University of Strathclyde

Department of Mechanical Engineering

CFD-based erosion modelling of simple and complex geometries

Malcolm Scott Wallace

PhD Thesis

2001

Abstract

Choke valves are important components in oil and gas production systems that are used to control the pressure and flowrate of fluids issuing from oil and gas reservoirs. The presence of sand in the production fluids can cause considerable damage to such components, and as sand is increasingly becoming an issue in oil and gas production, valve manufacturers need to find ways of reducing their product's susceptibility to solid particle erosion.

A CFD-based erosion modelling tool is achieved by first solving the fluid flow through the component of interest; tracking particles through the fluid and extracting impact data on all solid surfaces; and finally relating the particle impact data to erosive wear through a semi-empirical equation.

The present study has focussed on the development and validation of a CFD-based erosion modelling method for simple and complex geometries. Erosion testing has been carried out on a range of choke valve materials to provide the fundamental data required in constructing equations that relate erosion rate to particle impact velocity and angle. These equations have in turn been implemented in a commercial CFD code to provide the complete erosion modelling solution.

Validation of the method has been effected by comparing predicted results to experimental test data for both simple and complex geometries. Both single phase and abrasive flows have been considered in comparisons. For the simple geometries, reasonable agreement was obtained between predicted and measured pressure drop for the simplest cases, but predicted mass loss was considerably less than the measured amount. With the complex geometries (Multi-Orifice Sleeve choke valves), good agreement for pressure drop was obtained for some valve positions, but not so good for others. Significant differences were observed in mass loss predictions for the complex geometries, which raise questions as to the usefulness of CFD-based methods for predicting component lifetime.

Acknowledgements

I was an Associate of the Postgraduate Training Partnership (PTP) between the National Engineering Laboratory (NEL) and Strathclyde University during the course of this PhD. The PTP scheme was a joint initiative of the UK's Department of Trade and Industry (DTI) and the Engineering Sciences Research Council (EPSRC), and was supported by a grant from the DTI. I gratefully acknowledge grant support from both the EPSRC and NEL. Wood Group Pressure Control Ltd provided financial support for the work in this thesis, which is also gratefully acknowledged.

I would like to thank several people for their help and support throughout this project: my University supervisors, Dr William Dempster, and Dr Tom Scanlon; my NEL supervisor, Mr John Peters; my industrial sponsor, Mr Stephen McCulloch of Wood Group Pressure Control Ltd.; Dr Robert Woods, and Mr Dave Wheeler, of the University of Southampton; and Mr John Ogilvie of Wood Group Pressure Control Ltd. I must also thank my parents for all their understanding (especially when things got difficult) and support, and also my dear wife for her patience while this thesis was being completed. Above all I thank the God and Father of our Lord Jesus Christ for His daily preservation and care throughout the past four years. "For of him, and through him, and to him, are all things: to whom be glory for ever. Amen." Romans 11:36.

Malcolm Wallace

8th September 2001

Contents

Nomenclature

Symbol	Description	Units
a_P, a_{nb}	Centre coefficient and neighbouring coefficients for discretisation.	
b	Contribution of the constant part of the source term.	
C_η	Constant based on particle density and material elastic limit.	
C_λ	Constant characterising temperature dependence of flow stress.	
C_μ, $C_{1\varepsilon}$, $C_{2\varepsilon}$	Constants for k-ε turbulence model.	
C_A	Added mass coefficient.	
C_D	Drag coefficient.	
C_H	History coefficient.	
C_{ij}	Convective transport in Reynolds Stress Turbulence model.	
C_p	Specific heat capacity.	J/kgK
C_V	Valve flow coefficient.	litres /s $bar^{0.5}$
d_{ijk}	Diffusion in Reynolds Stress Turbulence model.	
D_n	Nozzle diameter.	mm
d_p	Particle diameter	m
d_t	Effective particle tip diameter.	m
e	Material restitution coefficient.	
E_e	Effective elastic modulus.	
E_{ij}	Mean fluid deformation rate tensor.	
E_{MM}	Erosion rate: mass loss of material per mass of particles	mg/g
E_p, E_b	Young's modulus for sphere and flat body.	
F(t)	Constant used by Sundararajan, 1991.	
F_{BH}	Basset History force.	N
F_D	Drag force.	N
F_G	Gravitational force.	N
F_{ij}	Body force generation in Reynolds Stress Turbulence model.	
F_L	Lift force.	N
F_{PG}	Pressure gradient force.	N
F_{VM}	Virtual mass force.	N
g	Gravitational acceleration vector.	m/s^2
H_i	Quasi-static indentation hardness.	
H_V	Hardness of material.	
I_p	Moment of inertia for spherical particles.	
k	Fluid turbulent kinetic energy	m^2/s^2
K_1	Parameter in Bitter's (1963b) erosion model.	
K_1, K_{12}, K_3	Empirical constants used by Grant and Tabakoff (1975).	
k_f	Ratio of vertical force to horizontal force.	
k_G	Radius of gyration of particle.	
K_m	Material dependent constant.	
k_P	Turbulent kinetic energy at point P.	m^2/s^2
K_V	Threshold velocity for deformation wear.	m/s
l_c	Contact depth	m
l_e	Characteristic length of eddy.	m
m_f	Mass of fluid displaced by particle.	kg
m_p	Particle mass	kg/s
M_P	Total mass of particles impacting material.	kg
n	Velocity exponent.	
n_s	Strain hardening exponent.	
P	Static pressure	Pa
P_{ij}	Shear generation in Reynolds Stress Turbulence model.	
p_s	Plastic flow stress.	N/m^2
Q	Volume flowrate	litres/s
Q_P	Energy used to produce deformation wear.	J
q_p, q_b	Poisson's ratios for sphere and flat body.	
R^ϕ	Scaled residual.	

r_p	Particle radius	m
S_{Mx}, S_{My}, S_{Mz}	Source terms in momentum equations.	
t	Time	s
t_c	Contact time.	s
t_e	Eddy lifetime.	s
T_L	Fluid Lagrangian integral time scale.	
t_r	Particle transit time in eddy.	s
u_τ	Friction velocity = $\sqrt{(\tau_w/\rho_w)}$.	m/s
u', v', w'	Fluctuating velocity components for fluid phase.	m/s
U, V, W	Mean components of fluid phase velocity vector **U**.	m/s
u, v, w	Instantaneous fluid velocities (of fluid velocity vector **u**).	m/s
U_P	Fluid velocity at point P.	m/s
u_p	Particle velocity.	m/s
u_r	Relative velocity between particle and fluid.	m/s
$V_\perp$	Particle velocity normal to surface.	m/s
$V_\parallel$	Particle velocity parallel to surface.	m/s
$\forall_d$	Volume of plastic zone beneath an impacting particle.	m^3
V_K	Characteristic velocity used by Hashish, 1987.	m/s
$\forall_M$	Volume loss of material (due to erosion)	m^3
V_N	Normal impact velocity.	m/s
$\forall_p$	Particle volume.	m^3
V_p	Particle impact velocity.	m/s
V_T	Tangential impact velocity.	m/s
W_{C1}, W_{C2}	Volume loss due to cutting wear.	m^3
W_D	Volume loss due to deformation wear.	m^3
x, y, z	Spatial coordinates	m
y^+	Dimensionless distance to the wall.	
y_E	Elastic load limit.	
y_E	Elastic load limit of a flat body.	
y_P	Distance from grid point P to the wall.	m
y_t	Depth of cut	m
α_0	Angle at which parallel particle velocity becomes zero.	deg
α_1	Characteristic particle impact angle used by Hashish, 1987.	deg
α_k	Plastically deformed material fraction.	
α_p, α	Particle impact angle.	deg
β_1	Parameter used by Hashish, 1987.	
δ_{ij}	Kronecker delta.	
δv_w	Volume of material removed (model of Hashish, 1987).	m^3
ε	Energy dissipation rate	m^2/s^3
ε_c	Critical strain for lip formation.	
ε_C	Cutting wear factor.	
ε_D	Deformation wear factor.	
ε_{ij}	Dissipation in Reynolds Stress Turbulence model.	
ϕ	General flow variable	
γ_c	Critical value of plastic strain.	
γ_1	Sphericity parameter.	
φ_{ij}	Pressure-strain in Reynolds Stress Turbulence model.	
κ	Karman constant.	
λ	Particle shape factor, Step length factor	
μ	Dynamic viscosity	kg/ms
μ_c	Maximum value of coefficient of friction.	
μ_{fr}	Coefficient of friction.	
μ_t	Turbulent viscosity	kg/ms
ν	Kinematic viscosity.	m^2/s
ρ	Fluid density	kg/m^3
ρ_m	Material density.	kg/m^3

ρ_w	Fluid density at the wall.	kg/m^3
σ_k, σ_ε	Prandtl numbers for k and ε.	
σ_m	Material flow stress.	N/m^2
σ_y	Yield stress.	N/m^2
τ	Dummy variable for time.	
τ_p	Particle relaxation time.	s
τ_w	Wall shear stress.	N/m^2
ΔP	Pressure drop.	bar
$\Delta\varepsilon_i$	Strain increment produced by particle impact.	
Ω_p	Particle angular velocity	rad/s
Ψ	Ratio of l_c to y_t.	

1.0 Introduction

1.1 Oil and Gas Production

Petroleum and its products have become essential ingredients for modern life. Many of the things which people enjoy and use would not be possible apart from the availability of oil and gas. It is not surprising that the petroleum production industry should be one of the largest in the world and that the price of oil should have significant influence on economic and political conditions within a country. As oil and gas becomes more difficult to extract in certain regions of the world, moves to drive down production costs will become increasingly important. Any measures that can be taken to increase production, or the lifetime of equipment, will be greatly welcomed by companies producing oil and gas. It is in this context of increasing equipment lifetime that the present study is set.

This study is concerned with one particular item of equipment used in the oil and gas production system: the choke valve. The choke valve is used to control the pressure and flowrate of fluids passing through the petroleum production system, and is the main controlling device between the subsurface reservoir and the processing units on the oil platform. As pressures within an oil and gas reservoir are typically much higher than can be sustained by the production system downstream, the choke valve must be able to dissipate high levels of fluid energy in order to achieve the required pressure drop across it. It is this suggestion of severe 'choking' that results in the choke valve being so called.

The way in which oil and gas wells are drilled, and production tubing installed, is a lengthy subject, and will not be discussed in detail here. However, in order to appreciate the function of the choke valve more fully, it is necessary to consider the various parts to an oil and gas production system. Figure 1.1 depicts schematically the key parts to a typical offshore installation. Production fluids enter the system at the base of the well. The actual well itself may extend for several metres into the oil and gas reservoir—depending on the orientation of the well (some are horizontal) and the height or width of the reservoir. On leaving the base of the well, fluid passes up through the production tubing to the surface. The production tubing is surrounded by what may be several layers of casing, until it reaches the final point at the surface where the casing structure will be at its widest (and strongest). What follows after reaching the surface will depend on the type of installation. In a typical case, the tubing (and some casing) will rise to the fixed platform at sea level, and terminate in the wellhead casing and christmas tree. The christmas tree is an important component which ultimately protects the downstream process stages (including production separators) from the reservoir pressure conditions. There are several gate valves within the christmas tree which

can act to shut in the well. Once fluid has passed through the christmas tree and choke valves, it is passed through the production separators and other process stages before transportation to shore.

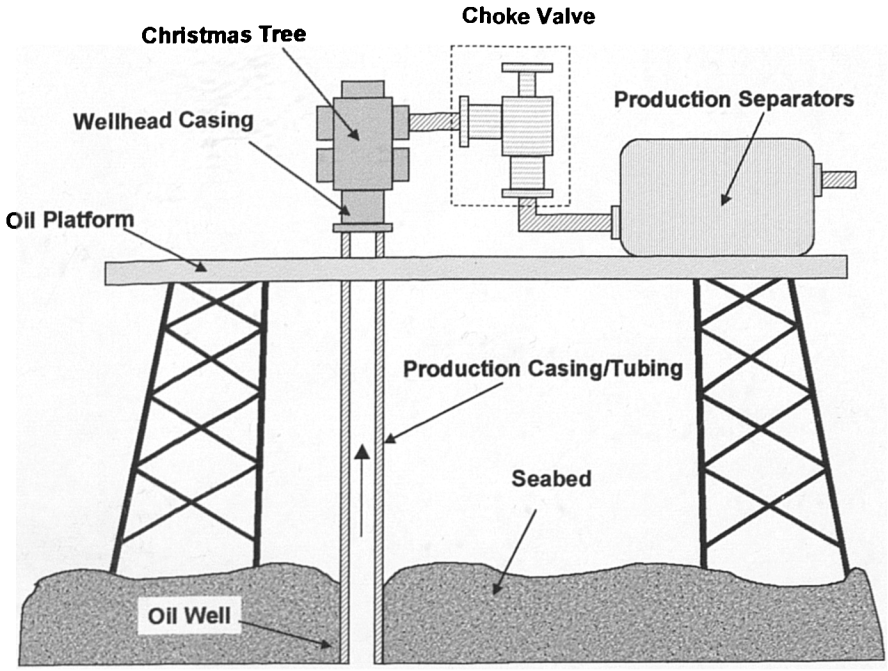

Figure 1.1 Schematic diagram of oil production system.

1.2 Choke Valve Design

There are several companies that manufacture choke valves for the oil and gas industry, each with their own design concepts and product ranges. The particular choke valve of interest in this project is one with a Multi-Orifice Sleeve (MOS) design, produced by Wood Group Pressure Control Ltd. A cross-sectional view of a typical MOS choke is shown in Figure 1.2(a). Figure 1.2(b) depicts the paths taken by fluid flowing through the valve for two stem positions. Vertical stem movement controls the total amount of tip hole area available for fluid to pass through.

Fluid must pass initially through the flow cage, which consists of rows of equally sized holes arranged round the circumference of a cylinder. After passing through the flow cage, fluid moves through the open area set by the position of the flow control tip. Self-impinging fluid jets form within the tip due to the arrangement of diametrically opposing holes. This self-impinging action is thought to be responsible for much of the energy loss through the valve.

The flow control tip and seat insert are generally made from erosion resistant materials such as tungsten carbides. Choice of materials for other components within the valve will depend on the conditions under which the valve is expected to operate: fluid composition will be significant in determining which materials to use.

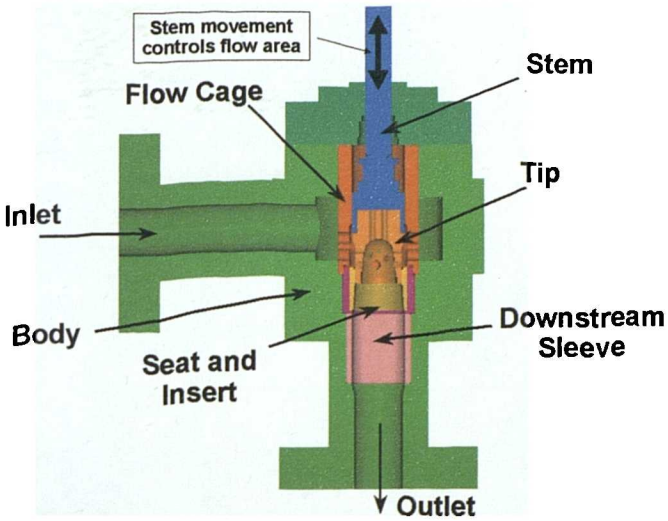

(a) Choke valve components.

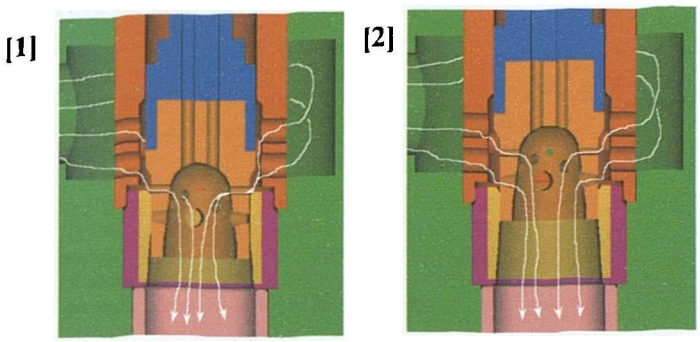

(b) Flow paths: [1] Partially open; [2] Fully open.

Figure 1.2 Cross-section of MOS Choke Valve and flow paths through the valve.

1.3 Sand Production

One of the problems facing operators is the possibility that a particular well will produce sand along with the oil and gas coming up from the reservoir. Whether a particular well will produce sand or not depends on the characteristics of the region surrounding the section of pipeline through which fluids are allowed to enter. This region (within the actual reservoir) is generally termed the 'formation', and the section of pipeline receiving fluids can be termed the 'perforation', as holes are generated (by explosives) through the tubing. This section of tubing is really the core part of the well. Figure 1.3 depicts this in more detail.

Under normal flowing conditions, sand grains tend to form arches at points where the fluid enters the perforated pipework (Figure 1.3). If the flowrate and pressure across the sand arch remain constant, the arch is likely to retain its shape, and little or no sand should enter the well. If there should be a change in production rate, or a well shut-in condition should be necessary, the arches are likely to be destroyed. It will then take some time for new arches to form under the new flowing conditions, during which time sand will be produced. Not all formations are suitable for the creation of arches.

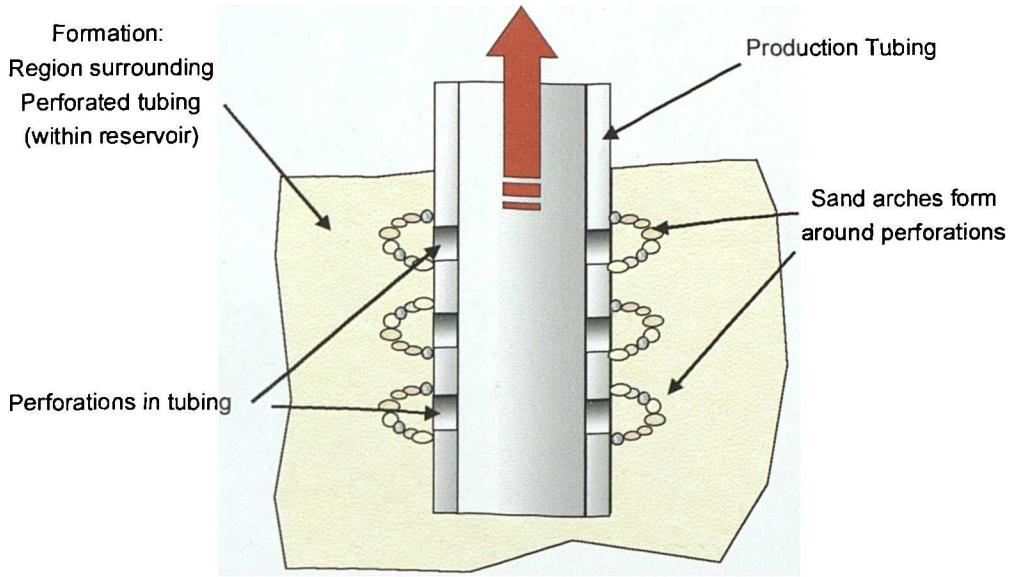

Figure 1.3 Illustration of sand arches around perforation holes.

Another factor that can initiate sand production is when water begins to enter the well along with the production fluids. Water will result in increased flow friction, which will have greater ability to carry sand grains with it. Reservoir pressure is generally low when water starts entering the well.

There are some ways in which sand production can be controlled. The most obvious way is to reduce production rates to a level where sand will not be swept into the well. This is not likely to be an economically viable solution to the problem. Another option is to simply let the well produce sand, and to dispose of it using facilities on the surface. However, removing sand from surface equipment, as well as cleaning and disposing of contaminated sand, will be expensive. Ultimately, the only way to tackle the problem may be to use some form of mechanical sand control device at the formation itself.

Gravel packs are one way in which sand influx can be reduced at the formation itself. These consist of clean, sized gravel held in place around the wellbore by means of a sized, wire wrapped screen. The advantages of gravel packs are that: they can give effective control of sand over long time periods; they do not deteriorate in the same way as some other

similar methods; and they can be used at any time in the life of a well. They can also result in high productivity from almost any type of formation. The disadvantages of gravel packs are that: the wellbore is restricted due to the presence of gravel; almost all well repairs require that the liner and gravel pack be removed before work commences; and screens have to be able to resist corrosion and erosion by the production fluids.

1.4 Erosion Problems and Solutions

Even when sand control methods are in place in a well, sand that does get through has the potential to cause significant damage to process piping and components. Every part of the system can potentially be affected, especially where fluids are moving at high velocity through small openings. Erosive wear is proportional to particle velocity, so that particles moving with a high velocity will cause far more damage than those with only a low velocity. As particle velocity depends on the underlying fluid velocity, one method of minimising erosion is simply to reduce the flowrate through the system as a whole. However, operators will be reluctant to reduce production flowrates as this will reduce revenue. There is also the problem of deciding the maximum flowrate allowable before erosion will become a problem. There have been several attempts made in the past to determine what these maximum flowrates (or threshold velocities) should be under various flowing conditions.

Although the production flowrate may be reduced to a level where erosion in pipelines is no longer a problem, the way in which these lower flowrates are achieved is by closing down the choke valves until sufficiently high pressure drops are achieved across them. Higher pressure drops mean that choke valves will see even greater potential to erode, as fluid acceleration within the valve will be high. Ultimately the potential for erosion of the choke valve is increased, and there are cases where choke valves have lasted for only a matter of days before internal components are almost completely destroyed. So while reducing the flowrate might prolong the life of process pipeline, the choke valve used to control the reduced flow is even more susceptible to erosion damage. Figure 1.4 shows the type of erosion often seen on the flow control tips of MOS choke valves. These are mild examples. There is therefore a need to design choke valves that are less susceptible to erosion.

The need for longer valve life means that choke valve manufacturers must improve valve design in order to counteract the potential for erosion. One of the strategies that can be employed is to use erosion-resistant materials for internal components. A considerable amount of effort has gone into developing new materials and coatings that promise to give significantly extended life under erosion conditions. Another strategy is to design valves in such a way as to reduce particle impact velocities, and also to attempt to control the angles

with which particles impact solid surfaces. The problem is how to determine the behaviour of particles within a choke valve and the subsequent erosion.

Figure 1.4 Typical erosion scars on a flow control tip.

1.5 CFD-Based Erosion Modelling

The advent of general-purpose commercial CFD (Computational Fluid Dynamics) codes has made it possible to predict fluid flow and particle motion through complex geometries. An extension of this capability is to extract the velocities and angles with which particles impact solid surfaces, and to somehow relate that information to erosive wear. Figure 1.5 illustrates this concept of CFD-based erosion modelling. The concept can be considered to have three stages:-

1. Predictions are made of the fluid flow field through the component of interest. The component geometry is used to create the computational mesh on which the governing equations of fluid flow will be solved. Appropriate boundary conditions are required before the flow solution can be obtained. As most flows will be turbulent in nature, it is likely that a turbulence model will be required in the fluid phase modelling.
2. Once the fluid phase behaviour has been adequately predicted, it is possible to track the movement of particles entrained within the fluid phase. Several thousand particle trajectories may be required in this step in order to obtain a good statistical representation of impact sites. Particle trajectories are calculated by solving the particle equation of motion for small time steps throughout the flow. When a particle strikes a solid surface it will lose some of its kinetic energy due to the collision, and will therefore rebound with a lower velocity (and possibly different angle) than at impact. Restitution coefficients are used to determine rebound velocity and angle.

3. The impact data generated by the particle trajectory calculations can be used to estimate the level of erosive wear taking place. Equations are developed which relate particle impact properties (e.g. impact velocity and angle) to the amount of material lost. These equations are generally semi-empirical, and will be specific to a certain material type. Successive impacts at each cell point on the surface are summed to give final erosion predictions when all particle trajectories have been calculated. The complete set of information is used to build up a map of erosive wear throughout the component.

This three-stage procedure has the potential to assist valve manufacturers in developing valves that are more resistant to solid particle erosion. Surfaces could be angled in ways that ensure particle impact angles cause the minimum amount of erosion damage. Surfaces receiving the greatest proportion of particle impacts could be reinforced at specific points.

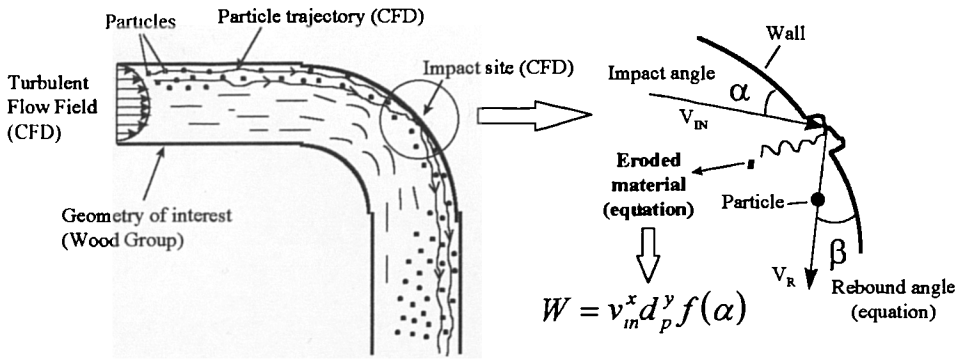

Figure 1.5 Erosion modelling concept.

In order to develop such a method, it is first essential to have a Computational Fluid Dynamics code that is able to accurately represent the geometry of interest. As choke valve geometries are often complex, a code with unstructured meshing capability is desirable. A method for calculating particle trajectories will also be required, and as this is often a feature of commercial CFD codes, it will probably not be necessary to develop this function oneself. The final requirement for the method is an equation that will relate particle impact data to erosive wear. This is the least well-defined part of the problem, and relies heavily on specific empirical data obtained by erosion testing of particular materials under chosen conditions. The uncertainty in predictions of erosion could be most affected by this final stage.

1.6 Aims and Objectives

The overall aim of this project is to develop, apply, and validate, a method for predicting the location and magnitude of solid particle erosion within Multi-Orifice Sleeve choke valves. The specific objectives to be achieved within this aim are to:-

1. Validate the use of a commercial CFD code for predicting the fluid flow field within simple and complex pressure-reducing geometries.
2. Obtain experimental erosion data for materials appropriate to choke valve construction, and to use this data in creating equations that will relate erosive wear to particle impact data.
3. Collate results of experimental testing that can be used to validate the overall method as a tool for predicting erosive wear within simple and complex geometries.
4. Assess the extent to which the method can predict solid particle erosion by comparing CFD predictions to the experimental data obtained in objective 3.
5. Draw conclusions as to the way in which component manufacturers might apply such methods, and how much weight can be placed on the resulting predictions.

1.7 Presentation of Material

The remainder of this thesis presents the work carried out in achieving the aims and objectives set out above. Chapter 2 begins with a review of previous CFD-based erosion modelling studies in order to identify the areas requiring further attention. The various aspects of modelling required in obtaining predictions of fluid flow and particle trajectories are outlined briefly, before going on to consider the subject of solid particle erosion. The main aims in considering solid particle erosion are to give some idea of the factors that influence erosive wear, the experimental methods often used to investigate these factors, and to gain some insight into the types of semi-empirical analytical equations that have been used to predict erosive wear in the past.

Stages 1 and 2 of the CFD-based erosion modelling procedure are essentially provided by the commercial CFD package used in the study. Development of the erosion equations, however, has required the experimental testing of several choke valve materials. The experimental testing, carried out using test facilities at the University of Southampton, is presented in Chapter 3 of this thesis. Most of the resulting test data is presented in various ways within the chapter. Chapter 4 of the thesis covers the generation of empirical erosion equations from the underlying test data. A software package known as TableCurve (2D and 3D) was utilised in generating appropriate equations. The overall CFD-based erosion modelling procedure is essentially defined by the end of Chapter 4.

Chapter 5 presents the results of some CFD modelling of a free liquid impinging jet. This was modelled in order to gain a deeper insight into the way particles are affected by the liquid carrier phase in a slurry jet erosion test facility. This has some significant implications for the way in which the results of such slurry testing are interpreted.

Having developed the required modelling tool, the subsequent task is to examine its effectiveness in predicting erosive wear. Ideally, each of the three stages should be validated in turn for both simple and complex geometries. A simple component was available for testing in the current study: Chapter 6 describes the experimental testing of various designs of this component for both single phase and abrasive flows. Chapters 7 and 8 go on to present the application of the CFD-based erosion modelling tool to these designs. Predictions of single phase flow are considered in some detail in Chapter 7, before going on to consider the actual prediction of erosive wear in Chapter 8. Comparisons are made with the testing for both single phase and abrasive flow.

As the ultimate aim in this study is the erosion modelling of complex choke valves, a considerable amount of effort has been devoted to doing so. Chapters 9 and 10 describe this effort. Test data for a choke valve at various open positions has been used to assess CFD predictions of pressure drop across the valve. The resulting comparisons give some indication as to the ability of CFD methods to predict hydrodynamic performance of valves. Another choke valve has also been considered, which was tested under abrasive flow conditions as part of a project carried out by a major oil company. The results of this testing have been made available, and have been used in assessing the ability of the erosion modelling tool to predict mass loss of valve components under erosive conditions.

Chapter 11 contains an overall discussion and summary of the work, and presents the conclusions arising from it. Several appendices containing relevant information follow.

1.8 Industrial involvement in project

This project was carried out under the Postgraduate Training Partnership between the University of Strathclyde and the National Engineering Laboratory. A third party to the project was Wood Group Pressure Control Ltd., who provided financial support for the project, along with relevant information and the components used in testing. There was therefore significant input from Wood Group Pressure Control Ltd. (WGPC) concerning the aims and objectives for this project—to ensure that their involvement was beneficial to the company. Most of the work was carried out at the National Engineering Laboratory, apart from two periods of time that were spent at the University of Southampton.

2.0 Review of CFD-Based Erosion Modelling

There have been many studies in which the concept outlined in section 1.5 has been applied to some extent. The range of applications is broad, from aerodynamic flows past turbine blades to flows inside pumps, pipes, bends, and other fittings. Experimental test facilities have also been analysed using the CFD-based technique. In reviewing the available literature, one of the main objectives has been to determine the extent to which the overall method has been validated for use as an engineering design tool. This validation includes examining the ability of the method to predict both the location, and the magnitude, of erosive wear caused by solid particles. After completing this initial part of the review, further attention will be given to the key parts that make up a CFD-based erosion modelling method.

2.1 Applications of CFD-Based Erosion Modelling

This part of the review is intended to give a broad outline of work carried out in the past. Rather than attempting to discuss everything by chronological order, the review will be split into sub-sections based on typical applications. Some applications are not particularly relevant to the present study (i.e. compressible gas flows) and so will not be covered in depth.

2.1.1 Turbomachinery flows

One of the first studies which could be said to have applied the three stage method outlined previously is by Grant and Tabakoff (1975), for gas-solid flows within rotating turbomachinery. Particle trajectories were calculated in a predetermined flowfield (not discussed in depth by the authors) using an inertial reference frame, and were based on the drag force acting on the particle. Correlations that determined the angle with which particles would rebound after impact were developed from experimental data. Erosion equations also came from experimental testing. Development of the rebound equations was based on the premise that the impact process could only be described by statistical means: this was reflected in the form of the equations. A Monte Carlo simulation model was incorporated to reproduce the random nature of the erosion process. Validation of the method was achieved by comparing predicted erosion with experimentally observed erosion for a specific test case. Predicted location of wear on the test blades was in good agreement with experimental data, as were predictions of actual mass loss for the stator and rotor blades. Predictions of mass loss for the inlet guide vanes were poor in the initial models—this was shown to be a result of the rotor blade geometry changing due to erosion. Thus the effect that geometry changes could have on erosion rate was noted early on.

The good agreement between experimental and predicted results can perhaps be attributed to the wealth of experimental data available to the authors from which to develop rebound and erosion correlations. However, it is also possible that good fortune played a part in the successful outcome of the modelling, as El-Sayed et al. (1985) state that the accurate prediction of erosion depends upon having a complete, three-dimensional, viscous, compressible solution for the gas flow in the blade passages. At the time of writing their paper, this was still a future prospect. El-Sayed et al. (1985) did not use a numerical procedure to obtain their three-dimensional flowfield through a stationary, low speed cascade. Instead they used laser Doppler anemometry to provide the basic particle-free flow. As in the previous study, they used correlations for particle rebound and erosion to supplement the trajectory predictions (which accounted only for the drag force). Their work clearly showed the need to consider secondary flows (and hence the need for full three-dimensional codes) in order to predict erosion properly. This suggests that simulations could be fairly sensitive to predictions of particle rebound. Hamed and Fowler (1983) modelled turbomachinery blade erosion by particle laden flows, but did not make any comparison with actual experimental data.

A more recent example of flow through turbomachinery components is the study of Drtina and Krause (1994) on abrasion of a Francis turbine guide vane. This differs from the previous two studies in that the fluid is an incompressible liquid. Agreement between simulation and actual field tests was poor in some areas of the geometry. This was attributed to limited information concerning the inflow conditions for both the fluid and particulate phases, indicating the dependency of simulations on inlet boundary conditions.

2.1.2 Flows in pump casings

The features of flows encountered in pump casings will be similar to those considered when modelling static turbine components. A number of studies have been carried out into erosion of pump casings. One of the earliest studies using an 'erosion modelling' approach was that of Roco and Addie (1983), who used a finite element method to solve the equation of motion for the slurry velocity (assuming inviscid flow). The concentration of solid particles was determined by solving the differential conservation equation of a solid contaminant. The convective velocity of solid particles was found by considering the dynamic equilibrium between various forces acting on the solids. The method did not directly yield particle trajectories. Erosion rate was determined by assuming that interaction work due to solid particle impingement is proportional to erosive wear. Experimental tests were carried out on samples of material held in a slurry flow to provide the constants of proportionality. It is difficult to tell how successful the method was, as no

quantitative or even detailed qualitative comparisons were made with experimental results. Tuzson (1984) also analysed pump erosion without actually calculating trajectories, but applied a scouring type of wear model thought to be more appropriate to sliding beds of particles around the casing wall. Order of magnitude agreement in erosion rate was obtained, along with good prediction of wear distribution.

Ahmad et al. (1986) went a stage further and calculated actual particle trajectories within a slurry pump impeller using a finite difference method for the inviscid liquid flow. The particle impact data was related to erosive wear using a simplified version of the empirical equations developed by Neilson and Gilchrist (1968). Relative erosion rates were predicted using the method, and compared to relative data obtained by experiment (involving several layers of paint to highlight eroded areas). There was said to be good agreement between prediction and experiment as far as point of maximum erosion is concerned, but the level of erosion was underestimated by the predictions. Several factors could have caused this, such as the neglect of circumferential velocity gradients in their analysis, the difficulty in finding the point of maximum wear experimentally, and the rough casting of the impeller. The method was used to examine the differences between two different types of pump in a later study (Ahmad and Goulas, 1986).

Minemura and Zhong (1995) combined a finite element method with a Lagrangian particle tracking method (using the particle equation of motion) to calculate particle trajectories within a pump casing. As in the previous studies, inviscid water flow was assumed (enabling use of the Laplace equation for the flow field), but a more complex formulation for trajectory calculations was applied, which could account for both particle spinning and collisions. A wear model based on the work of Bitter (1963a, b) was implemented, and the resulting predictions compared with previous experimental work of Roco et al. (1984). Fairly good agreement was obtained both in terms of wear magnitude and distribution. The effect of spinning and collisions was found to be negligible. The method was extended to account for changes in casing geometry by updating the finite element mesh after a pre-set level of wear at a boundary element (Zhong and Minemura, 1996). Figure 2.1 illustrates these changes in

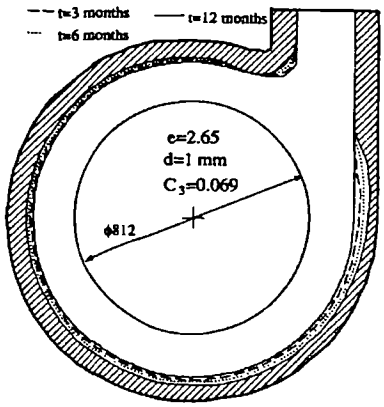

Figure 2.1 Deformation of casing due to wear (Zhong and Minemura, 1996).

geometry. No further statements were made regarding the ability of the method to predict erosion.

It is apparent that the erosion modelling technique has provided useful information in the field of pump design, with some studies finding fair agreement between predicted and actual wear.

2.1.3 Erosion of tube banks

Coal-fired boilers that utilise fluidised bed combustors frequently have problems due to particle erosion of tubes in the reheaters and economisers associated with the boiler. Several studies have been performed using fluid flow and particle modelling in attempts to understand the factors that affect erosion of the tube banks. Schuh et al. (1989) were possibly one of the first to consider flows past one or more tubes in a tube bank. They used a numerically generated, body-fitted, nonorthogonal, curvilinear coordinate grid to represent the flow domain around the tubes. A finite difference method was used to solve the flow equations in conjunction with the k-ε turbulence model, and a Lagrangian particle tracking procedure was used to calculate particle trajectories. The particle modelling implementation also included a stochastic turbulence dispersion model to simulate the effect of turbulence on the particle motion. A normalised form of Finnie's (1960) cutting wear model was used to predict relative erosion. Unfortunately no comparisons were made with experimental or field data in the study, which makes it difficult to assess the effectiveness of the method. However, it was possibly one of the first studies to apply a procedure similar to those in use today.

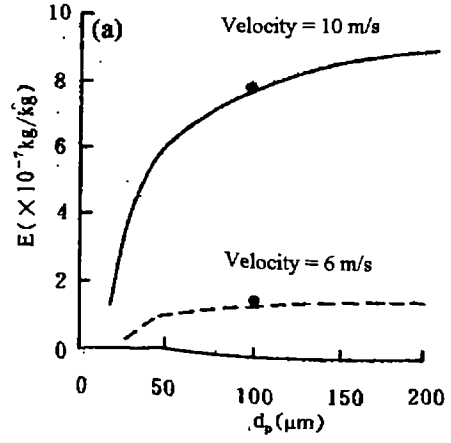

Figure 2.2 Erosion of first row tubes (Fan et al., 1994).

Jun and Tabakoff (1992) state that the flow solution obtained by Schuh et al. (1989) does not agree with experimental observations reported by another author. Jun and Tabakoff (1992) proceed to model the laminar flow across two tubes in line using a body-fitted grid, and track particles through the gas field by considering only the drag force acting on the particles. A finite volume method was used to solve the governing equations in primitive variable form, along with the k-ε turbulence model. A stochastic turbulence dispersion model was applied as part of the Lagrangian

particle tracking procedure. Particle rebound and erosion were predicted by empirical correlations. Although the gas flow past the tube banks was validated by comparison with previous research, no comparison is made for predictions of erosive wear. Fan et al. (1994) did have two experimental erosion values to compare their predictions of first row tube erosion against. The experimental data points agreed well with the prediction, but were insufficient to validate the method fully. Figure 2.2 shows the predicted erosion of first row tubes as a function of particle diameter, for two different free stream velocity levels. The experimental data points are included on this graph. Fan et al. (1999) used the method to investigate the effectiveness of adding fins to the tubes in order to reduce erosion. The presence of fins changes the gas flow field (and hence particle trajectories), so that particles impact the fins rather than the tubes themselves.

2.1.4 Erosion of pipe bends and related geometries

A fair amount of work has been carried out into the erosion modelling of pipe bends and related geometries. Blanchard et al. (1984) developed a two-dimensional theoretical model to predict particle trajectories round a 90^0 bend. However, the predictions of maximum wear location did not agree sufficiently well with experiment to warrant publication. This was attributed to the inability of the model to account for secondary flows. Rubini et al. (1985) were able to account for secondary flows in their computation of gas-particle flow round pipe bends with their fully-elliptic, three-dimensional, finite difference method for laminar and turbulent flows. No stochastic turbulent dispersion model was included in their Lagrangian particle tracking routine. Their predictions of wear location were compared against the experimental data of Mason and Smith (1972). Primary wear location was predicted to occur about 10^0 further downstream than the experimental data suggested, although the point was made that the actual pipe geometry eroded considerably before measurements were taken in the experiments. A secondary wear location was also predicted. No quantitative comparisons of erosion magnitude were made.

Actual quantitative comparisons of predicted penetration rate with experimental penetration rates were made by Wang et al. (1996) in their two-dimensional modelling of liquid- and gas-particle flows round 90^0 elbows. Their method did not consider the turbulent dispersion of particles, and utilised a two-layer mixing-length model to predict the turbulence of the fluid phase. Extensive comparisons of predicted penetration rates were made with the data of Bourgoyne (1989). Of these comparisons, 18 were for air-particle flow, and 3 were for mud-particle flow. With the air-particle flow, the average difference between measured and predicted penetration rate was 37.5 %, with the maximum difference being 56.1 %, and the minimum being 1.97 %. Differences were both above and below the

measured values, which suggests some element of inherent scatter in the method. For the liquid-particle flows, differences were 54.2 %, 171.1 %, and –42.7 %, which does indicate poorer performance for liquid flows. The authors acknowledge this, and cite the fact that secondary flows were not accounted for as being the possible reason for poorer predictions. Locations of maximum penetration rates were predicted fairly well, using the erosion model of Ahlert (1994). Another comparison was made between prediction and experiment for a gas-particle flow round a bend. Particle concentration was far higher for this model than for the previous models. The experimental data of Eyler (1987) was compared against predictions. Penetration rates normalised on the maximum value were compared in this instance, as the method could not well predict actual erosion due to the high concentration. Figure 2.3 shows the comparison between prediction and the experimental data of Eyler (1987). Agreement is very good.

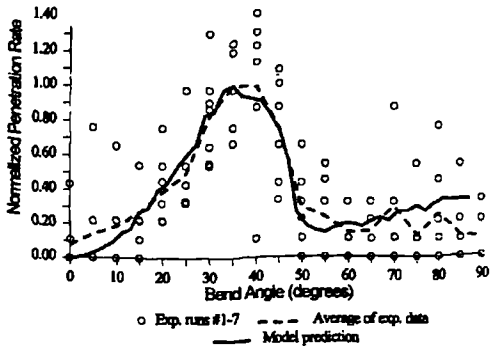

Figure 2.3 Predicted erosion profile of Wang et al. (1996) for an elbow.

More recent studies have also focused on erosion of pipe bends. Edwards et al. (2000) supplemented a commercial CFD code (CFX) with appropriate procedures to predict erosion on particle impact. The erosion model of Ahlert (1994) and its extension by McLaury (1996) (for aluminium) were used to predict erosive wear. Laser Doppler measurements of the flow structure round a bend (Enayet, 1982) were used to validate the CFD predictions of flow field. Reasonable agreement was obtained. Erosion predictions were validated by comparing predictions for a gas-particle flow against the same experimental data (Eyler, 1987) used in the comparison shown in Figure 2.3. Agreement for the predicted wear distribution is good, although actual erosion magnitude was not compared. Figure 2.4 shows comparison of these latest predictions with the original normalised experimental data (based on the findings of Eyler, 1987).

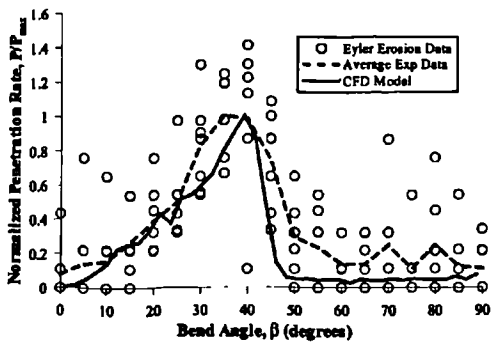

Figure 2.4 Comparison of bend erosion predictions with normalised test data. (Edwards et al. (2000)).

Keating and Nesic (2000) considered full 180^0 bends using the commercial CFD code PHOENICS in conjunction with a separate Lagrangian particle tracking code. Although the fluid velocity field was validated by comparison with experimental data, no comparisons were offered for the predictions of erosive wear (made with a modified form of Finnie's (1958) model). This makes it difficult to assess the effectiveness of the model. Hanson and Patel (2000) also used PHOENICS in predicting the life of pneumatic conveyor bends undergoing erosive wear. Their work was somewhat different in that they attempted to account for the shape of the wear scar as erosion continued. However, the shape of the scar was not used to alter the computational mesh for fluid phase calculations (Hanson, 2000).

Hengshuan and Zhong (1990) considered the erosion of rectangular section bends using a two-dimensional inviscid approach both with and without secondary flow. Finnie's model (Finnie, 1960, 1972) was used to predict the erosion rate. Comparison between predicted and actual distributions of erosion is favourable, with an improvement in prediction when secondary flow is accounted for.

It can be seen that the erosion of pipe bends can be fairly well predicted both in terms of wear distribution and in magnitude. This is perhaps to be expected, as although secondary flows do arise in pipe bends, the geometry is still quite simple, with the only solid surface being the outer boundary wall. The choice of erosion model has been that of Finnie (1958, 1960) in several cases, which suggests that even an early model such as this can give reasonable predictions of relative erosive wear.

2.1.5 Straight pipes and constrictions

A few studies are available where the object of the exercise has been to model erosion resulting from random perpendicular impacts of particles passing through a straight-walled pipe or constricted section. McLaury et al. (1996) modelled the erosion taking place within a straight choke geometry as shown in Figure 2.5. Their method was based around a two-dimensional axisymmetric CFD code, and accounted for turbulent dispersion of particles (with a stochastic model) as well as the 'squeeze film' effect (Clark and Burmeister, 1992) on particles impacting solid surfaces. An empirical equation based on experimental data was used to complete the prediction method (Ahlert, 1994). Direct comparison was made between experimentally obtained results and the erosion profiles predicted by the CFD technique. It was found that excellent quantitative agreement could be obtained only after the rapid erosion of the sharp edge at the entrance to the straight choke had been accounted for in the computational mesh. This edge had a significant effect on the turbulent kinetic energy levels at the entrance to the straight choke, and hence on the resulting erosion due to normal particle impacts against the walls. Figure 2.5 presents the two sets of predicted results. This

study underlines the need to properly account for the effect of eroded geometry on subsequent fluid mechanics behaviour (and hence particle transport). The same set of experimental data was used to validate the work of Edwards et al. (1998). There, however, no mention is made of accounting for the change in geometry profile, and agreement between the predictions and experiment are not quite so good.

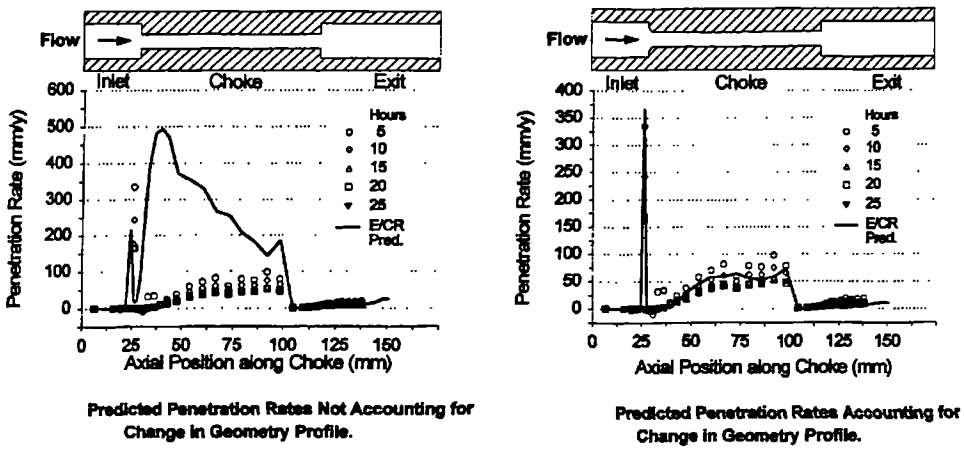

Figure 2.5 Comparison of penetration rates before and after accounting for change in geometry profile (McLaury et al.,1996).

2.1.6 Erosion of choke valves

A handful of studies have been published on the CFD-based erosion modelling of choke valves. Nokleberg and Sontvedt (1995) first mention the application of CFD techniques to analyse erosion problems with needle and seat choke valves, but do not present any real results until a later paper. In the later paper, Nokleberg and Sontvedt (1998) present erosion predictions for two types of choke valve: Needle and Seat, and External sleeve. The External sleeve choke valve is similar in concept to the MOS (Multi Orifice Sleeve) choke valve presented in chapter 1, as it embodies the principle of multiple self-impinging jets.

Their method is based on the structured mesh version of the Fluent commercial CFD package, and so has difficulty in accurately reproducing the valve internal geometries. Nevertheless, the predictions do follow experimentally observed trends fairly well, both in terms of mass loss and wear distribution. Actual erosion tests for the two types of valve give peak erosion rates around 2-3 times larger than calculated. Predictions are better for the Needle and Seat choke (where the internal geometry is fairly smooth and simple) than for the External sleeve choke valve. Figure 2.6 shows the comparison of predicted erosion profiles to experimentally obtained profiles for both types of choke valve. It is apparent that the method fails to predict the full extent of the erosion taking place along the cage length in the

External sleeve choke valve. This will be in part due to geometry changes during the erosion process, which the CFD method does not account for.

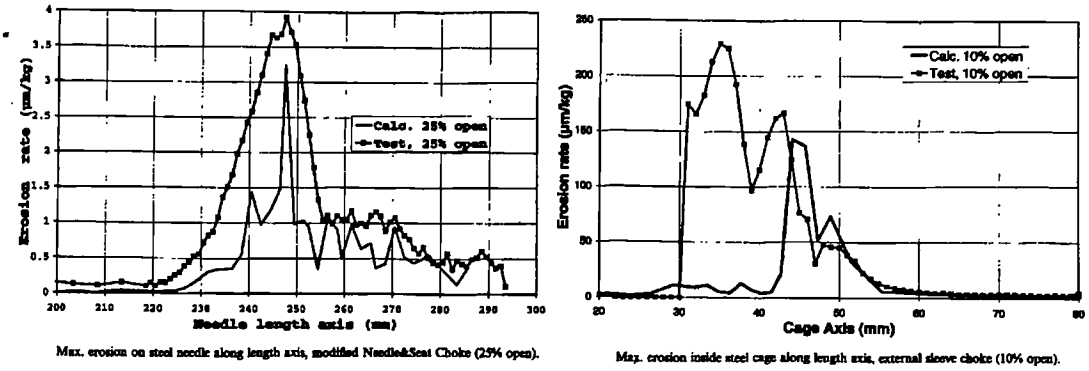

Figure 2.6 Comparison of predicted erosion profiles with measured. Nokleberg and Sontevdt (1998).

Forder et al. (1998) also considered Needle and Seat choke valves in their application of CFD-based erosion modelling techniques. Although detailed description has been made of their technique, no actual quantitative comparisons have been made between experimental and predicted erosion of choke valves. Again, a structured approach to mesh generation has been followed (using the commercial code CFX) which limits the ability of the method to represent complicated geometries accurately. The only comparison presented by Forder et al. (1998) has been for a flat plate undergoing erosion by a fully submerged jet. Good agreement is obtained. A hybrid empirical erosion model was used to represent both ductile and brittle erosion mechanisms.

No further erosion modelling studies involving choke valves have been found in the available literature. As far as is known at the time of writing, there are no other published studies where complex choke valve geometries have been modelled using an unstructured hybrid meshing strategy. The advantage of this strategy is that the complex geometries can be better represented. Also, there has only been a limited study of the ability of CFD codes to predict the hydrodynamic performance of choke valves (and indeed of valves in general). There is a definite need to consider both these aspects in more detail, so that valve manufacturers can evaluate the benefits CFD modelling has to offer in the design process.

The work by Nokleberg and Sontevdt (1998) has gone some way to demonstrate the potential usefulness of CFD-based erosion modelling in valve design. Their work is limited in that only a structured approach to mesh generation has been followed, and only limited information has been provided concerning the hydrodynamic predictions of the code. Although their predicted erosion profiles for the Needle and Seat choke compare well with

experiment, the predictions for an External sleeve choke have significant differences. This could be a result of the structured meshing strategy available to them.

The work undertaken in this thesis attempts to overcome the limitations of a structured mesh by using a flexible hybrid approach that permits the specification of tetrahedral, hexahedral and prismatic cells within the same computational domain. This enables accurate representation of the choke valve internal geometry. Test data has been made available to test the ability of CFD software to predict the hydrodynamic performance of the valve, and hence give some confidence in the CFD predictions of fluid flow field. It is only by predicting the correct flow field that particle impact sites can be expected to fall out correctly.

2.1.7 Summary

Various studies have been performed in the past using some form of 'CFD-based erosion modelling' technique. Not all have solved the primitive variable form of the Navier Stokes equations (indeed, one study used an experimentally obtained flow field), but in general they have followed the three-step process outlined in section 1.5. A small number of studies have reported good agreement between experimental and predicted results for certain applications. Erosion studies involving gas-particle flows in high speed turbomachinery applications have been successful—generally because the physical flow problem is more straightforward than in some internal flows, and good underlying empirical formulae have been available to use in the modelling technique. Such formulae have been developed using test rigs similar in nature to the actual components under consideration (hence ensuring that the fluid mechanics present in the erosion test rig are similar to what is present in the industrial flow).

The work of McLaury et al. (1996) for straight chokes gave excellent quantitative agreement between prediction and experiment. Nokleberg and Sontevdt (1998) also had good agreement for the simpler of the two choke designs they considered. Some authors avoid making direct quantitative comparisons altogether, which makes it difficult to provide an overall assessment of the technique used.

It can be concluded that CFD-based erosion modelling techniques have been shown to perform well when applied to simple geometries with relatively simple flows passing through them. When geometries become more complicated, or the flow physics become harder to predict, the success of erosion modelling techniques is likely to fall. Erosion of a Multi Orifice Sleeve type choke valve is a challenging application for these techniques, and little conclusive data has been published so far.

One of the difficulties in modelling complex valves is in representing the geometry sufficiently well. Unstructured hybrid mesh generation methods will be required to capture all of the important features inside such geometry. There are no published studies in which such meshing techniques are applied to complex valves.

Having given an overview of previous CFD-based erosion modelling studies, it is now proposed to look at each of the three key aspects in turn, and to discuss the relevant issues for each aspect.

2.2 Fluid Phase Modelling

The first step in an erosion modelling study is to obtain the fluid flow field through the geometry of interest. This will often be carried out using a general-purpose CFD code such as Fluent, Star-CD, and CFX (three of the main commercial packages worldwide). These packages have become increasingly popular during the last decade, and are slowly moving into the realm of Computer Aided Engineering design tools. Although most of the available commercial packages will offer a similar range of physical modelling options, not all have the option of hybrid mesh types, or even unstructured meshes.

2.2.1 Reynolds Averaged Navier Stokes Equations

Most commercial CFD packages solve the primitive variable form of the Navier Stokes equations. As most flows of industrial interest are turbulent in nature, it is not possible to solve the exact time-dependent form of the Navier Stokes equations for every flow: the computing power required would be colossal. (Some simple flows can be modelled using the basic equations directly: this is known as Direct Numerical Simulation (DNS)). For this reason, the basic Navier Stokes equations are generally recast into a time-averaged form by assuming that the instantaneous velocity appearing in the original equations can be represented by a mean component and a fluctuating component (i.e. $u = U + u'$). The resulting equations are known as the Reynolds Averaged Navier Stokes (RANS) equations.

Although the time averaging process eliminates the need for massive computing resource, the averaging process creates additional unknown terms called the 'Reynolds Stresses'. It is the aim of turbulence closure models to represent these terms in ways that embody the true underlying physics of the turbulent flow.

The Reynolds Averaged Navier Stokes (RANS) equations are given in their conservative form (for both compressible and incompressible flows) as (Versteeg and Malalasekera, 1995):-

Mass: $$\frac{\partial \rho}{\partial t} + div(\rho \mathbf{U}) = 0 \qquad (2.1)$$

x-momentum:-

$$\frac{\partial(\rho U)}{\partial t}+div(\rho U\mathbf{U})=-\frac{\partial P}{\partial x}+div(\mu\, grad\, U)+\left[-\frac{\partial(\rho\overline{u'^2})}{\partial x}-\frac{\partial(\rho\overline{u'v'})}{\partial y}-\frac{\partial(\rho\overline{u'w'})}{\partial z}\right]+S_{Mx} \tag{2.2a}$$

y-momentum:-

$$\frac{\partial(\rho V)}{\partial t}+div(\rho V\mathbf{U})=-\frac{\partial P}{\partial y}+div(\mu\, grad\, V)+\left[-\frac{\partial(\rho\overline{u'v'})}{\partial x}-\frac{\partial(\rho\overline{v'^2})}{\partial y}-\frac{\partial(\rho\overline{v'w'})}{\partial z}\right]+S_{My} \tag{2.2b}$$

z-momentum:-

$$\frac{\partial(\rho W)}{\partial t}+div(\rho W\mathbf{U})=-\frac{\partial P}{\partial z}+div(\mu\, grad\, \mathrm{W})+\left[-\frac{\partial(\rho\overline{u'w'})}{\partial x}-\frac{\partial(\rho\overline{v'w'})}{\partial y}-\frac{\partial(\rho\overline{w'^2})}{\partial z}\right]+S_{Mz} \tag{2.2c}$$

where **U** is the mean velocity vector (with components U, V, and W), and u', v', and w', are the fluctuating velocities associated with these mean components. All other symbols used in the above equations have been defined in the nomenclature.

In theory these equations can be used for any flow where instantaneous velocity predictions are not required. They should therefore be entirely applicable to flow through choke valves. However, the success of flow predictions lies heavily on the method used to predict the Reynolds Stress terms appearing in the momentum equations—turbulence closure models.

2.2.2 Turbulence closure models

Many of the CFD-based erosion modelling studies have used the standard two-equation k-ε model of Launder and Spalding (1974). The practice of solving two transport equations means that turbulent velocity and length scales can be independently determined. One transport equation is solved for k, the turbulent kinetic energy, and another solved for ε, the energy dissipation rate. The transport equation for turbulent kinetic energy (after Versteeg and Malalasekera, 1995) is given as:-

$$\frac{\partial(\rho k)}{\partial t}+div(\rho k\mathbf{U})=div\left[\frac{\mu_t}{\sigma_k}grad\, k\right]+2\mu_t E_{ij}.E_{ij}-\rho\varepsilon \tag{2.3}$$

where E_{ij} is the mean deformation rate tensor (matrix). The transport equation for the turbulence dissipation rate is:-

$$\frac{\partial(\rho\varepsilon)}{\partial t}+div(\rho\varepsilon\mathbf{U})=div\left[\frac{\mu_t}{\sigma_\varepsilon}grad\, \varepsilon\right]+C_{1\varepsilon}\frac{\varepsilon}{k}2\mu_t E_{ij}.E_{ij}-C_{2\varepsilon}\frac{\varepsilon^2}{k} \tag{2.4}$$

where $C_{1\varepsilon}$ and $C_{2\varepsilon}$ are dimensionless constants.

The turbulent viscosity is finally given by:-

$$\mu_t = \rho C_\mu \frac{k^2}{\varepsilon} \tag{2.5}$$

These equations are based on the Boussinesq hypothesis, which is that the Reynolds stresses can be related to the mean velocity gradients by

$$-\rho\overline{u_i'u_j'} = \mu_t\left(\frac{\partial u_i}{\partial x_j}+\frac{\partial u_j}{\partial x_i}\right)-\frac{2}{3}\left(\rho k+\mu_t\frac{\partial u_i}{\partial x_i}\right)\delta_{ij} \tag{2.6}$$

While using this hypothesis simplifies the task of turbulence closure, it does mean that the turbulent viscosity is assumed to be an isotropic scalar quantity, which is not always true. In cases where turbulence should definitely be anisotropic, turbulence models such as the standard k-ε model will give incorrect results. The standard k-ε model shown here has been derived for high Reynolds number flows, although there have been extensions to it for low Reynolds numbers (Jones and Launder, 1972).

A number of attempts have been made to improve on the standard k-ε model using other methods to formulate the transport equations. One of these is known as the RNG k-ε model of Yakhot and Orszag (1986), derived using a rigorous statistical technique known as renormalisation group theory. This is similar in form to the standard k-ε model, but has refinements that are said to improve its performance for a variety of flows. Some of the key features are that: an additional term appears in the ε equation that is said to improve accuracy for rapidly strained flows; the effect of swirl on turbulence is accounted for; and an analytical formula is used for turbulent Prandtl numbers—the standard k-ε model uses user-specified constants.

Another approach to turbulence modelling is to solve transport equations for each of the Reynolds stresses appearing in equation (2.2). The advantage in this is that any anisotropy inherent in a flow will be captured in the solution. Such turbulence models are generally referred to as Reynolds Stress Transport models (RSM). The general form of the transport equation for Reynolds stress $\overline{u_i'u_j'}$ is given by Launder (1989) as:-

$$\frac{\partial\overline{u_i'u_j'}}{\partial t}+C_{ij}=P_{ij}+F_{ij}+\frac{\partial}{\partial x_k}d_{ijk}+\varphi_{ij}-\varepsilon_{ij} \tag{2.7}$$

where: C_{ij} represents convective transport; P_{ij}, shear generation; F_{ij}, body force generation; d_{ijk}, diffusion; φ_{ij}, pressure-strain; and ε_{ij}, dissipation. The actual representation of each of these terms is not given here. Approximations are required for the diffusion, pressure-strain,

and dissipation terms: Launder (1989) presents a set that was heavily used throughout the 1980's.

Using the Reynolds Stress model for three-dimensional flow simulation means that seven extra transport equations are required over and above the basic Navier Stokes equations. This obviously introduces a far greater computational burden than for simulations using only two-equation turbulence models. There are very few CFD-based erosion modelling studies in which the Reynolds Stress model has been used in addition to the standard k-ε model.

Beyond the Reynolds Stress models lies the concept of Large Eddy Simulation (LES). In Large Eddy Simulations, the transient flow equations are solved for the mean flow and the *largest turbulent eddies*. Turbulence theory indicates that the largest eddies in a flow contain most of the energy, so that solving for these directly will improve the overall solution. The effects of the smaller eddies are modelled. LES is not at present a valid technique for general-purpose industrial simulations due to the large scale computing resource required. However, such a technique may well be required before the true flow phenomena taking place within the flow control tip of a choke valve can be obtained.

2.2.3 Wall functions

The standard k-ε turbulence model and its variants are only applicable to the fully turbulent, high Reynolds number, region of a flow. Viscous effects will dominate the flow behaviour close to a solid wall. There is therefore a need to account for the effect of a wall on the main turbulent flow. While it is possible to add low Reynolds number extensions to many of the popular turbulence models (and so apply the transport equations right up to a wall), it is generally accepted practice to apply wall functions that account for the near wall behaviour without requiring excessively small cells close to the wall. The standard wall functions of Launder and Spalding (1974) have been widely used. In this approach, the time-average velocity U_P of the fluid at the first grid point P away from the wall is supposed to obey the relation:-

$$\frac{U_P}{(\tau\ \rho)_w} C_\mu^{1/4} k_P^{1/2} = \frac{1}{\kappa} \ln\left[E y_P \frac{\left(C_\mu^{1/2} k_p\right)^{1/2}}{\nu} \right] \qquad (2.8)$$

where y_P is the distance from point P to the wall. This relation is valid when the dimensionless quantity y^+ has a value between 30 and 500. y^+ is given by:-

$$y^+ = \frac{\rho u_\tau y_P}{\mu} \qquad (2.9)$$

where u_τ, the friction velocity, is given by:-

$$u_\tau = \left(\frac{\tau_w}{\rho}\right)^{1/2} \tag{2.10}$$

It is assumed that the rate of turbulent energy dissipation equals the rate of energy production in the cell adjacent to the wall. For this reason, the wall function presented here can be termed an equilibrium wall function. There are also wall functions that effectively enable this constraint to be relaxed: these are subsequently termed non-equilibrium wall functions. Kim and Choudhury (1995) present such an approach.

2.2.4 Discretisation and solution algorithms

Discretisation is the process whereby the continuum transport equations are integrated over a control volume to form the basis for a numerical solution. The text by Patankar (1980) remains one of the classic introductions to this procedure, and so it will not be dealt with in detail here. A number of discretisation schemes are available to form the algebraic equations required for the numerical method: the particular formulation of these will depend on the accuracy sought from a solution, as well as the type of control volume used in the computational mesh.

A number of algorithms have been suggested to solve the system of algebraic equations resulting from the discretisation of the Navier Stokes and associated equations. One of the most well known algorithms is the SIMPLE (semi-implicit method for the pressure linked equations) algorithm of Patankar and Spalding (1972). This has subsequently been revised, giving rise to the SIMPLER (SIMPLE Revised) algorithm of Patankar (1980), and the SIMPLEC (SIMPLE Consistent) algorithm of Van Doormaal and Raithby (1979). Another popular method is the PISO (pressure-implicit with splitting of operators) algorithm developed by Issa et al. (1986). A selection of these algorithms is generally available in a good commercial CFD code.

The use of unstructured tetrahedral cells can introduce greater numerical error into a solution than would be present with a hexahedral mesh. Two ways of counteracting this effect are to either increase the number of cells in the computational mesh, or else to use a higher-order discretisation scheme. It is generally recommended practice to use at least a second order discretisation scheme regardless of the type of mesh. Some CFD vendors have developed higher order schemes aimed specifically at overcoming the problems caused by unstructured cell types. In the present study, second order discretisation has been used in almost all simulations—some have used third order discretisation (for hexahedral cells).

2.2.5 Mesh Generation

Appendix A presents an introduction to the unstructured meshing capabilities of the commercial CFD code used in the present study. It is not proposed to go into any further detail in this section.

2.2.6 Summary

The modelling approaches presented in section 2.2 for the fluid phase represent the methods generally used in industrial simulations of turbulent flow—for incompressible flows at least. The increasing use of these methods through commercial CFD packages suggests that the results they produce are valid enough to be used in engineering design studies. The expectation is that reasonable simulations of the flow through a choke valve will be obtained, although it is possible that some of the flow features will not be predicted. In particular, the complex three-dimensional flow structure within the flow control tip (where fluid jets impinge on one another to cause energy dissipation) is unlikely to be correctly predicted by two-equation turbulence models. Even higher order schemes like the Reynolds Stress Transport model (RSM), where a transport equation is solved for each of the Reynolds stresses in equation (2.2), may not correctly predict the flow. LES methods are out of reach for typical industrial flows at present.

Other flow features will depend more on correct mesh sizing than on the particular choice of turbulence model. Flow through sharp edged holes in the valve will be sensitive to the size of mesh cells surrounding the edge. There are regions of the valve that could almost represent flow between two parallel plates (region between the flow cage and the outside of the stem and tip). Correct mesh resolution will be important here to obtain correct flow profiles.

The emphasis in this study will be to apply the methods that are typically available for use in industrial flow simulations (i.e. through commercial CFD software), and to assess the results by comparison to experimental testing. It must be remembered that the main objective is to predict particle impact velocity on solid surfaces, and so that while not all flow features in the choke valve may be correctly predicted, it could be that the main features are sufficiently well defined to make the prediction of erosion a valid exercise.

2.3 Particle Trajectory Calculations

The second key element of an erosion modelling tool is the calculation of particle trajectories as they pass through the computational domain. These calculations will provide the vital information of velocity and angle as particles impact the solid surfaces of the domain. If the trajectory calculations are inadequate it is likely that the success of the overall erosion modelling tool will be limited. It is the aim of this section to examine the particle trajectory calculation in more detail.

The flows of interest in the present study will be turbulent in nature. Turbulence presents a difficulty in particle trajectory computations, as it will act to disperse particles from what might otherwise be a fairly smooth passage through the domain. Turbulent flows are characterised by random fluctuating velocities and rotational structures known as eddies. Particle trajectory calculations must account for these effects if realistic results are to be achieved.

2.3.1 Eulerian and Lagrangian solid particle modelling

There are essentially two approaches to the computational modelling of a discrete phase entrained within the continuous carrier phase: Eulerian or Lagrangian. In the Eulerian approach, the discrete phase is treated as being a continuum in a similar way to the carrier fluid phase. Differential equations are written for the particulate phase properties and solved alongside the equations for the fluid phase. Thus the particles act as interpenetrating continua dispersed throughout the fluid phase. This approach is suitable for cases where the particle loading is fairly high, and where it is not necessary to extract particle impact information at boundaries. Picart et al. (1986) developed a method that accounted for anisotropic effects in the turbulence field through second-order algebraic extensions to the k-ε model. A transport equation was written for the particle number density of spherical monosized particles, and particulate dispersion was accounted for. Tu et al. (1996) attempted to develop an Eulerian formulation that could better account for behaviour near an obstructing wall surface. The concept in mind was to define a particle-wall rebounding layer in which the collision process had a significant effect on incoming particles. While such developments continue to improve the Eulerian modelling procedure, it is not likely to become a suitable approach for erosion modelling studies for several years to come. This is due to the difficulty associated with obtaining actual particle impact velocities and angles at solid surfaces.

In the Lagrangian method, only the fluid carrier phase is solved by Eulerian equations. Individual particle trajectories are obtained by solving the particle equation of motion across many small time steps throughout the flow. In one-way coupling simulations

it is assumed that particles have no effect on the fluid flow: the flow field is obtained before trajectories are calculated. Two-way coupling simulations are required if particles do affect the flow solution: the overall computation becomes an iterative process. It may be necessary to calculate several thousand trajectories before a statistically meaningful representation of particle behaviour is obtained. The advantage with this approach is that particle impact velocities and angles can be determined at solid surfaces. As this information is vital for erosion modelling, the Lagrangian method for trajectory computations must be used.

The two main concerns involved in Lagrangian particle tracking are the forces to include in the particle equation of motion, and the method whereby the effect of turbulent velocity fluctuations is to be accounted for. Both elements will be addressed.

2.3.2 Forces acting on a solid particle

A particle moving in a fluid will experience a variety of forces acting upon it. These forces will determine the particular path taken by the particle as the fluid carries it along. Michaelides (1997) gives the earliest form of the equation for the *transient hydrodynamic force* acting on a sphere that was initially at rest, but now accelerating, in an infinite fluid at rest. This is given as:-

$$-F = 6\pi r_p \mu u_p + \frac{m_f}{2}\frac{du_p}{dt} + 6r_p^2\sqrt{\pi\rho\mu}\int_0^t \frac{\frac{du_p}{dt}}{\sqrt{t-\tau}}d\tau \qquad (2.11)$$

where: r_p is particle radius; μ is fluid dynamic viscosity; ρ is fluid density; u_p is particle velocity; m_f is mass of fluid displaced by the sphere; τ is a dummy variable for time, t. This is known as the Basset-Boussinesq-Oseen equation (B-B-O). The first term on the right-hand side is the steady-state drag force; second term is the added mass force; and the third term is the history integral force (or Basset force). The drag force acts in the direction of the relative velocity between the particle and the fluid. If the particle is accelerated relative to the fluid it will experience a resistance equal to the product of the acceleration and the virtual mass of the body. This is the added mass force (Jayanti and Hewitt, 1991). The Basset history force accounts for the influence of changes in the flow field surrounding the particle from steady-state conditions, and is important when the particle acceleration is high. Inclusion of this term greatly complicates particle trajectory calculations, as the force depends on the time-history of the particle trajectory.

Equation (2.11) is strictly only valid for conditions of low velocity and large acceleration, and does not truly apply at finite particle Reynolds numbers. A popular method of circumventing this limitation has been to introduce empirical coefficients, particularly for

the steady-state drag, which extend the range of application of the equation. Odar and Hamilton (1964) applied coefficients to all three terms in (2.11), resulting in

$$-F = \frac{1}{2} C_D \pi \rho r_p^2 u_p^2 + C_A m_f \frac{du_p}{dt} + C_H r_p^2 \sqrt{\pi \rho \mu} \int_0^t \frac{\frac{du_p}{dt}}{\sqrt{t-\tau}} d\tau \qquad (2.12)$$

where C_D is the drag coefficient, C_A the added mass coefficient, and C_H the history term coefficient. It should be remembered that this equation still only applies to the case of a sphere moving in a quiescent fluid. If the fluid were also moving, the relative velocity between the sphere and the fluid would be required.

There are other forces that also act on a particle moving through a fluid. The pressure-gradient force is the force required to accelerate the fluid that would occupy the particle volume V_p if the particle were absent. This force, in its full form, is given by Clift et al. (1978) as

$$\rho V_p \left[\frac{Du}{Dt} - \nu \nabla^2 u \right] \qquad (2.13)$$

where u is the instantaneous fluid velocity, and ν is the fluid kinematic viscosity.

Two lift forces may operate on a particle. The Magnus force originates from the non-linear terms of the Navier-Stokes equations, and is a lift force resulting from particle rotation at low Reynolds numbers. Jayanti and Hewitt (1991) give the Magnus force as being of the form

$$\frac{\pi}{8} \rho d_p^3 u_r \times \Omega_p \qquad (2.14)$$

where u_r is the relative velocity between the fluid and the particle, Ω_p is the angular velocity of the particle, and d_p is the particle diameter. Saffman (1965) showed that a small sphere in a slow shear flow experiences a lift force perpendicular to the flow direction, of magnitude:

$$1.615 \mu d_p^2 u_r \left[\frac{\rho}{\mu} \frac{du}{dy} \right]^{1/2} \qquad (2.15)$$

This is often referred to as the Saffman lift force.

Other forces that may act on a particle are the body force due to gravity,

$$m_p \mathbf{g} \qquad (2.16)$$

and the buoyancy force,

$$\rho \frac{\pi}{6} d_p^3 \mathbf{g} \tag{2.17}$$

where **g** is the gravitational acceleration vector.

It is often the case that some of these forces can be justifiably neglected. Meng and Van der Geld (1991) performed a comparative study of the Saffman lift, added-mass, pressure-gradient, and Basset history forces, for particles of various sizes moving in an inviscid liquid flow over a cylinder. They employed an estimation-iteration approach to solve the complex Basset history term. The results show that:-

- The Saffman lift force is always very small and can be ignored.
- Added-mass force is only important for large particles (particle sizes in study were 250, 1250 or 2500μm).
- Pressure-gradient force is generally important.
- Changes in the Basset history force are related to the steady drag force, and it can have considerable influence in particle trajectory calculations.

Based on the findings of Meng and Van der Geld (1991), it would be possible to neglect the Saffman lift force for erosion modelling calculations, as the particle sizes are generally small. Inclusion of the Basset history force greatly complicates particle trajectory calculations, and is generally neglected in erosion modelling studies. At least two of the major commercial CFD codes do not account for the Basset history force.

It is obvious that there are several forces acting on particles in a fluid flow. Not all forces need to be included in all simulations, but it will generally be the case (for industrial simulations at least) that the forces included in a calculation will be those that are made available to the user of a commercial CFD code.

The resulting particle equation of motion will have the general form:-

$$m_p \frac{d\vec{u}_p}{dt} = \vec{F}_D + \vec{F}_{VM} + \vec{F}_{PG} + \vec{F}_G + \vec{F}_{BH} + \vec{F}_L \tag{2.18}$$

where F_D is the steady drag force, F_{VM} is the virtual mass force, F_{PG} is the pressure gradient force, F_G are the forces due to gravity (body forces), F_{BH} is the Basset history force, and F_L are the lift forces. Some of these terms will require the particle velocity, u_P, as well as the fluid velocity u.

2.3.3 Modelling turbulent particle dispersion

The velocities required in the particle equation of motion are the instantaneous fluid and particle velocities at that instant in time. Unfortunately, the fluid phase equations are generally solved in their time-averaged form, so that instantaneous velocity information is not available. The fluid velocity can be viewed as being the sum of a mean velocity component and a fluctuating instantaneous component:-

$$u = U + u' \tag{2.19}$$

The mean component U is supplied by the solution of the time-averaged fluid phase equations in conjunction with an appropriate turbulence closure model. The fluctuating component must be generated by some other means. It is the objective of turbulent particle dispersion modelling to provide this other means. A comprehensive review and introduction to the subject has been given by Shirolkar et al. (1996).

Lagrangian particle tracking methods can also be described as separated flow models because the discrete phase calculation is performed in a separate step from the fluid phase calculation. The separated flow models can be split into two divisions: deterministic separated flow (DSF) models, and stochastic separated flow (SSF) models. Deterministic models simply ignore the fluctuating component of the instantaneous velocity, and obtain particle trajectories from the mean velocity field directly. This approach was adopted by Crowe et al. (1977) in their development of the Particle-Source-In Cell (PSI-CELL) method for gas-droplet flows. However this method does not address the fundamental problem of random fluctuations.

There are three types of stochastic separated flow model: those based on the eddy lifetime (or eddy interaction) concept; time correlated models that generate fluid particle and discrete particle trajectories simultaneously; and also Probability Density Function (PDF) propagation models. As the most popular approach to date has been the eddy interaction model, this type alone will be discussed here.

The eddy interaction model assumes that particles passing through the turbulent flow field will interact with a series of turbulent eddies of varying length and time scales. The smallest eddy size in a turbulent flow is given by the Kolmogorov length scale, and the corresponding eddy lifetime by the Kolmogorov time scale. Particles are often smaller than the Kolmogorov length scale. Each eddy with which the particle interacts must be characterised by a length scale, a time scale, and an instantaneous velocity that persists for the duration of the particle-eddy interaction. In the eddy interaction model, the fluctuating fluid velocity of the eddy is randomly sampled from a Probability Density Function (PDF)

based on local turbulence properties at the start of the particle-eddy interaction. The fluid turbulence closure model for the simulation gives the turbulence properties. A particle will interact with an eddy for the minimum of either the eddy lifetime or the transit time taken for the particle to cross the eddy and pass from it. Once the particle-eddy interaction has ended, the particle is assumed to immediately cross into a new eddy, and the process is repeated. In conventional eddy interaction models there is no link between the old eddy and the new eddy. The particle equation of motion is ideally solved only once for every particle-eddy interaction, over the time step given by the eddy-particle interaction time. One of the earliest implementations of such a model was that of Gosman and Ioannides (1981).

In the method suggested by Gosman and Ioannides (1981), the fluid turbulence was assumed to be isotropic and to possess a Gaussian probability distribution in the fluctuating velocity. The fluctuating velocity is therefore given by randomly sampling this distribution, so that

$$u' = \sqrt{2k/3} \tag{2.20}$$

where k is the turbulent kinetic energy. The time for which this velocity fluctuation will act on the particle is taken to be the minimum of either: (a) the eddy lifetime t_e, if the particle is moving slow enough, or (b) the transit time t_r, if the particle velocity enables it to leave the eddy before the eddy lifetime expires. A characteristic size for the eddy is given as

$$l_e = \frac{C_\mu^{3/4} k^{3/2}}{\varepsilon} \tag{2.21}$$

so that the eddy lifetime can be estimated to be

$$t_e = \frac{l_e}{|u'|} \tag{2.22}$$

The transit time is found from the solution to a simplified form of the particle equation of motion, i.e.

$$t_r = -\tau_p \ln\left[1.0 - \frac{l_e}{\tau_p |u - u_p|}\right] \tag{2.23}$$

where τ_p is the particle relaxation time given by:-

$$\tau_p = \frac{4}{3}\rho_p \frac{d_p}{\rho C_D |u - u_p|} \tag{2.24}$$

Although this approach is one of the earliest, it has nevertheless been applied in various forms in many studies. Among others, Govan et al. (1989), Adeniji-Fashola and Chen (1990), Sommerfeld et al. (1992), and Chang and Wu (1994) have used similar eddy interaction models that assume isotropic turbulence. It is apparent that, despite its limitations, it has achieved widespread use.

Graham (1995, 1996) has attempted to improve the eddy interaction model for isotropic turbulence by extending it to account for three main effects observed in particle dispersion experiments. These effects are:-

1. The crossing trajectories effect, or CTE, which results in reduced particle dispersion in the presence of a drift velocity. This can be accounted for by using the correct eddy length and fluid particle interaction time. The influence of gravity should also be included.
2. The inertia effect due to the density of the particles being greater than that of the fluid. This is modelled by allowing the maximum particle-eddy interaction time to become *greater* than the actual eddy lifetime.
3. The continuity effect where greater dispersion occurs in the drift velocity direction than at right angles to it. Calculating interaction times for each of the coordinate directions can model this effect.

2.3.4 Particle-Wall Interaction

It is important to have some understanding of the way in which particles behave upon impact with a solid wall in order to continue trajectory calculations after an impact event. Ideally, a simulation should be able to predict the correct rebound angle and velocity from the impact properties. The relationship between impact and rebound can be described in terms of restitution coefficients for a particular material. Figure 2.7 illustrates the type of notation employed. Restitution coefficients based on particle velocity ratio (V_2/V_1) give a measure of the momentum exchange on impact, and are therefore related to the energy available to damage the material surface by erosion. Although there are several studies examining particle-wall interaction modelling, there is considerable scope for further research.

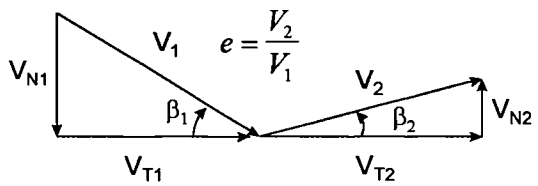

Figure 2.7 Impact and rebound notation for restitution coefficients.

Grant and Tabakoff (1975) developed particle rebound correlations for 200 μm diameter quartz sand particles impacting 2024 annealed aluminium alloy at velocities between 76.2 and 118.9 m/s in air. A purpose-built erosion wind tunnel was used for the experimental testing. High speed photography provided the particle impact and rebound measurements. Restitution ratios for normal and tangential velocity components were obtained in terms of impact angle. A later study by Tabakoff et al. (1987) applied Laser Doppler Velocimetry to measure impact and rebound velocities and angles for fly ash particles (around 5 μm) impacting aluminium and a titanium alloy in air. Other researchers, in their numerical predictions of solid particle trajectories, have used relations obtained by these authors. However, it is questionable as to whether they should be used for liquid-particle flows, where liquid viscosity and inertia effects govern particle-wall interaction.

Clark and Burmeister (1992) made an analysis of particle-wall interaction in liquid flows based on squeeze film theory. The film of liquid trapped between an impacting particle and the wall has a cushioning effect on the particle—the squeeze film effect. In order for a particle-wall collision to occur, the particle must have sufficient velocity to overcome the effect of the squeeze film. If the particle is to rebound after impact, it must again have sufficient residual kinetic energy to escape from the squeeze film region and escape into the main flow. Should the particle have insufficient rebound energy it will remain trapped by the squeeze film effects. Equations have been developed which allow estimation of the squeeze film effect. This theory has been successfully applied in erosion modelling studies (McLaury et al. (1996)).

2.3.5 Summary to particle trajectory calculations

The key issues involved in particle trajectory computations are: which terms to include in the particle equation of motion; how to correctly account for the effect of turbulent fluctuations; and how to model the particle-wall collision. Forces available for inclusion in the particle equation of motion will often be dictated by what is implemented in the commercial CFD package being used. The author does not know of any that implement the Basset history force (and it is possible that this has an important influence in some trajectory calculations). The turbulent dispersion model will also depend on what is available in the CFD code. It is likely to be based on the eddy interaction method, and may not represent state-of-the-art practice. However, trajectory simulations will at least reflect something of the influence of turbulent interaction. Particle-wall collisions are often modelled using relations for restitution coefficient, and some commercial codes will make provision for this. Applying other models for the wall collision process (e.g. squeeze film effect) will generally require user coding.

This chapter has not covered the issue of particle-particle collision models. This is because particle concentration levels in the flows of interest to the present study are unlikely to be high enough for such interaction to have an effect. Almost all CFD-based erosion modelling studies make the assumption that the level of particle concentration is not high enough to affect the continuous phase, and that an uncoupled Lagrangian model is therefore appropriate. As the particle concentrations in this study are less than 1% of mass, their effects on the continuous phase will be ignored.

The key data to be provided by particle trajectory calculations are particle impact angles and velocities on solid surfaces. It is this data that can be related to erosion rate through suitably defined empirical or semi-empirical equations.

2.4 Solid particle erosion

2.4.1 Introduction

Erosion due to solid particle impact has received considerable attention over the past century, and as a result a vast body of literature exists on the subject. As it would be almost impossible to attempt to cover it all, only that literature most pertinent to the present study will be reviewed. Of particular interest are studies in which an effort was made to derive equations (semi-empirical or otherwise) that relate erosive material loss to particle impact velocity and angle. Such equations will play a vital role in the success of a CFD-based erosion modelling tool. However, before these equations can be properly assessed, it will be necessary to achieve some understanding of solid particle erosion in general, and the way in which various variables affect the rate of material loss.

2.4.2 Mechanical properties of metals

The mechanical properties of metals give an indication of their behaviour under varying conditions of stress and strain. Stress is simply the applied force per unit area, while strain is a measure of relative elongation due to the applied force. The fundamental mechanical properties are ductility, malleability and toughness. The ductility of a material is its ability to deform under tension without fracture; malleability is its ability to deform under compression without fracture; and toughness indicates the material's ability to endure bending or applied shear stress without fracture. A number of mechanical tests have been devised which allow quantitative measurement of values related to these mechanical properties.

2.4.2.1 Tensile test

The tensile test involves applying increased tensile (stretching) loads to a specimen of known cross-sectional area, and measuring the length by which the specimen extends for each increment of force. This provides a force-extension diagram, of which a typical example for annealed low-carbon steel is shown in Figure 2.8. One of the specific values obtained from the tensile test is the yield stress given by:

$$\sigma_y = \frac{\text{Yield force (N)}}{\text{Original area of cross-section (m}^2\text{)}} \tag{2.25}$$

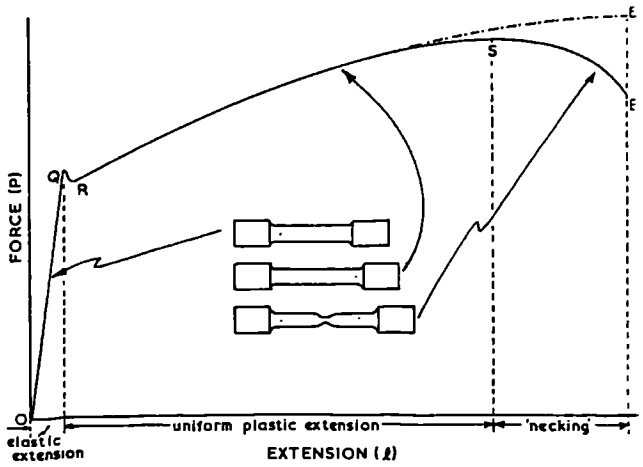

Figure 2.8 Force-extension diagram for an annealed low-carbon steel (Higgins, 1983).

Point Q on the force-extension diagram of Figure 2.8 shows the *elastic limit* of the specimen. If the applied load is removed at any point from 0 to Q, the material will return to its original dimensions as only *elastic deformation* has taken place. If the force is increased beyond point Q, a stage is reached at R where the specimen will deform suddenly for no increase in the applied load. This is the *yield point*, and indicates the onset of *plastic deformation*. If the load is now removed a small permanent deformation will remain. As the load is increased beyond R a point of maximum stress will be reached beyond which the material will fail. A typically *ductile* material, such as low-carbon steel, will exhibit 'necking' just before failure, whereas a typically *brittle* material will not show such 'necking' but rather fail suddenly as the maximum limit is reached. Figure 2.9 illustrates these two cases. The tensile strength of the material is defined as:-

$$\text{Tensile strength} = \frac{\text{Maximum force (N)}}{\text{Original area of cross-section (m}^2\text{)}} \tag{2.26}$$

Other values given by the tensile test are the percentage elongation and the percentage reduction in area.

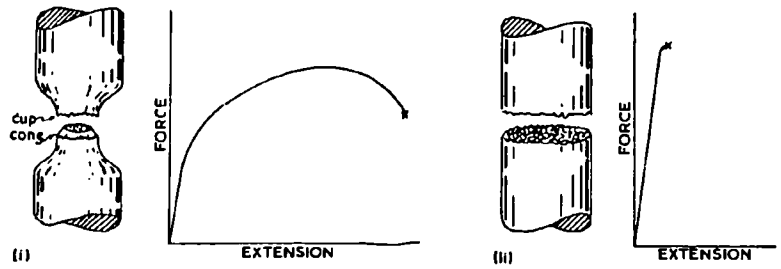

Figure 2.9 (i) Typically ductile fracture; (ii) typically brittle fracture (Higgins, 1983).

2.4.2.2 Hardness tests

Hardness can be thought of as a measure of a materials resistance to abrasion: early testing methods were based on this concept. More accurate methods, however, have been developed which measure the resistance of the material to plastic deformation under static pressure. A hardness index is obtained by dividing the static force by the surface area of the resulting impression. In the Brinell test, a hardened steel ball is pressed into the test piece surface to obtain a hardness index as described. The Vickers Hardness test uses a similar concept, but has a diamond square-based pyramid as the indenter. The Vickers Pyramid hardness number is the resulting index.

2.4.2.3 Impact tests

Impact tests provide a measure of the material toughness by recording material response to a mechanical shock. One test involves mounting a specimen beneath a pendulum striker that impacts with sufficient force to break the specimen.

2.4.2.4 Erosion response

The two typical material types (ductile and brittle) not only show different behaviour under fracture in the tensile test, but also respond differently under conditions of solid particle erosion. Figure 2.10 shows the erosion versus impact angle characteristic for typically ductile and brittle materials.

Material physical properties, such as melting point, density, and specific heat capacity, can also be of some importance in solid particle erosion studies.

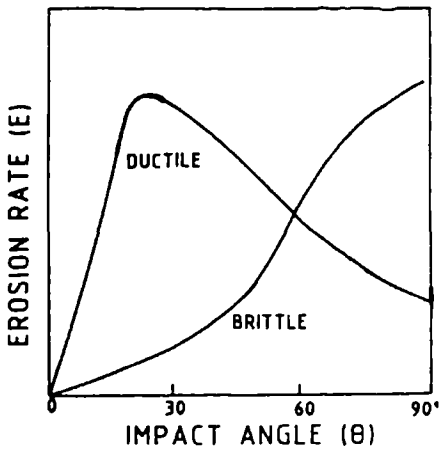

Figure 2.10 Erosion versus impact angle characteristics for typical ductile and brittle materials (Sundararajan and Roy, 1997).

2.4.3 Factors influencing solid particle erosion

The factors influencing solid particle erosion are perceived to be as follows (Tilly (1979), Finnie (1972), Sundararajan and Roy (1997)):-

1. Impact parameters: Particle velocity, rotation, and impact angle. Also the duration of exposure.
2. Particle properties: size, shape, hardness, and concentration.
3. Target material properties and stress level.
4. Environmental influence: Fluid phase and temperature conditions.

Each of these factors will be treated in turn, in order to develop an understanding of solid particle erosion.

2.4.3.1 Impact parameters

In the erosion modelling tool, impact parameters will be determined by the particle trajectory computations. These computations will provide data on particle impact velocity, angle, and concentration.

- *2.4.3.1.1 Particle impact velocity*

Numerous studies have shown that the amount of material removed in erosion increases as the particle impact velocity increases. It is generally accepted that erosion rate E_{MM} (mass loss of material per unit mass of abrasive) is proportional to the impact velocity raised to some exponent:-

$$E_{MM} \propto V_p^n \tag{2.27}$$

where V_p is the impact velocity (ms^{-1}) and n is the velocity exponent. It was originally thought (Finnie (1960), Neilson and Gilchrist (1968)) that this exponent had the value of 2.0, but extensive experimental testing by Finnie et al. (1967) for various impact angles has shown that it typically lies in the region 2.3 to 2.4 for ductile metals. Sundararajan and Shewmon (1983) concluded a mean value of 2.55 for normal impact. It has been suggested that this discrepancy between experimental and the original predicted exponent is due to particle rotation (Finnie, 1995). Higher exponents have been reported for brittle materials.

Grant and Tabakoff (1975) performed experiments in an erosion wind tunnel designed to provide a representative aerodynamic environment in which the specimens were placed. Test conditions would thus represent actual conditions of interest (turbomachinery applications) more closely. The data obtained (using 2024 aluminium alloy) indicated a velocity exponent of 2.8 for 20^0 impacts, and on the order of 4 for 90^0 impacts. Laitone (1979) suggested that these high values found experimentally are the result of aerodynamics effects alone. In his review article, Humphrey (1990) underlines the point that velocity exponents greater than 2 could result entirely from fluid mechanics effects, and not require a material related explanation.

It is also likely that the velocity exponent for spherical particles will be higher than that for angular particles. Hutchings et al. (1976) measured an exponent of 2.9 in experiments with 9.5 mm steel balls impacting mild steel at 30^0. Sheldon and Kanhere (1972) obtained an exponent of 2.8 with 2.3 mm steel spheres impacting a work-hardened aluminium alloy surface. The exponent fell to 2.34 for an annealed surface.

There is some evidence of a threshold velocity below which erosion will not occur (Tilly, 1979). Bitter (1963a) found a value of $0.67ms^{-1}$ for hardened steel balls impacting low carbon steel at 90^0 impingement.

- *2.4.3.1.2 Particle rotation*

Particle rotation may arise in two ways: the particle could be rotating before it hits the surface; it could also rotate as a result of the impact event itself. Hutchings et al. (1976) measured the particle rotation on rebound of 9.5 mm steel balls impacting mild steel. They concluded that the rotational energy of the rebounding ball could be neglected as it constituted less than 1 % of the initial linear kinetic energy.

Finnie and McFadden (1978) modified a previous theoretical analysis of Finnie (1960) to better account for the variation of particle rotation with initial impact velocity. Particles will dig deeper into a surface as the impact velocity increases, and as a result the rotation during impact will decrease and the resulting force acting on the particle will change

position. By accounting for this change of position, Finnie and McFadden (1978) were able to make a more realistic estimate of the velocity exponent.

The effect of particle rotation before impact is somewhat unknown and difficult to examine experimentally. For the present study it will be ignored.

- *2.4.3.1.3 Particle impact angle*

The amount of material removed in solid particle erosion is greatly affected by the angle at which the particle strikes the surface. There is a wide variation in the erosion versus impact angle characteristic between materials. Typically ductile materials (like metals and alloys) will have a characteristic which peaks somewhere in the region of 25^0, whereas typically brittle materials (like glass and ceramics) will show maximum erosion at 90^0. These typical responses are for erosion by angular particles: there is evidence to show that typically ductile metals will show maximum erosion at 90^0 when impacted by spherical particles (Reddy and Sundararajan, 1986). Figure 2.10 shows ductile and brittle material behaviour.

- *2.4.3.1.4 Duration of exposure*

Neilson and Gilchrist (1968) found that an aluminium specimen impacted by 210 μm aluminium oxide particles experienced an initial weight *gain* before settling to a steady erosion rate for all impact angles tested. The initial weight gain was greatest at 90^0 impact. Figure 2.11 shows some of the results. Tilly (1969) also found a weight gain at 90^0 impact, but not at 40^0 impact, for an aluminium alloy. Rather, the erosion rate was *greater* during the incubation period than at steady state. However, Neilson and Gilchrist (1968) appear to have made more frequent measurements of specimen mass in the early stages than Tilly (1969), which perhaps explains the differences. The results of Reddy and Sundararajan (1986) with spherical particles on copper and copper alloy show the erosion rate building up to the steady state value in the initial stages—but not increasing beyond it. It is apparent that there could be a number of contributing factors to the initial erosion behaviour of soft and ductile materials.

Tilly (1979) proposed that while soft and ductile materials will exhibit an incubation period, common engineering materials (including steel) will not, but will immediately erode at a steady state. The work of Levy et al. (1986) using two steels refutes this claim as it shows evidence of an initial peak erosion rate that is higher than the steady state value. Figure 2.12 shows results obtained for 1018 steel at various velocities using silicon carbide particles in the range 250 to 300 μm. It is noted that the frequency of measurement by Levy et al. (1986) was greater than that of Tilly (1969), which could explain the difference in observations.

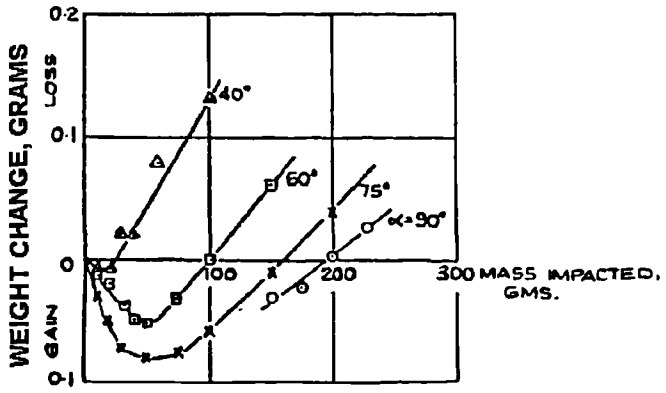

Figure 2.11 Weight change with impacted mass for 210 μm aluminium oxide particles impacting aluminium plates. (Neilson and Gilchrist, 1968).

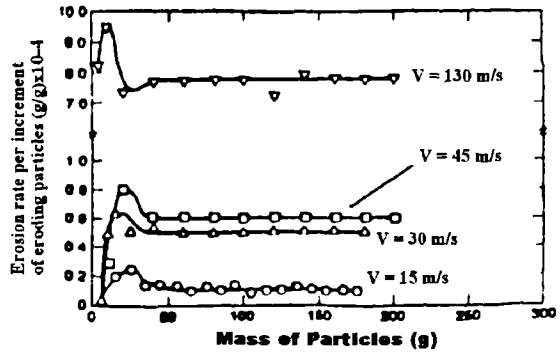

Figure 2.12 Incremental erosion rates of 1018 steel. Various particle velocities. (Levy et al., 1986).

2.4.3.2 Particle properties

- *2.4.3.2.1 Particle size effect*

It is a familiar observation that the erosion rate rapidly decreases when the particle size falls below about 100 μm: particles of 10 μm size have about a quarter the effectiveness of a 100 μm particle (Finnie, 1995). Figure 2.13 shows the results obtained by Tilly (1973), which clearly illustrate the effect. A proven explanation for the size effect has still to arise, even though at least a dozen (assessed by Misra and Finnie (1981)) have been proposed in the literature. As a further twist, Bahadur and Badruddin (1990) have shown that while the erosion rate of 18 Ni(250) maraging steel increased with increasing particle size for SiC and Al_2O_3 particles up to a certain value, it decreased almost linearly for increasing SiO_2 particle size without coming to a limiting value. An attempt was made to explain the effect in terms of relative contributions from different erosion mechanisms; however this may be somewhat subjective.

- *2.4.3.2.2 Particle shape*

Levy and Chik (1983) found that the erosion rate of AISI 1020 steel by angular steel grit was four times greater than that caused by spherical steel shot. This shows clearly the influence that particle shape has on the resulting erosion. Particle shape can also affect the variation of erosion with impact angle. Reddy and Sundararajan (1986) found that the maximum erosion of two ductile materials impacted by spherical steel shot occurred at 90^0 impact, and not around 25^0 as is normally expected for ductile materials. The same materials responded as expected when impacted by SiC particles (Roy et al., 1993). Several other investigators have observed similar results (Sundararajan and Roy, 1997).

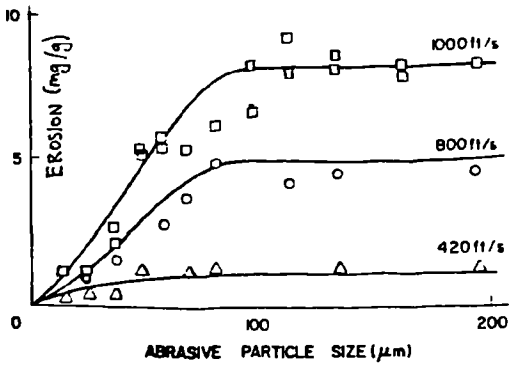

Figure 2.13 Illustration of particle size effect. (Data of Tilly (1973), in Misra and Finnie, (1981)).

- *2.4.3.2.3 Particle hardness*

It has been noted that the erosion rate will be independent of particle hardness when the particle hardness is at least twice that of the surface material (Sundararajan and Roy, 1997). Levy and Chik (1983) studied the erosion of AISI 1020 with five erodents, and concluded that the erosion rate remained constant when the particle hardness reached 700 kgf/mm^2. Figure 2.14 presents some of their results. Erosion rate is reduced when hardness falls below the critical value.

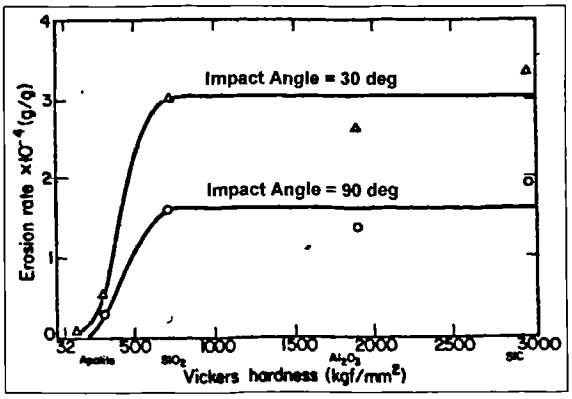

Figure 2.14 Effect of particle hardness. AISI 1020 steel. (Levy and Chik, 1983).

- *2.4.3.2.4 Particle concentration*

The concentration of particles impacting solid surfaces is not thought to have a significant influence on erosion rate (Sundararajan and Roy, 1997). Tilly and Sage (1970) examined the effect of dust concentration on erosion using two sizes of quartz dust. They found that the erosion rate *decreased* slightly as particle concentration increased. Figure 2.15 shows their results for a titanium alloy and a chromium steel. Uuemois and Kleis (1975) thought that as the concentration increased, the increased likelihood of particle-particle

collisions would prevent particles reaching the surface, and so decrease erosion. This theory has been considered in some detail by Andrews and Horsfield (1983), who show that *more,* rather than less, particles are likely to strike the surface as a result of collisions. Erosion rate is reduced at elevated flux levels because the incoming particles are deflected in a wide range of directions from the mean impact angle. Thus if the mean impact angle were 25^0, and the surface were typically ductile, erosion will reduce slightly with increased concentration as more particles will impact at angles other than 25^0 causing less damage as a result.

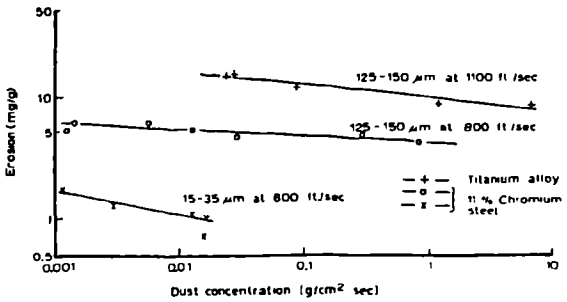

Figure 2.15 Dust concentration effects. (Tilly and Sage, 1970).

2.4.3.3 Properties of the target material

The differing responses of ductile and brittle materials to solid particle erosion have already been discussed. It seems reasonable to suggest that these responses, as well as the *erosion resistance* of a material, must in some way depend on the inherent mechanical and physical characteristics of the material. A considerable amount of effort has been made to relate a material's erosion behaviour to known mechanical and physical properties. If a universal relationship could be found, it would be possible to predict the amount of erosion for any material. This has yet to come.

- *2.4.3.3.1 Mechanical properties*

Early work by Finnie et al. (1967) indicated that the volume removed from annealed metals by eroding particles is proportional to the indentation hardness of the metal, as shown in Figure 2.16. This relation only holds for annealed metals: not for alloys. It was also shown that prior cold work to increase the hardness twofold of some annealed metals did not make them any more resistant to erosion. The effect of heat treatment on two steels to increase their hardness fourfold produced a slight *decrease* in their erosion resistance.

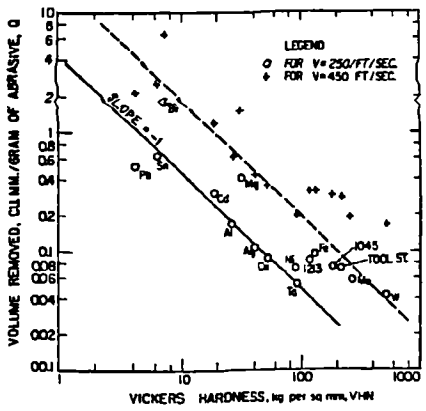

Figure 2.16 Volume loss as a function of hardness for $\alpha_p = 20^0$. (Finnie et al., 1967).

Sundararajan (1995) performed a comprehensive review of the effect of various strengthening mechanisms on erosion resistance of metallic materials. None of the mechanisms were able to significantly improve erosion resistance for all cases; indeed some served to reduce the resistance. It was also concluded that none of the static mechanical properties could be consistently related to erosion resistance. Materials are deformed at high strain rates under solid particle erosion—properties are not known under such unique conditions.

The conclusion that may be drawn from the literature is that the standard mechanical properties of a material do not necessarily indicate its resistance to solid particle erosion. Such behaviour must be determined from actual erosion tests.

- *2.4.3.3.2 Material stress level*

In applications such as turbine rotor blading, materials can be subject to significant tensile stresses. Tilly (1969) tested aluminium and steel specimens under gas-solid particle erosion conditions for a range of tensile stresses, but found no appreciable effect on the magnitude of the resulting erosion.

2.4.3.4 Environmental factors

- *2.4.3.4.1 Fluid phase*

Particles causing erosion are generally transported by a fluid, be it liquid or gas. It is the movement of this fluid phase that will determine the velocity and angle with which a particle impacts a solid boundary. Thus particles entrained in a fast moving gas will impact surfaces at high velocity and cause significant damage, while particles suspended in a slow moving liquid may not cause much erosion at all. The nature (laminar or turbulent) of the fluid phase will also have a significant effect.

Dosanjh and Humphrey (1985) performed a numerical analysis of the erosion caused by a particle-laden fluid jet impinging normally on a flat plate. Their results showed that as the jet turbulence intensity increased the magnitude of erosion (predicted using Finnie's (1960) cutting model) actually decreased, and that the point of maximum wear moved closer to the centreline of the jet. However, Finnie's cutting model has serious limitations in that it does not predict erosion at normal impact, even although it is known to occur experimentally. The findings of Dosanjh and Humphrey (1985) are therefore of limited value. It is quite possible that there have been no experimental studies on the effect of turbulence level in solid particle erosion.

Apart from governing the velocity with which particles strike a surface, the fluid will also determine the angle at which they impact. Tabakoff et al. (1983) analysed the trajectories of small particles approaching test specimens in an erosion wind tunnel. Significant proportions of the smallest particles considered (diameters less than 10 μm) were deflected away from the specimen, while particles with diameters less than 30 μm impacted over a wide range of angles. This has obvious implications for erosion tests carried out using sand-blast type apparatus, in which it is often assumed that the angle of impact is the angle between the specimen surface and the mean centre of the fluid jet. Benchaita et al. (1983) analysed the trajectories of particles flowing in a liquid jet, with similar conclusions.

- *2.4.3.4.2 Temperature*

Sundararajan and Roy (1997) have reviewed the available data on erosion behaviour at elevated temperatures. The review indicates that substantially less work has been carried out for high temperature erosion than for that at room temperature. Gat and Tabakoff (1978) examined the behaviour of several metals and alloys in an erosion wind tunnel. It was shown that the increase or decrease of erosion with temperature depends upon the impact angle and the thermal properties of the material. The erosion rate of three alloys at 20^0 impact angle all decreased for an increase in temperature. They did not exhibit such similar behaviour at the other impact angles used in the study.

Sundararajan and Roy (1997) have suggested that the temperature dependence of erosion can be classified into three groups. Materials in the first group exhibit a decreasing erosion rate with increasing temperature initially, but reach a minimum point beyond which erosion rate increases with increasing temperature. Second group materials erode independently of temperature until a critical point, beyond which erosion rate increases with temperature. In the third group materials erode with an increasing rate as the temperature rises.

2.4.3.5 Summary to Section 2.4.3

The amount of research carried out into the factors affecting solid particle erosion is vast. What has been presented so far can really only be considered to be a snapshot of some of the main factors involved. Even then, some of the behavioural trends observed in the various studies may only hold under a specific range of conditions, and cannot necessarily be considered universal. The main point to come out of this section is that erosion by solid particles is a complex phenomenon that does not easily lend itself to a set of fundamental rules that govern all cases. It is important to bear this in mind when attempting to develop analytical models for the erosion process.

2.4.4 Experimental techniques

A variety of experimental techniques have been presented in the literature for the study of solid particle erosion. Most studies appear to use some form of apparatus where particles are accelerated using compressed gas through a nozzle before impacting the specimen. A small proportion of erosion studies have used liquid-particle flows to erode specimens. Other techniques have also been used, such as vacuum free-fall apparatus and gas guns that propel single particles against stationary targets. Of primary interest to the present study are those techniques where liquid-particle flows are involved.

The quantitative data ideally required from an erosion experiment is as follows:-

1. Particle concentration or mass flux at the surface.
2. Particle impact velocities and angles.
3. Particle size distribution and characterisation.
4. Specimen erosion (volume loss, mass loss, or surface profile).

Not all of this data can be obtained for all types of erosion experiment. Particle impact angle and velocity are difficult to measure, particularly for liquid-particle flows. There is also wide variation in the significance attached to particle characterisation: some studies perform extensive examinations of particle shapes and sizes; others assume a single average diameter only.

The purpose of this section is to briefly review experimental techniques used in the past for solid particle erosion studies. In the present study, a method is required which will provide primary erosion data (erosion vs. impact angle characteristic) for materials of interest under conditions of liquid-particle flow.

2.4.4.1 Liquid-particle erosion studies

- *2.4.4.1.1 Continuous liquid-particle flow loops*

If a specific component (such as a valve or pipe bend) is to be tested under erosion conditions, the obvious approach will be to simply pump a particle-laden fluid through the component in question and observe its condition over time. The NEL low pressure abrasive flow valve test facility (Peters and Hardie, 1994) is a prime example of such an approach. Figure 2.17 shows the general layout. Clean water is supplied to the main piping system through a pressure control valve. Concentrated sandy water is taken from the mixing tank and injected into the main flow at the mixing section. The resulting slurry flow is passed through the valves or components to be tested before it enters a cyclone separator in which sand is removed from the water. Sand enters the mixing tank near the bottom; clean water at the top. Final separation of sand and water takes place in the mixing tank and through

various filters. This facility was designed specifically to test valves used by the oil and gas production industry through a procedure in which valves are opened and closed continuously during the course of the test. Valve performance in sandy service can thus be assessed. Particle concentration is measured using a dynamic sampling method; liquid flowrates are obtained from an electromagnetic flowmeter. Mass loss is measured by weighing components before and after testing. There is no established technique in this facility for measuring particle impact velocities or angles; neither have such measurements been made in the past.

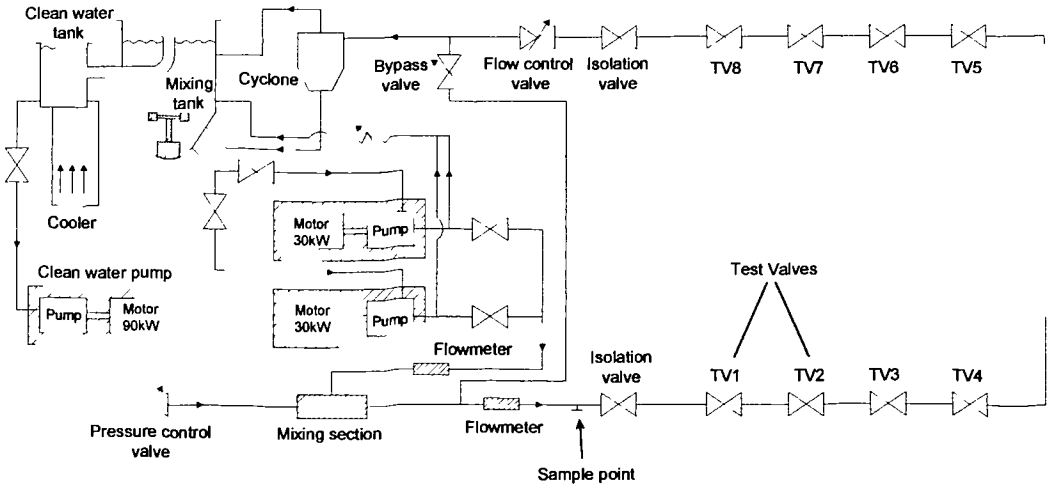

Figure 2.17 NEL low pressure abrasive flow valve test facility.

Kvenvold et al. (1994) used the medium pressure test rig of Det Norske Veritas Industry AS (DNVI) to examine erosion in choke valves. This test rig is capable of 15 bar operating pressure in 1 and 2 inch piping systems. Both oil and gas carrier phase can be supplied. McLaury et al. (1994) used a simpler version of the NEL facility to obtain erosion data for half-inch water elbows. A water and sand mixture was passed continuously through the elbows with a velocity of 2.8 ms^{-1} to obtain values of elbow penetration rate.

While the test rigs used in the above studies contained a separation stage to remove sand from the carrier phase, it is possible to design a facility without such components. Blanchard et al. (1984) examined the erosion of pipe bends using a facility in which the same sandy water was continuously circulated round the loop. Figure 2.18 shows this approach. The high pressure facility used by Graham and Ball (1989) is also without means for particle separation.

The main disadvantage in all of the test rigs mentioned so far is that they cannot easily provide the type of information ideally required by an erosion modelling tool, i.e. curves of erosion rate against particle impingement angle. One liquid-particle study that attempted to obtain such data was that of Roco and Addie (1983) in their development of an analytical model for predicting erosion in pump casings. Their approach was to simply place specimens, whose front edge was machined to a particular angle, in the middle of sandy water flow as shown in Figure 2.19. No account was made for the fact that particles are unlikely to impact the specimen at the angle between the specimen face and the mean flow direction—but rather at a range of angles due to the fluid mechanics of the liquid flow. The usefulness of the data obtained should therefore be questioned.

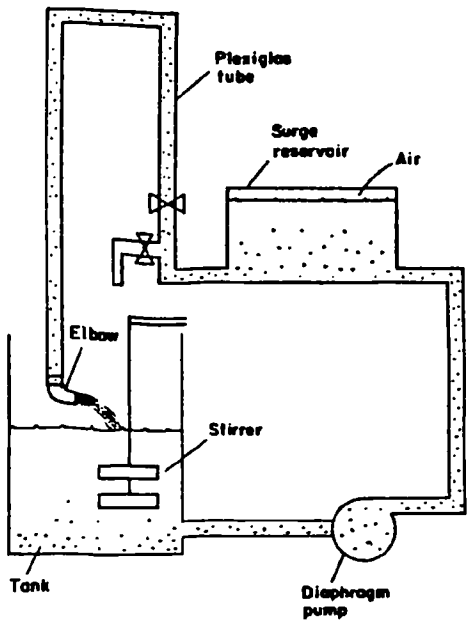

Figure 2.18 Continuous flow test loop used by Blanchard et al. (1984).

It would appear that no attempt has been made so far to obtain detailed experimental data of particle impact angle and velocity at the surface of erosion specimens in continuous liquid-particle flow loops. There are techniques that could potentially be used to obtain this data, such as Particle Image Velocimetry (PIV), Phase Doppler Anemometry (PDA), or even high speed photography.

- *2.4.4.1.2 Other liquid-particle techniques*

Another method for obtaining erosion data in liquid-particle flows is to use a nozzle to create an erosive jet impinging the surface at a particular angle. This was the method used by Forder et al. (1996) to obtain erosion-impact angle characteristics for specific materials. Benchaita et al. (1983) eroded metallic plates using a liquid-particle jet at 90^0 to the specimen surface using presumably the same test facility as Blanchard et al. (1984) without the bend. However, there will again be a wide spread of particle impact angles across the surface.

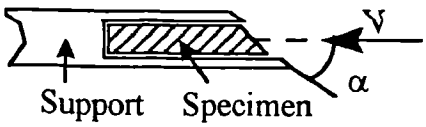

Figure 2.19 Specimen holder used by Roco and Addie (1983).

A fairly novel approach to erosion testing is the slurry pot erosion tester used consistently at the University of Kansas (Clark (1995), Wong and Clark (1993), Clark and Burmeister (1992)). The apparatus for liquid-particle erosion is shown as Figure 2.20. Cylindrical erosion specimens are held at either side of the central shaft that is driven through a toothed belt by an electric motor. Particles (generally glass beads) are added to the liquid and kept in suspension by the action of the rotating shaft. Impact velocity is estimated from the size of the crater left by the particle on the specimen surface. While this type of apparatus is convenient for laboratory tests, it again fails to provide actual measured particle impact angles at the specimen surface. The method used to predict velocity measurement appears to be successful—but will only apply to glass beads that leave a crater of measurable diameter on the specimen surface. Angular particles, such as occur in reality, tend to scratch and gouge the surface instead.

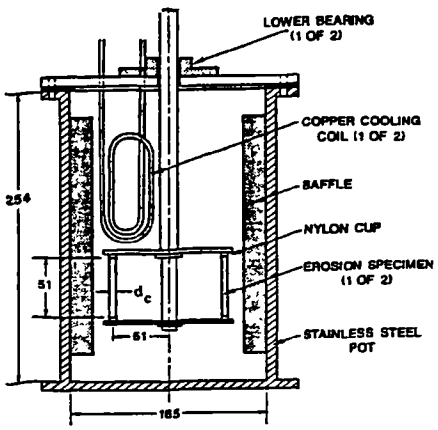

Figure 2.20 Slurry pot erosion tester of Clark (1995).

Clark (1993) has reviewed test methods and applications for liquid-particle erosion. The interesting suggestion is made that particle trajectory modelling and laboratory testing could be combined to produce more detailed data.

2.4.4.2 Gas-particle erosion studies

- *2.4.4.2.1 Sand blast type erosion testers*

By far the most popular method for obtaining primary erosion data is the sand blast type erosion tester. In this method, solid particles are entrained in a gas stream and accelerated through a nozzle before impacting specimens at the desired angle. ASTM standard G76 - 95 (1997) provides guidelines for this type of test. Figure 2.21 shows the typical layout. The nozzle length to diameter ratio should be greater than 25:1 to ensure an acceptable particle velocity distribution at the exit, with the recommended nozzle being a tube of 1.5mm inner diameter, 50mm long, manufactured from an erosion resistant material. Some means must be available whereby particle velocity can be measured, such as high speed photography or laser Doppler velocimetry. Specimen surfaces are to be prepared so as to obtain a surface roughness of 1 μm or less; specimens are weighed using an analytical balance. The standard provides data to be used in calibrating the tester as well as suggestions for test procedure and reporting.

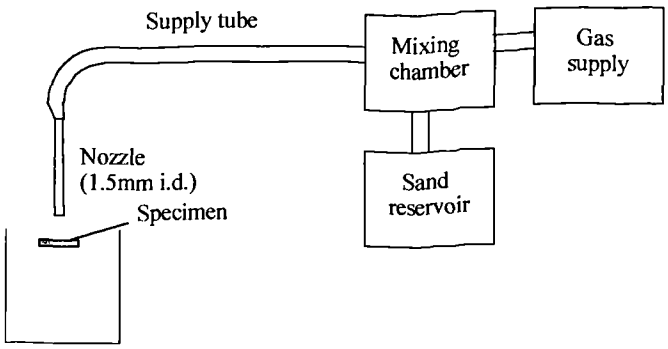

Figure 2.21 Typical layout of sand-blast type erosion tester.

Studies in which sand blast type erosion testers have been used include Hutchings (1981), Neilson and Gilchrist (1968), Shimoda et al. (1987), Reddy and Sundararajan (1986), Levy and Chik (1983), Head and Harr (1970), Jennings et al. (1976), Haugen et al. (1995), and Rao and Buckley (1984).

One of the key elements in an erosion study is the measurement of particle impact velocities. Double-flash photography has been used in a number of sand blast type tests, where velocities are estimated from the distance travelled by particles between exposures on the same piece of film. Neilson and Gilchrist (1968), Head and Harr (1970), and Smeltzer et al. (1970) have used this technique. Another technique has been the rotating disc method (Ruff and Ives, 1975), in which two rotating discs are fixed to a common shaft. Particles pass through a slit in the first disc to cause erosion of the second disc. Erosion exposures are made when the discs are stationary, and also when rotating at a known speed. Particle speeds can thereafter be calculated from the pair of marks eroded on the second disc. Hutchings (1981), Levy and Chik (1983), and Ives and Ruff (1979) all used this method.

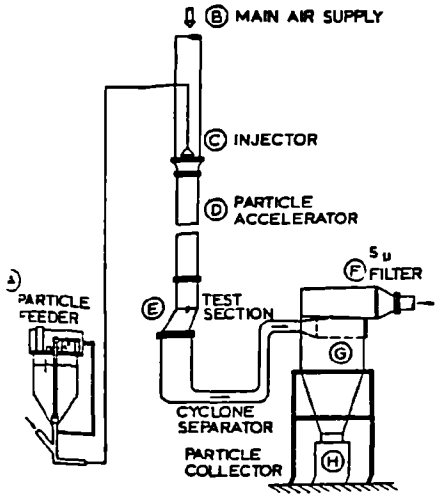

Figure 2.22 Erosion wind tunnel used by Tabakoff et al. (1979).

- *2.4.4.2.2 Erosion wind tunnels*

One criticism of sand blast type erosion tests is that they do not reproduce the fluid mechanics environment under which erosion may occur in practice. This inadequacy of the sand blast technique led to the development of an erosion wind tunnel facility at the University of Cincinnati for investigation of erosion in turbomachinery applications (Tabakoff et al., 1979). Figure 2.22 depicts this facility. The particle laden gas is accelerated

through a long tunnel before entering the test section in which the specimen is placed. Aerodynamic effects are preserved as the gas passes over and around the specimen. Particle velocities have been measured using high speed photography and Laser Doppler Anemometry in this facility.

The disadvantage with this test is that particles impacting the specimen will not necessarily do so at the angle between the specimen surface and the direction of the mean gas flow. Particles will rather tend to follow the fluid streamlines curving round the surface, particularly when the particles are light, resulting in a range of impact angles across the surface. This deflecting influence of the gas stream is significant for small particles; it does not have much effect on large particles. Tabakoff et al. (1983) carried out a numerical study to predict the particle trajectories at the specimen. Figure 2.23 shows some of their results.

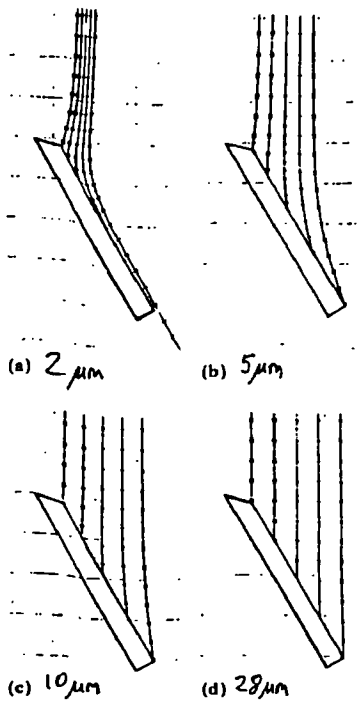

Figure 2.23 Particle trajectories in air flow. (Tabakoff et al., 1983)

Another factor found to affect the extent of erosion damage in this facility was the actual specimen size. Tabakoff (1983) used specimens of varying lengths to examine the effect. It was found that for a titanium alloy and a stainless steel, increasing the specimen length increased the erosion. Such effects arose because of the channelled gas flow over the surface. This casts doubts on the 'transferability' of test results outwith the erosion facility, as they appear to be dependent on the actual experimental set up itself. They may not be suitable for use in general purpose erosion modelling tools.

2.4.4.3 Summary of experimental techniques

The experimental methods typically used in solid particle erosion studies have been outlined. It is possible that the same technique could be used to study a whole range of factors thought to affect solid particle erosion.

One of the biggest problems with the various methods is the lack of conformity to an agreed standard. While there is a relevant ASTM standard for gas-particle erosion testing, it has been noted by others (Wood and Wheeler, 1998) that there are no instances in the literature where the guidelines have been followed. This makes it difficult to compare

material specific erosion data from different researchers, as the particular features of the test methods used may not be consistent.

Another important point made by some researchers is that the erosion experiments should recreate the fluid mechanics effects present in the real-life application of interest. This advice was followed in some of the testing carried out in the present study.

2.4.5 Erosion mechanisms

Much research has been conducted into the actual mechanisms whereby material is removed from an eroding surface. A fairly wide variety of opinions and theories have been offered over the past two decades or so, perhaps as a result of developments in Scanning Electron Microscopy (SEM) and other material examination techniques.

2.4.5.1 Ductile metal erosion

Finnie (1960) proposed that the erosion of ductile metals took place by an essentially cutting process in which the solid particle behaved in a manner similar to the tooth of a milling cutter. There has been some disagreement among authors as to the relative importance of this mechanism. Sundararajan (1991) stated that SEM examination of eroded surfaces did not indicate the ideal cutting proposed by Finnie, and went on to develop an analytical model that did not account for it. Hay and St. John (1993), however, performed gas-solid erosion studies which gave clear evidence of the significant contribution by cutting to erosive wear, when copper, mild steel, and heat treated surfaces were impacted by angular particles at 30^0. The problem is that erosion mechanisms are highly dependent on the particular combination of material, particles, and impact conditions.

Sundararajan (1991) assumed that erosion of ductile metals occurs by a process in which the plastic deformation beneath an impacting particle becomes localised near the material surface. This leads to the formation of a lip or microchip that is vulnerable to removal by further impacts. It is thought that this process is similar to the platelet mechanism described in some detail by Levy (1995).

In the platelet mechanism of erosion (Levy, 1995) material loss is said to occur by a combined extrusion-forging mechanism at all particle impacts. Impacting particles plough into the surface, extrude material, and thus form platelets or lips. Subsequent particles impacting this lip forge it into a distressed condition. It is then susceptible to removal by further impacts. Figure 2.24 shows a schematic of the surface cross-section during erosion. Initial impacts form platelets without loss of material, and as the particle kinetic energy is greater than that required to form the platelets, a work-hardened region develops beneath the softened surface region. Steady state erosion begins when the work-hardened region has

fully developed: in this condition it acts to increase the efficiency of subsequent particles impacting the surface. Platelets can then be formed, forged and removed at a steady rate. The work of Hutchings et al. (1976) using solid steel balls fired against metal surfaces appears to support the platelet mechanism theory.

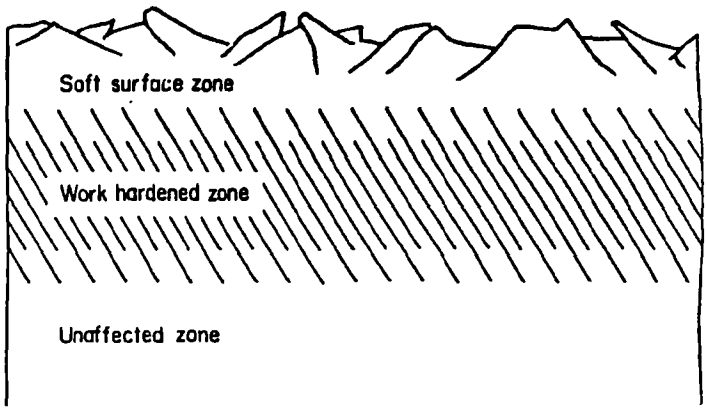

Figure 2.24 Cross section of eroding ductile metal surface. (Levy, 1995).

Jennings et al. (1976) suggested that *target melting* was the dominant erosion mechanism in tests carried out at high velocities with a variety of metals and particles. They admit, however, that results did not show which portion of the erosion process was thermal in nature (i.e. target melting), or which was mechanical in nature (e.g. cutting or platelet mechanism). The claim that target melting is the dominant mechanism is therefore thought to be somewhat dubious.

Rao and Buckeley (1984) performed a series of tests using aluminium alloy, copper, and 1045 steel specimens, being eroded by glass beads and crushed glass. They concluded that two or three erosion mechanisms could all be taking place under the one set of conditions. This is similar to the conclusion of Hay and St. John (1993) who found that no one erosion mechanism could be said to operate in all circumstances. This fact means that the analytical modelling of erosion processes is a difficult, if not impossible, task.

2.4.5.2 Erosion of brittle materials

Classically brittle materials show maximum material loss at normal impact angle and almost no material loss at shallow angles. In these materials, erosion is said to occur by the propagation and intersection of cracks produced by particle impacts (Finnie, 1960).

Bitter (1963a, b) developed an analytical erosion model that accounted for both cutting and deformation wear mechanisms. Cutting wear dominates in ductile materials, whereas deformation wear dominates in brittle materials. This deformation wear process arises when the material elastic limit is exceeded during a collision. Repeated impacts result in a plastically deformed surface layer. Deformation increases the elastic limit that will

eventually become equal to the hardness of the material and no longer be plastically deformable. In this hard and brittle condition the surface layer will be destroyed and fragments of it removed.

Levy (1995) describes the erosion of brittle scales on metals as being a process whereby the outer surface is cracked into small pieces that are separated from the underlying material by planar cracks. Continuing particle impacts remove the small cracked areas from the surface.

2.4.5.3 Summary

Research on erosion mechanisms does not appear to give conclusive results, and it is apparent that considerable effort would be required to understand all of the fundamental processes fully. As surface examination techniques become more sophisticated, it is likely that the understanding of erosion mechanisms will increase. This may be of some value in developing further analytical techniques to predict erosive wear.

2.4.6 Equations of Erosive Wear

The most important aspect of erosion research for the present study has been the development of empirical and analytical equations that will relate erosive material loss to properties of the particle-material system. Meng and Ludema (1995) reviewed wear models produced over several decades, and found 28 that were specifically for solid particle erosion. They found 33 parameters used in these equations overall, with there being an average of 5 parameters per equation. It was evident that each equation was the result of a very specific and individual approach. What has become clear from this and the work of the present study, is that no single equation exists that could be used to predict erosive wear from known standard material or particle parameters. Indeed, the conclusion can be safely drawn that no such universal analytical equation will ever be developed, and that there will always be some reliance on experimental testing to provide the empirical constants necessary in the various erosion models proposed so far.

The aim of this section is to present the models that have received most attention in the past and to give some insight into the basis of their derivation. Some of these models have been used in CFD-based erosion modelling studies.

2.4.6.1 Finnie's cutting model

The premise of the model derived by Finnie (1960) is that particles striking a ductile material at low angles of impact will remove material in a manner similar to that of a cutting tool, as shown in Figure 2.27. Erosion equations were derived by solving the equations of motion for the particle as it passes through the material surface. One of the basic assumptions made by the model is that the ratio k_f of vertical force to horizontal force on the impacting particle face remains constant throughout the cutting action. This is only true if particle rotation can be neglected. It is also assumed that the ratio of contact depth l_c, to y_t, the depth of cut, has a constant value ψ and that the particle cutting face is of uniform width. A constant plastic flow stress p_s arises upon impact.

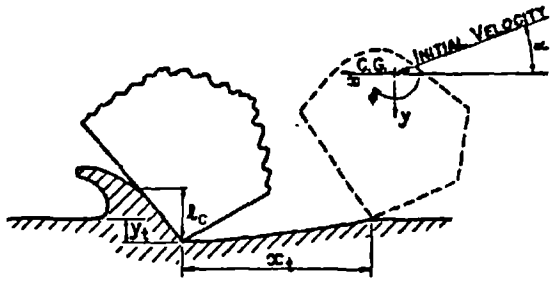

Figure 2.25 Abrasive particle impacting ductile surface. (Finnie, 1960).

If the impacting particle leaves the surface while cutting, the volume removed by a single abrasive grain of mass m_p and velocity V_p impacting at angle α_p is

$$V_M = \frac{m_p V_p^2}{p_s \psi k_f}\left(\sin 2\alpha_p - \frac{6}{k_f}\sin^2 \alpha_p\right) \text{ if } \tan\alpha_p \le \frac{k_f}{6} \qquad (2.28)$$

If the horizontal component of particle motion ceases while cutting, the volume loss is given by

$$V_M = \frac{m_p V_p^{\,2}}{p_s \psi k_f}\left(\frac{k_f \cos^2 \alpha_p}{6}\right) \text{ if } \tan\alpha_p \ge \frac{k_f}{6} \qquad (2.29)$$

When $tan\ \alpha_p$ is greater than $k_f/6$, the horizontal motion will stop during cutting and equation (2.29) will apply; otherwise equation (2.28) applies.

The analysis is extended to an overall mass of particles M_P by taking $k_f = 2$, $\psi = 2$, and assuming that only half of the particles will actually contribute to erosion. These assumptions are perhaps fairly arbitrary, but are necessary, as the quantities would prove difficult to measure. The resulting volume loss is given by

$$V_M = \frac{M_p V_p^2}{8 p_s}\left[\sin 2\alpha_p - 3\sin^2 \alpha_p\right] \qquad \alpha_p \le 18.5^0 \qquad (2.30)$$

and

$$V_M \approx \frac{M_P V_P^{\,2}}{24 p_s} \cos^2 \alpha_p \qquad \alpha_p \geq 18.5^0 \qquad (2.31)$$

The main quantity required for use of the model is the flow stress p_s, which must be obtained under conditions comparable to those of erosion. A preliminary erosion test is probably the simplest way to establish this.

The major shortcoming of the model is its inability to predict the erosion that will occur at normal impact, as can be seen from Figure 2.26, which shows relative volume removal with impact angle for three ductile materials. The model can only predict material loss adequately for impact angles up to around 45^0. Beyond this gross underprediction occurs. The model does appear to be able to predict the angle at which maximum erosion takes place.

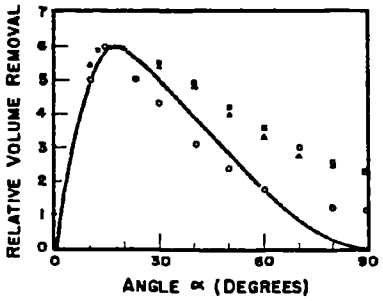

Figure 2.26 Prediction of volume removal with angle. (Finnie, 1960).

Finnie and McFadden (1978) later modified the cutting model to properly account for the dependence on velocity shown by ductile metals. They did so by relocating the resultant force acting on the particle tip to a more appropriate location, and including the equation for angular rotation in the solution. It was thought that the resulting model more correctly accounted for the effect of velocity. The results are not presented here, however, as certain parameters must be determined numerically during the calculation procedure, which makes the model considerably more complex.

2.4.6.2 Bitter's deformation model

Bitter (1963a) developed a model for the deformation erosion thought to occur at high angles of impact, particularly in brittle materials. He considered the energy balance of the plastic-elastic collision process, and showed that the energy Q_P used to produce deformation wear is given by

$$Q_P = \frac{1}{2} M_P \left(V_p - K_V\right)^2 \qquad (2.32)$$

where M_P is the total mass of impinging particles, V_p is the particle impact velocity, and K_V is the velocity of collision at which the elastic limit is just reached, i.e. the velocity below which no deformation wear occurs. The deformation wear factor ε_D is defined as the amount of energy required to remove one unit volume of material, so that deformation wear V_D (units volume loss) can be predicted by

$$V_D = \frac{\frac{1}{2} M_P \left[V_p - K_V\right]^2}{\varepsilon_D} \qquad (2.33)$$

It is the component of velocity normal to the surface that causes the deformation wear. Therefore if particles impinge at an angle other than 90^0, the deformation wear is given by

$$V_D = \frac{\frac{1}{2} M_P \left[V_p \sin\alpha_p - K_p\right]^2}{\varepsilon_D} \qquad (2.34)$$

This will be valid if $V_p \sin\alpha_p \geq K_V$. K_V can be determined for a spherical particle impacting a flat body by Hertzian contact theory (Bitter, 1963a) as

$$K_V = \frac{\pi^2}{2\sqrt{10}} y_E^5 \left(\frac{1}{\rho_p}\right)^{1/2} \left[\frac{1-q_p^2}{E_p} + \frac{1-q_b^2}{E_b}\right]^2 \qquad (2.35)$$

where: ρ_p is the density of the sphere; q_p, q_b are Poisson's ratios of sphere and flat body, respectively; E_p, E_b are Young's modulus' of sphere and flat body, respectively; y_E is the elastic load limit of the flat body.

The applicability of these equations was checked using experimental data: first for spherical cast iron pellets (0.3 mm diameter) impacting glass in a vacuum, and also for cast iron pellets (0.6 mm diameter) being blown onto glass at a higher velocity than in the first experiment. The model was shown to correlate the experimental data well, and correctly reproduced the trends observed. However, comparisons were only made at single velocities: it is not known how well the model captures the variation with velocity for a brittle material.

2.4.6.3 Bitter's cutting model

Bitter (1963b) also developed a model for the cutting wear that occurs when a particle strikes the surface at an acute angle. The particle velocity is resolved into two components: V_N normal to the surface, and V_T tangential to the surface. A shearing load will act on the body if V_N is greater than K_V, as a result of V_T. Both components decrease in the erosion process. By a rather lengthy derivation based on the assumption that the particle is spherical, Bitter (1963b) obtains the following equations for cutting wear:-

$$V_{C1} = \frac{2M_P C_\eta \left(V_p \sin\alpha_p - K_V\right)^2}{\sqrt{V_p \sin\alpha_p}} \left(V_p \cos\alpha_p - \frac{C_\eta \left(V_p \sin\alpha_p - K_V\right)^2}{\sqrt{V_p \sin\alpha_p}} \varepsilon_C \right), \alpha_p \leq \alpha_0 \qquad (2.36)$$

$$V_{C2} = \frac{\frac{1}{2} M_P \left[V_p^2 \cos^2\alpha_p - K_1 \left(V_p \sin\alpha_p - K_V\right)^{3/2}\right]}{\varepsilon_C}, \qquad \alpha_p \geq \alpha_0 \qquad (2.37)$$

where: V_{C1}, V_{C2} is the wear in units of volume loss which occurs when α_p is below and above α_0, respectively; α_0 is the angle for which V_T will just become zero when the particle leaves the body; C_η is a constant based on the particle density and material elastic limit; ε_C is the energy required to remove one unit of material by cutting wear. K_1 is based on an expression similar to (2.35).

The total wear taking place under solid particle erosion can be predicted from the set of equations (2.34), (2.36), and (2.37). Typical curves for the two idealised material types, ductile and brittle, are shown as Figure 2.27.

Two empirical constants are required by Bitter's model: the deformation constant ε_D, and the cutting constant, ε_C. These must be obtained under erosion conditions, such as through an erosion experiment using sand-blast techniques. Material properties are also required, including the particle density and elastic limit of the target material. The angle α_0 must be determined.

Comparisons between experimental erosion data and predicted results were made for the total set of wear equations (2.34), (2.36), and (2.37). Good agreement was obtained for the cases considered, although no comparison was made for the variation of erosion with impact velocity.

The validation data presented for the models of Bitter suggest that for the specific combinations considered, they could give good predictions of erosive wear. However, it is not known how well the equations reproduce variation of erosion with impact velocity, and so it may be that while they reproduce test data accurately at a particular velocity, they may not in fact be able to give similar good predictions at velocities outwith the test condition.

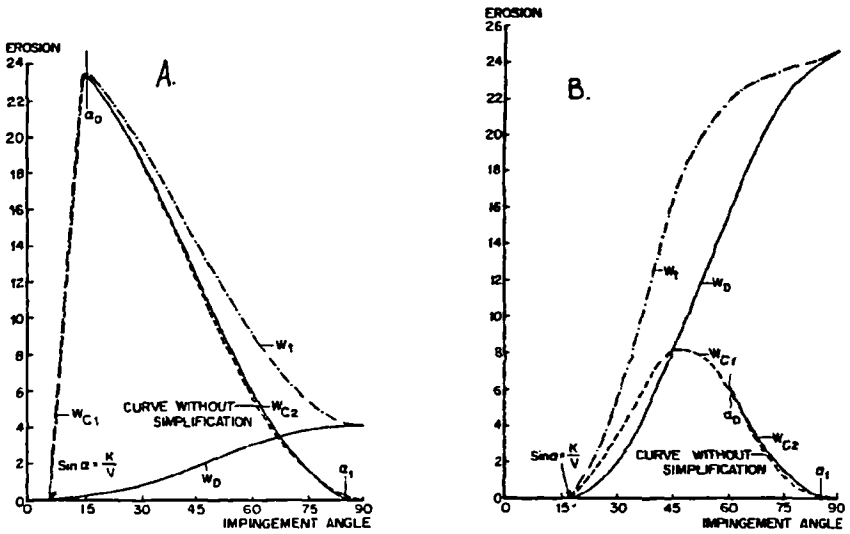

Figure 2.27 Erosion of: (a) ductile material; (b) brittle material.
(Bitter, 1963b).

2.4.6.4 Simplified model of Neilson and Gilchrist

Neilson and Gilchrist (1968) developed a simpler set of equations that could be used to correlate other experimental data. Similar factors to those considered by Bitter were accounted for, including both cutting and deformation wear. The equations are:-

$$V_M = \frac{\frac{1}{2} M_P V_p^2 \cos^2 \alpha_p \sin n_\omega \alpha_p}{\varepsilon_C} + \frac{\frac{1}{2} M_P (V_p \sin \alpha_p - K_V)^2}{\varepsilon_D}, \quad \alpha_p < \alpha_0 \qquad (2.38)$$

$$V_M = \frac{\frac{1}{2} M_P V_p^2 \cos^2 \alpha_p}{\varepsilon_C} + \frac{\frac{1}{2} M_P (V_p \sin \alpha_p - K_V)^2}{\varepsilon_D}, \quad \alpha_p > \alpha_0 \qquad (2.39)$$

where: V_M is the erosion produced by M_P mass of particles at angle of impact α_p and velocity V_p; ε_C is the unit of kinetic energy which must be absorbed by the surface in order to release one unit mass of material by cutting wear; ε_D is the corresponding energy parameter for deformation wear; K_V is the normal velocity component below which no erosion takes place in some materials; α_0 is the angle above which the residual parallel velocity component is zero; n_ω is a constant related to α_0 by

$$\alpha_0 = \frac{\pi}{2n_\omega} \qquad (2.40)$$

These equations are said to be perfectly general. Figure 2.28 shows the resulting curves for perspex. Several such curves are presented, and generally show good agreement between experiment and prediction, but do not show how well the models account for variation with velocity. Rather, it is shown that the empirical coefficients vary with impact velocity. This could make it necessary to generate relationships between the empirical coefficients and velocity themselves, which makes equations (2.38) and (2.39) less useful.

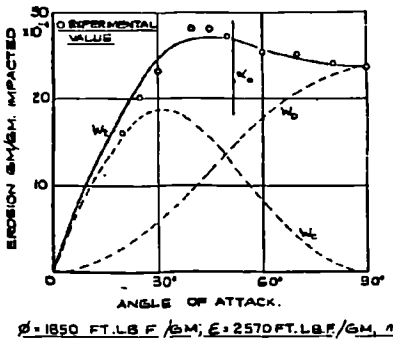

Figure 2.28 Erosion characteristic of perspex. Neilson and Gilchrist (1968).

2.4.6.5 Hutchings' fatigue model

Hutchings (1981) derived a model for erosion by spherical particles at normal impact. This was based on the criterion that a material fragment is removed when the maximum plastic strain within the fragment reaches a critical value γ_c. An average strain increment is associated with each impact, so that the mean number of impacts

required for material detachment can be predicted statistically. By assuming that all the particle kinetic energy is available to form the indentation, it can be shown that the erosion (mass loss from target per unit mass of particles) is given by

$$E_{MM} = 0.033 \frac{\alpha_k \rho_m \rho_p^{1/2} V_p^{3}}{\gamma_c^2 H_i^{3/2}} \tag{2.41}$$

where: α_k is the fraction relating the plastically deformed material around the indentation to the volume of the indentation; ρ_m is the density of the target material; ρ_p is the density of the impacting sphere; V_p is the impact velocity; H_i is the quasi-static indentation hardness. The dynamic hardness H_i can be measured from tests with single spheres. The factor α_k / γ_c cannot be measured independently but must come from actual erosion measurements.

Predicted erosion rates were compared with experimentally measured values for this model, showing that fair agreement could be obtained. Comparisons were made for a range of impact velocities, in order to justify the use of a cubic velocity exponent. It was suggested that the model did not predict the influence of particle density well enough, nor did it account for particle size, thus partly accounting for the difference between experiment and prediction.

2.4.6.6 Model of Hashish

The model proposed by Finnie (1960) did not consider any variation of the crater width during impact and erosion. Hashish (1987) extended this model to account for such variations. The particle tip involved in the cutting process is represented by a sphere in order to solve the equations of motion as the particle passes through the material. Three cases are considered:-

1. Shallow angle of impact: particle leaves material.

$$\frac{\delta v_w}{d_t^3} = \frac{7}{6}\left(\frac{V_p}{V_K}\right)^{2.5} \sin 2\alpha_p \sqrt{\sin \alpha_p}\left(1 - \frac{7}{3}\frac{\gamma_i}{\pi}\frac{\sin \alpha_p^{3/2}}{\cos \alpha_p}\right) \tag{2.42}$$

where: δv_w is the volume removed; d_t is the effective particle tip diameter; V_p is particle velocity; α_p is impact angle; V_K is defined as $V_K = \beta_1 d_t$. Equation (2.42) is valid for as long as the particle can exit the material after time $t_c = \pi/\beta_1$. β_1 is given by

$$\beta_1 = \sqrt{\frac{\pi \sigma_m d_t}{2 m_p}} \tag{2.43}$$

where: σ_m is the material flow stress and m_p is the mass of the impacting particle. γ_i in equation (2.42) is defined as

$$\gamma_t = 1 + \frac{m_p r_p^2}{I_p} \tag{2.44}$$

where: r_p is the particle radius, and I_p is the moment of inertia ($0.5 m_p r_p^2$ for spherical particles). This parameter can be used to reflect the sphericity of the particle.

The limiting angle for this mode of erosion α_0 can be found from

$$\tan\alpha_0 \sqrt{\sin\alpha_0} = \frac{3\pi}{14\gamma_i}\sqrt{\frac{V_K}{V_p}} \tag{2.45}$$

2. Intermediate angle of impact: V_T becomes zero in the rebounding phase.

For the range $\alpha_0 < \alpha_p < \alpha_1$ the volume removed is given by

$$\delta v_w = \frac{\pi d_t^3}{4\gamma_t}\left(\frac{V_p}{V_K}\right)^2 \cos^2\alpha_p \left(1 + \gamma_i \frac{\alpha_p - \alpha_0}{\alpha_1 - \alpha_0}\tan^2\alpha_p\right) \tag{2.46}$$

where α_1 is given by

$$\tan\alpha_1 \sqrt{\sin\alpha_1} = \frac{3}{7}\frac{\pi}{\gamma_t}\sqrt{\frac{V_K}{V_p}} \tag{2.47}$$

3. High angle of impact: V_T becomes zero in the impacting phase.

Volume loss is given by

$$\delta v_w = \frac{\pi d_t^3}{4}\left(\frac{V_p}{V_K}\right)^2 \sin^2\alpha_p \left(2 - \frac{90-\alpha_p}{90-\alpha_1} + \frac{1}{\gamma_t \tan^2\alpha_p}\right) \tag{2.48}$$

It is possible to include the effect of a threshold velocity in these equations if required.

As no comparisons were made between the results of this model and actual experimental data, it is difficult to assess the effectiveness of the method. Some parts of the model were used by Forder et al. (1998) in their CFD-based erosion modelling, with reasonable results being obtained.

2.4.6.7 Comprehensive model of Sundararajan

One of the criticisms of previous models is that they do not adequately account for all observed effects in ductile erosion. Sundararajan (1991) developed a comprehensive model for the erosion of ductile methods, based on the assumption that erosion occurs due to the localisation of plastic deformation, leading to lip formation and subsequent fracture. This concept is combined with the energy absorption theory developed by Brach (1988) for an impacting particle to produce the overall model.

For erosion at normal impact, it can be shown (Sundararajan, 1991) that

$$E_{MM} = \left(2^{n_s} C_\lambda / n_s C_p\right) F(t) V_p^2 \sin^2\left(1 - e^2\right) \qquad (2.49)$$

where: C_λ is a constant characterising the temperature dependence of the flow stress; n_s is the strain hardening exponent; C_p is the specific heat of the target material; and e is the restitution coefficient of the target material. F(t) is a numerical constant. Restitution coefficient is defined as the ratio of the normal component of rebound velocity to the normal component of the initial velocity of the solid particle. An expression for e is given by Tirupataiah et al. (1990) as

$$e = 1.9 H_V^{5/8} / E_e^{1/2} \rho_p^{1/8} V_p^{1/4} \qquad (2.50)$$

where: H_V is the hardness of the target material; E_e is the effective elastic modulus of the particle-eroding material system; and ρ_p is the particle density.

For erosion by particles impacting obliquely, the model of shear energy absorption developed by Brach (1988) is combined with localisation theory to produce the following equation for erosion rate:-

$$E_{MM} = \left\{C_\lambda (n_s + 1) V_p^2 / 2^{2-n_s} n_s C_P (1 + \lambda)\right\}\left\{\mu_{fr} / \mu_c\right)\left(2 - \mu_{fr} / \mu_c\right)\cos^2 \alpha_p \quad (2.51)$$

Where: λ is a particle shape factor, defined as r_p^2 / k_G^2, where k_G is the radius of gyration of the particle and r_p is the radius; μ_{fr} is the coefficient of friction; μ_c represents the maximum value of μ_{fr}. If $\mu_{fr} < \mu_c$, sliding exists between the particle and the target surface. If $\mu_{fr} = \mu_c$, sliding stops and the particle may roll.

As a first approximation, the total erosive wear due to particle impact is given by summing the results of equations (2.49) and (2.51). No direct comparisons were made between predictions made with this model and experimental data. It is therefore not known how well the model directly predicts erosion for real conditions.

Although the model of Sundararajan (1991) appears to be capable of explaining a large number of observed phenomena, it still has some serious shortcomings that were highlighted by Hay and St. John (1993). It was shown that the assumption made by Sundararajan (1991) that all material removed is strained to the critical strain is not always valid for erosion by angular particles. Sundararajan (1991) also assumed that $\lambda = 0$ for spherical particles—which is not physically correct (Hay and St. John, 1993). The model does not therefore truly account for particle shape, and must be modified to represent erosion behaviour with spherical particles.

The work of Hay has shown that it is difficult to develop a single comprehensive analytical model for solid-particle erosion of metals and alloys, as no single mechanism can be said to operate.

2.4.6.8 Simple model used by Haugen et al.

Haugen et al. (1995) performed an extensive experimental study to determine appropriate coefficients for an erosion equation of the form

$$E_{MM} = M_P K_m F(\alpha_p) V_p^n \tag{2.52}$$

where: M_P is the mass of sand hitting the target; K_m and n are constants which depend on the material and are determined by experiment; V_p is the particle impact velocity; $F(\alpha_p)$ is a function of the particle impact angle α_p. The form given for results based on carbon steel is

$$F(\alpha_p) = \sum_{i=1}^{8} (-1)^{(i+1)} A_i \left(\frac{\alpha_p \pi}{180} \right)^i \tag{2.53}$$

where the coefficients A_i depend on the type of material.

The main disadvantage with this type of model is that a large amount of experimental testing must be performed to obtain the required parameters. However, it is simple to implement, and appears to give useful results in engineering design simulations for choke valves. No detailed comparisons with experimental data are given for this model.

2.4.6.9 Statistical method used by Grant and Tabakoff

The philosophy adopted by Grant and Tabakoff (1975) was that erosion by small particles has to be described in a statistical sense due to the changing nature of the process with time. The eroded surface will gradually be covered with craters, so that the actual local impact angle between the particle and the surface could vary considerably from the geometric average.

Experimentally derived equations for 200μm quartz particles striking annealed 2024 aluminium alloy (under high speed gas flow conditions) are presented as follows. Restitution ratios are given by

$$V_{N_2}/V_{N_1} = 0.993 - 1.76\alpha_p - 1.56\alpha_p^2 - 0.49\alpha_p^3 \tag{2.54}$$

$$V_{T_2}/V_{T_1} = 0.988 - 1.66\alpha_p + 2.11\alpha_p^2 - 0.67\alpha_p^3 \tag{2.55}$$

Erosion per unit mass of impacting particles is given by

$$E_{MM} = K_1 f(\alpha_p) V_p^2 \cos^2 \alpha_p \left[1 - R_T^2\right] + f(V_p) \tag{2.56}$$

$$R_T = 1 - 0.0016 V_p \sin \alpha_p \tag{2.57}$$

$$f(\alpha_p) = \left[1 + CK(K_{12} \sin 2\alpha_0)\right]^2 \tag{2.58}$$

$$f(V_p) = K_3 (V_p \sin \alpha_p)^4 \tag{2.59}$$

where: K_1, K_{12}, K_3 are empirical constants depending on the particle-target system; C and K are not defined.

These equations are quite different to those of other models, in that the only parameters appearing are either particle impact properties or empirical coefficients. There does not appear to be any attempt to introduce underlying theoretical relationships. This approach is therefore similar to that of Haugen et al. (1995), although the resulting equations have a greater level of complexity. Both these studies support the suggestion that erosion equations can be developed based on empirical data alone.

Predicted erosion rates using equation (2.56) were compared with the underlying experimental results used to create them. Good agreement is observed between predicted and measured over ranges of both velocity and impact angle. Application of these equations to actual erosion predictions for engineering scenarios gave favourable results.

2.4.6.10 Summary to erosion equations

Only some of the erosion equations that appear to be most popular have been presented here. The equations vary widely in their form and content, and all depend to some extent on parameters that can only be obtained by specific erosion testing of materials. Some of the equations effectively reduce to curve fits of experimental data, which raises a question as to why the analytical development was necessary in the first place. Where several empirical coefficients (or erosion related parameters) are required, it is less likely that the erosion model could be transferred to cases other than those for which the equations were specifically derived. Thus the equations of Grant and Tabakoff (1975) could not readily be adapted to the case of liquid-particle erosion in choke valves as they were originally developed in the context of high speed turbomachinery flows.

A few of the studies investigated have adopted the approach of simply finding appropriate curves and surfaces to represent experimental data. Others have made some form of analysis into the way in which erosion will proceed. In the present study, the only parameters to come from the CFD simulation will be particle impact velocity and angle,

particle mass flowrate, and particle size (if a size distribution is specified at the inlet). Therefore it may not be essential to develop erosion equations that consider parameters other than these. Material parameters such as hardness and tensile strength etc. have been found to be poor indicators of erosion resistance in most cases, and so it may not be too important that the final erosion equations take these parameters into account. For these reasons, the approach to be adopted in the present study will be to find equations relating erosive wear to particle impact angle and velocity by considering fundamental experimental erosion data only. An attempt has been made to use the model of Neilson and Gilchrist (1968) in conjunction with experimental data obtained in the present study. This will be considered in a later section.

2.4.7 Summary to solid particle erosion

This section has attempted to outline the subject of solid particle erosion by considering first the two classic types of material (ductile and brittle); discussing some of the factors that influence erosive wear; describing some of the experimental techniques used in the past to investigate erosive wear; presenting briefly an indication of the possible mechanisms underlying erosion; and finally covering the more popular models that attempt to predict erosion from various parameters. Several conclusions can be drawn from this review. These are:-

1. Particle impact velocity is the most important factor in solid particle erosion, as the energy for material loss must come from the kinetic energy of the impacting particle. It will be important to capture the relationship between particle impact velocity and erosion for a particular material.
2. The range of experimental test techniques means that specific erosion data obtained for a particular material in one facility may not be comparable to data obtained in another facility. There does not appear to be much conformity amongst researchers in terms of facility design. This *means that further erosion testing will be required in the present* study, to ensure consistency between data for different types of material.
3. It is essential to know accurately the velocity and angle with which particles impact in experimental test methods. While this is possible for gas-particle test facilities (using optical and laser methods), it is almost impossible for liquid-particle facilities. The only alternative for liquid-particle facilities is to model the test method using CFD, and to make estimates of conditions at impact from that. There are no studies in the literature where a *free surface* liquid jet has been modelled in the context of erosive wear.

4. None of the erosion equations identified so far can be readily transferred to the CFD-based erosion modelling tool. All will require the availability of specific erosion test data for the materials of interest, and may not necessarily capture the erosion vs. velocity relationship indicated by the experimental data. It may be that simply finding equations that represent the underlying experimental data alone, should produce results as good as some of the more complicated expressions available.

2.5 Summary and Conclusions

In considering CFD-based erosion modelling studies carried out in the past, it has been noted that no studies have yet been published in which the component of interest has been the Multiple Orifice Sleeve choke valve. This has likely been a result of limited meshing capabilities of some of the commercial packages used by previous researchers. One of the key objectives of the present study is therefore to address this deficiency in current knowledge by applying unstructured hybrid meshing techniques to the erosion modelling of MOS choke valves. The work should provide useful information on the CFD modelling of such complicated valves generally.

Although some studies have shown excellent quantitative agreement between predicted erosion and experimental, these have tended to be for specific geometries such as pipe bends or straight section chokes. There has been no real quantitative comparison of CFD predictions with actual test data for more complicated geometries. This deficiency is again one that will be addressed in the present study.

Many researchers have attempted to develop complicated analytical expressions for erosive wear, none of which can be considered suitable for general purpose, universal use. In previous CFD-based erosion modelling studies, the trend has been to use one of these analytical expressions, with some adjustments to the empirical coefficients being made where necessary. An alternative approach will be taken in the present study, in that instead of using one of the previously developed models, equations will be sought that represent the experimental data directly. This should simplify the implementation of such equations in the CFD software.

3.0 Erosion Testing of Choke Valve Materials

3.1 Introduction

CFD-based erosion modelling tools require fundamental material erosion characteristics before an estimate of wear lifetime can be given. At present the only valid method for obtaining an erosion characteristic is to conduct experimental erosion tests on samples of the specific material in question, and to use this data in the construction of an equation covering the range of angles and velocities of interest.

A number of choke valve materials have been supplied for use in the current test programme. The industrial sponsor indicated which materials were most commonly used in choke valve manufacture, and arranged for delivery of appropriately sized samples made from each of the materials. Ten different materials were chosen for testing in total, and are listed as follows:-

1. AISI 4130
2. ASTM A564 630 (17.4 PH) 75k
3. ASTM A564 630 (17.4 PH) 105k
4. ASTM A182 F51 (Duplex)
5. ASTM A182 F55 (Duplex)
6. AISI 4130/Inconel 625 Overlay
7. Inconel 718
8. Tungsten Carbide SMS 25A
9. Tungsten Carbide VC-808
10. Tungsten Carbide DC(Z)05

Twenty samples per material were supplied for the first seven materials listed; fewer samples per material were supplied for the tungsten carbides. Not all materials were considered to have the same level of importance in the test programme—some were tested to a greater extent than others. Results for the testing of material 6 will not be presented as failures of the Inconel 625 overlay (thin metal layer on top of the AISI 4130 substrate) occurred during testing, and time was not available to investigate the reasons for this. Samples were generally 50 mm in diameter, and between 5.5 and 8 mm thick, depending on the material density. They were constrained to be less than 200 g in weight to ensure they could be measured on the analytical balance used in the tests. A material number and letter uniquely identified every sample. Thus '1A' represented AISI 4130 Sample A, and so on.

Materials 1 to 5 are fairly similar in that they are each some form of alloy steel. Comparative erosion studies in the past have not tended to consider such a narrow range of materials—the tendency is to use one or two of these more common materials, and to introduce more exotic alternatives for comparison. However, if solid particle erosion becomes the main factor in deciding which material to use, the valve manufacturer needs to know the difference in erosion performance between the available materials—even different grades of stainless steel. There are other factors driving material selection besides erosion, such as corrosion due to fluid properties, strength requirements due to high pressures, and so on. Testing this group of similar materials will provide useful information for the manufacturer in deciding whether any particular grade of steel has an advantage over another—at least for erosion conditions.

In summary, the specific objectives of this test programme were to:-

1. Test a range of choke valve materials using both air- and liquid-sand jetting techniques. Particle impact angle and velocity to be varied in both types of test.
2. Construct appropriate empirical erosion equations using the erosion data for each material (Chapter 4).
3. Model test apparatus using CFD techniques to see if additional information can be extracted from the test data (Chapter 5).

The relevant properties of the various materials tested are given in Table 3.1 below. Some of the hardness values were obtained by actual repeat measurements during the course of the study (indicated by *); others are values supplied by the manufacturer. Densities given for the three tungsten carbides are values supplied by the manufacturer; the rest are estimated values based on dimensional and mass measurements of selected samples. Surface roughness measurements represent average roughness taken over two or more samples. These measurements were made using a Form Talysurf 120L at the University of Southampton. Surface roughness should ideally have been consistent across all samples for all material types. This was not achieved during sample preparation (outwith the author's direct control).

The hardness values given in the table for tungsten carbides SMS-25A and VC-808 were obtained by converting from the Rockwell hardness number given by the manufacturer. As it is not known how true the conversions hold at such high hardness values, the original Rockwell hardness numbers are also given.

Table 3.1 Selected Material Properties

Material	Hardness (H_V)	Density (kg/m^3)	Surface roughness R_a (μm)
1. AISI 4130	240.9*	7790	0.28
2. ASTM A564 630 (17.4 PH) 75k	305.3*	7790	0.22
3. ASTM A564 630 (17.4 PH) 105k	335.4*	7730	0.016
4. ASTM A182 F51 (Duplex)	239.7*	7780	0.016
5. ASTM A182 F55 (Duplex)	279.7*	7740	0.012
7. Inconel 718	409.5*	8160	0.21
8. Tungsten Carbide SMS 25A	~1853.4 (HR_a = 92.0)	14930	0.015
9. Tungsten Carbide VC-808	~2243.5 (HR_a = 93.7)	14340	0.0071
10. Tungsten Carbide DC(Z)05	1817	15010	0.0096

3.2 Liquid-Sand Erosion Testing

The influence of a liquid on sand particles entrained within its flow will be significantly different from the effect of a gas. For this reason, it is important to account for both liquid and gas carrier phases when considering the solid particle erosion of specific materials. One drawback with liquid-sand erosion testing, however, is the difficulty in achieving high impact velocities without considerable expense. The test rig used in the present study operates under atmospheric conditions, and provides a maximum impact velocity of around 26 m/s.

3.2.1 Experimental Apparatus and Procedure

The liquid-sand slurry rig of Southampton University has been used to obtain results in the present study. Figure 3.1 depicts this test rig; Figure 3.2 depicts the sample holder.

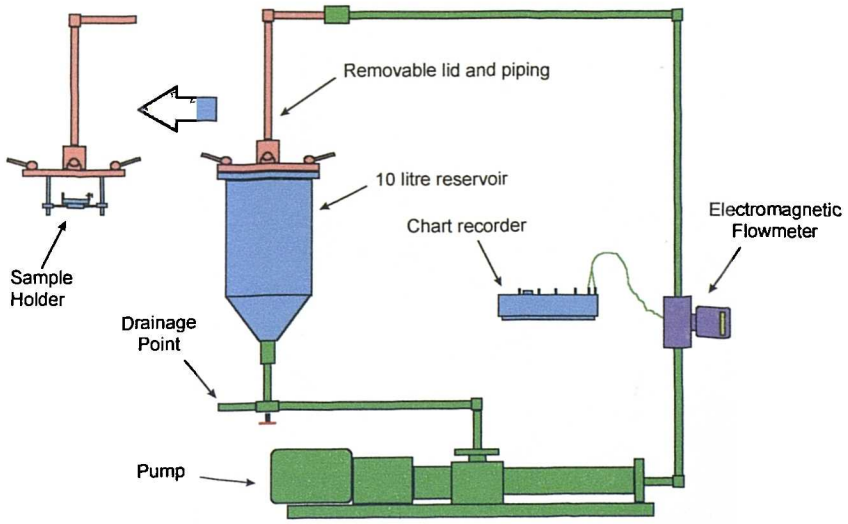

Figure 3.1 Layout of slurry rig.

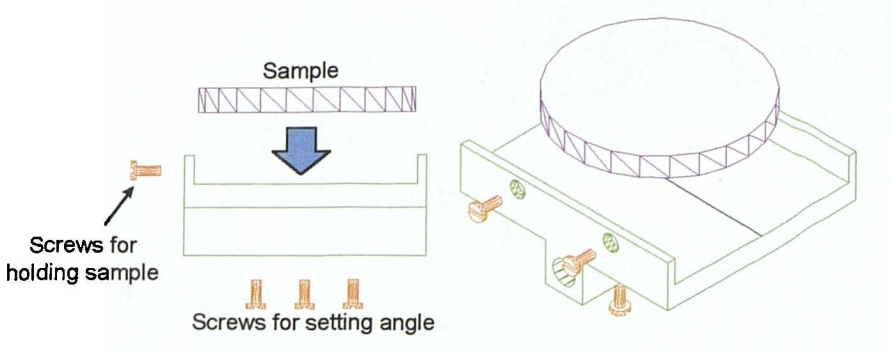

Figure 3.2 Sample holder for slurry rig.

Samples for testing are held in the sample holder beneath the top plate of the reservoir. This top plate, and a section of pipe attached to it, can be removed to give access to the reservoir and erosion specimen (Figure 3.1). Samples can be set to different impact angles and stand-off distance by adjusting the position of the sample holder. In this study, stand-off distance has been measured between the bottom surface of the top plate and the centre of the estimated jet impact site on the specimen. The actual distance from nozzle exit to specimen surface is about 10 mm greater than this value. Various nozzles can be fitted within the nozzle chamber above the top plate: a diameter of around 6 mm was used in the present study.

Water and sand were added to the reservoir before testing. The variable speed screw-type pump circulates this mixture continuously, and the flowrate is measured using an electromagnetic flowmeter. The output signal of the flowmeter is connected to a chart recorder so that an average flowrate can be determined from the continuous trace. The chart recorder was generally used at the start of a test to ensure the correct flowrate had been achieved.

The experimental test procedure can be summarised as follows:-

1. Specimen weighed to within ±0.02 mg using a Mettler AT201 analytical balance.
2. Approximately 9 kg of water was measured using a spring balance, and poured into the reservoir.
3. 189g of the selected grade of sand was added to the water in the reservoir. The pump ran while sand was being added. This amount of sand gave a concentration of approximately 2.1% by mass (in conjunction with 9 kg of water).
4. Specimen was set in the holder at the desired angle and stand-off distance (37mm ± 2mm). Angles were set using an angular Vernier gauge to within $\pm 2^0$ (estimated).
5. Top plate and pipe were placed over the reservoir. The pipe connected to the upstream piping through a coupling—four fasteners held the top plate on the reservoir.

6. Pump speed was set as necessary to give the required flowrate, which was recorded at the start of each test on the chart recorder. After ensuring correct flowrate, the rig was left running for the required period.
7. On completion of the test period, the pump was stopped, sample removed from the holder, and the rig flushed with clean water. Generally three complete flushings were carried out after each test.
8. Specimen was allowed to adjust to room conditions before re-weighing on the analytical balance. In general, several weighings were conducted for each sample to give an average final value.

3.2.2 Calibration of electromagnetic flowmeter

It was necessary to manually calibrate the electromagnetic flowmeter to ensure there had been no significant shift in reading since the previous calibration (date unknown). As removing the flowmeter from the test rig to calibrate in a separate facility was not an option, a manual method had to be devised. Figure 3.3 illustrates the method used.

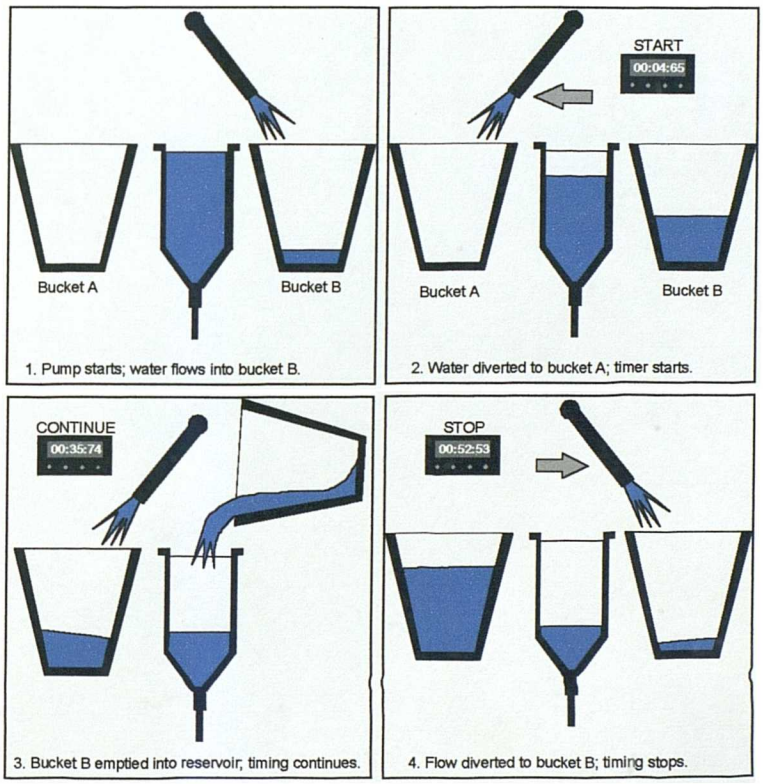

Figure 3.3 Illustration of method used in flowmeter calibration.

After completing the procedure in Figure 3.3, the mass of water in bucket A was weighed using a spring balance. The spring balance was itself calibrated in conjunction with both buckets to provide a more accurate measurement of water mass. Chart recorder reading is related to volume flowrate by the following equation:-

$$\text{Flowrate (litres/min)} = 0.26094 * \text{Chart position (mm)} - 2.33929 \qquad (3.1)$$

The chart recorder pen was set to 10 mm at rest.

3.2.3 Results from slurry testing

The complete set of tests carried out in the liquid-sand rig are summarised in Table 3.2. The numbers shown for each condition indicate the number of actual tests that were carried out for the specific material/test condition combination. Some of these were continuation tests using the same sample. Note that there were two separate stages to the test programme: the first phase took place between July to September 1999; the second phase between January and February 2000. This meant that some identical tests had to be carried out in both phases to assess the repeatability of results.

Table 3.2 Tests carried out on liquid-sand rig.

		Liquid-Sand Rig																			
		Low Energy					Medium Energy					High Energy					Highest Energy				
No.	Material / Impact Angle (deg)->	30	45	60	75	90	30	45	60	75	90	30	45	60	75	90	30	45	60	75	90
1	AISI 4130					1	1				1	1		1		1					1
2	ASTM A564 630 (17.4 SS) 75k						1		1		2	1				7					1
3	ASTM A564 630 (17.4 SS) 105k	1				1					7					1					
4	ASTM A182 F51 (Duplex)	1				1	1	1	1	1	1					3					
5	ASTM A182 F55 (Duplex)	1				1					1					1					
6	AISI 4130 / Inconel 625					1										1					
7	Inconel 718	1				6	1		1		2	1		1		2					2
8	Tungsten Carbide SMS-25A					1										4					
9	Tungsten Carbide VC-808					1					5					4					
10	Tungsten Carbide DC(Z)05					1															

Key: 1 = Carried out in Phase 1.

1 = Carried out in Phase 2.

2 = Carried out in both phases.

Four different energy levels have been defined in the above table. These represent the mean particle kinetic energy at impact for each energy level. An average particle diameter is used to calculate these mean values from

$$KE_p = \frac{1}{2} m_p V_p^2 \qquad (3.2)$$

where V_P is the mean particle impact velocity (ms^{-1}), and m_P is the typical particle mass (based on mean diameter for a particular sand grade). V_P is taken to be the average velocity of the liquid passing through the nozzle. Table 3.3 gives estimated particle kinetic energies for each of the four levels. Note that the "Highest Energy" level was not repeated systematically as the rig could not achieve the flowrate required at all angles of impact. The sand grade referred to in Table 3.3 is the supplier's designation, and is presented here for purposes of identification.

Table 3.3 Energy levels used in slurry erosion testing.

Energy Level	Sand Grade	Mean d_P	Avg. V_P	Est. KE_P
		(μm)	(m/s)	(J)
Low	110	135	15.19	3.97E-07
Medium	50	235	16.55	2.48E-06
High	50	235	22.60	4.63E-06
Highest	50	235	24.48	5.43E-06

The general approach in material testing was to run a test for long enough to establish steady state erosion of the particular material being considered. This meant that some tests had to be repeated initially to establish the required length of time for later tests.

3.2.3.1 Tests to determine times for achieving steady-state erosion

A sample (reference 7A) of Inconel 718 was eroded under low-energy conditions for a total of 300 minutes. The sample was removed every 60 minutes for weighing; sand was changed after each 60 minute interval. Another sample (7B) was eroded under similar conditions for 180 minutes, with no sand change. The results of these tests are plotted in Figure 3.4. Note that the unit of erosion rate is mass loss in mg (of eroded material) per gram mass of erodent (sand particles) impacting the specimen.

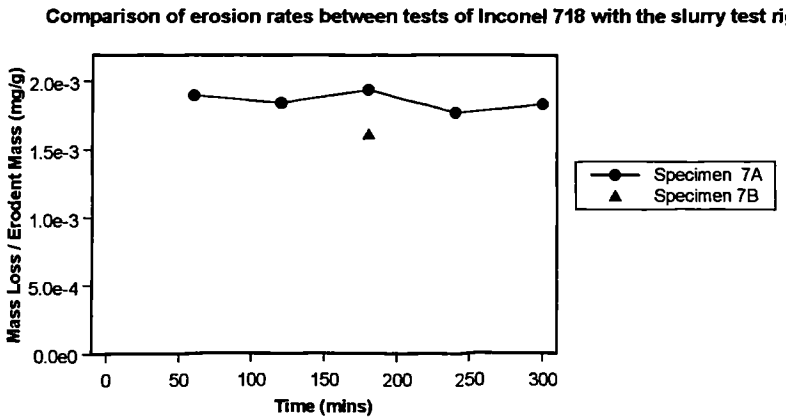

Figure 3.4 Erosion of Inconel 718; liquid-sand rig; low energy.

The fact that sample 7B eroded at a lower rate than sample 7A suggests that some sand degradation took place while testing 7B. Sand was changed every hour when testing 7A, but no sand change took place during testing of 7B.

Figure 3.5 shows results from the incremental testing of 17.4PH 105k at medium energy, with no sand changes. The erosion rate is observed to decrease from the initial level, before increasing slightly. There will be some reduction in erosion rate due to sand degradation. It is also possible that the erosion rate will be affected by gradual changes in shape of the erosion crater.

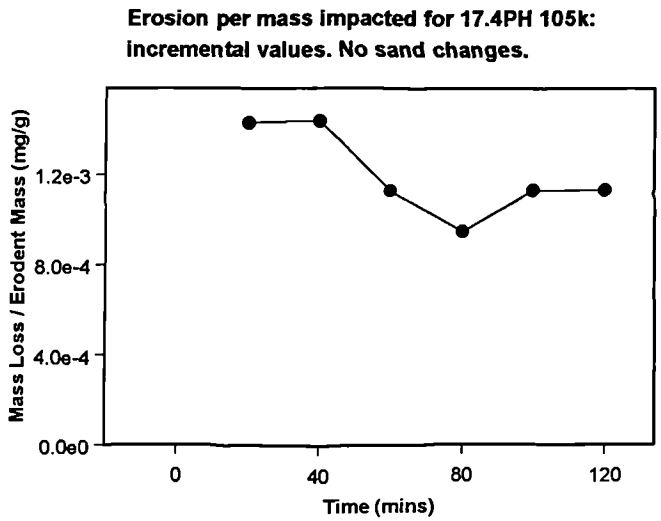

Figure 3.5 Incremental erosion of 17.4PH 105k with no sand changes; liquid-sand rig; medium energy.

Examination of these results suggests that test times of 300 minutes for low energy tests, and 60 minutes for medium energy tests, will be acceptable. High energy tests in the liquid-sand rig generally lasted for 20 minutes, as by this time significant material wear had taken place for most materials. The only materials not to erode sufficiently in these time scales were the tungsten carbides.

Steady-state erosion of tungsten carbides may not have been achieved in all tests with the liquid-sand rig. Figure 3.6 shows cumulative mass loss versus time for Tungsten Carbide SMS-25A when eroded at the high energy level. Steady state erosion has been achieved. Figure 3.7 shows cumulative mass loss for Tungsten Carbide VC-808 at two energy levels. Steady state erosion is observed at the high energy level. At medium energy, however, mass loss per test is so low that the uncertainty of mass measurement has significant influence on observed trends (i.e. scatter in readings could be greater than actual mass loss). These series

of tests indicate that steady state erosion was only achieved at the high energy level in the liquid-sand rig for tungsten carbide VC-808.

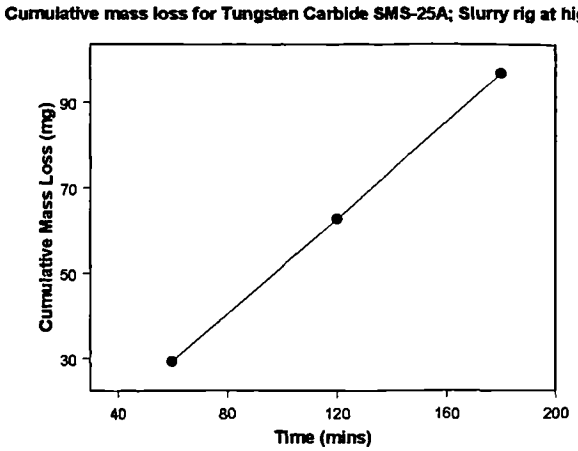

Figure 3.6 Erosion of Tungsten Carbide SMS-25A; liquid-sand rig; high energy.

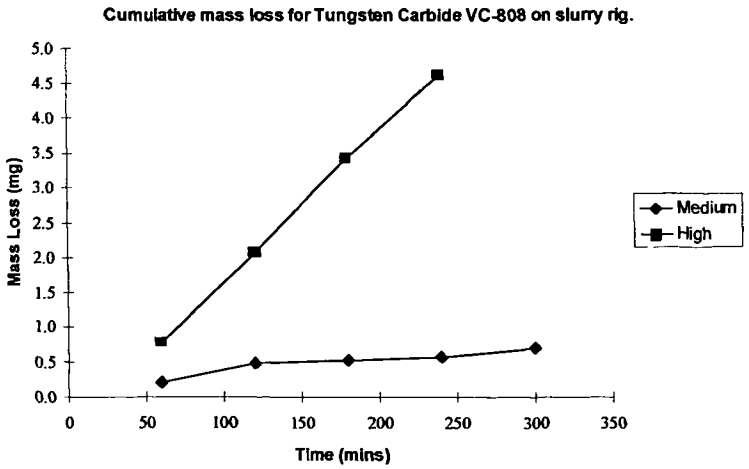

Figure 3.7 Erosion of Tungsten Carbide VC-808; liquid-sand rig; medium and high energy.

3.2.4.2 Repeatability

It is desirable to have testing techniques that give consistent results for repeat tests. Some materials were tested under the same conditions more than once to give an indication of repeatability. Significant differences have been found between results obtained in Phase 1 and results obtained in Phase 2 for identical test conditions. Table 3.4 lists high energy tests for 17.4PH 75k: there is a considerable reduction in erosion rate between the two phases of the test programme. Only one result was obtained in Phase 1 for this particular test, but the erosion rate of 6.83 mg/min is not approached by any of the Phase 2 results. Figure 3.8(a)

plots the data in Table 3.4: results obtained in Winter 2000 have been combined to give a single average value. Figure 3.8(a) also shows erosion rates of Duplex F51 samples. Again a significant reduction in erosion rate can be observed.

Several checks were made to eliminate any obvious reasons for the drop in erosion rate between the two phases. No changes had been made to the test rig at any time. The chart recorder used in the second phase of testing was the same as that in the first (and in any case a check calibration of the flowmeter was performed). Nozzle diameters were measured periodically to ensure no significant wear had taken place. Orientation of the top plate and influence of the sample holder (a new one was manufactured between the phases) were also considered. None of these factors were thought to cause reduction in erosion rate.

Table 3.4 *High energy tests of 17.4PH 75k at 90 degrees in slurry rig.*

Date	Time	Velocity	Mass loss (mg)	Erosion Rate (mg/min)	Specimen ID
8/6/99	20	22.61	136.59	6.83	2K
1/25/00	20	22.61	87.34	4.37	2H
1/25/00	20	22.61	81.49	4.07	2L
1/25/00	20	22.61	85.81	4.29	2T
1/26/00	20	22.62	89.25	4.46	2Q
1/27/00	20	22.45	78.80	3.94	2Q

The only other factor that would affect erosion rate significantly is sand size distribution. However, there was no reason to think that this should have changed to such an extent between the two test phases. As sand size distributions were not obtained in Phase 1, it was not possible to perform a comparison between Phases 1 and 2 in this regard. It is entirely likely that sand in both phases came from the same bags, which reduces the chance of size distributions being appreciably different.

Results from medium energy tests in both phases were also compared, as shown in Figure 3.8(b). This again shows a reduction in erosion rate for 17.4PH 75k, but a slight increase for 17.4PH 105k.

There is some inherent scatter in results obtained with the slurry rig, which makes it difficult to draw conclusions regarding changes in results between the two test phases. However, there does appear to be a definite reduction in high energy erosion rates, that cannot simply be dismissed as inherent scatter. Examination of eroded samples using an SEM (Scanning Electron Microscope) may have provided an explanation for the difference.

It is proposed to overlook the difference in erosion rates between the two test phases, and to view the results as a continuous set having error bands wide enough to encompass all the data.

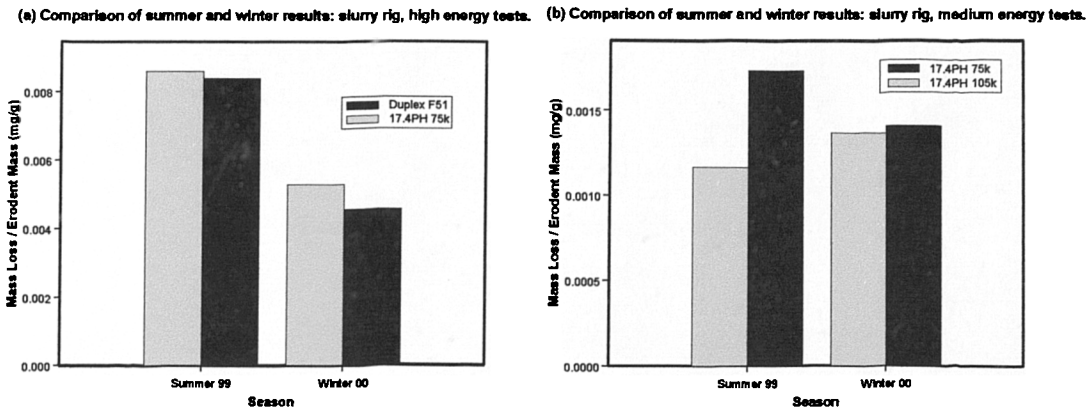

Figure 3.8 Comparison of results between test phases: high energy and medium energy.

3.2.4.3 Data at 90 degree impingement: metallic materials

As more tests were carried out for 90^0 impact angle than other angles, the 90^0 case will be considered first. All the data at 90^0 for the metallic materials (i.e. all materials excluding the tungsten carbides) has been plotted as a function of impact velocity in Figure 3.9. For conditions where more than one test has been performed (e.g. Inconel 718 at Medium Energy) a simple average has been taken of both the impact velocity (hence impact energy) and erosion rate. This may have some implications for the relative order of erosion resistance that materials exhibit, but at the same time it must be stressed that the level of scatter in the erosion data could be higher than the error introduced through taking average values. It would be necessary to repeat each test condition several times before an accurate representation of erosion resistance order could be obtained. The time and resources were not available to do so in the present study.

Erosion data obtained at the low and medium energy levels lies closely grouped together in the respective bands, and do not show any significant differences in erosion rates for the various materials. It could be postulated that to differentiate between material performance at low and medium energy conditions is not valid, as the scatter inherent in the erosion results could be of a larger scale than the actual differences in erosion rate between the materials. In effect, all the metallic materials behaved similarly at the low and medium energy levels—based on the currently available data.

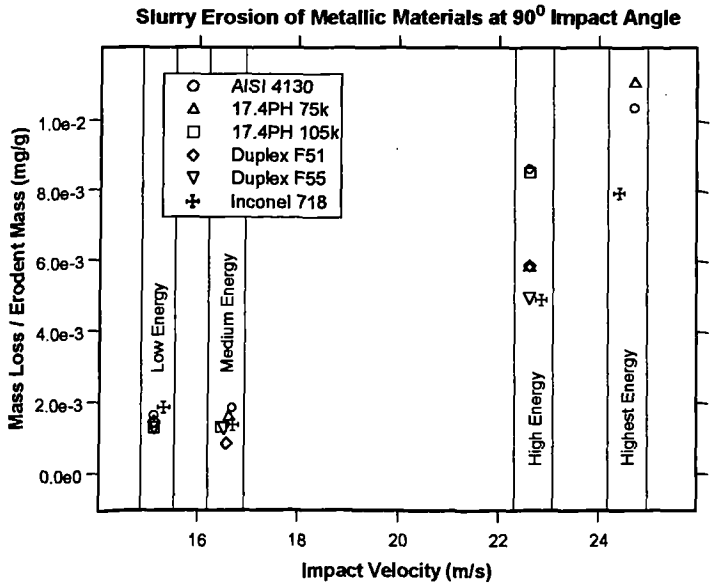

Figure 3.9 Results from erosion tests at 90 degree impact angle.

Something of the inherent scatter in the erosion data can be seen by examining the test results for Inconel 718, Duplex F51, and Duplex F55 in Figure 3.9. The erosion rate of Inconel 718 at Medium Energy is less than that at Low Energy. Similarly, the erosion rate of Duplex F51 at Medium Energy is also less than that at Low Energy. There is not much change in the erosion rate of 17.4PH 105k between the two levels. This suggests that the scatter inherent in the test method is too great to highlight differences in erosion resistance between impact velocities so close together. Many more repeat tests for each material would be required before firm conclusions could be drawn in respect of erosion resistance.

These findings for the low and medium energy levels lead to the conclusion that for this range of conditions in the slurry rig at least, particle kinetic energy is not an appropriate measure with which to correlate erosion data. Observe the same set of data used in Figure 3.9 plotted against kinetic energy in Figure 3.10. It can be seen that the apparent change in kinetic energy between low and medium levels is not reflected by a proportionally similar increase in erosion rate. This suggests that the kinetic energy may not be a suitable parameter for use in erosion testing. Only two sand grades were used in the erosion testing: Redhill 110 for low energy tests, and Redhill 50 for the other tests. When particle kinetic energies are defined by changing the particle size range, there is a risk that particle size effects will be mistaken for kinetic energy effects. That is, the cause of variance in erosion rate could be particle size rather than kinetic energy. It has been observed in the past that particle size does not have an effect above a certain size level: it is possible that such a phenomenon is observed here where

the higher sand size (Redhill 50) at medium velocity level does not give increased erosion rates above those obtained with the lower sand size (Redhill 110) at the lower velocity level.

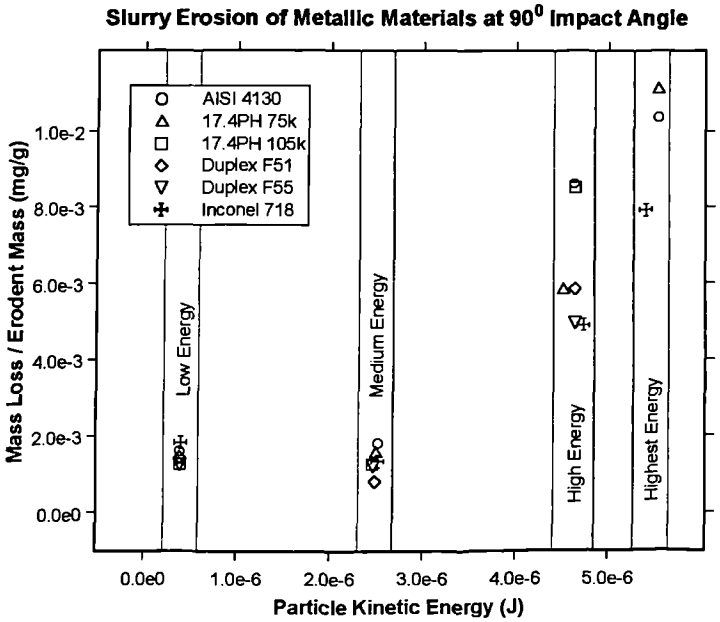

Figure 3.10 Results from erosion tests at 90^0 impact angle: plotted against particle kinetic energy.

For the present, erosion results will be considered to be a function of particle impact velocity, and not kinetic energy. This means that particle size as an erosion influencing parameter has not been of primary concern in this study, but has rather been viewed as having minor effect.

3.2.4.4 Data at other angles of impingement: metallic materials

Variation of erosion rate with impact angle has also been considered in the present test programme. Figure 3.11 shows results for AISI 4130 and Inconel 718 at the high energy level. Average data has been used where possible as before. The plots in Figure 3.11 are to some extent misleading, as at first sight they suggest that large differences exist between erosion rates at differing angles. However, closer examination of the y-axis scales show that the differences in erosion rate, particularly for AISI 4130, are very small. Erosion at 90^0 is just over 7% (of lower rate) higher than erosion at 30^0. This is within the inherent scatter of the results. For Inconel 718, it is found that the maximum erosion rate (at 60^0) is 12.3% greater than the lowest (at 30^0). Although some repeat tests were carried out at some angles, it was not possible to perform repeat tests at all angles—which would be required for a truly accurate picture of impact angle behaviour.

Three sets of data are available to explore impact angle behaviour at the medium energy level: 17.4PH 75k, Duplex F51, and Inconel 718. The results are shown in Figure 3.12. These plots exhibit the kind of trend that would be expected from ductile materials, where typically the maximum erosion occurs around 20^0 to 30^0 impact angle. The differences in erosion magnitude with angle are significantly greater at this energy level than the previous: Duplex F51 under 30^0 impact erodes 3.4 times faster than it does at 90^0 impact; Inconel 718 under 30^0 impact erodes just under twice as fast than it does at 90^0; and 17.4PH 75k around 1.2 times the 90^0 value. Thus for Inconel 718, it appears that the proportional increase in erosion rate at 30^0 impact is greater for the medium energy level than for the high energy level.

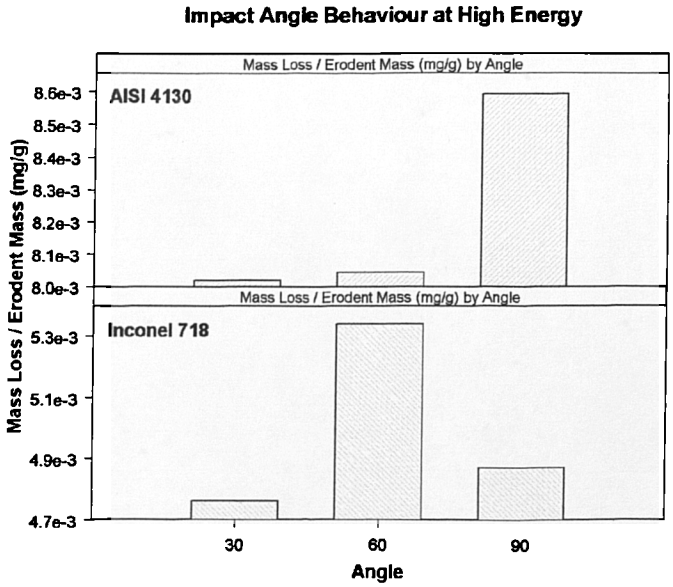

Figure 3.11 Slurry erosion data at high energy and three impact angles.

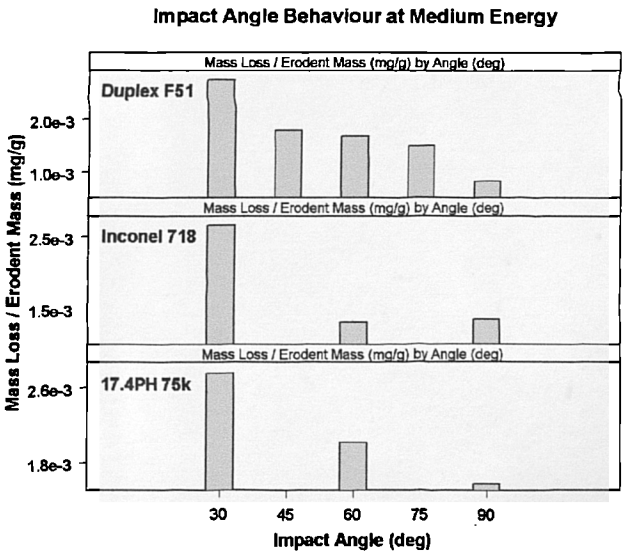

Figure 3.12 Slurry erosion data at medium energy and various impact angles.

Some materials have also been tested at the low energy level. As Inconel 718 has been tested at all three levels (two angles for low energy), it will be instructive to examine the form of impact angle behaviour across the three levels. Erosion rates are normalised based on the value at 90^0 impact, and plotted in Figure 3.13. It will be observed that the only data to follow the classical trend is the medium energy data—and even here the erosion rate at 60^0 is slightly lower than that at 90^0. It is possible that scatter inherent in the test method is masking the true trends that should be observed.

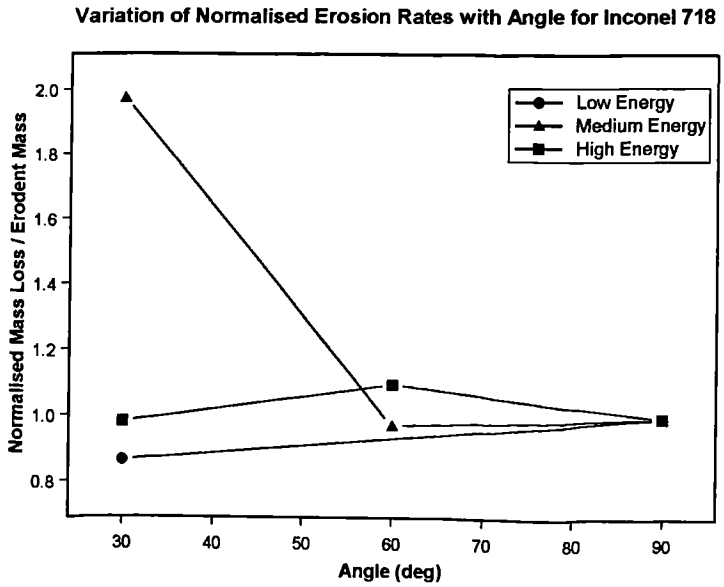

Figure 3.13 Normalised erosion rates for Inconel 718: Variation with angle.

3.2.4.5 Tungsten Carbide

Three separate tungsten carbides were tested with the slurry erosion rig. Only impact angles of 90^0 were considered with the slurry rig due to constraints on time (as the tungsten carbide samples took considerably longer to erode than the metallic materials).

All of the data points obtained for the tungsten carbides with the slurry rig are plotted on Figure 3.14. Average erosion values have been calculated where appropriate. Although some of these average values are based on repeat tests with the same specimen (and hence the final 'steady state' value may be more appropriate), taking the average does not give a significant difference in the final reported result. A logarithmic scale has been used to plot the erosion data in this instance, as the recorded values cover almost three orders of magnitude. Figure 3.15 shows the same data, plotted in conjunction with the data used to create Figure 3.9 previously, in order to give some indication of the superior erosion performance of tungsten carbides. It can be observed that Tungsten Carbides VC-808 and DC(Z)05 exhibit

erosion rates around three orders of magnitude lower than those of the metallic materials. This confirms the suitability of tungsten carbides for erosion applications.

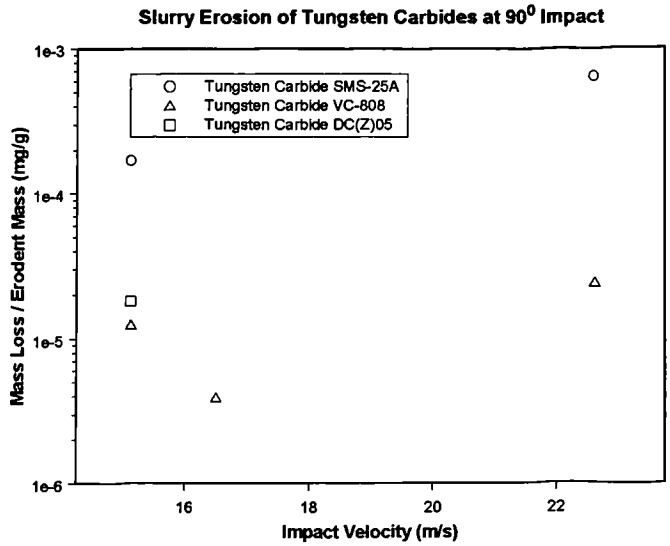

Figure 3.14 Slurry erosion data for tungsten carbides at 90^0 impact.

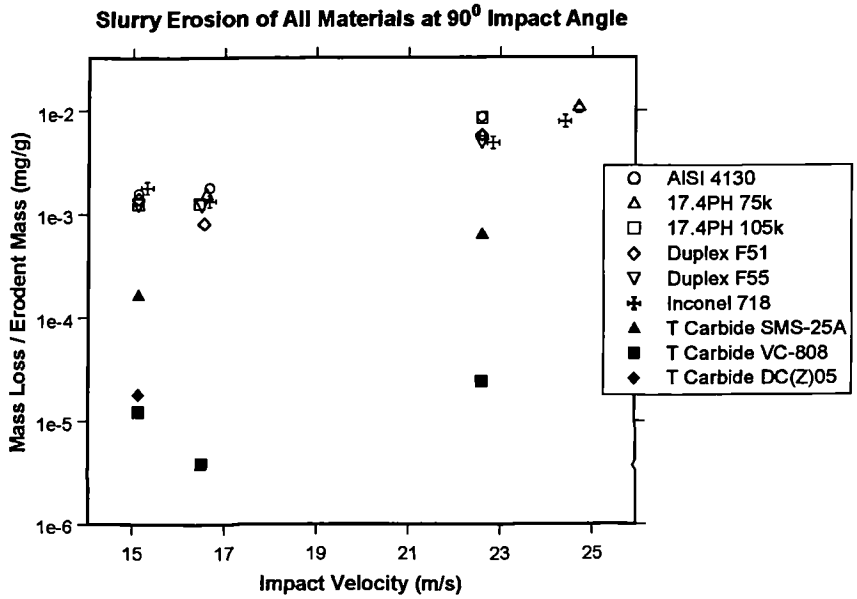

Figure 3.15 Slurry erosion data for all materials at 90^0 impact.

The erosion rate of Tungsten Carbide VC-808 at medium energy is lower than that at low energy. It is likely that steady state erosion was not achieved in the lower energy test for this material. Single five hour tests were conducted at low energy for both Tungsten Carbides VC-808 and DC(Z)05; as incremental erosion tests were not performed it is not possible to state whether true steady state erosion had been achieved.

3.2.5 Summary

Several materials have been tested under slurry erosion conditions for a range of impact angles and velocities. The data shows that erosion rates for the metallic materials are fairly similar, with no clear distinction between the relative erosion resistance of each material (although Inconel 718 does perform well at high energy levels). Scatter inherent in the test method makes it difficult to establish definite relationships between impact angle and erosion rate, although classical ductile behaviour can be observed for certain materials at the medium energy level. The three tungsten carbides tested exhibit far superior erosion resistance than any of the metallic materials. Of the three tungsten carbides considered, VC-808 and DC(Z)05 are clearly better than SMS-25A at resisting erosive wear.

3.3 Air-Sand Erosion Testing

Slurry erosion testing can only cover a limited velocity range. In order to test for erosion behaviour at high velocity, air-sand type test rigs must be used. One such test facility has been used in this study to obtain further data for the same set of materials listed previously.

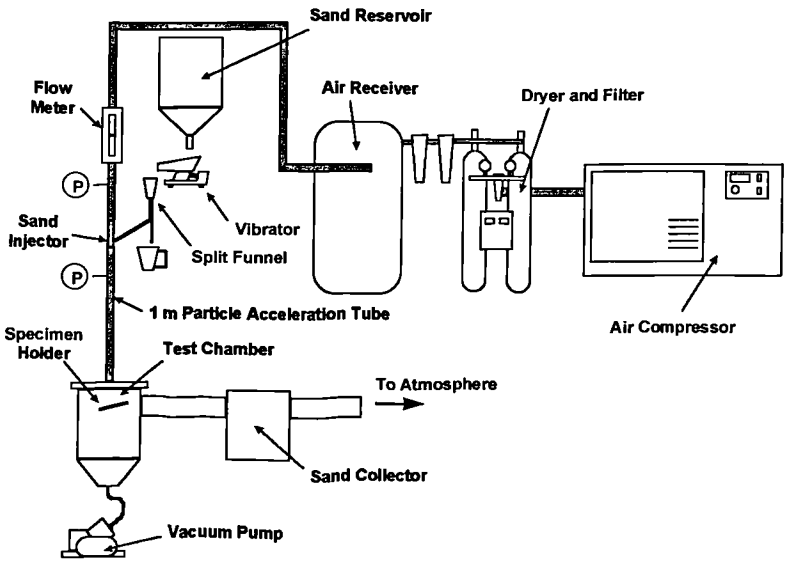

Figure 3.16 Air-sand erosion facility.

3.3.1 Experimental Apparatus and Procedure

The design and calibration of the test facility has been amply described by Wheeler and Wood (1998) and so will only be briefly described here. A schematic diagram of the facility is given in Figure 3.16. Air from the compressor is dried and filtered before being stored in a large pressure vessel (the 'air receiver'). Air is drawn from this vessel, through a

flowmeter and regulator (not shown), before passing through the sand injection system and acceleration tube. The acceleration tube has a constant diameter of 16 mm after the sand injection. Sand injection is effected by an arrangement shown in greater detail as Figure 3.17.

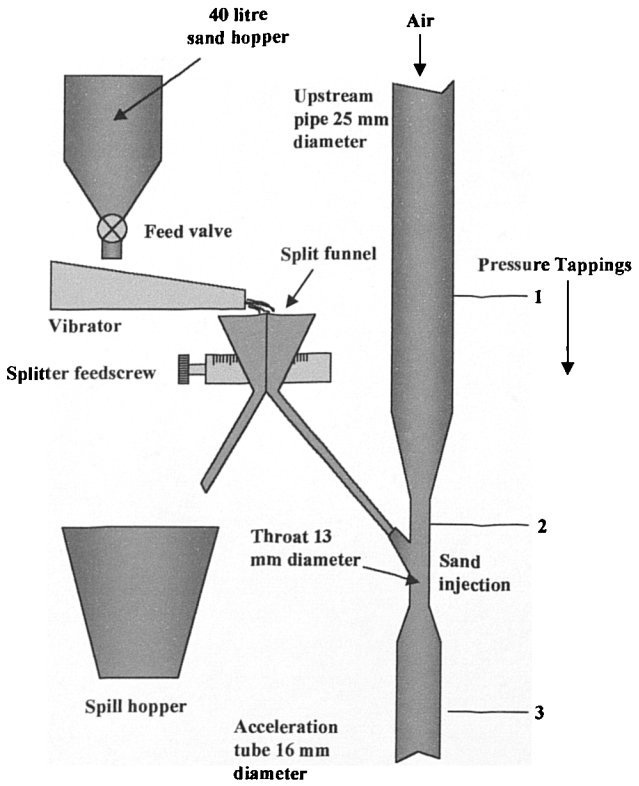

Figure 3.17 Sand injection system (after Wood and Wheeler, 1998).

Sand stored in the reservoir falls through a 2 mm orifice (attached to a ball valve) onto the shute of a vibration unit. This feeds the sand at a constant rate into a split funnel device whose position can be adjusted in order to produce different feed rates. Some of the sand falls into the pipe leading to the gas flow; the rest falls into a container for later use. Sand enters the gas stream in the throat of a venturi section, from which it will be accelerated over a distance of 1 m before impacting the specimen below.

The system was calibrated previously (Wheeler and Wood, 1998) to relate particle impact velocity to the gas flowrate passing through the flowmeter. Figure 3.18 presents the calibration curve obtained by means of high speed photography to measure the actual particle velocities at the specimen surface. The results of this previous work have been used in the present study as a measure of particle impact velocity.

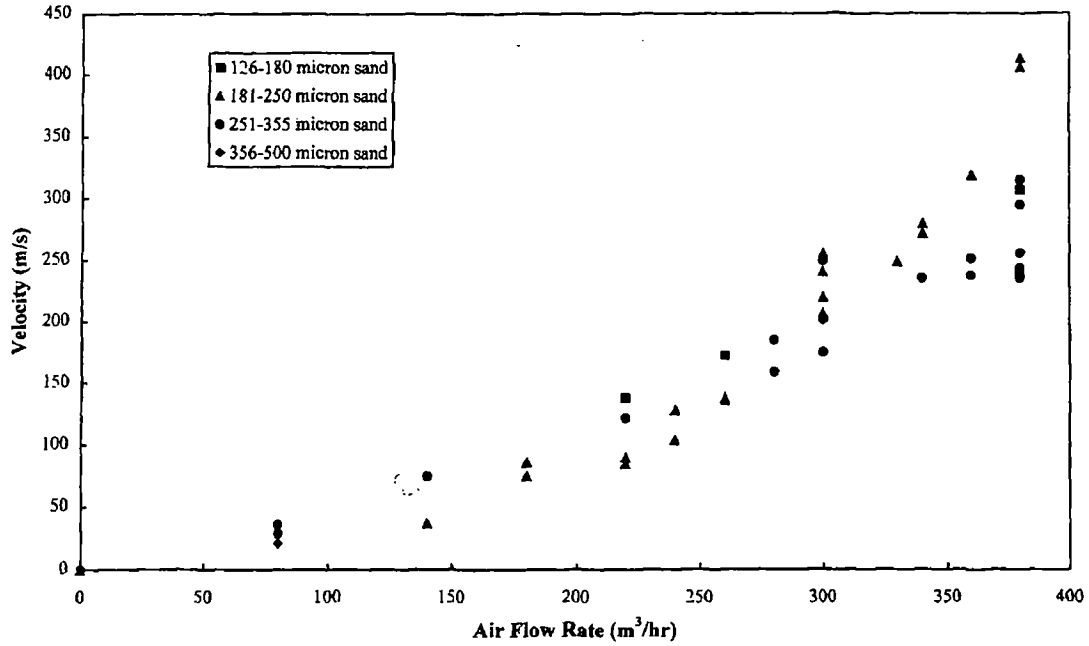

Figure 3.18 Calibration curve for air-sand test rig (Wheeler and Wood, 1998).

A mixture of three sand grades (known as 'Redhill mix') has been used for the air-sand testing. The typical sand size distribution resulting from the mixture is shown in Figure 3.19. Average particle size is taken to be 194 μm for Redhill mix. This is slightly less than the average particle size for Redhill 50 (used in the high energy tests on the slurry rig), which was given as 235 μm. It would have been useful to study the effect of using different sand grades had time been available.

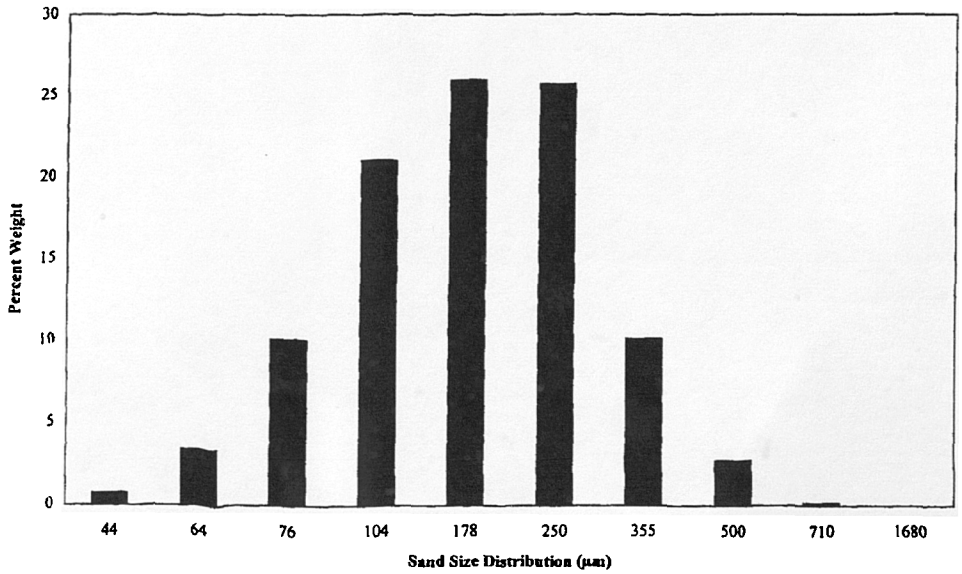

Figure 3.19 Sand size distribution for Redhill mix.

Two specimen holders were used in the experimental testing. The initial holder was the original design, and had the feature whereby samples were held in position by creating a vacuum seal at the back of the sample. Figure 3.20 illustrates the concept. This sample holder had a disadvantage in that it could not be easily used at angles other than 90^0. For this reason, a second sample holder was developed which could be used at any angle, without the need for a vacuum hose to be attached to the base of the sample. This has not been depicted here as it was similar in concept to that used on the slurry test rig (Figure 3.2).

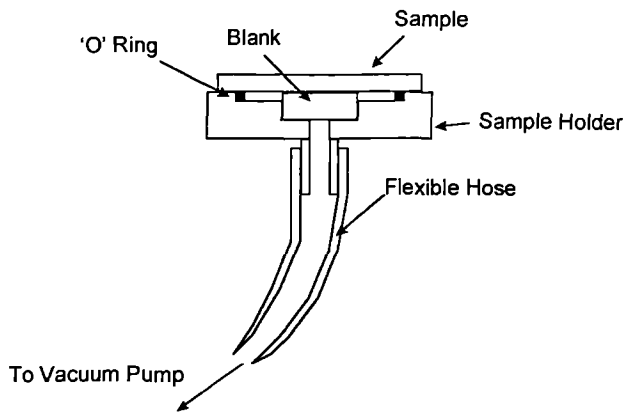

Figure 3.20 Arrangement for holding sample in place: Sample Holder 1.

The experimental procedure for testing with the air-sand rig can be summarised as follows:-

1. Specimen weighed to within ±0.02 mg using Mettler AT201 analytical balance.
2. Round blank attached to the back of the specimen using double-sided tape. This was only required when specimen holder 1 was used: with the second holder the sample could be held in place by screws.
3. Sample placed in test chamber; holder angle and stand-off distance (30 mm) adjusted if necessary. Lid of test chamber placed in position and sealed.
4. On/off valve of air-receiver opened to permit flow of air through the rig. Regulator valve adjusted until required flowrate registered on the flow meter.
5. Upstream and downstream pressures were recorded.
6. Vibration unit activated; ball valve beneath sand reservoir opened to start flow of sand. Split funnel was set at a fixed position for all tests.
7. Timing started when vibration unit was activated (as sand lay along the shute between tests).

8. Sand feed continued for allotted time span. On completion of time span, the vibration unit was de-activated and timing stopped. Regulator valve turned down and on/off valve closed.
9. Test chamber opened; sample removed from holder. Sample was cleaned with acetone, with care being taken to remove traces of double-sided tape after the blank was removed.
10. Sample allowed to adjust to room temperature conditions before being re-weighed on the analytical balance. Several repeat measurements were taken as for slurry testing.

3.3.2 Results from air-sand testing

As for the liquid-sand rig, there were two distinct phases to erosion testing on the air-sand rig: the first in July to September 1999; the second in January and February 2000. Most of the results were obtained in the second test phase for the air-sand rig. Table 3.5 presents the tests carried out on the air-sand rig.

Table 3.5 Tests carried out on air-sand rig.

		Air-Sand Rig														
		Low Velocity					Medium Velocity					High Velocity				
No.	Material / Impact Angle (deg)->	30	45	60	75	90	30	45	60	75	90	30	45	60	75	90
1	AISI 4130	1		1		1	1		2		3					
2	ASTM A564 630 (17.4 SS) 75k															
3	ASTM A564 630 (17.4 SS) 105k	1		1		3	1		2		10	1				3
4	ASTM A182 F51 (Duplex)	1		1		4	2		2		5	1				3
5	ASTM A182 F55 (Duplex)	2		2		1	1	1	2	1	4					1
6	AISI 4130 / Inconel 625	1		1		1					2					1
7	Inconel 718	1		1		1	1		2		5					1
8	Tungsten Carbide SMS-25A					2	3				6	2				4
9	Tungsten Carbide VC-808										3	2				2
10	Tungsten Carbide DC(Z)05					9	2				2	1				2

Key: 1 = Carried out in Phase 1.

1 = Carried out in Phase 2.

2 = Carried out in both phases.

The three velocity levels are defined in Table 3.6 below, along with the necessary gas flowrates and the estimated particle kinetic energy (based on a mean particle diameter of 194 μm).

Table 3.6 Velocity levels for air-sand testing.

Velocity Level	Flowrate (m^3/hr)	Mean Impact Velocity (m/s)	Mean Kinetic Energy (J)
Low	150	63	1.993e-5
Medium	250	148	1.100e-4
High	350	268	3.607e-4

3.3.2.1 Tests to determine times for achieving steady-state erosion

As for the liquid-sand erosion tests, it was important to have some understanding of the time required before steady state erosion conditions were achieved in air-sand testing. Figure 3.21 presents selected data for metallic materials showing the incremental mass loss over time. Such incremental tests were not carried out on all materials at all angles: the tests that were conducted were used to establish the testing times for other materials. Erosion rate data for the same set of tests are plotted in Figure 3.22. Figure 3.22 shows individual erosion rates after each period of testing for samples where more than three repeat tests were carried out. For example, four tests were carried out on Inconel 718 using the same sample each time. The first and second tests were of five minute duration, and the third and four test were of ten minute duration—giving a total test time of thirty minutes. The average erosion rate from each series of tests has been shown on the graph as horizontal lines running next to each data set.

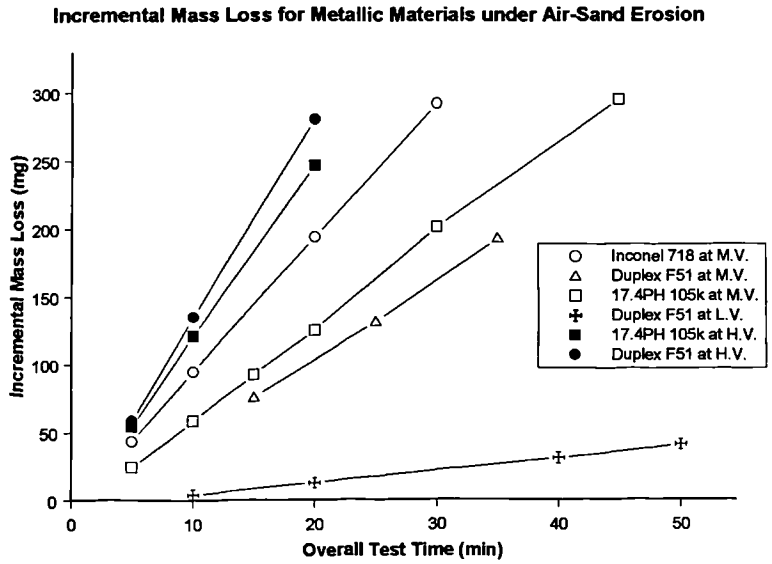

Figure 3.21 Incremental mass loss for selected metallic materials under air-sand erosion.

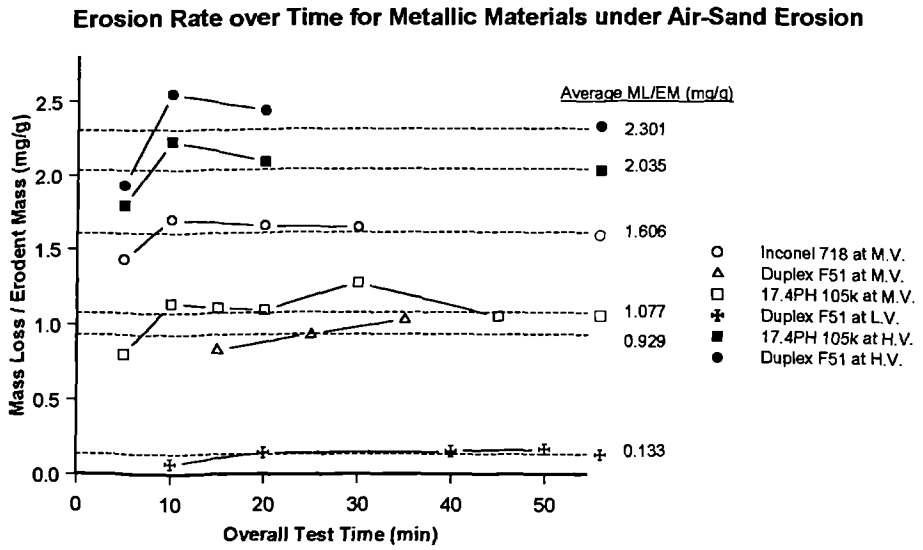

Figure 3.22 Air-sand erosion rates for repeat tests on the same samples.

The data shown in Figure 3.22 indicates that the initial erosion rate obtained after a short period of testing may be somewhat lower than the steady state erosion rate after two or three consecutive tests. This has some implications for cases where only one erosion test was carried out for a particular specimen: the erosion rate reported may be slightly lower than would be obtained if a series of tests were carried out. Time limitations meant that repeat tests could not be performed for every material/erosion condition combination.

Similar tests were carried out for the tungsten carbides. Figure 3.23 shows results from some incremental mass loss tests carried out with the air-sand rig. It will be observed that the mass loss reported for Tungsten Carbide DC(Z)05 at Low Velocity is actually negative (i.e. mass gain), and does not increase to appreciable levels until after at least two hours of testing. This is due to the very low levels of erosion taking place in each test period, and exemplifies the superior performance of this particular grade of tungsten carbide.

As before, results from the same set of tests can be plotted as a series of erosion rates in order to assess how appropriate it is to use an average value where possible. Figure 3.24 presents this data. A greater amount of scatter is observed in the data compared to the previous set for metallic materials. The most consistent test among those presented in Figure 3.24 is that of Tungsten Carbide VC-808 at Medium Velocity: minimal variation in erosion rate is noted. It must also be remembered that the actual recorded erosion rates are very low in comparison to the previous sets of data, so that accurate measurement of erosion rate is difficult. The testing of Tungsten Carbide VC-808 at Low Velocity is interesting in that the

erosion rate does appear to reach a steady state (albeit low) value. Another interesting observation is that the erosion rate of Tungsten Carbide SMS-25A at High Velocity is lower than that at Medium Velocity.

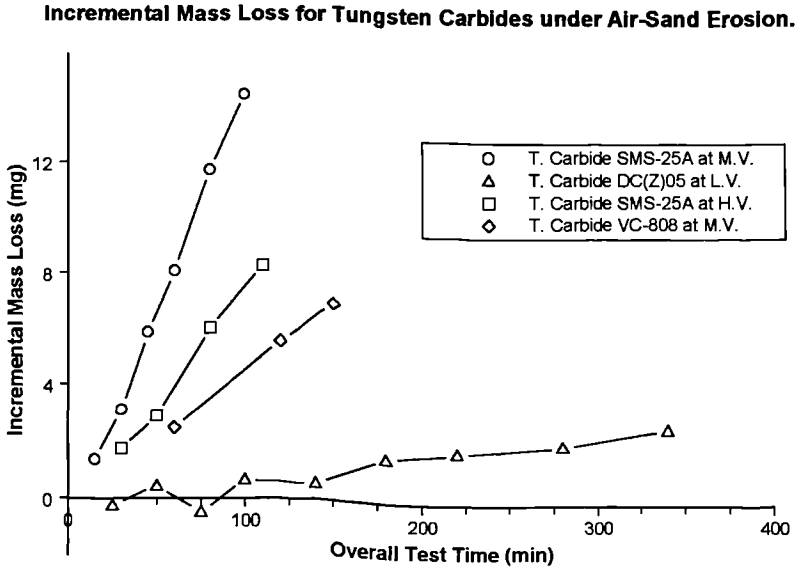

Figure 3.23 Incremental mass loss for selected tungsten carbide erosion tests.

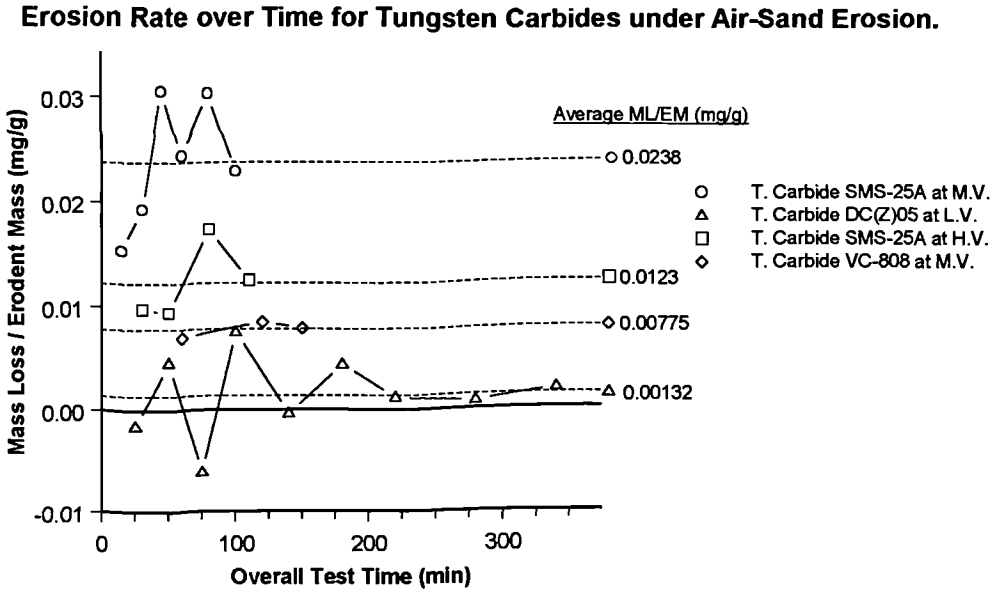

Figure 3.24 Erosion rates for repeat tests on the same samples: tungsten carbides.

3.3.2.2 Repeatability of testing with the air-sand rig

The air-sand testing also took place over two distinct time periods, although most of the testing was carried out in the second phase. All of the tungsten carbide work was carried out in the second phase. Figure 3.25 presents erosion data for materials where similar tests (at

90^0 impact angle) were carried out in both phases. For example, Duplex F55 was tested at medium velocity in both 1999 and 2000. The graph shows two data points for 1999 (as two consecutive tests were performed on the same sample) and also two data points for 2000 (two tests on the same sample). Note that none of the samples from the 1999 phase were re-used in the 2000 test phase. Some of the samples were only tested for one period of time, such as 17.4PH 105k in the 2000 test phase (see Figure 3.25). The graph therefore gives some idea of the intermediate erosion rates as well as comparing data between the two phases.

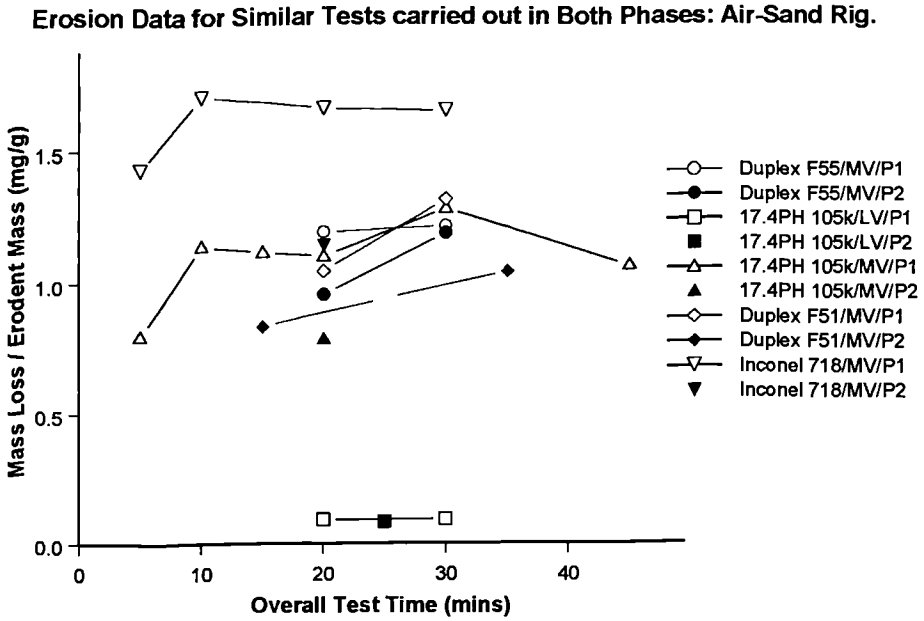

Figure 3.25 Erosion data for similar tests carried out in both phases: air-sand rig.

The same data shown in Figure 3.25 has been re-plotted as a bar graph in Figure 3.26, where instead of individual erosion rates from a series of tests, the overall mean erosion rates (where available) have been presented. The first erosion rate on Figure 3.26 (for Duplex F55 at Medium Velocity) is based on the two individual test results shown before in Figure 3.25, and so on. Figure 3.26 indicates a clear trend in that erosion results from the second phase are generally lower than those in the first phase. This does suggest that something has changed between the first phase of testing and the second, especially as the slurry erosion results behave in a similar manner.

No clear reason has been found to explain the apparent decrease in erosion rate for samples tested in the second phase. The fact that such a decrease is observed in both the slurry and the air-sand rig suggest that the cause lies with the sand used in testing, outdoor temperature, or some aspect of the test samples. Sand used in the testing comes in large sacks

that are simply stored unopened until required. Sand grades are stamped on the sacks in fairly large letters, which means that use of the wrong sand grade is unlikely. It is not known how much the sand size distribution varies between sacks or even within different regions inside the sack itself. There could potentially be some settling of the sand during storage, which could result in sand size distributions being skewed towards the low or high regions of the range. Outdoor temperature is not thought to be a major cause of change, as the difference between the two phases is simply not large enough: maybe around 15-20^{0}C. The only change in the samples used was that those in the second phase had been kept in storage for a period of five months. It is unlikely that any form of material change could have occurred in such a short time.

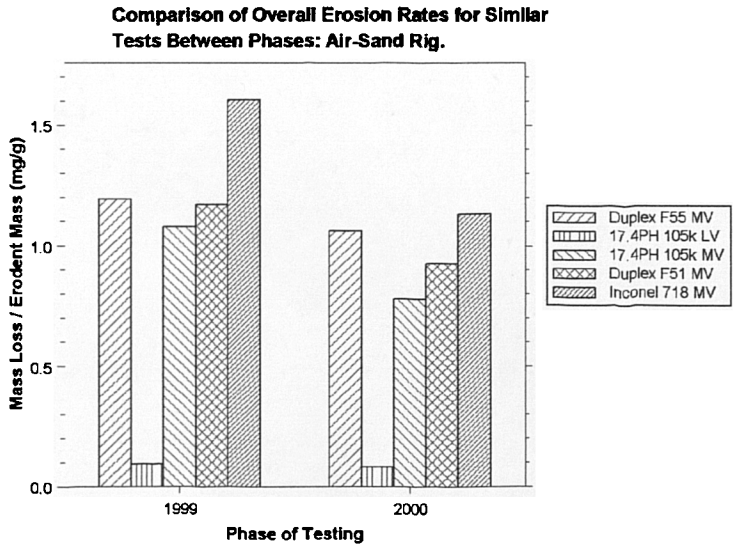

Figure 3.26 Overall erosion rates for similar tests carried out in both phases.

It is proposed to simply view the differences in erosion rate between the test phases as an uncertainty band to be applied to all results. In one way this is not disadvantageous, as the complex nature of erosion does not lend itself to precise quantitative predictions from equations based on accurate data—presuming such data can be obtained.

3.3.2.3 Data at 90^0 impingement: metallic materials

As for the slurry testing, most of the tests in the air-sand rig were carried out at 90^0 impingement—especially when repeat tests were required. All results from testing of metallic materials at 90^0 impingement have been plotted as a function of mean impact velocity in Figure 3.27 below. Note that a logarithmic scale has been used for Mass Loss per Erodent Mass in order to show the relative erosion rates at low velocity more clearly.

It is apparent from Figure 3.27 that no clear order of material erosion resistance exists for all impact velocities. Duplex F51 comes out as being the least erosion resistant material at low impact velocity, but lies somewhere in the middle for medium and high impact velocity. Inconel 718, which was one of the best metallic materials under slurry erosion conditions, appears to be the worst material under medium and high velocity air-sand erosion conditions. Again, one of the reasons for not being able to rank materials more rigorously is that repeat tests were not carried out for all materials, and there is also the issue of decreased erosion rate in the second phase.

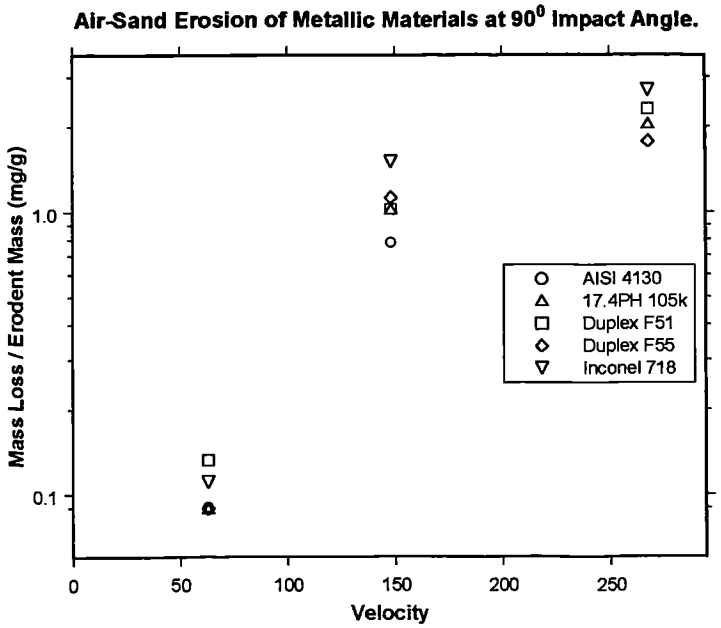

Figure 3.27 Results from air-sand erosion tests at 90^0 impact angle: metallic materials.

3.3.2.4 Data at other angles of impingement

Erosion tests were carried out at impact angles other than 90^0 for most materials. Figures 3.28 to 3.30 present the available data for metallic materials at the three different velocity levels. Only two metallic materials were tested at an alternative impact angle for 268 m/s: this data is shown in Figure 3.30.

The data presented in Figure 3.28 for 63 m/s impact velocity follows the classical ductile trend in general: maximum erosion occurs around 30^0 impact angle. Duplex F51 appears to have maximum erosion at 90^0 impact angle, and not around 30^0. It is suspected that this result is somewhat spurious, and is not likely to represent the true behaviour of Duplex F51. Some random set of variations in test conditions may have combined to cause such a

result: or the sample itself could have had features resulting in such an increased erosion rate. The expected behaviour is apparent for Duplex F51 at the 148 m/s velocity level (Figure 3.29). However, at this level, the maximum erosion rate for Inconel 718 is at 90^0, and the behaviour of Duplex F55 across the angle range is not entirely clear. One of the reasons for clear trends not being readily apparent in these data sets is that repeat tests could not be performed at all conditions. Table 3.5 indicates which tests were repeated.

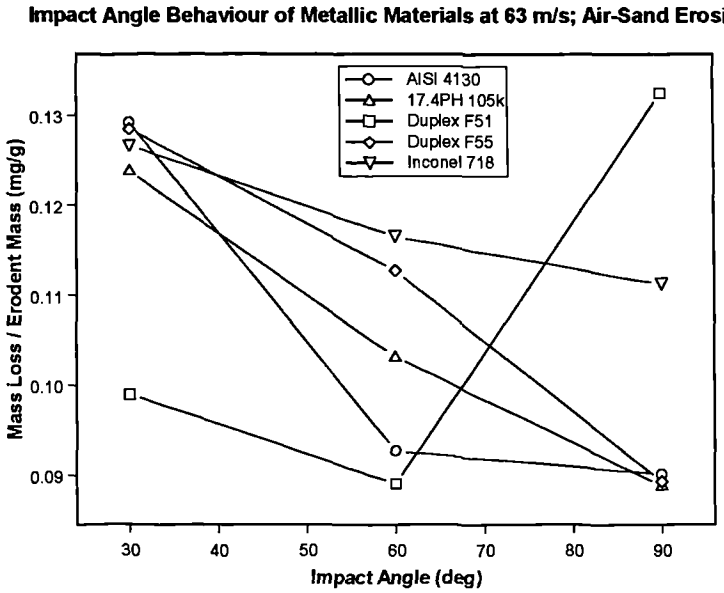

Figure 3.28 Impact angle behaviour for metallic materials at 63 m/s impact velocity.

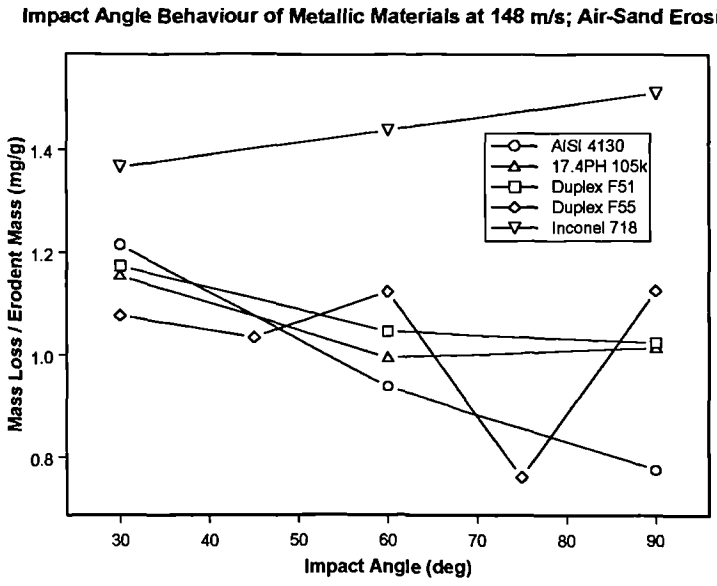

Figure 3.29 Impact angle behaviour for metallic materials at 148 m/s impact velocity.

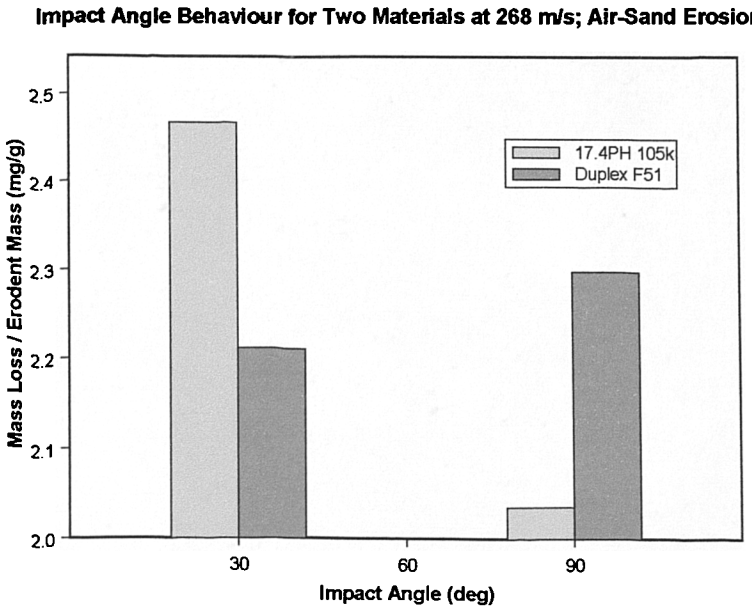

Figure 3.30 Impact angle behaviour of 17.4PH 105k and Duplex F51 at 268 m/s impact velocity; air-sand erosion.

It is possible that some change in the nature of the erosion process for a specific material does take place as velocities are increased. Inconel 718 had the greatest erosion resistance for metallic materials under slurry erosion conditions, but at higher velocities it apparently does not perform so well. Electron microscope examination could have provided some evidence for erosion mechanisms at the various velocities, had it been possible to apply this technique.

3.3.2.5 Erosion data for tungsten carbides

A limited number of tests were carried out using the three different tungsten carbides. Most of these tests were at a 90^0 impact angle, although some were performed at 30^0. Figure 3.31 presents the available data for a 90^0 impact angle.

An interesting phenomenon is observed for Tungsten Carbide SMS-25A, where the erosion rate at 268 m/s is lower than that at 148 m/s. This suggests that the erosion mechanism at 268 m/s is different from that at 148 m/s. Again, electron microscope examination would be required in order to understand this behaviour more fully. Tungsten Carbide DC(Z)05 exhibits some form of steady-state erosion beyond 148 m/s, as the erosion rate at 268 m/s is not much greater than that at 148 m/s.

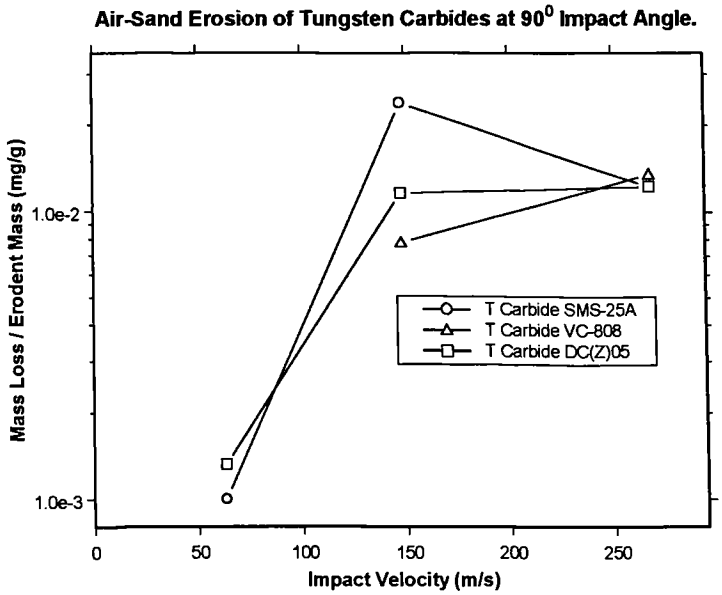

Figure 3.31 Air-sand erosion of tungsten carbides at 90^0 impact angle.

Some erosion tests were also carried out at 30^0 impact for the tungsten carbides, although only at the medium and high velocity levels due to limitations on time. The results of these tests are shown in Figures 3.32 and 3.33 below.

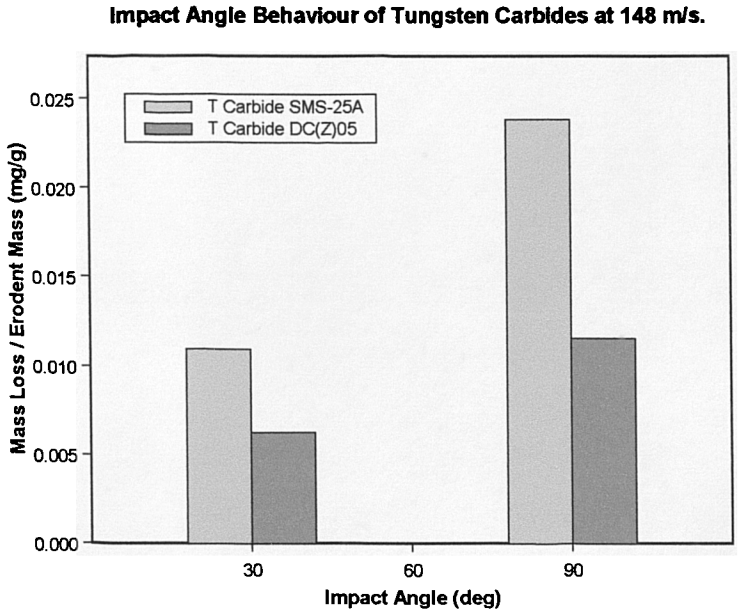

Figure 3.32 Impact angle behaviour of tungsten carbides at 148 m/s.

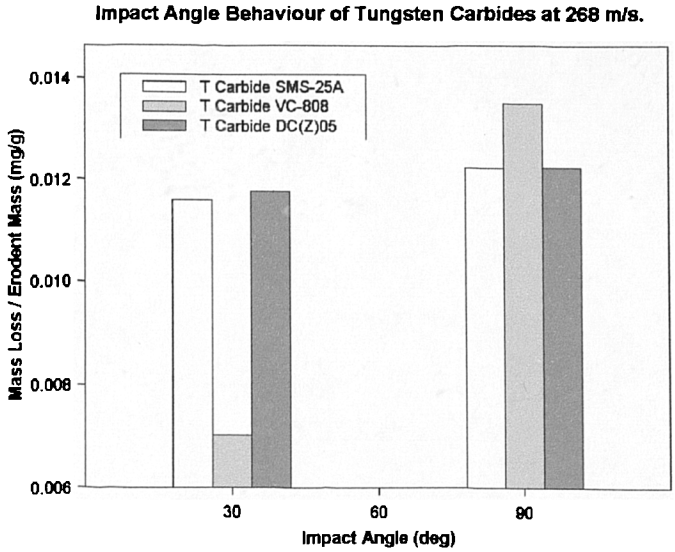

Figure 3.33 Impact angle behaviour of tungsten carbides at 268 m/s.

Figures 3.32 and 3.33 confirm the general understanding that tungsten carbides exhibit maximum erosion at 90^0 impact. The difference between erosion at 30^0 and that at 90^0 is most significant for Tungsten Carbide SMS-25A at 148 m/s impact velocity, where the erosion rate at 90^0 is 118 % greater than that at 30^0. The erosion rate of Tungsten Carbide DC(Z)05 at 90^0 is 83 % greater than that at 30^0. There will be some element of uncertainty in these figures, due to the limited number of data points available for each erosion rate in Figure 3.33, but they do indicate a significant increase in damage when particles impact at 90^0. This has definite implications for choke valve design, where it will be advantageous to eliminate 90^0 particle impacts as far as possible.

The only appreciable increase in erosion rate with angle at high velocity is for Tungsten Carbide VC-808, where the erosion rate at 90^0 is 93 % higher than that at 30^0. Again, the limited number of repeat tests will have influenced these results. The first test for Tungsten Carbide VC-808 at 30^0 gave an erosion rate of 0.0045 mg/g; the second test gave 0.00956 mg/g. The average value of 0.00703 mg/g has been reported. If final erosion rates had been used to calculate the increase in erosion rate between 30^0 and 90^0, the increase would be on the order of 63.2 %. However, this is still appreciable. It would have been useful to test the tungsten carbides at angles other than 30^0 and 90^0, and with significantly more repeat tests, in order to identify any difference in impact angle behaviour between the grades VC-808 and DC(Z)05.

3.3.3 Summary of air-sand testing

A number of samples were tested repeatedly under the same conditions to determine the minimum lengths of time to run tests for a steady state erosion result. In most cases, the test time was adequate. Some differences were found between tests carried out in the summer of 1999 and the winter of 2000, in that the erosion rates determined in the second phase were generally lower than those in the first phase. No clear reason has been discovered for this trend, but it must lie in either the sand size distribution or some shift in test rig calibration.

Testing of metallic materials at 90^0 impact shows that the materials which had highest erosion resistance in the slurry testing do not necessarily have highest resistance in the air-sand testing: this applies to Inconel 718 in particular. Classical ductile behaviour is observed for most metallic materials at low impact velocity (63 m/s), although the trends are not so clear at medium impact velocity. The tungsten carbides consistently show maximum erosion at 90^0 impact angle for both medium and high impact velocities.

3.4 Combined Erosion Data

If it can be assumed for the moment that erosion mechanisms will be similar in both slurry and air-sand erosion, then it is possible to consider all of the erosion data as a continuous set. A distinction will be made initially between the metallic materials and the tungsten carbides.

3.4.1 Combined data for metallic materials

The average erosion rates for all the metallic materials (17.4PH 75k excepted) at 90^0 impact angle, across the whole velocity range (where possible), have been plotted on the same graph in Figure 3.34. Note that logarithmic scales are specified for both axes. It is again apparent that there is no clear trend as to which materials perform best under erosion conditions. Inconel 718 has the lowest erosion resistance under low energy conditions on the slurry rig, but then has comparatively good resistance under high energy conditions on same rig. By medium and high velocity on the air-sand rig, however, Inconel 718 has become the worst performing metallic material. There must certainly be a sand size issue for the low and medium energy conditions on the slurry rig, as the group of data points at low energy are almost equal to that of the medium energy condition.

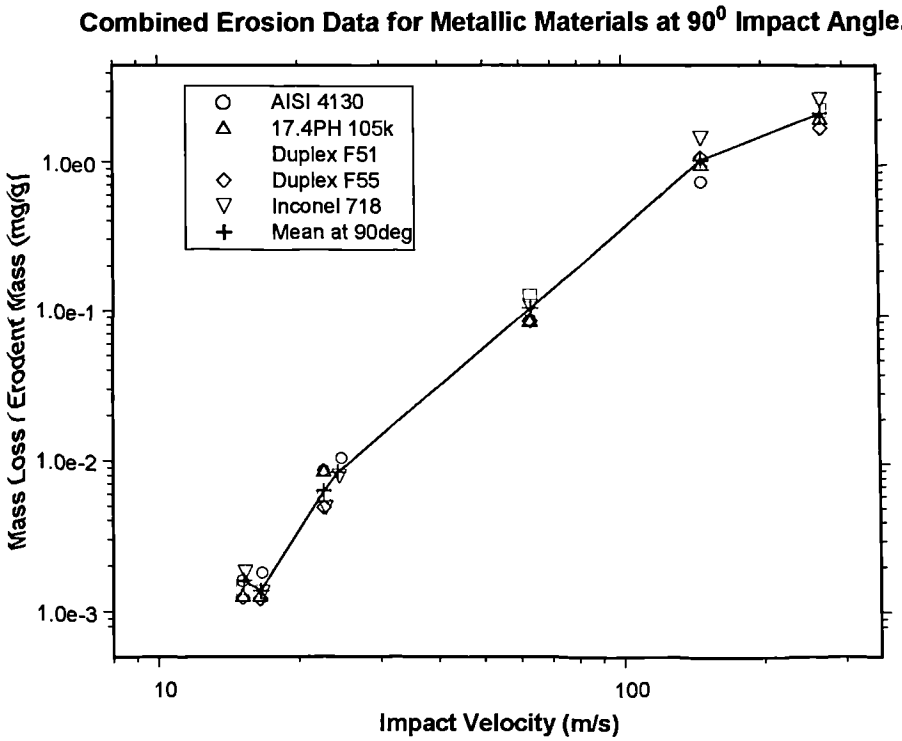

Figure 3.34 Combined erosion data for metallic materials at 90^0 impact angle.

The fact that no clear trends emerge suggests that insufficient repeat tests were carried out for each material, and also indicates something of the random scatter inherent in the test method. It could be concluded that as no one material has a clear advantage over another, the choice of particular metallic material will have no great impact on the erosion lifetime of a choke valve product, e.g. AISI 4130 will do as well as Inconel 718 under certain erosion conditions. (There are other issues, such as corrosivity of fluids, which also govern the selection of materials).

A mean value of erosion rate at each velocity has been plotted in Figure 3.34 with the rest of the data. The mean value was arrived at by simply finding the mean erosion value based on all specific tests carried out at the appropriate velocity and angle. This could result in some mean values being disproportionately influenced by materials where several repeat tests were carried out on the same specimen, as each of the individual tests would be counted in the mean value. However, the error introduced by cases where only one test has been carried out (and hence giving a result which could be at one particular end of the scatter range) is likely to be more significant than that of taking the mean erosion value across all tests at a particular velocity and angle. The mean data appears to be fairly central throughout

the series, although it is weighted towards the erosion rate of Inconel 718 at the low energy level on the slurry rig (due to several repeat tests on the same specimen).

Mean data has also been generated for impact angles other than 90^0. Figure 3.35 presents the variation of the mean data set with impact angle for several velocity levels. The data set is not ideal in that some of the plots do not follow classical trends (e.g. mean erosion rate at 60^0 for low velocity on the air-sand rig is less than that at 90^0), and also there are no points for 60^0 impact angle erosion at low energy on the slurry rig, and high velocity on the air-sand rig. However, it is still possible to use the data in further analysis.

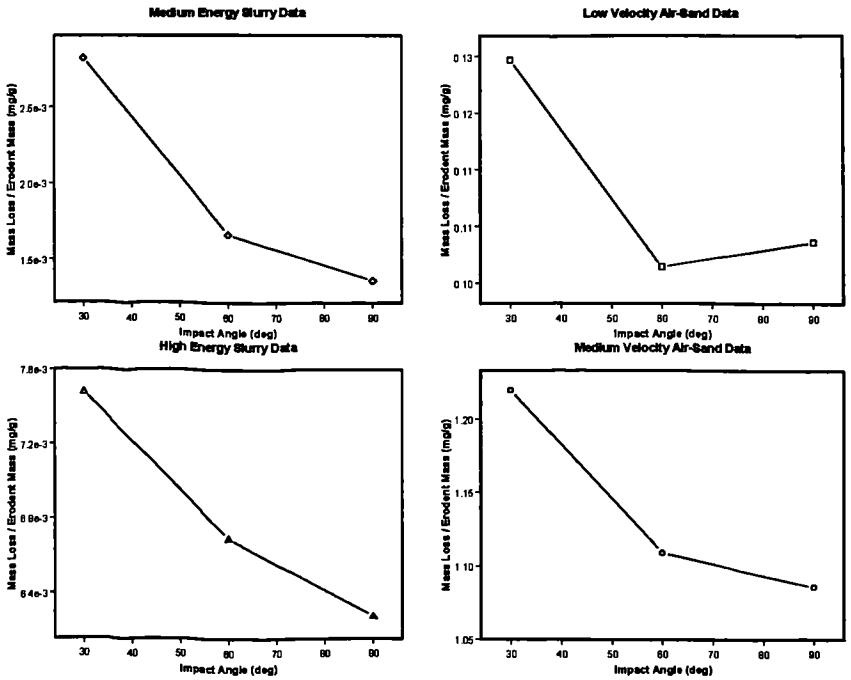

Figure 3.35 Mean erosion data at various velocity levels.

The mean erosion data will be used in the following chapter as a basis for equation fitting, in order to develop relations for use in the CFD software. Error bands can be defined as the difference between the maximum and minimum recorded erosion rates at a particular velocity level. This should give some indication as to the uncertainty associated with predictions for metallic materials. Appendix B shows this uncertainty analysis. It is shown there that the maximum uncertainty for testing of metallic materials is ± 35.7 % (for Duplex F55 under slurry erosion). This large uncertainty means that it is certainly appropriate to generate equations representing the mean metallic data, and to attach an uncertainty of ± 35.7 % to the predicted results.

3.4.2 Combined data for tungsten carbides

Only Tungsten Carbide VC-808 was tested sufficiently to give an indication of behaviour across the whole range of test velocities. The available data (at 90^0 impact angle) for all three tungsten carbides is plotted in Figure 3.36. No mean data points have been calculated for the tungsten carbides due to the large difference in performance between Tungsten Carbide SMS-25A and the other two, and also due to the fewer data points available.

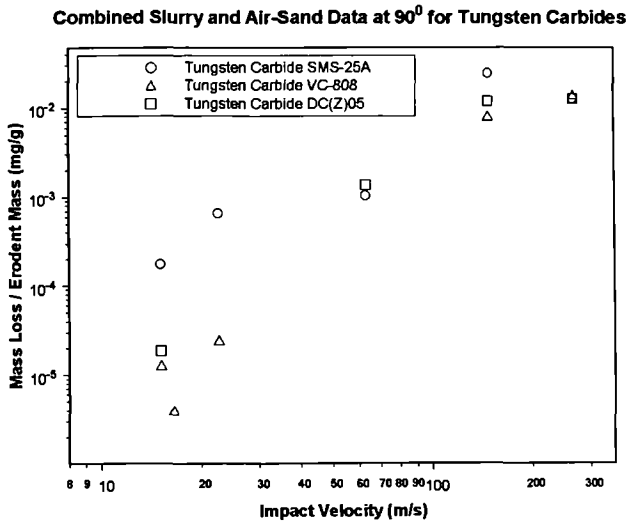

Figure 3.36 Combined data for tungsten carbides.

3.4.3 Summary

The main purpose in plotting combined sets of data is to show that for the metallic materials at least, there exists a fairly well defined mean trend through all the data. This has important implications for creating empirical erosion equations, as if a mean trend exists, it makes sense to generate a mean equation also. This is indeed the approach to be taken initially.

3.5 Summary of Chapter 3

A range of erosion tests has been carried out for materials used in choke valve construction. Both liquid-sand and air-sand testing has been performed. The main aim of the testing was to build up sufficient data sets for each material that would allow construction of empirical equations based on particle impact velocity and particle impact angle. Limitations on test time available meant that not every material could be tested at all permutations of velocity and angle. This will have an effect on the generation of empirical equations, as there

will not be sufficient data to create an equation considering both velocity and angle for some materials.

The set of data obtained from experimental testing is far from perfect. There is an anomaly between results obtained in the first round of testing and those in the second. No firm reason has been discovered to explain this anomaly. The variation will be considered to be part of the uncertainty inherent in the results, and may actually serve to ensure that predictions made with the CFD-modelling tool are not taken to be accurate values. It would not be wise to do this even with a 'perfect' data set.

The uncertainty analysis shown in Appendix B gives the *average* uncertainty for testing of metallic materials as being ± 14.6 %. This is really only an estimate of the uncertainty, and does not account for any systematic errors that may have been present. The average uncertainty for tungsten carbide testing is ± 26.2 %. The uncertainty for DC(Z)05 has been excluded in this estimate, as some of the earlier test points were definitely not in the steady state. It is likely that some of the other uncertainty estimates will also include test points where steady state conditions had not been achieved, which may mean that uncertainties are higher than they should be. The two different test phases have also contributed to the uncertainty of results.

No comparisons have been made with erosion data obtained by other researchers. This would be a useful exercise, as it would give some indication as to how consistent erosion data are between different test facilities. It has been remarked previously as to the lack of conformity between test methods: it would be very useful to carry out some form of intercomparison exercise.

No Scanning Electron Microscope examinations have been carried out on the eroded samples. It would certainly have been useful to perform such examinations, as they would have given a better understanding of the apparent changes in relative erosion resistance of some materials—as particle impact velocity increased. It may also have given reasons for the differences between results obtained in Phase 1, and those in Phase 2, for the same materials and test conditions.

4.0 Empirical Erosion Equations

There are three possible approaches to obtaining equations that relate particle impact data to erosive wear. The first approach (and most universal) would be to derive a purely analytical formula that would be valid under all conditions, and only require the insertion of commonly known material properties before it could be applied. Such a formula does not exist, and it is unlikely that one will ever be produced, due to the complex nature of erosion phenomena.

The second approach is to combine a theoretical understanding of erosion phenomena with empirical data. Underlying theory (which can vary considerably from author to author in the literature) is used to construct a basic framework for the erosion equation, and the unknown coefficients are supplied from actual erosion testing similar to that presented in Chapter 3. Thus a semi-empirical formula is obtained. This approach is by far the most popular in the literature, and has been almost always applied in CFD-based erosion modelling studies.

The third possible approach is to develop equations based on empirical data alone, without making any reference to possible underlying mechanisms of erosion. There are some examples of this approach in the literature, such as the study of Grant and Tabakoff (1975), and that of Head and Harr (1970). Both made use of statistical methods in developing their equations.

In this study, an initial attempt was made to apply an erosion formula developed by previous researchers—that of Neilson and Gilchrist (1968). On finding that this did not adequately represent the experimental data, further equations were developed using two- and three-dimensional equation fitting software. These were the equations ultimately used in most of the CFD based erosion modelling work. Wallace et al. (2000) describe the application of the initial erosion model to CFD predictions of erosion.

4.1 Equations based on the model of Neilson and Gilchrist (1968)

Neilson and Gilchrist (1968) developed some simple erosion equations based on the premise that two different mechanisms are present in the erosion process: cutting and deformation. This followed on from the work of Bitter (1963a,b) who presented an exhaustive theoretical basis for his equations. However, Neilson and Gilchrist felt that the work of Bitter was too complex to be readily applied, and so developed simplified relations for quick correlation of experimental data.

The equations of Neilson and Gilchrist as applied in this study are:-

$$W = M_P \left\{ \frac{\frac{1}{2} V_p^2 \cos^2 \alpha_p \sin 2\alpha_p}{\varepsilon_C} + \frac{\frac{1}{2} V_p^2 \sin^2 \alpha_p}{\varepsilon_D} \right\} \qquad \alpha_p \leq \alpha_0 \qquad (4.1)$$

$$W = M_P \left\{ \frac{\frac{1}{2} V_p^2 \cos^2 \alpha_p}{\varepsilon_C} + \frac{\frac{1}{2} V_p^2 \sin^2 \alpha_p}{\varepsilon_D} \right\} \qquad \alpha_p > \alpha_0 \qquad (4.2)$$

where W is the wear rate (mg/s), M_P is the mass of impacting particles (g/s), V_p is the particle impact velocity (m/s), α_p is the impact angle (radians), and ε_C and ε_D are the cutting and deformation wear coefficients respectively. α_0 is the cut-off angle (radians).

Coefficients have been determined for AISI 4130 steel undergoing slurry erosion only. Slurry erosion data at the medium and high energy levels have been used in generating the coefficients. This data is plotted on Figure 4.1 for reference. Data at the high energy level does not follow the ideal ductile trend (in that maximum erosion occurs at 90^0 instead of around 30^0), which means that the equations cannot truly follow the observed trend.

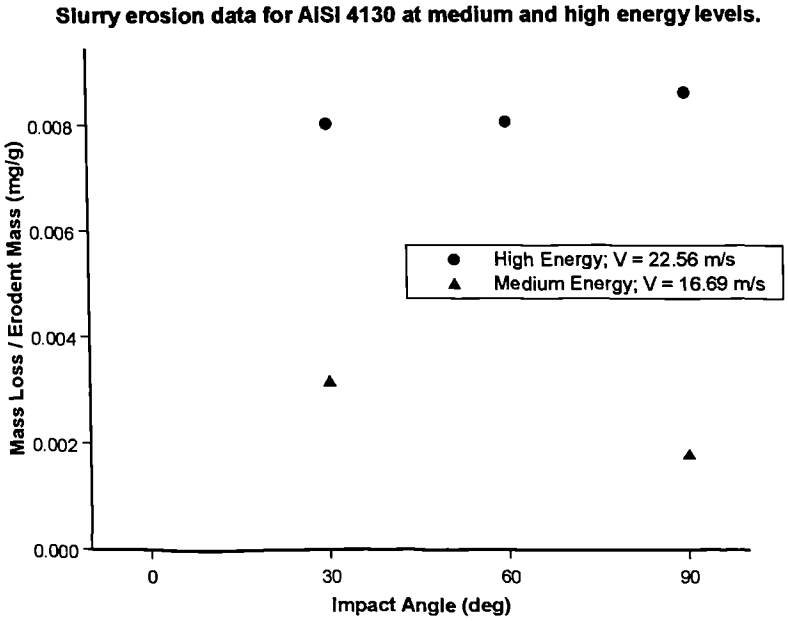

Figure 4.1 Slurry erosion test data for AISI 4130 steel.

Data at only one energy level at a time can be used to generate the coefficients. Therefore, two sets of coefficients have been determined: the first using data at the medium energy level, and the second using data at the high energy level. The resulting coefficients are given in Table 4.1. For this data, the cut-off angle (α_0) has been determined to be 45^0 ($\pi/4$ radians).

Table 4.1 Coefficients for equations 4.1 and 4.2.

Coefficient Set	Energy level for data	Cutting wear coefficient ε_C	Deformation wear coefficient ε_D
A	Medium	33316.9	77419.7
B	High	29624.8	29624.8

The resulting behaviour of equations 4.1 and 4.2, when applied to the same conditions used in the underlying experiments, can be seen in Figures 4.2 and 4.3. Figure 4.2 shows the erosion versus impact angle relationship at the two energy levels (corresponding to average impact velocities of 16.69 m/s for medium energy, and 22.56 m/s for the high energy), using equations 4.1 and 4.2 in conjunction with the medium energy coefficients (set A). Figure 4.3 shows a similar plot using the high energy coefficients (set B).

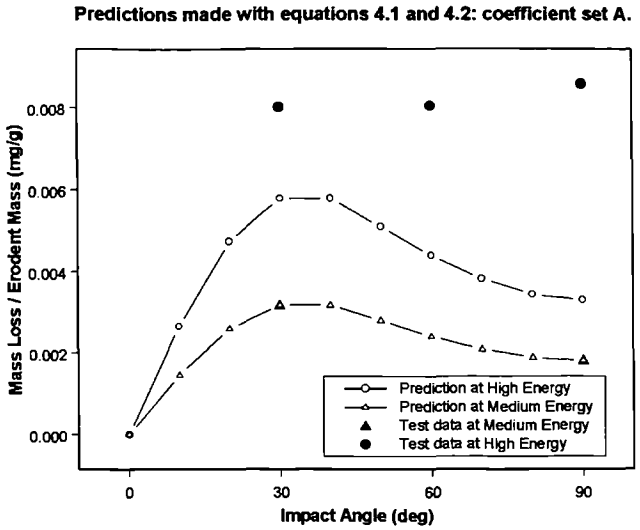

Figure 4.2 Comparison of predicted and measured results using coefficient set A.

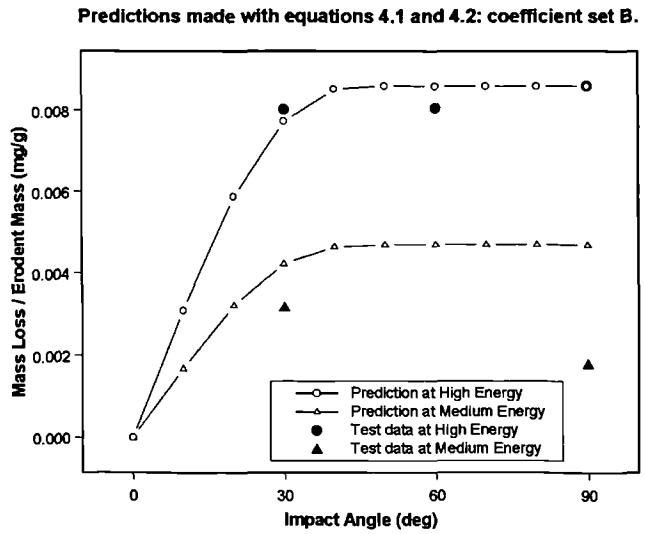

Figure 4.3 Comparison of predicted and measured results using coefficient set B.

It will be apparent that in Figure 4.2, the equations using coefficient set A are able to correctly predict the measured erosion at the medium energy level, but underpredict erosion at the high energy level. In Figure 4.3, the equations using coefficient set B can predict the measured erosion at the high energy level, but overpredict erosion at the medium energy level. The relationship between erosion rate and impact velocity has not been represented sufficiently well in the equations—assuming that the experimentally observed trend is true.

This limited application of Neilson and Gilchrist's model suggests that it is not able to capture the erosion rate versus velocity variation implied by the experimental data. It does appear to predict the correct relationship between erosion rate and impact angle at the medium energy level, but unfortunately the data does not provide a well defined trend at the high energy level. There will need to be some adjustment of the experimental data when creating equations in order to capture the expected trends, and to mask out what may be spurious results from the testing.

In order to ensure the velocity variations suggested by the test data were repeated in the erosion equations, it was decided to use equation fitting software (TableCurve 2D and 3D) to generate further relationships based on the test data alone. Educated estimates of data points were provided where the test data sets were incomplete, or where individual points did not suit the expected trend sufficiently well.

4.2 Erosion equations based on test data only: mean data sets

The equations to be presented in this section are a selection of those created using TableCurve 2D and 3D equation fitting software. Raw data was supplied to these packages in tabular form, and the software cycled through the many forms of equations within it to find those that could represent the data sufficiently well. It was then necessary to visually examine plots produced by these equations to determine the ones that gave the closest possible representation of the data. Generally two or three equations were chosen for each set of data, and further manual examination carried out using spreadsheet software to examine equation behaviour at the limits of the impact velocity and impact angle ranges. From these further studies the best equations for each data set could be chosen.

4.2.1 Equations for mean erosion of metallic materials across all impact angles

In Chapter 3, a set of mean erosion rate data was developed for the metallic materials under consideration. This data has been used here to generate a number of equations for mean erosion rate. The benefit in creating such equations is that predictions from the CFD package will not favour one metallic material over against another, but rather

give a result with a broad uncertainty that could cover a range of materials. The first set of equations ignores the influence of impact angle, and is based on two-dimensional sets of erosion rate versus impact velocity data.

The mean erosion data is plotted on its own in Figure 4.4 below. Three sets of points are presented: one set for each of the three impact angles considered. It is apparent that the differences between these points, when viewed as a whole, is small enough to permit generation of an overall mean data set using all available data regardless of impact angle. Such a data set has been produced. The overall mean data is based on the initial sets of mean data for each of the impact angles. Thus each point on the overall mean line will be based on three underlying points, one for each impact angle. This avoids overall mean data being weighted towards the more popular 90^0 impact erosion rates.

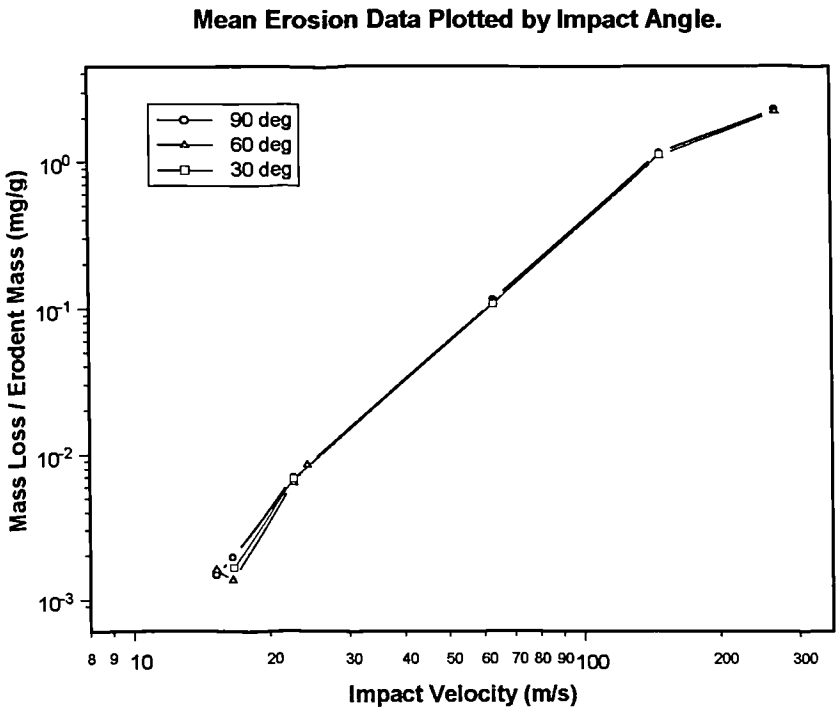

Figure 4.4 Plot of averaged erosion data.

Figure 4.4 indicates that the difference in erosion rates between different impact angles is apparent most at the lower impact velocities (and at the medium energy slurry test in particular). The approach taken when creating empirical equations has been to fit subsets of the data as appropriate, in order to preserve features of erosion behaviour at the lower velocities.

4.2.1.1 Overall mean equation using all velocities: $E = f(V_p)$

The first equation to be presented is one that covers all data from the lowest to the highest velocity level. Mean erosion rates for each velocity level were produced by taking the average across the three impact angles at each velocity. Thus the resulting data effectively eliminates the dependency on impact angle. Only the mean data set was used in creating the overall equation: there were no additional estimated data points included in the set. The resulting equation (generated by TableCurve 2D) is:-

$$\ln E_{MM} = \frac{(a_1 + b_1 V_p)}{(1 + c_1 V_p + d_1 V_p^2)} \tag{4.3}$$

where coefficients a_1 to d_1 are given in Table 4.2; E_{MM} is the mass loss of material per mass of sand impacting (mg/g); and V_p is the particle impact velocity (m/s). This equation has been plotted in Figure 4.5 along with the underlying mean data used to create it.

Table 4.2 Coefficients for Equation 4.3.

Coefficients	Values
a_1	-7.69614
b_1	1.0337E-02
c_1	5.5536E-02
d_1	6.9451E-05

It will be noted that equation 4.3 (and indeed none of the software generated equations) does not pass through zero erosion at zero velocity. This is unphysical, but to have constrained the equations to pass through zero would have made it almost impossible to fit them to the data in this way. The equations will be taken to only apply when the impact velocity is above some threshold level, which could be chosen according to the discretion of the equation user. A minimum level of 1 m/s would not be inappropriate.

Although equation 4.3 captures the air-sand data well, it does not give the correct gradient when passing through the slurry data. For this reason, two further equations have been created, one for the slurry data only, and another for the air-sand data plus the high energy point of the slurry data.

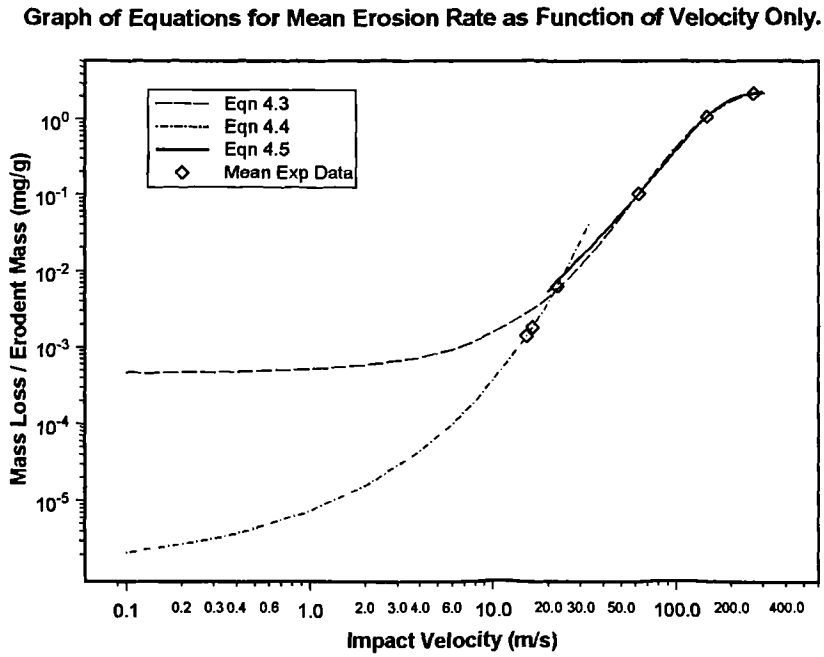

Figure 4.5 Graph showing plots of equations 4.1 to 4.3, along with underlying mean experimental data (eliminating angle dependency).

4.2.1.2 Mean equation for slurry data only: $E = f(V_p)$

Using only the mean slurry data in the 2D equation fitting software gives the following relation:-

$$\ln E_{MM} = a_2 + b_2\sqrt{V_p} \quad \left(V_p \leq 25.0\,\text{ms}^{-1}\right) \tag{4.4}$$

where coefficients a_2 and b_2 are given in Table 4.3, and the other parameters are as before. Note that no additional estimated data points were required in the generation of this equation. The resulting predictions have been plotted in Figure 4.5. This equation is only applicable for V_p less than 25.0 m/s (conservative bound) as unrealistically high erosion rates will be returned beyond this.

4.2.1.3 Mean equation for high energy slurry data and all air-sand data: $E = f(V_p)$

Considering the high energy point from the mean slurry data, along with the mean air-sand data produces the following equation:-

$$E_{MM}^{-1} = a_3 + b_3\frac{\ln V_p}{V_p^2} + \frac{c_3}{V_p^2} \quad \left(25.0 \leq V_p \leq 268.0\right) \tag{4.5}$$

where coefficients a_3 to b_3 are given in Table 4.3. This has also been plotted in Figure 4.5 for comparison with the previous equations. A lower velocity limit of 25.0 m/s has been set for this equation, and a higher velocity limit of 268.0 m/s.

Table 4.3 Coefficients for equations 4.4 and 4.5.

Coefficient	Value
a_2	-13.6346
b_2	1.81915
a_3	0.623859
b_3	-31627.08
c_3	163632.7

The main difference between the three mean equations lies in their behaviour at lower velocities. The overall equation (4.3) gives higher erosion rates at velocities below about 22.0 m/s than the mean slurry equation (4.4). Only the mean slurry equation correctly follows the gradient of the line through the three slurry erosion points.

Setting the correct level of erosion rate at low velocity limits is a somewhat arbitrary task, as no slurry tests were performed at impact velocities less than the nominal 15.3 m/s of the low energy test. This means that the true low velocity behaviour is not known from the available test data. However, the nature of the slurry test is such that the impact velocities reported here are artificially high as they stand: this will be discussed in a later chapter. The approach adopted has been to select equations that follow the implied velocity/erosion gradient at slurry points, and to accept the resulting low velocity behaviour as being representative of what may happen in real situations. There will be a threshold velocity for each particular material, below which no erosion will occur.

If these equations are to be used in simulations, the recommendation is that both equations 4.4 and 4.5 should be used after finding the point where both curves meet (at 24.247 m/s). Equation 4.3 does not follow the low velocity data sufficiently accurately to be of general use.

4.2.2 Three-dimensional surface fits for mean data

While it may be useful to have simple equations which relate erosion to impact velocity alone, an equation that reflects the dependence on impact angle will possibly provide greater accuracy in CFD modelling applications. To this end, several equations have been generated using TableCurve 3D which relate erosion rate to both impact angle and velocity. Generally several equations were generated for each set of data: the most appropriate ones will be presented here.

4.2.2.1 Mean angle relationships at various velocities.

One of the problems faced when using the current data set to fit equations is that no tests were conducted at low velocities and low impact angles. The lowest velocity considered was around 15.3 m/s, while the lowest impact angle was 30^0. It has therefore been necessary to generate additional data to ensure the analysis software returns plausible results. A set of equations was created to represent the erosion versus impact angle behaviour at specific velocities, i.e. 2D equations relating erosion rate to impact angle alone. These 2D equations were then used to estimate additional data points for the 3D equations.

- Erosion versus impact angle for: $V_p = 16.5$ m/s

Erosion rate was set to 10^{-8} mg/g (effectively zero) at an impact angle of 0.1^0 to provide a lower limit on the curve. The equation chosen has the form:-

$$E_{MM}^{-1} = a_4 + b_4 \frac{\ln \alpha_p}{\alpha_p^2} + \frac{c_4}{\alpha_p^2} \qquad (4.6)$$

where a_4 to b_4 are appropriate coefficients. As the same form of equation has been used at all velocity levels, it is only necessary to report the different coefficients here. Table 4.4 provides this data.

- Erosion versus impact angle for: $V_p = 22.6$ m/s

The same approach was followed as previously, with an estimate of $E_{MM} = 10^{-8}$ mg/g at $\alpha_p = 0.1^0$. Coefficients are reported in Table 4.4.

Table 4.4 Coefficients for Impact Angle Relationships

Mean V_p (m/s)	Coefficient	Value
16.5	a_4	926.1372
	b_4	-946656.26
	c_4	2704884.5
22.6	a_5	174.0650
	b_5	-75777.30
	c_5	221401.9
63.0	a_6	9.99679
	b_6	-4547.172
	c_6	13678.80
148.0	a_7	1.019555
	b_7	-453.7075
	c_7	1367.036

- Erosion versus impact angle for: $V_p = 63.0$ m/s

Air-sand data was used at this velocity. It was found that the equation could not be fitted to the experimental data as originally defined: the erosion value at 60^0 was less than that at 90^0. Equation (4.6) requires erosion at 60^0 to be somewhere between the 30^0 and 90^0 values—below that at 30^0, and higher than that at 90^0. A mean rate was therefore calculated for erosion at 60^0, to ensure the correct trend would be followed. An additional point was also included at 15^0 to effect the desired trend: this was taken to be half the erosion rate at 30^0. Subsequent coefficients are given in Table 4.4.

- Erosion versus impact angle for: $V_p = 148.0$ m/s

An additional point at 15^0 was again included for this velocity—taken to be half the erosion rate at 30^0 as before. Coefficients are in Table 4.4. Figure 4.6 presents plots of all four equations.

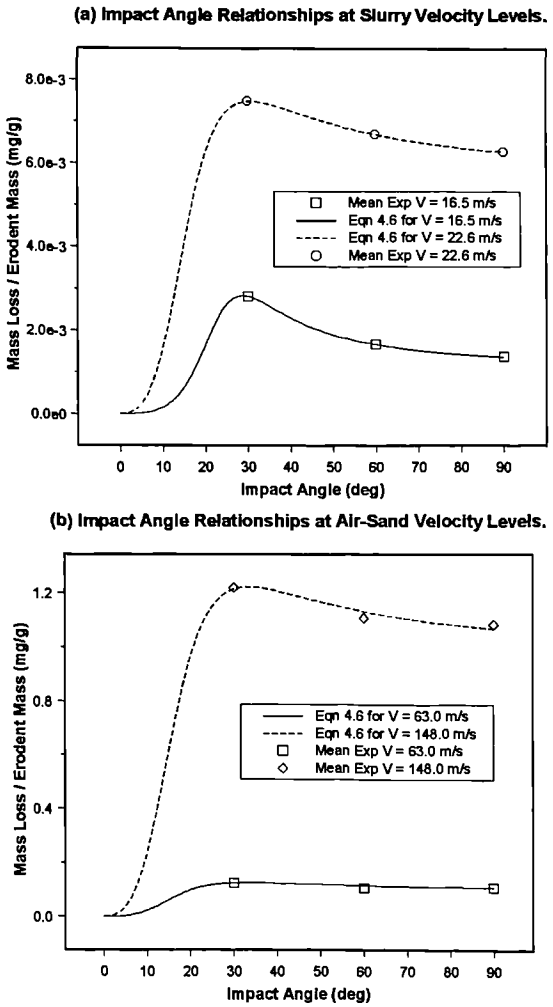

Figure 4.6 Impact angle relationships for mean erosion data (metallic materials).

4.2.2.2 Surface for mean slurry data only: $E = f(V_p, \alpha_p)$

The initial approach in creating an equation relating erosion rate to both impact angle and velocity for the mean slurry data, was to allow the equation to take whatever form best suited the data (i.e. not constraining it to pass through zero). Some equations were generated in which low velocity erosion rates were estimated, but there was little difference between the behaviour of these equations at low velocity and others where there were no additional low velocity estimates. Equation 4.7 is the final surface chosen from this initial exercise:-

$$\ln E_{MM} = a_8 + b_8 V_p + c_8 \ln \alpha_p + \frac{d_8}{\alpha_p} \qquad (4.7)$$

α_p is the particle impact angle (degrees), and coefficients a_8 to d_8 are given in Table 4.5.

Another equation was also created using a composite approach. First, a simple power law curve fit was used to find the exponent n for a relation of the form $E \propto K \cdot V^n$ where K is an empirical constant. Thereafter another function was generated to provide a multiplier that imitated the angle relationship of equation 4.6. The final composite relation is:-

$$E_{MM} = 3.4771\text{E-}08 V_p^{3.9059} \cdot 4\xi(1-\xi) \quad \text{where } \xi = e^{-\left(\frac{\alpha_p - 0.0109}{39.657}\right)} \qquad (4.8)$$

The suitability of these equations can be analysed by generating two-dimensional plots of erosion against velocity for particular impact angles, and also erosion against impact angle for particular velocities. Figure 4.7 shows erosion rate as a function of velocity for an impact angle of 90^0. The mean experimental data for 90^0 impact erosion is plotted, and curves generated using equations 4.4, 4.7 and 4.8. (Equation 4.4 is for mean erosion disregarding impact angle at slurry velocities. The graph shows that equation 4.7 gives results similar to this at low impact velocities.) While equation 4.7 can predict the correct erosion levels between 15 m/s and 22 m/s, the low velocity behaviour is not satisfactory. Ideally the erosion rate would fall to zero at zero velocity—in the same way as equation 4.8. Instead, equation 4.7 almost approaches a constant value as the velocity falls. This could result in erosion predictions being higher at low impact velocities than they should be.

Equation 4.8 underpredicts the erosion rate at 90^0 impact angle across the whole velocity range considered. Had the impact angle been set to 30^0 (and the appropriate mean experimental data presented), the agreement would be much closer. The problem is that the

second part of equation 4.8 (accounting for impact angle effects) has a greater difference between erosion rates at 30^0 and at 90^0 than is observed in the experimental data. The advantage of equation 4.8, however, is that it does fall to zero erosion at zero velocity.

Table 4.5 Coefficients for Equation 4.7.

Coefficient	Values
a_8	-4.99294
b_8	0.197034
c_8	-0.92912
d_8	-36.2032

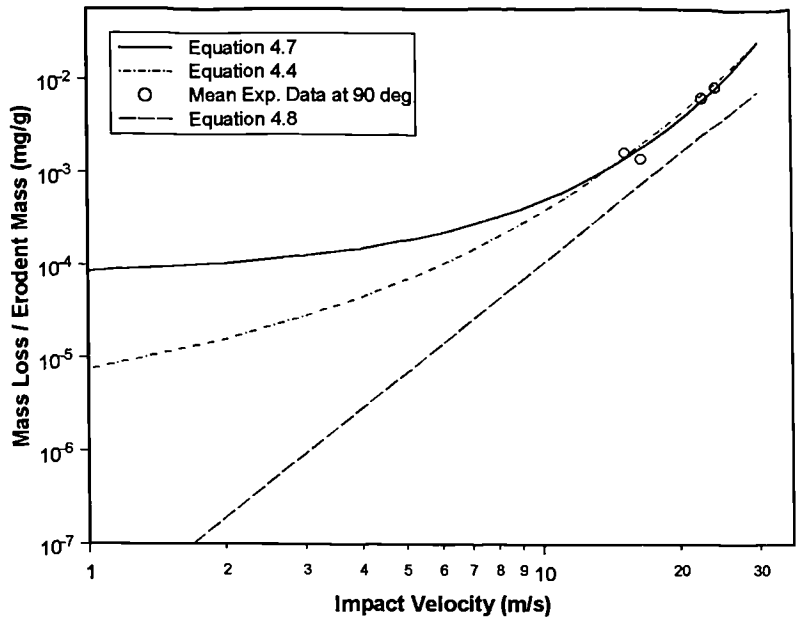

Figure 4.7 Comparison of various functions with experimental erosion rates as a function of velocity.

The advantage of three-dimensional equations is that they can give some indication of change in erosion rate due to impact angle. This behaviour is illustrated in Figure 4.8, where the predicted erosion rates using equations 4.7 and 4.8 are plotted against impact angle for two velocities: 16.5 m/s and 22.6 m/s (medium and high energy levels on the slurry rig). The predictions are compared with the mean experimental data at impact angles of 30^0, 60^0, and 90^0, as well as equation 4.4 using coefficients for velocities of 16.5 m/s and 22.6 m/s. Equation 4.7 performs better than equation 4.8 in terms of reproducing the erosion rate versus impact angle relationship, and also has a much smaller change between erosion rate at 30^0 and 90^0 in comparison to equation 4.8.

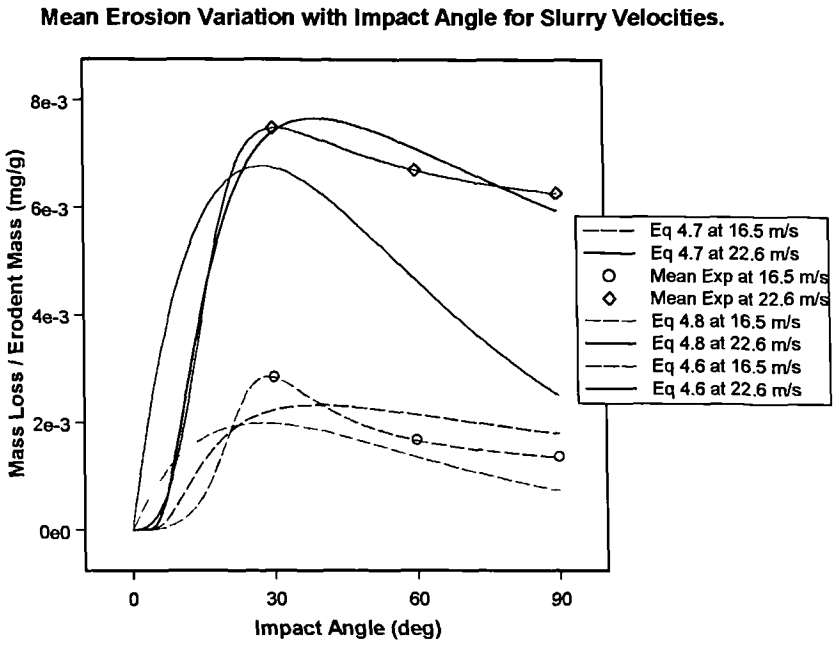

Figure 4.8 Evaluation of equations 4.7 and 4.8 as a function of impact angle.

The result of this analysis would be to recommend equation 4.7 for use when velocities are above 10 m/s or so, and to use equation 4.8 when velocities are below this.

4.2.2.3 Surface for all mean data: $E = f(V_p, \alpha_p)$

A surface has been created which covers the entire velocity range from 15.1 m/s to 268 m/s. Estimates of erosion rate were made at a velocity of 1 m/s (and for a range of impact angles) using equation 4.7 given previously. Equation 4.6 with the four sets of coefficients was also used to generate additional estimated data for the appropriate velocity levels. The resulting equation is:-

$$\ln E_{MM} = a_9 + b_9(\ln V_p)^2 + c_9 \ln V_p + \frac{d_9}{\sqrt{V_p}} + e_9 \frac{\ln V_p}{V_p} + \frac{f_9}{V_p} + g_9\sqrt{\alpha_p}\ln\alpha_p + h_9\frac{\alpha_p}{\ln\alpha_p} + i_9 \ln\alpha_p$$

Limits on use: $\alpha_p \geq 2.0^0$; $V_p \geq 2.0$ m/s (4.9)

where a_9 to i_9 are the empirical coefficients given in Table 4.6, V_p is the particle impact velocity (m/s), and α_p is the impact angle (deg). The equation is plotted as a function of velocity for an impact angle of 90^0 in Figure 4.9. Mean experimental data at 90^0 is shown for comparison, along with a plot of equation 4.9 (which applies to slurry velocities only).

Table 4.6 Coefficients for Equation 4.9.

Coefficients	Values
a_9	-845.6141
b_9	-13.24336
c_9	201.0870
d_9	2278.403
e_9	-638.2688
f_9	-1457.711
g_9	-1.434076
h_9	2.486511
i_9	6.037049

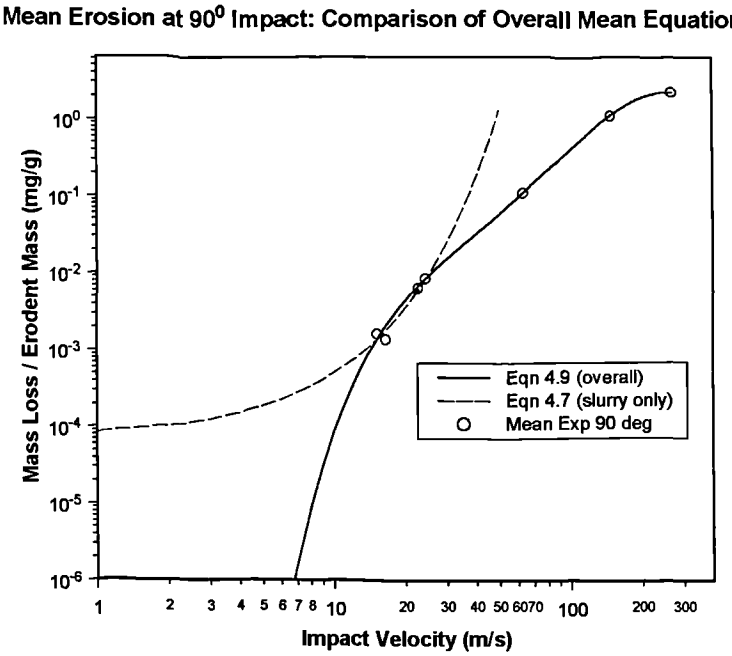

Figure 4.9 Comparison of Equation 4.9 with other data.

Equation 4.9 should not be used at velocities lower than 2.0 m/s, as the function tends to infinity when velocity falls below 1.0 m/s. The practice to be adopted in the present study is to use equation 4.7 for velocities up to 22.322 m/s (the point where equations 4.7 and 4.9 meet), and to use equation 4.9 for velocities beyond this—in cases where a mean metallic erosion rate is applicable.

The impact angle behaviour of equation 4.9 has also been explored. Figures 4.10 and 4.11 show predicted variation of erosion rate with impact angle for four velocity levels of 16.5 m/s, 22.6 m/s, 63.0 m/s, and 148.0 m/s. Note that equation 4.9 cannot be used when $\alpha_p = 1^0$ exactly, as this will cause a division by zero in one of the terms. The lower limit for equation 4.10 is therefore set to $\alpha_p = 2.0^0$.

The main advantage to using equations 4.7 and 4.9 is that particles impacting at low angles will not cause a disproportionately high amount of erosion— as would occur if one of the two-dimensional equations based on only impact velocity were used. Some benefit will also come from the fact that the classical ductile impact angle relationship is loosely followed as impact angle increases. These equations are only valid for metallic materials similar to those in the group tested. They will be useful for studies where a relative comparison of erosion performance in a component is required, and not actual lifetime values—although they will still give some idea of the likely order of lifetime possible.

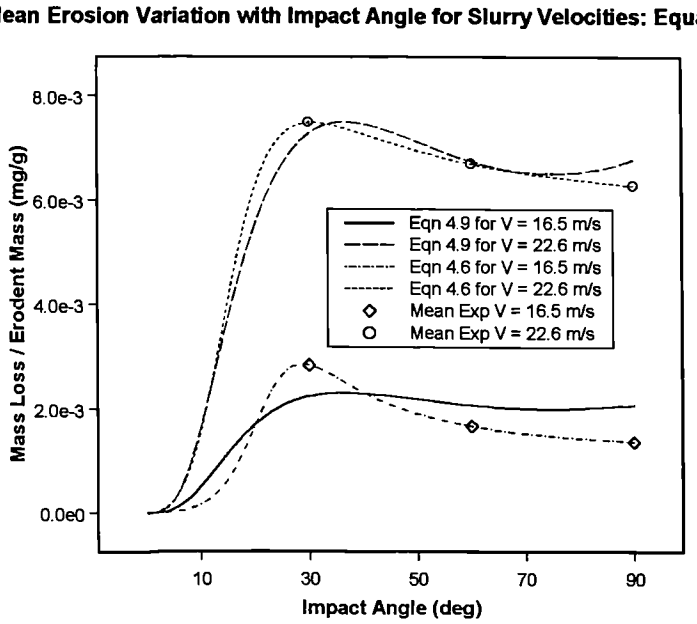

Figure 4.10 Equation 4.9 at various impact angles: slurry velocities.

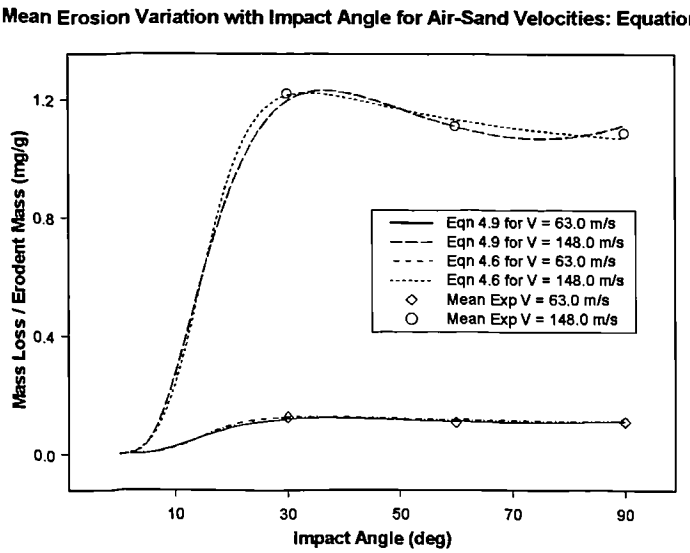

Figure 4.11 Equation 4.9 at various impact angles: air-sand velocities.

4.3 Erosion Equations for Specific Materials

Although the mean equation for metallic materials will have its uses in evaluating competing designs for erosion resistance, there may be times when an equation for a specific material is more desirable. The tungsten carbides were not included in the mean equation due to their vastly superior erosion resistance: it is therefore necessary to develop equations for these materials also.

4.3.1 Erosion equations for tungsten carbides

There is a difficulty in creating equations for tungsten carbide, as the amount of data available is not quite sufficient to produce equations that account for the effect of both impact velocity and angle for all three materials. Equations based on velocity alone will be presented for all three tungsten carbides, and one equation based on both angle and velocity will be given for Tungsten Carbide DC(Z)05.

4.3.1.1 Mean equation for Tungsten Carbide SMS-25A: $E = f(V_p)$

The available erosion rate data for Tungsten Carbide SMS-25A has been averaged across all angles at each velocity level to create a set of mean data. Where tests have been performed at more than one angle for a particular velocity, the averaging has been performed by first finding the mean value for all tests at a particular angle and velocity (as there were repeat tests at the same conditions), and then taking the mean across the two angles (30^0 and 90^0). No tests were performed at 60^0 impact angle.

The trend shown by the combined slurry and air-sand data for Tungsten Carbide SMS-25A is difficult to use in creating an overall equation. Several equations were created for this particular grade of tungsten carbide. The first two will not be presented here, but are given in Appendix C. After using these equations initially, a further two equations were created, one of which covered the slurry velocities, and the other covering the higher air-sand velocities. The equation for slurry velocities is:-

$$\ln E_{MM} = a_{tc1} + b_{tc1}\sqrt{V_p} \qquad V_p \leq 22.59 \text{ m/s} \qquad (4.10)$$

where E_{tc} is the mass loss per erodent mass (mg/g) and the coefficients are given in Table 4.7. The second equation, covering velocities up to the medium velocity on the air-sand rig (148 m/s) is given as:-

$$\ln E_{MM} = a_{tc2} + b_{tc2}V_p^2 \ln V_p \qquad 22.59 \text{ m/s} < V_p \leq 148.0 \text{ m/s} \qquad (4.11)$$

where the coefficients are also given in Table 4.7. These two equations are plotted as a function of velocity (along with the underlying mean experimental data) in Figure 4.12.

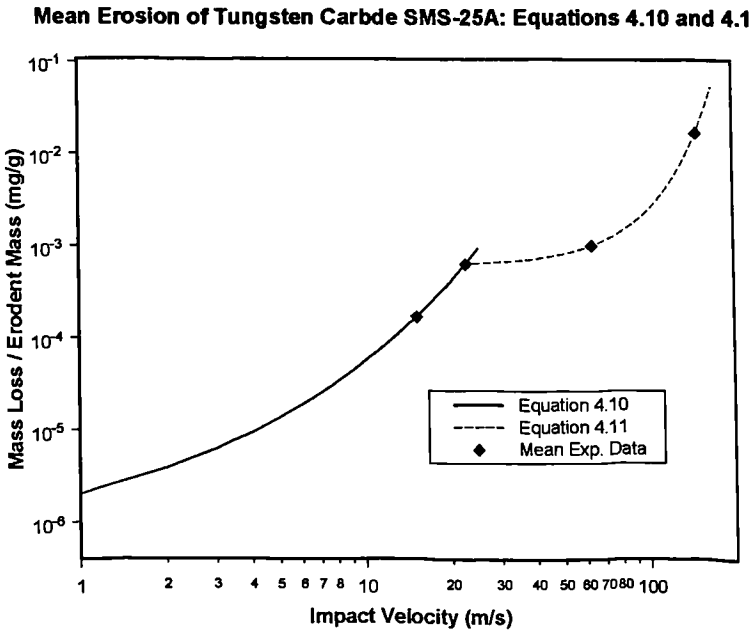

Figure 4.12 Mean erosion of Tungsten Carbide SMS-25A: Equations 4.10 and 4.11.

Table 4.7 Coefficients for equations 4.10 and 4.11.

Coefficients	Values
a_{tc1}	-14.64553
b_{tc1}	1.532546
a_{tc2}	-7.410363
b_{tc2}	3.06688e-5

4.3.1.2 Mean equation for Tungsten Carbide VC-808: $E = f(V_p)$

One equation has been obtained to correlate the mean erosion of Tungsten Carbide VC-808. No low velocity estimates were necessary to generate the equation. The equation covers the whole velocity range, and is given as follows:-

$$E_{MM} = \frac{a_{tc3}}{\left(1+\exp\left(\frac{-\left(V_p - b_{tc3}\right)}{c_{tc3}}\right)\right)} \qquad (4.12)$$

where the coefficients a_{tc3} to c_{tc3} are given in Table 4.8. The equation is plotted alongside the underlying mean data in Figure 4.13 below. Note that the mean data point at medium energy level (16.5 m/s) on the slurry rig has been disregarded.

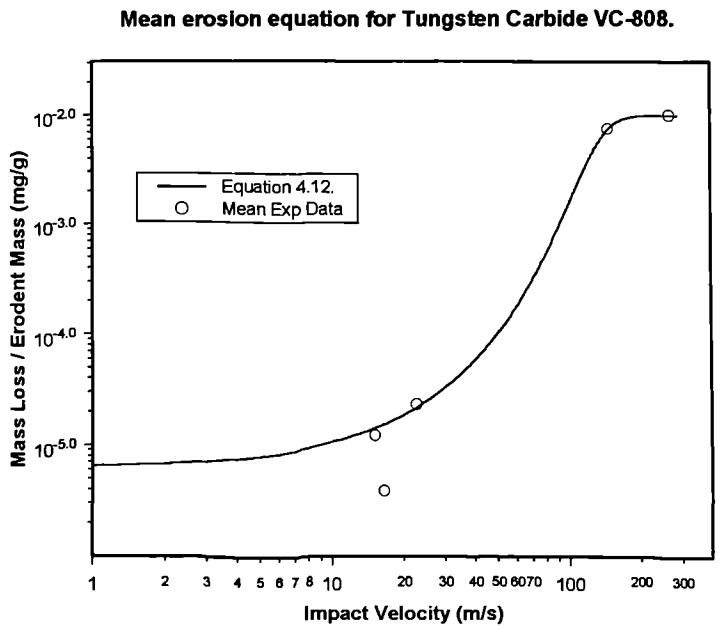

Figure 4.13 Plot of equation 4.12 for mean erosion of Tungsten Carbide VC-808.

Table 4.8 Coefficients for equations 4.12 and 4.13.

Coefficients	Value
a_{tc3}	0.010281
b_{tc3}	128.6473
c_{tc3}	17.2936
a_{tc4}	-19.4372
b_{tc4}	-6.0985E-04
c_{tc4}	3.16444

4.3.1.3 Mean equation for Tungsten Carbide DC(Z)05: $E = f(V_p)$

An equation has been produced across the whole velocity range for Tungsten Carbide DC(Z)05, and is given as:-

$$\ln E_{MM} = a_{tc4} + b_{tc4} V_p^{\frac{3}{2}} + c_{tc4} \ln V_p \qquad (4.13)$$

where coefficients a_{tc4} to c_{tc4} are given in Table 4.8. The equation is plotted in Figure 4.14 below, along with equation 4.12 for comparison.

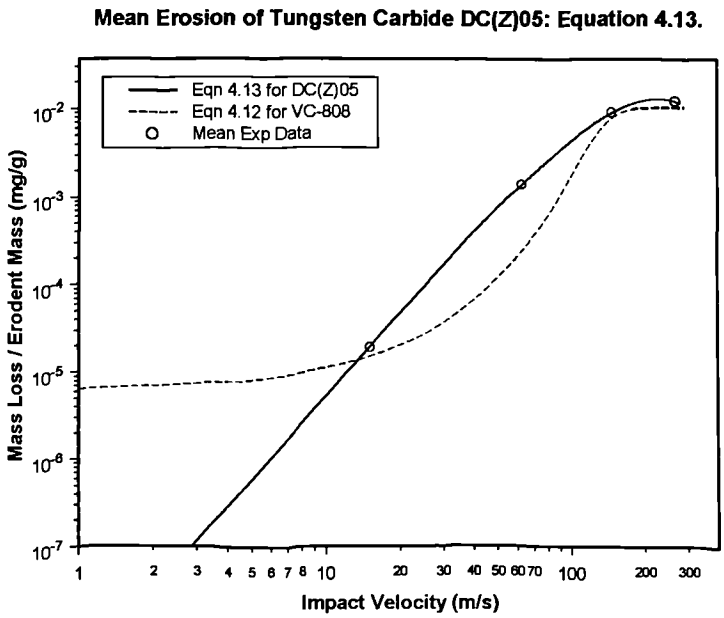

Figure 4.14 Plot of equation 4.13 for mean erosion of Tungsten Carbide DC(Z)05.

There is obviously a considerable difference between equations 4.13 and 4.12 in the shape of curve produced. Several more tests at intermediate velocities would be required to properly establish the nature of the relationship between erosion and velocity. However, the equations should give some indication of erosion levels when used in CFD based erosion modelling software.

4.3.1.4 Further equation for Tungsten Carbide DC(Z)05: $E = f(V_p, \alpha_p)$

An attempt was made to generate an equation that accounted for both impact angle and velocity using the data for Tungsten Carbide DC(Z)05. The underlying data was created by assuming that the erosion at 30^0 impact angle would be half that at 90^0. Only velocities up to 148 m/s were accounted for in the data set, and although erosion tests had been carried out at 30^0 impact angle for velocities of 148 m/s and 268 m/s, these data points were ignored in the data set (to ensure a good fit). An estimate of 10^{-8} mg/g erosion rate was used for impact angles of 0.1^0 at all velocities, along with a low velocity estimate of 10^{-9} mg/g (at all impact angles). The resulting equation is:-

$$\ln E_{MM} = a_{tc5} + b_{tc5}\sqrt{V_P}\ln V_P + c_{tc5}\sqrt{V_P} + d_{tc5}\ln \alpha_p \qquad (4.14)$$

where the coefficients a_{tc5} to d_{tc5} are given in Table 4.9. The equation is plotted as a function of velocity (and impact angle of 90^0) in Figure 4.15. Equation 4.13 is also shown for comparison.

Table 4.9 Coefficients for equation 4.14.

Coefficients	Values
a_{tc5}	-23.34645
b_{tc5}	-0.502562
c_{tc6}	3.830384
d_{tc5}	0.630930

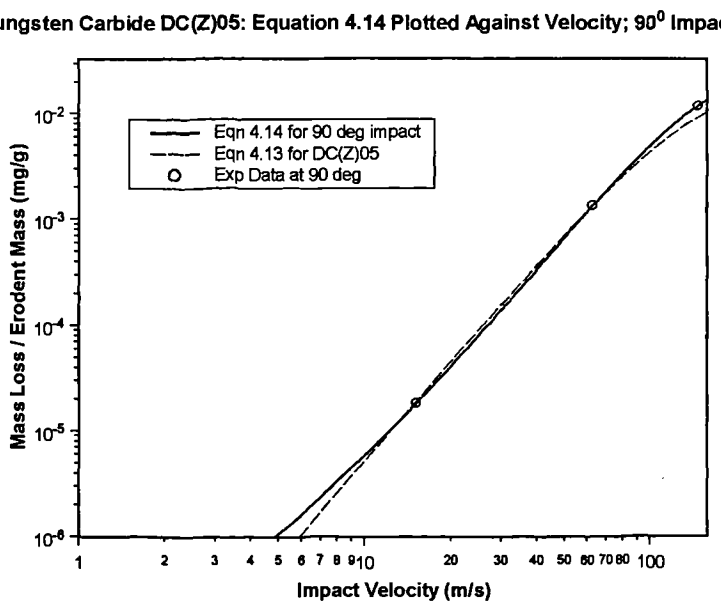

Figure 4.15 Tungsten Carbide DC(Z)05: Equation 4.14 as a function of velocity.

There does not appear to be a great deal of difference in Figure 4.15 between predictions using equation 4.13 and those using equation 4.14. However, equation 4.14 has the distinct advantage that it can predict the effect of impact angle as well as velocity.

Equation 4.14 can be plotted as a function of impact angle at specific velocities. Figure 4.16 shows the predicted erosion rate versus impact angle for an impact velocity of 148 m/s. The two experimental data points obtained at this velocity (for 30^0 and 90^0 impact) are shown for comparison, as is the underlying data used to generate the equation. Only the 90^0 impact point of the underlying data set is based on experimental testing: the other points are estimated as discussed previously. Similarly shaped curves are obtained at other velocity levels.

Figure 4.16 shows that equation 4.14 predicts maximum erosion at 90^0, which is the accepted behaviour for brittle materials like tungsten carbide. The advantage of equation 4.14 over equation 4.13 is that glancing particles in the CFD modelling will not cause as much damage as the perpendicular impacts: which behaviour should be observed in the field. No such equations were developed for the other two tungsten carbides.

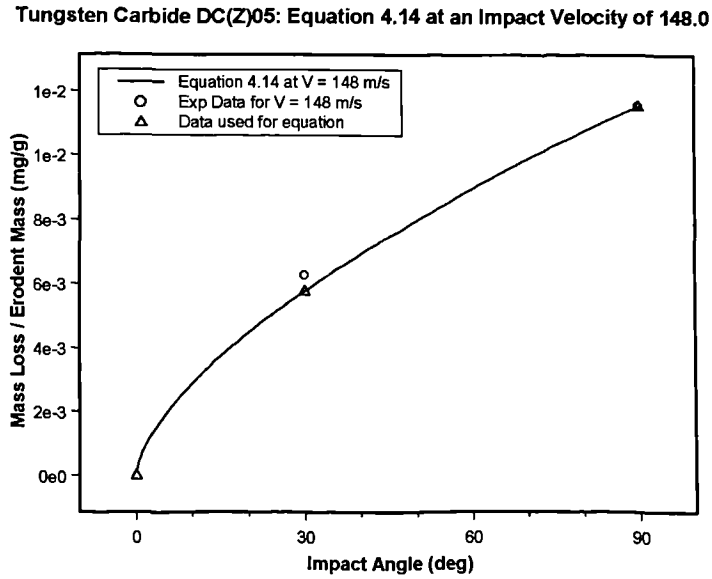

Figure 4.16 Plot of equation 4.14 at impact velocity of 148.0 m/s.

4.3.2 Equations for Duplex F51

A number of equations were obtained for Duplex F51. The amount of data available to base equations on is less than that used for the mean metallic materials equations. The developed equations will be dealt with briefly.

4.3.2.1 Mean equation based on velocity: $E = f(V_p)$

An equation relating erosion rate to impact velocity alone is given in Appendix C, along with appropriate plots.

4.3.2.2 Equation accounting for angle and velocity: $E = f(V_p, \alpha_p)$

An equation has also been constructed for Duplex F51 that accounts for the effect of both impact angle and velocity. Some of the experimental data was ignored when developing this equation. Specifically, erosion rates at the following conditions were ignored: V_p = 15.13 m/s and $\alpha_p = 90^0$; V_p = 16.57 m/s and $\alpha_p = 45^0$, 75^0; V_p = 63.0 m/s and $\alpha_p = 90^0$; also data at V_p = 22.6 m/s and 268 m/s. Additional estimates were required at low impact angles: erosion rate at 0.1^0 was taken to be 0.1% of the erosion at 30^0. Estimates of erosion at 0.1 m/s were also used. The equation which results is:-

$$\ln E_{MM} = a_{df1} + b_{df1} \ln V_p + c_{df1} \alpha_p \ln \alpha_p + d_{df1} \sqrt{\alpha_p} \ln \alpha_p + e_{df1} \sqrt{\alpha_p} \quad (4.15)$$

where coefficients a_{df1} to e_{df1} are given in Table 4.12. The equation is plotted against velocity in Figure 4.17 below.

Table 4.10 Coefficients for equation 4.15.

Coefficients	Values
a_{dfl}	-23.78876
b_{dfl}	2.89125
c_{dfl}	0.024506
d_{dfl}	-1.21708
e_{dfl}	5.41775

The mean 3D equations (4.7 and 4.9) have also been plotted alongside equation 4.15 in Figure 4.17, at an impact angle of 90^0. It can be seen that Equation 4.15 does represent the velocity variation of Duplex F51 erosion fairly well, and may give better low velocity predictions than equation 4.7.

Figure 4.18 examines the behaviour of equation 4.15 with impact angle. Four different velocity levels are shown, with the available experimental data being plotted alongside the equation in each. Agreement with experimental data is best at the highest velocity level considered: 148.0 m/s. At some of the slurry velocity levels, the equation only loosely represents the experimental variations.

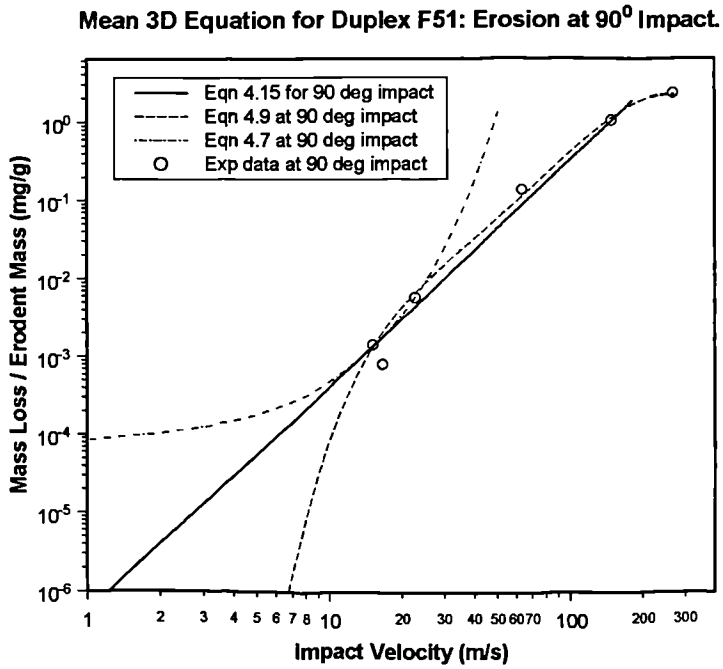

Figure 4.17 Plot of equation 4.15 for 90^0 impact angle.

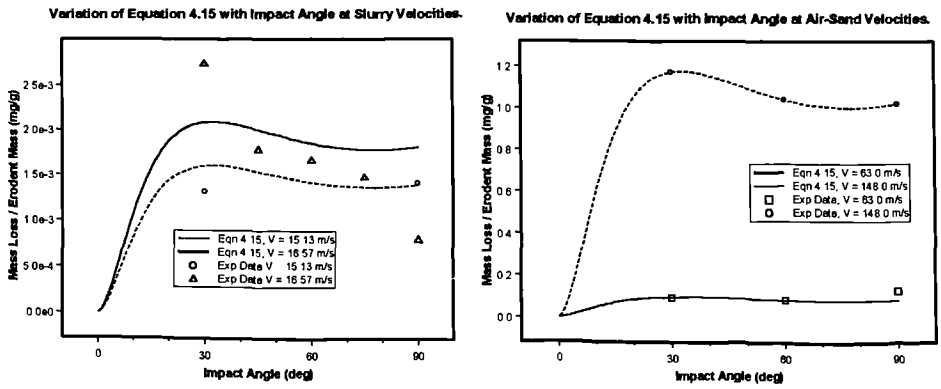

Figure 4.18 Plot of equation 4.15 at various velocities.

4.3.3 Other materials

Equations for AISI 4130 and 17.4 PH 105k are given in Appendix C. Both equations account for the effect of impact angle and velocity on erosion rate. They are not included here to prevent cumbersome repetition of similar concepts.

4.4 Summary and conclusions

The desired objective of developing empirical erosion equations for use in the CFD-based erosion modelling tool has been achieved. Equations have been obtained in two ways: first by calibrating an existing set of erosion equations (model of Neilson and Gilchrist), and secondly by using curve and surface fitting software to generate further equations based on the underlying experimental data alone. The advantage in the latter approach is that the generated equations will follow the experimental trends to a higher degree than the calibrated semi-empirical equations. Generating equations based on only experimental data does not make use of possible existing relationships between erosion rate and known properties of materials (e.g. hardness, particle diameter etc.) However, as such relationships are only tentatively known, it is perhaps not unreasonable to have excluded them for the present study. Future work could look at taking some of the more probable relationships into account.

A mean equation for metallic materials has been developed that should be useful for modelling studies where component designs are being compared relative to one another, and where some idea of the 'real life' component longevity is also desired. Various additional equations have been generated for specific materials, and in particular for the tungsten carbides. The equations for tungsten carbides are based on a relatively small number of test points, and so should be treated with care in CFD-based erosion studies. Some of the later

equations for specific metallic materials (i.e. Duplex F51) may give better results than the initial mean equations, especially in the low velocity regions.

Ultimately the only way to test the validity of the equations presented in this chapter is to use them in CFD-based erosion modelling simulations where experimental data for both the flow and erosion sides of the case are available. Performing such validation is the basis for the bulk of the work remaining in this thesis.

Before going on to consider the validation work, it will be instructive to consider some CFD modelling that attempted to predict actual particle impact velocities for a liquid jet impacting a flat surface—as in the slurry jet erosion testing. The outcome of such modelling has significant implications for the type of erosion equation developed in this chapter. Chapter 5 presents such a study.

5.0 Liquid Jet Modelling: Effect of liquid on true impact angle and velocity

5.1 Introduction

In almost all erosion testing studies where a liquid-jet impact facility has been used, the impact angle and velocity reported are the mean impact angle between the nozzle central axis and the specimen surface, and the mean liquid velocity through the nozzle. While it is generally recognised that the actual particle impact angle and velocity at the surface will be different from this, there have been very few attempts to measure or predict the actual values. Figure 5.1 illustrates the deflection of particle trajectories from the mean path, as well as the reduction in velocity due to the stagnation region (for 90^0 impact). There will be similar effects at impact angles other than 90^0.

There have been some studies in which numerical predictions were made of a free surface liquid impinging jet. One example is that of Fujimoto et al. (1999) who solved conservation equations in primitive variable form for the laminar flow of an incompressible jet, in order to evaluate convective heat transfer between the jet and solid surface. Their model considered only the liquid phase: the free surface boundary was tracked as part of the numerical procedure. Fujimoto et al. (1999) validated their simulations by comparing results against the experimental measurements of Stevens and Webb (1992, 1993a, b). These papers give LDV (Laser Doppler Velocimetry) measurements of the flow structure of impinging free liquid jets at perpendicular impact, and provide excellent data with which to validate numerical predictions.

In this chapter, the work of Stevens and Webb (1992, 1993a, b) will be compared against CFD predictions of the same jets used by them experimentally, in order to gain some understanding of the difference between actual particle impact properties on a surface, and those used for data correlation in the slurry jet erosion testing. The modelling work is not exhaustive, and is only intended to be illustrative of what could be obtained by further modelling of actual erosion test conditions. Modelling actual test apparatus would require considerably more work than has been possible to do in the current time frame.

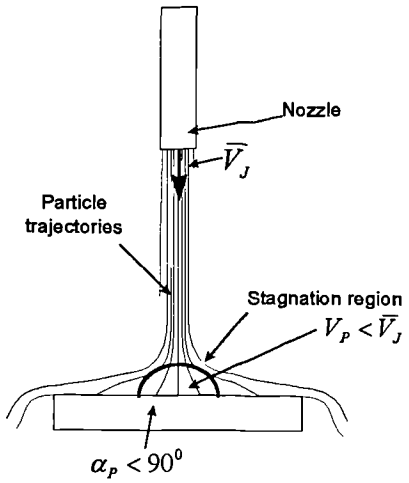

Figure 5.1 Liquid jet impacting specimen at 90^0.

5.2 Modelling Technique

Modelling the free surface flow of a liquid jet is a somewhat more difficult task than the flow of a single phase incompressible fluid. It is necessary to model both a liquid and a gas phase for the free liquid jet problem, and to employ some means of tracking the interface between the gas phase and the liquid phase. In this study, the volume-of-fluid (VOF) method (Hirt and Nichols, 1981) has been used to model the liquid jet in surrounding air. The VOF model predicts the flow of two or more immiscible fluids by solving a single set of momentum equations, and tracking the volume fraction of each fluid throughout the domain. The interface between phases is tracked by solving the continuity equation for the volume fraction of one or more of the phases. Within cells containing the interface, a geometric reconstruction technique (Youngs, 1982) is used to represent the interface in order to enable calculation of face fluxes for these cells.

In this study, the jet has been modelled as an axisymmetric problem only. For this reason, three-dimensional effects that might occur with a real jet (such as jet break up in random directions) will not be reproduced. An idealised problem has been chosen for study in order to correspond with the experimental measurements available. However, the experimental studies of Stevens and Webb were conducted using dimensions and conditions under which break up would not occur (to enable LDV measurement of velocities). It is suspected that jet break up would have been present to some extent in the slurry tests presented in Chapter 3— as the ratio of nozzle diameter to height was higher than in the experimental test cases, thus giving more room for air entrainment and subsequent break up.

5.3 Model Validation

Two cases from the work of Stevens and Webb (1992, 1993a, b) have been selected for comparison with CFD predictions. The relevant parameters are listed in Table 5.1. The nozzle diameters are greater than that used in the slurry erosion testing (where nozzle diameter was 6 mm), and the nozzle-to-plate distances (height) are lower. In the slurry testing, the ratio of height to nozzle diameter was over 7, whereas in the validation studies, this ratio is one for case 2, and less than one for case 1. However, a personal communication with Stevens (2000) indicates that for height to nozzle ratios up to 4, there was no measurable effect on the flow structure inside the impingement region—for the velocity ranges considered in the work. Successful CFD results for the validation cases will therefore give a good indication of the basic flow behaviour likely to be present in the slurry testing, and certainly enough data with which to draw basic conclusions concerning the relation of particle impact velocities to liquid velocity through the nozzle.

Table 5.1 Parameters for validation cases.

Case	Nozzle D (mm)	Nozzle-plate distance (mm)	Reynolds No.
1	23.0	17.25	37,000
2	10.9	10.9	37,000

Experimental data presented by Stevens and Webb (1993a) includes radial velocity profiles moving out from the centre line of the impinging jet, free surface velocities, and liquid layer depth measurements (though not all for these cases: other cases were also considered in their research). Normalised RMS turbulence across the liquid layer depth has been reported for case 1. There is certainly sufficient data to properly validate CFD modelling for a free liquid jet impingement.

5.3.1 CFD model parameters

Both cases were modelled using the same approach. A hexahedral structured mesh was created for the particular geometry in question, with greater cell density in the liquid jet region than in the air region. The centre-line of the liquid jet formed the axis of rotation for the axisymmetric model. Figure 5.2 shows dimensions of the solution domain for both cases.

Inlet boundary conditions were obtained by calculating the required mass flowrate for the particular Reynolds number and nozzle diameter, and using this to calculate fully developed flow profiles (velocity and turbulence) from a periodic model of a pipe section. Three turbulence models have been used: initially the standard k-epsilon model (Launder and

Spalding, 1974), thereafter the RNG k-epsilon model (Yakhot and Orszag, 1986), and finally the Reynolds Stress Model (Launder, 1989). Standard wall functions have been used in all cases. The differential viscosity option was activated in the RNG k-epsilon model to see if this provided improved predictions near the stagnation region of the impinging jet: results suggest that it did.

A constant pressure boundary was specified at the outlet. The air-volume fraction was set to 1.0 at this boundary to ensure only air could flow back into the domain. Turbulence intensity was set to 1.0%. Use of the geo-reconstruct linear interpolation scheme for interface location required a transient solution. The time-steps required were generally in the order of $5x10^{-5}$ to $1x10^{-4}$s. Air filled the whole domain at t = 0.0 s. When calculations began, liquid gradually flowed from the nozzle, impacted the flat surface, and moved out to the pressure boundary. The PISO algorithm (Issa et al., 1986) was used in solving the model, along with the PRESTO! scheme (PREssure STaggered Option) for pressure interpolation. The momentum and turbulence equations were solved with the second-order upwind discretisation scheme.

In the multiphase model, the implicit body force treatment and surface tension options were activated. The former parameter improves flow predictions when strong body forces such as gravity are present, while the surface tension model is that of Brackbill et al. (1992). The surface tension coefficient was left at the default value for water (0.0735 N/m).

Other important conditions were the specification of gravity (9.81 m/s^2) in the axial direction, activation of specified operating density (air), and setting the reference pressure location in the region of lighter fluid density. Some of these settings are obviously specific to the CFD package used (Fluent version 5.4), but they will be useful for anyone wishing to repeat the models with the same package.

Table 5.2 outlines the CFD solutions that have been obtained. Note that the original meshes were adapted after the initial solution to ensure sufficient cell density in the liquid layer. Abbreviations used to describe the turbulence models are given in Table 5.3.

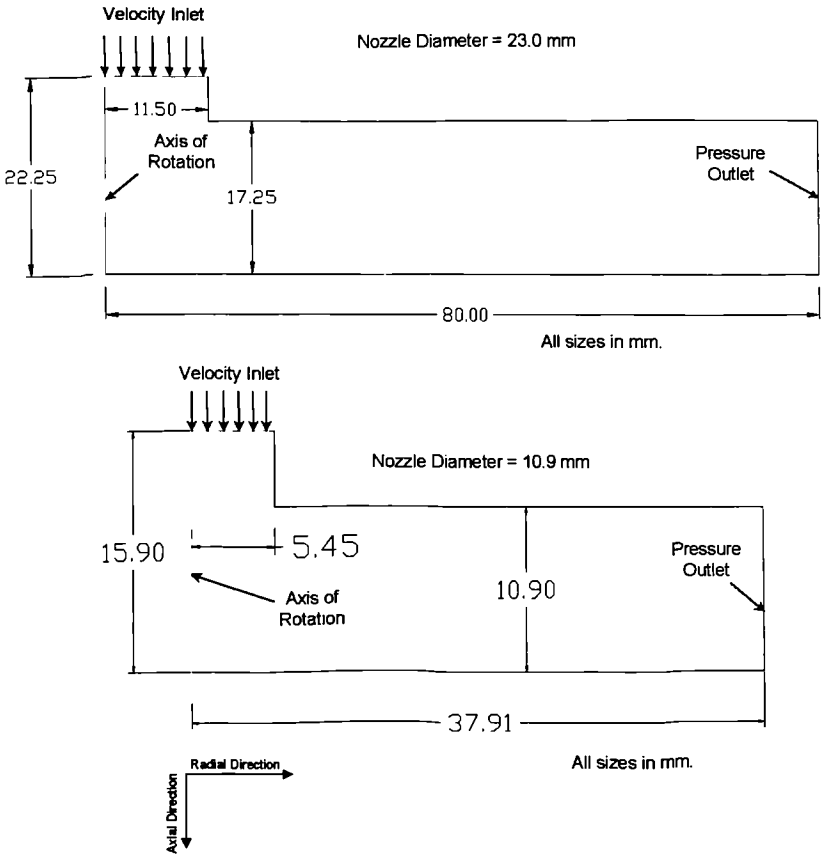

Figure 5.2 Mesh dimensions for 23.0 mm and 10.9 mm nozzles.

Table 5.2 Details of solutions obtained.

Case No.	D_n (mm)	Mesh	Turbulence	Δt (s)	Comments
1	23.0	9665 cells	ske; swf	$1x10^{-4}$	
2	23.0	Adapted from 1	ske; swf	$1x10^{-4}$	Continued from 1.
3	23.0	As 2	rngke; swf	$1x10^{-4}$	Continued from 2.
4	23.0	As 2	rsm; swf; wr	$1x10^{-4}$	Continued from 3.
5	23.0	As 2	rngke; neqwf	$1x10^{-4}$	Continued from 3.
6	23.0	17600 cells	rngke; swf	$5x10^{-5}$	
7	23.0	As 6	rsm; neqwf; wr	$3x10^{-5}$	Continued from 6.
8	10.9	4600 cells	ske; swf	$5x10^{-5}$	
9	10.9	Adapted from 8	ske; swf	$3x10^{-5}$	Continued from 8.
10	10.9	As 9	rngke; swf	$5x10^{-5}$	Continued from 9.
11	10.9	As 9	rsm; swf; wr	$5x10^{-5}$	Continued from 10.

Table 5.3 Explanation of turbulence model abbreviations.

Abbreviation	Meaning
ske	Standard k-ε turbulence model
rsm	Reynolds Stress Model
swf	Standard wall functions
wr	Wall reflection option ON
rngke	RNG k-ε turbulence model
neqwf	Non-equilibrium wall functions

5.3.2 Comparison of results for $D_n = 23.0$mm

Radial velocities along horizontal lines above the base surface (from Stevens and Webb, 1993b) are compared with the CFD predictions in Figure 5.3. H is the vertical distance from the flat surface onto which the jet impinges. Uncertainty in velocity measurements is said to be less than 5%. Data from CFD cases 2, 6, and 7 have been used in the comparison with experiment. CFD predictions agree fairly well at the lowest level compared, but as the height increases, CFD modelling begins to overpredict the radial velocity. Note that the axial direction is in line with the liquid jet; the radial direction is from the axis of rotation to the outlet (as in Figure 5.2).

Predicted and measured radial velocity profiles on vertical lines at two distances from the axis of rotation are presented in Figure 5.4. Data from CFD cases 2, 6, and 7 are again used. Agreement is fairly good along the profile at 11.5 mm from the axis, with case 6 possibly being the closest to the experimental data. The maximum velocity near the surface for case 6 is approaching the experimentally measured value. At 28.75 mm from the axis, case 6 is again closest to the measured values. This suggests that the combination of the RNG k-ε model and the fine mesh give significant improvements over the coarse mesh and standard k-ε model. Results obtained with the RSM model are no better than those with the RNG k-ε model. Comparing the results from other cases with experimental data suggests that there is no real benefit in using the RSM model for the liquid jet model—in terms of velocity predictions at least.

One reason for differences between predictions and experiment is that y^+ values were lower than the minimum limit ($y^+ \sim 30$) for the valid application of wall functions. This was certainly so within the stagnation region. It would have been difficult to ensure y^+ values were within the constraints along the whole length of the wall, as to do so would have meant less mesh resolution for the axial velocity profiles within the liquid layer. A better approach (had there been time) would have been to apply a two-layer model or a turbulence model having low Reynolds number extensions—thus removing the need for wall functions (and associated y^+ constraints) altogether.

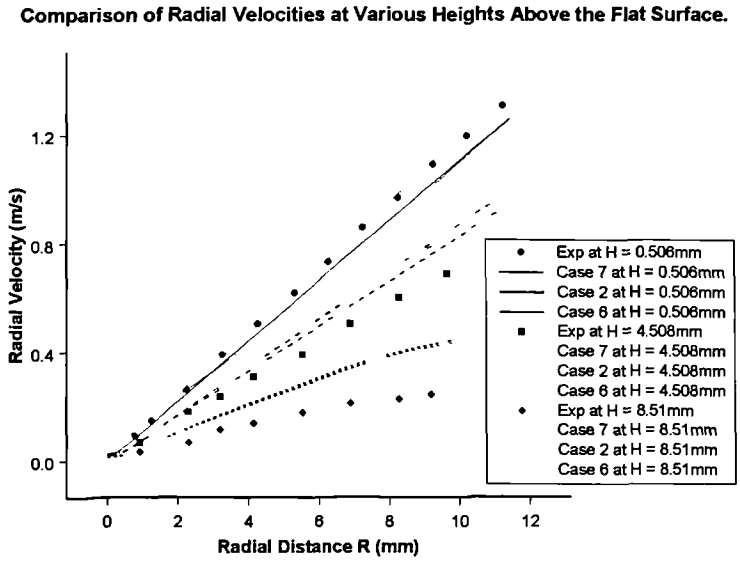

Figure 5.3 Radial velocities along horizontal lines: comparison with experiment (D_n = 23.0 mm) .

The experimental data includes measurements of the liquid layer height. These measurements are compared with the CFD predictions of layer height in Figure 5.5. The position of the free surface in the CFD predictions was taken to be the point where air volume fraction fell to 0.5. There is good agreement between the measurement and prediction for all cases considered. Case 6, which gave the closest results to the experiment in terms of radial velocity prediction, gives the poorest result in terms of liquid layer height.

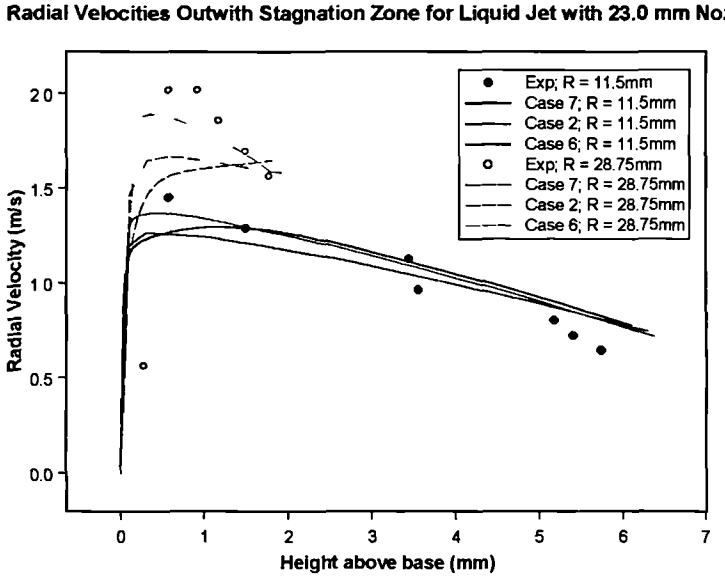

Figure 5.4 Radial velocity profiles outwith stagnation zone: comparison with experimental data for three CFD cases (D_n = 23.0 mm).

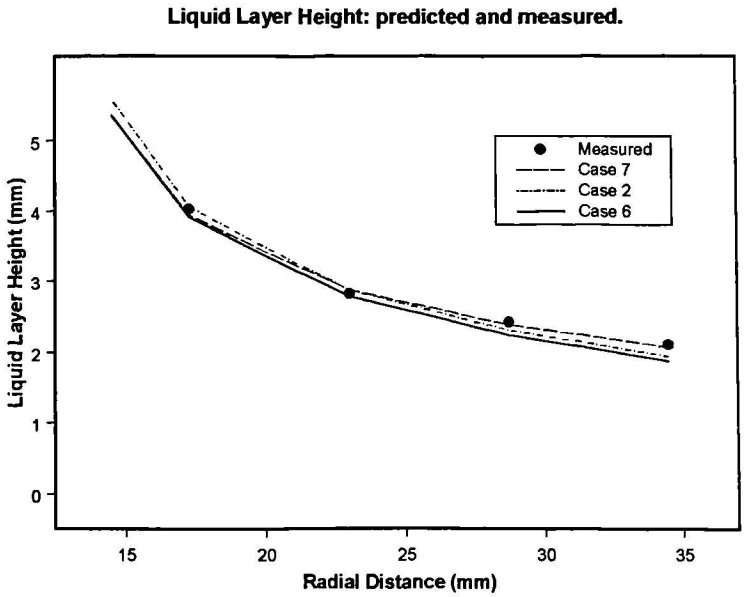

Figure 5.5 Comparison of predicted and measured liquid layer height (D_n = 23.0 mm).

Figure 5.6(a) shows the two phases predicted by the CFD model (outlining jet structure), and Figure 5.6(b) shows the velocity magnitudes within the liquid and air regions.

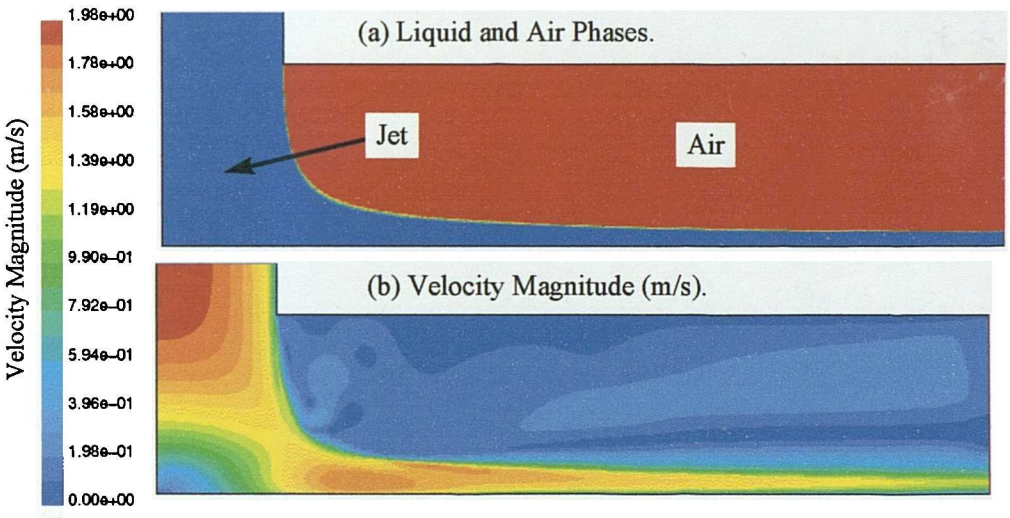

Figure 5.6 Liquid jet structure and velocity magnitudes: Case 7 (D_n = 23.0 mm).

Stevens and Webb (1993a) also measured the Root Mean Square (RMS) of the fluctuating velocity in the radial direction at various distances from the axis of rotation. Figure 5.7 compares predicted and measured RMS of fluctuations at a distance of 11.5 mm from the axis of rotation. Four of the cases in Table 5.2 have been selected for comparison. In the cases using either the standard k-ε or RNG k-ε turbulence models, the quantity used to compare against measured data is derived from the turbulent kinetic energy as:-

$$\overline{v'} = \sqrt{\frac{2}{3}k} \tag{5.1}$$

where k is the turbulent kinetic energy (m^2/s^2) given by the CFD solution. Turbulent kinetic energy itself is defined as:-

$$k = \frac{1}{2}\left(\overline{u'^2} + \overline{v'^2} + \overline{w'^2}\right) \tag{5.2}$$

where u', v', and w' are the fluctuating velocities in each of the co-ordinate directions. Where the Reynolds Stress turbulence model has been used, it was possible to extract the radial stress, and compare the square root of this with the experimental data directly.

Figure 5.7 shows that the Reynolds Stress turbulence model is clearly better at predicting the turbulence quantities than the other models. A comparison at only one position has been shown here, but the trends are similar at other positions. The RNG k-ε model is considerably better than the standard k-ε model in this instance, but not as good as the Reynolds Stress model due to the underlying isotropic assumption of the RNG k-ε model.

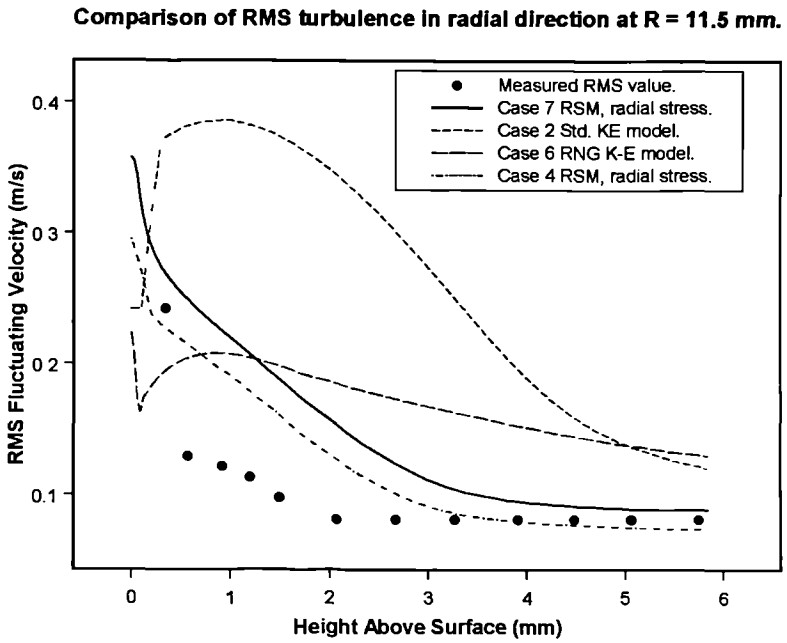

Figure 5.7 Comparison of turbulence quantities at a radial distance of 11.5 mm from the axis of rotation (D_n = 23.0 mm).

This comparison of measured and predicted data for the case with a nozzle diameter of 23.0 mm has served to show that the CFD method can predict the true velocities and turbulence to a reasonable extent. The reason for carrying out this comparison is to give some

credibility to the CFD predictions of axial velocity (assuming that credible prediction of radial velocity secures credible prediction of the axial velocity), and hence to show the true behaviour of particles in a slurry jet (as particle behaviour is directly dependent on fluid behaviour). No comparisons will be presented here for the 10.9 mm nozzle in order to avoid unnecessary repetition of similar material. Results will follow similar trends.

5.3.3 CFD predictions of axial velocity

Axial velocity profiles at various heights above the base surface are shown for case 6 in Figure 5.8. The inlet velocity profile is included for comparison. The deceleration of the fluid approaching the base surface is clearly seen. At 0.506 mm above the surface, the fluid velocity is a fraction of the inlet velocity.

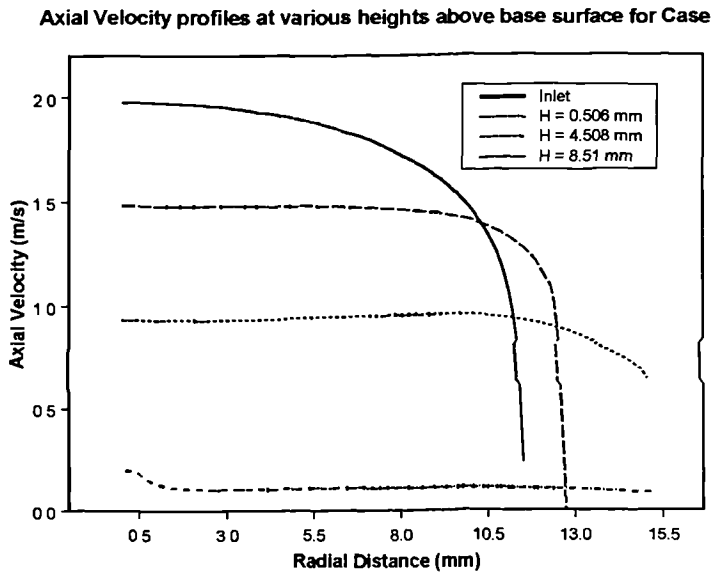

Figure 5.8 Axial velocity profiles at various heights (H, mm) above base surface (D_n = 23.0 mm).

Stevens (2000) considered nozzle-to-plate spacings up to a value of 4. It was found that for this range, nozzle-to-plate spacing did not have any measurable effect on the flow structure or heat transfer within the impingement region of the jet. Thus the result in Figure 5.8, that the axial velocity is around half the inlet velocity at approximately 0.2 nozzle diameters above the plate surface (4.508 mm), is likely to hold true for nozzle-to-plate spacings several times larger than considered here. The nozzle-to-plate spacing used in the slurry rig was around 7.8, which is almost twice the maximum distance considered by Stevens. There will be some differences in the flow structure at a z/d of 7.8 from that considered here, with an increasing likelihood of jet break up before the plate. However, the

general behaviour within the stagnation region should be similar, and conclusions drawn from the limited study in this chapter should at least be indicative of what took place in the slurry rig itself.

5.4 Particle tracking for 23.0 mm nozzle

The main aim in this chapter is to investigate the actual particle impact parameters in comparison to the fluid axial velocity at the inlet. Particle tracking has therefore been carried out using the flow solution obtained in Case 7 of Table 5.2. The following particle tracking parameters have been set for this simulation:-

Particle size	235 μm
Particle density	2668 kg/m^3
Particle concentration	1.0 % by mass
Particle mass flowrate	0.006704 kg/s
Liquid mass flowrate	0.6704 kg/s
Particle inlet velocity	1.614 m/s
Liquid average axial velocity at inlet	1.614 m/s
Gravitational acceleration	Activated
Stochastic Turbulence Dispersion	Activated
Random Eddy Lifetime	Activated
Number of particle trajectories	40,000
Restitution coefficients	$\varepsilon_N = \varepsilon_T = 1.0$

The particle tracking algorithm employed makes no difference between the liquid phase and the gas phase. Particles could therefore leave the liquid phase and enter the gas phase. In reality, this is unlikely to occur, as particles will tend to be carried exclusively by the higher inertia of the liquid phase (and indeed this tended to be the case in the CFD simulations). There may therefore be some room for improvement in the particle tracking algorithm to better account for the different characteristics of the two phases, and to ensure that particles always remain within the liquid (unless released by jet breakup).

Predicted particle impact velocity and angle along the base surface are shown in Figure 5.9. The range of particle impact velocities are clearly significantly lower than the particle velocities at the inlet, where it is likely that they will have the same velocity range as the liquid itself. Peak particle impact velocity is around 0.8 m/s—half of the particle velocity at the nozzle. Velocities within the stagnation region are very much lower than this, as well as those further out from the peak position. This is a clear indication that using the average liquid velocity at the nozzle is not a valid indicator of particle impact velocity at the surface.

The nominal particle impact angle for a slurry test is the angle between the specimen surface and the vertical centre-line of the jet. For the cases considered here, the nominal particle impact angle is 90^0. Particle impact angles plotted on Figure 5.9 show that this is not the case, but rather that particles have a wide spread of impact angles along the surface. Indeed, the maximum angle predicted is not actually 90^0, but around 73^0. The average impact angle will be much lower than this value.

The maximum impact angle at a radial distance of 0.0 mm is less than 90^0. This result arises because of the way in which particle impact angles were recorded and exported from Fluent. A single average value of impact angle (or velocity) was stored for each computational cell lying on the surface beneath the jet. Each time a particle impacted a particular cell, the average value was updated (hence necessitating the storage of running total number of impacts, and running total summation of the impact angles and velocities). The results presented here were exported from Fluent based on cell nodes, which means that the result stored at a cell centre is transferred to coordinates at the cell corners (or nodes) by linear interpolation. This has clearly resulted in some loss of accuracy at the radial zero position, where true perpendicular impacts would be expected.

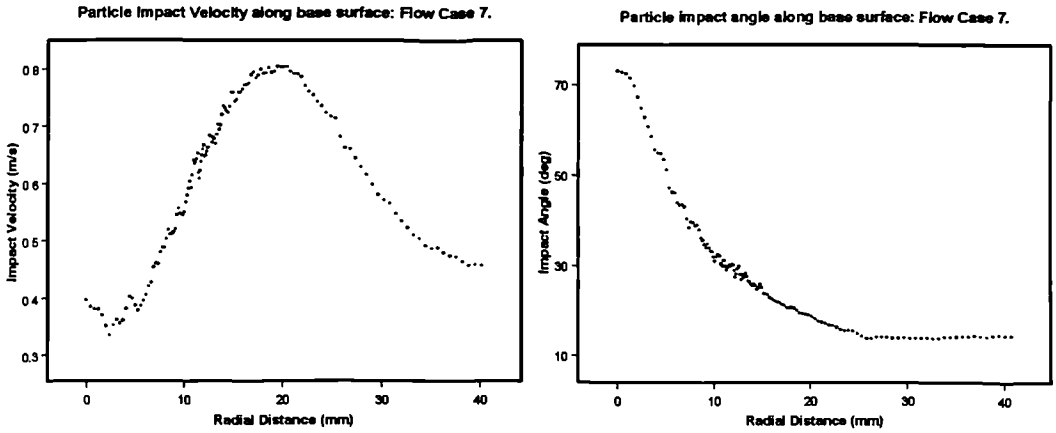

Figure 5.9 Particle impact velocity and angle along base surface (D_n = 23.0 mm).

5.5 Conclusions

A free liquid jet impacting a flat plate has been modelled using CFD techniques. The model has been validated by direct comparison to experimental data obtained with Laser Doppler Velocimetry. Reasonable agreement is obtained between the predicted flow structure and the experimentally obtained structure—indicating that the CFD predictions of axial velocity approaching the surface (which were not measured experimentally) should be close to

the true behaviour. Examination of the liquid axial velocity profiles show that the axial velocity approaching the surface is under half the inlet velocity.

Application of particle tracking to the flow model gives an estimate of particle impact angle and velocity along the surface. These results show clearly that the particle impact velocity is far less than the average liquid velocity passing through the nozzle. Particle impact angle is also significantly different from the overall angle between the jet centre-line and the plate top surface.

The final conclusion from this limited study of free liquid jets is that the particle impact velocity reported in the slurry testing (for 90^0 impingement at least) is around twice the actual impact velocity that would have occurred at the surface. This results from the long established practice of taking the particle impact velocity to be the average liquid velocity through the nozzle. The implication for the erosion equations developed in Chapter 4 is that erosion rate is likely to be underpredicted in CFD based erosion modelling studies where these equations are used—at least for the slurry velocity range. It may be possible to improve the equations by correcting the underlying velocities used in their construction, or to apply a correction to the impact velocity supplied by the particle tracking before using the equation. Future studies should definitely consider this improvement.

The study presented in this chapter is by no means an exhaustive investigation into particle impact behaviour in free liquid jets. Further work needs to be carried out for jets having nozzle diameters and nozzle-to-plate spacings closer to those for the actual slurry rig used in Chapter 3. It may be that a specific numerical code should be written to better account for the physical phenomena taking place in the liquid jet, and also to incorporate a more sophisticated particle tracking model than has been used (in order to account for the free surface). Application to overall angles other than 90^0 is also required, although this would be somewhat more difficult to apply, as it would be necessary to use a three-dimensional approach. There is clearly a considerable area of research requiring attention before erosion equations developed from slurry jet testing can be considered to truly represent test conditions.

6.0 Experimental Testing of Simple Geometry

The erosion modelling tool for the present study comprises a flow solution using the single phase modelling capabilities of Fluent, particle trajectory calculations using a Lagrangian method, and ultimate erosion predictions using the empirical equations developed in Chapter 4. Implementing the empirical equations in Fluent is fairly straightforward through the use of User Defined Functions. This will be covered in more detail in Chapter 8.

However, having constructed a method for CFD-based erosion modelling, it is necessary to have suitable geometries and conditions for which to apply the method. Two types of geometry will be considered in the present study: simple and complex. The reason for doing so is that the CFD methods are more likely to obtain the correct flow field and particle trajectories for a simple geometry than for a complex geometry, and so enable the actual erosion predictions (using the empirical equations of Chapter 4) to be assessed more directly. If the flow phenomena in a complex geometry are not predicted correctly, then the accuracy of particle trajectory calculations (and hence impact velocities and angles) will also be reduced. This will mask any uncertainty that should properly be attributed to the empirical equations.

The simple geometry used in this study has been termed 'flow restrictor', and can be thought of as a component placed in a pipeline that presents a fixed resistance to the flow. Thus for a specific flowrate, a fixed pressure drop will take place across the component. The background to the development of this component has its basis in an attempt to extend choke valve lifetime—this background will be dealt with first. The complex geometry (to be considered later) is the Multi-Orifice Sleeve choke valve manufactured by Wood Group Pressure Control Ltd.

6.1 Background to flow restrictor

Before discussing the need for a flow restrictor, it is necessary to introduce some basic information regarding the way in which choke valves are specified. One of the most widely used parameters in valve selection is known as the valve flow coefficient, C_V. This is generally defined by industry in non-SI units as

$$C_V = Q\sqrt{\frac{SG}{\Delta P}} \tag{6.1}$$

where Q is the volume flowrate in US gallons/min, ΔP is the pressure drop across the valve (psi), and SG is the specific gravity of the fluid passing through the valve. For SI units, Q will

be in litres/s, and ΔP will be in bar. C_V will therefore have the units of (gallons min^{-1} $psi^{-0.5}$) in non-SI units, and the units of (litres s^{-1} $bar^{-0.5}$) in SI units. Units of litres and bar are used for the SI version, as to use m^3 and Pa produces results that are so small as to be meaningless (i.e. differences become too small to appreciate). It should be stressed that the normal usage in the oil and gas valve industry is to use the non-SI version of C_V.

A typical C_V characteristic for a choke valve is shown in Figure 6.1. This is based on what is termed an 'equal percentage' characteristic. The curve shows how the valve C_V will vary depending on the position of the valve flow control tip. Valve position has been presented in terms of percentage valve lift in Figure 6.1. The MOS choke valve to be considered later in this study has a characteristic based on the equal percentage principle.

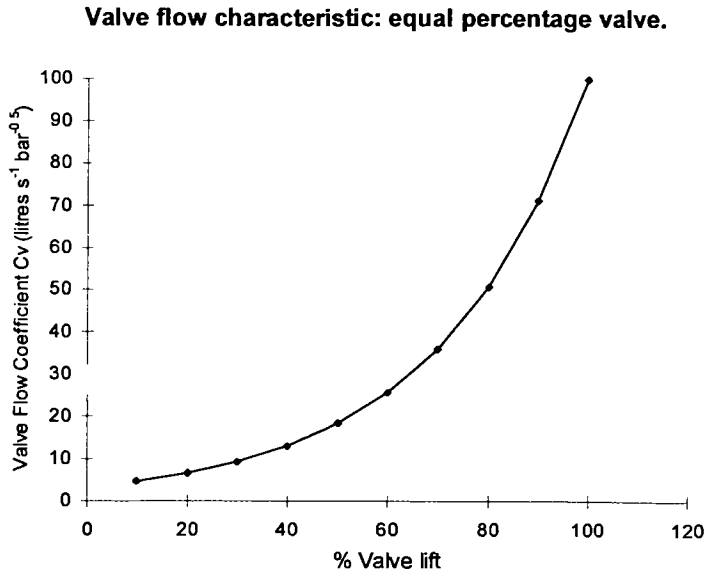

Figure 6.1 Equal percentage valve characteristic.

The stem position of a choke valve determines the equivalent orifice diameter of the open area presented to the flow. A small amount of stem travel (from fully closed position) will present only a fraction of the total possible area to the flow, and a low C_V will result. When the stem travel is near the fully open position, most of the available area is open to the flow, and the resistance caused by the valve will be at or near its minimum value. The size of choke valve required for a particular application must therefore be carefully selected based on estimates of flowrates likely to be encountered in service.

The pressure drop required across a choke valve will be set by: the upstream pressure, the downstream working pressure, and the flowrate set by the operator. Pressure drop in system piping will also need to be considered. However, once a system has been designed and installed, it is likely that the same level of pressure drop will be maintained across the choke valve for an extended period of time. As the valve wears away due to erosion, it will be gradually closed to ensure the same pressure drop (and flowrate) is maintained. When the valve can no longer be closed sufficiently to control flowrate, it will be necessary to replace the valve.

Most of the pressure drop caused by the valve will take place across the flow cage and control tip. High fluid velocities will occur within this region as fluid passes through the various small holes and openings of the cage and tip. If there were some means whereby the open area presented to the flow by the control tip could be increased for the same flowrate (while maintaining the same pressure drop across the valve), it would be possible to reduce fluid velocities within the tip. Reduced fluid velocities will result in slower particle impacts, and as erosion is proportional to velocity, the amount of wear should also be reduced.

One way in which the control tip open area can be increased is to have more than one Pressure Reduction Stage (PRS) within the same valve body (Figure 6.2). By moving some of the overall valve pressure drop (which remains fixed) to regions of the valve other than the flow control tip, the erosion seen by the tip should be reduced. In the present study, the approach adopted has been to include an additional component within the valve that presents a fixed resistance to the flow. As some of the valve pressure drop takes place across this component, the amount of stem travel can be increased, as less pressure drop is required across the control tip. Increased stem travel results in more open area available for the fluid to pass through, and as a result fluid velocities passing through the tip will be decreased.

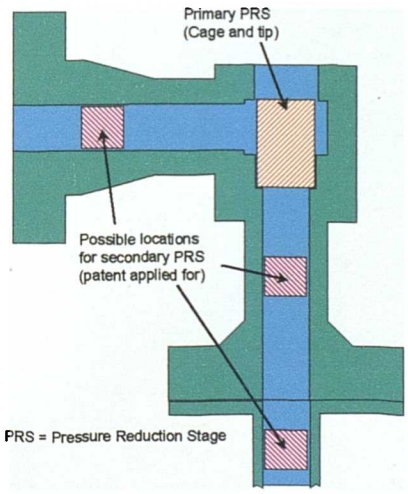

Figure 6.2 Pressure Reduction Stages (PRS) in a MOS choke valve.

The component used to provide the additional fixed resistance to the flow has been termed a 'flow restrictor'. Three different designs of restrictor have been developed for the present study—these are shown in Figures 6.3 to 6.5. Actual dimensions are given in Appendix D. The upstand restrictor was the first one to be developed, with the aim of the upstand being to provide an initial deflection to the oncoming flow. This design was altered to give the fluted restrictor concept, in which the initial obstruction was retained, but with long flutes being machined in the nose section to act as additional friction surfaces to the fluid. The final design (Figure 6.5) built on the first two designs by still having a nose section, but also ensuring that the flow profile through the individual holes was as symmetric about the hole centre as possible (for four of the holes). CFD analysis was used to aid the progressive development of the restrictor.

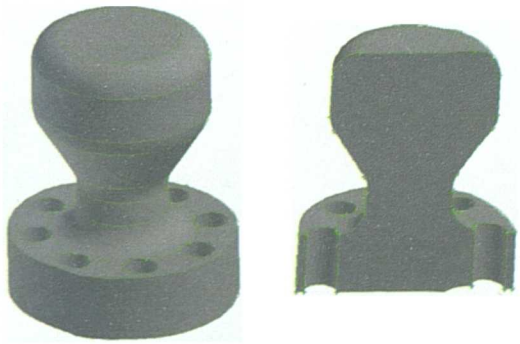

Figure 6.3 Upstand restrictor.

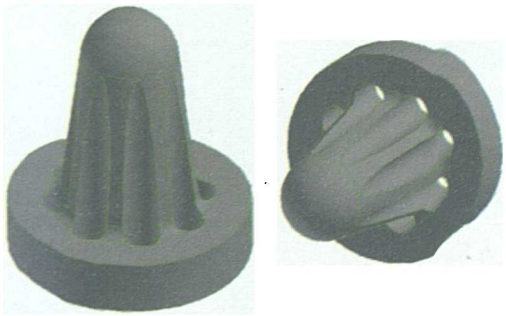

Figure 6.4 Fluted restrictor.

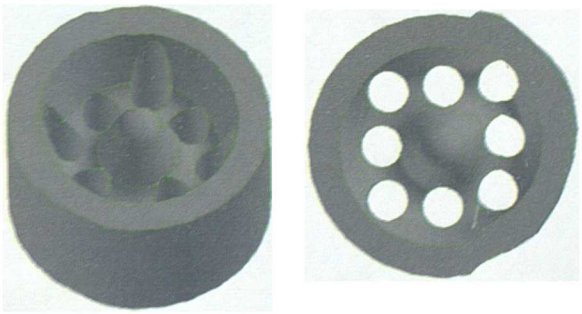

Figure 6.5 Valley restrictor.

The effect of an additional fixed resistance within the valve can be examined by simple hand calculation. The overall system of a valve plus restrictor is represented as two flow resistances in series. The pressure drop across each resistance is calculated in turn:-

$$\Delta P_{valve} = \left(\frac{Q}{C_{Vvalve}}\right)^2 \qquad (6.2) \qquad\qquad \Delta P_{restrictor} = \left(\frac{Q}{C_{Vrest}}\right)^2 \qquad (6.3)$$

where Q is the flowrate in litres/s, and ΔP is the pressure drop in bar across either the valve or restrictor. C_V will be in units of litres s^{-1} $bar^{-0.5}$. It is possible to calculate the pressure drops across both the valve and restrictor using the correct C_V value for each. Valve C_V will obviously change with position. Restrictor C_V is constant, and must be found from experimental testing, CFD simulation, or appropriate extrapolation of such data. The flowrate is set to 1 litre/s for the pressure drop calculation. Once the total pressure drop has been calculated (sum of equations 6.1 and 6.2), the overall C_V for valve and restrictor can be calculated from the usual expression for C_V (neglecting the effect of specific gravity for an incompressible flow):-

$$C_{Vtotal} = \frac{Q}{\sqrt{\Delta P_{total}}} \qquad (6.4)$$

It follows that this three-step calculation reduces to the following:-

$$C_{Vtotal} = \frac{C_{Vvalve} \cdot C_{Vrest}}{\sqrt{C_{Vrest}^2 + C_{Vvalve}^2}} \qquad (6.5)$$

Using equation 6.5, it is possible to observe how the original valve C_V characteristic will be altered as a result of the restrictor. The effect that a restrictor has on a valve characteristic curve is illustrated in Figure 6.6. Two additional characteristics have been generated (for two possible restrictors), and are shown along with the underlying valve characteristic. The first is for a case where the restrictor inserted into the valve has the same C_V value as the valve maximum C_V ($RC_V = VC_{Vmax}$ in Figure 6.6). The second case is where the restrictor has half the C_{Vmax} of the valve. Ultimately, the restrictor reduces the maximum overall C_V value of the valve characteristic. For the case where restrictor C_V equals the maximum valve C_V, the overall combined maximum C_V is around 30% lower than the maximum C_V the valve would have on its own. When restrictor C_V is half the maximum valve C_V, the combined maximum C_V is around 40% of the original valve C_V. There will need to be some care taken in specifying the C_V of the restrictor to be added to the valve.

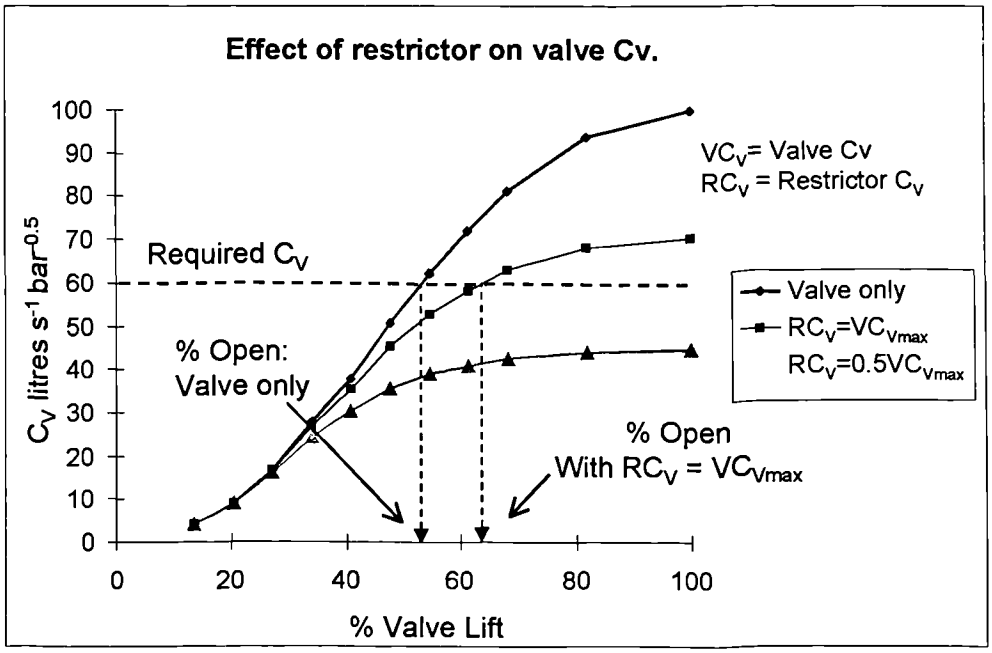

Figure 6.6 Illustration of effect restrictor has on valve C_V characteristic.

Figure 6.6 also illustrates the benefit of having a restrictor in a valve. Consider the case where the original required C_V is around 60 litres s^{-1} $bar^{-0.5}$ (shown on the graph by a horizontal dotted line). If the valve alone is used to provide this C_V, the valve will operate at around 53% open (shown on the graph by "% open, Valve only"). Should a restrictor having the same C_V as the maximum valve C_V be added, the overall C_V characteristic curve for the valve changes to the middle curve on the plot. In order for the combined system to provide an overall C_V of around 60 litres s^{-1} $bar^{-0.5}$ as before, the valve itself must be opened to around 67%—over 10% increase in open position from before. This increase in open position means that greater open areas are presented to the flow for the same flowrate as before, so that lower fluid velocities will be present within the valve. A reduction in erosion rate will result.

6.2 Restrictor Flow Testing

Several prototype restrictors were flow and erosion tested using the abrasive flow facility at the National Engineering Laboratory. The flow testing (using clean water) will be dealt with first, before going on to look at the results of erosion testing. Flow testing was carried out to determine the C_V value associated with a particular restrictor design and hole size. As only measurements of flowrate and pressure drop were required from the restrictor flow testing, it was found that these tests could be performed fairly quickly.

6.2.1 NEL abrasive flow loop

Figure 6.7 depicts the general layout of the NEL abrasive flow loop. This was originally designed for the abrasive flow testing of valves for the oil and gas industry. Water is taken from the clean water tank and passed through a pump having a 90 kW motor attached to it. Sand water mixture is added to the clean water using two sand injection pumps powered by 30 kW motors. The sand water mixture comes from a mixing tank, where a large paddle rotates with sufficient speed to keep the sand in continuous suspension. After the mixing section, the slurry flows through either 50 mm pipework or 100 mm pipework (as required) in which are installed the valves or other components to be tested. Once the slurry has passed through the test components, it enters into a hydrocyclone that acts as a preliminary stage in separating the sand from the water. Concentrated sand mixture from beneath the cyclone enters the base of the mixing tank, while the cleaner water enters the tank at the top. A weir is in place at the top of the mixing tank for clean water to overflow into the clean water storage tank adjacent. There is thus a continuous cycle.

Flowrate is measured using electromagnetic flowmeters—one for the 100 mm line and another for the 50 mm line. All instrumentation on the test facility is monitored continuously from a central control room. Pumps and valves are also controlled from the same point.

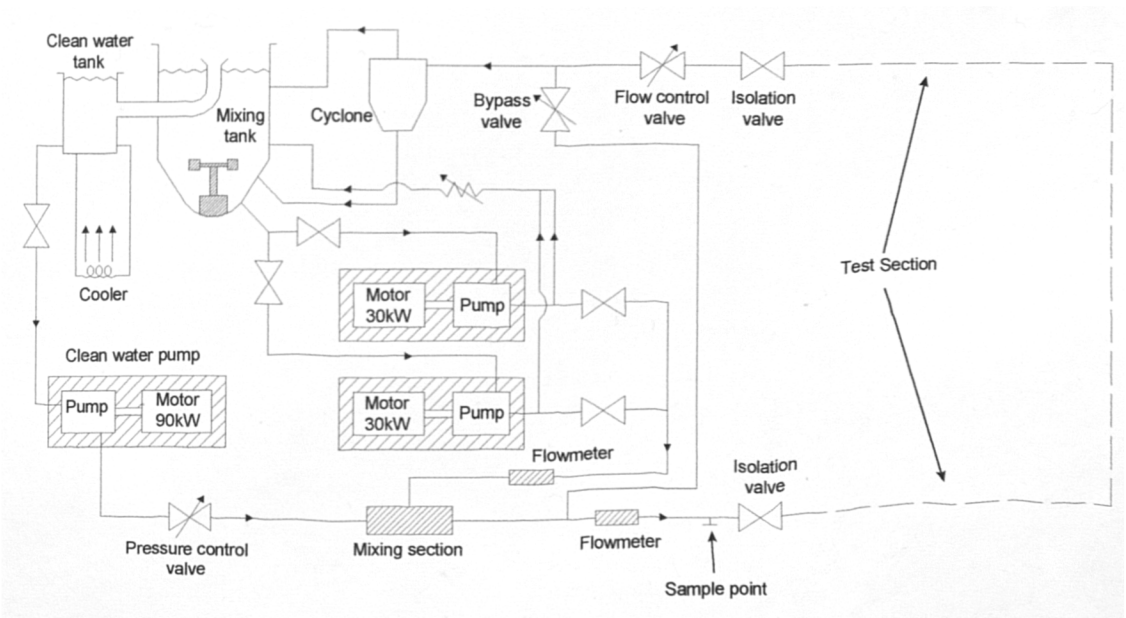

Figure 6.7 NEL abrasive flow facility.

6.2.2 Test procedure

The restrictor to be tested was installed between lengths of 50 mm pipework. A spool piece was manufactured by WGPC Ltd. to hold the restrictor during testing. Figure 6.8 gives a schematic diagram of the spool piece (test section) and adjacent pipework. As the figure shows, there is at least 30D of straight piping before the restrictor test section, which should be adequate to ensure a fully developed flow profile (although this depends on the upstream configuration). Static pressure measurements were made 2D upstream and 6D downstream of the restrictor. Flowrate was measured upstream of the restrictor section using a 100 mm electromagnetic flowmeter. Pressure transducers and the flowmeter were calibrated previously.

The required flowrate through the restrictor section was set primarily using a flow control valve downstream of the restrictor. In some tests, it was necessary to open the bypass loop of the facility in order to obtain a lower flowrate than was available using the flow control valve alone. Once a desired flowrate had been achieved, the flow was allowed to settle before logging measurements of upstream and downstream static pressure, volume flowrate, and water temperature. Although the logging rate was varied in some tests, a scan rate of 0.5 Hz (i.e. one scan every 2s) for 3 minutes was generally used to obtain data. The aim in flow testing was to obtain measurements of pressure and flowrate for three different flowrates per restrictor. The logged data was used to give average measurements for each point.

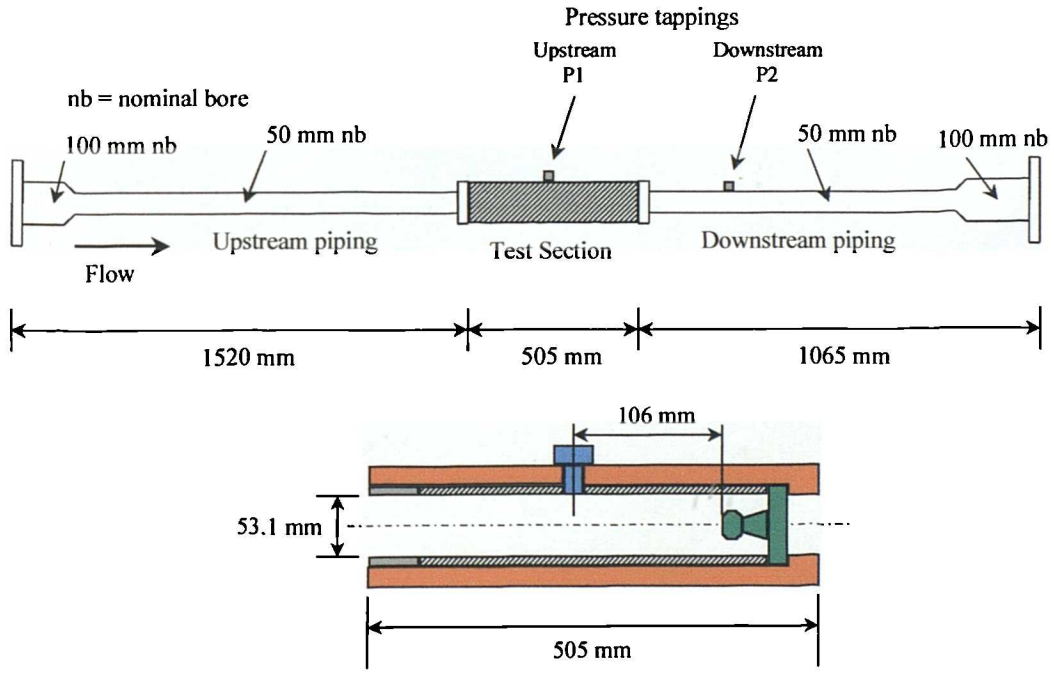

Figure 6.8 Restrictor test section and associated piping.

6.2.3 Results of restrictor flow testing

Six restrictors have been tested in total. The design and hole sizes are listed as follows:-

1. Upstand with 8 mm straight holes.
2. Upstand with 8 mm angled holes (60^0 angle).
3. Upstand with 11 mm straight holes.
4. Upstand with 5 mm straight holes.
5. Fluted with 11 mm straight holes.
6. Valley with 11 mm straight holes.

The above list indicates the order of flow testing. Table 6.1 provides the complete set of results for all restrictors tested. Additional testing was carried out with the 11 mm upstand design to investigate the effect of logging rate and time on the final results. The data obtained from this additional testing is shown in Table 6.2. C_V values have been calculated using equation 6.1.

Table 6.1 Results of restrictor flow testing.

Description	TBS (s)	Log Time (mins)	Flowrate (litres/s)	P1 (bar)	P2 (bar)	ΔP (bar)	Cv SI	Average Cv SI
Upstand 8mm straight holes	30	10	5.72	8.23	7.30	0.93	5.94	
	30	10	9.92	14.38	11.37	3.01	5.72	
	30	10	13.99	14.04	8.07	5.97	5.73	**5.8**
Upstand 8mm angled holes	30	10	5.62	8.49	7.18	1.31	4.91	
	30	10	10.02	14.43	10.49	3.93	5.05	
	30	10	13.96	14.08	6.41	7.67	5.04	**5.0**
Upstand 11mm straight holes	30	10	10.01	14.35	13.56	0.79	11.30	
	30	10	15.53	13.78	11.82	1.96	11.10	
	30	10	25.21	12.28	6.85	5.43	10.82	**11.1**
Upstand 5mm straight holes	2	5	4.91	11.57	5.44	6.13	1.98	
	2	3	5.33	13.17	5.88	7.29	1.97	
	2	3	5.45	13.41	2.82	10.59	1.67	**Use**
	2	3	5.63	14.31	2.62	11.69	1.65	**2.0**
Fluted 11mm straight holes	2	3	9.70	14.42	13.82	0.60	12.52	
	2	3	16.08	13.91	12.21	1.70	12.33	
	2	3	24.30	12.67	8.73	3.95	12.24	**12.4**
Valley 11mm straight holes	2	3	9.88	14.59	13.88	0.71	11.74	
	2	3	15.55	14.09	12.44	1.65	12.10	
	2	3	20.29	13.43	10.66	2.77	12.20	
	2	3	28.09	11.92	6.48	5.44	12.04	**12.0**

TBS = Time between scans; P_1 = upstream static pressure; P_2 = downstream static pressure;

$\Delta P = P_1 - P_2$

Table 6.2 Additional points taken during investigation of logging parameters.

Description	TBS (s)	Log Time (mins)	Flowrate (litres/s)	P1 (bar)	P2 (bar)	ΔP (bar)	Cv SI	Average Cv SI
Upstand 11mm straight holes	1	2	19.69	13.34	10.07	3.27	10.9	
	2	2	19.69	13.38	10.12	3.26	10.9	
	5	5	19.69	13.35	10.13	3.22	11.0	
	15	10	19.68	13.33	10.08	3.25	10.9	
	30	10	19.67	13.25	10.10	3.15	11.1	**11.0**
	2	3	25.46	12.30	6.78	5.52	10.8	
	2	3	10.08	14.41	13.54	0.87	10.8	**10.8**

Results for the upstand restrictor with 5 mm holes are effectively limited to a single flowrate. Choked flow occurred with this restrictor, which meant that it was only possible to achieve a maximum flowrate of around 5.3 litres/s before choked flow. This has significant implications for valve operation.

Table 6.2 investigates the effect of time between scans and log time in more detail. It can be seen that there is little difference between the results obtained, which indicates that the results presented in Table 6.1 are fairly consistent—even though different logging parameters were used for the second half of Table 6.1.

6.2.4 Uncertainty in Measurements

Appendix D gives details of the procedure adopted to estimate the uncertainty in measurement of C_V. Average uncertainty for results shown in Table 6.1 is estimated to be under 2 % of C_V; for Table 6.2 the average uncertainty is expected to be under 3 %.

It will be noted that high uncertainties resulted during flow testing of the 11mm upstand restrictor at 10 litres/s (Table D.5). The cause of this high uncertainty appears to be significant variation in the pressure measurements. Irregular fluctuations of the pressure readings were observed in all tests, but some had larger relative fluctuations than others. Data for the fluted restrictor in Table D.4 also has high uncertainty attached to it. Examination of the data for these tests shows the highest fluctuations (i.e. highest standard deviation) to come from the downstream pressure transducer, where the flow might be expected to be less stable than that seen by the upstream transducer. The combination of this and low pressure drop across the restrictor results in large variations in the calculated C_V.

6.2.5 Choked flow condition

Choked flow occurred in the 5mm hole upstand restrictor. This means that a point was reached where no increase in flow through the restrictor was observed for an increase in pressure drop across the restrictor. There are obvious implications here for a valve containing

a restrictor, as a choked flow condition may be reached far sooner in the modified valve than in one having no restrictor. Further work is required to examine ways in which the onset of cavitation (that leads to choked flow) could be predicted. It is also the case that the downstream pressure in field conditions will be much higher than was possible to achieve in the present test facility, which may help to reduce the likelihood of a choked flow condition.

6.2.6 Summary

The flow testing of restrictors provides actual data with which to compare CFD predictions of pressure drop across the components. Ideally, the data would include velocity profile measurements upstream and downstream of the restrictor. It was not possible to perform such measurements in the present study for a variety of reasons including limited timescale and cost.

6.3 Erosion testing of restrictors

An important objective in the restrictor testing programme was to evaluate their performance under abrasive flow conditions. Four prototype restrictors were tested under abrasive flow conditions to examine their resistance to solid particle erosion. The restrictors tested were as follows:-

1. Upstand with 11 mm straight holes; AISI 4130.
2. Upstand with 11 mm straight holes; Duplex F51.
3. Fluted with 11 mm straight holes; AISI 4130.
4. Valley with 11 mm straight holes; AISI 4130.

6.3.1 Test procedure

As before, the NEL abrasive flow loop was used for testing. In the erosion tests, the two sand injection pumps were used in conjunction with the main pump. Sand was added to the water contained in the mixing tank. This tank contains a stirrer that keeps the sand in suspension in the lower regions of the tank. The two sand injection pumps take sand-water slurry from the lower half of the mixing tank, and feed into the main flow at the mixing section. Pipework leading to and from the sand injection pumps is of 50 mm diameter; the remaining pipework (from the main pump, and after the mixing section) is 100 mm diameter. The increased pumping capacity meant that a flowrate of 28 litres/s could be set for the erosion tests.

Restrictors were weighed to within 10 mg using an electronic scale. Measurements were made before and after testing. Sand concentration measurements were made using the iso-kinetic sampling technique outlined in Appendix D. The average concentration throughout the erosion tests was 0.43% by mass. A total of 14 concentration measurements were made over the whole test program, and are given in Table 6.5. Photographs of the restrictor were taken before and after testing. Silica sand (Chelford 50) was used in testing, having a rounded shape of average diameter 275 μm ± 25 mm. Density is 2650 kg/m^3.

6.3.2 Results of erosion tests

The main results for the four erosion tests are given in Table 6.3. Measurements of flowrate, upstream pressure, downstream pressure, and temperature were logged every minute throughout the test period. These measurements have been used to give overall average values. The table shows C_V values at the start and end of test periods: it was found that restrictor C_V increased throughout erosion tests as a result of material loss. Sand concentration measurements are average values: Table 6.4 gives the actual measurements.

Table 6.3 Results of erosion testing.

Test	Description	Time	Mass Before	Mass After	Sand Conc.	Mass loss	Erosion rate	Flowrate	Cv Start	Cv End
		(hrs)	(g)	(g)	(% mass)	(g)	(g/hr)	(litres/s)	SI	SI
1	US, 4130	14	688.98	669.09	0.53	19.89	1.42	28.14	11.8	13.5
2	US, Duplex	15	688.37	673.66	0.39	14.71	0.98	28.49	11.7	13.5
3	Fluted, 4130	14	690.30	681.15	0.44	9.15	0.65	29.34	12.6	14.4
4	Valley, 4130	14	838.93	830.77	0.39	8.16	0.58	28.57	12.9	14.7

Table 6.4 Sand concentration measurements.

No.	Time	Sand Mass (g)	% Conc.
1	Before Test 1	49.23	0.49
2	Before Test 1	51.21	0.51
3	Before Test 1	45.97	0.46
4	Before Test 1	52.54	0.53
5	Before Test 2	39.69	0.40
6	During Test 2	34.54	0.35
7	During Test 2	38.58	0.39
8	During Test 2	41.64	0.42
9	During Test 2	50.69	0.51
10	Before Test 3	43.63	0.44
11	Before Test 4	46.88	0.47
12	After Test 4	32.38	0.32
13	After Test 4	38.83	0.39
14	After Test 4	37.47	0.37

6.3.2.1 Upstand restrictor with 11 mm straight holes: AISI 4130

This was the first restrictor to be tested under erosion conditions. The restrictor was subjected to the erosive flow for a continuous 14 hours at approximately 28 litres/s. Figure 6.9 shows the change in Cv throughout the test. Photographs of the restrictor before and after testing are shown in Figure 6.10.

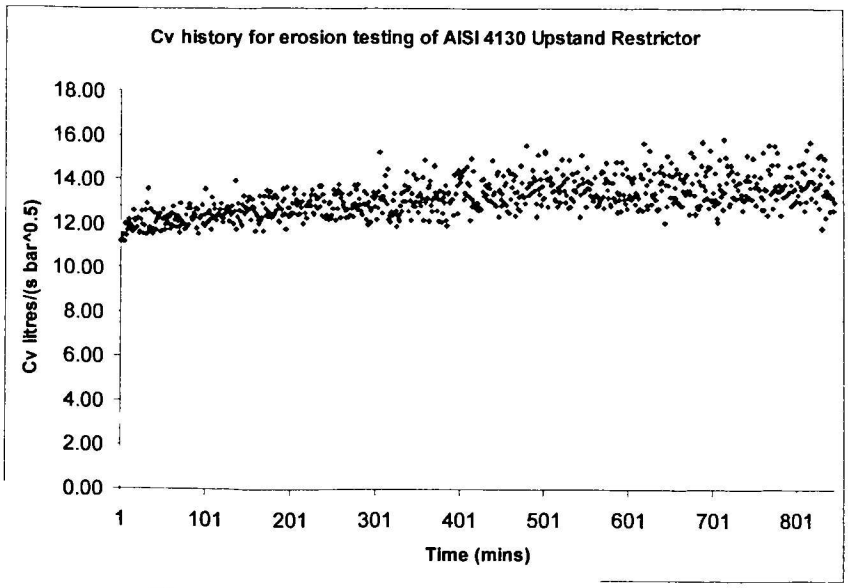

Figure 6.9 Change in C_V during erosion test 1.

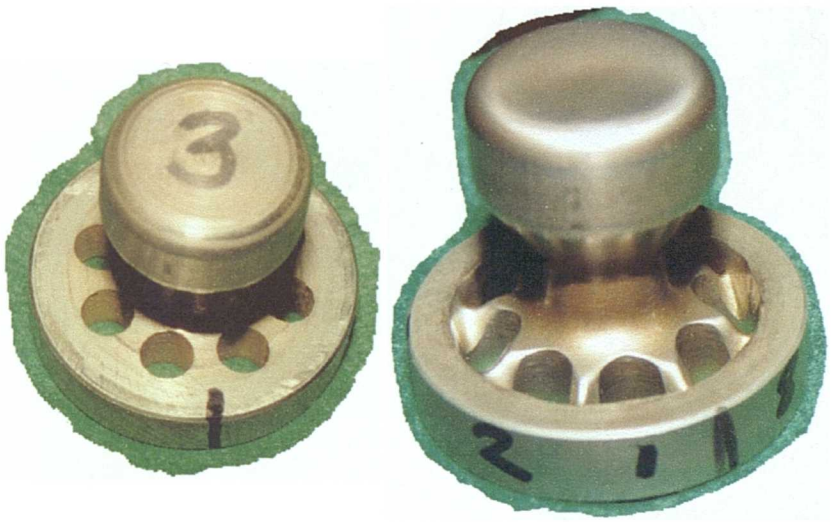

Figure 6.10 Upstand restrictor (AISI 4130) before and after erosion testing.

6.3.2.2 Upstand restrictor with 11 mm straight holes: Duplex F51

This restrictor was identical in geometry to the previous restrictor, but was made from Duplex F51 stainless steel instead of AISI 4130 low alloy steel. As the rate of erosion seemed high during the previous test, it was decided to test the Duplex restrictor in four stages, each

of 5 hours duration. It was thought that this would give a clearer understanding of the erosion process. Mass loss measurements and photographs were taken between each stage of the test.

Table 6.5 gives the specific measurements for this test. Stage 2 was split in two due to an unexpected rig shutdown. Figure 6.11 is a plot of the erosion rate in each 5 hour period of the test: it can be seen that the erosion rate decreases as time increases. Figure 6.12 shows the combined plot of C_V values for all four stages of the test. Photographs of the specimen before, during, and after the test are provided in Figure 6.13.

Table 6.5 Results taken during erosion testing of Duplex F51 Upstand design.

Period	Time (hrs)	Mass Before (g)	Mass After (g)	Sand Conc. (% mass)	Mass loss (g)	Erosion rate (g/hr)	Flowrate (litres/s)	Cv Start SI	Cv End SI
1	5	688.37	682.8	0.43	5.57	1.11	28.2	11.7	13.1
2	5	682.8	677.78	0.37	5.02	1.00	28.7	12.6	13.1
3	5	677.78	673.66	0.42	4.12	0.82	28.7	13.1	13.5
4	5	673.66	669.69	0.51	3.97	0.79	28.7	13.1	13.4

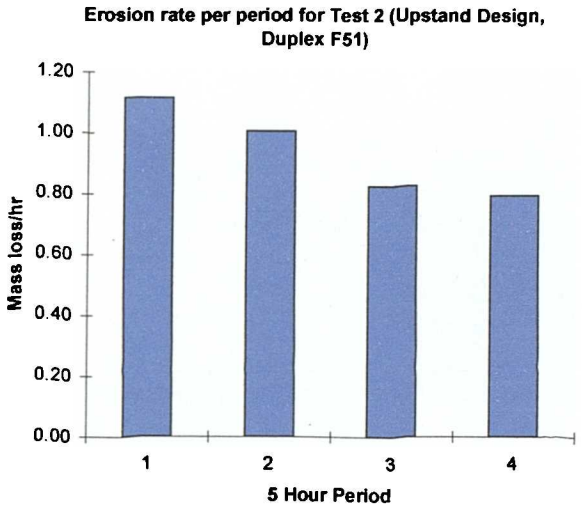

Figure 6.11 Erosion rate in each 5 hour period for Test 2.

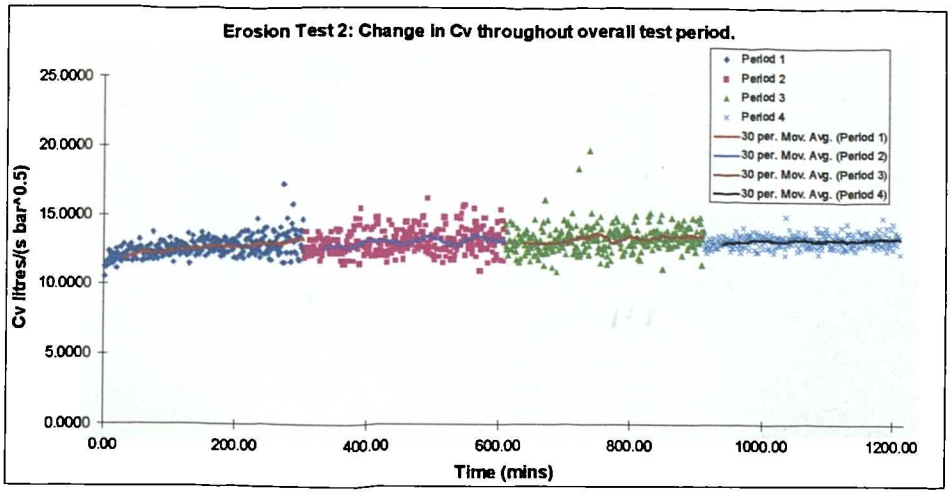

Figure 6.12 Change in C_V during erosion Test 2.

Before Testing | After 5 hours | After 10 hours | After 15 hours | After 20 hours

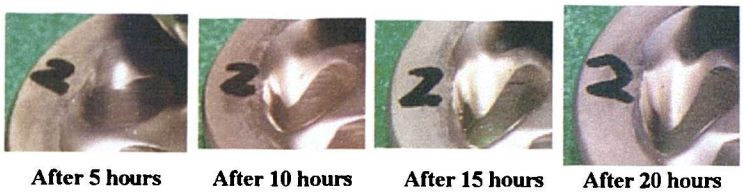

After 5 hours | After 10 hours | After 15 hours | After 20 hours

Figure 6.13 Photos of Duplex F51 Upstand restrictor during multiple erosion tests.

6.3.2.3 Fluted restrictor with 11 mm straight holes: AISI 4130

This restrictor was tested in the same way as the first upstand restrictor: for 14 hours continuously. Although the mass loss overall was much less than for the upstand restrictor design, there were signs of cavitation erosion taking place within the holes: Figure 6.14 shows a photograph of this erosion. Erosion was also observed in the side wall of the sleeve leading up to the restrictor base plate in all three of the above erosion tests, as shown in Figure 6.15. The sleeve was repaired between tests two and three. This erosion was caused by localised flow recirculation next to the wall, and was one of the reasons for ensuring the final restrictor design (Figure 6.5) did not have any orthogonal corners where flow could recirculate in the same way.

Figure 6.14 Erosion of fluted restrictor: AISI 4130.

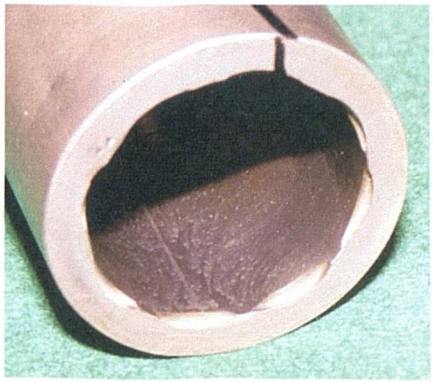

Figure 6.15 Erosion of sleeve end.

6.3.2.4 Valley restrictor with 11 mm straight holes: AISI 4130

This restrictor was designed to eliminate cavitation erosion in the holes, and solid particle erosion on the side walls. Both objectives were achieved. Figure 6.16 shows photographs of the restrictor before and after testing. Although the mass loss is not much different from the previous test, the wear has taken place in a much more uniform manner. There is evidence of wear on the side walls within the restrictor, as well as the more obvious wear between the holes. Restrictor C_V again increases throughout the duration of the test, as shown in Figure 6.17.

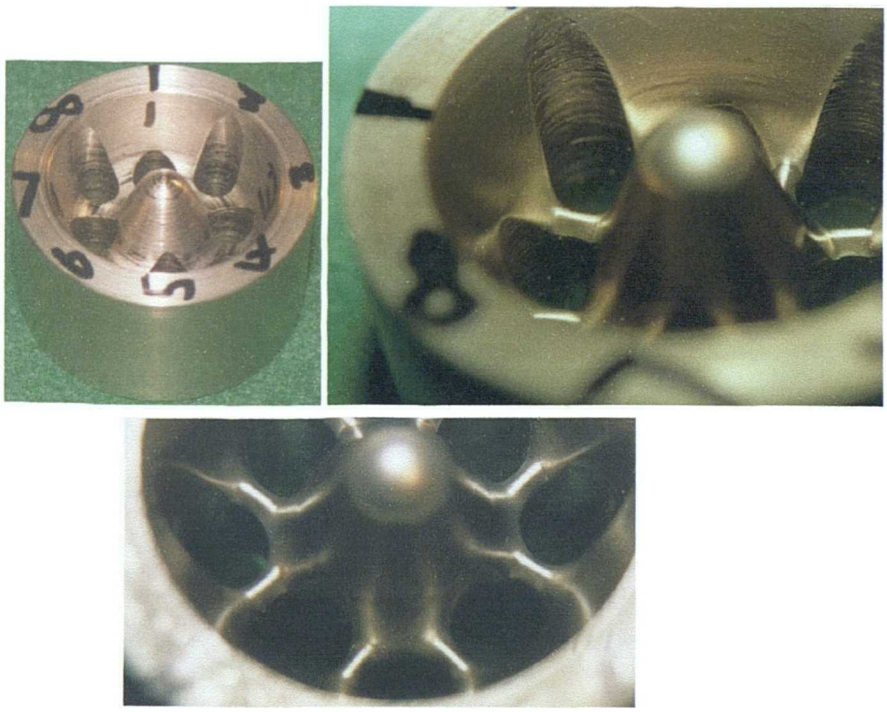

Figure 6.16 Erosion testing of valley restrictor.

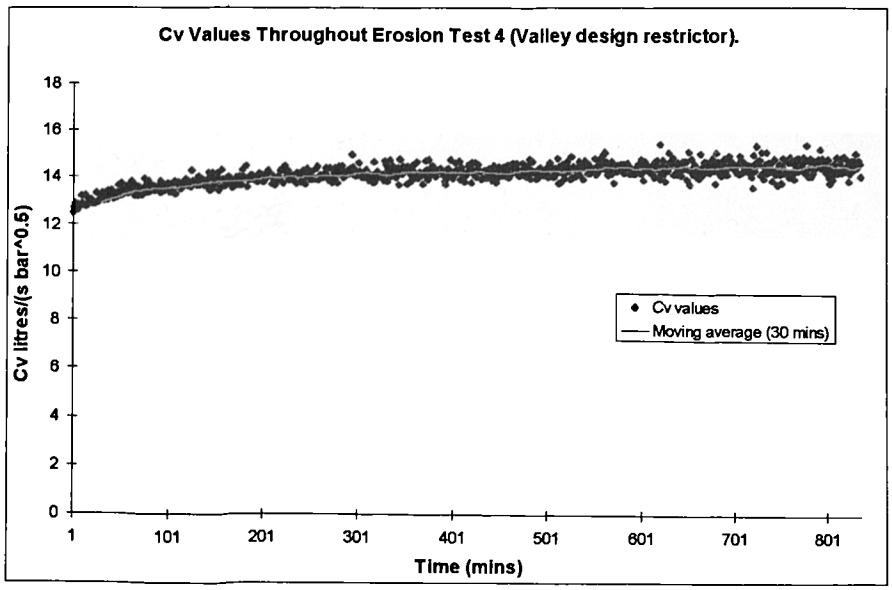

Figure 6.17 Change in C_V during erosion testing of valley restrictor.

6.3.3 Discussion of results

The upstand restrictor was severely eroded in both cases (AISI 4130 and Duplex F51). Examination shows the bulk of erosion to occur on the material between adjacent holes, towards the outer diameter of the restrictor. Particles are moved towards the outer diameter as a result of the upstand. Erosion of the Duplex restrictor was somewhat less than that of the AISI 4130 restrictor, due to the greater erosion resistance of the Duplex material. It is thought that the erosion profile between the holes will retain its shape throughout the restrictor lifetime, but simply move downwards as more material is lost. Figure 6.13 seems to confirm this, where the erosion profile can be seen to increase in the vertical direction, but still retain the same basic shape. There will ultimately come a point where the material between the holes is insufficient to hold the upstand in place: at this point the restrictor will fail. Very little erosion is observed on the upstand itself, indicating that particle velocities were not high enough to remove material.

The fluted restrictor was intended to provide greater channelling of the flow through the holes, as well as having more material between the holes for longer lifetime. While material loss occurred as expected between the holes, material was also removed in line with the fluted edges within each hole themselves. This was unexpected, and is likely to be a result of localised cavitation within the hole. Flute geometry may be responsible for the localised cavitation, as fluid shoots over the edge of the flute before entering the hole. This accentuates the separation and recirculation immediately after the flute edge, resulting in localised

cavitation. Thus there could be a combination of particle and cavitation erosion, which is known to be much more severe than either of these mechanisms alone (Madadnia and Owen, 1995). This is possibly due to particles being propelled onto the surface with far higher velocities when a bubble collapses than they would have otherwise.

A common feature of the first three erosion tests was the damage caused to the surrounding sleeve (Figure 6.15). Peak damage occurred at the point where the bridge between holes met the wall (although the sleeve only rested on the surface). This clearly indicates damage caused by particles rebounding off the surface between the holes and onto the perpendicular sidewall.

The final restrictor was designed in such a way as to eliminate both cavitation and side wall erosion. CFD modelling (to be presented later) gave additional insight into fluid behaviour, which was useful in arriving at an alternative design. Testing of the final valley design showed improved erosion performance. Although the overall mass loss was not much less than that of the fluted restrictor, it was spread more evenly across the whole of the restrictor upper surface—not just at specific points. No cavitation erosion was observed, and the side wall erosion obtained previously was also eliminated. It is expected that the valley design will have significantly longer lifetime than the previous designs, and is the way forward for restrictors that are to be used in field conditions.

Restrictor C_V changed by a small amount in all of the erosion tests carried out, with the typical rise being in the order of 22% above the original C_V measured in clean water. It should be noted that the initial C_V recorded during erosion testing is around 6.5% higher than the C_V recorded with clean water—suggesting some influence of the sand content on measured C_V. This could mean that either the fluid behaviour has been affected by the presence of sand (as sand will affect the flow more and more as concentration increases), or else that the sand influences the methods used to measure pressure and flowrate. It is likely that C_V will settle at a constant value after the initial erosion has taken place: hence the restrictor/valve combination should be designed for the final prospective restrictor C_V rather than the initial C_V. Allowing for a 25% increase in C_V should be sufficient.

6.4 Conclusions to restrictor testing

Restrictor C_V has been measured under both clean and abrasive flow conditions. There is some effect of sand content on measured C_V, in that initial C_V in erosion tests was around 6.5% higher than the average C_V from clean water tests. Erosion tests have shown that

C_V increases due to material loss, with the increase being in the order of 25% of original clean water C_V.

The valley design restrictor is the most erosion resistant, as it causes wear to be more evenly spread over the whole impacted surface. It also eliminates side wall erosion, and gave no evidence of the cavitation damage observed in the fluted design. It is recommended that the valley design, or variants of it, be used in actual restrictors for installation in the field.

The testing gives a source of experimental data with which to compare CFD predictions. Test results are limited in that only overall measurements of pressure drop and mass loss have been made. Profiles for both flow and erosion quantities would be the ideal type of measurements for comparison with CFD results, but it has simply not been possible to make such measurements in the present study. The results available will, however, enable at least an overall assessment of the CFD techniques to be made, but finding reasons for any poor predictions will not be so easy.

7.0 CFD Modelling of Single Phase Flow through Restrictors

The first step in applying a CFD-based erosion modelling technique to a component is to correctly predict the single phase flow. It is reasonable to assume that the particle trajectory calculations will only reflect true behaviour if the underlying fluid phase has been modelled correctly. In this chapter, work carried out to validate the CFD modelling technique for single phase flow through the restrictors discussed in the previous chapter will be presented. Experimental test data from the previous chapter has been used to provide validation data for the CFD predictions. The commercial CFD package, Fluent, has been used in all predictions.

7.1 Modelling techniques

7.1.1 Governing equations of fluid flow

The equations governing the turbulent flow of a Newtonian fluid have been used to predict the single phase flow through the restrictors. The Reynolds Averaged Navier Stokes equations solved by Fluent for incompressible turbulent flows are written in Cartesian tensor form as:-

$$\frac{\partial \rho}{\partial t} + \frac{\partial}{\partial x_i}(\rho u_i) = 0 \tag{7.1}$$

$$\rho \frac{Du_i}{Dt} = -\frac{\partial p}{\partial x_i} + \frac{\partial}{\partial x_j}\left[\mu\left(\frac{\partial u_i}{\partial x_j} + \frac{\partial u_j}{\partial x_i} - \frac{2}{3}\delta_{ij}\frac{\partial u_l}{\partial x_l}\right)\right] + \frac{\partial}{\partial x_j}\left(-\rho\overline{u_i' u_j'}\right) \tag{7.2}$$

Equation 7.1 is the mass conservation equation, and equation 7.2 is the momentum conservation equation. The Reynolds stress term can be seen on the far right hand side of equation 7.2.

7.1.2 Turbulence modelling

Three turbulence models were used in this study: the k-ε model of Launder and Spalding (1972), the RNG k-ε model of Yakhot and Orszag (1986), and the Reynolds Stress model of Launder (1989). The governing equations for these models will not be given here, as they have already been discussed in Chapter 2.

7.2 Modelling of upstand restrictor with 8 mm straight holes

All of the restrictor geometries tested in the abrasive flow facility have been modelled at least once with CFD techniques. Some have been modelled using several different meshes in an attempt to find the approach giving the best results. As the upstand design with 8 mm straight holes has received the most attention in CFD modelling, it will be dealt with first.

7.2.1 Computational Meshes

Several meshes have been created for the upstand restrictor with 8 mm diameter straight holes. As the restrictor has rotational symmetry, it is only necessary to model one hole in the CFD model (one-eighth of the annulus). Figure 7.1 shows the general form of computational mesh used in the restrictor modelling. Two diameters of straight pipe are modelled upstream of the restrictor, and six diameters downstream. Some of the later models had shorter lengths of upstream and downstream piping, but in general 2D upstream and 6D downstream were used. This was to correspond with the locations of the pressure tappings in the experimental tests.

Table 7.1 lists the computational meshes that were created for the 8 mm straight hole upstand restrictor. The reason for creating so many meshes was that results for this particular restrictor did not correspond well with the experimental data, and so a further investigation of meshing strategy was carried out. It is generally accepted practice in CFD simulations to perform a mesh sensitivity study. This is made difficult in the present study by the use of hybrid meshes that contain unstructured tetrahedral and hexahedral sections. It becomes difficult to refine meshes in an ordered way—especially for unstructured tetrahedral sections. In this section, mesh resolution has been reported in terms of cell length in the axial direction, at points where the flow changes rapidly (i.e. at the start and end of the holes). A comparison for the meshes in Table 7.1 will be given later.

In Table 7.1, SG represents Simplified Geometry, and AG represents Accurate Geometry. The simplified geometry refers to the mesh where some of the curvature present in the actual restrictor was replaced by angular joints in the computational mesh. Figure 7.2 illustrates the simplification. The column titled 'Transition Regions' refers to the number of sections in the mesh containing unstructured tetrahedral cells. Only two meshes were created using entirely hexahedral cells: the rest all had at least one tetrahedral transition section.

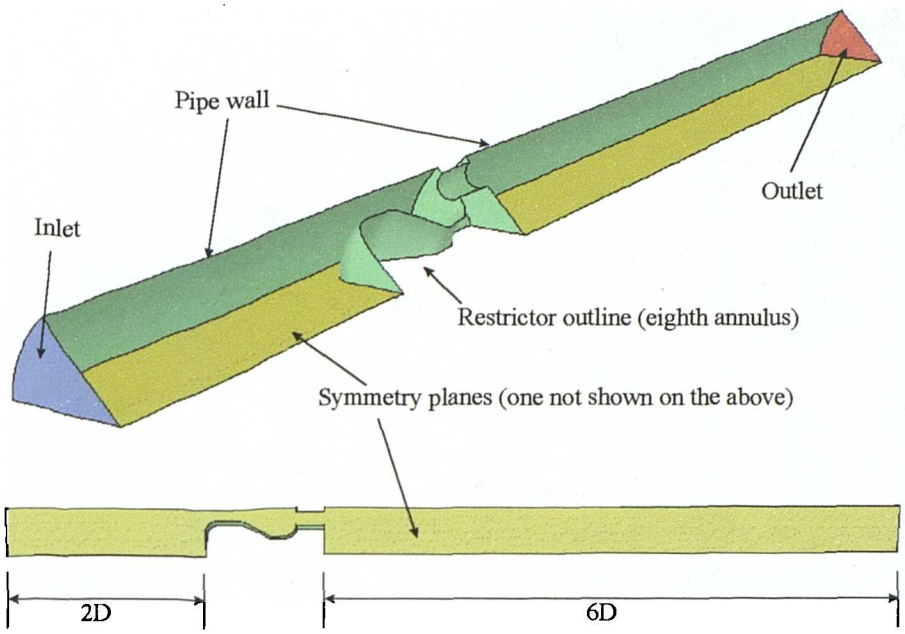

Figure 7.1 Typical arrangement for computational mesh.

Table 7.1 Computational meshes for 8mm upstand restrictor with straight holes.

Description	Ref.	No. Cells	Transition Regions
Eighth annulus; SG.	MR8Sa	261k	1
Eighth annulus; AG.	MR8Sb	148k	3
	MR8Sc	440k	3
	MR8Sd	512k	3
	MR8Se	207k	2
	MR8Sf	58k	3
	MR8Sg	92k	2
	MR8Sh	371k	1
	MR8Si	172k	0
	MR8Sj	438k	0

7.2.1.1 Mesh with simplified geometry: MRS8a

It was initially thought that the curvature appearing in the actual restrictor geometry could be neglected in the CFD representation. Subsequent meshes used the true restrictor geometry to avoid any adverse effects on the CFD predictions. Figure 7.3 highlights the key features of this mesh.

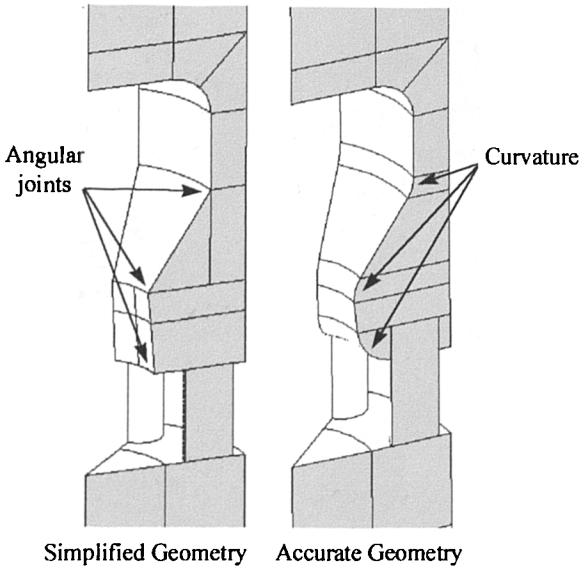

Figure 7.2 Difference between simplified and accurate geometry.

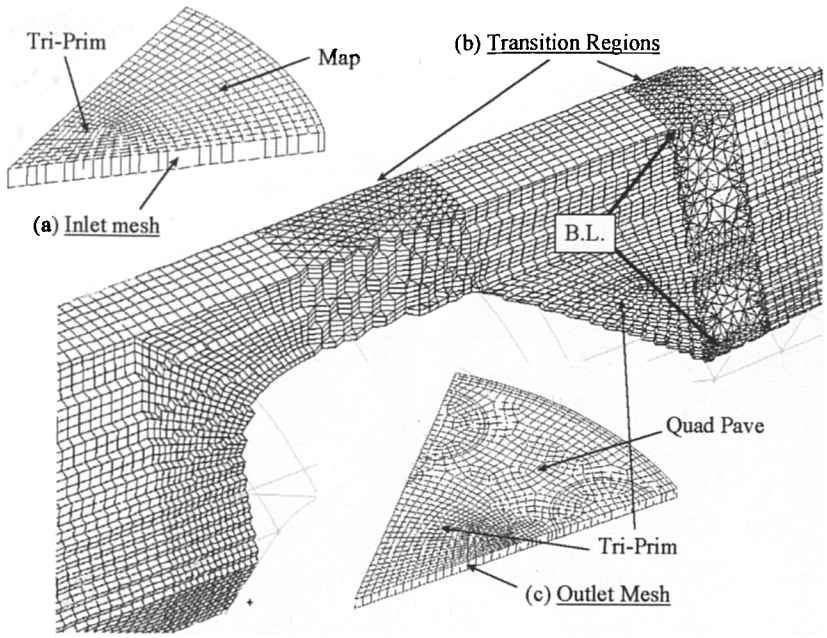

Figure 7.3 Features of initial mesh for upstand restrictor: Mesh R8S-A.

The inlet section (Figure 7.3(a)) of the mesh (2D upstream length) was created using hexahedral cells. A tri-primitive mesh was used close to the pipe centreline, and a regular mapped mesh from this to the pipe wall. This mesh was swept down through the domain until just above the upstand of the restrictor. The inlet mesh ends on the top surface of the restrictor upstand.

Two transition regions were required for this mesh. Only one of these was a true unstructured tetrahedral section: the other contains five-sided wedge-shaped cells as shown in Figure 7.3(b). The advantage in having wedge-shaped cells is that they are quadrilateral in the flow direction, which should improve the flow solution. The tetrahedral transition section is necessary to join two incompatible hexahedral sections. Hexahedral cells are used to mesh the restrictor holes (two half holes) and adjacent surfaces. This can be seen on the section of outlet mesh shown as Figure 7.3(c). The outlet mesh was created by sweeping the mesh on the downstream face of the restrictor through the length of the outlet. Cell aspect ratio does increase considerably towards the final outlet boundary of the mesh, due to the length of piping included.

Only this mesh uses the simplified geometry: the rest all follow the true restrictor geometry accurately. It should also be noted that boundary layers (B.L.) were specified on either side of the unstructured tetrahedral transition region. These five-sided prismatic cells provide better solution of the flow near the solid boundaries.

7.2.1.2 First mesh using accurate geometry: MR8Sb

Meshes MR8Sb and MR8Sc are similar to each other in layout: only the cell sizes and density changed between the models (with MR8Sc having a significantly more refined mesh). Mesh MR8Sb has three unstructured tetrahedral transition regions: two before the holes, and one immediately after the holes. The aim of this was to allow more appropriate meshing of the inward sloping region of the upstand (upstream of the holes) and to enable efficient meshing of the outlet sections (with mapped hexahedral cells) downstream of the holes. Figure 7.4(a) shows the upstream transition regions. Prismatic boundary layers were specified at the outer faces of the transition regions.

The internal mesh structure shown in Figure 7.4(b) illustrates the type of quad-paved face that has been used in many of the meshes. Corners 1 and 2 have been identified to aid location of the cutting plane on which the quad mesh has been displayed. The volume mesh between point 1 and the downstream face of the second upstream transition region was created by sweeping the quad-paved face upwards towards the upstream transition region. The tetrahedral transition regions were created after the hexahedral regions.

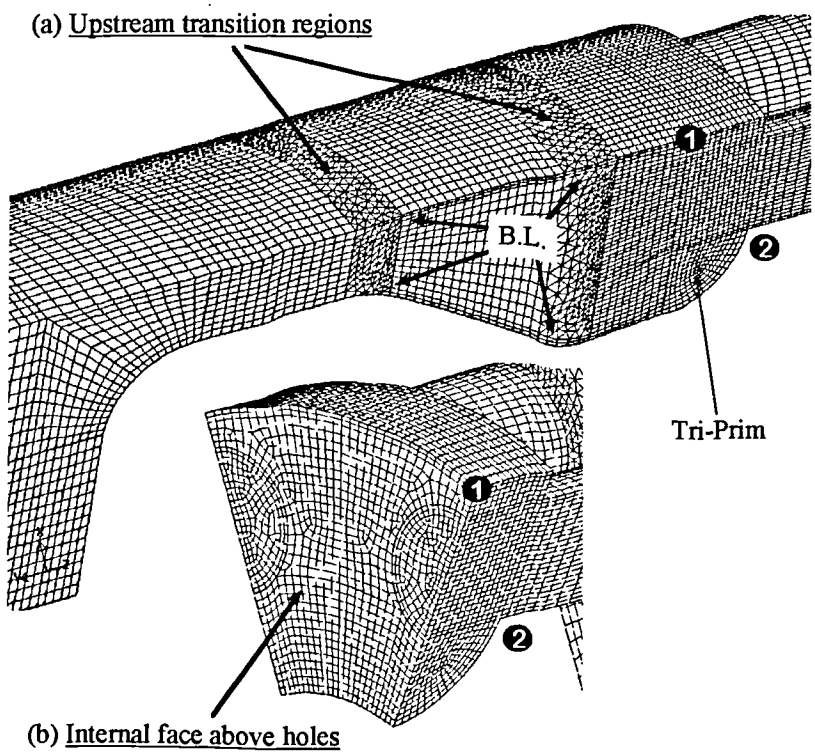

Figure 7.4 Main body of mesh for MR8Sb.

The outlet section of the mesh starts with a third tetrahedral transition region as shown in Figure 7.5(a). Immediately below the transition region is a hexahedral mesh as shown in Figure 7.5(b). The inner part of the outlet mesh is formed by a tri-primitive quad face being swept down through the domain. The outer section is a regular mapped hexahedral mesh. Using this approach reduces the number of cells required in the long outlet region.

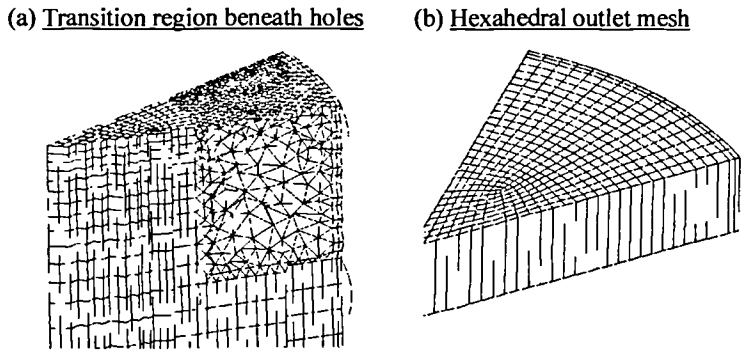

Figure 7.5 Main features of outlet mesh for MR8Sb.

It will be observed that the mesh shown here closely follows the true curved geometry. An attempt has also been made to use hexahedral cells whenever possible, which accounts for the three tetrahedral transition regions. Boundary layers have been used in all three transition

regions to provide five-sided prism cells at the inner and outer edges (apart from the third transition region where a boundary layer is only specified on the outer wall).

7.2.1.3 Refinement of previous mesh: MRS8c

This mesh is based on the same underlying strategy as the previous mesh, where three tetrahedral transition regions are used to connect hexahedral sections. However, in this mesh an attempt was made to concentrate cells more closely round the sharp edges of the holes through the restrictor base. Figure 7.6 illustrates this mesh at either side of the holes.

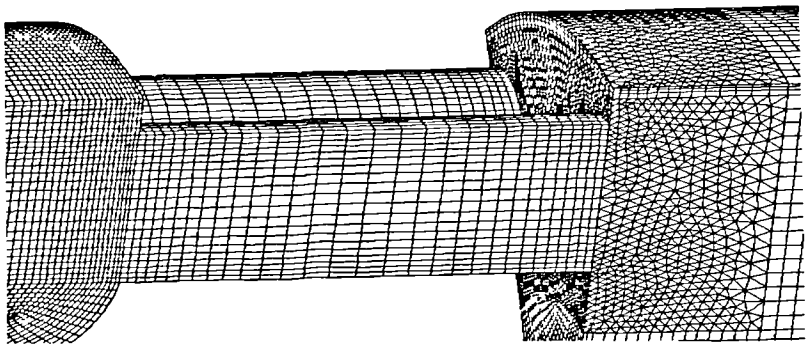

Figure 7.6 Mesh through holes for Mesh MR8Sc.

7.2.1.4 Mesh MR8Sd

Although the geometry continues to be the same for this mesh as for the previous mesh, a different approach was adopted. Greater care was taken to group cells closer to the hole entrance and exit than in the previous meshes (Figure 7.7(b)). The arrangement of transition regions was also changed. Figure 7.7(a) shows the position of the three tetrahedral transition regions. The first transition region now appears in the sloping section of the upstand: hexahedral cells were specified here previously. A short section of hexahedral mesh follows the first transition region, before meeting the second tetrahedral section, which maps cells onto the quad-paved face created by the holes and surrounding geometry. The third transition region is not immediately after the hole exit as in previous meshes, but rather comes after a short section of wedge-type mesh created by a downwards sweep of the unstructured tri-pave face on the downstream side of the restrictor holes. This wedge section was included to provide higher quality cells immediately after the restrictor holes. Figure 7.8 illustrates the meshing arrangement downstream of the holes.

It will be noted that mesh MR8Sd has the greatest number of cells out of all the meshes presented here, and indeed should represent the greatest level of refinement. In particular, an attempt has been made to ensure adequate cell resolution (at least in the direction of flow) near the hole edges.

Another feature is that the inner part of the outlet mesh does not have a tri-primitive initial face, but rather a tri-pave face. This means that the inner part of the outlet mesh consists of wedge cells along the whole length of the outlet. The remainder of the outlet mesh is a regular hexahedral mapped mesh (after the tetrahedral transition section).

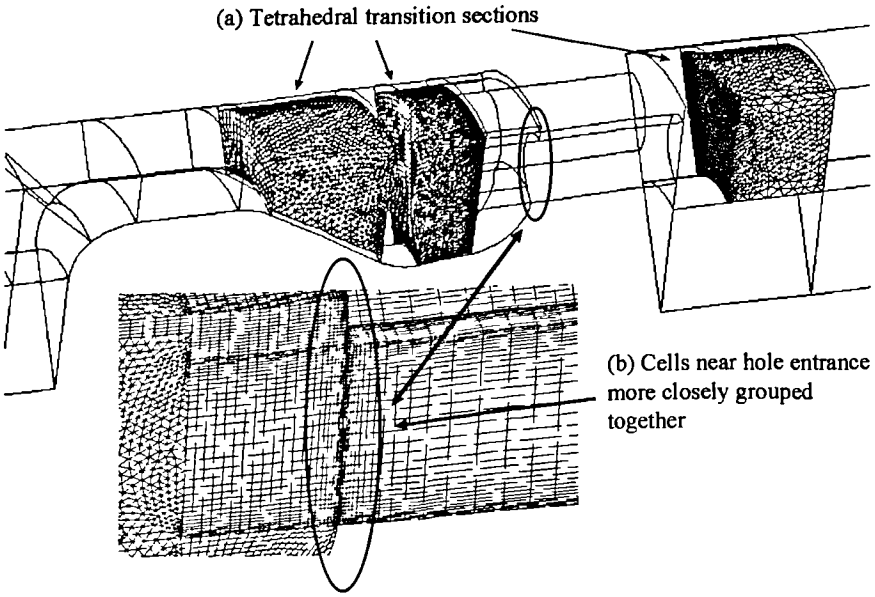

Figure 7.7 Transition regions and cell grouping near hole entrance for MR8Sd.

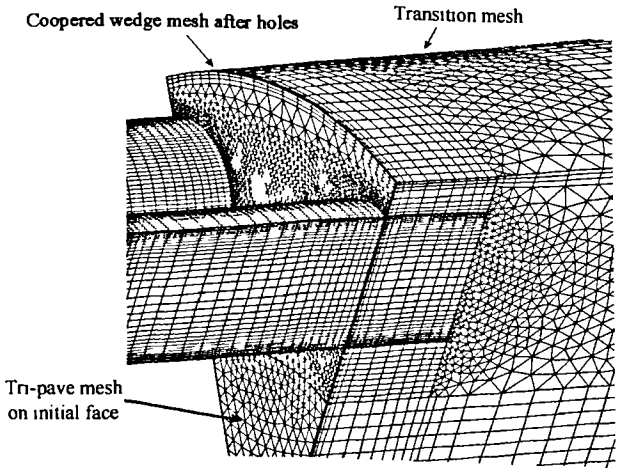

Figure 7.8 Mesh following holes for MR8Sd.

7.2.1.5 Mesh MR8Se

Although the main aim of this mesh was to continue grouping cells close to hole edges while reducing the overall number of cells, an additional feature is that only two tetrahedral transition sections are specified. The middle transition region of the previous mesh is removed, and instead a continuous hexahedral region is generated. Figure 7.9 illustrates the resulting mesh. The two remaining tetrahedral sections are similar to those used in the previous mesh. A tri-pave face is again used to create the inner part of the outlet mesh. As in most cases, prismatic boundary layers have been created on the inner and outer surfaces of unstructured tetrahedral sections.

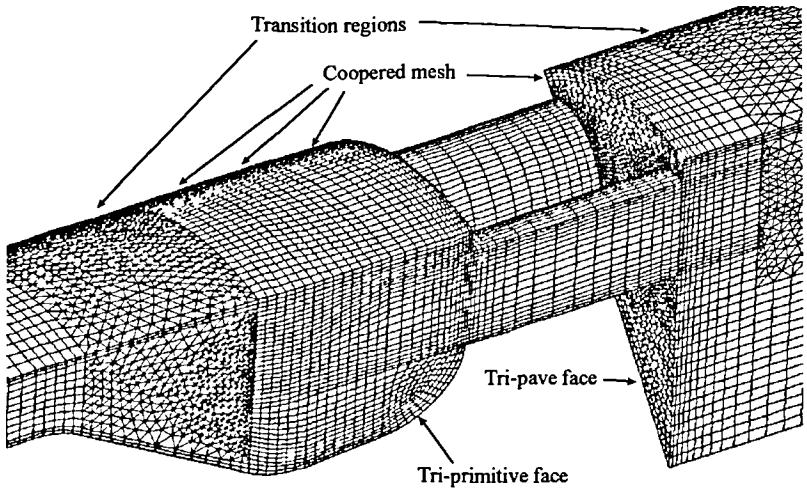

Figure 7.9 Features of Mesh MR8Se.

7.2.1.6 Mesh MR8Sf

The previous two meshes were intended to be high quality meshes with adequate numbers of cells. One question, which needs to be addressed, is the minimum number of cells required to provide a meaningful flow solution. Mesh MR8Sf is the coarsest mesh developed so far, having around 58,000 cells. Figure 7.10 presents the main features of this mesh, which contains three tetrahedral transition regions within it, although one only partially covers the radial cross-section of the geometry. It is apparent that significantly fewer cells have been specified throughout the mesh.

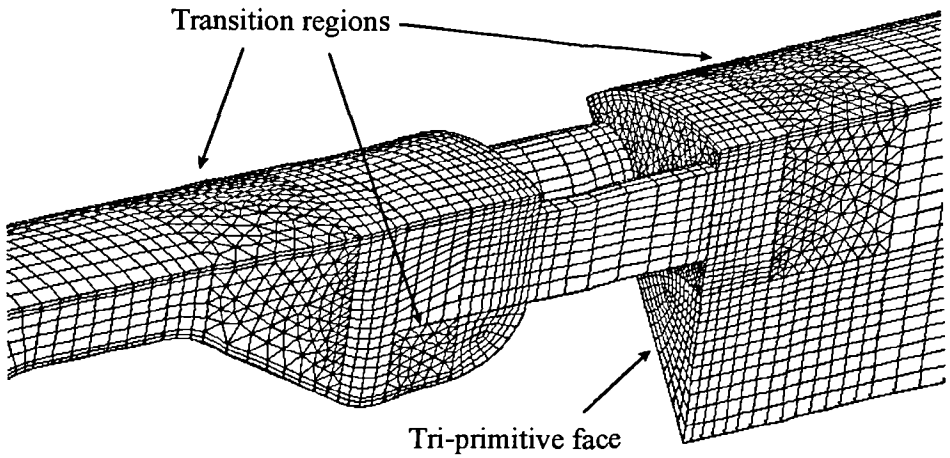

Figure 7.10 Main features of Mesh MR8Sf.

7.2.1.7 Mesh MR8Sg

The aim of this mesh was to reduce the number of changes in cell type throughout the domain. An enlarged tetrahedral region was therefore specified before the restrictor holes. Figure 7.11 illustrates this difference. The mesh is fairly coarse with around 92,000 cells.

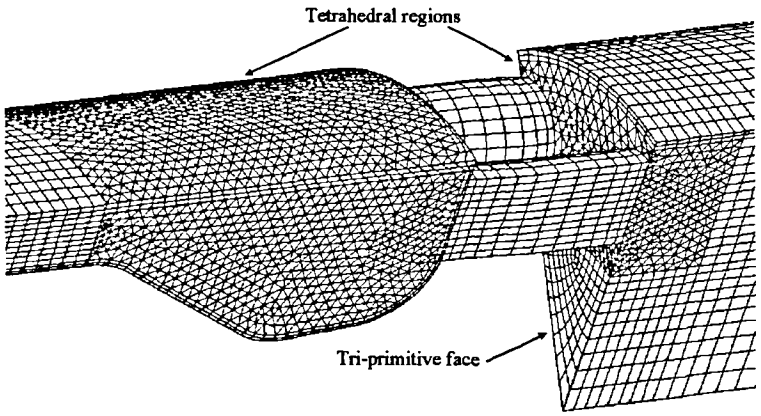

Figure 7.11 Tetrahedral regions and holes of Mesh MR8Sg.

7.2.1.8 Mesh with extended tetrahedral region: Mesh R8Sh

All of the meshes considered so far have tetrahedral transition regions. In most instances, the aim has been to minimise the amount of tetrahedral cells if possible. This particular mesh takes an alternative approach, and has a tetrahedral region which begins before the top surface of the upstand, and continues to the leading face of the restrictor holes. An extended boundary layer is set on the surface of the upstand itself, to improve flow modelling close to the surface. Figure 7.12 illustrates the mesh.

The outlet of mesh MR8Sh is created by sweeping the top face after the holes down through the outlet pipe. Figure 7.12 shows the resulting mesh some way down the outlet section. A tri-primitive face forms the inner section of the outlet mesh, while the remainder has the imprint of the restrictor holes. Note that this mesh had only one diameter of pipe upstream of the restrictor, and just over four diameters downstream.

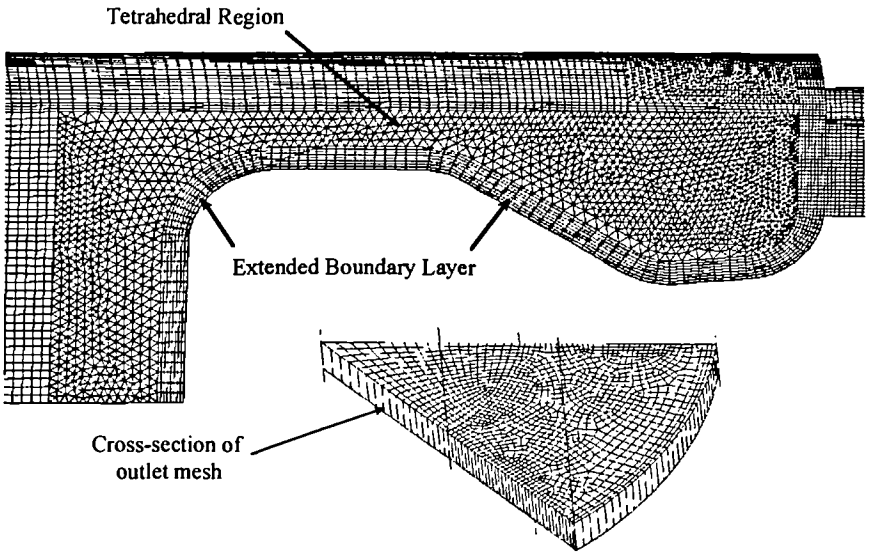

Figure 7.12 Enlarged tetrahedral section of Mesh MR8Sh.

7.2.1.9 Mesh with hexahedral cells only: MR8Si and MR8Sj

Two meshes were created using only hexahedral cells. The second mesh (MRSj) is a refined version of the first. Figure 7.13 shows the upstand and hole sections of Mesh MR8Si. A single hole has been modelled in this mesh, rather than two half holes. This was thought to make the task of creating the mesh easier. The joint between the inlet mesh and the main restrictor mesh is possibly the region most likely to cause problems in obtaining a solution, as cells will be skewed somewhat at the joint. This shows the disadvantage in using an entirely hexahedral mesh: all adjacent regions must be compatible in order to continue the progression of cells.

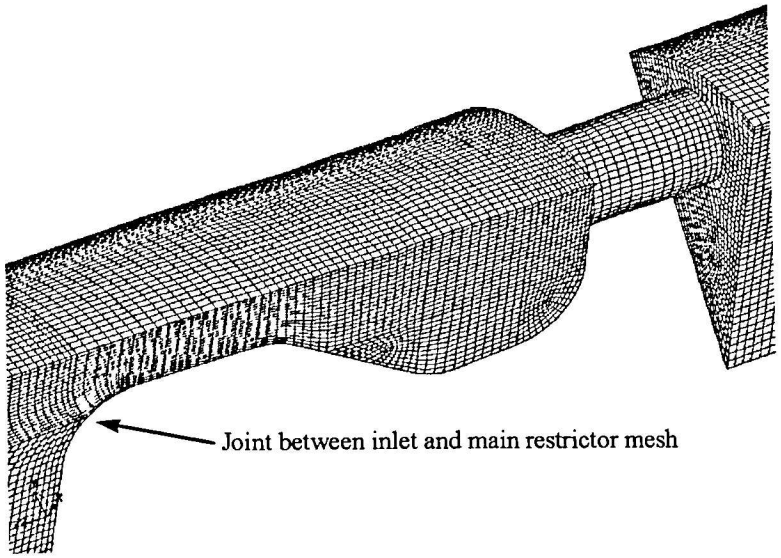

Figure 7.13 Part of Mesh MR8Si: fully hexahedral.

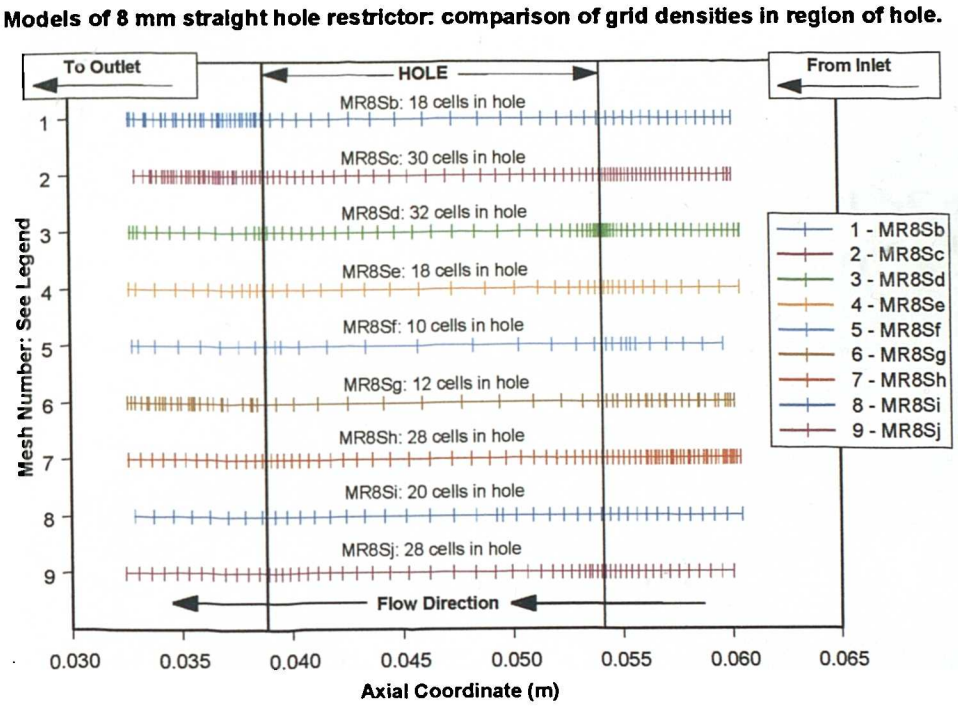

Figure 7.14 Comparison of mesh resolution in hole regions.

7.2.1.10 Comparison of mesh resolution in hole region

Figure 7.14 presents a comparison of cell centre positions in the axial direction for all meshes considered so far—apart from MR8Sa. Each short vertical line in the figure is the approximate position of the cell centre. Flow is from right to left, which means that the inlet would be further to the right of the cells included in the figure, and the outlet much further to

the left. The exact number of cells specified in the hole for each mesh has been included on the figure.

It will be seen that in mesh MR8Sd, the cells are closely grouped together at the leading edge of the hole. The distance between the cell centre immediately upstream of the hole and the leading edge of the hole, is less than 0.001 D_P—where D_P is the pipe diameter. This corresponds to the recommendation of Erdal and Andersson (1997) who found that, for successful modelling of an orifice plate, the position of this upstream cell centre should be within 0.001 D_P. They modelled an orifice plate 11 mm thick, and set 15 cells in the axial direction along its length. In mesh MRSd, 32 cells have been set for a 15.24 mm thick 'plate'. However, the flow features will be somewhat different from that observed in an orifice plate simulation. These recommendations have been applied to see the difference that is made to the solution. It is known that for orifice plates, the sharpness of the leading edge of the hole is one of the most crucial parameters for correct correlation between pressure drop and flowrate. The pressure drop is heavily dependent on the sharpness. However, the ratio of hole diameter to pipe diameter in this simulation is much smaller than that in the work of Erdal and Andersson (1997), and so their findings cannot be conclusively applied to the current study.

Hole cell distributions for other meshes have been set in keeping with the underlying design criteria for each mesh. When a coarse mesh has been developed, the number of cells in the hole has been similarly reduced. In retrospect, it would have useful to examine the effect of hole cells in more detail, without necessarily changing the rest of the mesh. However, in a three-dimensional mesh it would be difficult to isolate effects to one cause alone, as the cell distribution in other co-ordinate directions would also need to be considered.

7.2.1.11 Summary to Computational Meshes

It will be apparent that a large number of computational meshes have been created in the course of the study of restrictors. Creating each mesh generally took up 60 to 70 % (rough estimate) of the total time spent with a model, depending on the number of actual flow solutions obtained. The more complex meshes took around 2-3 days to create, while some of the simpler ones (i.e. those with fewer changes in mesh type), were created in less than a day. Setting up and running each model (to obtain a flow solution) was comparatively quick—as little as 10 minutes would be required to set a model running. Solution time (on a Windows NT machine having dual Intel Pentium II 400 MHz processors) was in the order of 12-36 hours. Models were run as parallel cases whenever possible.

One of the main problems encountered in creating computational meshes was in setting up the underlying CAD geometry in the Fluent pre-processor. Each section of mesh had to be defined as a geometrical entity (i.e. distinct block in the overall 3D solid model). Bugs in the pre-processor caused some problems, as did some of the restrictions imposed on the user by the software. These tended to increase the amount of time spent in mesh creation; but as experience with the software grew, it was possible to work around the limitations.

It is difficult to include detailed discussion on every mesh created for use in restrictor modelling. An attempt has been made to briefly outline the main features of the various meshes, as well as something of the rationale behind their creation. The actual predicted results must be considered before the influence of meshing strategy on results will be known.

7.2.2 Flow Solutions

At least one prediction of flow and turbulence properties has been made for each of the meshes described above. The minimum level of prediction has been for a single flowrate using fully-developed flow profiles at the inlet, in conjunction with the standard k-ε turbulence model. These settings will be discussed more fully as appropriate. All successfully converged solutions obtained using the various meshes are summarised in Table 7.2.

Table 7.2 Summary of solutions obtained for upstand restrictor with 8mm straight holes.

Models	Cells	Turbulence	Discretisation	Q_T (litres/s)
MR8Sa-1	261k	ske; swf	2o; sp	10.00
MR8Sb-1	148k	ske; swf	2o; sp	9.92
MR8Sb-2	148k	ske; noneq	2o; sp	9.92
MR8Sb-3	148k	ske; swf	2o; 2op	9.92
MR8Sb-4	148k	ske; noneq	2o; 2op	9.92
MR8Sc-1	440k	ske; swf	2o; sp	9.92
MR8Sd-1	512k	ske; swf	2o; sp	9.92
MR8Se-1	207k	ske; swf	2o; sp	9.92
MR8Se-2	207k	ske; swf	2o; 2op	9.78
MR8Sf-1	58k	ske; swf	2o; sp	9.92
MR8Sf-2	58k	rsm; swf; wr	2o; sp	9.92
MR8Sf-3	58k	rsm; swf; wr	2o; sp	9.78
MR8Sg-1	92k	ske; swf	2o; sp	9.92
MR8Sg-2	92k	rsm; swf; wr	2o; sp	9.92
MR8Sh-1	371k	ske; swf	quick; sp	9.78
MR8Sh-2	371k	rsm; swf; wr	quick; sp	9.78
MR8Sh-3	371k	ske; swf	2o; sp	9.92
MR8Si-1	172k	ske; swf	2o; sp	9.78
MR8Si-2	172k	ske; swf	2o; prsto	9.78

Models	Cells	Turbulence	Discretisation	Q_T (litres/s)
MR8Si-3	172k	ske; swf	2o; sp	9.92
MR8Sj-1	172k	ske; swf	2o; sp	9.78

In Table 7.2, the relevant mesh has been indicated in the first part of the unique solution identifier. Where more than one solution has been obtained with a specific mesh, the second part of the identifier is incremented ('flow solution 1', 'flow solution 2', etc). The abbreviated turbulence and discretisation parameters are explained in Table 7.3.

Table 7.3 Explanation of turbulence and discretisation parameters.

Abbreviation	Meaning
ske	Standard k-ε turbulence model
rsm	Reynolds Stress Model
swf	Standard wall functions
wr	Wall reflection option ON
rngke	RNG k-ε turbulence model
neqwf	Non-equilibrium wall functions
2o	Second order discretisation
sp	Standard pressure interpolation
quick	QUICK discretisation
2op	Second order pressure interpolation
prsto	PRESTO! pressure interpolation

7.2.2.1 Inlet Boundary Conditions

Fully developed flow profiles were set at all inlets in all cases. These flow profiles were obtained by first running a periodic solution which considered only a short section of the inlet pipe length. A typical example is shown in Figure 7.15. Periodic boundaries are set at either side of the pipe section, with symmetry planes set as appropriate. In most cases the RNG k-ε turbulence model was used initially, with the Reynolds Stress Model being activated if actual stress components were required (e.g. when the actual restrictor case was to be run with the RSM turbulence option). The mass flowrate was the only input required for this type of model: the solver ran until the solution had come to a steady state (no change in flow variables) and the specific flowrate had been achieved.

All meshes used for periodic profile calculations have the same cross-section as the inlet to the actual restrictor computational domain. This means that no interpolation of flow profile takes place in the restrictor model.

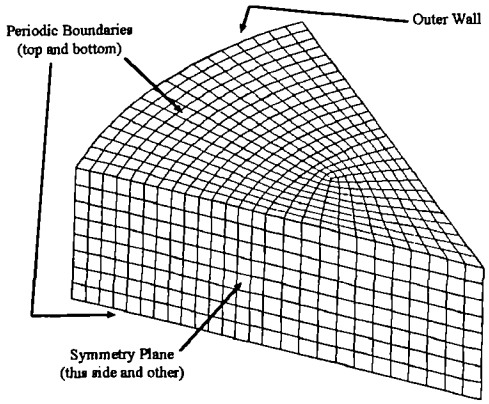

Figure 7.15 Example of mesh used for periodic profile calculations.

7.2.2.2 Solver Parameters and Convergence

The properties of water at 20^0C have been used for the incompressible fluid in all cases. Second order upwind discretisation has also been used in all cases (apart from a few periodic profile cases where a higher order scheme may have been specified instead). Solution algorithm has generally been the SIMPLE (Patankar and Spalding, 1972) or SIMPLEC (Van Doormal and Raithby, 1979) algorithms for steady flow cases, and the PISO (Issa et al., 1986) algorithm for unsteady cases. The particular choice of algorithm is not expected to influence the final solution (Jang et al., 1986).

Selected flow variables (e.g. velocity magnitude or turbulent kinetic energy) have been monitored at one or two specific points in the flow domain during solver iterations. Monitoring variables at specific points serves to indicate when a steady state solution has been achieved. In addition to this, the solver plots a scaled residual imbalance for each quantity being solved. This should generally fall by several orders of magnitude for a successfully converged solution. The scaled residual is defined by first examining the discretisation equation for a single cell, which is given for a general variable ϕ at a cell P as:

$$a_P \phi_P = \sum_{nb} a_{nb} \phi_{nb} + b \qquad (7.1)$$

where a_P is the centre coefficient, a_{nb} are the influence coefficients for the neighbouring cells, and b is the contribution of the constant part of the source term S_C in $S = S_C + S_P\phi$. The scaled residual is defined as:

$$R^{\phi} = \frac{\sum_{cells\ P} \left| \sum_{nb} a_{nb}\phi_{nb} + b - a_P\phi_P \right|}{\sum_{cells\ P} |a_P\phi_P|} \qquad (7.2)$$

In general for the work presented in this study, the scaled residual for each property came to a minimum steady state value that was generally several orders of magnitude lower than the initial reported values. The way in which the above definition is applied varies slightly depending on the particular variable of interest. More information can be found in the Fluent manual.

7.2.2.3 y^+ values

The fundamental law underlying the wall functions used in this study is only valid when the quantity y^+ (equation 2.9) lies in the range 30 to 500 for all cells next to the wall. In some of the cases considered here, the y^+ values fell below the lower limit in certain regions of the mesh. Although the maximum y^+ limit was not really an issue in most of the 8 mm straight hole restrictor studies, there were some in which y^+ values fell below the lower limit. Mesh MR8Sd had the greatest range of cells for which the minimum y^+ fell below this lower limit. Figure 7.16 shows the y^+ values up to a maximum of 30 for flow solution MR8Sd-1. Low y^+ values will have an adverse affect on the simulation results.

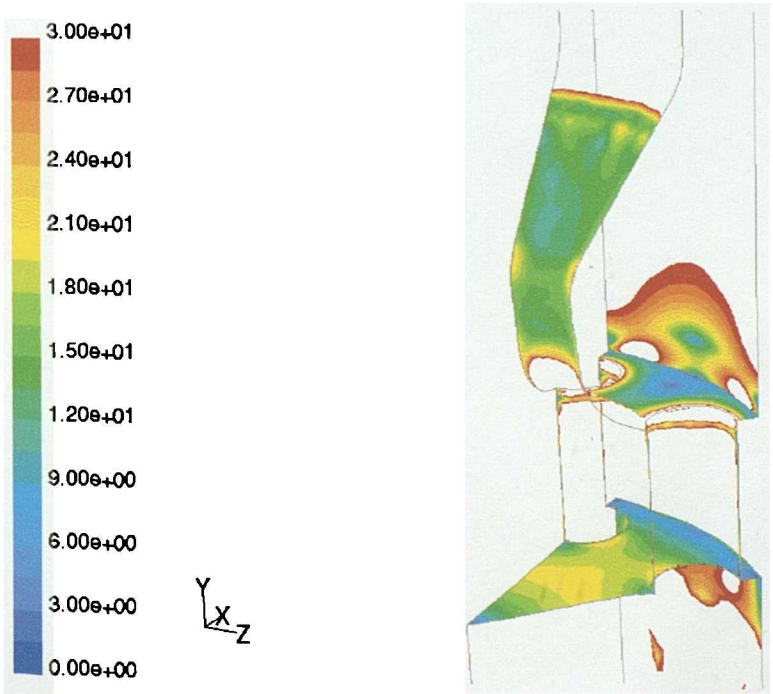

Figure 7.16 regions of low y^+ value for flow solution MR8Sd-1.

Flow solutions using mesh MR8Si had y^+ values *conforming* to the required limits across almost the whole mesh—apart from some cells on the side of the upstand. These results will therefore be the least affected by low y^+ values.

Further work is required to quantify what significance low y^+ values will have on predicted results. Such a study would need to be comparative, in that the effects of y^+ must be considered along with all other factors that could reduce the accuracy of predictions. In their study of flow through orifice plates, Erdal and Andersson (1997) reported y^+ values as low as seven in some parts of their mesh. They were still able to make predictions of pressure drop to within 3 % of measured values, which suggests that y^+ played only a minor role in determining the accuracy of their predictions. Other factors such as mesh distribution were of far more importance.

7.2.2.4 Predictions of pressure drop and flow coefficient

The first stage in modelling the restrictors was to obtain predictions of pressure drop (and hence flow coefficient C_V) for direct comparison with the experimentally obtained values. The experimental data against which the CFD predictions will be compared has been presented previously in Table 6.2. Experimental data for the 8 mm straight holed upstand restrictor is shown again for ease of reference, in Table 7.4. Three data points are available from the testing, all of which combine to give an average flow coefficient for the particular restrictor geometry in question. Note that abbreviations in Table 7.4 follow those in Table 6.2. The worst case uncertainty in the table is estimated to be 1.41 % of C_V. This uncertainty is for individual readings of C_V: the uncertainty for average C_V will be higher.

Table 7.4 Experimental data for 8 mm straight upstand restrictor.

TBS	Log Time	Flowrate	P1	P2	ΔP	Cv
(s)	(mins)	(litres/s)	(bar)	(bar)	(bar)	SI
30	10	5.72	8.230	7.302	0.928	5.80
30	10	9.92	14.379	11.369	3.010	5.64
30	10	13.99	14.038	8.067	5.970	5.66

In the first stages of modelling restrictors, the flowrate chosen was generally the middle flowrate of Table 7.4, i.e. 9.92 litres/s. Some CFD models were also run using a corrected version of this flowrate, obtained using the correction described in Appendix D. The corrected flowrate is 9.78 litres/s. This explains the reason for having some repeat CFD models with slightly adjusted flowrates in Table 7.2.

Table 7.5 presents the CFD predictions of overall pressure drop and flow coefficient for all successful models obtained so far. An estimate of error as compared with the experimental values has been determined from the following:-

$$\% \text{ Difference} = \left[\frac{\text{CFD Prediction} - \text{Experimental Value}}{\text{Experimental Value}}\right] \times 100\ \% \qquad (7.3)$$

This relation will be used for comparison of both pressure drop and flow coefficient: the relevant columns in Table 7.5 are headed 'Diff.' to indicate the application of equation 7.3.

Table 7.5 Predictions of pressure drop and flow coefficients for models of the upstand restrictor with 8 mm straight holes.

Model	CFD Flow (litres/s)	Exp. Flow (litres/s)	Pdif CFD (bar)	Pdif Exp (bar)	% Diff.	Cv CFD SI	Cv Exp. SI	% Diff.
MR8Sa-1	10.00	9.92	4.45	3.01	47.8	4.74	5.72	-17.1
MR8Sb-1	9.92	9.92	4.16	3.01	38.3	4.86	5.72	-15.0
MR8Sb-2	9.92	9.92	4.29	3.01	42.5	4.79	5.72	-16.3
MR8Sb-3	9.92	9.92	4.04	3.01	34.4	4.93	5.72	-13.8
MR8Sb-4	9.92	9.92	4.08	3.01	35.5	4.91	5.72	-14.1
MR8Sc-1	9.92	9.92	4.23	3.01	40.7	4.82	5.72	-15.7
MR8Sd-1	9.92	9.92	4.15	3.01	38.0	4.87	5.72	-14.9
MR8Se-1	9.92	9.92	4.16	3.01	38.3	4.86	5.72	-15.0
MR8Se-2	9.78	9.78*	4.02	3.01	33.4	4.88	5.64	-13.4
MR8Sf-1	9.92	9.92	4.19	3.01	39.1	4.85	5.72	-15.2
MR8Sf-2	9.92	9.92	3.85	3.01	27.9	5.06	5.72	-11.6
MR8Sf-3	9.78	9.78*	3.74	3.01	24.2	5.06	5.64	-10.3
MR8Sg-1	9.92	9.92	4.51	3.01	49.7	4.67	5.72	-18.3
MR8Sg-2	9.92	9.92	3.92	3.01	30.4	5.01	5.72	-12.4
MR8Sh-1	9.78	9.78*	4.17	3.01	38.5	4.79	5.64	-15.0
MR8Sh-2	9.78	9.78*	3.67	3.01	22.1	5.10	5.64	-9.5
MR8Sh-3	9.92	9.92	4.31	3.01	43.1	4.78	5.72	-16.4
MR8Si-1	9.78	9.78*	4.06	3.01	35.1	4.85	5.64	-14.0
MR8Si-2	9.78	9.78*	4.00	3.01	33.1	4.89	5.64	-13.3
MR8Si-3	9.92	9.92	4.18	3.01	39.0	4.85	5.72	-15.2
MR8Sj-1	9.78	9.78*	4.04	3.01	34.4	4.86	5.64	-13.7
MR8Sk-1	9.78	9.78*	4.35	3.01	44.5	4.69	5.64	-16.8

Some of the experimental flowrates in the table have an asterisk attached to them (i.e. at a flowrate of 9.78 litres/s). This flowrate is essentially the corrected version of 9.92 litres/s (the flowrate given by the flowmeter). The reason for doing this was to see whether using the corrected flowrate gave improved comparison between predicted and actual results. The results with this corrected flowrate are generally better than those with the uncorrected flowrate, which suggests that uncertainty in the flowrate measurement has some part to play in

the difference between predicted and actual results. A graphical representation of the data in Table 7.5 has been produced, and is shown in Figure 7.17.

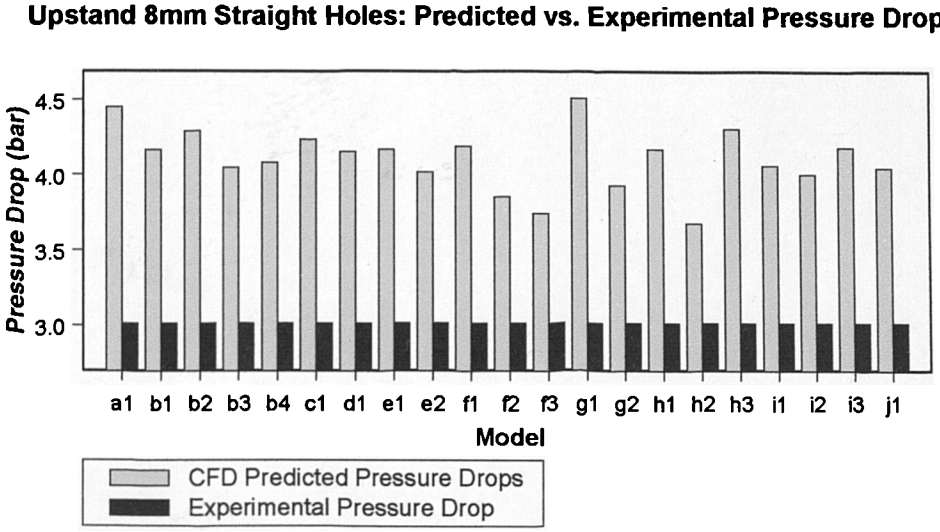

Figure 7.17 Comparison of predicted and experimental pressure drop data.

It is apparent from Figure 7.17 that the cases giving closest agreement to the experimental data are f-2, f-3, and h-2. The Reynolds Stress Model was used in these cases. The error in pressure drop prediction falls to under 30% of the experimental value.

There are therefore significant differences between experimental and CFD predictions of pressure drop for the upstand restrictor with 8 mm straight holes. With the cases attempted so far, there does not appear to be any real benefit of a fine mesh over a coarse mesh—indeed it seems that a coarse mesh enables use of the Reynolds Stress turbulence model, which results in improved predictions. However, it is unlikely that this is truly the case—a finer mesh will generally improve results to a point where no further improvement is possible.

It is interesting to note that it is the coarse meshes that give the closest results to experimental measurements. These are the meshes that have lowest resolution at the sharp corners of the hole entrance (and exit). Corners in the actual manufactured prototypes were not well finished, which means that the CFD models represent much sharper corners than were present in the real prototype. A sharper edge will give rise to a higher pressure drop: the CFD predictions are higher than the measurements. It is therefore suggested that one of the main causes for CFD over-prediction of pressure drop comes from modelling a sharper edge than was present in the prototype.

Several attempts were made to apply the Reynolds Stress turbulence model to fine grid meshes, but it was found that solutions tended to become unstable and did not approach a steady state solution. For this reason most of the cases in Table 7.5 use the standard k-ε turbulence model with standard wall functions. The RNG k-ε model proved even harder to apply than the Reynolds Stress model. No successfully converged solutions were obtained with the RNG k-ε model for the upstand restrictor with 8 mm straight holes, although many attempts were made. The 'success' of the standard k-ε model is probably a result of its simpler and more approximate nature than either the RNG k-ε or Reynolds Stress models. As less of the true flow physics are being accounted for, so it should become easier to obtain some form of converged solution. Although the standard k-ε model may not be capturing all of the flow features, it appears to be giving predictions with some degree of consistency. The results do suggest that using the standard k-ε model will be partly responsible for over prediction of pressure.

A fair degree of grid independence can be seen for the pressure drop predictions with the standard k-ε model and standard wall functions. Pressure loss for models b-1, c-1, d-1, e-1, and f-1 is around 4.17 bar on average. The largest deviation from this is 0.06 bar (1.43% of average), which indicates a consistent prediction. The flow profiles that follow support this result. Some element of grid independency is seen for cases that used the Reynolds Stress model also. Comparing pressure drop prediction for cases f-3 and h-2 shows that the results are within 0.07 bar of each other.

As the flow coefficient considers the square root of pressure drop, the error in CFD prediction of this quantity is less than that for the actual prediction of pressure drop. To predict flow coefficient to within 15 % is probably acceptable for this type of geometry and application, although care will be required when specifying the choke valve C_V to be used in conjunction with the restrictor.

In order to further understand the effect of mesh construction on flow predictions, it is necessary to look at predicted flow profiles throughout the domain. Before looking at profiles in detail, however, it will be constructive to consider the typical flow behaviour predicted by the CFD modelling.

7.2.3 Typical flow behaviour

One of the main advantages of CFD modelling is that the flow properties are predicted in every part of the computational domain. This includes flow close to walls, around corners, within holes and so on. In some cases, it would be almost impossible, and certainly expensive, to use experimental techniques for obtaining the same data. Enhanced flow visualisation is therefore a distinct advantage of CFD over experimental methods. In this particular section, the intention is to build up a visual picture of the flow features within the restrictor.

7.2.3.1 Flow before restrictor holes

Various features of the flow field predicted by the standard k-ε turbulence model are outlined here. In all cases considered so far, the flow has been modelled as fully developed two diameters upstream of the restrictor. The first obstruction presented to the flow is the upstand section of the restrictor. This causes flow to accelerate locally, and to deflect around the bluff end of the upstand, as shown in Figure 7.18. The accelerated flow passes by the widest section of the upstand to enter the enlarged region before the holes (Figure 7.19).

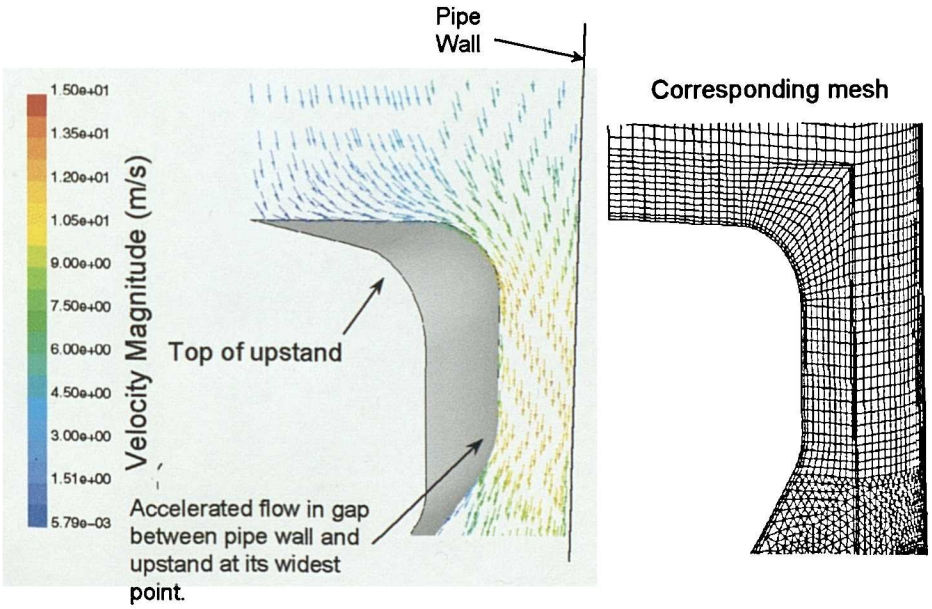

Figure 7.18 Velocity vectors of flow passing upstand section for Case MR8Se-1.

Flow separation occurs just following the top radius of the upstand, which results in a large recirculation region beneath the slope of the upstand. The slow moving recirculation region on the inner walls creates a velocity gradient across the annulus which will result in a weak shear layer approximately in line with the vertical edge of the upstand's widest section.

Contours of turbulent kinetic energy on a plane passing between the holes (central plane) are shown in Figure 7.20. The weak band of shear can be observed. The rapid straining of the fluid at the top outer edge of the upstand also causes increased levels of turbulence—at least according to the standard k-ε model used for the solution from which these graphics come.

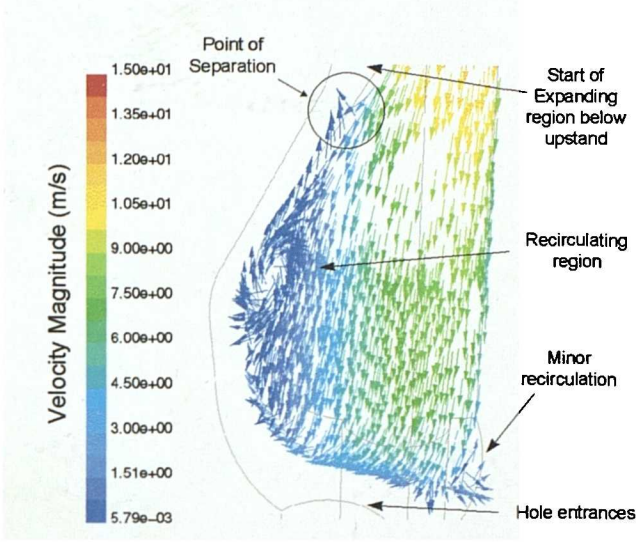

Figure 7.19 Separating flow and recirculating region below upstand for Case MR8Se-1.

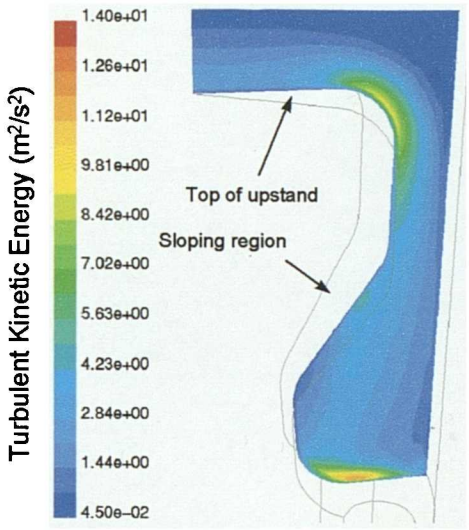

Figure 7.20 Turbulent kinetic energy on central plane around upstand for Case MR8Se-1.

7.2.3.2 Flow through holes

When the fluid reaches the restrictor holes, there will obviously be rapid changes in direction and velocity, which result in large pressure losses and turbulence levels. One concern with the flow through the holes is whether the local static pressure will fall below the fluid vapour pressure, as this could result in cavitation with associated noise and damage potential. This has been examined in more detail for the fluted and valley restrictors.

Fluid accelerates rapidly as it enters the restrictor holes (Figure 7.21(a)). This rapid acceleration results in significant pressure loss across the leading edge of the hole. Separation and reattachment are observed to take place within the length of the hole, which presents a challenge to the turbulence models in terms of successfully predicting energy loss. The mesh is not sufficiently refined for case MR8Se-1 to show actual recirculation within the separation region, so vectors from the appropriate region have been selected from case MR8Sd-1 (the most refined case considered). These are shown as Figure 7.21(b). The existence of separation and reattachment within the hole will be prime causes for poor CFD predictions.

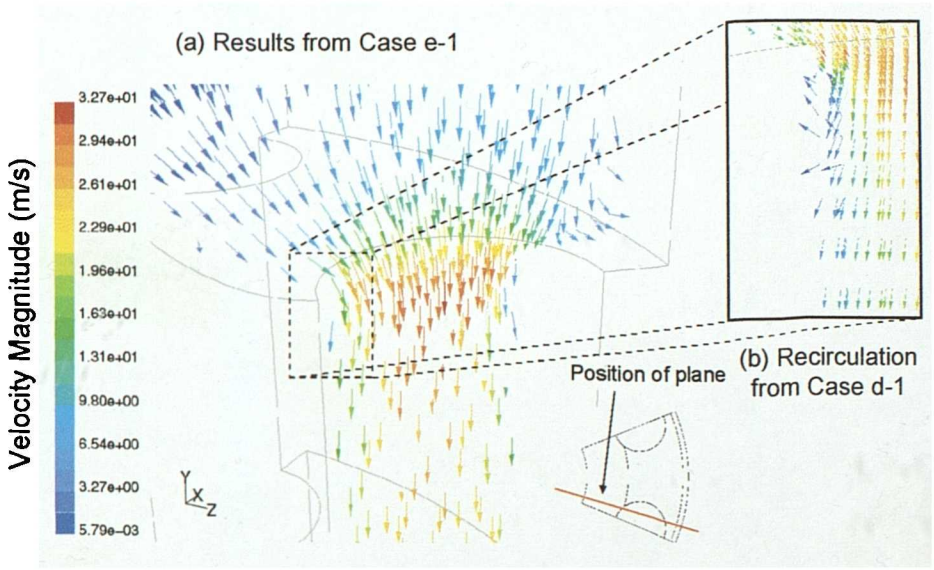

Figure 7.21 Velocity vectors of flow entering restrictor hole for Cases e-1 and d-1.

7.2.3.3 Flow beyond holes

Fluid behaviour after the restrictor holes is characterised by large recirculation regions and mixing jets, which again present a challenging problem for CFD analysis. Figure 7.22 illustrates some of the complex motion by way of pathlines. These can be thought of as the path a fluid particle would take if released along lines just before the hole exit. Both views in Figure 7.22 are of the same set of lines: fluid moves from a vertical plane near the hole centre to the region between the two half-holes. A three-dimensional recirculatory motion is developed.

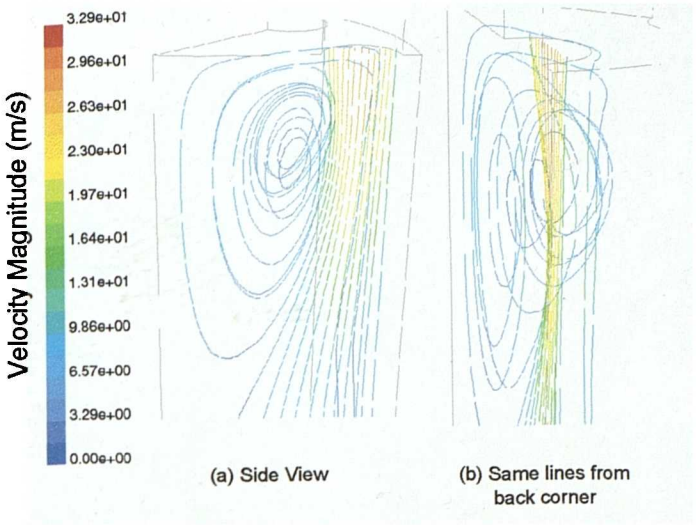

Figure 7.22 Pathlines showing three-dimensional motion beneath holes: Case d-1.

Once the recirculatory motion has died away, fluid will once again have a uniform flow direction, and ultimately return to the fully developed flow conditions of the inlet. An estimate of the downstream length required before fully developed flow is re-established will be given in a later section.

7.2.4 Profiles of predicted data

7.2.4.1 Static pressure

The primary objectives in examining the static pressure profile predicted by the CFD modelling is to first of all determine the length of downstream piping required before all recoverable pressure has been restored; and secondly to assess the likelihood of cavitation at the downstream pressures used in the experimental testing. Profiles obtained using different meshes will be compared as a matter of course.

There is a slight difference between the flowrates used in similar cases. Some of the cases shown in Table 7.2 have a flowrate of 9.92 litres/s, whereas others have 9.78 litres/s. The reason behind this difference is that the latter flowrate is a corrected version of the former: the calibration equation for the electromagnetic flowmeter was used in the correction. An attempt has been made to re-run some cases with both flowrates so as to provide a better comparison with experiment.

Figure 7.23 shows the static pressure profiles for models obtained using Mesh MR8Sb. As the mesh remains identical for all solutions, the effect of different solver parameters can be clearly seen. The most significant factor to affect the result is the use of second order pressure interpolation: this gives a reduced overall static pressure drop which is more in line with the experimental result. Non-equilibrium wall functions increase the overall pressure drop from the result obtained using standard functions. If comparing results with experimental data alone, it is shown that standard wall functions provide a better solution. The line along which this data is taken lies on the right hand symmetry plane (when the restrictor lies vertical with the upstand to the top).

There is not a great deal of difference between the four solutions beyond the top surface of the hole. This suggests that the flow behaviour upstream of the hole has more effect on the pressure drop than that downstream of the hole. It will be instructive to examine profiles of other flow properties at several locations upstream of the holes.

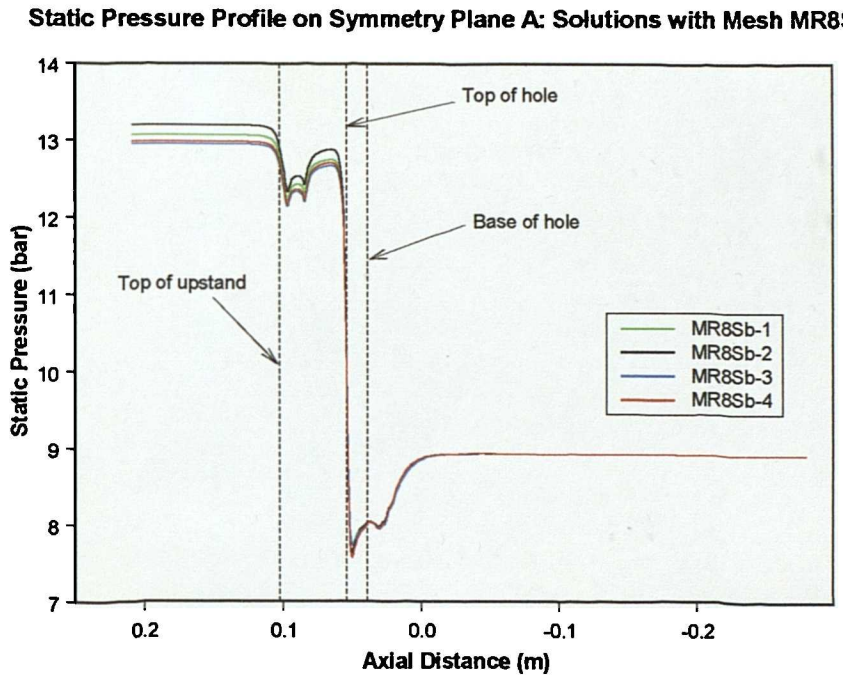

Figure 7.23 Static pressure profile along axial direction for cases MR8Sb-1 to b-4.

The effect of different meshing strategies on the static pressure distribution is shown by comparing cases MR8Sb-1, MR8Sc-1, MR8Sd-1, MR8Se-1, MR8Sf-1, MR8Sg-1, MR8Sh-3, and MR8Si-3. Figure 7.24 presents this comparison. Note that node data is presented for all profiles—unless stated otherwise. It is interesting to note that the majority of

the solutions (apart from MR8Sg-1) are all fairly close in terms of profile. This does give some confidence in the repeatability of the CFD solutions using different meshes.

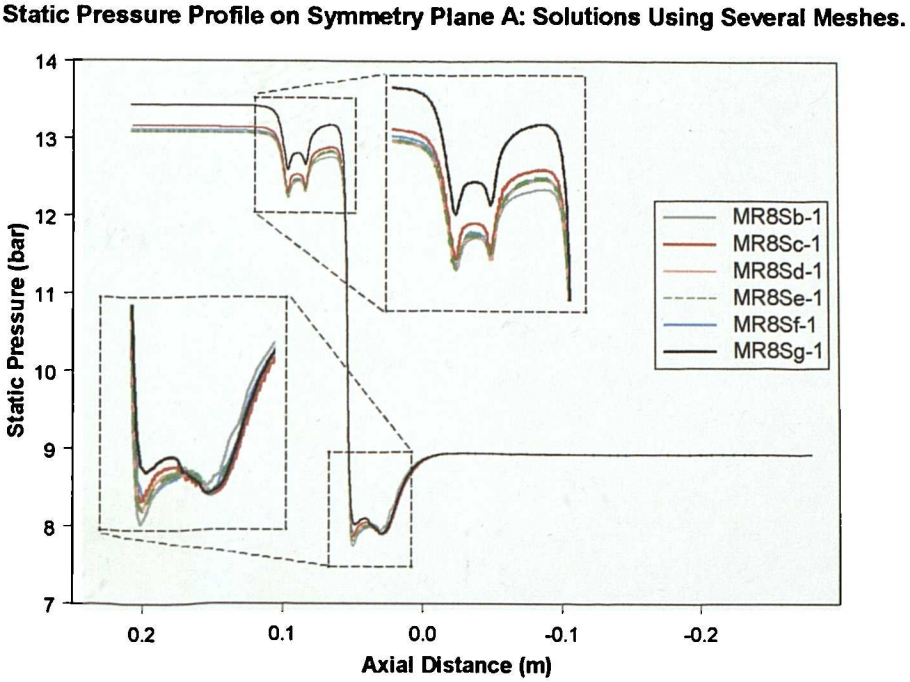

Figure 7.24 Comparison of static pressure profiles with various meshes.

7.2.4.2 Velocity Data

Particle impact velocity will be directly dependent on the fluid velocity close to the surface. It may therefore be more important to consider the variation in fluid velocity profiles with different meshing strategies and modelling parameters than it is to consider the variation in static pressure profile. However, the disadvantage with contemplating velocity profiles is that there are no experimental profiles available with which to compare results. Static pressure drop is the only property that can be validated in this way.

Velocity profiles have been obtained at several locations throughout the restrictor domain. Figure 7.25 identifies these locations with the geometric distances used to specify them. Actual geometric definitions in terms of co-ordinates differ between meshes, but the generic locations remain the same. Lines are created on three different planes (for eighth annulus meshes) as shown (Figure 7.25 (d)). Note that the lines that lie along the symmetry plane are rotated by 0.1^0 inwards to avoid problems when creating the lines in Fluent.

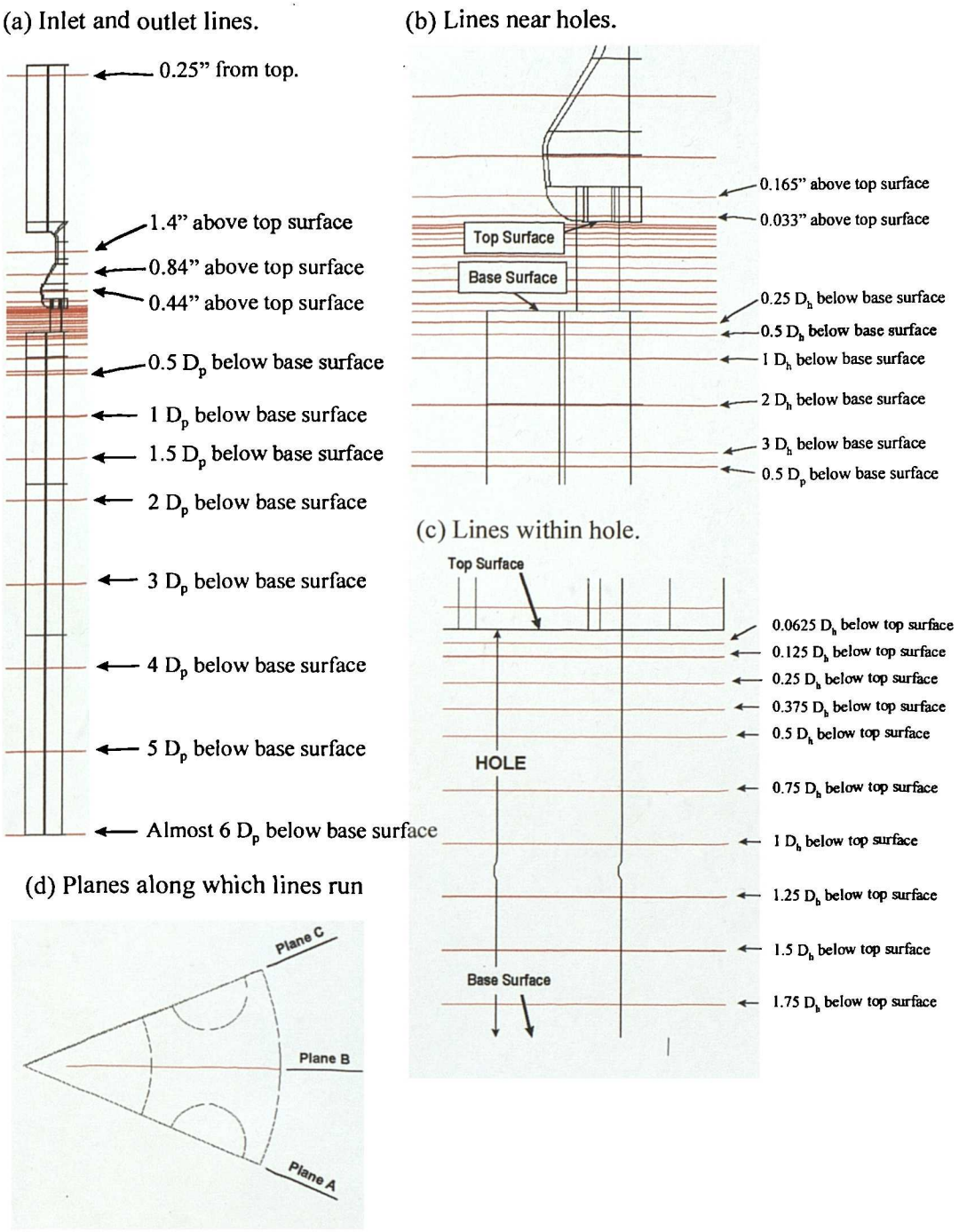

Figure 7.25 Lines used to extract data.

As the mesh used for case MR8Sd-1 has the most number of cells, the velocity data obtained throughout the length of the restrictor domain will be presented in full. This will give some indication as to the flow development taking place before and after the restrictor, as well as the fluid behaviour near and within the holes. Figure 7.26 shows axial velocity profiles along planes A and B for all six lines above the top surface. Figure 7.27 presents the profiles

within the restrictor hole itself (plane A), and Figure 7.28 presents selected profiles for lines downstream of the restrictor base surface (planes A and B).

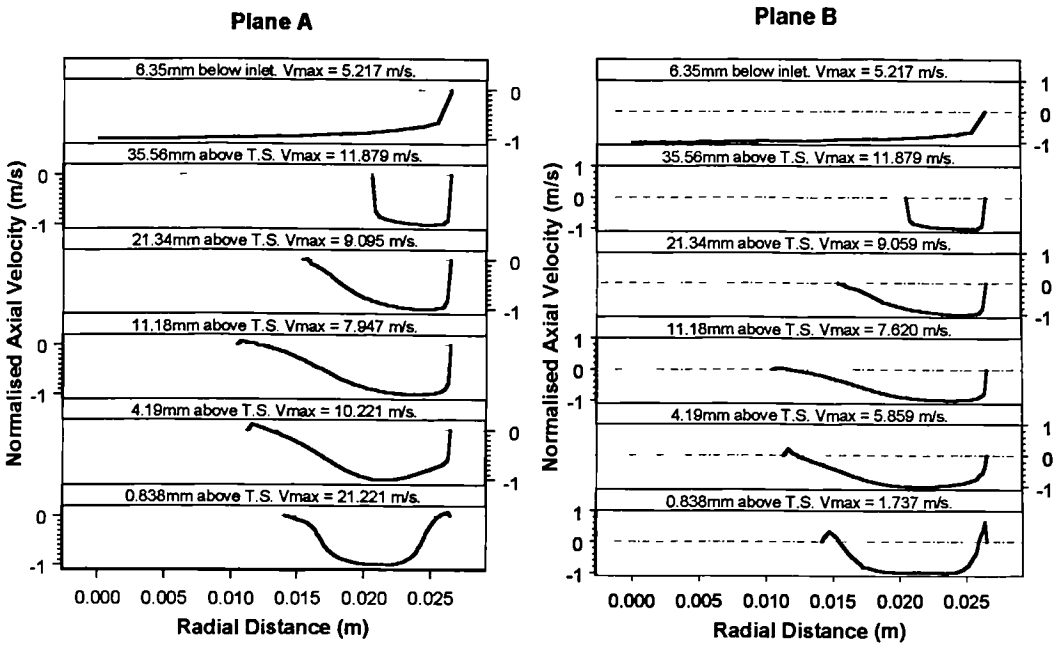

Figure 7.26 Axial velocity profiles before holes for Case MR8Sd-1.

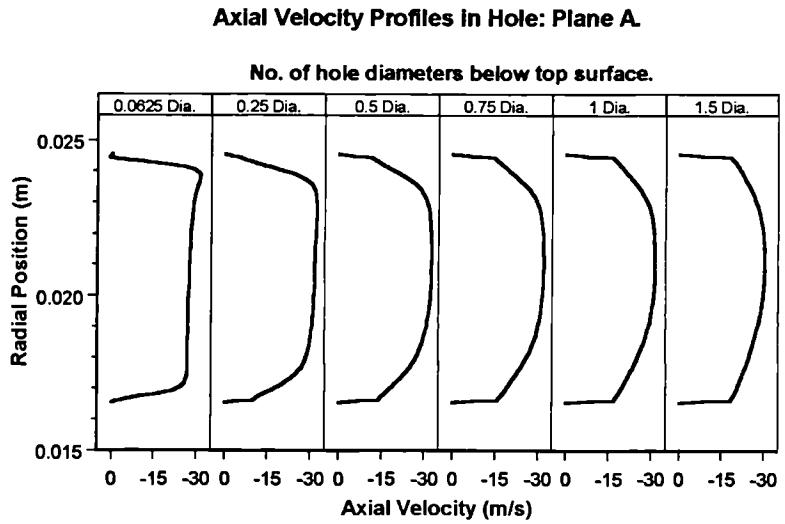

Figure 7.27 Axial velocity profiles in restrictor hole: MR8Sd-1; Plane A.

In Figure 7.26, profiles have been normalised by finding the maximum axial velocity on a line, and dividing the individual points by this maximum value. The normalised velocities extend from 0 to -1 (although recirculation causes the normalised velocity to be greater than 0 at some points) as the restrictor orientation in the actual CFD cases meant that axial velocities were negative (downwards direction). To obtain the true velocity from the profile plots, the

maximum value given should be multiplied by the plotted value. The resulting velocity will be the true value.

Actual velocities are presented for flow in the restrictor holes in Figure 7.27, as the magnitudes are all fairly similar. Some recirculation can be observed at 0.625 D_h (first plot) where the velocity is greater than 0. The velocity profile will not reach its fully developed state before the exit of the hole.

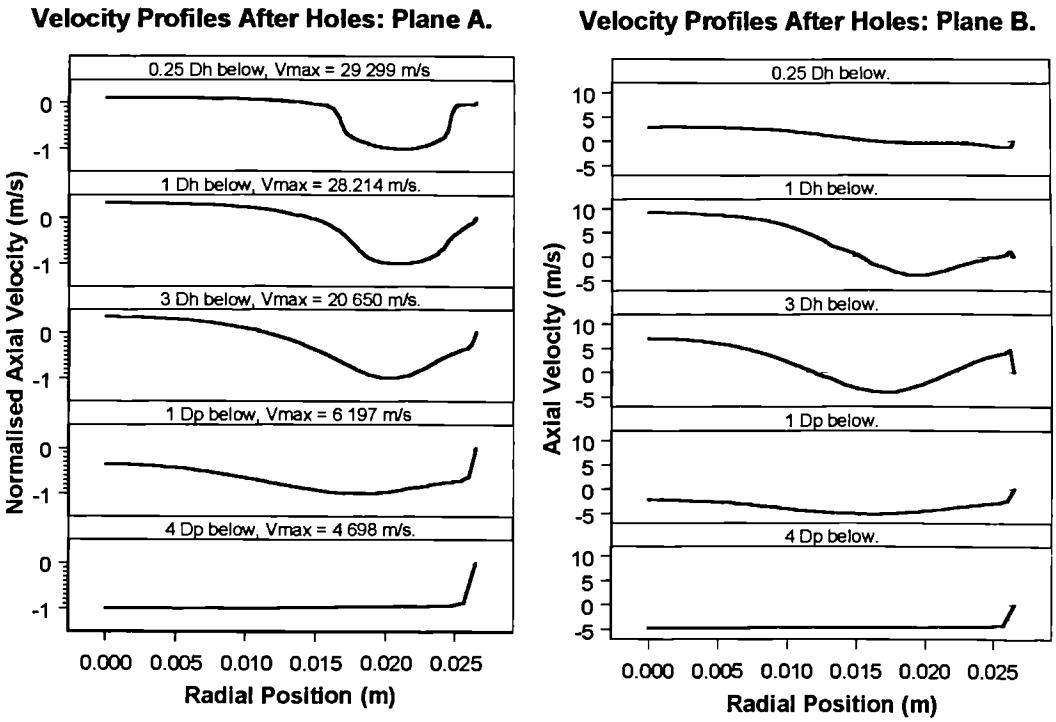

Figure 7.28 Axial velocity profiles after restrictor holes: MR8Sd-1; Planes A and B.

Velocity profiles after the outlet (Figure 7.28) show that a strong recirculation region exists beneath the restrictor. The recirculation dissipates before one pipe diameter downstream of the restrictor is reached. No clear evidence is given in the profiles for recirculation between the holes and pipe outer wall, although there will undoubtedly be some level of motion immediately after the restrictor.

One of the concerns in this model has been to find the length required after the restrictor for fully-developed flow to be re-established. Comparing the outlet profiles downstream of the restrictor with the inlet profile set before the restrictor can test this. Figure 7.29(a) compares the inlet axial velocity profiles with those at 4, 5, and 6 pipe diameters downstream of the restrictor. Turbulent kinetic energy profiles are compared in a similar way in Figure 7.29(b). It is apparent that both axial velocity and turbulent kinetic energy profiles

still have some way to go before a fully developed condition is re-established. The effect of this on the upstream solution is not fully known, especially since the static pressure recovery has taken place well before the outlet boundary of the CFD model. Some later models only accounted for 4 pipe diameters after the restrictor: these could be somewhat affected by too short an outlet section.

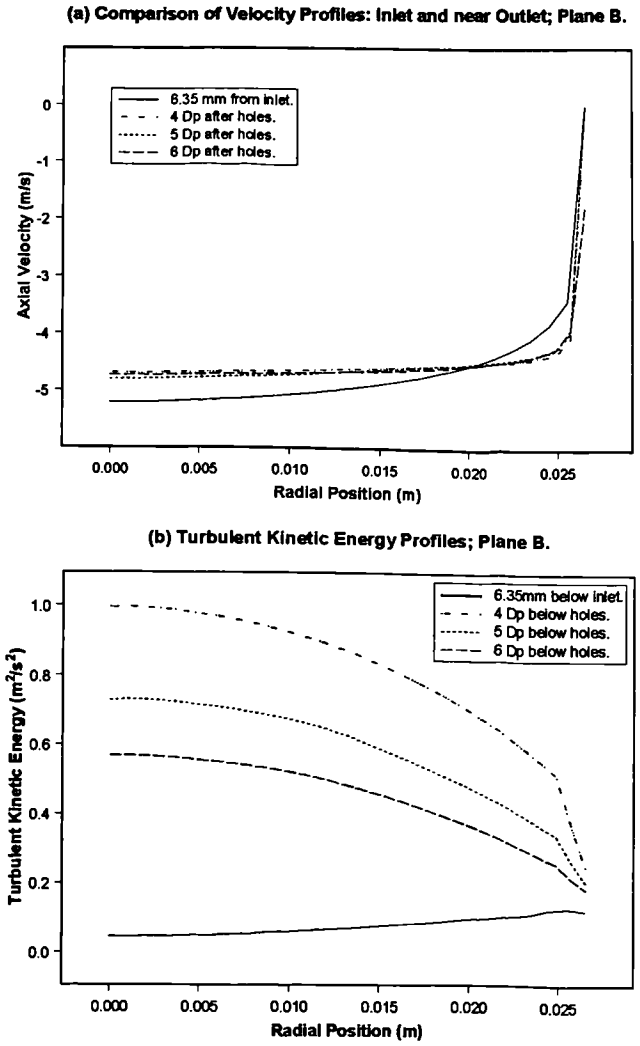

Figure 7.29 Comparison of inlet and outlet profiles for MR8Sd-1; Plane B.

The difference in velocity profiles resulting from two different flowrates (9.92 litres/s and 9.78 litres/s) is shown in Figure 7.30. Profiles at locations before, and after the holes are chosen for plotting the data. Cases MR8Si-1 and MR8Si-3 are used in the comparison (as both flowrates were considered with the underlying mesh). There is a fairly significant difference in the peak velocities reached, which means that only cases having the same flowrate should be compared.

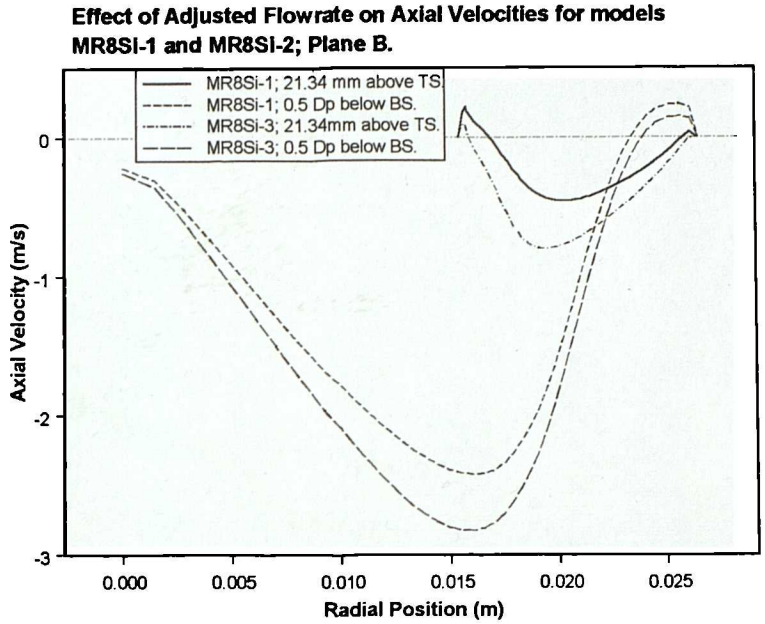

Figure 7.30 Comparison of Axial Velocities for MR8Si-1 and MR8Si-3; Plane B.

The effect of meshing strategy and cell density on axial velocity profiles has been considered. Figure 7.31 compares profiles from a location before the holes for all meshes containing one or more tetrahedral transition regions (and considering only an eighth annulus). The comparison indicates that a certain number of cells are required before the recirculation close to the inner wall of the upstand is achieved. Cases MR8Se-1, Mr8Sf-1, and MR8Sg-1 do not predict the recirculation indicated by the others.

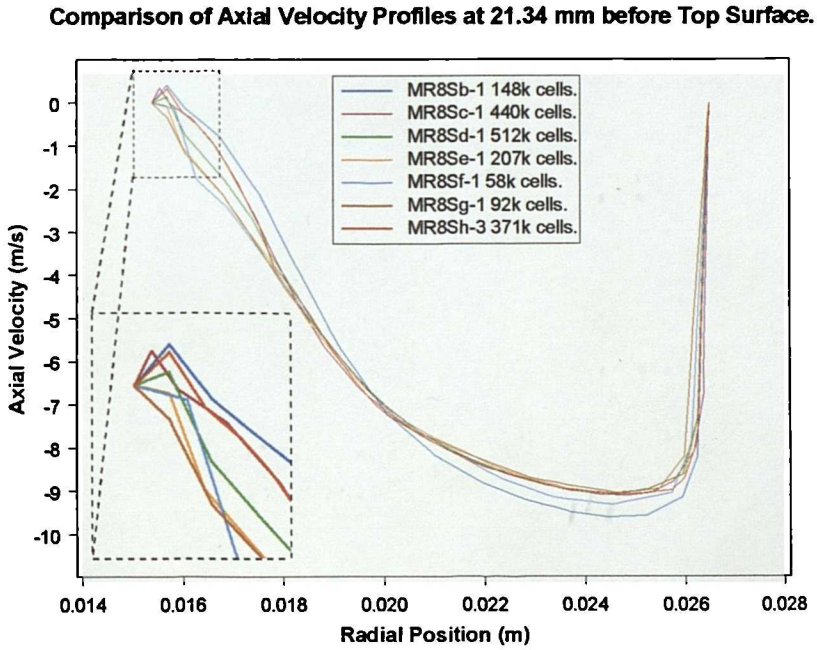

Figure 7.31 Axial velocity profiles from various cases at 21.34 mm before holes; Plane A.

Further comparisons of axial velocity profiles are made at a line immediately before the top surface, as the velocity there will have significant effect on the particle impact velocity. Figure 7.32 shows velocity profiles from the same set of models as in Figure 7.31, for the line 0.838 mm above the top surface on Plane B. Most of the meshes produce similar profiles, although that of MR8Sf-1 does not follow the others close to the restrictor upstand wall. The minimum velocity predicted by Case MR8Sb-1 is lower than that of the others. There is likely an insufficient number of cells close to the wall regions in all of the cases, as the peak velocities in the recirculations are somewhat sharply defined. Greater cell density would possibly generate a smoother transition in the change of flow direction. Overall, however, this comparison shows that there is not likely to be a great difference in particle impact velocities predicted using various computational meshes—provided the cell density is sufficient to begin with. This is important, as it suggests that predictions of erosion upstream of the holes will not be as dependent on the computational mesh as other quantities (e.g. static pressure).

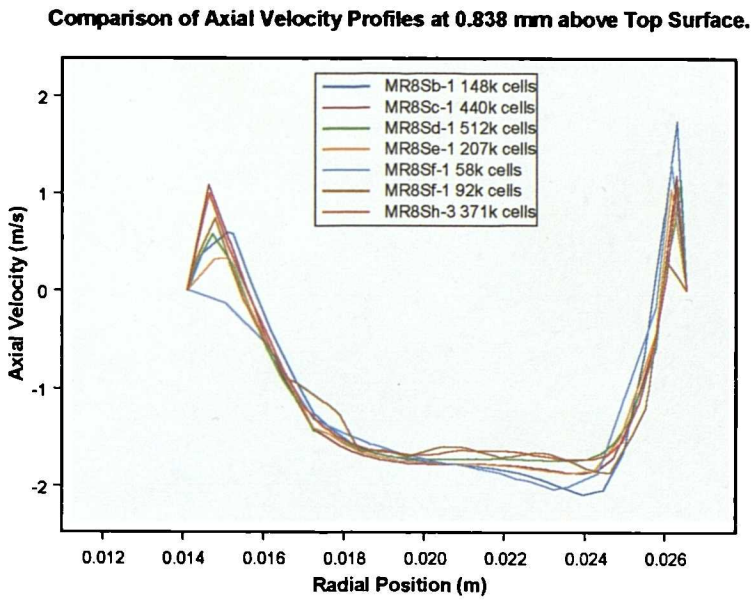

Figure 7.32 Axial velocity profiles just before the top surface; Plane B.

7.2.4.3 Turbulence Properties

The particular turbulence model used will affect predictions of turbulent kinetic energy and dissipation rate. Although the standard k-ε model has had to be used for most of the cases presented here, it is by no means the most advanced model available. However, real difficulties were found in attempting to apply other turbulence models to the problem: only some successful solutions with the Reynolds Stress Transport model have been obtained.

Choice of wall function has an obvious effect on turbulence predictions, as do other parameters particular to certain turbulence models.

Comparison is made between turbulent kinetic energy profiles predicted using various meshes. Figure 7.33 compares profiles at half a pipe diameter downstream of the restrictor base using the same six meshes as in Figure 7.31. Profiles are given for Plane A. Differences between the profiles are more distinct for turbulent kinetic energy than for axial velocity. Although all of the profiles have the same general shape (caused by the shearing fluid on either side of the submerged liquid jet), the magnitude of turbulent kinetic energy varies. This variation is almost constant along the whole length of the profiles. There may again be a problem with insufficient cells next to the walls, as the profile changes rapidly across a very short distance. Standard equilibrium wall functions were used in all cases shown in Figure 7.33.

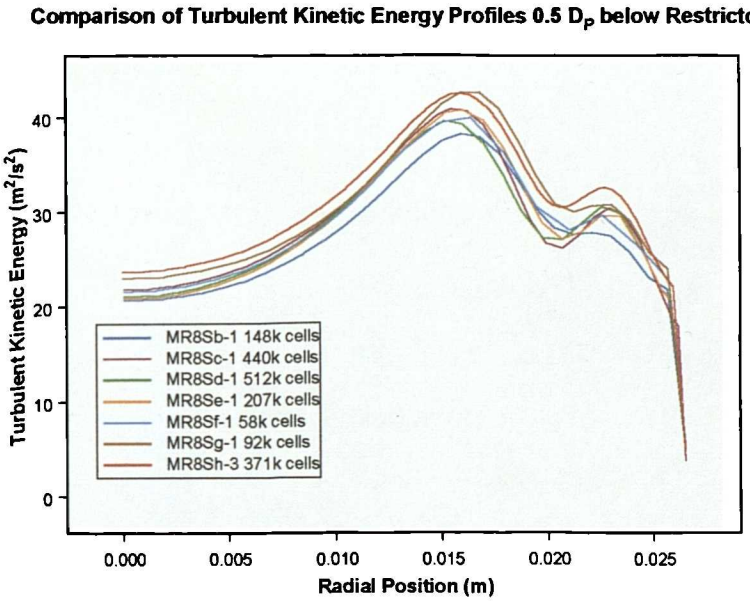

Figure 7.33 Comparison of turbulent kinetic energy profiles on Plane A for various meshes.

The effect of different wall functions, as well as choice of pressure interpolation scheme, can be examined by observing the turbulent kinetic energy profiles generated with the four cases based on Mesh MR8Sb. Figure 7.34 presents the comparison. Using non-equilibrium wall functions has an obvious impact on the kinetic energy profile, especially in the region between the outer jet shear layer and the wall. The use of second-order pressure interpolation is not so significant, with there being little change in the shape of the profile.

Another important comparison is between cases using the standard k-ε turbulence model and those using the Reynolds Stress model. Figure 7.35 compares cases MR8Sf-1, MR8Sf-2, MR8Sg-1, and MR8Sg-2. The same location on Plane A has been used as previously. While the shape of the profiles remain similar, it is clear that the standard k-ε model overpredicts turbulent kinetic energy magnitude in comparison to the results of the Reynolds Stress model. Standard wall functions were used in all cases.

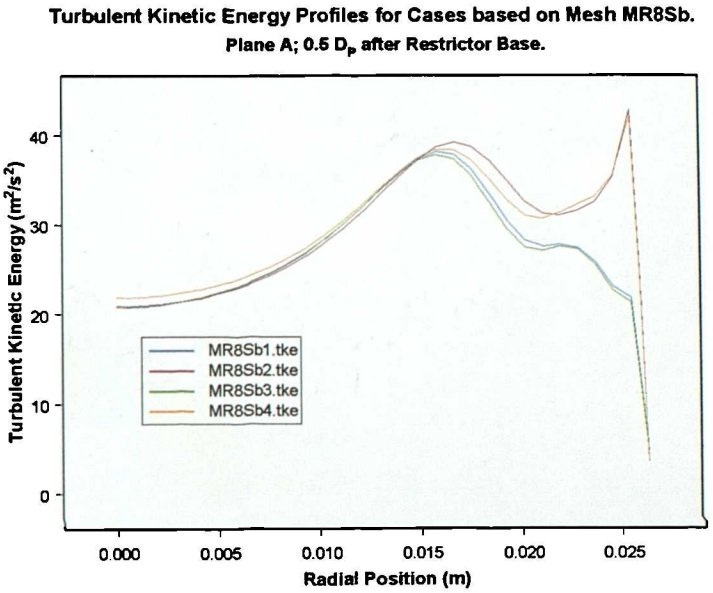

Figure 7.34 Comparison of turbulent kinetic energy profiles for cases that using Mesh MR8Sb.

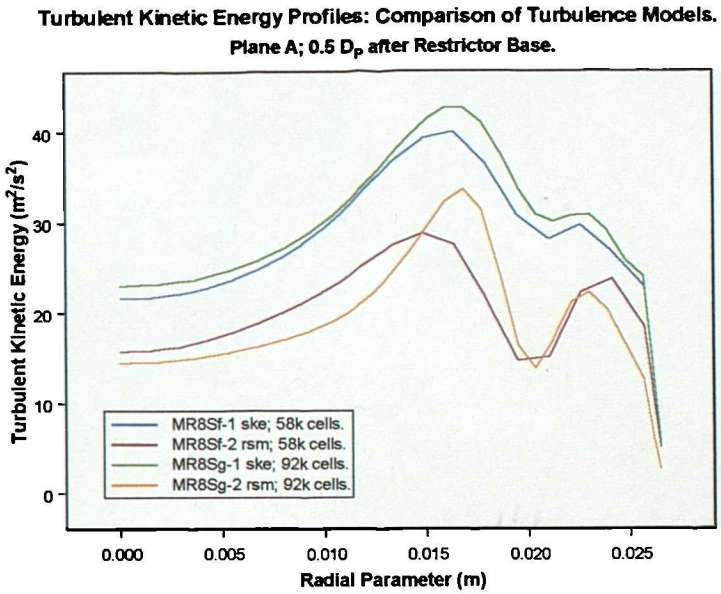

Figure 7.35 Turbulent kinetic energy profiles produced by different turbulence models. Plane A; 0.5 D_P after restrictor.

7.2.5 Summary of modelling with 8mm straight upstand restrictor

Considerable effort has gone into modelling single phase flow through the 8 mm straight holed upstand restrictor. This was a direct result of poor initial agreement between CFD predicted, and experimental measured, static pressure drop. It was not possible to obtain agreement better than around 22% of the experimental value. Applying an extensive range of meshes to the problem leads to the conclusion that either some physical phenomena taking place in the flow are not being correctly represented in the CFD model, or else the geometry modelled is not an accurate representation of the component tested. Incomplete modelling of physical phenomena could be related to the curvature of the geometry: some turbulence models are known to have difficulty in providing correct solutions when high levels of curvature are involved. Inaccurate representation of geometry is also possible, as the leading edges of restrictor holes in the CFD models are probably much sharper than those that were present in the test pieces (particularly when mesh density is high). As edge sharpness has a significant effect on pressure loss in orifice plates, it is likely that it will have a considerable influence on the pressure loss of restrictors. It would be necessary to measure profiles experimentally in order to pinpoint the exact cause of discrepancy.

7.2 Upstand restrictors with 8 mm angled, and 5 mm straight, hole geometries

CFD models were created for the upstand restrictor having 8 mm angled holes, and also for the upstand restrictor with 5 mm straight holes. Results were similar to those for the 8 mm straight holed restrictor, in that differences between experimental and predicted static pressure drop of around 35% were obtained. The specific modelling work will not be presented here to avoid unnecessary repetition.

Restrictors that were used in erosion testing all had 11 mm straight holes (for three different geometries). The single phase modelling of these restrictors will now be discussed, before going on to consider actual erosion modelling using the equations developed in Chapter 4.

7.3 Single phase modelling of upstand restrictor with 11 mm straight holes

Only one computational mesh has been created for the upstand restrictor with 11 mm straight holes. The main features of this mesh are shown in Figure 7.36. Only one tetrahedral transition region has been defined for this mesh. The region beneath the inwards sloping section of the upstand is meshed using a special form of hexahedral mesh alongside a regular

mapped mesh. In the outlet region, the unstructured hexahedral surface mesh at the base of the restrictor is swept down through the six diameters of pipe. The inner part of the outlet mesh is formed using a tri-primitive quadrilateral face. Around 357,000 cells were used in this mesh.

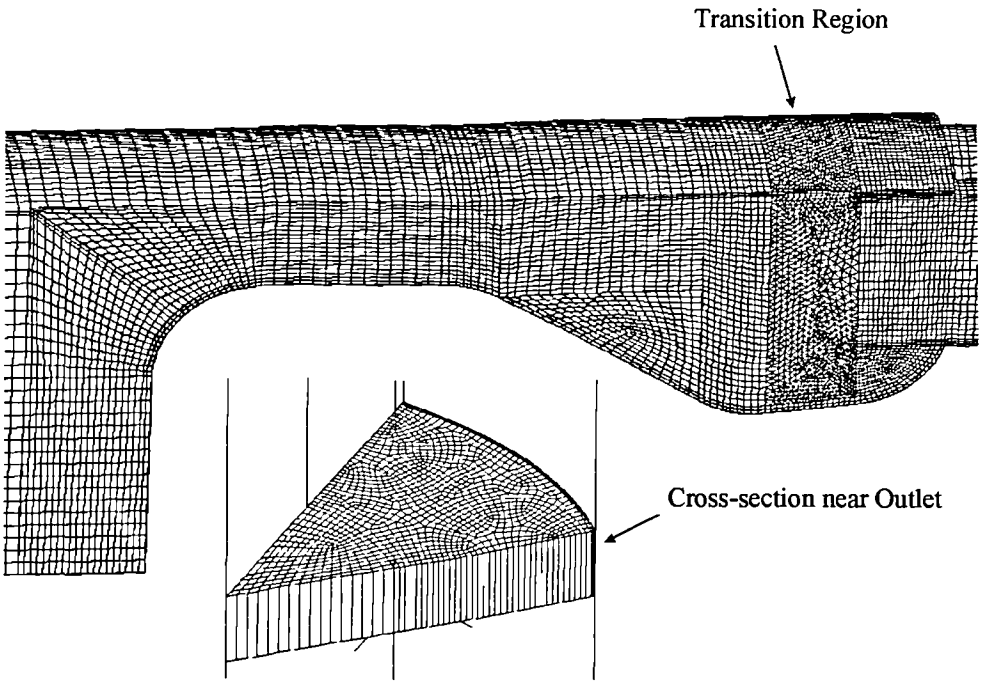

Figure 7.36 Main features of mesh for 11mm straight holed upstand restrictor.

Table 7.6 presents the successful flow solutions obtained using this mesh. Note that the mesh has been designated MU1. The experimental data appropriate to this mesh is given for clarity in Table 7.7, and the actual comparisons between the experimental data and CFD predictions are made in Table 7.8.

Table 7.6 Cases obtained with Mesh MU1.

Models	Cells	Turbulence	Disc^{n}.	Q_T (litres/s)
MU1a	357k	ske; swf	2o; sp	25.25
MU1b	357k	rsm; swf; wr	2o; sp	25.25
MU1c	357k	ske; swf	2o; sp	28.14
MU1d	357k	ske; noneq	2o; sp	28.14
MU1e	357k	ske; swf	2o; sp	10.08

Table 7.7 Experimental Data for 11mm Upstand Restrictor.

TBS (s)	Log Time (mins)	Flowrate (litres/s)	P1 (bar)	P2 (bar)	dP (bar)	Cv SI
30	10	10.01	14.35	13.56	0.79	11.30
30	10	15.53	13.78	11.82	1.96	11.10
30	10	25.21	12.28	6.85	5.43	10.82
2	3	10.08	14.41	13.54	0.87	10.79

Table 7.8 Comparison of predicted and experimental data.

Model	CFD Flow (litres/s)	Exp. Flow (litres/s)	Pdif CFD (bar)	Pdif Exp. (bar)	% Diff.	Cv CFD SI	Cv Exp. SI	% Diff.
MU1a	25.25	25.21	5.83	5.43	7.35	10.45	10.81	-3.35
MU1b	25.25	25.21	4.99	5.43	-8.15	11.30	10.81	4.49
MU1c	28.14	28.14	7.24	5.21	38.85	10.46	12.32	-15.14
MU1d	28.14	28.14	7.32	5.21	40.39	10.40	12.32	-15.60
MU1e	10.08	10.08	0.94	0.87	8.24	10.38	10.80	-3.88

In Table 7.8, the experimental flowrates for MU1c and MU1d are those set during the erosion testing of restrictors—and hence contained sand in the fluid. The experimental pressure drop given in Table 7.8 at a flowrate of 28.14 litres/s is an average figure based on measurements made in the first hour of erosion testing. Points were recorded every 60s during the testing. It will be observed that this average pressure drop for 28.14 litres/s is less than the pressure drop recorded during single phase testing at 25.25 litres/s. Some of this reduction at the higher flowrate will be due to erosion of the restrictor holes, but there may also be some effect due to the presence of particles in the fluid.

Good agreement (within 10%) can be observed between experimental and predicted pressure drops for cases MU1a, MU1b, and MU1e. Poor agreement is observed for the erosion testing cases MU1c and MU1d. This suggests that a coupled solution (where the presence of particles is accounted for in the fluid equations) may have been a more appropriate method for the CFD predictions. However, the time required to carry out such a calculation would have been prohibitive. The experimental pressure drop at erosion testing conditions is certainly less than it would have been if the restrictor had been tested under clean liquid flow at the same flowrate.

Figure 7.37 shows y^+ values below 30 for case MU1a. It can be seen that the regions where the y^+ values become lower than they should are on the outer pipe wall following the restrictor. This will have some effect on the predicted unrecoverable pressure drop across the restrictor.

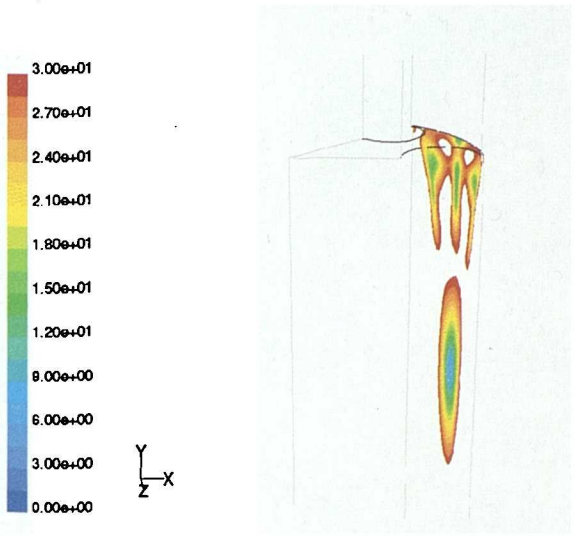

Figure 7.37 y^+ values falling below the lower limit of validity for case MU1a.

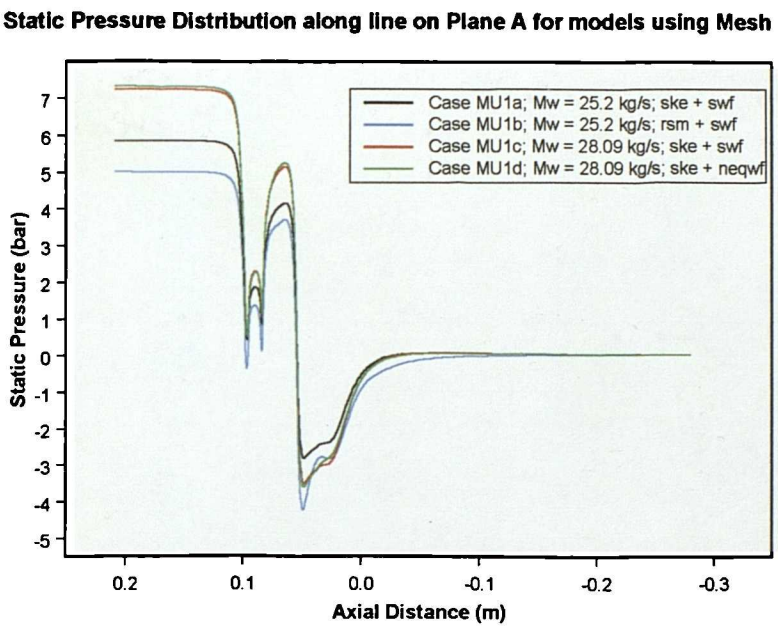

Figure 7.38 Static pressure along line passing through hole centre on Plane A. Cases using Mesh MU1 (apart from case MU1e).

Profiles of static pressure through the computational domain are shown for the first four cases (MU1a to MU1d) in Figure 7.38. There is very little difference between the results of cases MU1c and MU1d. More significant differences are observed between case MU1a and MU1b—due to use of the Reynolds Stress turbulence model for case MU1b. The shape of the profile for case MU1b is different from that of MU1a, indicating that the use of the Reynolds Stress turbulence model has quite an impact on results. It is difficult to say which particular model gives the best solution for cases MU1a and MU1b, as the experimentally measured static pressure drop lies somewhere in between the predicted pressure drops.

Velocity profiles are considered in Figure 7.39 for a line at 21.34 mm above the top surface of the base, and in Figure 7.40 for a line 0.838 mm above the same surface. There is very little difference between the profiles from MU1c and MU1d in Figure 7.39 on the whole, although little recirculation is predicted in MU1d close to the upstand wall (left hand side of the plot). Fairly significant differences are observed between the profiles from MU1a and MU1b in Figure 7.39, as the profile obtained with the Reynolds Stress turbulence model has a flatter shape than that obtained with the standard k-ε model. Both predict recirculation near to the upstand surface.

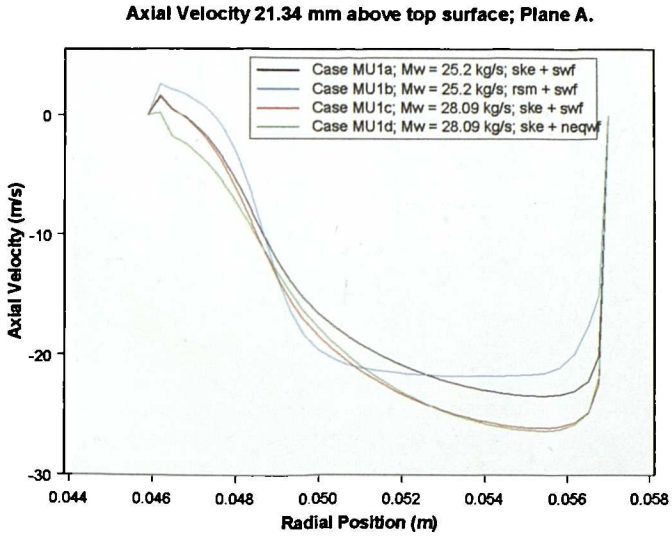

Figure 7.39 Axial velocity profiles 21.34 mm above top surface of base on Plane A. Cases using Mesh MU1 (apart from case MU1e).

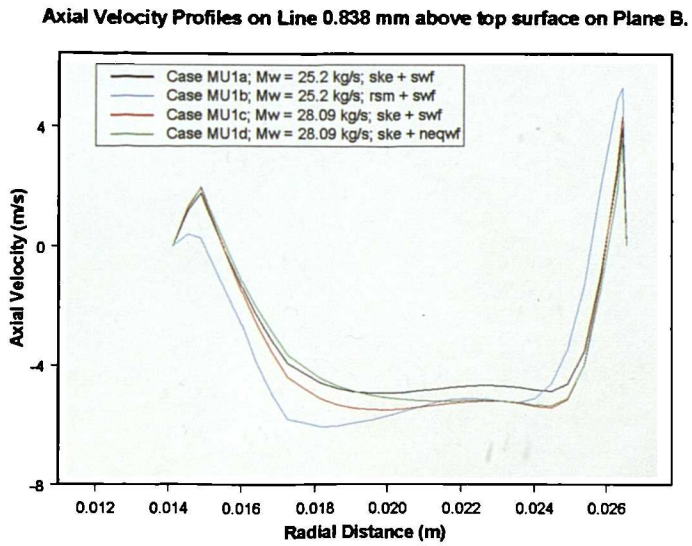

Figure 7.40 Axial velocity profiles 0.838 mm above top surface of base on Plane B. Cases using Mesh MU1 (apart from case MU1e).

The axial velocity profiles shown in Figure 7.40 are all fairly similar in shape, apart from that of case MU1b, which indicates faster moving fluid towards the inside of the annulus. It is interesting to note that the peak axial velocity predicted in case MU1b is higher than that of cases MU1c and MU1d—which are both for a higher overall flowrate.

Turbulent kinetic energy profiles are compared at a location 0.5 D_P downstream of the restrictor base in Figure 7.41. There is a considerable difference between the turbulent kinetic energy levels predicted by MU1a and MU1b. This suggests definite overprediction of turbulent kinetic energy by the standard k-ε model. There is no major difference between the results of the other two cases in Figure 7.41, apart from a small 'spike' near the wall when non-equilibrium wall functions are used.

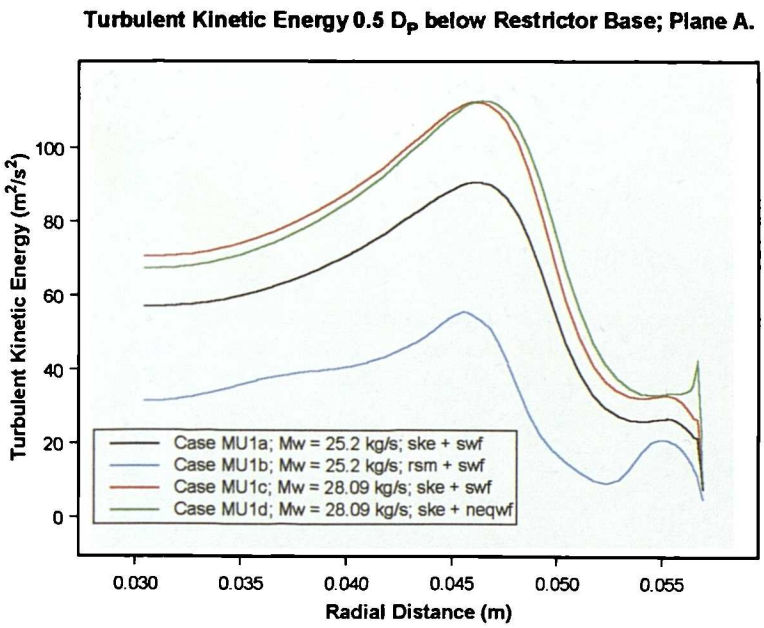

Figure 7.41 Turbulent kinetic energy profile on Plane A; 0.5 D_P below restrictor base. Cases MU1a to MU1d.

Comparing profiles from MU1a with those of MU1c indicates very little change in the form of solution with the increase in flowrate. Changing solution parameters such as wall function or turbulence model has an obvious effect on the results, but not simply a change in flowrate.

7.4 Fluted restrictor with 11 mm straight holes

This intermediate restrictor was tested in both single phase and abrasive flow conditions. As with the previous geometry, only one computational mesh has been created for this restrictor design, and again an eighth annulus has been modelled. Figure 7.42 presents the

main features of the mesh. The mesh has been presented in a different orientation from previous meshes to highlight the shape of the fluted section. Two tetrahedral transition regions were used in this mesh. No prismatic boundary layers could be set along the main fluted region before the holes, due to the nature of the geometry. This means that tetrahedral cells are directly adjacent to the wall on the main upstand surface of the restrictor. Around 197,000 cells were used in the mesh.

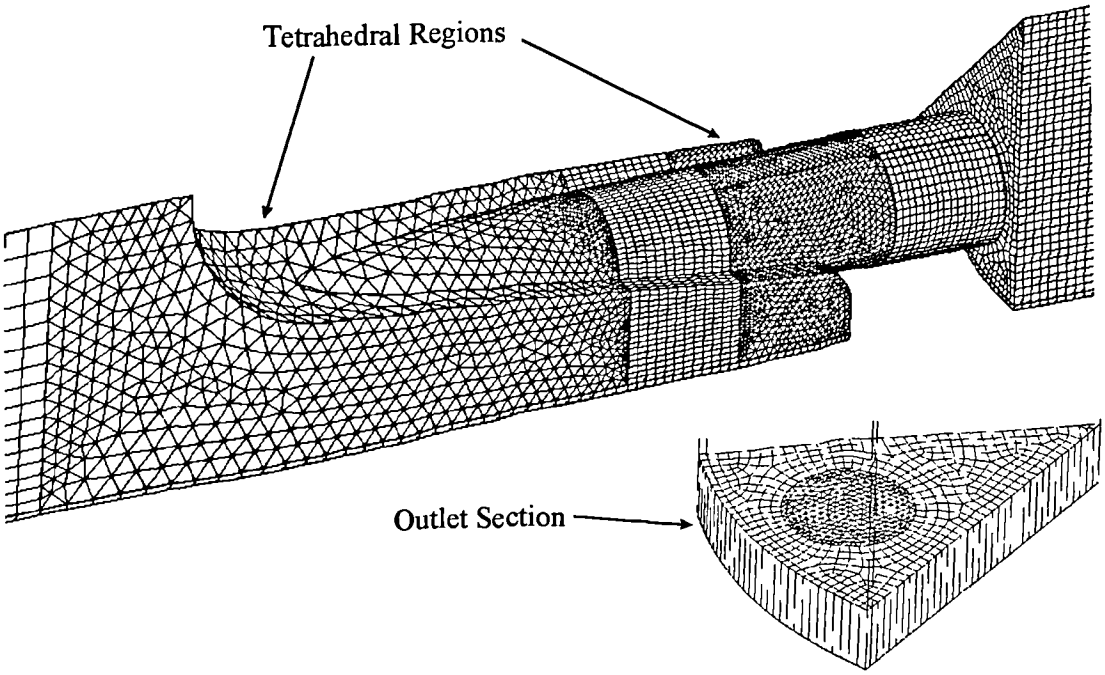

Figure 7.42 Main features of Mesh MF1 (Fluted Restrictor).

Solutions obtained using this mesh are listed in Table 7.9 below. Table 7.10 presents the available clean flow experimental data for the restrictor, and Table 7.11 compares predicted results with experimental. No profiles will be considered for this particular restrictor to prevent unnecessary repetition. However, the issue of cavitation will be considered.

Table 7.9 Cases using Mesh MF1 (Fluted Restrictor).

Models	Cells	Turbulence	Disc^{n}.	Q_T (litres/s)
MF1a	197k	ske; swf	2o; sp	9.92
MF1b	197k	ske; swf	2o; sp	29.39
MF1c	197k	ske; neqwf	2o; sp	9.92
MF1d	197k	rsm; neqwf; wr	2o; sp	9.92
MF1e	197k	rsm; neqwf; wr	2o; sp	29.39

Table 7.10 Clean flow experimental data for fluted restrictor.

TBS (s)	Log Time (mins)	Flowrate (litres/s)	P1 (bar)	P2 (bar)	dP (bar)	Cv SI
2	3	9.70	14.42	13.82	0.60	12.52
2	3	16.08	13.91	12.21	1.70	12.33
2	3	24.30	12.67	8.73	3.95	12.24

Table 7.11 Comparison of CFD predicted and experimental data.

Model	CFD Flow (litres/s)	Exp. Flow (litres/s)	Pdif CFD (bar)	Pdif Exp. (bar)	% Diff.	Cv CFD SI	Cv Exp SI	% Diff.
MF1a	9.92	9.72	0.77	0.60	28.88	11.28	12.54	-10.08
MF1b	29.39	28.44	6.77	4.95	36.82	11.30	12.79	-11.66
MF1c	9.92	9.72	0.77	0.60	28.32	11.30	12.54	-9.89
MF1d	9.92	9.72	0.80	0.60	32.96	11.11	12.54	-11.47
MF1e	29.39	28.44	7.04	4.95	42.24	11.08	12.79	-13.35

In the above table, the experimental flowrate given for MF1b and MF1e is the average flowrate based on data from the first hour of erosion testing. Flowrates increased gradually during the course of erosion tests. The flowrate used in the CFD model at erosion conditions is the average flowrate across the entire erosion test period. It would perhaps have been better to use the flowrate given in the above table instead of the overall average value.

The predicted results in Table 7.11 do not compare too favourably with the experimental results. One of the reasons for this is that the CFD flowrates do not quite match the experimental test flowrates. There could be a fairly significant error due to this. Also, evidence of cavitation erosion was discovered in the erosion testing. This could mean that fluid phenomena were present in the actual tests that were not accounted for in the CFD modelling. Examination of y^+ values for case MF1b show that y^+ increases above the upper level of validity on the base of the restrictor. This may not affect the results too adversely, as the main flow of fluid is not parallel to this face, but rather orthogonal to it.

In order to assess the likelihood of cavitation phenomena, the absolute static pressure on restrictor surfaces must be obtained from the CFD predictions. In the erosion testing, the average downstream static pressure was around 8.06 barg, which means around 9.07 bar absolute. The absolute static pressures in the CFD model are obtained by simply adding this 9.07 bar to the predicted result (as gauge static pressure was set to zero at the outlet boundary). Figure 7.43 presents the absolute static pressure at all face cell points on the top surface and hole of the fluted restrictor. It will be apparent that the static pressure on these inner walls does indeed fall well below the vapour pressure of the liquid (taken to be 0.02337 bar for water at 20^0C). The CFD model is therefore indicating very real potential for

cavitation—as is borne out by the results of erosion testing with the fluted restrictor. This highlights the usefulness of CFD predictive tools: it would have been almost impossible to predict cavitation potential by hand calculation, as the only pressure measurements available were at the 2 D_P upstream and 6 D_P downstream locations.

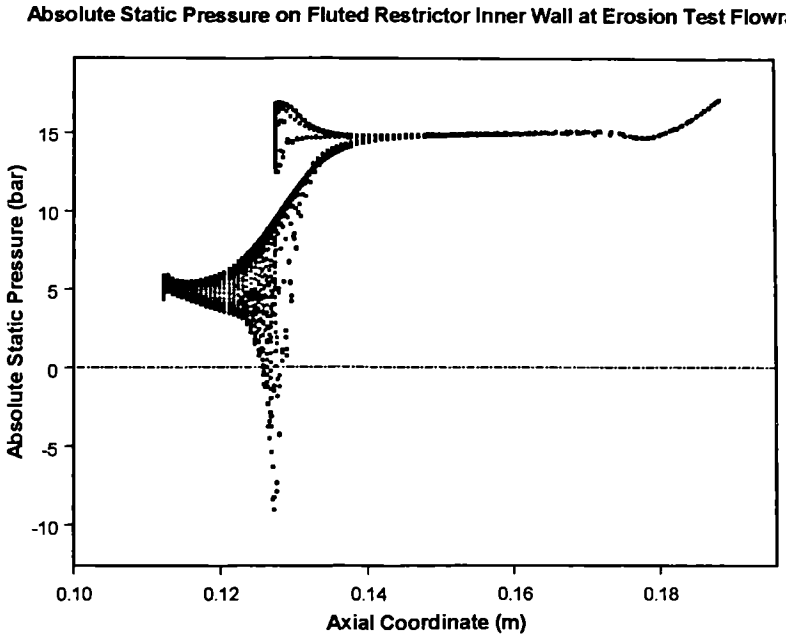

Figure 7.43 Absolute static pressure predictions on upper wall of fluted restrictor. Flowrate = 29.39 litres/s.

The static pressure map predicted by the CFD model (gauge pressure) is displayed on the restrictor and pipe walls in Figure 7.44. This gives a better indication of where the low pressure points occur in the model than the plot of Figure 7.43. Comparison with the suspected cavitation erosion (Figure 6.14) shows that the low pressure spot predicted by the CFD model is just upstream of the eroded area in the actual test specimen. This confirms the ability of the CFD model to predict areas likely to be eroded by cavitation phenomena. It also highlights the danger in CFD methods, in that results can be predicted that are physically impossible—the 'negative' absolute pressure in the above figure must be regarded as an imaginary artefact.

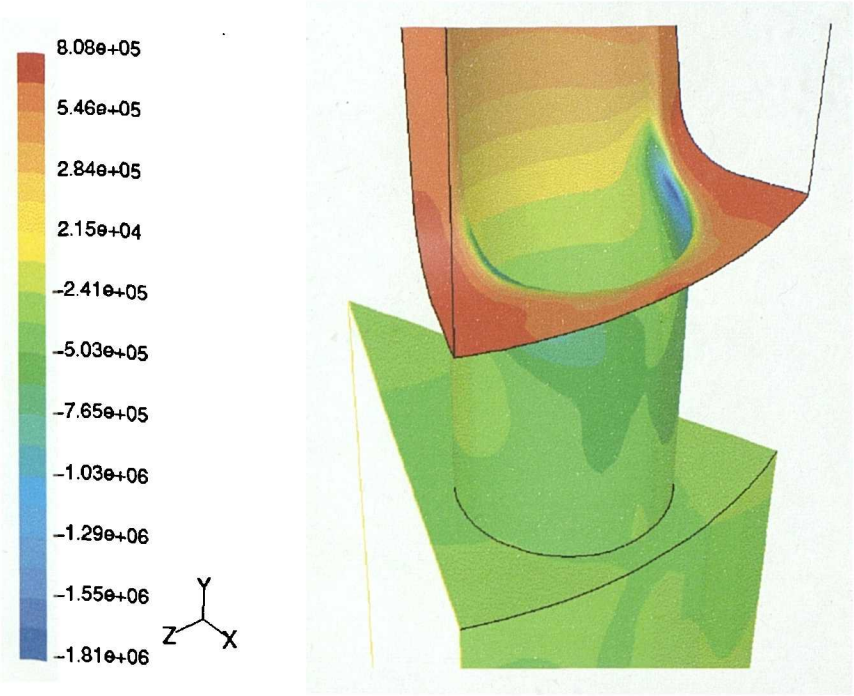

Figure 7.44 Static pressure on restrictor surfaces (gauge pressure).

7.5 Valley restrictor with 11 mm straight holes

This restrictor represents the final outcome of the test programme. It was designed to overcome the problems found with the previous models (pipe wall erosion with the upstand and fluted restrictors, and also cavitation erosion within the hole of the fluted restrictor). Two computational meshes were developed for this model: one with 281,000 cells (MV1), and another with around 460,000 cells (MV2). Figure 7.45 presents the main features of the mesh containing 281,000 cells (MV1). One tetrahedral transition region is required, which fills a volume starting just above the top nose of the restrictor, and ends just inside the holes. Boundary layers have been set on the upper surface of the restrictor, but could not be set within the holes themselves.

Table 7.12 lists the solutions obtained using Meshes MV1 and MV2. Appropriate single phase experimental data is presented in Table 7.13, and predicted results are compared with experimental results in Table 7.14.

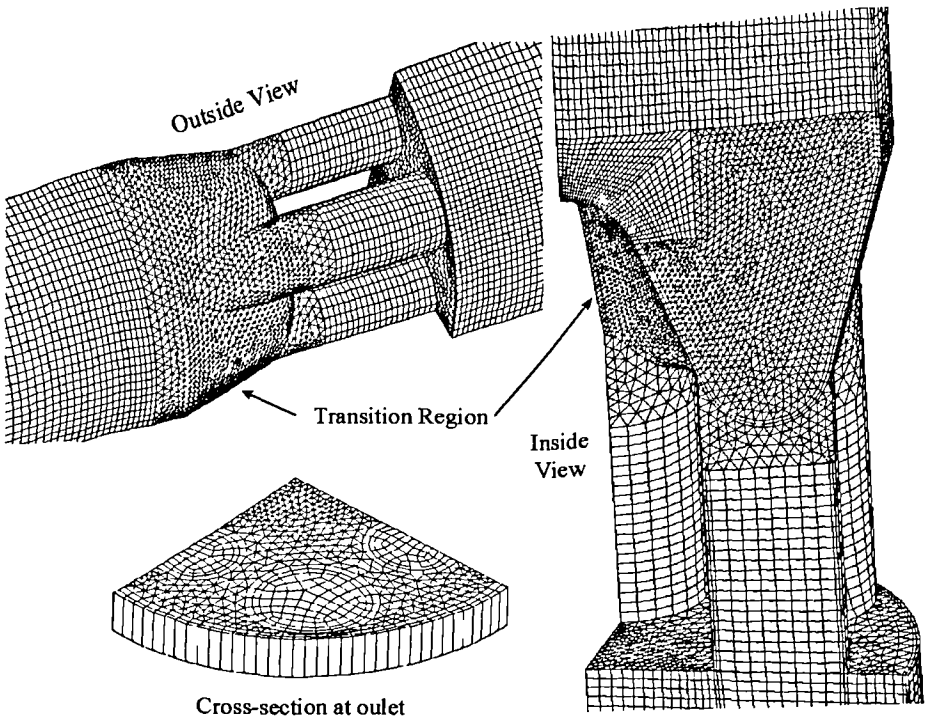

Figure 7.45 Main features of Mesh MV1 (valley restrictor).

Table 7.12 Cases using Meshes MV1 and MV2 (valley restrictor).

Models	Cells	Turbulence	Disc^{n}.	Q_T (litres/s)
MV1a	281k	ske; swf	2o; sp	9.90
MV1b	281k	rsm; swf; wr	2o; sp	9.90
MV1c	281k	ske; swf	2o; sp	28.57
MV1d	281k	ske; neqwf	2o; sp	9.90
MV2a	460k	ske; swf	2o; sp	9.90
MV2b	460k	ske; neqwf	2o; 2op	9.90
MV2c	460k	rsm; neqwf; wr	2o; 2op	9.90
MV2d	460k	rsm; swf; wr	2o; 2op	9.90
MV2e	460k	ske; swf	2o; sp	28.57

Table 7.13 Single phase experimental data for valley restrictor.

TBS	**Log Time**	**Flowrate**	**P1**	**P2**	**dP**	**Cv**
(s)	**(mins)**	**(litres/s)**	**(bar)**	**(bar)**	**(bar)**	**SI**
2	3	9.88	14.59	13.88	0.71	11.74
2	3	15.55	14.09	12.44	1.65	12.10
2	3	20.29	13.43	10.66	2.77	12.20
2	3	28.09	11.92	6.48	5.44	12.04

Table 7.14 Comparison of experimental and predicted results for valley restrictor.

Model	CFD Flow (litres/s)	Exp. Flow (litres/s)	Pdif CFD (bar)	Pdif Exp. (bar)	% Diff.	Cv CFD SI	Cv Exp SI	% Diff.
MV1a	9.90	9.89	0.80	0.71	12.15	11.10	11.75	-5.51
MV1b	9.90	9.89	0.73	0.71	2.75	11.60	11.75	-1.28
MV1c	28.57	27.89	6.51	4.52	43.99	11.19	13.11	-14.64
MV1d	9.90	9.89	0.79	0.71	11.45	11.14	11.75	-5.21
MV2a	9.90	9.89	0.75	0.71	5.57	11.44	11.75	-2.61
MV2b	9.90	9.89	0.75	0.71	5.59	11.44	11.75	-2.61
MV2c	9.90	9.89	0.68	0.71	-4.39	12.03	11.75	2.34
MV2d	9.90	9.89	0.68	0.71	-4.16	12.01	11.75	2.22
MV2e	28.57	27.89	6.17	4.52	36.32	11.50	13.11	-12.27

In the above table, experimental flowrates at MV1c and MV2e are based on data from the first hour of erosion testing. Table 7.14 shows fairly good agreement between experimental and predicted results when the single phase data is used for comparison. Differences between predicted and measured results increase for the erosion case. As with the previous restrictor, the flowrate used in the CFD model for erosion conditions is actually the average experimental flowrate over the whole test period.

There is a clear improvement in results obtained using Mesh MV2 over those based on Mesh MV1. This indicates that the solution obtained with Mesh MV1 is by no means mesh independent. It is possible that no real mesh independent solutions have been obtained in the present study due to the nature of the problem and the limitations on maximum mesh size imposed by the available hardware.

There are no real problems with y^+ values for these cases, apart from a few localised points where they approach either the lower or higher limit of validity. It is unlikely that this will be a major source of error in these cases.

The holes of the valley restrictor are arranged on two centre diameters: an inner and an outer. It is instructive to compare axial velocity profiles for holes lying on the inner centre diameter with those lying on the outer centre diameter for this restrictor. Figure 7.46 presents this comparison for cases MV1a and MV2d. It will be apparent that the profile in hole 2 (lying on the outer diameter) is somewhat skewed, whereas that in hole 1 (lying on the inner diameter) is fairly uniform. This suggests that greater erosion could occur in hole 2, where the velocity is skewed towards one side of the hole, than in hole 1 where fluid passes through in a uniform manner. Actual erosion predictions could help elucidate this. Figure 7.46 also indicates a significant difference between the solution of MV1a and that of MV2d. Case MV2d does use the Reynolds Stress turbulence model as well as having a greater number of

cells. It is likely that the turbulence model is causing most of the change from the profile shape predicted by case MV1a.

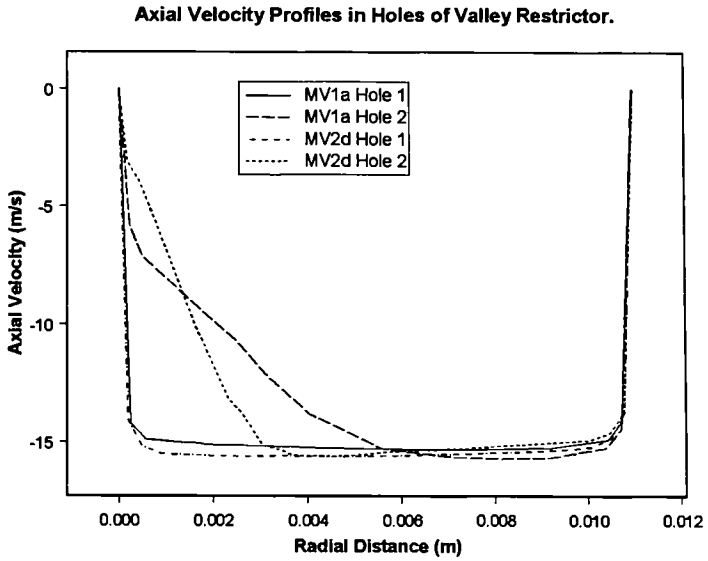

Figure 7.46 Axial Velocity profiles in hole of valley restrictor.

The possibility of cavitation has again been examined. Figure 7.47 shows a similar plot to that of Figure 7.43, but this time for case MV2e. The absolute pressure does fall below the vapour pressure of the liquid at a fairly specific point, but not by the same extent observed for the fluted restrictor in Figure 7.43. The flowrate in case MV2e is near to the actual flowrate used in the erosion tests. No clear evidence of cavitation erosion was observed for the valley restrictor, so it is likely that the design has improved sufficiently to prevent such phenomena occurring to a significant level.

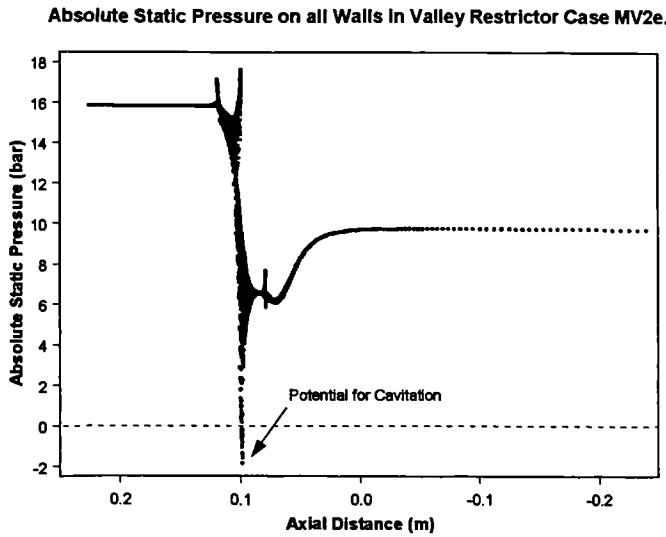

Figure 7.43 Absolute static pressure on all walls of restrictor in case MV2e.

7.6 Summary and conclusions to chapter

This chapter has covered the CFD modelling of single phase flow through the various restrictor designs. The main conclusion to come out of this work is that predictions of static pressure drop across restrictors are best for the valley restrictor design, and worst for the upstand restrictor design. Some of the restrictor models considered during the project have not been presented here, namely the upstand restrictors having 8 mm holes angled at 60^0, and also with 5 mm straight holes.

One concern in modelling the restrictors was whether sufficient cells had been applied in the actual restrictor holes. Work carried out for the upstand restrictor with 8 mm straight holes suggests that this may not be the main factor in determining the success of pressure drop predictions. Representation of the restrictor hole leading edge could have a more significant effect. It is likely that the restrictor models in this study have corners that are better defined geometrically than in the prototypes themselves. There is less of an effect for the valley restrictor, as the geometry does not change so rapidly as in the upstand restrictors.

It would have been useful to compare predicted velocity profiles with actual measured profiles, as this would have given a better indication of the CFD code performance, and have helped to highlight where the CFD code is failing. An encouraging outcome of the work has been the ability of the code to predict the likelihood of cavitation occurring in the restrictor. This was exemplified for the case of the fluted restrictor, where actual testing had indicated a region in which damage was caused by cavitation phenomena rather than erosion.

The use of a Reynolds Stress turbulence model is likely to improve predictions overall. Again, this cannot be truly verified without additional data, but simple comparison of static pressure drop predictions do seem to indicate improvements with the Reynolds Stress model. Use of this model could have benefits in erosion modelling, as the effect of anisotropic flow on particle behaviour can be accounted for.

Having considered the modelling of single phase flow past the simple geometries, attention can now turn to predicting the erosion due to solid particles for the same geometries.

8.0 Predictions of Erosive Wear in Components of Simple Geometry

The restrictor tests have provided experimental data with which to validate CFD-based erosion modelling predictions. As the restrictors geometries can be considered simple in comparison with Multi-Orifice Sleeve Choke Valves, they can be used in an initial validation of the CFD-based technique. In this chapter, the equations presented in Chapter 4 are used to obtain predictions of mass loss over a 14 hour period—corresponding to the length of time for which restrictors were subject to abrasive flow.

8.1 Particle tracking in Fluent

8.1.1 Particle force balance

Fluent predicts the trajectory of a particle by integrating the force balance on the particle. This is written for the x direction in Cartesian coordinates (Fluent Users Manual) as:-

$$\frac{du_p}{dt} = \frac{3}{4}\frac{C_D}{d_p}\left(\frac{\rho}{\rho_p}\right)(u-u_p)|u_p-u| + g_x\frac{(\rho_p-\rho)}{\rho_p} + \frac{1}{2}\frac{\rho}{\rho_p}\frac{d}{dt}(u-u_p) + \left(\frac{\rho}{\rho_p}\right)u_p\frac{\partial u}{\partial x} \quad (8.1)$$

where all forces are per unit particle mass, and the symbols are as defined in the nomenclature. The drag coefficient, C_D, is given by

$$C_D = a_1 + \frac{a_2}{\mathrm{Re}} + \frac{a_3}{\mathrm{Re}^2} \quad (8.2)$$

The a_x coefficients are given by Morsi and Alexander (1972) for several ranges of relative Reynolds number, Re. This relative Reynolds number is defined as

$$\mathrm{Re} = \frac{\rho d_p |u_p - u|}{\mu} \quad (8.3)$$

Fluent is also able to include the Saffman lift force if required. While this was generally activated in the present study, it is unlikely to have had any significant effect on the particle trajectories for the type of flow considered here (Meng and Van der Geld, 1991).

8.1.2 Stochastic tracking

Fluent accounts for the effects of turbulent dispersion on particle motion using what is termed 'the Discrete Random Walk (DRW) model', based on the eddy lifetime concept. The fluctuating fluid velocity component for each particle-eddy interaction is sampled by assuming that the fluctuations obey a Gaussian probability distribution. Thus

$$u' = \zeta\sqrt{\overline{u'^2}} \tag{8.4}$$

where ζ is a normally distributed random number, and the multiplier is the local root-mean-square (rms) value of the velocity fluctuations. When an isotropic turbulence model is used (such as the standard k-ε model), the rms values can be found as:

$$\sqrt{\overline{u'^2}} = \sqrt{\overline{v'^2}} = \sqrt{\overline{w'^2}} = \sqrt{2k/3} \tag{8.5}$$

where k is the turbulent kinetic energy (m^2/s^2).

When the Reynolds Stress Model is used, non-isotropy of the turbulence can be accounted for, and so the rms components of fluctuating fluid velocity are given by:

$$u' = \zeta\sqrt{\overline{u'^2}}\ ;\ v' = \zeta\sqrt{\overline{v'^2}}\ ;\ w' = \zeta\sqrt{\overline{w'^2}} \tag{8.6}$$

The fluctuating velocity component acts over a characteristic eddy lifetime given by either the constant

$$\tau_e = 2T_L \tag{8.7}$$

or as a random variation about T_L:

$$\tau_e = -T_L \log(r) \tag{8.8}$$

where r is a uniform random number between 0 and 1, and T_L is the fluid Lagrangian integral time scale. For the k-ε turbulence models, this is given by

$$T_L \approx 0.15\frac{k}{\varepsilon} \tag{8.9}$$

and for the Reynolds Stress Model it is given by:

$$T_L \approx 0.30\frac{k}{\varepsilon} \tag{8.10}$$

This stochastic tracking option was activated in all particle trajectory calculations performed in the present study. The only flow simulations used in particle trajectory calculations have been those that used the standard k-ε turbulence model, and so the fluctuating velocity components will have the same magnitude in each coordinate direction. This may result in particles not being propelled in the direction they ought to be under some

flow structures. It would have been useful to consider solutions where the Reynolds Stress Model was used, but time was not available to do so.

8.1.3 Parameters controlling particle tracking

In Fluent, a number of inputs are required from the user to determine the way in which particle tracking will proceed. Some of these may have a significant effect on predictions of erosive wear, and so will be considered here in turn. The inputs are as follows:-

1. Particle Injection Type: Particles can be injected into the computational domain at any point. They can be injected from a single point, along a line, or from every cell face lying on a particular plane or boundary. In the present study, particles are injected at each face on the velocity inlet boundary. Thus if there are 600 faces on the inlet boundary for a particular mesh, 600 particle trajectories will be modelled per stochastic try (see next).

2. Number of stochastic tries: This parameter, in conjunction with the number of points on the particle injection surface, will determine the overall number of trajectories to be modelled. The total particle mass flowrate remains constant regardless of the number of tries: the individual mass flowrate associated with each particle trajectory is adjusted accordingly. The number of stochastic tries should be such that particle properties passing through a plane (or impacting a surface) will remain constant over several separate predictions of particle behaviour. If the solution changes between predictions (for the same flow solution) then it is likely that an insufficient number of particles are being tracked.

3. Random Eddy Lifetime: Activating this will generate a random eddy lifetime for particles according to equation (8.8). This may result in a more realistic solution.

4. Step Length Factor, λ: This is used to determine the time step used by Fluent to integrate the equation of motion for the particle. It is based on an estimate of the time a particle is likely to take to traverse a particular continuous phase control volume. Thus the actual integration time step will be given by

$$\Delta t = \frac{\Delta t'}{\lambda} \tag{8.11}$$

where $\Delta t'$ is the estimated time step, λ is the step length factor, and Δt is the resulting integration time step. λ is therefore roughly the number of steps used in the calculation of a particle path through each computational cell (control volume).

5. Maximum number of steps: This sets the maximum number of steps that will be allowed in any particle trajectory. When a particle trajectory calculation exceeds this overall number of steps, the calculation for that particular trajectory will be aborted.

6. Scale flowrate by face area: An option that allows particle mass flowrate for each trajectory to be scaled according to the area of the cell face from which the trajectory begins. A large cell face will therefore have a correspondingly large mass flowrate, whereas the flowrate from a smaller face will be reduced.

The only way in which to determine the effect that each of these parameters has on erosion predictions is to perform a sensitivity study on each parameter. Such a study has been carried out, although the number of permutations has been restricted somewhat to fit in with time available to complete the work. This work will be presented shortly.

8.1.4 Particle rebound

Provision is made in Fluent for specifying constant or varying values of normal and tangential restitution coefficient on solid surfaces. Setting both ε_n and ε_t to 1.0 means that a particle will lose no kinetic energy on impact with a wall, and will rebound with the same angle as it had on impact. As this is not realistic behaviour, it is necessary to provide equations that predict the appropriate restitution coefficient from the particle impact angle. A number of these equations have been developed by various researchers, usually based on experimental measurements made with high speed gas-solid flows. As no equations have been developed for use in liquid-solid flows, it is proposed to simply use the gas-solid equations in order to introduce some element of impact angle dependent energy loss into the calculations. Table 8.1 presents some of the equations available in the literature, together with the experimental conditions used to obtain them, where known. Each equation is plotted for comparison in Figure 8.1. Notation for restitution coefficients has been given previously in Figure 2.7.

There are some common features among the curves plotted in Figure 8.1. Energy loss in the normal direction tends to be highest at 90^0 impact (as would be expected for a 'head-on collision'). For the tangential coefficient, maximum energy loss would appear to occur around an impact angle of 30^0. It is intended to discount equation sets R2 and R4 as they do not display the same general characteristics as the other equations. Predictions will be obtained using the other four equation sets, and compared to see what sort of variations result.

Table 8.1 Equations for restitution coefficients.

Ref.	Source	Conditions	Et	En
R1	Vittal and Tabakoff (1987)	Sand particle on 410 stainless steel. Velocity not known. Gas flow.	$\varepsilon_T = 1.0 - 2.12\alpha_P + 3.0775\alpha_P^2 - 1.1\alpha_P^3$	$\varepsilon_N = 1.0 - 0.4159\alpha_P + 0.4994\alpha_P^2 - 0.292\alpha_P^3$
R2	Tabakoff and Eroglu (1988): Flat Plate	15 μm fly ash particles on 2024 Aluminium flat plate. 98 m/s in gas flow??	$\varepsilon_T = 1.0 - 2.64204\alpha_P + 8.38479\alpha_P^2 - 10.80932\alpha_P^3 + 4.62071\alpha_P^4$	$\varepsilon_N = 1 - 1.08969\alpha_P - 1.40079\alpha_P^2 + 3.65638\alpha_P^3 - 1.75401\alpha_P^4$
R3	Tabakoff and Eroglu (1988): Convex Cylinder Surface	As above.	$\varepsilon_T = 1.0264 - 0.92161\alpha_P - 0.11439\alpha_P^2 + 1.00663\alpha_P^3 - 0.38995\alpha_P^4$	$\varepsilon_N = 0.93359 - 1.20042\alpha_P + 0.97736\alpha_P^2 - 0.07948\alpha_P^3 - 0.15118\alpha_P^4$
R4	Tabakoff and Eroglu (1988): Concave Cylinder Surface	As above.	$\varepsilon_T = 1.01549 + 0.01426\alpha_P - 2.9042\alpha_P^2 + 4.42507\alpha_P^3 - 1.80741\alpha_P^4$	$\varepsilon_N = 0.96187 - 4.12609\alpha_P + 9.55722\alpha_P^2 - 8.62842\alpha_P^3 + 2.67599\alpha_P^4$
R5	Forder et al. (1998)?	Not given.	$\varepsilon_T = 1 - 0.78\alpha_P + 0.84\alpha_P^2 - 0.21\alpha_P^3 + 0.028\alpha_P^4 - 0.022\alpha_P^5$	$\varepsilon_N = 0.988 - 0.78\alpha_P + 0.19\alpha_P^2 - 0.024\alpha_P^3 + 0.027\alpha_P^4$
R6	Grant and Tabakoff (1975)	200 μm quartz on 2024 aluminium alloy. V = 76.2 to 118.9 m/s. Gas flow.	$\varepsilon_T = 0.988 - 1.66\alpha_P + 2.11\alpha_P^2 - 0.67\alpha_P^3$	$\varepsilon_N = 0.993 - 1.76\alpha_P + 1.56\alpha_P^2 - 0.49\alpha_P^3$

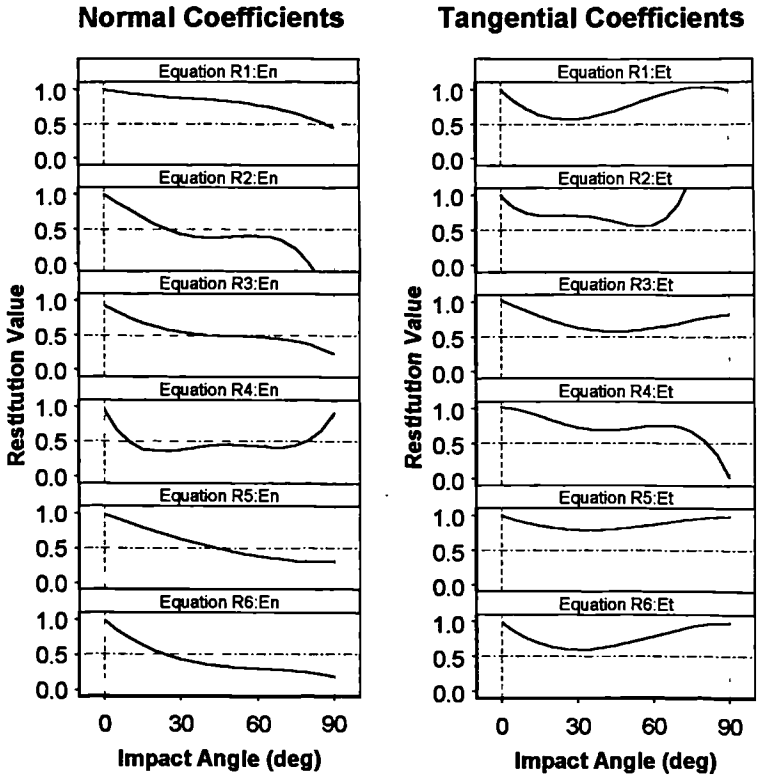

Figure 8.1 Plot of equations for normal and tangential restitution coefficients.

8.1 User Defined Functions for Erosion Predictions

The equations developed in chapter 4 have been implemented in the Fluent software by means of User Defined Functions (UDFs). These are sections of code written in the C programming language that carry out calculations defined by the user. Function headers are provided for a variety of tasks, such as adding source terms to the governing equations, initialising the flow field, setting boundary conditions, and so on. Several headers are available

for the discrete phase model, and include provision for custom drag laws, non-standard body forces, and customised output files among others. Implementation of erosion equations is also allowed. It is not possible (at the time of writing) to calculate particle rebound behaviour by means of a User Defined Function. This means that the squeeze film effect of Clark and Burmeister (1992) cannot be applied in the Fluent software. Only polynomial equations such as those in Table 8.1 can be used.

Table 8.2 summarises the User Defined Functions that have been developed for use in Fluent. The relevant equations from Chapter 4 are identified, as well as the threshold velocities over which the equations will be applied. Appendix E contains the actual User Defined Functions themselves for future reference. Note that they have been combined into one single function that enables any of the individual material equation sets to be selected from the Fluent user interface. This will save having to re-compile every time a different function is desired.

The way in which particle impacts were recorded, and erosion predictions obtained, is summarised as follows:-

1. A particle impacts a solid wall and the Erosion UDF is called. Particle impact angle, impact velocity, and mass flowrate, are passed to the Erosion UDF, along with the impacted cell face ID. The actual cell in which the particle resides can also be found.
2. If the impact angle is above the specified minimum, erosion rate (in mg/s) is calculated for the current impact using the impact velocity, impact angle, and particle mass flowrate supplied, in conjunction with the appropriate empirical equation. The actual equation used may depend on the particle impact velocity (as some UDFs use a different equation for each of two velocity ranges).
3. Mass loss is calculated by multiplying the erosion rate by the appropriate time period.
4. Total erosion rate for a face is updated (i.e. total erosion rate so far + current erosion rate). Total mass loss for the face is updated likewise.
5. Total number of particle impacts on the face is updated (i.e. total number of impacts so far + 1).
6. Total impact velocity on the face is updated (i.e. total impact velocity for face so far + current impact velocity). Total impact angle is updated likewise.
7. Average impact velocity so far is calculated as: total impact velocity for face so far / total number of impacts on face. Average impact angle so far is calculated likewise.

In this way, total erosion rate and mass loss can be found for all cell faces lying on a solid wall. Average impact angle and velocity for these faces are also stored. Once a calculation has completed, all stored quantities can be plotted as contour maps, or output as numerical quantities using the appropriate facilities of Fluent.

Table 8.2 User Defined Functions for Erosion Predictions.

ID	Name	Materials	Equations	Velocity Range (m/s)	Angle Range (deg)
F1	Mean_2d_1	Metallic	4.4 & 4.5	0.1 to 268; change at 24.247	2.0 to 90.0
F2	Mean_3d_1	Metallic	4.7 & 4.9	0.1 to 268 m/s; change at 22.322	2.0 to 90.0
F3	Mean_3d_2	Metallic	4.8 & 4.9	0.0 to 268 m/s; change at 24.756	2.0 to 90.0
F4	M_tcA_2d_1	Tungsten Carbide SMS-25A	Appendix C.1	1.0 to 148.0	2.0 to 90.0
F5	M_tcA_2d_2	Tungsten Carbide SMS-25A	Appendix C.3	1.0 to 63.0	2.0 to 90.0
F6	M_tcA_2d_3	Tungsten Carbide SMS-25A	4.10 & 4.11	1.0 to 148.0; change at 22.590	2.0 to 90.0
F7	M_tcB_2d_1	Tungsten Carbide VC-808	4.12	1.0 to 268.0	2.0 to 90.0
F8	M_tcC_2d_1	Tungsten Carbide DC(Z)05	4.13	1.0 to 148.0	2.0 to 90.0
F9	M_tcC_3d_1	Tungsten Carbide DC(Z)05	4.14	1.0 to 148.0	1.0 to 90.0
F10	M_dupf51_2d_1	Duplex F51	App. C.4	1.0 to 268.0	2.0 to 90.0
F11	M_dupf51_3d_1	Duplex F51	4.15	1.0 to 148.0	1.0 to 90.0
F12	M_aisi_3d_1	AISI 4130	App. C.5	1.0 to 268.0	1.0 to 90.0
F13	M_ph105k	17.4 PH105k	App. C.6	1.0 to 268.0	1.0 to 90.0

8.3 Preliminary Studies

The restrictor flow solutions for which erosion predictions will be obtained are: MU1c, MF1b, MV1c, and MV2e. All of these use the standard k-ε turbulence model. Preliminary studies to investigate the influence of certain defining parameters have been carried out using MU1c and MV1c. These will be briefly discussed.

One of the first considerations in predicting erosion is the optimum number of particle trajectories required for a consistent solution. Ideally, the number of trajectories should be such that increasing them will make no difference to the final result: the prediction will be independent of the number of trajectories. To investigate this for case MU1c, step length factor was set to 20 (fairly high value), random eddy lifetime and 'scale flowrate by face area' were activated, and particle inlet velocity was set to the average fluid inlet velocity (12.715 m/s for MU1c). Normal and tangential restitution coefficients were set to 1.0 on all solid surfaces. Particle mass concentration was taken to be 0.43% (average for erosion tests),

particle diameter was set to 250μm (0.009252"), and particle density was taken to be 2668 kg/m^3. Particle mass flowrate for the eighth annulus is therefore 0.015098 kg/s. Table 8.3 summarises the resulting total restrictor mass loss (TML) as the number of tries was increased.

Table 8.3 Effect of stochastic tries on mass loss.

Ref.	Tries	Trajectories	TML (g)	ER (g/hr)
PS1	20	13500	4.19	0.299
PS2	30	20250	4.085	0.292
PS3	40	27000	4.2996	0.307
PS4	50	33750	4.2413	0.303
PS5	60	40500	4.1437	0.296
PS6	70	47250	4.2544	0.304
PS7	80	54000	4.177	0.298

PS# = Preliminary Study No...
TML = Total Mass Loss
ER = Erosion Rate

As no real trend is observed in Table 8.3, it is necessary to look at profiles of mass loss along a line to understand the effect that increasing particle count has. Figure 8.2 presents plots of mass loss (over 14 hours) for a line lying on the top surface of the upstand base. Note that a smoothing algorithm has been applied to each set of data (same parameters in all sets) to remove some of the scatter that would be observed if only the points themselves had been plotted. The lines are beginning to converge on one another by the point where 70 and 80 tries are being specified. Below this there is no clear indication as to which line is most accurate. Ultimately, experimentally measured profiles would be required to compare these lines of data against.

The results of further investigations into the effect of particle tracking parameters are presented in Table 8.4. Some results are given where the random eddy lifetime option was deactivated, and others have various step length factors (SLF). It is clear that using random eddy lifetime (REL) decreases the predicted mass loss. Presumably the particles impact surfaces with reduced impact velocities to cause the drop in material loss. Effect of step length factor is inconclusive from Table 8.4.

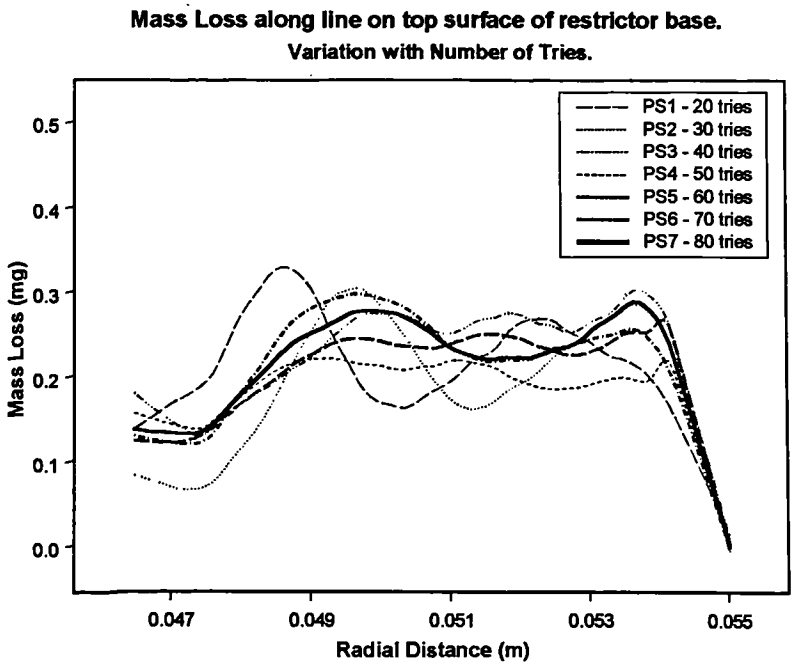

Figure 8.2 Variation of mass loss distribution according to number of tries.

Table 8.4 Further effects of tracking parameters.

Ref.	Tries	Trajectories	SLF	REL	TML (g)	ER (g/hr)
PS8	30	20250	20	Off	4.708	0.336
PS9	40	27000	20	Off	4.609	0.329
PS10	50	33750	20	Off	4.662	0.333
PS11	60	40500	20	Off	4.54	0.324
PS12	100	67500	20	Off	4.533	0.324
PS13	100	67500	10	Off	4.591	0.328
PS14	100	67500	5	Off	4.587	0.328
PS15	100	67500	10	On	4.186	0.299
PS16	120	81000	10	On	4.138	0.296

Further such studies were carried out using case MV1c. One clear conclusion that could be drawn from these studies was that scaling the particle flowrate by face area causes a definite reduction in predicted mass loss (in addition to the reduction caused by random eddy lifetime). This suggests that a more conservative prediction (in that mass loss will be higher) could be obtained by de-activating both random eddy lifetime and the scaled flowrate option. However, the solution would be technically less accurate, and so further predictions will continue to use both these options.

The effect of step length factor can be observed for the case of the valley restrictor in Figure 8.3. Three computations are presented. Random eddy lifetime is not used in these predictions, neither is flowrate scaled by face area at injection. Mass loss along a line on the

downstream pipe wall is presented. There is a fairly significant change in the profile shape when step length factor is reduced to 10, and even more when reduced to 5. In order to reduce the time it takes to run an erosion prediction, it was decided that a step length factor of 15 would be used (this being the median factor between 10 and 20).

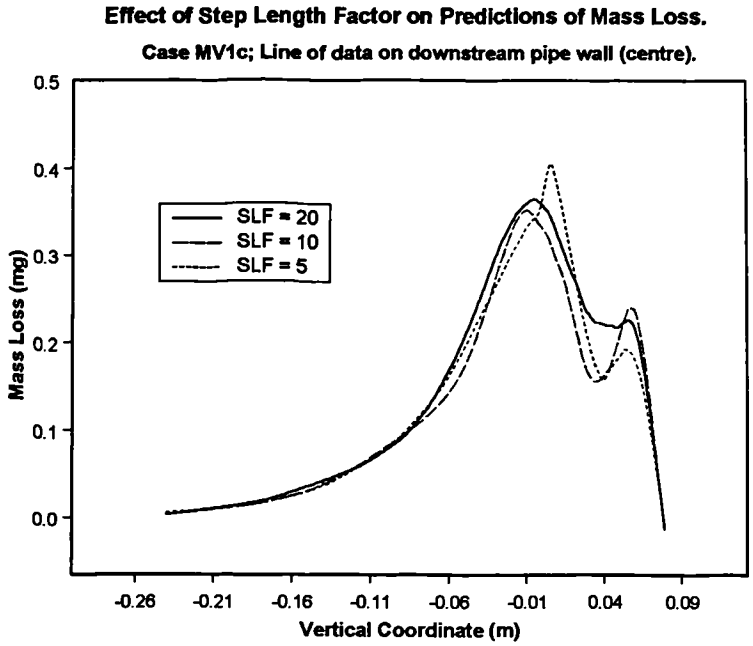

Figure 8.3 Effect of step length factor on predictions with valley restrictor.

8.4 Erosion predictions for upstand restrictor with 11 mm straight holes

Predictions of erosion will be made for each restrictor using the erosion equations specified in Table 8.2, and the rebound equations of Table 8.1 (although not all rebound equations will be used). When compared with the available experimental data, these predictions will give some indication as to the ability of the CFD-based erosion modelling method to make estimates of actual material loss. It will also be instructive to look at the erosion maps produced by the simulations, and to again compare these with the experimental findings. Flow solution MU1c has been used throughout.

The first step in the erosion modelling has been to use a range of rebound equations in conjunction with erosion function F2 (first mean 3D equation) in order to determine the most suitable rebound equation for use in the simulations. In these predictions, 120 stochastic tries have been implemented (81,000 trajectories) with random eddy lifetime on, and scaling particle flowrate by face area. A step length factor of 15 has been used throughout. Table 8.5 presents the pertinent results.

Table 8.5 Effect of rebound equation.

Ref.	No. Tries	Rebound Eqn.	Total Mass Loss (g)	ER (g/hr)
UML1	120	$\varepsilon_n = \varepsilon_t = 1$	4.1376	0.296
UML2	120	R1	4.0411	0.289
UML3	120	R3	4.2116	0.301
UML4	120	R5	4.2234	0.302
UML5	120	R6	4.0645	0.290

UML# = Upstand Mass Loss No...

As equation set R5 gives the highest prediction of mass loss (and hence is most conservative), it is proposed to use this in all further predictions. There is not a great deal of difference between the mass loss predicted using the assumption of no kinetic energy loss, and the mass loss predicted with the rebound equations. This suggests that the rebound behaviour is not critical for this type of flow (incompressible liquid flow). For a gas flow, the rebound behaviour could have much greater significance.

Having determined an appropriate set of rebound equations, it is possible to go on to apply the various erosion equations to the upstand restrictor models. For these final erosion predictions, 120 stochastic tries have been applied in conjunction with a Step Length Factor of 15. Rebound equations R5 have been set on all solid surfaces. Table 8.6 presents the results. Comparisons with erosion testing will be made in a later section.

Predicted mass loss on the top surface of the restrictor base is shown in Figure 8.4. Both images show the same set of data, but in the second the scale has been reset to 1.0 mg loss in order to show more clearly the extent of predicted erosion damage. All areas coloured red in this second image have a mass loss of 1.0 mg or more. A 14 hour time interval was used in calculating the mass loss. These plots are from prediction UML10 (using the Mean_3d_2 UDF).

Table 8.6 Erosion predictions for MU1c with various UDFs.

Ref.	Erosion UDF	Lower Angle (deg)	TML (g)	ER (g/hr)
UML6	Mean_3d_1	5.0	4.2354	0.3025
UML7	M_aisi_3d_1	1.0	6.4546	0.4610
UML8	M_dupf51_3d_1	1.0	3.7520	0.2680
UML9	M_tcC_3d_1	1.0	0.02524	0.0018
UML10	Mean_3d_2	5.0	3.7185	0.2656
UML11	Mean_3d_2	2.0	3.8411	0.2744

TML = Total Mass Loss
ER = Erosion Rate

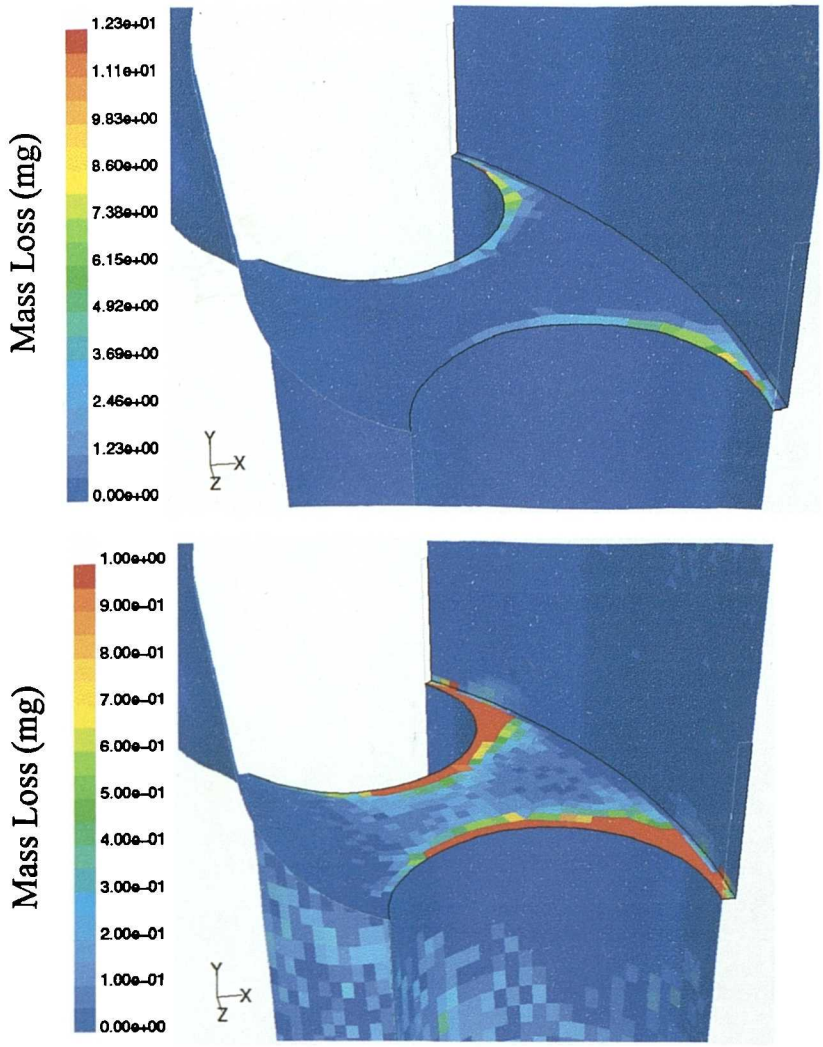

Figure 8.4 Predicted mass loss on top surface of restrictor base (after 14 hours).

The predicted mass loss map indicates some localised erosion of the upstream pipe wall at the point where the hole is closest to the wall (almost on the symmetry plane). This does correspond to the location of erosion observed on the pipe sleeve under actual test conditions. What happens after initial erosion at this point is not clear (as no modelling of eroded geometry has been attempted), but it is possible that fluid behaviour past this point contributes to greater erosion of the pipe wall as time proceeds.

Particle impact angle and velocity are shown in Figure 8.5. Particles impact areas immediately round the hole entrances with angles at which erosion will be a maximum (for ductile materials), indicating the swift removal of the original sharp edges. The particle impact map does help to understand the fluid behaviour approaching the restrictor base top surface. It is obvious that fluid approaching the surface between holes must change direction slightly to pass through either hole. Particles follow the fluid path and therefore create an impact pattern

having fairly high impact angles in the centre of the surface, but significantly lower angles approaching the holes. While impact velocities are not as high on these leading edges of the holes as they are within the holes, the rate of particles impacting the leading edges will be much higher than on the sides of the holes themselves. Particles impacting the top surface at points round the rim of the hole appear to do so with a slightly higher impact velocity than others further away from the hole. Had a finer mesh been specified round the rim of the hole, there might have been an even narrower band of higher velocity particles than indicated in Figure 8.5. This behaviour will obviously encourage rapid destruction of the sharp edges at the entrance to the holes.

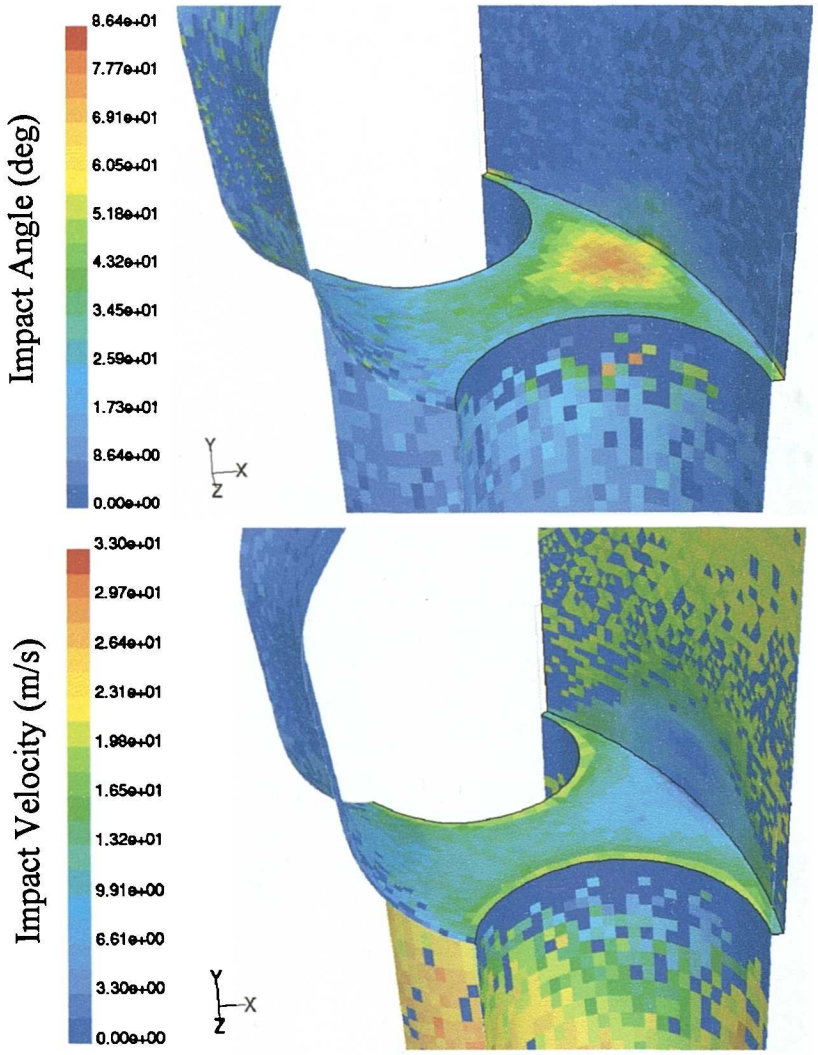

Figure 8.5 Average particle impact angles and velocities for upstand restrictor.

8.5 Erosion predictions for valley restrictor with 11mm straight holes

Similar erosion predictions have been made for the valley restrictor as were made for the upstand restrictor. Predictions based on flow solution MV1c will be considered first.

Particle concentration was again taken to be 0.43% by mass (which comes to 0.030655 kg/s for the quarter annulus). Particle inlet velocity was the liquid average velocity of 12.913 m/s. Particle size and density were as before. Step length factor was again set to 15, random eddy lifetime was activated, and particle inlet flowrate was scaled by face areas. 80 stochastic tries were used for each prediction (giving 92,400 trajectories) in conjunction with rebound equation set R5. Table 8.7 presents the results obtained with various erosion UDFs.

Table 8.7 Predicted mass loss for flow solution MV1c.

Ref.	Erosion UDF	Lower Angle (deg)	TML (g)	ER (g/hr)
VML1	Mean_3d_1	5.0	2.5452	0.1818
VML2	M_aisi_3d_1	1.0	4.5604	0.3257
VML3	M_dupf51_3d_1	1.0	2.9945	0.2139
VML4	M_tcC_3d_1	1.0	0.01978	0.0014
VML5	Mean_2d_1	5.0	5.3264	0.3805
VML6	Mean_3d_2	5.0	2.7851	0.1989

VML# = Valley Mass Loss No...

Contours of predicted mass loss are shown in Figure 8.6 in the same way as before—the scale of the second plot being set to a maximum of 1.0 mg. Results from prediction VML6 are shown. There is little erosion predicted on the upper sloping surfaces (the valley) of the restrictor. Most of the erosion takes place around the edges of the holes. In the experimental restrictor, hole edges were eroded at the base of the valley, creating a pointed ridge for the fluid to pass over. There is a point of maximum erosion predicted at the innermost point of the central hole for this restrictor. While significant erosion may have taken place at this point in the initial stages of the erosion testing, there is no obvious gouge or scar remaining there on the eroded prototype. There is definitely material loss on the inner valley surface adjacent to the hole, but it is not known what stages were involved in the development of the erosion at that point.

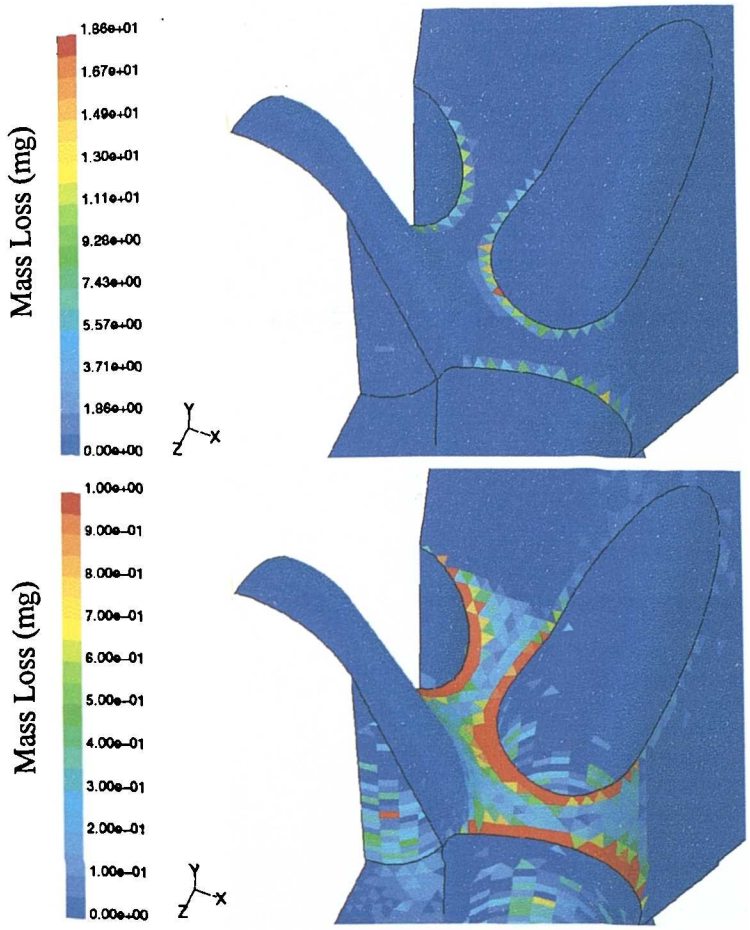

Figure 8.6 Predictions of mass loss using case MV1c.

Particle impact angle is plotted in Figure 8.7, along with particle impact velocity. Impact angles around hole edges are less acute than for the upstand restrictor. This will benefit both ductile and brittle materials, as the impact angles are likely to be below the range for maximum erosion of ductile materials (and brittle materials erode most at normal impact). Impact velocities around the holes are in the same range as for the upstand case. However, although the velocities are similar, the shallower impact angles will result in a reduced rate of erosion compared to the upstand case.

There appears to be a region of high mass loss in the restrictor hole (red patch in the bottom-left of the lower half of Figure 8.6. It should be noted that the Mass Loss range in this figure has been set to a maximum of 1.0 mg. The corresponding patch in the top picture does not show up so clearly. It may be that a particle has somehow become 'trapped' in a near-wall cell, and artificially caused a greater amount of mass loss than there ought to be. This was clearly observed in one or two other instances, and may be an intermittent bug in the Fluent software.

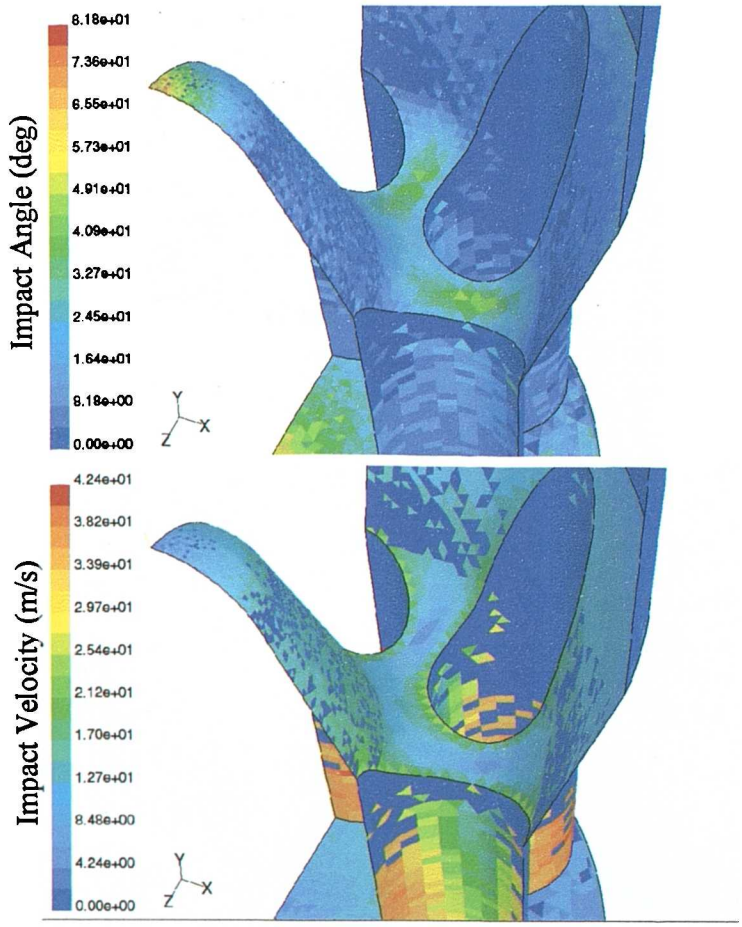

Figure 8.7 Particle impact angle and velocity for case MV1c.

8.6 Erosion predictions for fluted restrictor with 11 mm straight holes

A smaller number of predictions were made for the fluted restrictor with 11 mm straight holes. Particle mass concentration was again set to 0.43%, which resulted in an actual particle mass flowrate (for the eighth annulus) of 0.01577 kg/s. Particle inlet velocity was set to the average fluid velocity of 13.1827 m/s. Particle diameter and density were as before. 400 stochastic tries were required with this model (flow solution MF1b) to obtain 83,200 actual trajectories. Step length factor was set to 15 for all predictions, and the random eddy lifetime option was activated. Particle flowrate was again scaled by cell face area at the inlet. Gravitational acceleration was specified. Table 8.8 presents the predicted results.

Table 8.8 Predicted mass loss for fluted restrictor (MF1b).

Ref.	Erosion UDF	Lower Angle (deg)	TML (g)	ER (g/hr)
FML1	Mean_3d_2	5.0	2.635	0.188
FML2	Mean_3d_1	5.0	3.172	0.227
FML3	M_dupf51_3d	1.0	2.930	0.209
FML4	M_aisi_3d_1	1.0	4.733	0.338

Predicted mass loss for run FML4 are presented in Figure 8.8. No significant erosion is predicted on the sides of the hole for this geometry, even though there was material loss observed in the actual test component. This underlines the fact that the wear mechanism within the holes is cavitation (or cavitation combined with erosion) rather than solely solid particle erosion.

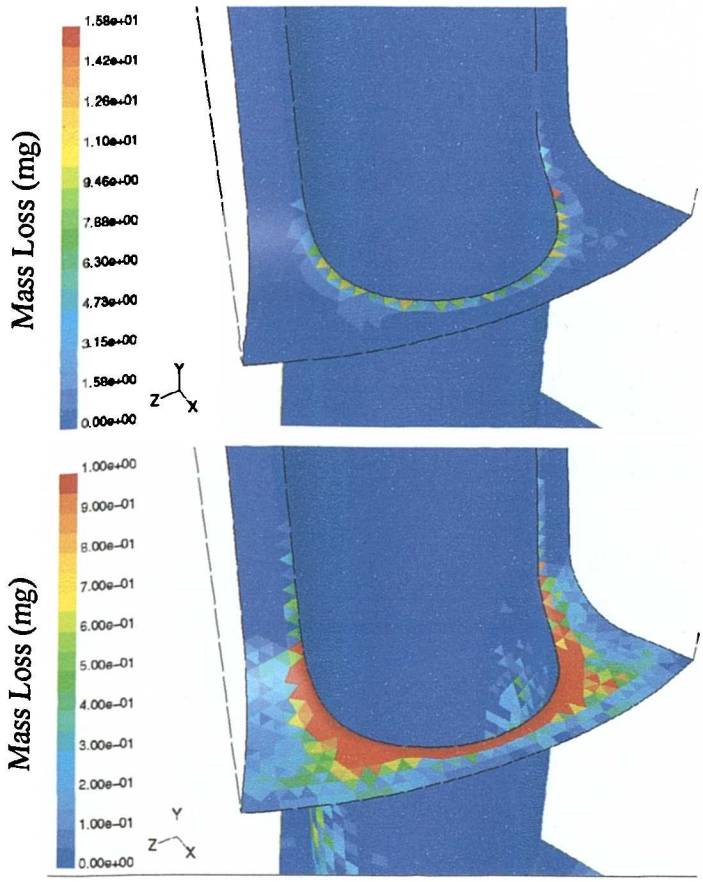

Figure 8.8 Predicted mass loss for fluted restrictor (case FML4).

Plots of particle impact angle and velocity for the same run are shown in Figure 8.9. It is clear from the velocity predictions that particles do impact on the walls inside the hole. This is likely to combine with the cavitation taking place on the surface of the hole to cause more severe damage than would have been obtained with the cavitation alone.

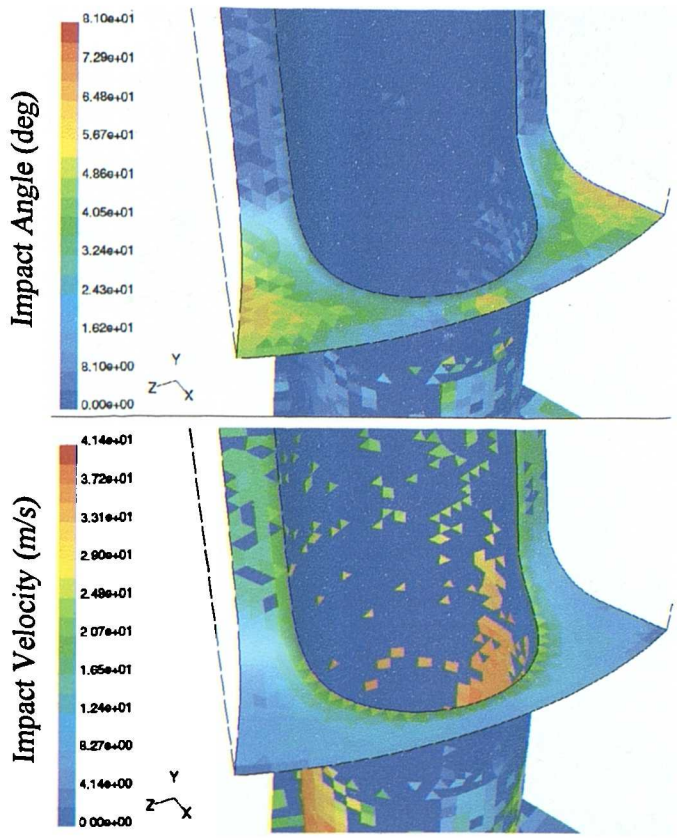

Figure 8.9 Particle impact angle and velocity for fluted restrictor.

The main limitation with all of the erosion predictions made so far is that they only account for the original un-eroded geometry. In the actual tests, the initial surface shapes would only have applied right at the start of the test period. Deformation of the surfaces due to erosion would have commenced as soon as fluid began to flow.

8.7 Comparison of erosion predictions with test results

There are two ways in which predictions can be compared with the actual experimental test results. Direct comparisons can be made between the overall measured erosion rates and the predicted, and comparisons can also be made of relative erosion rate between geometries for predicted and actual data.

8.7.1 Direct comparison

8.7.1.1 Upstand restrictor

Two sets of results were obtained for the upstand restrictor: the first was for a straight 14 hours test period (with an AISI 4130 specimen); the second was carried out in four stages each of 5 hours duration (Duplex F51 specimen). For the first test, total mass loss after 14

hours was 19.89g, giving an average erosion rate of 1.42 g/hr. In the second set of testing, total mass loss after 15 hours was 14.71g, giving an average erosion rate of 0.98 g/hr. Figure 8.10 compares the erosion rate predictions of Table 8.6 (for upstand restrictor) with these two measured results.

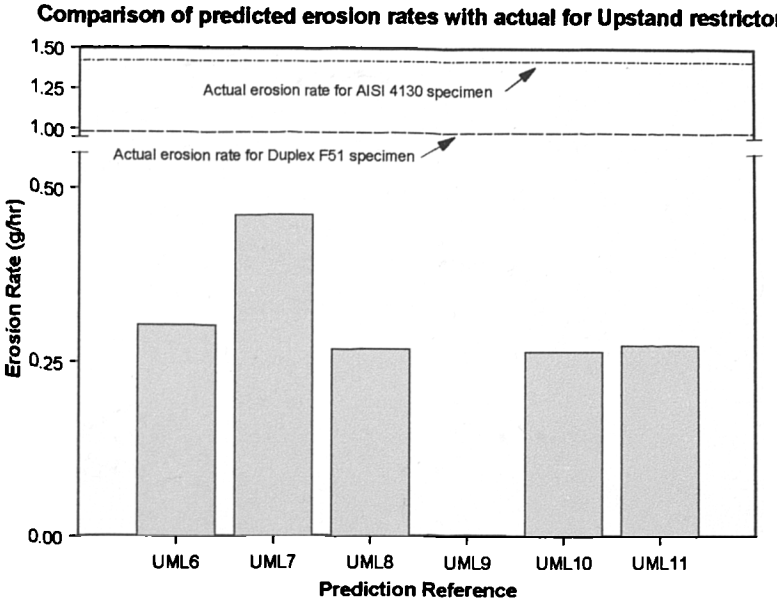

Figure 8.10 Comparison of predicted and measured erosion rates (from Table 8.6).

Predicted erosion rate (prediction UML7 in Table 8.6) for the AISI 4130 specimen is 67.5% lower than the corresponding experimental value. For the Duplex F51 specimen, prediction UML8 is 72.65% lower than the experimental value. The mean predictions are similar to the Duplex F51 prediction.

It is possible that some cavitation erosion was present in the holes of the upstand restrictor. This was not clearly observed after testing, as the sides of the holes were considerably deformed by erosion, and any evidence of cavitation erosion may have been removed by continuous solid particle erosion.

In the experimental testing, the erosion rate of the Duplex F51 specimen does decrease with time—so that the erosion rate after 15 hours of testing is almost 30% lower than it was at the start. However, it would not be strictly correct to compare the final erosion rate with the overall value obtained from CFD predictions, as the geometry after 15 hours of testing is considerably different from that at the start.

8.7.1.2 Valley restrictor

Only one specimen was tested for the valley restrictor, in a single erosion period. Measured mass loss was 8.16 g, giving an average erosion rate of 0.58 g/hr. This result is compared with the predictions of Table 8.7 in Figure 8.11 below.

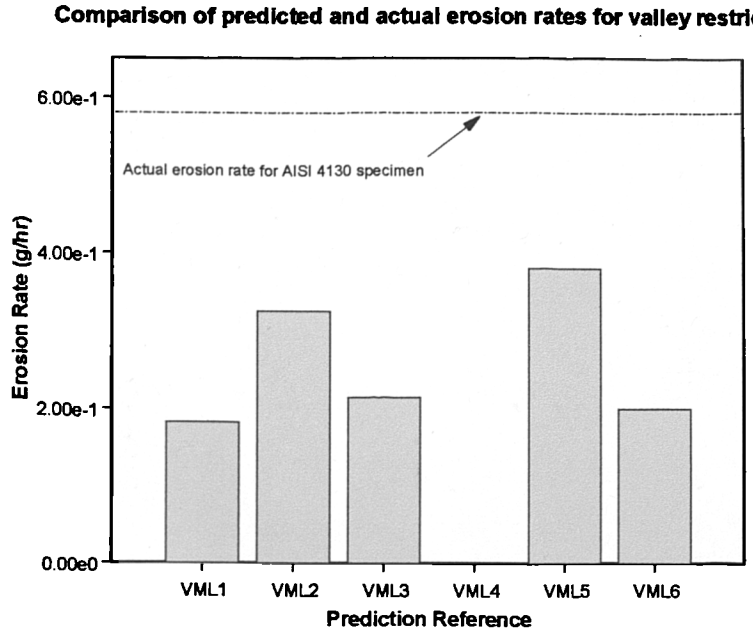

Figure 8.11 Comparison of predictions (Table 8.7) for valley restrictor.

The predicted erosion rate with the AISI 4130 UDF is 43.8% lower than the actual erosion rate. This is an improvement on predictions for the upstand restrictor, which suggests that cavitation erosion could indeed have been present in the actual tests for the upstand restrictor. The valley restrictor design is not so amenable to cavitation phenomena—material loss is much more likely to be a result of solid particle erosion alone. This could explain the improved performance of the CFD modelling.

8.7.1.3 Fluted restrictor

The actual erosion rate for the fluted restrictor (AISI 4130 specimen) was found to be 0.65 g/hr. Using the AISI 4130 UDF gives a prediction of 0.338 g/hr, which is 48% lower than the actual. It is perhaps unexpected that the difference between measured and predicted erosion should be the same for the fluted restrictor as for the valley restrictor, as there was undoubtedly cavitation erosion present in the fluted restrictor that the CFD model would not predict. This indicates that there are other factors affecting how well the CFD model predicts erosion apart from cavitation phenomena. Relative geometry change could be a significant

factor—in that geometry changes taking place on the fluted restrictor could affect the flow to a greater extent than the geometry changes of the valley restrictor. There is also the issue of particle rebound phenomena, and how much that is affected by fluid flow across surfaces as well as the underlying material type.

These direct comparisons of actual mass loss with predicted mass loss give a quantitative measure of the performance of the CFD-based erosion modelling technique. One of the main reasons for differences between predicted and actual mass loss will be that liquid velocities reported in the slurry erosion tests (from which the empirical equations came) were much higher than the true particle impact velocities at the sample surface. The fact that CFD predictions are lower than the actual measurements is consistent with this hypothesis.

8.7.2 Relative comparisons

The measured erosion rate of the upstand restrictor (made from AISI 4130) is taken to be the base level for relative comparisons. Figure 8.12 compares the measured relative erosion rates against the CFD predicted relative erosion rates. CFD predictions are those made using material specific UDFs (i.e. M_aisi_3d_1 and M_dupf51_3d), although for a true relative comparison only the AISI 4130 predictions should be considered. It is apparent that the CFD predictions do not closely follow the trends of the measured values, although they do at least identify the upstand restrictor as being the least resistant to erosion.

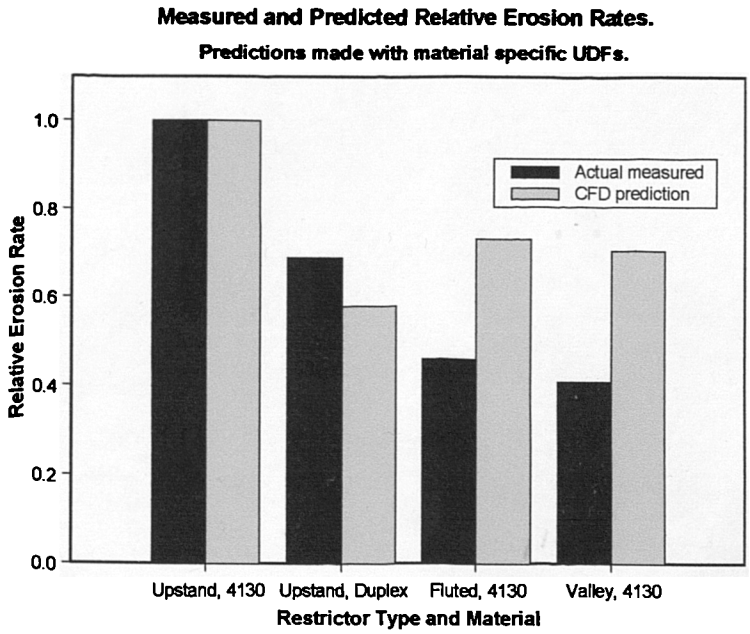

Figure 8.12 Measured and predicted relative erosion rates.

The level of difference in erosion rate between the fluted and valley restrictor designs is not as large in the predictions as it is in the actual tests. This again throws some doubt on the ability of the CFD method to predict relative erosion rates between different geometries. However, the fluid mechanics effects caused by different geometries will have a major influence on whether the relative erosion can be predicted correctly or not.

A similar graph is shown in Figure 8.13 where the predicted relative erosion rates are based on the mean three-dimensional UDFs, Mean_3D_1 and Mean_3D_2. The first UDF gives a reasonable result in predicting relative erosion rate, with at least the correct trend being returned to some degree. The second UDF, however, does not predict the expected difference in erosion rate between the fluted and valley restrictors. It is interesting to note that all the equations do at least predict the reduction in erosion when changing from the upstand geometry to one of the other two geometries. There may be features of the other two geometries which make it difficult to obtain the correct particle impact sites.

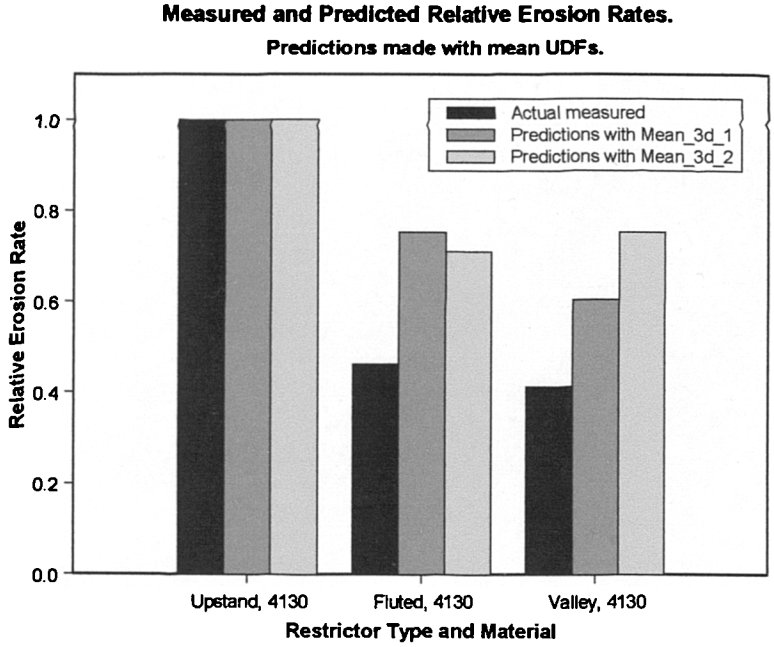

Figure 8.13 Measured and predicted relative erosion rates where mean equations have been used for the predictions.

8.8 Summary and conclusions

This chapter has presented the erosion modelling of flow restrictors. Some initial studies were performed to help understand the effect of various particle tracking parameters on the predictions. It was found that activating the random eddy lifetime option, and scaling particle flowrate by cell face area on the inlet surface, both reduced the overall predicted mass

loss. Step length factor also affected calculations, with a final figure of 15 being chosen for the erosion predictions. Several equations have been identified for the restitution coefficients used to calculate particle rebound parameters. Repeat studies with some of the equations showed that of Forder et al. (1998) to be adequate (as it gave a fairly conservative result).

Erosion predictions have been made for three of the restrictor flow cases: MU1c, MV1c, and MF1b. Several erosion functions were used for each case. Comparing the predictions against results of abrasive flow testing show that the CFD method underpredicts erosion rate by up to 72.6% of the measured value. Trends suggested by relative erosion rates are reproduced in the CFD predictions to some extent, but the magnitude of reduction between the upstand and fluted restrictors, and between the fluted and valley restrictors, is not predicted to be as large as it is. However, the mean three-dimensional erosion function (Mean_3d_1) did capture the trend qualitatively, if not quantitatively.

The erosion predictions have not been as successful as would be desired. Several possible causes for this have been identified. One is that the underlying erosion data used in developing the empirical equations use particle impact velocities that are too high. This alone will cause underprediction of erosion rates. Another cause of underprediction is that cavitation erosion may have occurred in all of the restrictors for at least some of the abrasive flow test period. It certainly took place in the fluted restrictor. The CFD model will not reproduce this material loss. Geometry changes will be another significant cause of poor predictions. This is especially so for the upstand restrictor (for which predictions were poorest) due to the scale of deformations taking place. Changes on the valley restrictor were not so pronounced, which is why reasonable predictions are obtained for this geometry.

Further work could be done to improve the predictions for these geometries. The first would be to re-define the empirical erosion equations based on true particle impact velocities at the surface. Applying squeeze film theory to particle impacts would help to reproduce true behaviour at the surface. A step beyond these tasks would be to model the actual geometry changes taking place on the restrictors, in order to capture the true fluid mechanics phenomena as time progresses.

9.0 Modelling of Single Phase Flow through Complex Geometries

The ultimate aim of the work carried out in this project has been to apply the CFD-based erosion modelling technique to the MOS choke valve. This valve represents a complex geometry and therefore requires considerably more effort to model than the simpler restrictor geometries considered previously. This chapter presents the work carried out in modelling flow of single phase fluids only. Data from previous testing has been made available to validate the CFD modelling.

9.1 Choke valve testing: Three inch valve

A three inch (76.2 mm) nominal bore choke valve was tested at NEL in 1988 for Seaboard Lloyd (now Wood Group Pressure Control). Results of this testing are presented in NEL report No. SELL/01. The aim of the tests was to measure valve flow coefficient over a range of flowrates and valve settings according to a relevant standard. Figure 9.1 depicts the test arrangement.

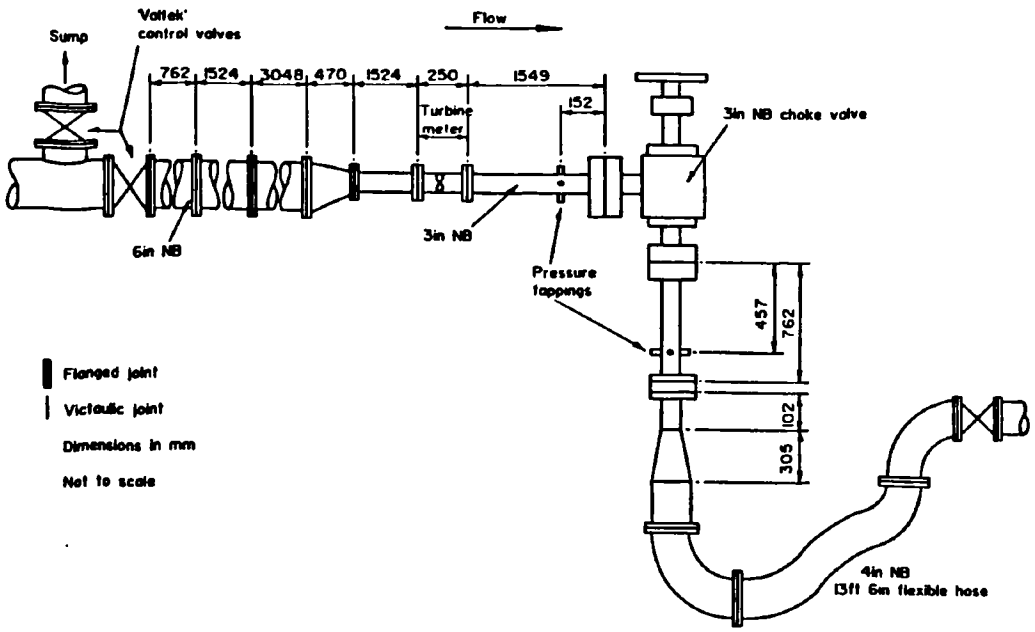

Figure 9.1 Valve test arrangement.

As the original test report is commercially confidential, only those results directly relevant to this project will be presented. In the test procedure, measurements were made of static pressure at two points: 2 pipe diameters upstream, and 6 pipe diameters downstream, of the valve under test. The pressure drop across the valve alone was found by subtracting the

estimated pressure drop in the piping from the overall measured value. Flowrate through the valve was measured with a turbine flowmeter. A total of ten valve positions were considered, with three different flowrates being set for each position. This provides a wide range of data with which to validate the CFD modelling capability.

9.1 Computational meshes for Three inch choke valve

The three inch choke valve has been modelled in four different stem positions: 100%, 81%, 68.1%, and 36% open. These figures refer to the percentage of total valve open area presented to the flow. Valve stem positions have been set by either calculating the correct position for the required percentage area, or else by referring to the stem marking standard supplied by the manufacturer. Creating computational meshes proved to be a difficult and time-consuming process for the complex valve geometry. A mesh had to be entirely re-created each time the valve position changed—although this task was made easier by the solid modelling approach taken by the Fluent pre-processor. As the entire valve solid model was created in AutoCAD, it was only necessary to move the position of the stem and tip in the AutoCAD model to generate a new geometry. Using the previous Fluent pre-processor where surface models were required would have been far more time-consuming than the Gambit method.

Some of the main meshes will be described briefly in turn, in order to give some indication as to how these valve geometries can be modelled. Such information will be useful for future work. Table 9.1 lists all of the computational meshes for the three inch choke valve. Key parts of the choke valve inner volume are shown for reference in Figure 9.2. This figure shows the fluid-filled volumes rather than the actual valve components surrounding the volumes. Each computational mesh was generally divided up into these sections—and each section meshed individually.

Table 9.1 Computational Meshes created for the three inch choke valve.

Ref.	Valve Position % open area	No. of Cells	Comments
MC100a	100	99k	
MC81a	81	399k	
MC68a	68.1	225k	
MC36a	36	180k	
MC36b	36	267k	
MC36c	36	359k	
MC36Ra	36	458k	Tip rotated 15^0
MC36Rb	36	470k	Adapted from MC36Ra
MC36Rc	36	482k	Adapted from MC36Rb

9.2.1 100% open — Mesh MC100a

This was the first mesh created for the three inch choke valve, and is the least refined mesh of all. Unstructured tetrahedral cells have been used for the gallery, cage holes, gap volume, tip holes, and tip inner volume. Mapped hexahedral cells have been used in the inlet and outlet sections. Figure 9.2 presents the pertinent features of this mesh, and highlights the sections mentioned. It will be apparent that the mesh is fairly coarse in comparison with the restrictor meshes of Chapter 7. No boundary layers were specified in this mesh: tetrahedral cells sit directly on surfaces where used.

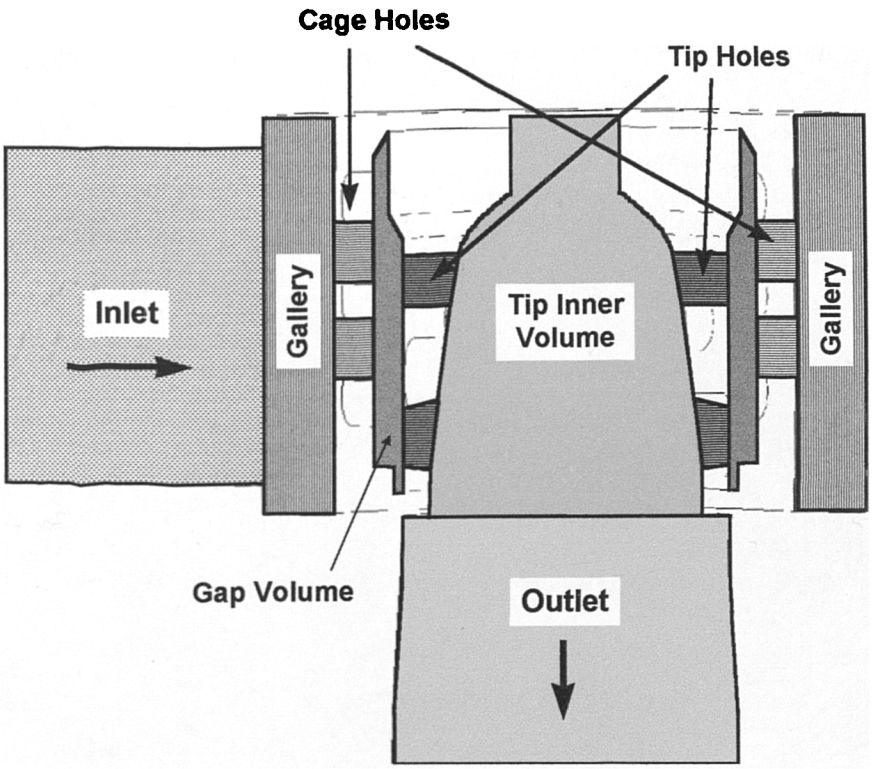

Figure 9.2 Main sections of choke valve meshes (flow regions).

The valve meshes generally included 2D of pipe upstream of the valve and 6D of pipe downstream. This was to match the positions of the upstream and downstream pressure tappings in the actual tests.

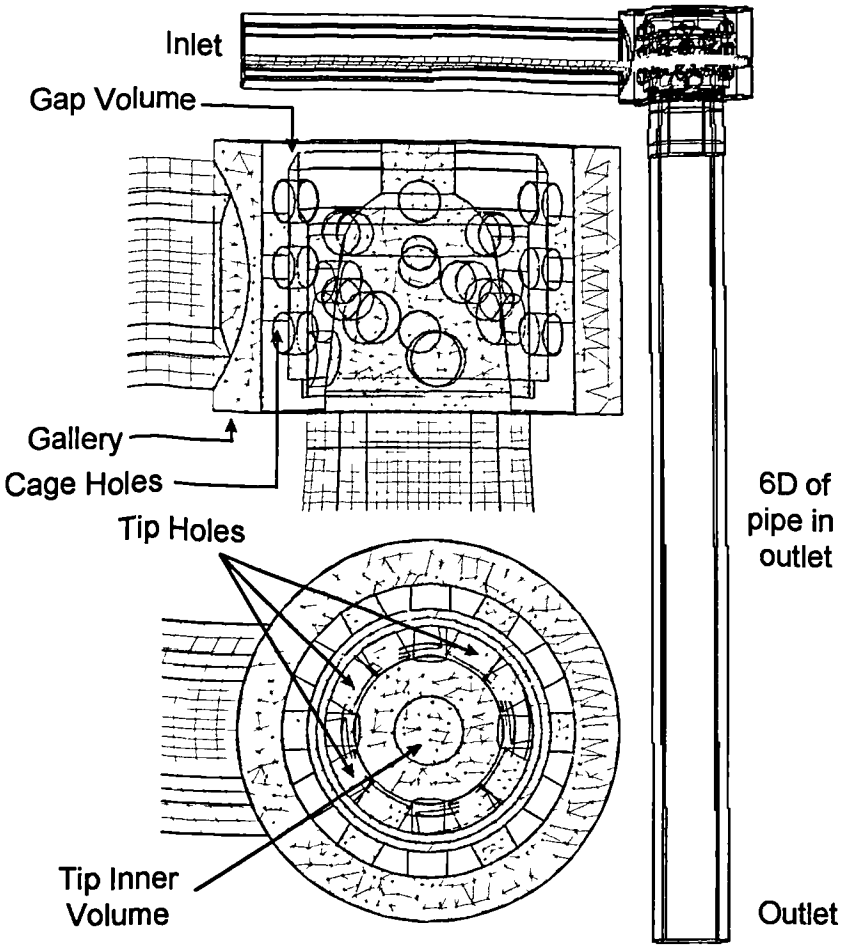

Figure 9.2 Features of Mesh MC100a (100% open).

9.2.2 81% open — Mesh MC81a

The tip holes in the previous mesh were all fully open to the flow. In this 81 % open mesh, the bottom row of tip holes are half covered by the edge of the valve seat (base of the gap volume). Figure 9.3 presents several views of the meshed regions within the valve. Tetrahedral cells were used in the entire gallery region of this mesh, without specifying any boundary layers (Figure 9.3(a)). This does mean that the gallery mesh is fairly coarse in comparison to the mesh within other parts of the valve. An attempt was made to use hexahedral cells in part of the gap volume for this mesh. Figure 9.3(b) shows how the top row of cage holes, and part of the second row, are meshed with unstructured hexahedral cells. This hexahedral mesh is continued into the gap volume. Beneath this hexahedral section, wedge shaped cells are used in the cage holes (triangular face extruded along the length of the hole), and unstructured tetrahedral cells in the rest of the gap volume. This approach results in a higher quality mesh for the thinnest region of the gap volume.

Wedge shaped cells are again used for all of the tip holes (Figure 9.3(d)) and completely unstructured tetrahedral cells for the tip inner volume. The outlet length of the mesh is created with a multi-block hexahedral mesh, the last section of which is shown in Figure 9.3(d). The large aspect ratio at this point can be clearly seen.

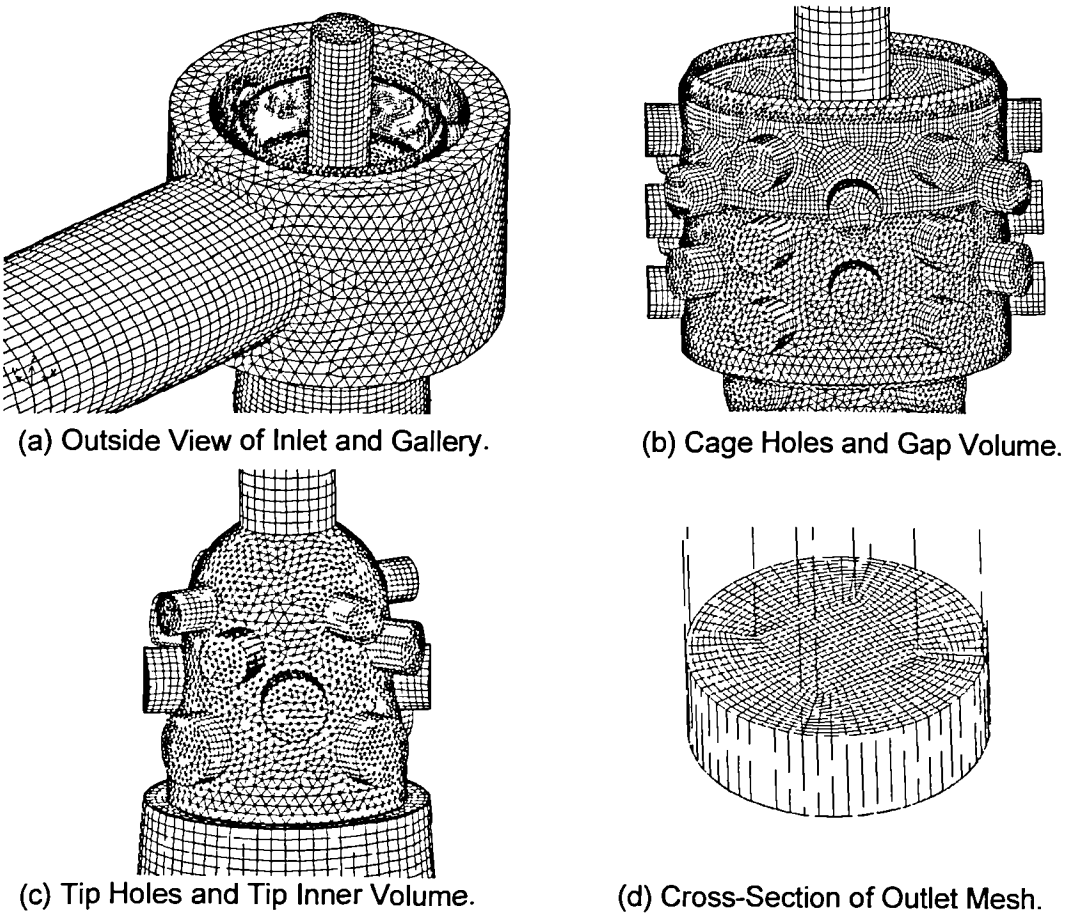

(a) Outside View of Inlet and Gallery.

(b) Cage Holes and Gap Volume.

(c) Tip Holes and Tip Inner Volume.

(d) Cross-Section of Outlet Mesh.

Figure 9.3 Computational Mesh MC81a.

9.2.3 Initial mesh for 36% open — Mesh MC36a

Four meshes were created for the 36% open case, as it was found that predicted results did not compare too well with the experimental results for this position. Holes in the bottom row of the control tip are only fractionally open to the flow for this position, which does cause some difficulties in meshing. It was not possible to specify as many cells as would have been desired around these narrow gaps of the geometry—which may mean that some of the physical behaviour is not adequately predicted.

The initial mesh, MC36a, is similar to mesh MC100a in that the gallery, cage holes, gap volume, tip holes, and tip inner volume are meshed entirely with unstructured tetrahedral cells. No wedge shaped cells were used at any point in this mesh. Inlet and outlet sections are of hexahedral multi-block design as before. It should be noted that the order in which meshes are presented here is not chronological: mesh MC36a was created after mesh MC100a, and before MC81a. Mesh MC36a can be thought of as a fairly coarse mesh for this type of geometry. Figure 9.4 presents a plan view of the mesh from the top, which shows clearly the use of tetrahedral cells in the aforementioned regions. The gallery mesh here is an improvement on that used for mesh MC100a.

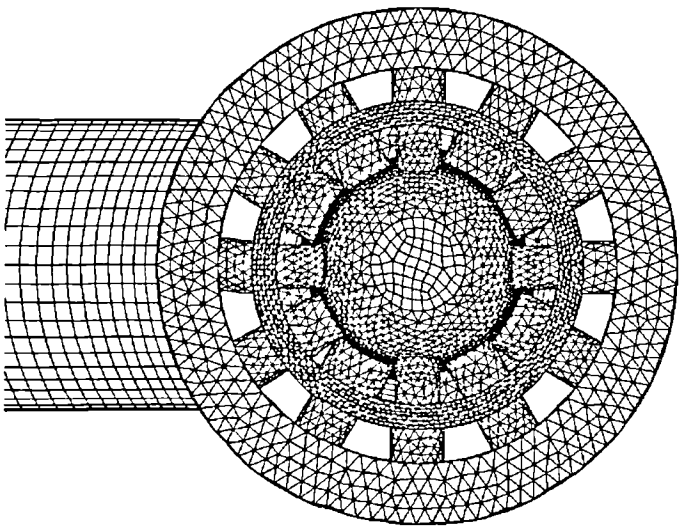

Figure 9.4 Plan view of Mesh MC36a.

9.2.4 Additional meshes for 36% open case

Mesh MC36b was a continuation of mesh MC36a with an increased number of cells. No real improvement was made in terms of meshing strategy. A different approach was adopted in Mesh MC36c, where the intention was to remove most of the tetrahedral meshing from the gallery. There is still a need to have a tetrahedral section where the inlet mesh meets the gallery mesh, but unstructured hexahedral meshing can be used elsewhere (Figure 9.5(a)). The cage holes were meshed with a multi-block hexahedral mesh, in which the inner cylinder has a paved quadrilateral face swept through its length, and the outer cylinder has a regular mapped hexahedral mesh.

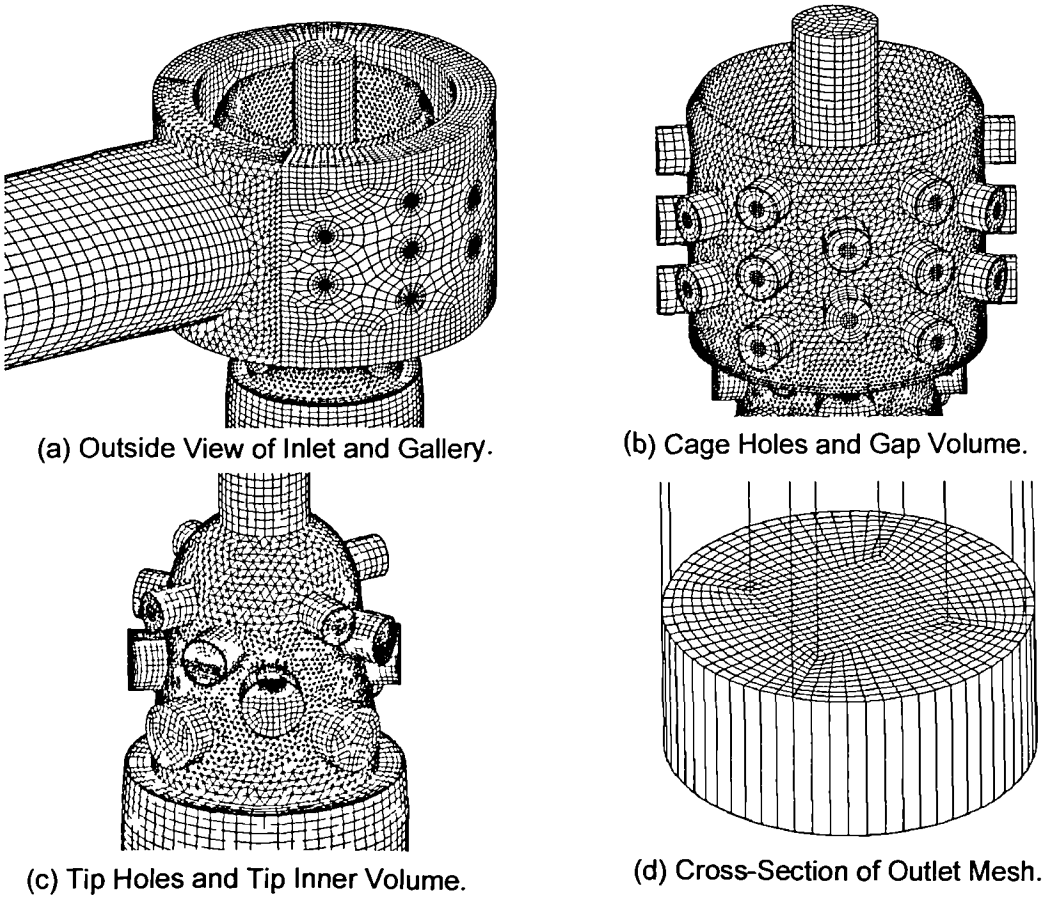

Figure 9.5 Computational Mesh MC36c

The gap volume of Mesh MC36c uses unstructured tetrahedral meshing throughout the entire volume, although cells are more densely populated towards the base of this region.

In Mesh MC36Ra the flow control tip is in the same vertical position as before, but has been rotated 15^0 around the central vertical axis compared to the previous meshes. The aim behind this was to examine the effect of flow control tip orientation on flow behaviour. Actual component orientations are not recorded in real valves, so the computational meshes do not necessarily represent the true orientation of valve internals that was present in the NEL flow tests. Figure 9.6 shows the outer gallery mesh for this valve, as a slightly different approach was adopted to that of previous meshes.

Mesh MC36Ra was adapted twice based on results of simulation using the original mesh. Adaption increases the number of cells in certain areas according to rules set by the user. In this instance, pressure gradient was used as the criterion for cell adaption.

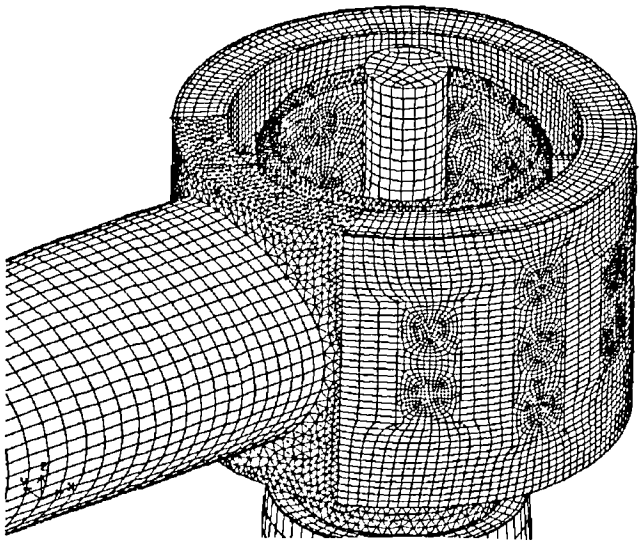

Figure 9.6 Outside view of Mesh MC36Ra.

9.2.5 68.1% open case: Mesh MC68a

One of the concerns about the 36% open case was that some of the tip holes were only fractionally open—and it was thought this could be the cause of differences between experimental and predicted results. The 68.1% case was created in order to explore this further. In the 68.1% case, the bottom row of tip holes are fractionally open—as opposed to the third row of holes for the 36% open case. Mesh MC68a is a fairly coarse mesh, in that around 225,000 cells were used. A finer mesh was created at a later stage, but a successful flow solution was not obtained.

9.2.6 Summary of valve meshes

Creating the various meshes outlined here was a time-consuming task, and in the early stages it took over a week to create a single mesh. The complexity of the valve meant that a considerable amount of domain decomposition had to take place before the mesh could be created. The narrow gap between the inside of the flow cage, and the outside of the tip, was the most difficult region to mesh properly. Often several attempts had to be made to ensure the tetrahedral cells were not unduly skewed, and to have three or more cells across the width of the gap. Overall meshing strategy improved with practice, which means that some of the later meshes are of a higher quality than those created at the beginning. This may have some effect on the predicted results. However, it will be difficult to quantify the influence of meshing strategy on results due to the complex nature of the geometry.

9.2 Results of CFD modelling for three inch choke valve

There are several ways to assess the results of CFD modelling for the choke valve. One of the first steps is to compare the predicted valve pressure drops with those measured in flow testing at NEL. This will give some measure of validation for the CFD models.

9.3.1 C_V and pressure drop: comparison of predicted and measured values

Obtaining successfully converged solutions for the three inch choke valve meshes proved difficult in some cases. Table 9.2 presents the solutions obtained using the meshes, along with comments on how well the solution converged. Oscillatory convergence was obtained in several cases, although the magnitude of the residual oscillations varied from case to case. These oscillations are thought to be purely numerical artefacts, and do not suggest any form of periodic flow within the valve itself. It is possible that transient behaviour does take place within the valve, but capturing these numerically is outwith the scope of the current project. The available computational resources were unlikely to have been able to predict such phenomena. In Table 9.2, 'osc' in the convergence column indicates that oscillatory convergence was obtained. 'Good osc' means that while oscillations were present, the residual magnitude was small. 'Poor osc' suggests that the residual magnitudes were higher.

The predicted pressure drops of Table 9.2 are compared against actual test data where possible in Table 9.3. It will be apparent that good agreement between predicted and actual C_V values is obtained for the 100% and 81% open cases, but not so good for the 36% open case. The 68.1% case is moderate in comparison to the 36% case, but not as good as the 81% case. Rotating the flow control tip by 15^0 has a fairly significant impact on the predicted C_V values, with disparity between predicted and actual increasing to around 20%. The error in pressure drop prediction will be even higher.

It is possible that having tip holes that are only fractionally open does affect how well the model predicts true pressure loss. However, it may also be that the CFD has difficulty in predicting the flow through holes of small diameter. When the valve is only 36% open, the flow is forced to pass through the top two rows of the tip. If the valve is 100% or 81% open, most of the flow can pass through the larger diameter holes in the bottom two rows of the tip. Even at 68.1% open, most of the third row tip holes are open to the flow. It would be possible to extract the mass flowrate through each hole of the cage and tip for all the models, and to compare distributions through the tip—but this would be a lengthy and time-consuming exercise.

One problem in running CFD models with high flowrates (such as 120.75 litres/s) is that the y^+ values reported on solid walls of the model exceed the recommended maximum of 500. Using lower flowrates (e.g. 6.14 litres/s) brought the y^+ values within this limit. However, there is only a slight change in the resulting C_V value when this approach is taken. There was not much scope for adjusting the mesh in order to ensure y^+ values were within the limits of validity for these models, due to the length of time required to develop the mesh and obtain solutions.

Table 9.2 Solutions obtained for three inch choke valve.

Models:	Cells	Turbulence	Discretis-ation	Flowrate (litres/s)	ΔP (bar)	C_V SI	Convergence
MC100a-1	99k	ske; swf	2o; sp	20.02	1.06	19.40	Good
MC100a-2	99k	ske; swf	quick; 2op	50.61	6.86	19.32	Good
MC100a-3	99k	ske; swf	quick; sp	120.75	39.41	19.23	Osc
MC36a-1	180k	ske; swf	2o; sp	15.41	3.03	8.85	Fair
MC36b-1	267k	ske; swf	2o; sp	15.41	2.96	8.96	Osc
MC36b-2	267k	ske; swf	2o; sp	120.75	180.78	8.98	Good OS
MC36c-1	359k	ske; swf	2o; sp	6.13	0.54	8.31	Good
MC36c-2	359k	ske; swf	2o; sp	120.58	206.00	8.40	Osc
MC81a-1	399k	ske; swf	quick; sp	18.08	1.07	17.50	Poor Osc
MC81a-2	399k	ske; swf	2o; sp	120.75	46.85	17.64	Poor Osc
MC36Ra-1	458k	ske; swf	2o; sp	120.75	212.09	8.29	Fair
MC36Ra-2	458k	ske; swf	2o; sp	85.38	106.17	8.29	Osc
MC36Rb-1	470k	ske; swf	2o; sp	85.38	109.75	8.15	Osc
MC36Rc-1	482k	ske; swf	2o; sp	85.38	111.03	8.10	Fair Osc
MC36Ra-3	458k	ske; swf	2o; sp	6.14	0.56	8.22	Fair
MC68a-1	225k	ske; swf	2o; sp	120.75	66.46	14.81	Poor Osc
MC68a-2	225k	ske; swf	2o; sp	6.14	0.17	14.72	Poor Osc

Table 9.3 Comparison of predicted and experimental results for three inch (76.2 mm) choke.

Model	CFD Flow (litres/s)	Exp. Flow (litres/s)	ΔP CFD (bar)	ΔP Exp. (bar)	% Diff.	Cv CFD SI	Cv Exp SI	% Diff
MC100a-1	20.02	20.02	1.06	1.04	2.43	19.40	19.65	-1.25
MC100a-2	50.61	50.61	6.86	6.70	2.46	19.32	19.55	-1.21
MC100a-3	120.75		39.41			19.23	19.71	-2.40
MC36a-1	15.41	15.41	3.03	2.25	34.82	8.85	10.28	-13.87
MC36b-1	15.41	15.41	2.96	2.25	31.82	8.96	10.28	-12.90
MC36b-2	120.75		180.78			8.98	10.28	-12.65
MC36c-1	6.13		0.54			8.31	10.28	-19.16
MC36c-2	120.58		206.00			8.40	10.28	-18.28
MC81a-1	18.08	18.08	1.07	1.09	-1.71	17.50	17.34	0.90
MC81a-2	120.75		46.85			17.64	17.39	1.43
MC36Ra-1	120.75		212.09			8.29	10.28	-19.35
MC36Ra-2	85.38		106.17			8.29	10.28	-19.40

Model	CFD Flow (litres/s)	Exp. Flow (litres/s)	ΔP CFD (bar)	ΔP Exp. (bar)	% Diff.	Cv CFD SI	Cv Exp SI	% Diff
MC36Rb-1	85.38		109.75			8.15	10.28	-20.73
MC36Rc-1	85.38		111.03			8.10	10.28	-21.19
MC36Ra-3	6.14		0.56			8.22	10.28	-20.05
MC68a-1	120.75		66.46			14.81	15.63*	-5.26
MC68a-2	6.14		0.17			14.72	15.63*	-5.81

* These are interpolated C_V values.

9.3.2 Flow visualisation

As in the restrictor work, the use of CFD enables visualisation of the flow behaviour at all points within the geometry of interest. Understanding the flowfield within a choke valve is somewhat more complicated, but is likely to be of significant interest to the valve manufacturer. Some space will therefore be devoted to exploring the fluid flow field in more detail.

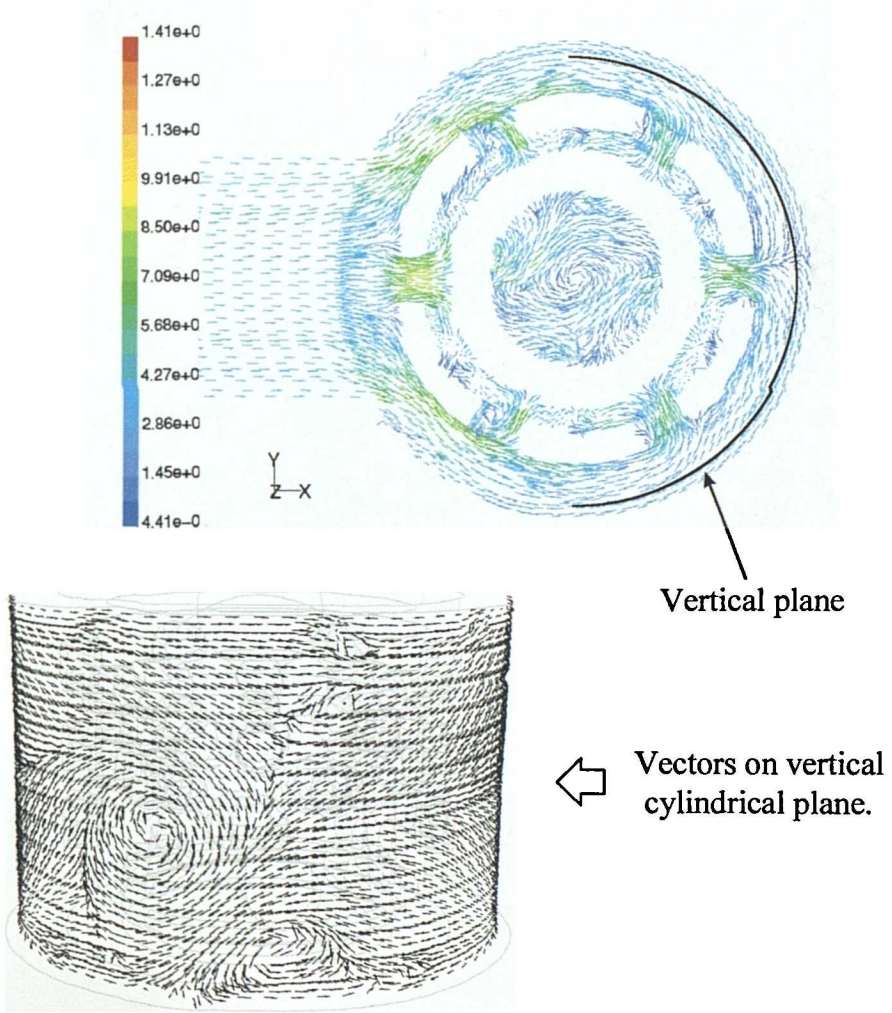

Figure 9.7 Velocity vectors on planes in gallery for case MC100a-1.

9.3.2.1 Flow around gallery

The first change a fluid will experience on passing through the valve will be the deflection caused by the cage, and subsequent movement round the gallery. Figure 9.7 shows some velocity vectors plots from case MC100a-1 for a horizontal plane passing through the second row of cage holes from the top, and a vertical plane located in the rear of the gallery. Visualising three-dimensional flow is somewhat difficult, but vector plots do give at least some idea of the motion taking place. The horizontal vectors indicate recirculatory motion as the fluid passes through cage holes not directly in line with the flow. This could cause sand impingement on one side of the holes in question. The vertical vector plot suggests that for this case, the flow meeting at the rear of the gallery is not symmetric. This could possibly be a result of incomplete convergence as a similar plot for case MC36a-1 shows symmetric behaviour at the same position (Figure 9.8). Case MC100a-2 (higher flowrate than case MC100a-1) shows a single rotational motion at the rear of the gallery, perhaps confirming the existence of asymmetric flow for the fully open case (Figure 9.8).

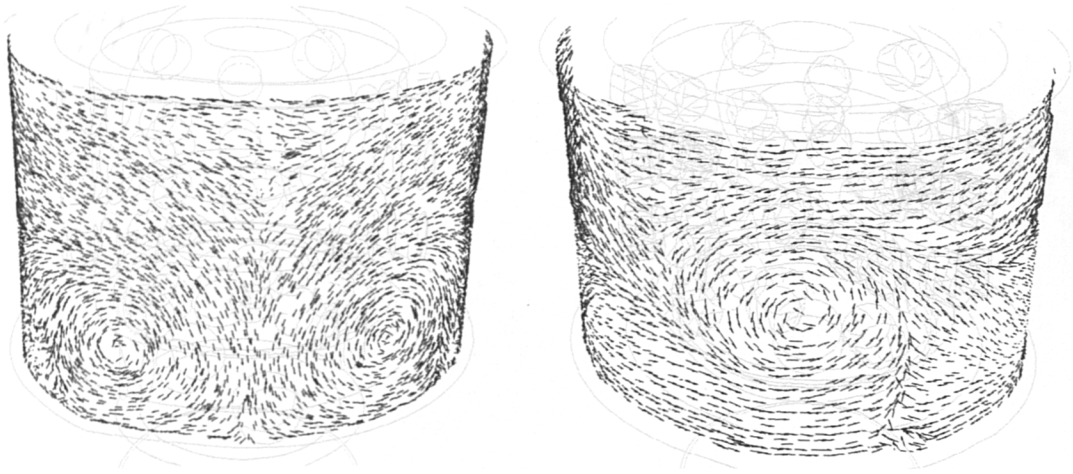

Case MC36a-1 Case MC100a-2

Figure 9.8 Velocity vectors at rear of gallery for cases MC36a-1 and MC100a-2.

9.3.2.2 Flow in gap region, tip holes, and tip inner volume

The gap region of the choke valve proved to be one of the most difficult to mesh in an adequate way. In the 36% open case, it was possible to use unstructured hexahedral cells for the upper portions of the mesh (where the cage holes faced only the blank surface of the stem). Where the cage holes faced some of the tip holes, however, it was necessary to use tetrahedral cells. The main drawback was that some parts of the mesh had only a few cells across the gap

with which to resolve the flow. True flow structure may not have been obtained in all cases attempted.

Figure 9.9 shows velocity vectors on a vertical plane in the gap region of case MC36b-1. This figure clearly shows the complex fluid motions taking place within this region—definitely asymmetric. The positioning of holes within the flow control tip causes the asymmetric flow. A helical pattern is used rather than a symmetrical one. It is not possible to make any sort of statement as to the validity of these velocity field predictions, as experimental data is not available. However, making any sort of meaningful measurements for such a complex flow would be a task of considerable difficulty. The density of velocity vectors is higher at the base of the gap in Figure 9.9 as cells were concentrated more towards this region.

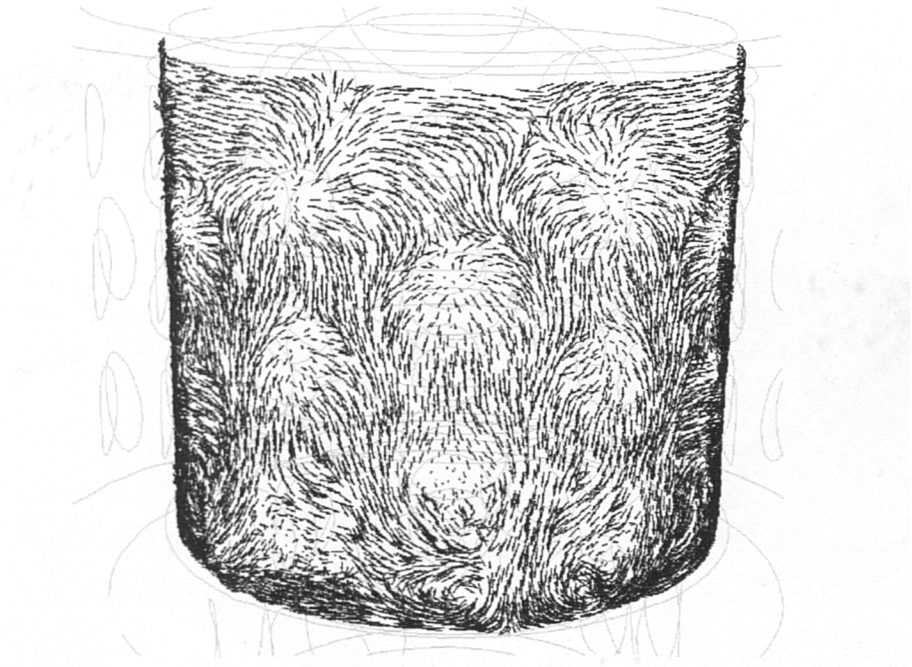

Figure 9.9 Velocity vectors in gap region of case MC36b-1.

Velocity vectors on a horizontal plane cutting through the top row of tip holes for case MC36b-1 is shown in Figure 9.10. The vector colours indicate actual velocity magnitudes. Inlet flowrate for this case was 15.41 litres/s. It is clear that the arrangement of tip holes in relation to the cage holes causes the fluid to rotate in a specific direction within the tip inner volume. For the top row of tip holes at least, there is not the same level of unbalanced flow as was observed before in some of the cage holes. This may mean that erosion in the top row of tip holes will not be as unbalanced as in the cage holes. However, the relative rate of erosion

in the tip holes will be expected to be much higher than that of the cage holes, due to the higher fluid velocities entering the tip.

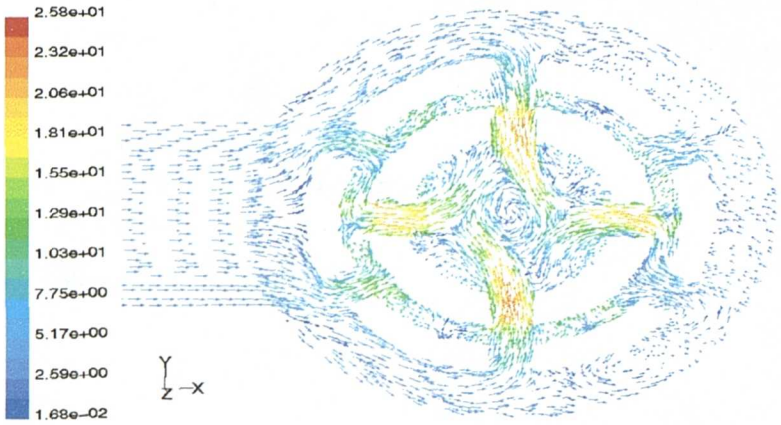

Figure 9.10 Velocity vectors (m/s) on horizontal plane passing through top row of tip holes for case MC36b-1.

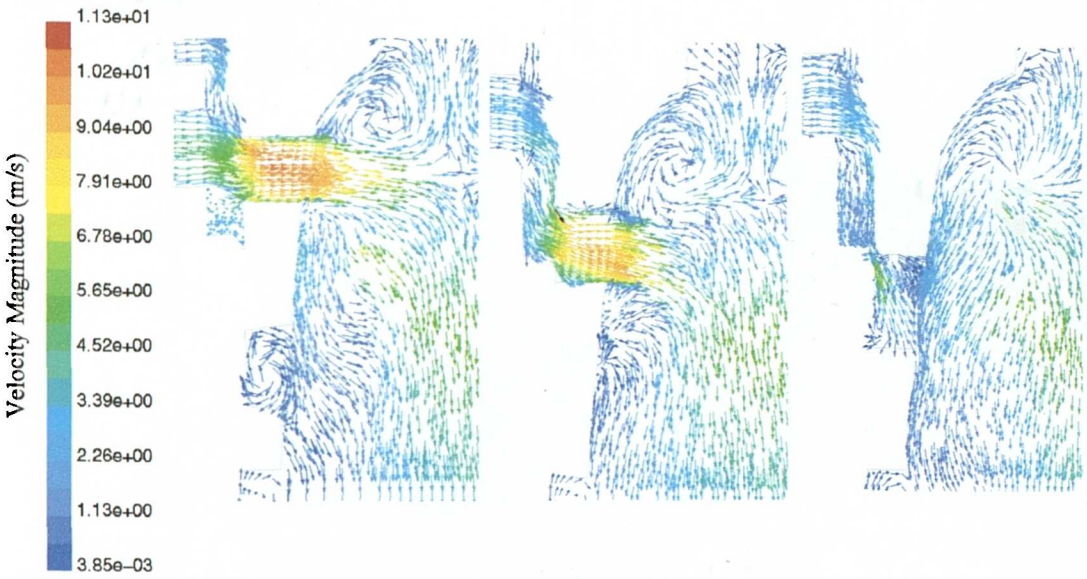

Figure 9.11 Velocity vectors (m/s) on vertical planes passing through centre of tip holes for case MC36c-1 (Flowrate = 6.13 litres/s).

Examination of vertical vector plots on planes passing through the tip holes shows that maximum velocity levels do not necessarily occur at the point where open area is smallest (i.e. fractionally open hole). This may arise when tip holes are almost directly in line with the cage holes at some of the valve positions. Figure 9.11 presents three vector plots from case MC36c-1 showing velocity vectors on vertical planes passing through each of the top three rows of tip holes. The highest velocities are observed in the top and second rows, but not so much in the third row (where the small gap at the top occurs). This suggests that the

fractionally open hole may not have much effect on the overall pressure drop through the valve.

Fluid movement within the tip itself is characterised by multiple rotating eddies. In some positions, the arrangement of the tip holes does encourage fluid to rotate in one direction only. Figure 9.12 shows velocity vectors on horizontal planes cutting through the tip inner volume at three different vertical positions for the 36% open case, MC36c-1. The first plane is just above the top row of tip holes, the second is half-way between the second and third row of holes, and the third just cuts through the base of the bottom row of holes. Note that the vectors shown for the third plane indicate the velocity components lying on the plane itself (i.e. not true three-dimensional vectors as in the first two plots. The plots show something of the complex fluid motion that must be taking place within the tip inner volume. It would require more complete modelling methods (such as Large Eddy Simulation) to capture the true fluid behaviour within this region.

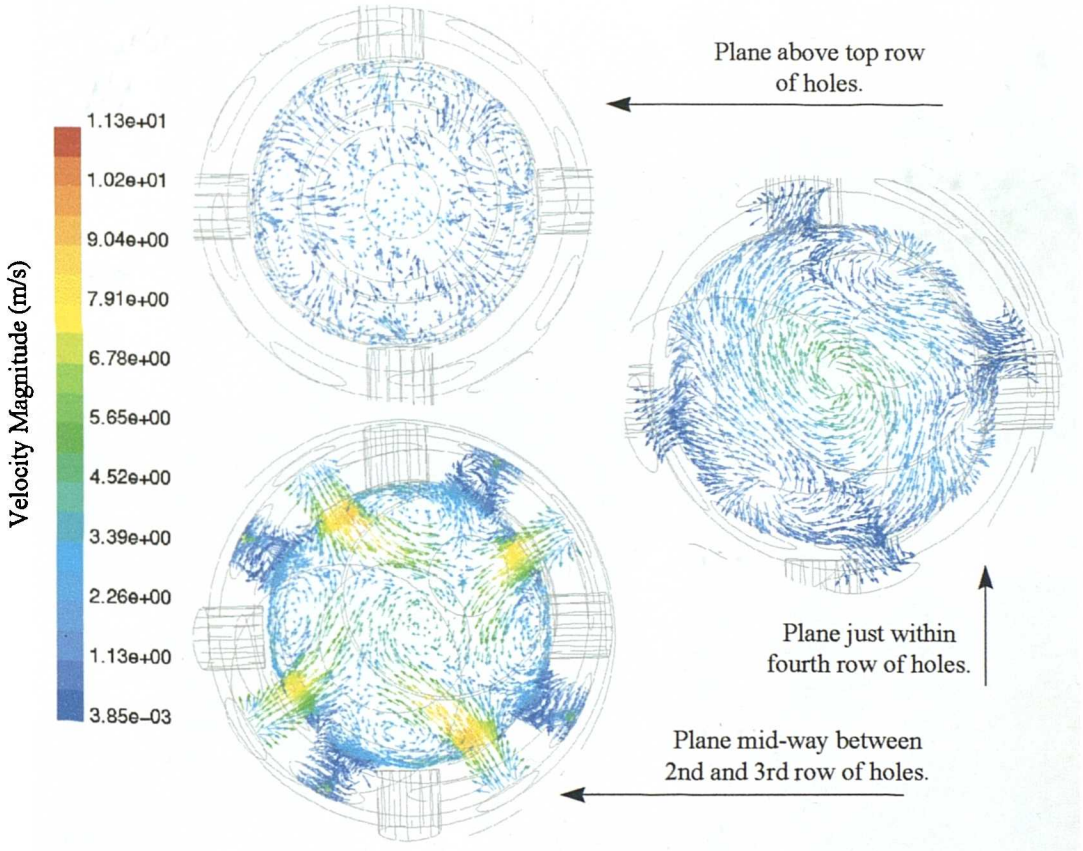

Figure 9.12 Velocity vectors within tip inner volume for case MC36c-1.

9.3.2.3 Flow in the outlet length

In general, a length of pipe six diameters long was added to the outlet of the valve. This was to correspond with the measurement locations in the actual testing. Figure 9.13 presents axial (flow direction) velocity profiles at various intervals along the length of the outlet for case MC36Ra-3. There are just under 11 pipe diameters of length from the base of the tip inner volume to the outlet boundary of the CFD model. Figure 9.13 indicates very little change between the axial velocity profile at 4 D_P and at the outlet (almost 11 D_P). This suggests that for the axial velocity at least, there has been sufficient length specified in the outlet.

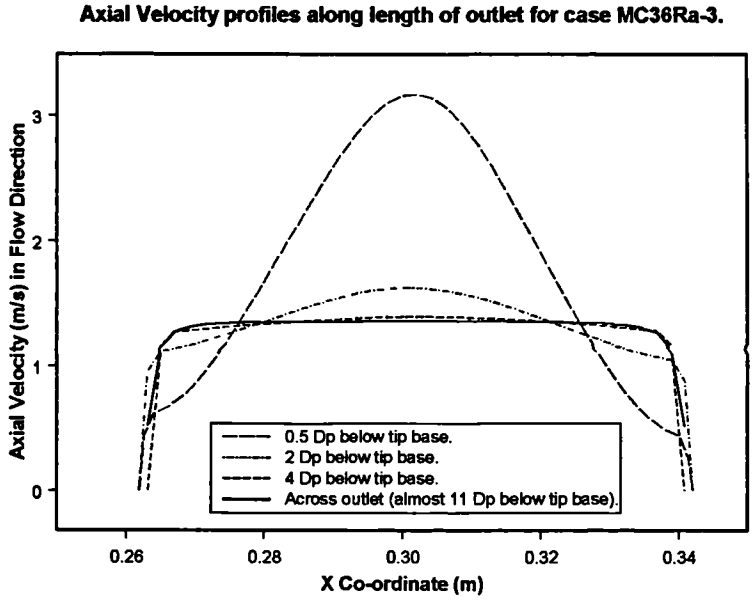

Figure 9.13 Axial velocity profiles along length of outlet for case MC36Ra-3.

Turbulent kinetic energy profiles along the outlet are plotted in Figure 9.14. This indicates a considerable reduction in the energy level from the base of the tip to the outlet. It is unlikely that the standard k-ε model will have predicted the energy levels correctly, as the velocity vector plots have given evidence of highly anisotropic flow within the tip inner volume. Figure 9.15 compares the inlet and outlet turbulent kinetic energy profiles—showing that even with over 10 pipe diameters length after the base of the tip, the profile has not recovered its fully developed form.

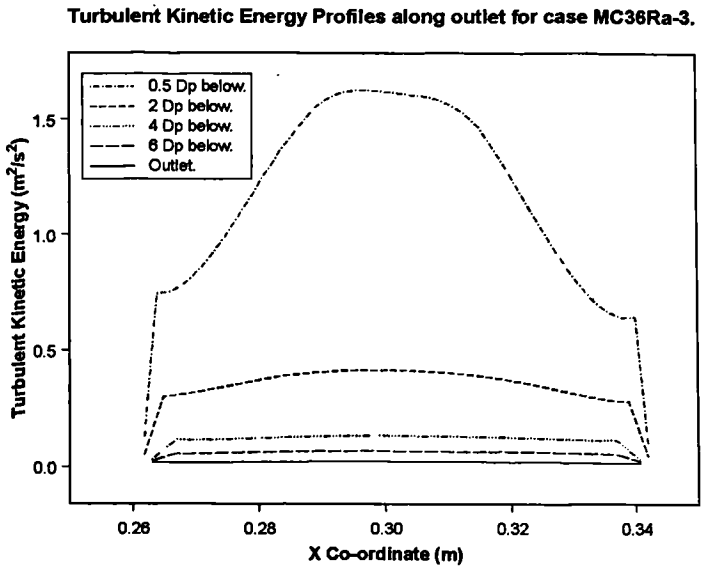

Figure 9.14 Turbulent kinetic energy on X axis at various positions along outlet of case MC36Ra-3.

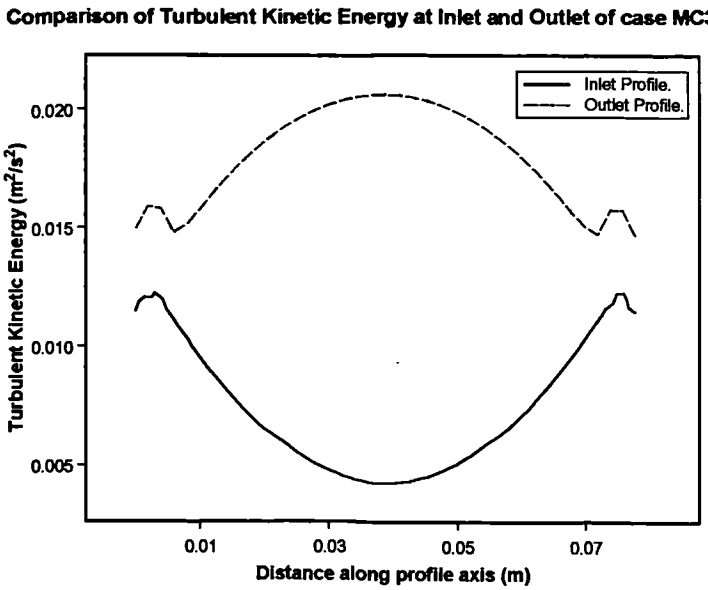

Figure 9.15 Profiles of turbulent kinetic energy at inlet and outlet of case MC36Ra-3.

The three-dimensional motions taking place within the choke valve are perhaps best described through pathlines released from various points throughout the valve. While visualisation in this way is fine on the computer screen (where the model can be rotated and re-sized as desired), it is not so useful (for such complex geometry) for visualisation on paper.

9.3 Comparison of Turbulent Kinetic Energy Profiles in Tip

Some idea of grid sensitivity can be obtained by comparing normalised profiles of turbulent kinetic energy along the same horizontal line in the flow tip. Figure 9.16 shows this comparison for cases MC36a-1, MC36b-1, MC36b-2, and MC36c-2. The profiles have been normalised, as the same flowrate has not been used in all cases. Reasonably good comparison is observed between the profiles obtained using meshes MC36a and MC36b. When using mesh MC36c, there is a distinct change in the profile in the centre region of the tip, although it is fairly consistent with the other profiles elsewhere. Out of the three meshes, mesh MC36c has the greatest number of cells, which suggests that the flow should be better resolved for this mesh than for the others. However, it is difficult to draw definite conclusions from these profile comparisons, as complete convergence was not obtained in all cases.

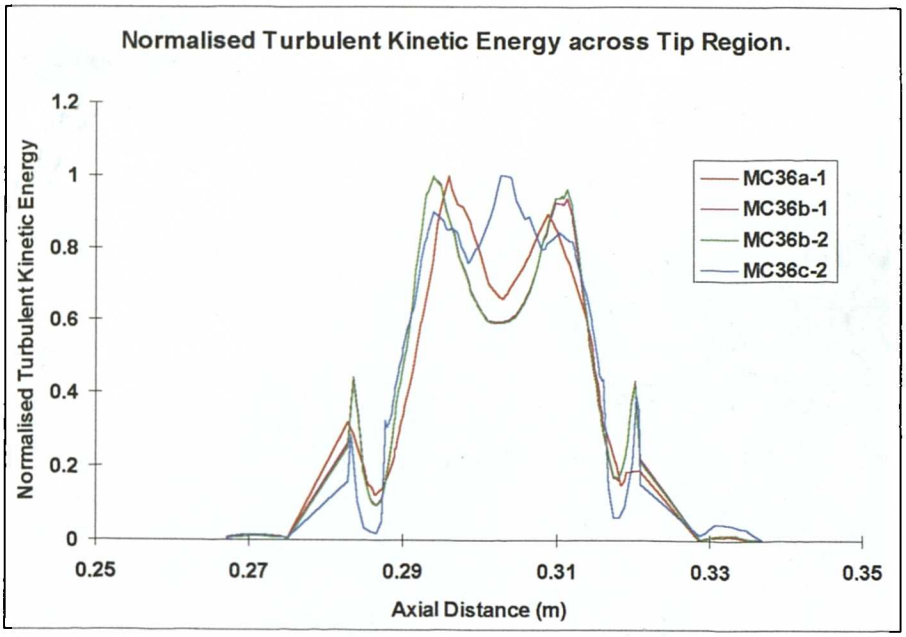

Figure 9.16 Profiles of normalised turbulent kinetic energy inside flow control tip.

9.4 Summary to chapter

This chapter has explored the modelling of single phase flow through choke valves. By comparing predicted results against measured test results, it has been shown that the accuracy of CFD predictions varies with the valve open area. Good agreement was obtained for cases where the valve was 100 % or 81 % open, but as the valve approached more fully closed positions, the agreement was not so good.

The angular position of the flow control tip within the valve has a definite effect on pressure drop. As the actual positions were not recorded during the test procedure, it was not possible to reproduce the exact geometry seen by the test fluid. Rotating the flow control tip by 15^0 in the 36% open position produced a general increase in the difference between predicted and measured C_V.

This work has shown that the computational mesh has an effect on the accuracy of predictions (depending on the valve position). It has not been possible to perform a conventional grid sensitivity study for the choke valve, as the computational resources available could only allow for a mesh of up to approximately 500,000 cells. It is likely that insufficient numbers of cells were specified in the choke valve to fully resolve all the important features of the flow. Flow within the gap region in particular is affected by inadequate meshing, as the narrow circumferential gap does not lend itself to easy meshing. Cells in the upper region of this gap (when valve was partially closed) tended to be wide and thin (high aspect ratio).

In some valve positions, residuals plotted during the solution process did not approach steady state values as desired, but oscillated about some mean level. Solutions for the valve at 81% and 68.1% positions had this problem in particular. This again indicates insufficient numbers of cells in the computational domain. Some level of oscillation was seen in the residual plots of almost all the solutions obtained. The oscillations could also suggest transient phenomena, but a transient run on one model indicated that a purely numerical cause was more likely.

No successful solutions have been obtained with a turbulence model other than the standard k-ε model. Some attempts were made to use the RNG k-ε model, but these failed to converge. Likewise, an attempt to use the Reynolds Stress model at the 36% position did not come to a converged solution.

It is likely that over two million cells would be required to successfully model the three inch choke valve in its various positions. While creating the mesh might not be any more time consuming than it was in this study, the time to solve the model would be vastly increased unless several processors could be used in a parallel solution. In this study, typical solution time ranged from 16 hours to well over 36 hours—depending on the number of cells and quality of the mesh. Some cases were continued for several days to see whether a converged solution would result or not.

The three inch valve has not been modelled under abrasive flow conditions as no actual test data is available with which to compare predictions. However, another choke valve of similar design (albeit with fewer holes in the flow cage) has been tested under controlled (abrasive flow) conditions, and the results of this testing will be compared with CFD based erosion predictions—in the following chapter.

10.0 Modelling of both single phase flow and erosion in a choke valve

The final stage in this project has been to apply the CFD-based erosion modelling technique to a complex geometry: the Multi Orifice Sleeve choke valve. As the whole aim of the project has been to assess the usefulness of CFD-based techniques in predicting erosion of such valves, it will be appropriate to consider the simulation in some detail. Results from an abrasive flow test (carried out in the UK by a major oil company) on a MOS choke valve have been made available, and these will be used to provide validation data for the CFD technique.

10.1 Choke valve geometry and computational mesh

A cross-section view of the choke valve to be considered in this chapter is presented in Figure 10.1. The basic design of the valve is similar to those of the previous chapter, but here there are not so many holes in the flow cage, and the dimensions are smaller. The choke has a nominal 1 inch (25.4 mm) equivalent diameter (based on area available to the flow through the tip).

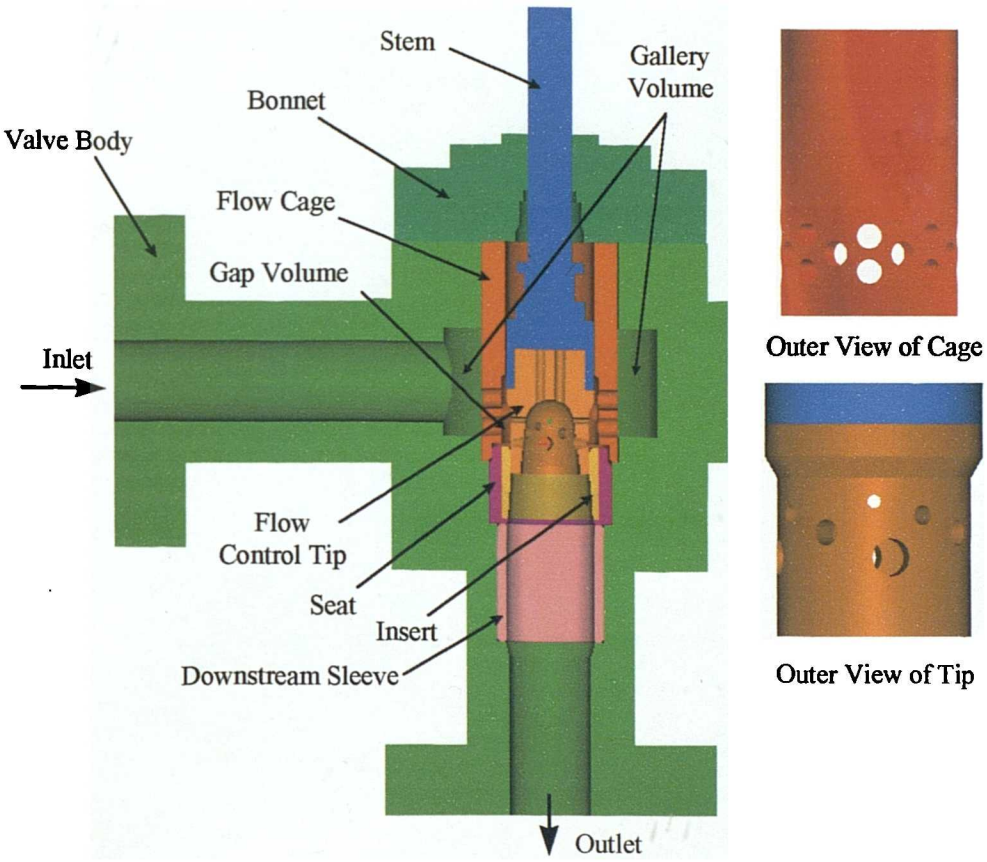

Figure 10.1 Cross-sectional view of choke valve.

This valve has been modelled in the position chosen for actual testing—around 50% open (33/64ths position). When the valve is in this position, the bottom row tip holes are completely covered, the third row of tip holes is almost fully closed (a fraction of open area remains), and the second row of tip holes is almost fully open. Figure 10.2 shows this more clearly. The orientation of the tip during testing has not been taken into account.

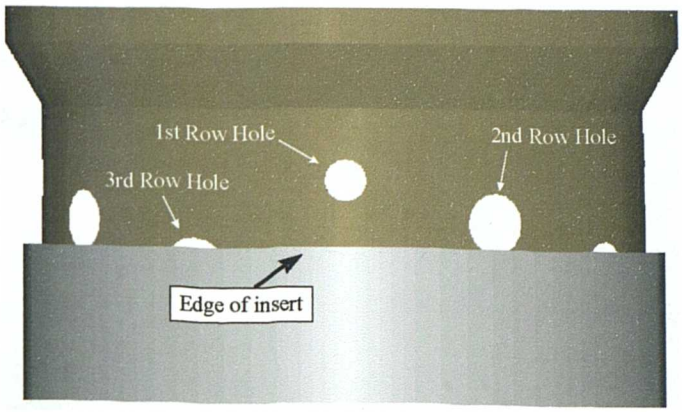

Figure 10.2 Position of tip at 33/64ths.

Only one mesh has been created for the valve at this position. The mesh contains over 586,000 cells, which makes it just within the capability of the available computational resource. Figure 10.3 shows the outside of the inlet and gallery mesh—a tetrahedral transition section has been used to join the hexahedral inlet and gallery regions. A cross-section through part of the gallery, cage hole and gap volume has also been shown to highlight the way in which the mesh has been constructed. The tetrahedral face on the lower half of the gallery inner wall (where the cage holes come through) has been extruded outwards to form wedge shaped cells in the lower half of the gallery volume. The upper half of the gallery mesh has also been formed by the extrusion (Cooper) process—with a paved hexahedral mesh being extruded to form true hexahedral cells on the upper half of the gallery. Having larger cells in the upper half of the gallery should not affect the flow solution adversely, as flow is only moving around the outside of the cage in this upper region. A greater density of cells is required in the lower half as flow is turning into the holes of the cage.

The gap volume is formed from a combination of hexahedral cells in the upper portion, and unstructured tetrahedral cells in the lower portion (where the top holes enter the volume). Quadrilateral paved cells have been used on some surfaces in the tetrahedral region—pyramid cells will be formed on these faces to enable tetrahedral volume meshing. Figure 10.4 shows the mesh used for the gap volume.

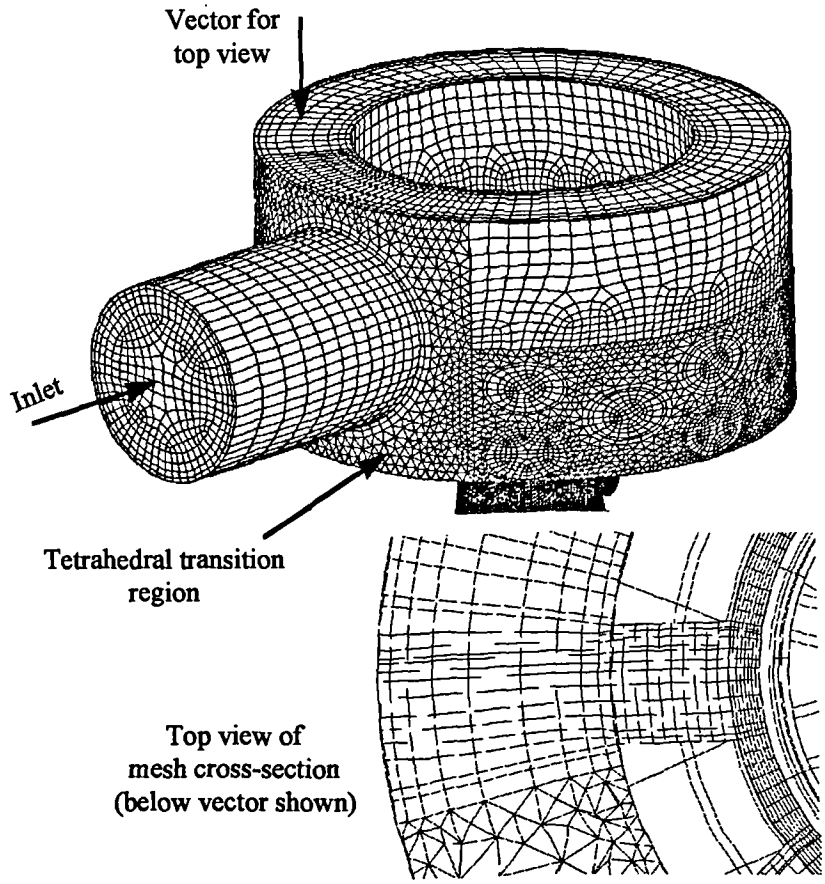

Figure 10.3 Inlet and gallery sections of choke valve mesh.

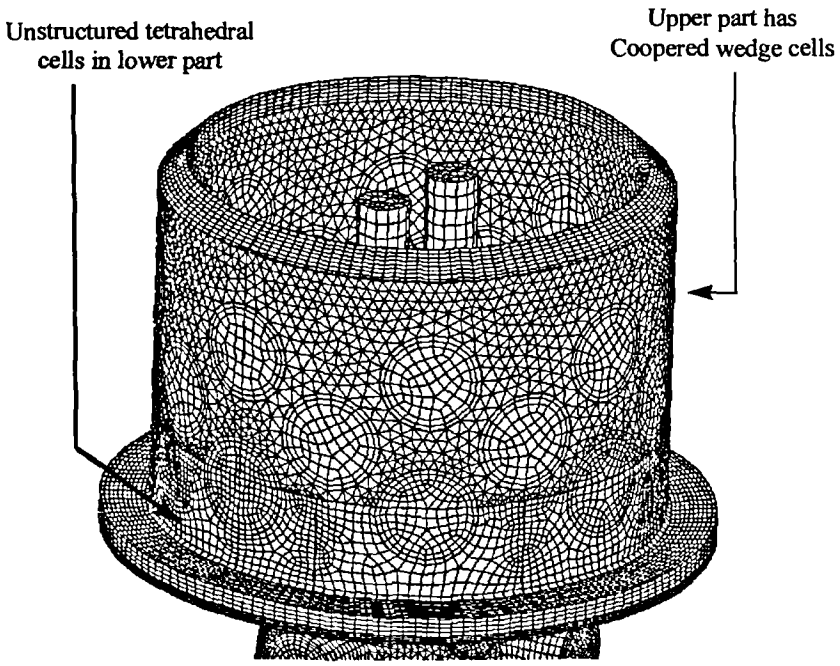

Figure 10.4 Mesh in gap volume of choke valve.

Tip holes have been meshed with wedge or hexahedral cells in general, and a combination of tetrahedral and hexahedral cells has been used in the tip inner volume. A cylinder meshed with true hexahedral cells forms the innermost core of the tip inner volume—this being surrounded by unstructured tetrahedral cells from the core to the outer wall. Tetrahedral cells surround all sides of this hexahedral core (including the region from the base of the hexahedral core to the top of the outlet section). Figure 10.5 depicts these features.

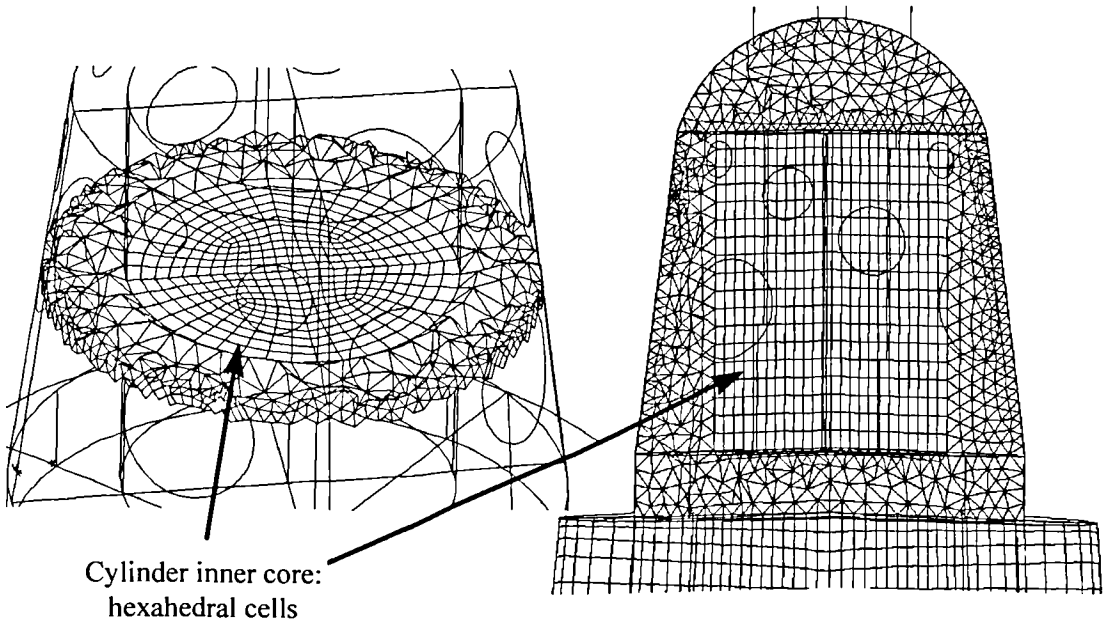

Figure 10.5 Meshing arrangement for tip inner volume.

The outlet section of this mesh extends for 10 pipe diameters beyond the actual valve exit. A hexahedral mesh was formed in the same way as the cylindrical core of the tip inner volume—by splitting the circular cross-section into quarters, and meshing each quarter with a quadrilateral 'tri-primitive' mesh. This face is swept in the vertical direction to create a hexahedral volume mesh. Figure 10.6 shows the mesh at the very outlet of the computational domain.

Although only one mesh has been presented here, several meshes were created prior to this final one, in order to produce as high quality a mesh as possible with the resources available. One of the aims was to maximise the proportion of hexahedral or wedge cells in the mesh, as Figures 10.3 to 10.5 show. This should help minimise numerical diffusion and obtain a more accurate solution.

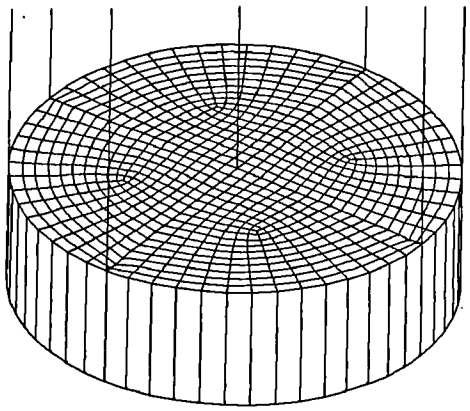

Figure 10.6 Cross section of mesh at the outlet.

10.2 Single phase flow modelling

10.2.1 Test conditions

In the actual valve testing, the valve was mounted in a test facility that consisted essentially of a 100 mm diameter pipe loop within which the test valves were mounted, and through which water and sand slurry was circulated using a diesel driven triplex pump. Although the main test loop used 100 mm pipework, the valve was placed in a section giving 0.5 m upstream and 1.14 m downstream of 50 mm diameter pipework. This matches the inlet and outlet diameters of the choke valve (52.3 mm). The following conditions applied to the abrasive flow test considered here:-

Inlet Pressure:	89 barg
Outlet Pressure:	34 barg
Flow Rate:	7.934 kg/s (126 US gal/min)
Sand Content:	0.89% by mass
Test duration:	6 hours
Sand type and size:	Redland 30 with average diameter 440 μm.

As no specific single phase flow tests were carried out for this valve, it will be necessary to compare the single phase CFD simulation with the above measurements. The uncertainty of the above measurements is not known.

10.2.2 CFD solutions

Two CFD solutions have been obtained for this valve. Both cases use the standard k-ε turbulence model. The first case uses standard wall functions, and the second case uses non-equilibrium wall functions. Table 10.1 presents the relevant results from the flow solutions

(and compares them to the measured values). Second order upwind discretisation was used for the momentum and turbulence properties, and the standard interpolation scheme for pressure. Inlet boundary conditions were calculated from a periodic model of pipe flow at the required flowrate (giving fully developed flow profiles). The same mesh has been used in both cases.

Table 10.1 Results from choke valve modelling.

Case	CFD $\dot{Q}_w$ (litres/s)	Test $\dot{Q}_w$ (litres/s)	ΔP_{CFD} (bar)	ΔP_{EXP} (bar)	ΔP % dif.	C_V CFD	C_V Exp	C_V % dif.
1	7.95	7.95	47.9	55.0	-12.93	1.15	1.07	7.17
2	7.95	7.95	49.4	55.0	-10.12	1.13	1.07	5.48

These results would indicate that case 2, where non-equilibrium wall functions were used, gives a better prediction of valve pressure drop than case 1. The non-equilibrium functions relax the constraint that turbulent kinetic energy and its dissipation rate must be equal at the wall. The error in pressure drop prediction from the above table is around 13% of the experimental value for case 1. However, the true difference between predicted and measured values cannot be known, as the uncertainty inherent in the test measurements has not been reported. Uncertainty in pressure drop figures could be around 2 or 3% of reading, and similarly for the test flowrate measurement.

10.2.3 Predicted flow structure

Fluid velocities for this simulation were found to be significantly higher than those experienced in the restrictor simulations. Figure 10.7 presents velocity vectors on vertical planes passing through the tip holes having any open area for the flow (i.e. top three rows). The maximum velocities are around 107 m/s, which is significantly higher than that observed in the restrictor models (around 30 to 40 m/s). There is rapid acceleration of the fluid between the gap region and the holes: this will mean that a significant proportion of the valve energy loss takes place as the fluid passes through the tip holes.

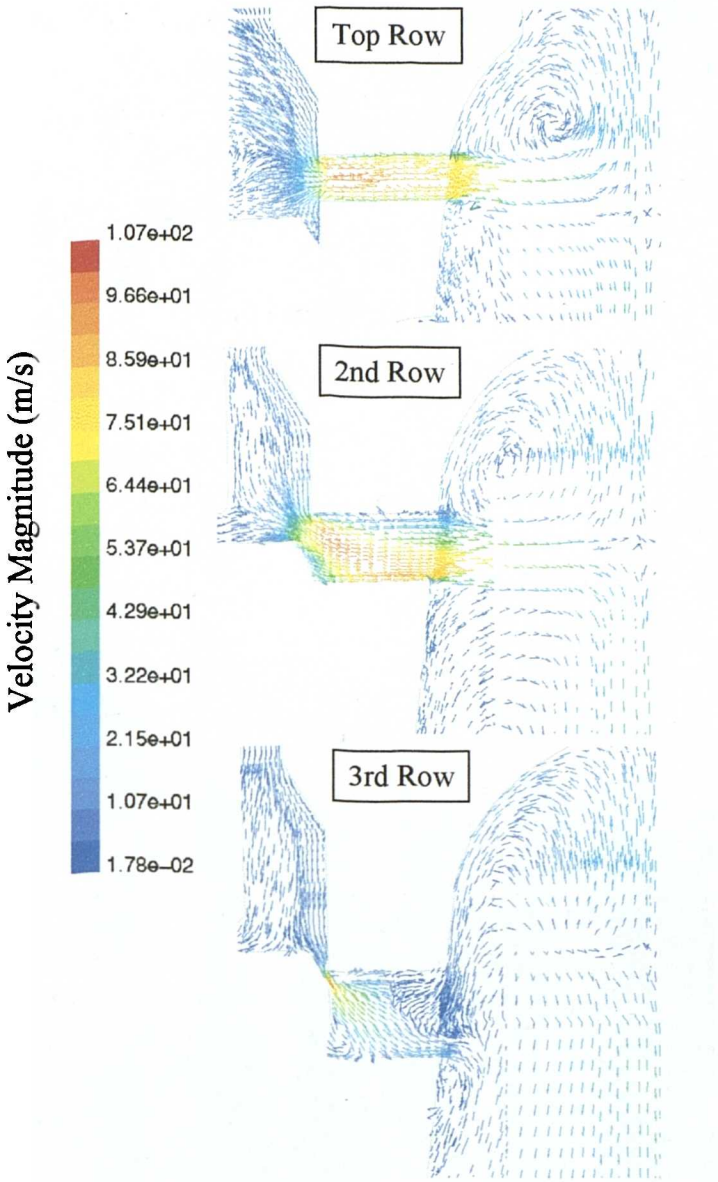

Figure 10.7 Velocity vectors on vertical planes passing through tip holes.

10.2.4 Static pressure loss

The rapid fluid acceleration through the tip holes causes significant energy loss. It would appear that most of the pressure loss occurs across the first two rows of tip holes, as indicated by Figure 10.8. This figure shows the absolute static pressure (based on a downstream pressure of 34 barg) on all walls of the gap region, tip holes, and tip inner volume. Some localised cavitation may take place within this valve, as the predicted minimum (numerical) absolute static pressure is well below zero (even with 34 barg outlet pressure). This suggests that some of the material loss in the tip holes could be a result of cavitation phenomena in addition to solid particle erosion. Having such a large proportion of the total

pressure drop across the tip holes must contribute to erosion damage. There does not appear to be any significant pressure loss across the holes of the flow cage, which could raise questions as to the necessity of the flow cage at all.

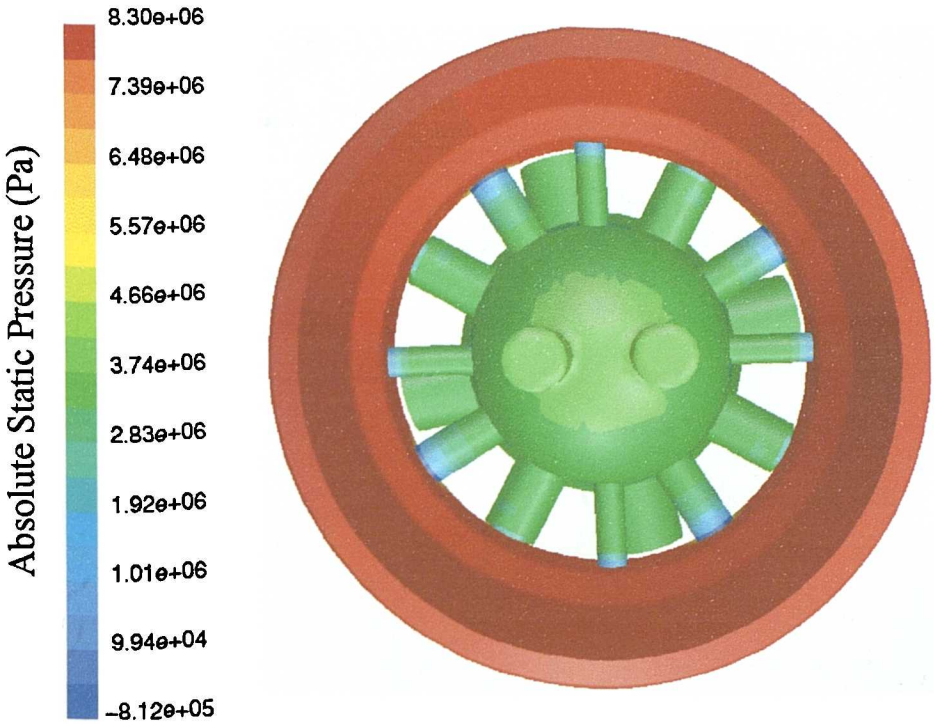

Figure 10.8 Absolute static pressure on surfaces of gap region, tip holes, and tip inner volume.

10.3 Erosion modelling

In the valve testing, two sets of choke trim material were considered (i.e. two different grades of tungsten carbide were used in two separate tests). The test conditions given earlier apply to the case where a tungsten carbide similar to Tungsten Carbide DC(Z)05 was used for the trim components. This tungsten carbide will be referred to as 'Trim 1'. The other valve test (which had very similar test conditions to that being considered) used a tungsten carbide closer to Tungsten Carbide SMS-25A of Chapter 3. Components in this second test will be referred to as 'Trim 2'. UDFs for all three tungsten carbide materials considered in Chapter 3 will be applied in erosion modelling, but predictions made using the equations for Tungsten Carbide SMS-25A will be compared against the mass loss measurements from the second test using Trim 2.

The actual conditions for the testing to be considered here are as given in section 10.2.1. For the simulation, sand particle diameter was set to the average specified diameter for the sand used in testing: a diameter of 440 μm. Sand density was taken to be 2668 kg/m^3, as it came from the same source as that used in the erosion testing described in Chapter 3. Sand particle inlet velocity was set to be the average fluid inlet velocity (3.64 m/s); mass concentration was 0.89% (resulting in a particle mass flowrate of 0.07062 kg/s for a water flowrate of 7.9342 kg/s). Step length factor was set to 15, rebound equation set R5 of Table 8.1 was used on all solid surfaces, and a maximum number of 40,000 time steps was permitted. 84,000 particle trajectories were obtained for each simulation. The effects of gravity were not considered in all simulations: this will be discussed in more detail shortly.

As the choke valve consists of several different materials, it was necessary to repeat the particle tracking for each different material type required. This is because specific material types cannot be attached to different surfaces with the present User Defined Functions. It would be possible to do this for each computational mesh, but to do so would be time consuming if several different models were being considered (e.g. different valve open positions). The same expressions for restitution coefficient (set R5 of Table 8.1) were used throughout. If different materials had been accounted for in a single simulation, then appropriate expressions could have been used for each material (had suitable expressions been available for all the materials considered). This would further ensure the correct particle paths were obtained.

10.3.1 Predictions of mass loss

10.3.1.1 Gravity off

Table 10.2 compares predicted mass loss with the measured mass loss for key components within the valve when the effects of gravitational acceleration are not accounted for in the particle tracking. The User Defined Functions used in doing so are identified.

It is obvious from Table 10.2 that CFD predictions of mass loss are considerably different from the measurements. Predictions for erosion of tungsten carbide are lower than the actual measurements by more than an order of magnitude. The tip material in actual testing was a tungsten carbide similar to that to which the UDF 'M_tcC_3d_1' corresponds. This was also used for the seat insert. 17.4 PH 105k was used for the stem, seat, and flow cage. Predictions for the seat (part of which is tungsten carbide) using 'M_ph105k' UDF are closer to the measured value, but it is not known what proportion of the mass loss came from

the tungsten carbide insert, and what came from the seat. The downstream sleeve in the valve was not made from 17.4PH 105k stainless steel—so there will be some error as a result of UDF not corresponding to the correct material.

Table 10.2 Comparisons between measurements and predictions.

Component	UDF	Measured (g)	Predicted (g)	% Difference
Tip 1	M_tcC_3d_1	2.9	0.143	-95.1
Seat 1	M_tcC_3d_1	0.5	0.011	-97.8
Seat 1	M_ph105k	0.5	2.357	371.4
Outlet* 1	M_ph105k	3.36	0.264	-92.1
Tip 2	M_tcA_2d_3	8.2	1.186	-85.5
Seat 2	M_tcA_2d_3	1.3	0.0876	-93.3

*Measured value is for downstream sleeve plus an additional sleeve in the outlet pipe section (length not known); prediction is for whole length of outlet (plus pipe). Assume most erosion will occur in the downstream sleeve.

Figure 10.10 shows the predicted mass loss in and around the top tip hole directly in line with the inlet. This hole appears to receive most erosion damage of all the top row tip holes, which is possibly a consequence of it being in line with the valve inlet. There will be a fairly direct path from the inlet flow to this particular tip hole. Externally this hole will be rounded at its entrance. Comparison with Figure 10.13 (photographs of actual eroded tip holes) shows that the CFD prediction is similar to what is found in reality. There is a greater level of erosion at the base of the top tip hole in Figure 10.13 than is predicted by the CFD model. This may be a result of not accounting for gravitational acceleration in the CFD model.

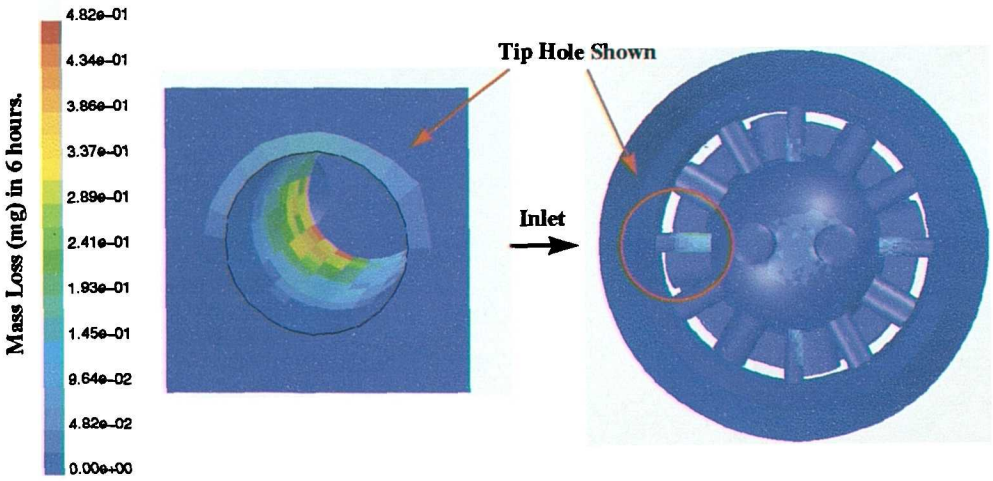

Figure 10.10 Predicted mass loss of top row tip hole (in line with inlet).

Figure 10.11 shows the predicted mass loss for a second row tip hole. There will be significant loss of material in the base of the hole, as well as around the sides of the entrance

to the hole. This is consistent with the actual erosion observed (in Figure 10.13), where there are erosion scars at the sides of the hole (lower half). It is likely that the initial erosion proceeded according to the predicted wear map, and as material loss increased, the fluid flow behaviour was such as to cause 'tear dropping' on the front surface of the tip. There will also have been some gap between the tip outer surface and the insert inner surface (not accounted for in the CFD model) due to finite machining tolerances.

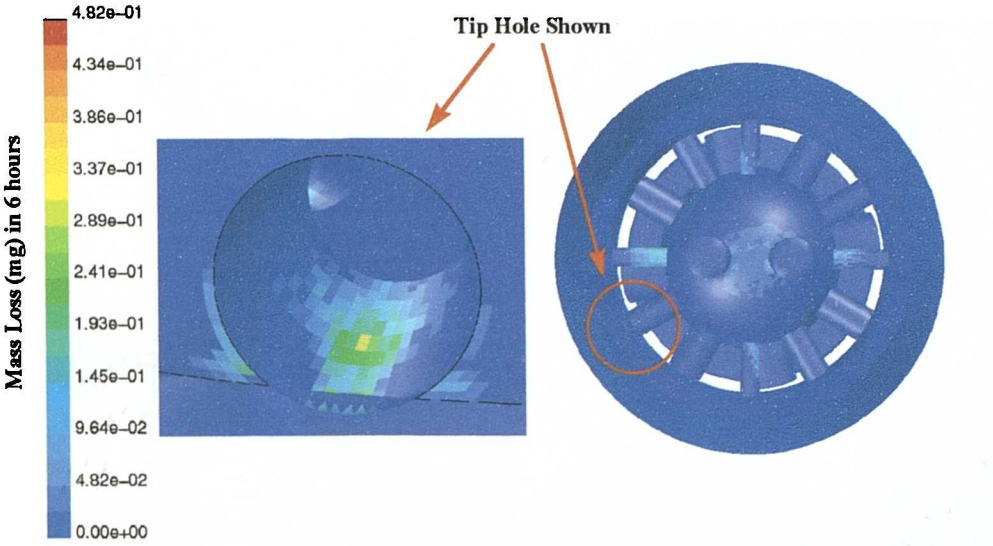

Figure 10.11 Predicted mass loss of 2nd row tip hole (RHS of inlet).

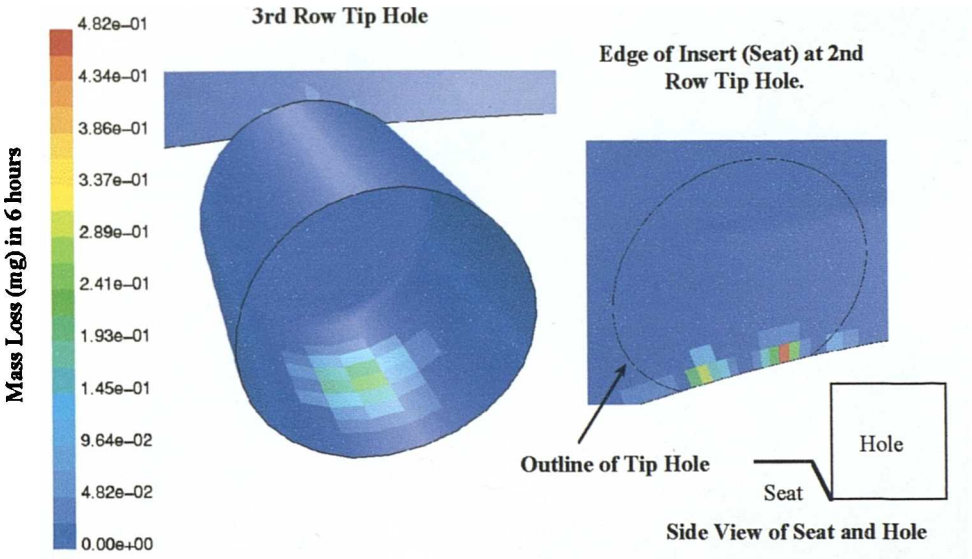

Figure 10.12 Mass loss on 3rd row tip hole, and chamfered edge of the seat insert.

Figure 10.12 shows the predicted mass loss on a third row tip hole, and also on the edge of the insert (seat) at the entrance to a second row tip hole. The viewing position has changed for the third row tip hole in Figure 10.12: the hole is positioned as though viewed

from *inside* the tip inner volume. The edge of the seat can be seen at the outside of the hole. Erosion is predicted at the very base of this hole, at the point where particles will impact after passing through the small gap. Comparing this with Figure 10.13 suggests that the CFD is indeed predicting the initial erosion map, and that as time progresses the action of the fluid (in response to an eroding surface) will be to gouge out material at the front of the hole.

Erosion of the seat and insert is also considered in Figure 10.12, at the point where the edge of the insert meets the entrance to a second row tip hole. A high level of erosion will take place on this point, which will cause fluid to jet down into the second row tip hole—and possibly being the mechanism from which 'tear drop' scars originate.

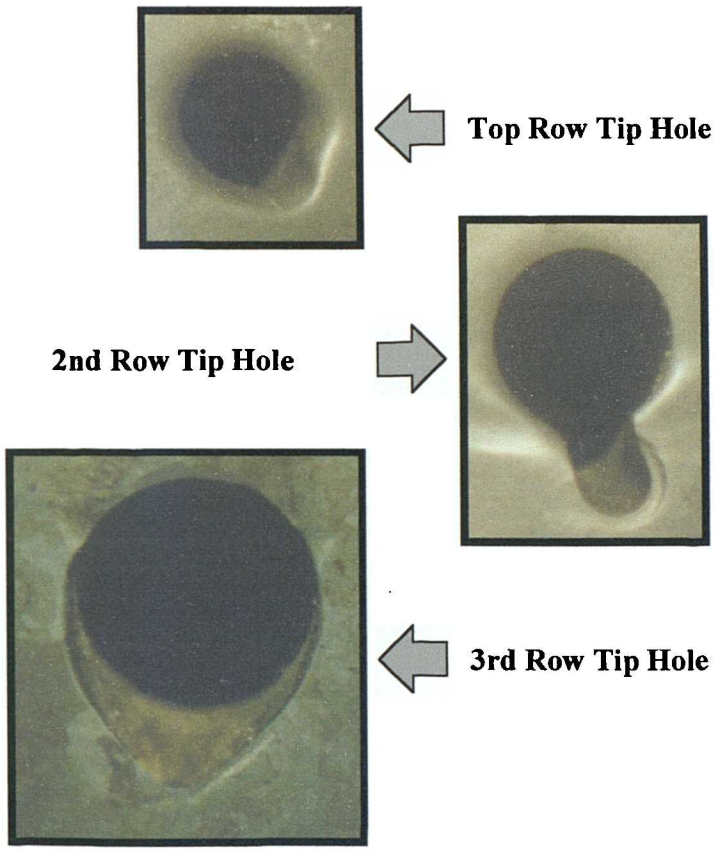

Figure 10.13 Actual erosion on tip holes of tested valves.

10.3.1.2 Gravity on

The initial approach to obtaining solutions with gravitational acceleration activated, was to set the direction of acceleration vertically downwards (i.e. the valve would be in an upright position with the outlet vertically in line with the inlet). However, it was found that a significant proportion of the particle trajectories (around 18%) did not escape from the computational domain. This resulted from certain trajectories becoming 'trapped' in certain

areas of the mesh where predicted flow conditions (in conjunction with downwards gravity) caused particles to recirculate indefinitely. Figure 10.14 shows one location where this type of condition occurred—in one of the fourth row tip holes.

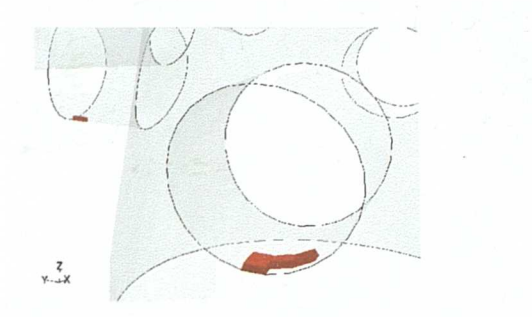

Figure 10.14 Region of large particle impacts (due to infinite trajectories): fourth row tip hole.

This problem did not occur when the direction of gravity was changed to the positive Y axis as shown in Figure 10.15. It is not uncommon for valves like these to be installed in such an orientation—this being the only way possible when inlet and outlet pipes lie on the same horizontal plane. The valve orientation during testing was similar to this, except that the valve was flipped round the other way (so that gravity would act in the opposite direction to that modelled). There should not be any significant effect in specifying gravity to act in the negative Y direction. When gravity was activated in this way, the proportion of trajectories not completing fell to around 3%.

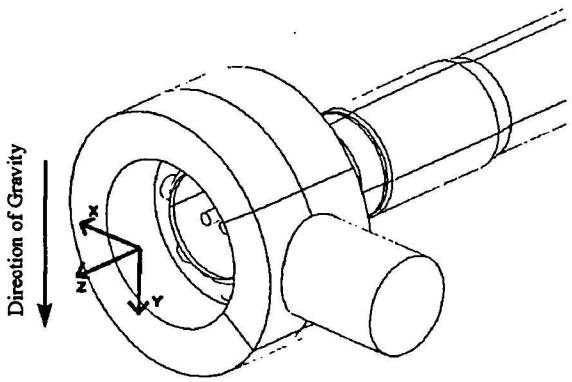

Figure 10.15 Direction of gravitational acceleration.

Predictions of mass loss made with gravitational acceleration activated are shown in Table 10.3. The reason for such high differences between predicted and actual mass loss for the seat is that the area of the seat surface (the insert) receiving most particle impacts is made from tungsten carbide in reality. When the tungsten carbide is replaced by 17.4 PH105k

stainless steel in the CFD model, the same number of particle impacts will result, but as the material is far less erosion resistant than tungsten carbide, the mass loss from it will be much higher. This results in the large overpredictions reported in Tables 10.2 and 10.3 when UDF M_ph105k is used.

Table 10.3 Predictions made with gravity on.

Component	UDF	Measured (g)	Predicted (g)	% Difference
Tip 1	M_tcC_3d_1	2.9	0.1412	-95.1
Seat 1	M_tcC_3d_1	0.5	0.0107	-97.86
Seat 1	M_ph105k	0.5	2.347	369.4
Outlet 1	M_ph105k	3.36	0.267	-92.05
Tip 2	M_tcA_2d_3	8.2	1.173	-85.7
Seat 2	M_tcA_2d_3	1.3	0.0892	-93.1

The differences between measured and predicted erosion in Table 10.3 are not much lower than in Table 10.2, which shows that gravity alone is not responsible for the large uncertainty.

10.3.2 Particle impact angle and velocity

Although the actual magnitude of the predictions are not as close to the measured as would be desired, there is still useful information to be gained from the particle impact properties provided by the erosion modelling function. Particle impact velocities on the flow control tip are shown in Figure 10.16. The top row tip hole is highlight (left hand side) to show the velocities within the bore. Maximum velocities appear towards the end of the hole. A second row tip hole is also highlighted, which again shows higher velocities on the inner side of the hole. This is what would be expected for flow through the holes, as the fluid will obviously accelerate through the hole.

Particle impact angles on the outer surface of the tip are shown in Figure 10.17. The highest angles on the tip surface are observed to be opposite the holes in the cage. There are also fairly high angles of impact on the surface of the seat, which suggests particles are being directed downwards onto the seat by the flow through the cage.

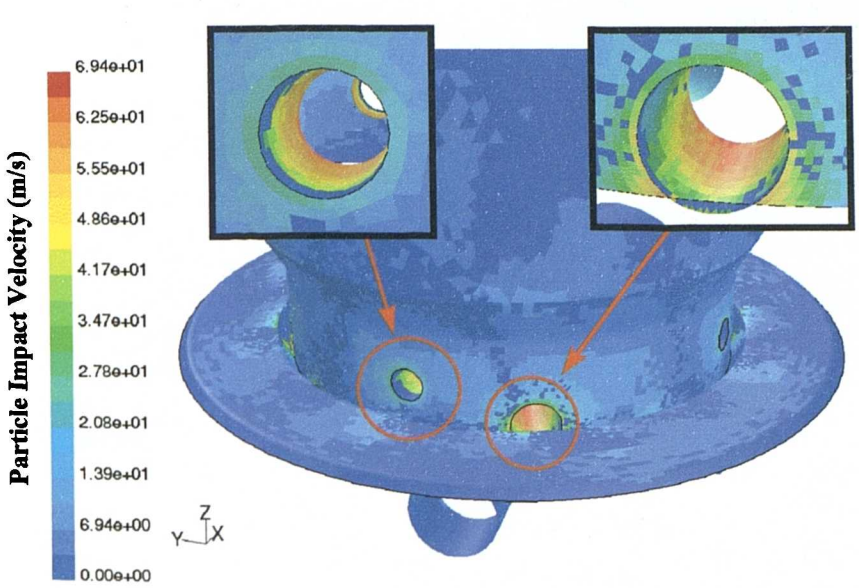

Figure 10.16 Particle impact velocities on tip (two holes highlighted).

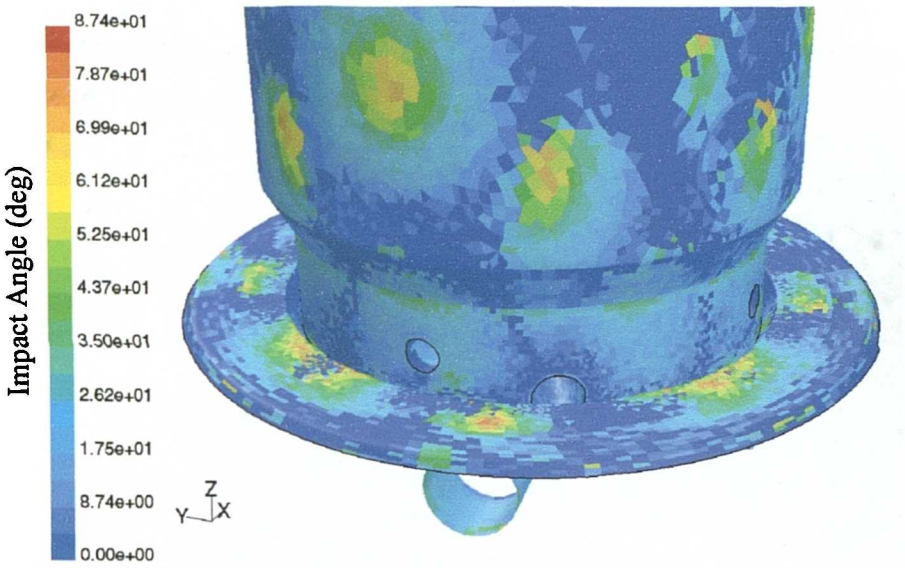

Figure 10.17 Particle impact angles on tip.

10.3.3 Discussion of erosion modelling

The predictions of mass loss for the choke valve considered here do not sufficiently match up with the measurements made for the actual test valve for the method to be used to predict valve lifetime. Predictions do highlight the areas most likely to suffer rapid erosion damage, which is of definite use in choke valve design.

There are several possible reasons for predictions not matching actual measurements. The first is that the erosion functions do not predict mass loss sufficiently well at the higher impact velocities seen by the choke valve. Velocities in the restrictor components were in the

velocity range closer to that used in obtaining slurry erosion data, so that there may have been a better correspondence between conditions used to obtain the equations, and conditions in the component itself. When velocities increase above 30 m/s, or so, the underlying data moves into the range where air-sand erosion data was used in constructing the equations. There may be a fundamental difference between the magnitude of air-sand erosion and liquid-sand erosion at these higher velocities, although there are few studies in the literature where this effect has been examined.

Absolute static pressure predicted by the CFD modelling suggests that localised cavitation could have been present in some of the valve tip holes. The combination of cavitation and erosion would increase the amount of material loss in the tip holes considerably—a factor that would definitely not have been mirrored in the CFD predictions. It would be necessary to develop empirical erosion equations that accounted for wear loss due to both cavitation and particle impact before this additional wear mechanism could be included. Although some testing has been carried out on specific components under such conditions, the author is not aware of any attempt to develop actual predictive equations.

Behaviour of particles close to the surface may also be different in the valve from that predicted by the CFD model. In the CFD technique, particles cannot slide along surfaces to cause abrasive (or sliding) wear—they can only impinge and rebound. Any sliding wear in the actual valve would not therefore be detected by the CFD model.

The geometry of the choke valve is considerably more complex than the restrictor geometry. Particles must follow tortuous paths through holes, sharp turns, and self-impinging jets. It is possible that neglecting some of the forces in the particle equation of motion has made it impossible for the CFD to predict the true trajectory in such a complex flow. There are clearly some deeper issues which need to be addressed besides questioning the validity of the empirical erosion equations.

There are also other parameters affecting the particle tracking that could be considered in more detail. A single particle size of 440 μm was used for all predictions. In the actual testing, periodic measurements of sand size distribution suggested that the true mean particle size was lower than this—although that was partly attributed to the sand sampling method employed. Application of an actual sand size distribution to the particle tracking may return different results from what has already been obtained. Particle rebound equations could also affect the modelling results, especially as the set of equations used here do not necessarily

hold for tungsten carbide—they were said to be applicable to AISI 4130 steel. Unfortunately time ran out in this study to be able to carry out these additional studies, but they would certainly be a useful starting point for further investigations.

10.4 Conclusions

A choke valve has been modelled in a position that corresponds to the position used for an actual abrasive flow test on an identical valve. The CFD prediction of pressure drop corresponds fairly well to the measured pressure drop—the prediction being around 13% higher than the measurement. Examination of the static pressure drop on valve inner surfaces suggests that much of the pressure loss takes place through the holes in the tip.

Predictions of mass loss using the empirical equations of Chapter 4 do not correspond to the actual measurements made during testing. The predicted locations of mass loss are in agreement with the test findings, which does provide some level of validity to the results.

Further work is required to establish whether the real cause of poor mass loss predictions are the empirical erosion equations, or whether the particle tracking algorithm itself needs to be revised. If particle impact velocities are not predicted correctly, there will obviously be a significant impact on the results. The validity of erosion equations based on air-sand erosion test data also needs to be considered.

11.0 Closure

The overall aim of this project was to develop, apply, and validate a method for predicting the location and magnitude of solid particle erosion within simple and complex geometries. Several objectives were determined as being key goals on the way to achieving the overall aim of the project. The extent to which these objectives have been achieved, and the conclusions that result, form the basis for the discussion which now follows.

11.1 Discussion of objectives

11.1.1 Validation of commercial CFD code for simple and complex geometries

Two types of geometry have been considered in the CFD modelling work: simple (restrictor components) and complex (Multi-Orifice Sleeve choke valves). Several CFD models were developed for each type of component, and the predicted results were compared against actual test data relating flowrate through the component to pressure drop across the component. This has given some measure of the ability of a commercial CFD code to predict the correct pressure drop across these types of component.

The most time consuming part of the CFD modelling process is in creating the computational mesh. This will typically take up 60 to 70 % of the overall analysis time, and could mean several hours to several days (or even weeks) depending on the complexity of the geometry. Post-processing results of converged solutions could take around 20 % of the time, depending on the level of detail required from the solution. Actually setting up and running CFD cases is comparatively quick (in terms of man-time), although cases could take several hours (or days) to converge. This running time is not included in the estimated ratios presented here.

The reason for attempting to validate the performance of the CFD code in predicting single phase incompressible flows through components, is that the fluid flow field ultimately determines the path taken by particles within the component. Predicting the correct fluid flow field is essential to predicting true particle trajectories. Had it been possible, the ideal way to validate the single phase CFD predictions would have been to compare predicted velocity fields against actual velocity fields, measured using Laser Doppler Velocimetry or similar techniques. This may be a feasible option for the restrictor geometries considered, but it is most unlikely for the MOS choke valves due to the complexity of their internal geometry. All that has been possible in the present study has been to compare measurements of pressure

drop with CFD predictions at identical flowrates. While this gives some indication as to how well the CFD model can predict the interchange between kinetic and potential energy, it does not provide the quantitative information on velocity fields that would be desired. In most of the solutions obtained, pressure drop is overpredicted. This would suggest that fluid velocities could have been higher than they would be in reality. However, it is unlikely that a 30% overprediction of pressure drop would have meant a similar 30% overprediction of velocity: the ratio will be somewhat lower.

Although the comparisons of predicted to measured pressure drop do not give the level of validation that would ideally be desired for an erosion modelling study, they are very useful for valve manufacturers whose main concern might be to use CFD as an alternative to actual flow testing. CFD predictions of pressure drop for the valley restrictor were closest to the actual measured values. This restrictor was designed to minimise any possible cavitation phenomena thought to be present in some of the earlier restrictor designs. As this restrictor design is the one used for actual production components, the manufacturer can have confidence that the CFD prediction of C_V will be within 6% of the true value (for clean liquid flow).

Further work is required before CFD techniques can be recommended for regular use in predicting pressure drop across MOS choke valves at different stem positions. A far more rigorous validation study is required, in which valves are tested under tightly controlled single phase flow conditions. Positioning of valve components should be carefully noted and recorded before testing, and valve stem travel should be confirmed to correspond to the valve position indicator. Several flowrates should be applied for each valve position, using as high a downstream pressure as is practically possible. Laser Doppler Velocimetry measurements could be obtained for flow downstream of the valve outlet to provide a basis for validating CFD velocity and turbulence predictions. This would be a fairly straightforward undertaking, provided the appropriate LDV equipment could be obtained on loan or otherwise.

Computational resources for modelling MOS choke valves also need to be upgraded before developing further models. The resource available for the present study has been a Personal Computer having Dual Intel Pentium II 400 MHz processors, 512 Mb RAM, and running under Windows NT 4.0 operating system. A more appropriate level of computational resource would be a machine having 2.0 Gb of RAM, four or more processors, and a Unix operating system or similar. This would give the flexibility to create meshes having cells more densely packed in regions of small gaps, as well as allowing longer lengths of downstream

piping after the valve body. If such computational resource was available, there is little doubt that the application of a commercial CFD software package would considerably improve the research and development capability of choke valve manufacturers.

In summary therefore, the validation of a commercial CFD package for simple and complex geometries has been carried out, but not to as great an extent as would be desired for the erosion modelling study. This results from not being able to compare measured fluid velocity profiles against predicted profiles.

11.1.2 Empirical erosion data and equations

Two types of erosion test were carried out on a range of materials commonly used in choke valve manufacture. Material specimens were tested under different velocities and impact angles to build up a map of erosive wear. These results were used in generating empirical equations relating erosion to particle impact velocity and angle.

One of the main uncertainties in the results of the erosion testing arose from the fact that two separate periods of testing were required to cover all of the material types. Repeat erosion testing of similar materials under what should have been identical test conditions gave different results. Several avenues were explored to discover reasons for this anomaly, but none gave conclusive results. It is possible that sand size distributions changed between the two test periods. The need for two separate periods arose from delays in obtaining material specimens in time for the start of the first test period, as well as other problems with the sample holders for the two test rigs. A new holder had to be manufactured for the air-sand test rig between the two test periods. It would have been better to use test rigs belonging to NEL itself, had such been available.

Erosion equations have been developed based entirely on empirical data alone. The reason for doing this was that many of the previous attempts to develop analytical equations for erosion (based on understanding of material behaviour etc.) have not given rise to any conclusive universal model for the process. It was thought more appropriate to base equations on actual data to ensure the trends observed were captured as accurately as possible. Using an erosion equation previously determined by other researchers (and simply calibrating it with the current empirical data) could result in observed trends being lost. There did appear to be a fairly well defined trend for variation of erosion with velocity for the metallic materials tested—so much so that equations based on the mean data were constructed. It would be a useful future exercise to compare the predictions made by these equations with some of the

semi-analytical equations given in the literature. The current equations could possibly be improved by such comparison.

The work carried out in modelling liquid jet impact has shown that particle impact velocities in the slurry erosion test rig are significantly less than the average liquid velocity through the nozzle. This will have a considerable impact on the results of erosion modelling using these equations, as material loss will be underpredicted. Further work is required to revise the particle impact velocities reported in the erosion tests, and to develop new equations based on the revised velocities. Such equations would be likely to predict material loss to a more accurate degree than is possible at present.

11.1.3 Experimental erosion testing of actual components

A series of tests were carried out at NEL using simple components whose function was to restrict the flow. Three components of different design were tested under abrasive flow conditions. Definite signs of cavitation erosion were observed for one of the components (the fluted restrictor), and it is suspected the same may have occurred in one of the other designs also (the upstand restrictor). Tests lasted for around 14 hours (although one restrictor was tested in 4 stages, each of 5 hours duration). Mass loss was measured before and after each test.

Although the tests do provide a basis for validating the CFD-based erosion modelling technique, there were limitations to the test method which do not allow as full a validation as would have been desired. Having a single test period of 14 hours (for three out of the four tests performed) meant that intermediate worn states of the component were not observed. A better method would have been to test the component for only an hour (or less) at a time, and to weigh and examine it after each short period. It was not possible to do so in the current project due to the cost that would have been incurred. Had a smaller scale facility been available, such an approach may have been possible.

Only mass loss measurements were made in the restrictor testing. While this gives an overall basis for validation, it does not permit detailed analysis of the ability of a CFD method to predict geometry changes taking place on the surface of the component. Actual geometrical measurements would be required to examine such a process. The shape of the restrictor components makes dimensional measurements fairly difficult to do without considerable expense. If geometry changes were to be considered in future work, then an even simpler component should be used.

Chapter 10 uses results from a choke valve test that was not carried out by NEL, and was therefore outwith the immediate control of the author. As there have been few other similar tests on these type of choke valves, the study of Chapter 10 is a unique comparison between test and simulation for high pressure slurry flow through an MOS choke valve. The tests were carried out under controlled conditions on an established test facility at pressure drops approaching field conditions. Sand concentration in these tests was considerably higher than would be expected in the field (although there are some cases where such concentrations occur), but this was necessary to effect appreciable erosion in as short a time as possible. The test data was considered to be entirely suitable for use in validating the CFD-based erosion modelling technique.

11.1.4 Predictions of erosion in simple and complex geometries

CFD-based predictions of mass loss for the restrictor components were in general lower than the corresponding experimental measurements. The main reason for this was taken to be the practice of using mean liquid velocity through the nozzle for the particle impact velocity in the slurry jet testing. The best prediction of material loss (for the valley restrictor) was 43.8 % lower than the measured value. This could be improved by adjusting the erosion equations appropriately.

Mass loss distribution predicted by the CFD method is consistent with what would have been the initial areas of wear seen by the restrictor at the start of the test period. However, the shape of the surface (particularly for the upstand restrictor) would have started to change as soon as the slurry started to flow. Erosion of the sharp-edged hole had an observable effect on the pressure drop being continuously monitored across the restrictor. Attempting to predict these geometry changes would be a useful step forward in the area of erosion modelling.

Predictions of material loss for a MOS choke valve were not as close to the true erosion as the predictions for restrictors. In some cases, predictions for the choke valve were more than an order of magnitude lower than the expected values. There are several possible reasons for this. Firstly, the fluid flow field for the choke valve may not be predicted correctly, especially in the narrow gap between the cage inner wall and the tip outer surface. It was not possible to put as many cells in this region as would have been desired. Also, the main component for which predictions of mass loss were compared to experiment was the flow control tip. This was made of tungsten carbide in the test valve, with two different tungsten

carbides being applied in two separate tests. Empirical data for the tungsten carbide equations was not as complete as some of the other materials (as it took longer to test) and so the equations may not be capturing the true erosion versus impact parameters relationship.

Incomplete modelling of particle behaviour on solid surfaces may be another factor in the underprediction of mass loss for the choke valve. Only particles that impact and rebound can be modelled at present: different behaviour may occur in the actual valve, such as a bed of particles sliding along parts of a surface.

Further work is required to determine which of the possible reasons for underprediction is the correct one. As suggested before, it will be helpful to perform a far more rigorous validation of the CFD predictions of single phase flow to ensure that the right trends are coming out of the simulations. When a greater degree of confidence about the single phase flow is obtained, it will be possible to examine the influence of particle tracking algorithm, empirical erosion equations, particle rebound behaviour etc. in more detail.

11.1.5 Usefulness of CFD-based erosion modelling to valve manufacturer

In its present state, the CFD-based erosion modelling tool developed in this project can be used to predict initial wear locations in both simple and complex geometries. These predictions will be fairly reliable, and should be useful when designing components to be more erosion-resistant. It is also possible to obtain some indication of relative erosion rate (particularly for metallic materials), which will enable assessment of alternative designs.

At present the method cannot be used to predict the actual lifetime of a component under erosion conditions. It does not seem sensible to convert a mass loss prediction having a 70% error band into a corresponding component lifetime, unless the minimum possible lifetime were to be used. To do even this, however, would require some consistency in predictions across different components, which has not been conclusively shown in the present study (e.g. difference in prediction error between restrictor and choke valve models). If it is the case that no prediction is available at all for a component, and the geometry is fairly simple (e.g. flow restrictor), then there may indeed be some merit in making an actual estimate of component life.

Some improvements could be made to the empirical erosion equations and particle tracking procedure (e.g. accounting for squeeze film effects as particles approach the wall in liquid flows) in order to improve erosion predictions. Modelling geometry changes could also be a significant step forward in erosion studies. It may be possible to do this manually using

an unstructured meshing technique, but to do so automatically would require considerable effort. Use of a commercial code having a flexible moving mesh facility could make this easier.

The underlying single phase modelling that has come out of this project is likely to be of considerable use to choke valve manufacturers. While there are areas needing further attention, the work has shown the usefulness of CFD methods in choke valve analysis and design. Using computational techniques eliminates the need for flow testing, and enables several competing designs to be assessed without having to manufacture a prototype for each. The meshing strategies developed throughout the project will assist future workers attempting similar models—thus saving time.

11.2 Original contribution

The work contained in this thesis has contributed to knowledge in the following specific ways:-

1. Modelling of single phase flow through Wood Group Pressure Control MOS choke valves: There have been no CFD studies in the literature where the geometry of interest is the MOS choke valve manufactured by WGPC. Indeed, there are only a handful of CFD studies where the component is a choke valve of any type at all. The few studies that are available have been for simpler types of valves, and have not used hybrid meshing techniques. This study has compared predicted pressure drops with measured pressure drops for a range of valve positions, and has shown that there may be deeper issues that CFD modelling must address.

2. Further testing of materials used in choke valve manufacture: A range of materials used in choke valves were tested using slurry and air-sand erosion test facilities. While some of these materials have been tested before, this work extends the data available for use in constructing empirical erosion equations for use in CFD erosion modelling. Several issues were raised (such as repeatability of test method) that warrant further attention by those concerned with erosion testing in the academic community.

3. Development of empirical erosion equations: Almost all other CFD-based erosion modelling studies have used semi-analytical erosion equations to relate particle impact data to material loss. This imposes restrictions on the trends that will be modelled—regardless of what the underlying empirical data may suggest. In this study, equations were created entirely from empirical data, and so follow the observed trends more closely.

There are obvious limitations in the equations (such as not passing through zero), but they do serve to suggest alternative ways in which material loss could be related to particle impact.

4. Tracking particles through a model of liquid jet in air: There are no studies in the literature where particles have been tracked through a free liquid jet impinging a flat plate. This study has considered a case for which experimental data were available (to provide validation), and has shown that particle impact velocities on the surface of the plate are considerably less than the average liquid velocity through the nozzle. Particle impact angles also differ from the mean angle between the plate and jet centre line.

5. Testing of components designed to extend choke valve life: The restrictor components considered in this study were intended to extend the life of choke valves in erosive service. Several prototype designs were tested in the NEL abrasive flow facility, under both single phase and abrasive flow conditions. This work has generated additional data with which to compare the results of CFD-based erosion modelling studies, and can thus act as validation cases in the future. Field trials of the concept have shown it to significantly extend valve lifetime. A patent has been applied for.

6. CFD modelling of restrictor components (single phase and erosion): The work carried out to predict pressure drop across the restrictor components has explored the ability of CFD codes to predict energy loss through long orifices. It has also been possible to predict areas of material loss at the start of erosion testing. This unique comparison underlines the need to account for geometry changes in erosion modelling.

7. Quantitative comparison of erosion predictions for an MOS choke valve: The availability of specific erosion test data for the type of choke valve manufactured by WGPC has enabled direct comparison of predicted erosion with actual erosion under controlled conditions. There is only one other published study in the literature where this type of comparison has been made—for valves with simpler internal geometry than the MOS choke valve. The results suggest that there is still work to be done before CFD modelling techniques can be routinely used to predict lifetime of choke valves in erosive service.

11.3 Conclusion

A CFD-based erosion modelling technique has been developed using the commercial CFD package Fluent, and has been applied to a range of simple and complex geometries. The success of this method in predicting component lifetime is limited. The best predictions of

material loss for a simple geometry was 43.8% lower than the experimentally measured value. When applied to complex geometries, the predictions were over an order of magnitude different from the measurements (for the tungsten carbide flow control tip). In both simple and complex geometries, the CFD technique can predict the locations of initial wear, and for simple geometries at least, can give some indication as to relative erosion rates between competing designs.

References

Adeniji-Fashola, A., Chen, C.P. (1990) Modelling of confined turbulent fluid-particle flows using Eulerian and Lagrangian schemes. International Journal of Heat and Mass Transfer, Vol. 33, No. 4, pp. 691-701.

Ahlert, K.R. (1994) Effects of particle impingement angle and surface wetting on solid particle erosion of ANSI 1018 steel. M.S. Thesis, University of Tulsa.

Ahmad, K., Baker, R.C., Goulas, A. (1986) Computation and experimental results of wear in a slurry pump impeller. Proceedings of the Institute of Mechanical Engineers, Vol. 200, No. C6, pp. 439-445.

Ahmad, Kl, Goulas, A. (1986) On the use of particle trajectories for the prediction of erosion in slurry pumps. ASME, Fluids Engineering Division (Publication), FED, Vol. 38, pp. 125-133.

Andrews, D.R., Horsfield, N. (1983) Particle collisions in the vicinity of an eroding surface. Journal of Physics D: Applied Physics, Vol. 16, pp. 525-538.

ASTM (1997) Standard test method for conducting erosion tests by solid particle impingement using gas jets. G76-95 1997 Annual Book of ASTM Standards, Vol. 03.02, No. G76-95.

Bahadur, S., Badruddin, R. (1990) Erodent particle characterisation and the effect of particle size and shape on erosion. Wear, Vol. 138, pp. 189-208.

Benchaita, M.T., Griffith, P., Rabinowicz, E. (1983) Erosion of metallic plate by solid particles entrained in a liquid jet. Journal of Engineering for Industry, Vol. 105, pp. 215-221.

Bitter, J.G.A. (1963a) A study of erosion phenomena, Part 1. Wear, Vol. 6, pp. 5-21.

Bitter, J.G.A. (1963b) A study of erosion phenomena, Part 2. Wear, Vol. 6, pp. 169-190.

Blanchard, D.J., Griffith, P., Rabinowicz, E. (1984) Erosion of a pipe bend by solid particles entrained in water. Journal of Engineering for Industry, Vol. 106, pp. 213-217.

Bourgoyne, A.T. (1989) Experimental study of erosion in diverter systems due to sand production. SPE/AIDC 18716. Presented at 1989 SPE/IADC Drilling Conference held in New Orleans, Louisiana, pp. 807-816.

Brach, R.M. (1988) Impact dynamics with applications to solid particle erosion. Journal of Impact Engineering, Vol. 7, No. 1, pp. 37-53.

Brackbill, J.U., Kothe, D.B, Zemach, C. (1992) A continuum method for modeling surface tension. Journal of Computational Physics, Vol. 100, pp. 335-354.

Chang, K.-C., Wu, W.-J. (1994) Sensitivity study on Monte Carlo solution procedure of two-phase turbulent flow. Numerical Heat Transfer, Part B, Vol. 25, pp. 223-244.

Clark, H.McI. (1993) Test methods and applications for slurry erosion—a review. Tribology: Wear Test Selection for Design and Application, ASTM STP 1199, Eds. A.W. Ruff, R.G. Bayer, pp. 113-132.

Clark, H.McI. (1995) A comparison of particle impact in gas-solid and liquid-solid erosion. Wear, Vol. 186/187, pp. 465-472.

Clark, H.McI., Burmeister, L.C. (1992) The influence of the squeeze film on particle impact velocities in erosion. International Journal of Impact Engineering, Vol. 12, No. 3, pp. 415-426.

Clift, R., Grace, J.R., Weber M.E. (1978) Bubbles, Drops and Particles. Academic Press, New York.

Crowe, C.T., Sharma, M.P., Stock, D.E. (1977) The Particle-Source-In Cell (PSI-CELL) model for gas-droplet flows. Transactions of the ASME, Journal of Fluids Engineering, June 1997, pp. 325-332.

Dosanjh, S., Humphrey, J.A.C. (1985) The influence of turbulence on erosion by a particle-laden fluid jet. Wear, Vol. 102, pp. 309-330.

Drtina, P., Krause, M. (1994) Abrasion on a Francis turbine guide vane: Numerical simulation and field tests. 17th IAHR Symposium, 1994, Paper 31.

Edwards, J.K., McLaury, B.S., Shirazi, S.A. (1998) Supplementing a CFD code with erosion prediction capabilities. ASME Fluids Engineering Division Summer Conference 1998, Paper FEDSM98-5229.

Edwards, J.K., McLaury, B.S., Shirazi, S.A. (2000) Evaluation of alternative pipe bend fittings in erosive service. FEDSM2000-11245, Proceedings of the ASME Fluids Engineering Division Summer Meeting, June 11-15, 2000, Boston, MA.

El-Sayed, A.F., Lasser, R., Rouleau, W.T. (1986) Effects of secondary flow on particle motion and erosion in a stationary cascade. International Journal of Heat and Fluid Flow, Vol. 7, No. 2, pp. 146-154.

Enayet, M., Gibson, M., Taylor, A., Yianneskis, M., (1982) Laser-Doppler measurements of laminar and turbulent flow in a pipe bend. International Journal of Heat and Fluid Flow, Vol. 3, pp. 213-219.

Erdal, A., Andersson, H.I. (1997) Numerical aspects of flow computation through orifices. Flow Measurement and Instrumentation, Vol. 8, No. 1, pp. 27-37.

Eyler, R.L. (1987) Design and analysis of a pneumatic flow loop. M.S. Thesis, West Virginia University.

Fan, J., Sun, P., Zheng, Y., Zhang, X., Cen, K. (1999) A numerical study of a protection technique against tube erosion. Wear, Vol. 225-29, pp. 458-464.

Fan, J., Zhou, D., Hua, Q., Cen, K. (1994) Numerical computation of particle-laden gas flows past staggered tube banks undergoing erosion. Powder Technology, Vol. 80, pp. 1-10.

Finnie, I. (1960) Erosion of surfaces by solid particles. Wear, Vol. 3, pp. 87-103.

Finnie, I. (1972) Some observations on the erosion of ductile metals. Wear, Vol. 19, pp. 81-90.

Finnie, I. (1995) Some reflections on the past and future of erosion. Wear, Vol. 186/187, pp. 1-10.

Finnie, I., (1958) The mechanism of erosion of ductile materials. Proceedings of the 3rd US National Congress of Applied Mechanics, pp. 527-532.

Finnie, I., McFadden, D.H. (1978) On the velocity dependence of the erosion of ductile metals by solid particles at low angles of incidence. Wear, Vol. 48, pp. 181-190.

Finnie, I., Wolak, J., Kabil, Y. (1967) Erosion of metals by solid particles. Journal of Materials, Vol. 2, No. 3, pp. 682-700.

Forder, A., Thew, M., Harrison, D. (1998) A numerical investigation of solid particle erosion experienced within oilfield control valves. Wear, Vol. 216, pp. 184-193.

Forder, A.F., Thew, M.T., Harrison, D. (1996) A CFD model to analyse erosion within oilfield control valves. Third CFX International Users Conference, pp. 415-427.

Fujimoto, H., Hatta, N., Viskanta, R. (1999) Numerical simulation of convective heat transfer to a radial free surface jet impinging on a hot solid. Heat and Mass Transfer, Vol. 35, pp. 266-272.

Gat, H., Tabakoff, W. (1978) Some effects of temperature on the erosion of metals. Wear, Vol. 50, pp. 85-94.

Gosman, A.D., Ioannides, E. (1981) Aspects of computer simulation of liquid-fuelled combustors. AIAA 19th Aerospace Sciences Meeting, Paper AIAA-81-0323.

Govan, A.H., Hewitt, G.F., Ngan, C.F. (1989) Particle motion in a turbulent pipe flow. International Journal of Multiphase Flow, Vol. 15, No. 3, pp. 471-481.

Graham, D.H., Ball, A. (1989) Particle erosion of candidate materials for hydraulic valves. Wear, Vol. 133, pp. 125-132.

Graham, D.I. (1995) An improved eddy interaction model for numerical simulation of turbulent particle dispersion. ASME, Fluids Engineering Division, (Publication) FED, Vol. 228, pp. 161-167.

Graham, D.I. (1996) An improved eddy interaction model for numerical simulation of turbulent particle dispersion. Journal of Fluids Engineering, Vol. 118, pp. 819-823.

Grant, G., Tabakoff, W. (1975) Erosion prediction in turbomachinery resulting from environmental solid particles. Journal of Aircraft, Vol. 12, No. 5, pp. 471-478.

Hamed, A., Fowler, S. (1983) Erosion pattern of twisted blades by particle laden flows. Journal of Engineering for Power, Transactions of ASME, Vol. 105, pp. 839-843.

Hanson, R. (2000) Private communication.

Hanson, R., Patel, M.K. (2000) Development of a model to predict the life of pneumatic conveyor bends subject to erosive wear. FEDSM2000-11246, Proceedings of the ASME Fluids Engineering Division Summer Meeting, June 11-15, 2000, Boston, MA.

Hashish, M. (1987) An improved model of erosion by solid particle impact. Proceedings of the 7th International Conference on Erosion by Liquid and Solid Impact, Cambridge, UK, pp. 66-1, 66-9.

Haugen, K., Kvernvold, O., Ronold, A., Sandberg, R. (1995) Sand erosion of wear-resistant materials: Erosion in choke valves. Wear, Vol. 186/187, pp. 179-188.

Hay, S., St John, D.H. (1993) Models of gas-solid particle erosion of metals and alloys. National Conference Publication, Institution of Engineers, Australia, Vol. 93, No. 1, pp. 215-219.

Head, W.J., Harr, M.E. (1970) The development of a model to predict the erosion of materials by natural contaminants. Wear, Vol. 15, pp. 1-46.

Hengshuan, C., Zhong, X. (1990) Numerical analysis and experimental investigation of erosion in variable rectangular-section bends by solid particles. Chinese Journal of Mechanical Engineering (English Edition), Vol. 3, No. 1, pp. 111-118.

Hirt, C.W., Nichols, B.D. (1981) Volume of Fluid (VOF) method for the dynamics of free boundaries. Journal of Computational Physics, Vol. 39, pp. 201-225.

Humphrey, J.A.C. (1990) Fundamentals of fluid motion in erosion by solid particle impact. International Journal of Heat and Fluid Flow, Vol. 11, No. 3, pp. 170-195.

Hutchings, I.M. (1981) A model for the erosion of metals by spherical particles at normal incidence. Wear, Vol. 70, pp. 269-281.

Hutchings, I.M., Winter, R.E., Field, J.E. (1976) Solid particle erosion of metals: the removal of surface material by spherical projectiles. Proceedings of the Royal Society, London, Series A, Vol. 348, pp. 379-392.

Issa, R.I., Gosman, A.D., Watkins, A.P. (1986) The computation of compressible and incompressible recirculating flows by a non-iterative implicit scheme. Journal of Computational Physics, Vol. 62, pp. 66-82.

Ives, L.K., Ruff, A.W. (1979) Electron microscopy study of erosion damage in copper. ASTM STP 664, Erosion: Prevention and Useful Applications, pp. 5-35.

Jang, D.S., Jetli, R., Acharya, S. (1986) Comparison of the PISO, SIMPLER, and SIMPLEC algorithms for the treatment of the pressure-velocity coupling in steady flow problems. Numerical Heat Transfer, Vol. 10, pp. 209-228.

Jayanti, S., Hewitt, G.F. (1991) Review of literature on dispersed two-phase flow with a view to CFD modelling. Report AEA APS – 0099 from AEA Petroleum Services, AEA Technology, Harwell Laboratory, Oxon, OX11 ORA.

Jennings, W.H., Head, W.J., Manning, C.R. (1976) A mechanistic model for the prediction of ductile erosion. Wear, Vol. 40, pp. 93-112.

Jun, Y.-D., Tabakoff, W. (1992) Numerical simulation of a dilute particulate flow over tube banks. ASME, Fluids Engineering Division (Publication) FED, Vol. 144, pp. 125-133.

Keating, A., Nesic, S. (2000) Particle tracking and erosion prediction in three-dimensional bends. FEDSM2000-11249, Proceedings of the ASME Fluids Engineering Division Summer Meeting, June 11-15, 2000, Boston, MA.

Kim, S.E., Choudhury, D. (1995) Near-wall treatment using wall functions sensitised to pressure gradient. ASME, Fluids Engineering Division (Publication) FED, Vol. 217, pp. 273-280.

Kvenvold, O., Sandberg, R., Nokleberg, L. (1994) Erosion of pressure/flow control valves due to impact of sand particles. Valve Workshop 1994, Flow Centre, National Engineering Laboratory, East Kilbride, Glasgow.

Laitone, J.A. (1979) Aerodynamic effects in the erosion process. Wear, Vol. 56, pp. 239-246.

Launder, B.E. (1989) Second-moment closure: present...and future? International Journal of Heat and Fluid Flow, Vol. 10, No. 4, pp. 282-300.

Launder, B.E., Spalding, D.B. (1974) The numerical computation of turbulent flows. Computer Methods in Applied Mechanics and Engineering, Vol. 3, pp. 269-289.

Levy, A., Aghazadeh, M., Hickey, G. (1986) The effect of test variables on the platelet mechanism of erosion. Wear, Vol. 108, pp. 23-41.

Levy, A.V. (1995) Solid Particle Erosion and Erosion-Corrosion of Materials, ASM International (Book).

Levy, A.V., Chik, P. (1983) The effects of erodent composition and shape on the erosion of steel. Wear, Vol. 89, pp. 151-162.

Madadnia, J., Owen, I. (1995) Erosion in conical diffusers in particulate-laden cavitating flow. International Journal of Multiphase Flow, Vol. 21, No. 6, pp. 1253-1257.

Mason, J.S., Smith, B.V. (1972) The erosion of bends by pneumatically conveyed suspensions of abrasive particles. Powder Technology, Vol. 6, pp. 323-335.

McLaury, B. (1996) Predicting solid particle erosion resulting from turbulent fluctuations in oilfield geometries. PhD Thesis, Department of Mechanical Engineering, University of Tulsa.

McLaury, B.S., Shirazi, S.A., Shadley, J.R., Rybicki, E.F. (1994) A particle tracking method to predict sand erosion threshold velocities in elbows and tees. ASME, Fluids Engineering Division (Publication) FED, Vol. 189, pp. 145-153.

McLaury, B.S., Shirazi, S.A., Shadley, J.R., Rybicki, E.F. (1996) Modeling erosion in chokes. ASME, Fluids Engineering Division (Publication) FED, Vol. 236, No. 1, pp. 773-781.

Meng, H., Van der Geld, C.W.M. (1991) Particle trajectory computations in steady non-uniform liquid flows. ASME, Fluids Engineering Division (Publication) FED, Vol. 118, pp. 183-193.

Meng, H.C., Ludema, K.C. (1995) Wear models and predictive equations: their form and content. Wear, Vol. 181-183, pp. 443-457.

Michaelides, E.E. (1997) Review—The transient equation of motion for particles, bubbles, and droplets. ASME Journal of Fluids Engineering, Vol. 119, pp. 233-247.

Minemura, K., Zhong, Y. (1995) Numerical prediction of erosion wear on pump casing under solid-water two-phase flow. Advances in Multiphase Flow, pp. 561-572.

Misra, A., Finnie, I. (1981) On the size effect in abrasive and erosive wear. Wear, Vol. 65, pp. 359-373.

Morsi, S.A., Alexander, A.J. (1972) An investigation of particle trajectories in two-phase flow systems. Journal of Fluid Mechanics, Vol. 55, No. 2, pp. 192-208.

Neilson, J.H., Gilchrist, A. (1968) Erosion by a stream of solid particles. Wear, Vol. 11, pp. 111-122.

Nokleberg, L., Sontvedt, T. (1995) Erosion in choke valves—oil and gas industry applications. Wear, Vol. 186/187, pp. 401-412.

Nokleberg, L., Sontvedt, T. (1998) Erosion of oil and gas industry choke valves using computational fluid dynamics and experiment. International Journal of Heat and Fluid Flow, Vol. 19, pp. 636-643.

Odar, F., Hamilton, W.S. (1964) Forces on a sphere accelerating in a viscous fluid. Journal of Fluid Mechanics, Vol. 18, pp. 302-314.

Patankar, S.V. (1980) Numerical heat transfer and fluid flow. Hemisphere Publishing Corporation.

Patankar, S.V., Spalding, D.B. (1972) A calculation procedure for heat, mass, and momentum transfer in three dimensional parabolic flows. International Journal of Heat and Mass Transfer, Vol. 15, pp. 1787-1806.

Peter, J.S., Hardie, A. (1994) Experiences with abrasive flow type-testing of valves. Valve Workshop 1994, Flow Centre, National Engineering Laboratory, East Kilbride, Glasgow.

Picart, A., Berlemont, A., Gouesbet, G. (1986) Modelling and predicting turbulence fields and the dispersion of discrete particles transported by turbulent flows. International Journal of Multiphase Flow, Vol. 12, No. 2, pp. 237-261.

Rao, P.V., Buckley, D.H. (1984) Particulate erosion mechanisms. NASA Technical Memorandum 83551.

Reddy, A.V., Sundararajan, G. (1986) Erosion behaviour of ductile materials with a spherical non-friable erodent. Wear, Vol. 111, pp. 313-323.

Roco, M.C., Addie, G.R. (1983) Analytical model and experimental studies on slurry flow and erosion in pump casings. Slurry Transportation, Vol. 8, pp. 263-276.

Roco, M.C., Nair, P., Addie, G.R., Dennis, J. (1984) Erosion of concentrated slurries in turbulent flow. Journal of Pipelines, Vol. 4, No. 3, pp. 213-221.

Roy, M., Tirupataiah, Y., Sundararajan, G. (1993) Effect of particle size on the erosion of Cu and its alloys. Materials Science and Engineering, Vol. A165, pp. 51-63.

Rubini, P., Boysan, F., Swithenbank, J. (1985) The computation of gaseous particle laden flow around pipe bends. 2nd International Conference on Multi-Phase Flow, London, pp. 229-243.

Ruff, A.W., Ives, L.K. (1975) Measurement of solid particle velocity in erosive wear. Wear, Vol. 35, pp. 195-199.

Saffman, P.G. (1965) The lift on a small sphere in a slow shear flow. Journal of Fluid Mechanics, Vol. 22, No. 2, pp. 385-400.

Schuh, M.J., Schuler, C.A., Humphrey, J.A.C. (1989) Numerical calculation of particle-laden gas flows past tubes. AIChE Journal, Vol. 35, No. 3, pp. 466-480.

SELL/01 (1988) Flow tests on a 3-inch nominal bore choke valve. National Engineering Laboratory, East Kilbride, Glasgow, G75 0QU.

Sheldon, G.L., Kanhere, A. (1972) An investigation of impingement erosion using single particles. Wear, Vol. 21, pp. 195-209.

Shimoda, K., Hojo, H., Yukawa, T. (1987) Method for the prediction of erosion by logarithmic-normal size distributed particles. Proceedings of the 7th International Conference on Erosion by Liquid and Solid Impact, Cambridge, UK, pp. 68-1, 68-8.

Shirolkar, J.S., Coimbra, C.F.M., Queiroz McQuay, M. (1996) Fundamental aspects of modelling turbulent particle dispersion in dilute flows. Progress in Energy and Combustion Science, Vol. 22, pp. 363-399.

Smeltzer, C.E., Gulden, M.E., Compton, W.A. (1970) Mechanisms of metal removal by impacting dust particles. Journal of Basic Engineering, Sept 1970, pp. 639-654.

Sommerfeld, M., Zivkovic, G. (1992) Recent advances in the numerical simulation of pneumatic conveying through pipe systems. Computational Methods in Applied Sciences, C. Hirsch (Editor), Elsevier Science Publishers, pp. 201-212.

Stevens, J., (2000) Personal Communication.

Stevens, J., Webb, B.W. (1992) Measurements of the free surface flow structure under an impinging, free liquid jet. Transactions of the ASME, Journal of Heat Transfer, Vol. 114, pp. 79-84.

Stevens, J., Webb, B.W. (1993a) Measurements of flow structure in the radial layer of impinging free-surface liquid jets. International Journal of Heat and Mass Transfer, Vol. 36, No. 15, pp. 3751-3758.

Stevens, J., Webb, B.W. (1993b) Measurements of flow structure in the stagnation zone of impinging free-surface liquid jets. International Journal of Heat and Mass Transfer, Vol. 36, No. 17, pp. 4283-4286.

Sundararajan, G. (1991) A comprehensive model for the solid particle erosion of ductile materials. Wear, Vol. 149, pp. 111-127.

Sundararajan, G. (1995) The solid particle erosion of metallic materials: The rationalisation of the influence of material variables. Wear, Vol. 186/187, pp. 129-144.

Sundararajan, G., Roy, M. (1997) Solid particle erosion behaviour of metallic materials at room and elevated temperatures. Tribology International, Vol. 30, No. 5, pp. 339-359.

Sundararajan, G., Shewmon, P.G. (1983) A new model for the erosion of metals at normal incidence. Wear, Vol. 84, pp. 237-258.

Tabakoff, W. (1983) Experimental study on the effects of specimen sizes on erosion. Wear, Vol. 86, pp. 65-72.

Tabakoff, W., Eroglu, H. (1988) LDV measurements of solid particle rebound parameters and effect of surface shape on erosion. ASME, Fluids Engineering Division (Publication) FED, Vol. 64, pp. 174-177.

Tabakoff, W., Hamed, A., Beacher, B. (1983) Investigation of gas particle flow in an erosion wind tunnel. Wear, Vol. 86, pp. 73-88.

Tabakoff, W., Kotwal, R., Hamed, A. (1979) Erosion study of different materials affected by coal ash particles. Wear, Vol. 52, pp. 161-173.

Tabakoff, W., Malak, M.F., Hamed, A. (1987) Laser measurements of solid-particle rebound parameters impacting on 2024 aluminium and 6A1-4V titanium alloys. AIAA Journal, Vo. 25, No. 5, pp. 721-726.

Tilly, G.P. (1973) A two-stage mechanism of ductile erosion. Wear, Vol. 23, pp. 87-96.

Tilly, G.P. (1979) Erosion caused by impact of solid particles. Treatise on Materials Science and Technology, Vol. 13, pp. 287-319.

Tilly, G.P., Sage, W. (1970) The interaction of particle and material behaviour in erosion studies. Wear, Vol. 16, pp. 447-465.

Tirupataiah, Y., Venkataraman, B., Sundararajan, G. (1990) The nature of the elastic rebound of a hard ball impacting on ductile, metallic target materials. Materials Science and Engineering, Vol. A124, pp. 133-140.

Tu, J.Y., Lee, B.E., Fletcher, C.A.J. (1996) Eulerian modelling of particle-wall collisions in confined gas-particle flows via a Lagrangian approach. ASME, Fluids Engineering Division (Publication) FED, Vol. 236, No. 1, pp. 751-758.

Tuzson, J.J. (1984) Laboratory slurry erosion tests and pump wear rate calculations. Transactions of the ASME, Journal of Fluids Engineering, Vol. 106, pp. 135-140.

Uuemois, H., Kleis, I. (1975) A critical analysis of erosion problems which have been little studied. Wear , Vol. 31, pp. 359-371.

Van Doormaal, J.P., Raithby, G.D. (1984) Enhancements of the SIMPLE method for predicting incompressible fluid flows. Numerical Heat Transfer, Vol. 7, pp. 147-163.

Versteeg, H.K., Malalasekera, W. (1995) An introduction to Computational Fluid Dynamics Longman Scientific and Technical, ISBN 0-582-21884-5.

Vittal, B.V.R., Tabakoff, W. (1987) Two-phase flow around a two-dimensional cylinder. AIAA Journal, Vol. 25, No. 5, pp. 648-654.

Wallace, M.S., Peters, J.S., Scanlon, T.J., Dempster, W.M., McCulloch, S., Ogilvie, J.B. (2000) CFD-based erosion modelling of multi-orifice choke valves. FEDSM2000-11244, Proceedings of the ASME Fluids Engineering Division Summer Meeting, June 11-15, 2000, Boston, MA.

Wang, J., Shirazi, S.A., Shadley, J.R., Rybicki, E.F. (1996) Application of flow modeling and particle tracking to predict sand erosion rates in 90 degree elbows. ASME, Fluids Engineering Division (Publication) FED, Vol. 236, No. 1, pp. 725-734.

Wong, K.K., Clark, H.McI. (1993) A model of particle velocities and trajectories in a slurry pot erosion tester. Wear, Vol. 160, pp. 95-104.

Wood, R.J.K., Wheeler, D.W. (1998) Design and performance of a high velocity air-sand jet impingement erosion facility. Wear, Vol. 220, pp. 95-112.

Yakhot, V., Orszag, S.A. (1986) Renormalization group analysis of turbulence. 1. Basic Theory. Journal of Scientific Computing, Vol. 1., No. 1, pp. 3-51.

Youngs, D.L. (1982) Time-dependent multi-material flow with large fluid distortion. In K. W. Morton and M. J. Baines, editors, Numerical Methods for Fluid Dynamics. Academic Press, 1982.

Zhong, Y., Minemura, K. (1996) Measurement of erosion due to particle impingement and numerical prediction of wear in pump casing. Wear, Vol. 199, pp. 36-44.

Appendix A: Mesh types available in Fluent

The pre-processor associated with Fluent is known as 'Gambit'. This package enables construction of computational meshes containing both structured and unstructured sections of mesh (hybrid meshing). This document outlines the various cell types available, and the way in which these can be used to create computational meshes.

A.1 Two-dimensional cells and face meshes

In two-dimensional models, computational domains are constructed from entities known as faces. Faces are constructed from a series of edges that combine to form a closed loop. Cells are created on faces. There are two basic cell types that can be created on a face: quadrilateral (quad) and triangular (tri). Figure A.1 depicts these two basic face cell types.

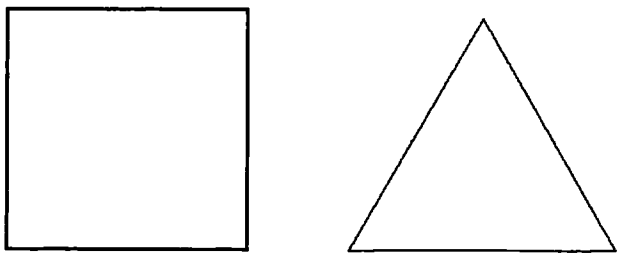

Quadrilateral Face Triangular Face

Figure A.1 Basic cell face types.

Quadrilateral cells can be arranged on a face in a number of ways. The most fundamental method is to create mapped faces, where the number of cells on one edge equals the number of cells on the opposite edge. Although the face on which the cells are created could have more than four edges, the mesh itself requires that there be only four edges—so an 'effective' four sided face must be specified for cells to be mapped between. Figure A.2(a) presents a typical mapped mesh, where the lines used to create the cells are adjusted to follow the shape of the outer edges. Various 'smoothing' algorithms are available to preserve the fundamental orthogonal cell shape as far as possible. (These smoothing algorithms can be applied to all face types). Two alternative ways to create quad faces are also shown in Figure A.2. Figure A.2(b) presents an unstructured (paved) quad face that does not have the same restrictions as the mapped face. Figure A.2(c) shows a fairly specific type of mesh that only applies when it is desired to have quad cells in a three-sided face. This is known as a tri-

primitive quad face. Some or all of the edges could be replaced by arcs, rather than having straight lines.

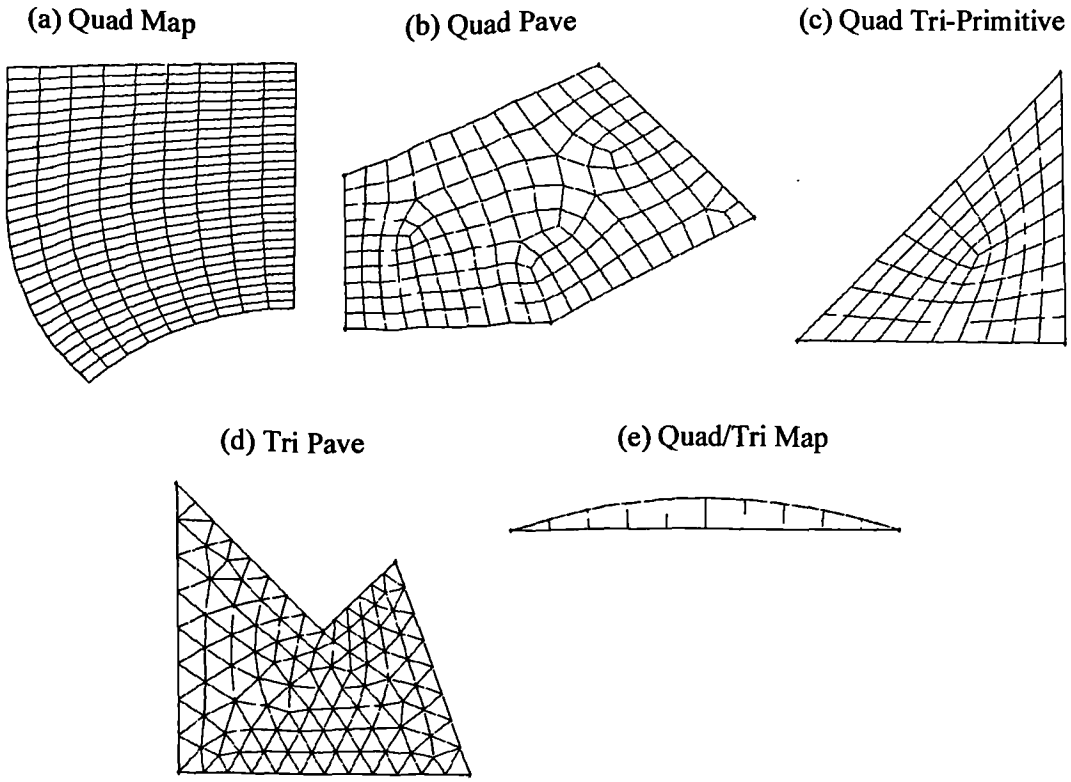

Figure A.2 Methods of creating face meshes with basic cell types.

The most flexible type of cell to use in a face mesh is the triangular (tri) cell. These cell types are always arranged using the paved option. Figure A.2(d) gives an illustration of this type of mesh. Only the number of cells applied on the outer edges controls the cell density within the face. A combination of quad and tri cells can be used in the special case shown in Figure A.2(e), where two tri cells are specified at the corners of the mesh, and quad cells are used in between.

A.2 Three dimensional cells and volume meshes

Volume meshes are generated by first creating enough face meshes to guide the volume meshing process, and selecting which type of volume mesh to create. The basic volume cells are shown in Figure A.3. Hexahedral and tetrahedral cells are the main cell types used in volume meshes, although wedge shaped cells are also very useful. Wedge cells are created when a triangular face is swept (or extruded) along a path normal to the face: this is a process known as 'Coopering', and the resulting mesh is often referred to as a 'Cooper mesh'.

Any face can be used to create a Cooper mesh—not necessarily a triangular one. A paved quadrilateral face can be used to create a Cooper mesh.

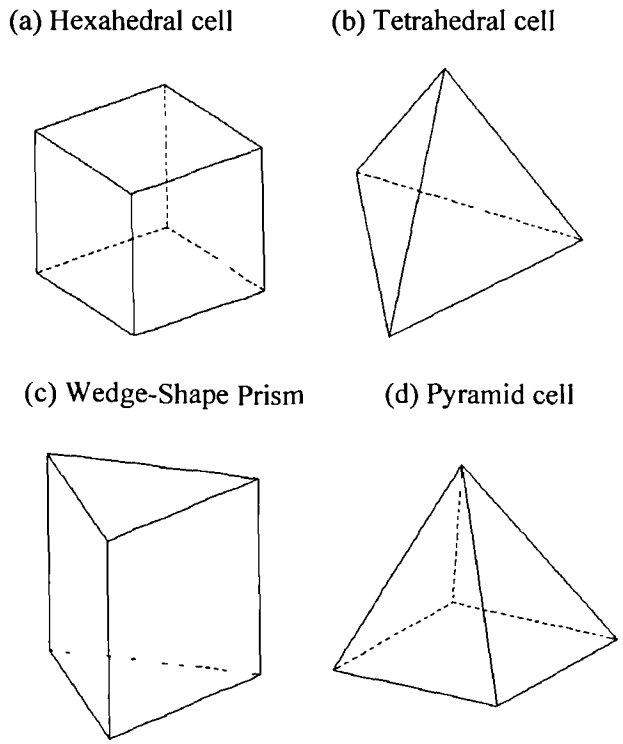

Figure A.3 Basic volume cells.

The type of volume meshes typically created using the cells of Figure A.3 are shown in Figure A.4. Figure A.4(a) is the most basic type of volume mesh, being constructed using mapped hexahedral cells only. Hexahedral cells have also been created in the mesh of Figure A.4(b), where the Cooper method has been used to sweep (or extrude) the bottom quadrilateral paved face upwards through the volume. Five-sided wedge cells are created in the Cooper mesh of Figure A.4(c), using the underlying triangular face on the bottom surface. Finally, an unstructured tetrahedral mesh has been used to create the mesh shown in Figure A.4(d). Each face of the mesh shown here contains triangular cells, but this need not necessarily be the case. Pyramid cells are created on quadrilateral faces if the adjacent volume is to be filled with tetrahedral cells. Figure A.5 illustrates this process.

(a) Mapped hexahedral mesh.

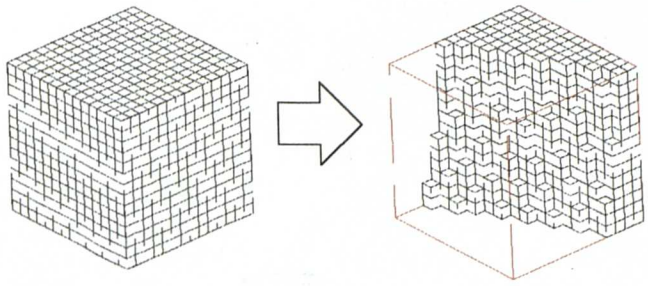

(b) Cooper mesh: Based on paved quadrilateral face.

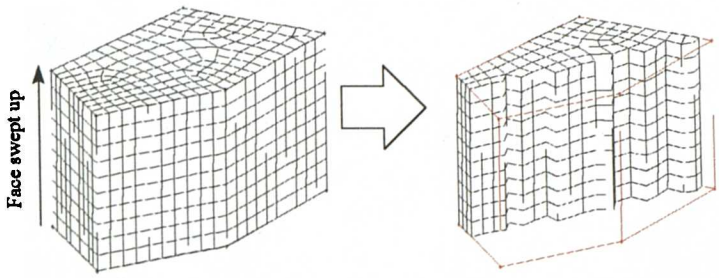

(c) Cooper mesh: Based on triangular face.

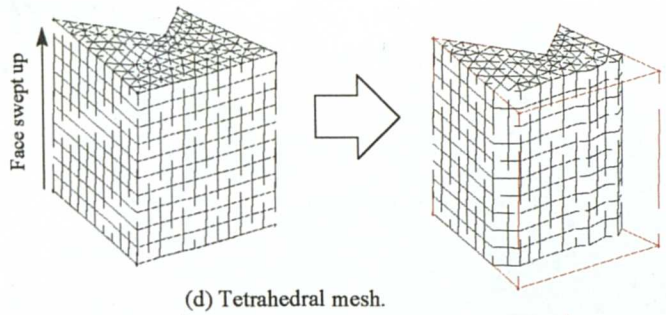

(d) Tetrahedral mesh.

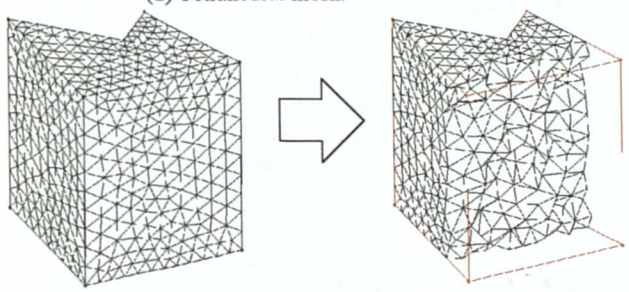

Figure A.4 Examples of volume meshes.

A.3 Boundary Layers

Figure A.5 illustrates another important feature available in Gambit: that of boundary layers. Boundary layers are used in cases where the main volume mesh must be generated using tetrahedral cells, but it is desired to maintain a high quality hexahedral (or prismatic) mesh close to a solid surface. For example, a simulation of air flow over a body could benefit from hexahedral cells close to the surface of the body, but require unstructured tetrahedral cells for the rest of the domain to avoid sudden changes in cell volume (or large aspect ratios).

Figure A.6 gives further illustrations of this technique. Boundary layers can be grown from surfaces having triangular cell types—in a similar way to the method used in Cooper meshing (Figure A.6(b)).

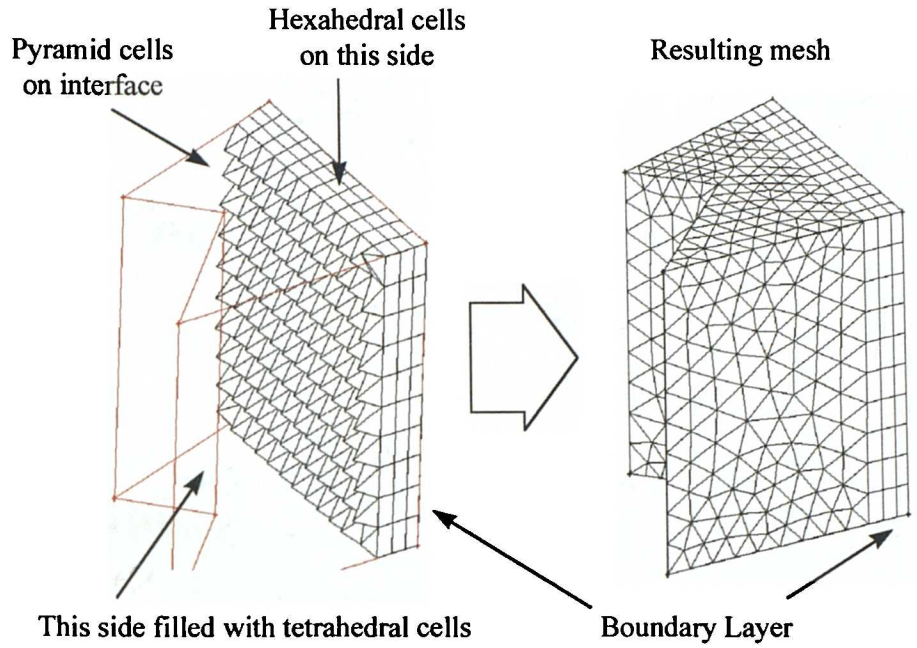

Figure A.5 Pyramid cells on interface for a hybrid mesh.

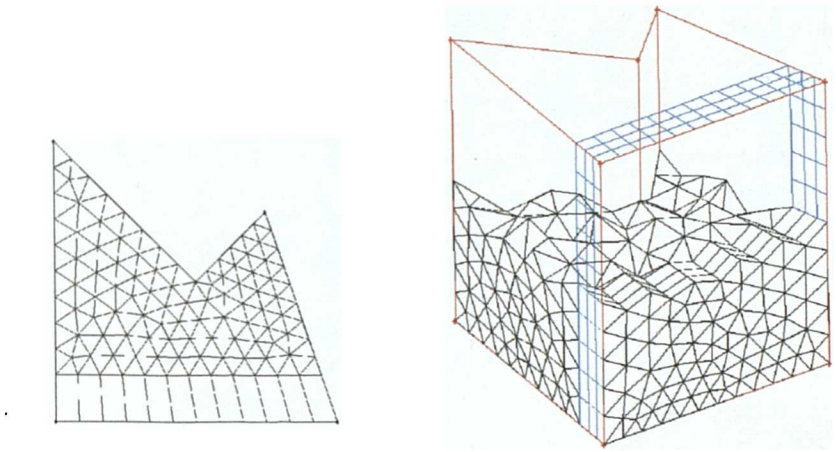

(a) Face mesh with Boundary Layer

(b) Volume mesh: boundary layer from a face containing triangular cells.

Figure A.6 Further illustrations of boundary layers.

Appendix B: Consideration of uncertainty in erosion testing

In order to gain some insight into the uncertainty of results in erosion testing, an analysis has been performed for all cases where 3 or more erosion tests were carried out at the same test conditions. The results of this analysis are shown in Table B.1.

The 'Test Rig' column indicates whether the air-sand (A-S) test rig, or the slurry test rig (L-S) was used in the particular series of tests being considered. The number of points indicates the number of separate tests carried out at the particular angle and velocity being considered. The maximum, minimum, and mean values of E_{MM} (Mass Loss / Erodent Mass, mg/g) for the series of test points are given.

Two approaches have been taken in estimating the uncertainty. Values shown in the column headed '% D/M' are calculated from:-

$$\%D/M = \left[\frac{Max - Min}{Mean}\right] \times 100\% \qquad \text{(B.1)}$$

Values shown in the final column are given by:-

$$\%U = \frac{2}{Mean} \times \frac{s_p(E_{MM})}{\sqrt{n}} \times 100\% \qquad \text{(B.2)}$$

where $s_p(E_{MM})$ is the standard deviation (based on the whole population) of all the recorded erosion rates at the test conditions. n is the number of points recorded. A coverage factor of 2 has been allowed in the above uncertainty estimate.

The average uncertainty given by the final column is 27.4 % of the mean erosion rate. This will be lower than the true uncertainty, as uncertainties in instrumentation and particle impact velocity have not been accounted for. It is clear that these erosion tests are not as accurate as would be desired. Some of the higher uncertainties will be a result of incomplete testing for some of the materials, in that the earlier tests in a series did not achieve a steady state erosion condition. This will have been especially the case in testing tungsten carbide DC(Z)05 (hence the high uncertainty). Another factor will be the time gap between the two periods of testing. These uncertainties must be borne in mind when applying the final erosion equations to a CFD-based erosion modelling simulation.

Table B.1 Estimates of uncertainty.

		Test conditions				Mass Loss / Erodent Mass (mg/g)				
Ref.	Material	Test Rig	Angle (deg)	Velocity (m/s)	No. Points	Max (mg/g)	Min (mg/g)	Mean (mg/g)	% D/M	% U
1	AISI 4130	A-S	90	148	3	9.27E-01	6.46E-01	7.77E-01	36.1	17.1
2	Inconel 718	L-S	90	15.32	6	1.94E-03	1.61E-03	1.82E-03	18.2	4.8
3	Inconel 718	A-S	90	148	5	1.70E+00	1.13E+00	1.51E+00	37.6	12.5
4	17.4PH 105k	L-S	90	16.42	6	1.44E-03	9.22E-04	1.16E-03	44.1	14.4
5	17.4PH 105k	A-S	90	63	3	9.27E-02	8.21E-02	8.89E-02	11.9	6.2
6	17.4PH 105k	A-S	90	148	10	1.27E+00	7.79E-01	1.02E+00	48.4	9.1
7	17.4PH 105k	A-S	90	268	3	2.22E+00	1.79E+00	2.04E+00	21.1	10.2
8	Duplex F51	L-S	90	22.61	3	8.40E-03	4.55E-03	5.84E-03	65.9	35.7
9	Duplex F51	A-S	90	63	4	1.67E-01	6.75E-02	1.32E-01	74.9	29.0
10	Duplex F51	A-S	90	148	5	1.31E+00	8.29E-01	1.03E+00	46.5	13.9
11	Duplex F51	A-S	90	268	3	2.55E+00	1.93E+00	2.30E+00	26.7	13.4
12	Duplex F55	A-S	90	148	4	1.20E+00	9.47E-01	1.13E+00	22.8	9.3
13	T.C. SMS-25A	L-S	90	22.62	4	7.05E-04	5.61E-04	6.38E-04	22.6	9.2
14	T.C. SMS-25A	A-S	30	148	3	1.57E-02	5.67E-03	1.09E-02	92.2	43.6
15	T.C. SMS-25A	A-S	90	148	6	3.06E-02	1.53E-02	2.38E-02	63.9	18.8
16	T.C. SMS-25A	A-S	90	268	4	1.73E-02	9.42E-03	1.23E-02	64.6	25.8
17	T.C. VC-808	L-S	90	16.51	5	7.60E-06	1.41E-06	3.89E-06	159.4	55.8
18	T.C. VC-808	L-S	90	22.62	4	2.77E-05	1.54E-05	2.37E-05	51.9	20.7
19	T.C. VC-808	A-S	90	148	3	8.47E-03	6.94E-03	7.75E-03	19.7	9.3
20	T.C. DC(Z)05	A-S	90	63	9	7.47E-03	-6.13E-03	1.32E-03	1031.7	188.6

Appendix C: Extra Erosion Equations

C.1 Equations for Tungsten Carbide SMS-25A

Three additional equations for Tungsten Carbide SMS-25A are presented here. The first equation used all of the available test data (slurry and air testing) with no additional estimates at low velocity. The resulting equation is:-

$$\ln E_{MM} = a_1 + b_1 V_p^{\frac{5}{2}} + c_1 (\ln V_p)^2 \qquad \text{(C.1)}$$

where the coefficients are given in Table C.1.

The second equation again used all of the slurry data, but did not use the high velocity point of the air-sand data (to improve the shape of the curve before 148 m/s). The equation is:-

$$\ln E_{MM} = a_2 + b_2 V_p^3 + \frac{c_2}{V_p^2} \qquad \text{(C.2)}$$

where the coefficients are given in Table C.1. This equation has been plotted along with the previous equation (and the mean experimental data used in creating them), on Figure C.1.

Table C.1 Coefficients for equations C.1 and C.2.

Coefficients	Values
a_1	-11.54991
b_1	-2.68206E-06
c_1	0.328734
a_2	-7.05503
b_2	9.2901E-07
c_2	-219.3511

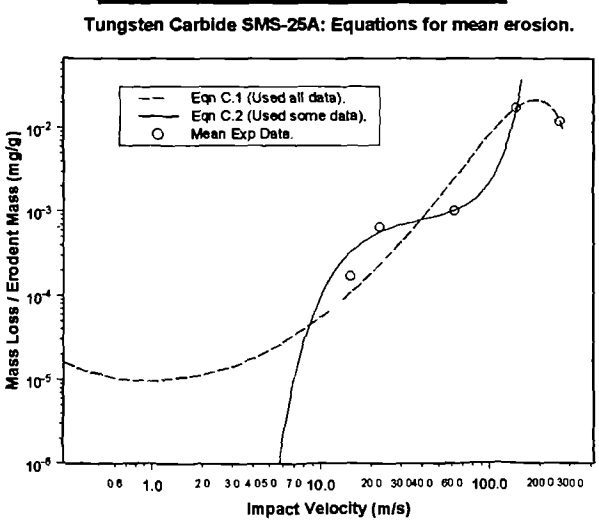

Figure C.1 Graph of equations C.1 and C.2 for Tungsten Carbide SMS-25A.

It will be apparent that equation C.1 does not seem to fit the mean experimental data particularly well, and that equation C.2 produces quite a different curve from equation C.1. The best curve to use would probably be that of equation C.2, as it captures the mid-range trends better than equation 4.11. However, further data would be required to establish the true experimental trend at velocities between 63.0 m/s and 148 m/s, as without this the shape of the curve is somewhat arbitrary.

Two further equations for Tungsten Carbide SMS-25A were also developed, which considered all of the slurry data and only the first point of the air-sand data. The most suitable of these two equations is given as follows:-

$$E_{MM}^{-1} = a_3 + \frac{b_3}{V_p^2} + c_3 \exp^{-V_p} \qquad \text{(C.3)}$$

where the coefficients are given in Table C.2. This equation is only valid for velocities up to 63.0 m/s, and is plotted in Figure C.2. Obviously the equation fits the data well, with the curve passing through the three mean experimental points used. It should be noted that an additional estimated erosion rate was used in creating the equation: the erosion at impact velocity of 0.01 m/s was taken to be 10^{-9} mg/g. This probably accounts for the steep drop in erosion rate as velocity decreases. As in previous cases, the lack of experimental data at low velocities makes it difficult to estimate suitable additional points. Perhaps the work of other researchers could be used to overcome this difficulty.

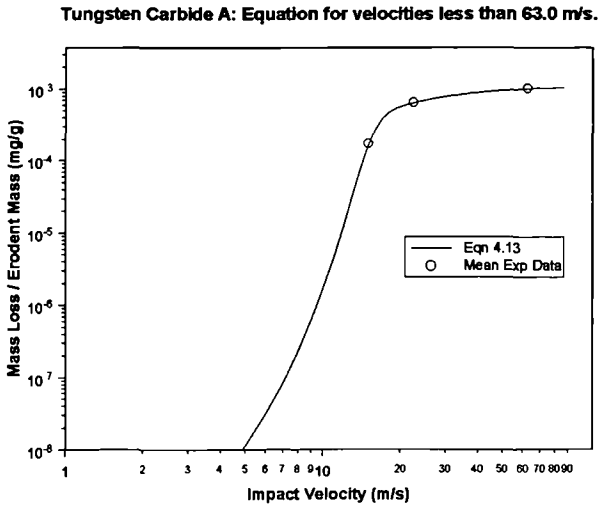

Figure C.2 Plot of equation C.3 for Tungsten Carbide SMS-25A.

Table C.2 Coefficients for equation C.3.

Coefficients	Values
a_3	916.233496
b_3	332469.256
c_3	1.3202E+10

C.2 Mean equation for Duplex F51

The data available at each velocity level was averaged to provide a basic set of data for constructing an equation relating erosion rate to impact velocity only. An additional low velocity estimate was added to the data set to help create the equation:-

$$\ln E_{MM} = a_4 + b_4 V_p^2 + c_4 \ln V_p \qquad \text{(C.4)}$$

where the coefficients are given in Table C.3. The equation has been plotted in Figure C.3 along with predictions of equation 4.9 (mean 3D equation for metallic materials) at an impact angle of 60^0. There is no great difference between the predicted erosion with equation C.4 and that with equation 4.9 at 60^0 impact, indicating the validity of equation 4.9 for this material. The low velocity behaviour of equation C.4 is more desirable than that of 4.9 (at least in appearance).

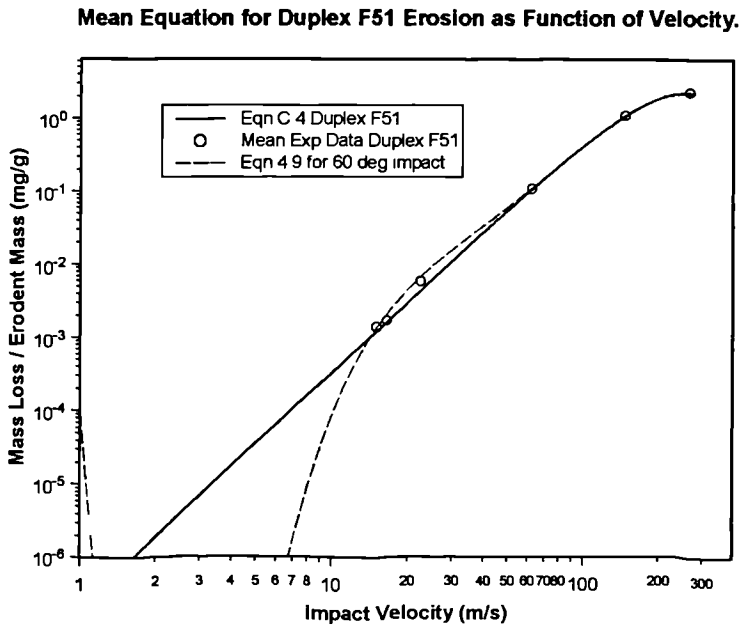

Figure C.3 Plot of equation C.4 for mean erosion of Duplex F51.

Table C.3 Coefficients for equation C.4.

Coefficients	Values
a_4	-15.392869
b_4	-2.3329E-05
c_4	3.19839753

C.3 Equation for AISI 4130, accounting for both angle and velocity

An additional equation has been generated for AISI 4130 that accounts for variation in both impact angle and velocity. Test data at 60^0 and 90^0 impact angle has been ignored at the 22.4 m/s velocity level. Additional estimates of erosion rate were made for impact angles of 0.1^0 where possible, and a low velocity estimate of 10^{-9} mg/g was set at $V_p = 0.1$ m/s (for an impact angle of 30^0; the estimate at 90^0 was taken to be 70% of the 30^0 estimate). Erosion rate at 0.1^0 impact angle is taken to be 0.001 times that at 30^0 impact angle. The following equation results:-

$$\ln E_{MM} = a_5 + b_5 \ln V_p + c_5 \alpha_p + d_5 \alpha_p \ln \alpha_p + e_5 \sqrt{\alpha_p} \qquad \text{(C.5)}$$

where the coefficients are given in Table C.5 below. The equation is plotted as a function of velocity (for an impact angle of 90^0) in Figure C.4. Actual experimental data at 90^0 impact angle are included on the plot, as are plots of equations 4.7 (3D equation for slurry erosion of metallic materials) and 4.9 (3D equation for air-sand erosion of metallic materials) at the relevant angle. It can be seen that equation C.5 predicts slightly lower levels of erosion than equation 4.9 in the region between the highest slurry velocities and the maximum air-sand velocity. Equation 4.7 has a different characteristic from equation C.5 at the lower velocities.

C.4 Equation for 17.4 PH 105k, accounting for both angle and velocity

Data used to create this equation consisted of test data at low and high energy conditions on the slurry rig for a 90^0 impact angle, low and medium velocity data at all angles on the air-sand rig, and additional estimates of erosion at 0.1^0 impact angle for the air-sand velocities. Test data at 268 m/s on the air-sand rig was not used. In all cases, the final erosion rate was used, rather than the average. The resulting equation, that accounts for both particle impact angle and velocity, is:-

$$\ln E_{MM} = a_6 + b_6 \ln V_p + c_6 \sqrt{\alpha_p} \ln \alpha_p + d_6 \ln \alpha_p \qquad \text{(C.6)}$$

where the coefficients are given in Table C.4. At 90^0 impact angle, the above equation follows the previous equation (for AISI 4130) fairly closely (slightly lower magnitude), as can be seen from Figure C.4.

Table C.4 Coefficients for Equation C.6.

Coefficients	Values
a_6	-16.5448955
b_6	2.65723537
c_6	-0.08295079
d_6	1.45726325

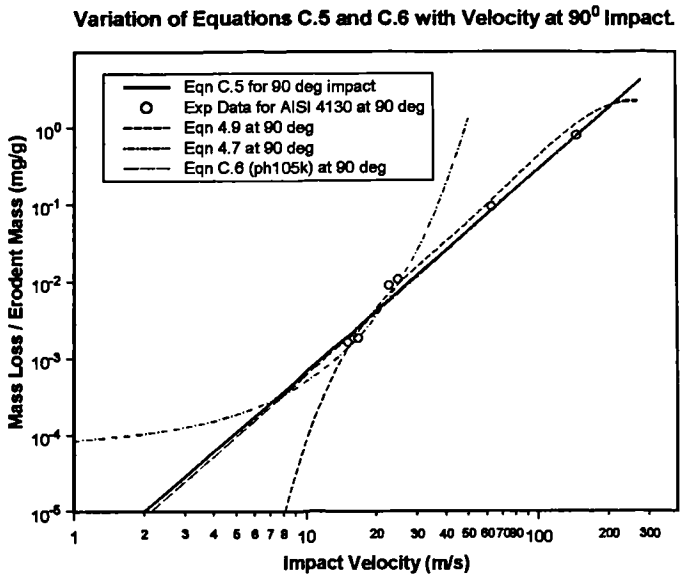

Figure C.4 Equations C.5 and C.6 plotted against velocity at 90^0 impact.

Appendix D

D.1 Dimensional drawings of restrictors

Note that these drawings remain the property of Wood Group Pressure Control Ltd., and should not be reproduced without their permission. All dimensions are in inches unless otherwise indicated.

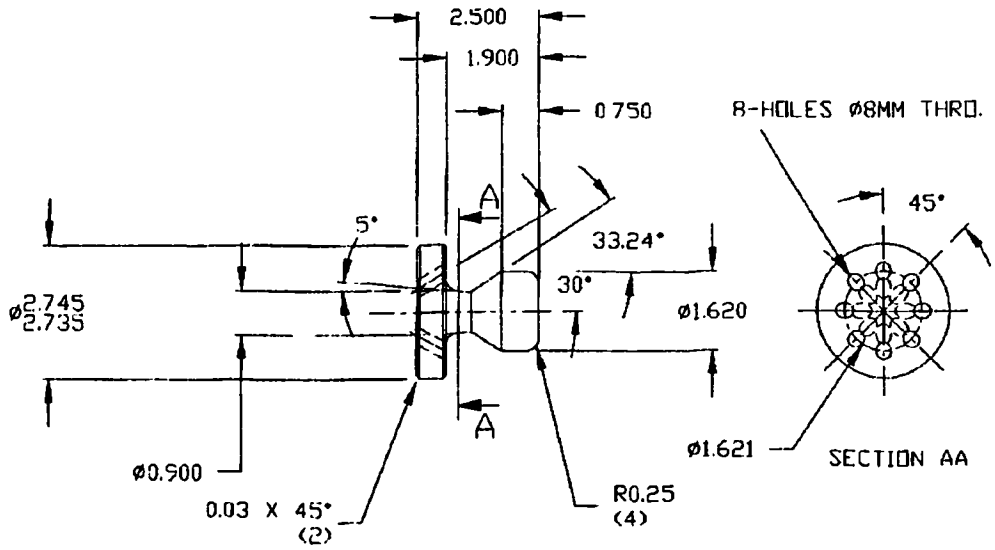

Figure D.1 Upstand restrictor with 8 mm angled holes.

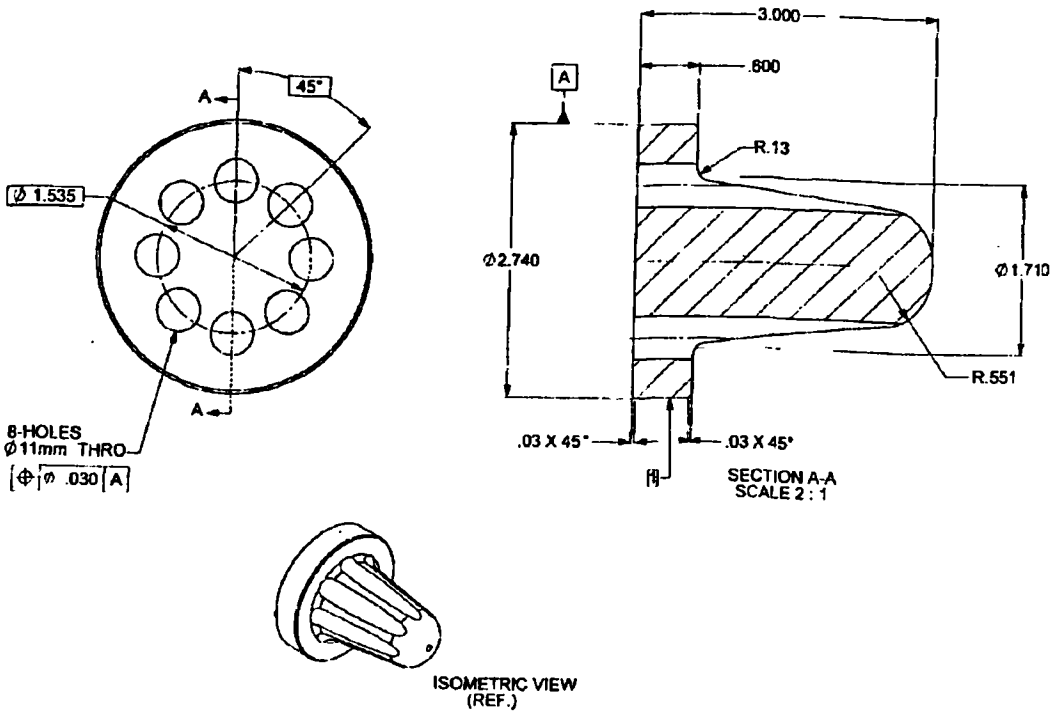

Figure D.2 Fluted restrictor with 11 mm straight holes.

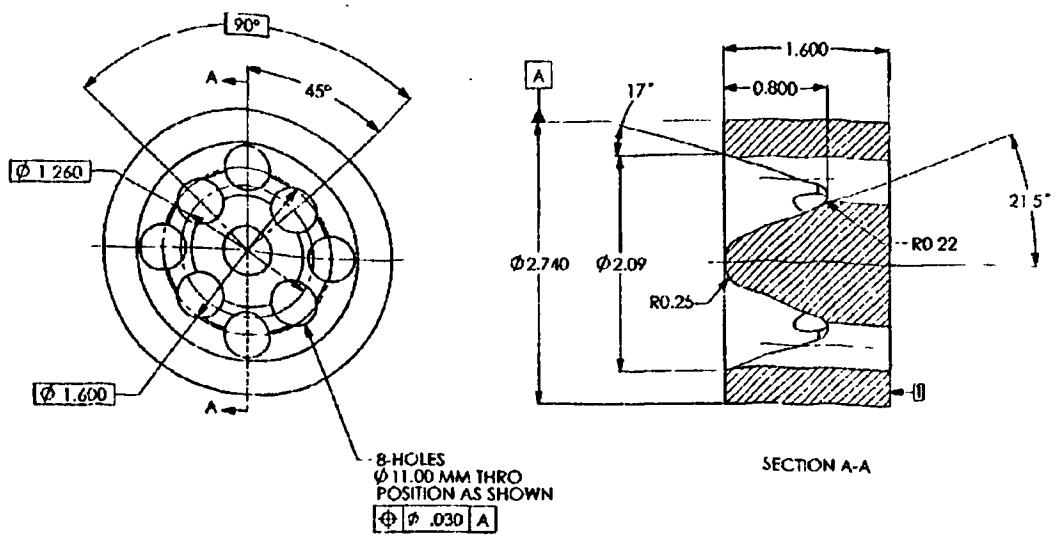

Figure D.3 Valley restrictor with 11 mm straight holes.

D.2 Sand sampling technique

In the NEL abrasive flow facility, sand concentration was found using an iso-kinetic sampling procedure. This is based on the principle that the mixture velocity in the sampling tube should be the same as that in the main pipe. Figure D.4 depicts the sampling arrangement. The required flowrate Q_S in the sampling tube is calculated from

$$Q_S = A_S \cdot V_P \qquad \text{(D.1)}$$

where V_P is the main pipe velocity (given by the EM flowmeter), and A_S is the area of the sample tube (calculated from sample tube diameter, D_S). Knowledge of the sample flowrate can be used to calculate the time it would take for a 10 litre bucket to fill if this flowrate is indeed present in the sample tube. The three valves shown on Figure D.4 are adjusted in a trial-and-error process until the bucket fills in the predicted time. Once this time has been achieved, it is reckoned that fluid is passing through the tube at flowrate Q_S. Sand sampling will therefore be at iso-kinetic conditions.

Sand is separated from the sample mixture by first rapidly stirring the liquid in the bucket so that sand is pulled into the centre of the bucket. The sand is allowed to settle, and excess water is then removed using a siphon tube. Clean water is added to the wet sand remaining at the centre of the bucket base, and the new liquid-sand mixture is stirred rapidly. Another siphon is set up and used to suck the wet sand from the base of the bucket, in order to pass it through filter paper in a funnel. This continues until all sand is deposited in the filter paper. The filter paper containing the sand is dried overnight. Final sand mass can be found by weighing both filter paper and sand—then subtracting the weight of the filter paper.

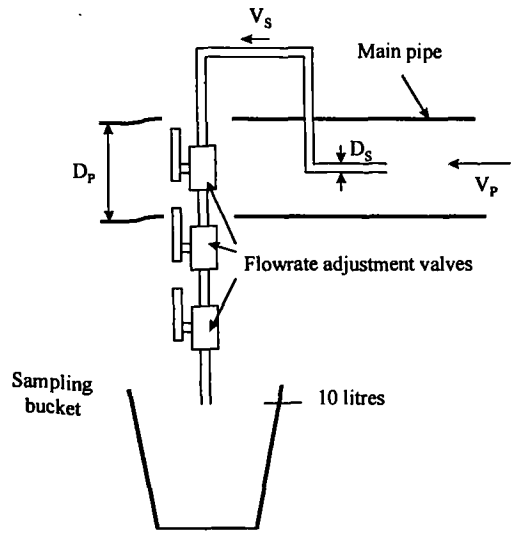

Figure D.4 Schematic of sampling arrangement.

D.3 Uncertainty analysis for flow coefficient

The procedure adopted in estimating measurement uncertainty is based on the ISO Guide to the Expression of Uncertainty in Measurement. C_V is given by

$$C_V = Q\sqrt{\frac{SG}{\Delta P}} \tag{D.2}$$

where Q is the volume flowrate in US gallons/min, ΔP is the differential pressure in psi, and SG is the specific gravity of water at the measured temperature, given by

$$SG = \frac{\rho_w}{\rho_{w@15^0C}} \tag{D.3}$$

where ρ_w is the density at a particular temperature (^{0}C) and the reference density is that at 15^{0}C (999.0103 kg/m^3). The uncertainty of each component in the equation will be treated in turn, before arriving at a statement of combined uncertainty.

D.3.1 Uncertainty in Volume Flowrate

Volume flowrate was measured by a 4 inch electromagnetic flowmeter (Fischer & Porter Model L10D1464, Serial No. 9002L2203AI) calibrated previously using a reference turbine meter (3 inch, No. AOT 27048/k3). The data from this calibration is presented in Table D.1. The turbine meter was calibrated using the NEL weightank (uncertainty = ±0.1% of flow).

Table D.1 Data for check calibration of EM flowmeter.

Point	Frequency	Reference Flow	Magus Reading	Corrected Flow	% Diff C-Ref	% Unc EM flow
	(Hz)	(litres/s)	(litres/s)	(litres/s)		
1	228.6252	15.2935	15.1912	15.2581	-0.231	0.249
2	300.4749	20.0997	20.0606	20.1124	0.063	0.210
3	378.7062	25.3329	25.3172	25.3528	0.079	0.187
4	523.8333	35.0409	35.0838	35.0892	0.138	0.166
5	604.7054	40.4507	40.4580	40.4468	-0.010	0.160
6	630.0031	42.1429	42.1178	42.1014	-0.098	0.159

Mean Turbine Meter k Factor = 14.9492 pulses/litre.

Uncertainty of mean k factor is ±0.14% (i.e. u(k) = 0.02093 pulses/litre.

Range is 10 to 41 litres/s.

The Magus reading is the EM flowmeter signal as displayed on the computerised Data Acquisition Unit. A correction can be applied to the EM meter signal from the plotted data in Figure D.5.

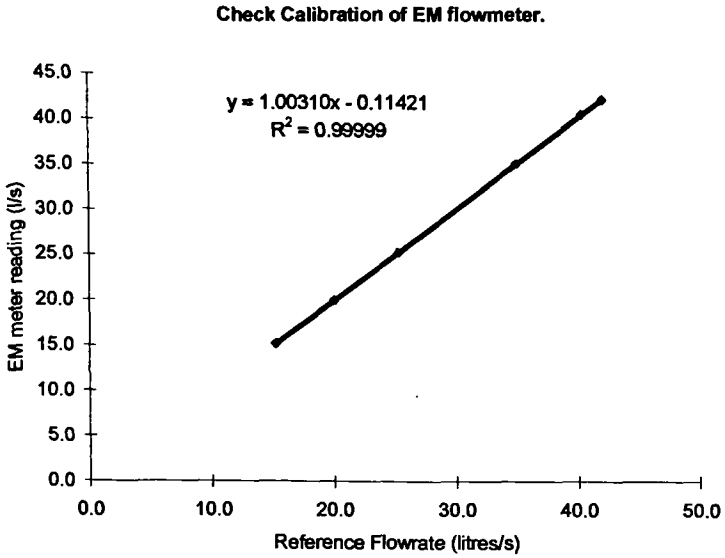

Figure D.5 Check calibration of EM flowmeter.

The correction equation shown in Figure D.5 can be rearranged to give a correction for the EM reading:-

$$\text{Corrected Flow (l/s)} = 0.996908 \cdot \text{EM reading (l/s)} + 0.113859 \qquad \text{(D.4)}$$

The standard deviation for the corrected flow is given as:-

$$s_{cf}^2 = \frac{1}{N}\sum\left(mq_{em} + b - q_{cf}\right)^2 \qquad \text{(D.5)}$$

where m = 0.996908 and b = 0.113859 from equation (D.4), q_{em} is the individual reading from the EM flowmeter, and q_{cf} is the individual reference (or 'corrected') flow value. Applying this equation to the data in Table D.1 gives s_{cf} = 0.031303 litres/s. The overall uncertainty for flowrate will include this value, as well as the uncertainty in reference meter calibration. Thus the uncertainty due to flowrate is:-

$$u(Q) = \sqrt{\left[\frac{dQ}{dk}\right]^2 u^2(k) + u^2(Q_c)} \; ; \qquad \frac{dQ}{dk} = -\frac{Q}{k} \tag{D.6}$$

where $u^2(k)$ = 0.00043802 (pulses/litre)^2, and $u^2(Q_c)$ = 0.0009799 (litres/s)^2. Final values of uncertainty for each flowrate are presented as a percentage of the EM flow in Table D.1.

D.3.2 Uncertainty of pressure measurement

Two Druck pressure transducers (Model PTX 610, serial No.s 594454 and 478188) were used to measure upstream and downstream static pressure. These transducers had been previously calibrated using a Budenberg deadweight tester. The calibration data for the deadweight tester is presented in Table D.2. True pressure measurements have been corrected using

$$P_c = \frac{g_{nel}}{g_n} \cdot P_{true} \tag{D.7}$$

where g_{nel} is 9.8155 m/s^2, and g_n is 9.80665 m/s^2.

Table D.2 Calibration data for Budenberg Deadweight Tester.

Nominal pressure (psi)	True pressure (psi)	Corrected Pressure (psi)	% difference
10	9.9974	10.006	0.0642
200	200.002	200.182	0.0912
400	400.002	400.363	0.0907
600	599.995	600.536	0.0894
800	799.987	800.709	0.0886
1000	999.98	1000.882	0.0882
1200	1199.96	1201.043	0.0869
1400	1399.95	1401.213	0.0867
1600	1599.93	1601.374	0.0859
1800	1799.9	1801.524	0.0847

The uncertainty in nominal pressure (as the pressure transducers are calibrated against this) is taken to be made up of three components: mean % difference, uncertainty in mean % difference, and uncertainty in true pressure. This can be combined by:-

$$u(P_n) = \sqrt{\left(\frac{\Delta P}{100} \cdot P_n\right)^2 + \left(\frac{\Delta P}{100} \cdot P_n\right)^2 \cdot u^2(\Delta P) + u^2(P_T)} \qquad \text{(D.8)}$$

where P_n is the nominal pressure (psi), P_T is the true pressure (psi), and ΔP is the mean percentage difference between the corrected true pressure and nominal pressure. ΔP = 0.086%, and $u(\Delta P) = s_{\Delta P} = 0.007414\%$, from the above table.

True pressure is given by

$$P_T = \frac{F_L}{A_e} = \frac{m_L g}{A_e} \qquad \text{(D.9)}$$

where F_L is the force due to applied load m_L, and A_e is the effective piston area given by:

$$A_e = A_0(1 + ap) \qquad \text{(D.10)}$$

The calibration certificate states that A_0 = 40.319 mm^2 ±0.0022 mm^2, and a = 9.2 x 10^{-6} MPa^{-1} ±0.5 x 10^{-6} MPa^{-1}. Only the uncertainty in A_o will be considered here, as calculations indicate the uncertainty in a is negligible. Uncertainty in applied mass can be taken as a constant 0.000988 % of total mass. Assuming rectangular distributions for uncertainty of m_L and A_0 gives

$$u(m_L) = \frac{0.000988}{100} \cdot \frac{m_L}{\sqrt{3}} = 5.70422 \times 10^{-6} \cdot m_L \text{ g} \qquad \text{(D.11)}$$

and

$$u(A_0) = \frac{0.0022}{\sqrt{3}} = 0.00127 \text{ mm}^2 \qquad \text{(D.12)}$$

Uncertainty of A_e will be taken to be $u(A_0)$, i.e. $u(A_e)$ = 0.00127 mm^2. These uncertainties are combined to give the overall standard uncertainty in true pressure:

$$u(P_T) = \sqrt{\left[\frac{P_T}{m_L}\right]^2 \cdot u^2(m_L) + \left[\frac{P_T}{A_e}\right]^2 \cdot u^2(A_e)} \qquad \text{(D.13)}$$

Application of equation D.13 to the data given in Table D.2 shows the uncertainty in true pressure to be an almost constant value of 0.0032 % for all pressures. Thus the uncertainty in true pressure can be neglected.

Calculation of equation (D.8) shows that the main component of uncertainty is the mean % difference. The overall uncertainty in the Budenberg pressure measurement will therefore be taken as ±0.086% of reading. This figure will be used when considering uncertainty of pressure measurement using the two Druck transducers. Table D.3 presents the calibration data for the two Druck transducers.

Table D.3 Calibration data for pressure transducers.

NOT No. 1188			NOT No. 1180		
Applied Pressure (psig)	Reading (psig)	% difference	Applied Pressure (psig)	Reading (psig)	% difference
10	10.253	2.530	10	10.061	0.610
50	50.253	0.506	50	50.128	0.256
150	150.254	0.169	150	150.169	0.113
200	200.254	0.127	200	199.934	-0.033
362	362.005	0.001	362.5	362.5	0.000
250	250.004	0.002	250	250.001	0.000
200	200.254	0.127	200	199.934	-0.033
150	150.254	0.169	180	180.028	0.016
50	50.253	0.506	50	50.128	0.256

The maximum % difference for NOT No. 1188 is 0.506%, while the maximum for NOT No. 1180 is 0.256%—discounting the difference at 10 psig. These values will be used in the final C_V uncertainty estimate.

Final uncertainty in pressure measurement is taken to be the sum of the component percentage uncertainties: calibration uncertainty plus the two mean differences for the two transducers. This gives

$$u(\Delta P) = (0.086 + 0.506 + 0.256)\% = 0.848\% \qquad \text{(D.14)}$$

D.3.3 Uncertainty due to Density

For the C_V values presented in Table 6.1, no account was made for the variation of density (or specific gravity) with temperature. There will therefore be some uncertainty as a result of this. The maximum temperature recorded in the flow tests of Table 6.1 did not exceed 25 ^{0}C. Water density at this temperature is 997.009 kg/m^3. Therefore, the maximum error in specific gravity will be taken as:-

$$u(SG) = \frac{\rho_{w@15^0C} - \rho_{w@25^0C}}{\rho_{w@15^0C}} = 0.002 \qquad \text{(D.15)}$$

D.3.4 Overall uncertainty in C_V

The final value for uncertainty of C_V will be given by

$$u(C_V)=\sqrt{\left[\frac{\partial C_V}{\partial Q}\right]^2\cdot u^2(Q)+u^2(SG)+\left[\frac{\partial C_V}{\partial \Delta P}\right]^2\cdot u^2(\Delta P)+u^2(C_{V\_R})} \qquad \text{(D.16)}$$

where the partial differentials are replaced as follows:

$$\frac{\partial C_V}{\partial Q}=\frac{C_V}{Q};\quad \frac{\partial C_V}{\partial \Delta P}=\frac{1}{2}\frac{C_V}{\Delta P} \qquad \text{(D.17)}$$

The individual uncertainty components are:

u(Q): Given by equation (D.6).

u(SG): Constant u(SG) = 0.002.

u(ΔP): u(ΔP) = 0.00848 * ΔP bar.

$C_{V\ R}$: Random uncertainty of C_V. This is given by

$$u(C_{V\ R})=s(\overline{C_V})=\frac{s(C_v)}{\sqrt{n}} \qquad \text{(D.18)}$$

where n is the number of samples in the population, and $s(C_V)$ is the standard deviation of the whole population. This random component must come from the original data obtained in each C_V test.

Uncertainties evaluated using equation (D.16) are given for each of the restrictor flow tests in Table D.4. Note that the final uncertainty has been doubled (i.e. giving a coverage factor of 2) and converted into a percentage of the overall C_V (% U).

Table D.4 Restrictor C_V data with uncertainty estimates.

Description	Hole D (mm)	TBS (s)	Log Time (mins)	Flowrate (litres/s)	P1 (bar)	P2 (bar)	dP (bar)	Cv SI	% U SI
Upstand 8mm straight holes	8	30	10	5.72	8.23	7.30	0.93	5.94	1.41
	8	30	10	9.92	14.38	11.37	3.01	5.72	1.09
	8	30	10	13.99	14.04	8.07	5.97	5.73	1.00
Upstand 8mm angled holes	8	30	10	5.62	8.49	7.18	1.31	4.91	1.43
	8	30	10	10.02	14.43	10.49	3.93	5.05	1.09
	8	30	10	13.96	14.08	6.41	7.67	5.04	1.00
Upstand 11mm straight holes	11	30	10	10.01	14.35	13.56	0.79	11.30	1.09
	11	30	10	15.53	13.78	11.82	1.96	11.10	0.98
	11	30	10	25.21	12.28	6.85	5.43	10.82	0.93
Upstand 5mm straight holes	5	2	5	4.91	11.57	5.44	6.13	1.98	1.58
	5	2	3	5.33	13.17	5.88	7.29	1.97	1.49
	5	2	3	5.45	13.41	2.82	10.59	1.67	1.49
	5	2	3	5.63	14.31	2.62	11.69	1.65	1.48
Fluted 11mm straight holes	11	2	3	9.70	14.42	13.82	0.60	12.52	8.18
	11	2	3	16.08	13.91	12.21	1.70	12.33	2.99
	11	2	3	24.30	12.67	8.73	3.95	12.24	1.06
Valley 11mm straight holes	11	2	3	9.88	14.59	13.88	0.71	11.74	2.49
	11	2	3	15.55	14.09	12.44	1.65	12.10	1.23
	11	2	3	20.29	13.43	10.66	2.77	12.20	1.03
	11	2	3	28.09	11.92	6.48	5.44	12.04	0.94

Table D.5 Additional 11mm restrictor data with uncertainty estimates.

Description	Hole D (mm)	TBS (s)	Log Time (mins)	Flowrate (litres/s)	P1 (bar)	P2 (bar)	dP (bar)	Cv SI	% U SI
Upstand 11mm straight holes	11	1	2	19.69	13.34	10.07	3.27	10.89	1.23
	11	2	2	19.69	13.38	10.12	3.26	10.90	1.47
	11	5	5	19.69	13.35	10.13	3.22	10.98	1.49
	11	15	10	19.68	13.33	10.08	3.25	10.92	1.71
	11	30	10	19.67	13.25	10.10	3.15	11.09	2.48
	11	2	3	25.46	12.30	6.78	5.52	10.84	1.37
	11	2	3	10.08	14.41	13.54	0.87	10.79	9.19

Examination of these two tables shows that the majority of results have uncertainties lower than 2 % of C_V. This level of accuracy is likely to be sufficient for most calculations in which C_V is required.

Appendix E: User Defined Functions for Erosion Modelling

The following is the entire C function used in Fluent in order to apply the erosion equations developed in Chapter 4.

```
#include "udf.h"
#include "dpm.h"
#include "sg.h"
#include "surf.h"
#include "prop.h"

double mypi - 3.141592654;
double hours   6.0;
double mean2d_lowvel(double);
double mean2d highvel(double);
d uble mean3d lowvel(double, d uble);
d uble mean3d highvel(d uble, double);
d uble mean3d_lowvel_c mp(d uble, double);
d uble mean3d lvw(double);
double tcA 2d 1(double);
d uble tcA 2d 2(double);
double tcB 2d 1(double);
d uble tcC 2d 1(double);
d uble tcC 3d 1(d uble, d uble ;
d uble dupf51 2d 1 d uble);
d uble dupf51_3d 1(d uble, d uble ;
d uble aisi 3d 1(d uble, d uble);
d uble phl 5k 3d 2 d uble, d uble ;
d uble tcA 2d 3 d uble ;
double tcA 2d 4 d uble ;

/* This is the main UDF f r mean er sion  f metallic materials. The function accounts for
b th particle impact vel city and angle. */

/* Revised  n 2 th September 2  0: version 4. Set lower angles to 2.0 degrees.*/
/*3rd Oct ber. Additi nal UDS f r penetrati n rate. */
/* 3rd Oct ber 20  ; make C UDSI st rage incremental; ie. add values each time. */
/* 3rd October 2   ; additı nal equation for tungsten carbide A: SMS 25A. */

enum
{
        iart,    /* Impact angle running total. */
        iarav,   /* Impact angle running average. */
        ivrt,    /*Impact vel city running total (m/s). */
        ivrav,   /* Impact Vel city running average (m/s). */
        errat,   /* Er si n rate in mg/s. */
        pcnt,    /* C unt of particles impacting specific face. */
        ml ss, /* Mass l ss in mg. */
        prate, /* Penetrati n rate in mm/year */
        N REQUIRED UDS
};

DEFINE DPM EROSION mean 2d 1, p, t, f, normal, alpha, Vmag, mdot
{
        d uble A[ND_ND ;
        d uble fa;
        d uble andeg;
        d uble mlyear;
        d uble penrate    .0;
        d uble matdens   780 .0;
        double et   0. ;
        d uble lowang   2.0, ninety   90.0;
        double lowvel   0.1, midvel = 24.24663, hivel = 268;
        double oneghty   18 . ;
        int newpid - p->part id;
        int oldpid;
        cell_t c0   RP_CELL & p->cCell));
        Thread *t0   RP THREAD(& p->cCell));
        andeg = alpha *  neghty / mypi;
        if ((andeg >- l wang) && (andeg <- ninety )
        {
                if ((Vmag >  lowvel) && (Vmag <  midvel))
                {
                        et - 1000 * mdot * mean2d lowvel(Vmag); /* mdot is in kg/s; convert to g/s */
                }
                else if ((Vmag > midvel) && (Vmag < hivel))
                {
                        et - 1000 * mdot * mean2d_highvel(Vmag); /* et is in mg/s */
                }

                else
                {
                        et - 0.0;
                }
```

```
                mlyear - et * 60.0 * 60.0 * 24.0 * 365;
                F UDSI(f,t,errat)   F UDSI(f,t,errat) + et;
                F_UDSI(f,t,mloss) - F_UDSI(f,t,mloss) + (et * 60.0 * 60.0 * hours); /* mass loss in mg */
                C UDSI(c0,t0,errat)   C UDSI(c0,t0,errat) + et;
                C_UDSI(c0,t0,mloss)   C_UDSI(c0,t0,mloss) + (et * 60.0 * 60.0 * hours);
                F AREA(A, f, t);
                fa - NV MAG(A);
                penrate   1000.0 * (mlyear / (1000.0 * 1000.0 * matdens * fa));
                C UDSI(c0,t0,prate)   C UDSI(c0,t0,prate) + penrate;
                F UDSI(f,t,prate)   F UDSI(f,t,prate) + penrate;
                        /* Following calculates the accretion rate */
                F STORAGE R(f, t, SV DPMS ACCRETION)   F STORAGE R(f, t, SV_DPMS_ACCRETION) +
                        (mdot / fa);
                /* Following stores count of particles impacting a face */
                F_UDSI(f,t,pcnt)   F UDSI(f,t,pcnt) + 1.0;
                C UDSI(c0,t0,pcnt)   C UDSI(c0,t0,pcnt) + 1.0;
                F STORAGE R(f, t, SV DPMS EROSION) = F STORAGE R(f, t, SV DPMS EROSION) + 1.0;
                /* Store of running t tal impact angle; calculation of running average */
                F UDSI(f,t,iart) - F_UDSI(f,t,iart) + andeg;
                F UDSI(f,t,iarav)   F UDSI(f,t,iart) / F UDSI(f,t,pcnt);
                C UDSI(c0,t0,iart)   C UDSI(c0,t0,iart) + andeg;
                C UDSI(c ,t ,iarav)   C UDSI(c0,t0,iart) / C_UDSI(c0,t0,pcnt);
                /* Store of running total impact velocity; calculation of running average */
                F UDSI(f,t,ivrt)   F UDSI(f,t,ivrt) + Vmag;
                F UDSI(f,t,ivrav)   F UDSI(f,t,ivrt) / F_UDSI(f,t,pcnt);
                C UDSI c ,t ,ivrt)   C UDSI(c0,t0,ivrt) + Vmag;
                C UDSI c ,t ,ivrav)   C UDSI(c0,t0,ivrt) / C_UDSI(c0,t0,pcnt);
        }
}

DEFINE DPM EROSION(Mean 3d 1, p, t, f, n rmal, alpha, Vmag, mdot)
{
        d uble A[ND_ND];
        d uble fa;
        d uble andeg;
        double mlyear;
        d uble penrate    . ;
        d uble matden    78  . ;
        double et    . ;
        double lowang   2. , ninety   9 .0;
        d uble l wvel   1. , midvel   22.322, hivel   30 ;
        d uble  neghty   18 . ;
        int newpid   p->part id;
        int oldpid;
        cell t c    RP_CELL & p->cCell  ;
        Thread *t    RP THREAD & p->cCell) ;
        andeg   alpha *  neghty   mypi;
        if ((andeg >  l wang  &&  andeg <  ninety )
        {
                if   Vmag >  l wvel  &&  Vmag <  midvel))
                {
                        et   1  0 * mdot * mean3d_l wvel(Vmag, andeg); /* mdot is in kg/s; convert to g/s */
                }
                else if   Vmag > midvel) &&  Vmag < hivel)
                {
                        et   1    * md t * mean3d highvel(Vmag, andeg);
                }
                else
                {
                        et    . ;
                }
                mlyear   et * 6 .0 * 60.0 * 24.0 * 365;
                F_UDSI f,t,errat    F_UDSI(f,t,errat) + et;
                F UDSI f,t,ml ss  - F_UDSI(f,t,ml ss) + (et * 60.0 * 60.0 * hours); /* mass loss in mg */
                C UDSI c ,t0,errat) - C_UDSI(c ,t ,errat) + et;
                C UDSI(c0,t ,mloss) = C_UDSI(c0,t0,mloss) + (et * 60.0 * 60.0 * hours);
                F_AREA(A, f, t);
                fa - NV MAG A ;
                penrate   1   .0 * (mlyear / (1000.0 * 1000.0 * matdens * fa));
                C UDSI(c ,t0,prate) - C UDSI(c0,t ,prate) + penrate;
                F_UDSI(f,t,prate) = F UDSI(f,t,prate) + penrate;
                        /* F ll wing calculates the accretion rate */
                F_STORAGE R(f, t, SV_DPMS_ACCRETION) - F_STORAGE_R(f, t, SV_DPMS_ACCRETION) +
                        (md t / fa);
                /* Following stores count of particles impacting a face */
                F UDSI(f,t,pcnt)   F UDSI(f,t,pcnt) + 1.0;
                C_UDSI(c0,t0,pcnt)   C_UDSI(c0,t0,pcnt) + 1.0;
                F STORAGE R(f, t, SV DPMS EROSION) - F STORAGE_R(f, t, SV_DPMS_EROSION) + 1.0;
                /* Store of running total impact angle; calculation of running average */
                F UDSI(f,t,iart) - F_UDSI(f,t,iart) + andeg;
                F_UDSI(f,t,iarav) - F_UDSI(f,t,iart) / F_UDSI(f,t,pcnt);
                C UDSI(c0,t0,iart) - C UDSI(c0,t0,iart) + andeg;
                C UDSI(c0,t0,iarav) = C UDSI(c0,t0,iart) / C_UDSI(c0,t0,pcnt);
                /* Store of running total impact velocity; calculation of running average */
                F_UDSI(f,t,ivrt)   F_UDSI(f,t,ivrt) + Vmag;
                F UDSI(f,t,ivrav)   F UDSI(f,t,ivrt) / F UDSI(f,t,pcnt);
                C_UDSI(c0,t0,ivrt)   C_UDSI(c0,t0,ivrt) + Vmag;
                C UDSI(c0,t0,ivrav)   C UDSI(c0,t0,ivrt) / C_UDSI(c0,t0,pcnt);
```

```
        }
}

DEFINE DPM EROSION(Mean 3d 2, p, t, f, normal, alpha, Vmag, mdot)
{
        double A[ND_ND];
        double fa;
        double andeg;
        double mlyear;
        double penrate   0.0;
        double matdens   7800.0;
        double et   0.0;
        double lowang   2.0, ninety   90.0;
        double lowvel   1.0, midvel   24.75596, hivel - 300;
        double oneghty   180.0;
        int newpid   p->part id;
        int oldpid;
        cell t c0   RP CELL &(p->cCell));
        Thread *t0   RP THREAD &(p->cCell));
        andeg   alpha * oneghty / mypi;
        if ((andeg >  lowang) && (andeg <  ninety))
        {
                if ((Vmag >  l wvel) && (Vmag <= midvel))
                {
                        et   10 0 * mdot * mean3d_lowvel_comp(Vmag, andeg);
                                /* md t is in kg/s; convert to g/s */
                }
                else if ((Vmag > midvel) && (Vmag < hivel))
                {
                        et   1    * md t * mean3d highvel(Vmag, andeg);
                }
                else
                {
                        et    . ;
                }
                mlyear   et * 6 .0 * 6 .0 * 24.0 * 365;
                F UDSI f,t,errat    F UDSI(f,t,errat) + et;
                F UDSI(f,t,ml ss)   F UDSI f,t,mloss) + (et * 60.0 * 60.0 * hours); /* mass loss in mg */
                C UDSI(c ,t ,errat    C UDSI(c0,t0,errat) + et;
                C UDSI(c ,t ,ml ss    C UDSI(c0,t0,mloss) + (et * 60.0 * 60.0 * hours);
                F AREA A, f, t ;
                fa   NV MAG A ;
                penrate   1   .0 * (mlyear / (1000.0 * 1000.0 * matdens * fa));
                C UDSI c ,t ,prate    C UDSI(c0,t0,prate) + penrate;
                F UDSI f,t,prate    F_UDSI f,t,prate) + penrate;
                        /* F ll wing calculates the accretion rate */
                F ST RAGE R f, t, SV DPMS_ACCRETION) - F_STORAGE_R(f, t, SV_DPMS_ACCRETION) +
                         md t / fa ;
                /* F ll wing st res c unt of particles impacting a face */
                F UDSI f,t,pcnt    F UDSI(f,t,pcnt) + 1.0;
                C UDSI c ,t0,pcnt  - C_UDSI(c0,t0,pcnt) + 1.0;
                F STORAGE R f, t, SV DPMS EROSION) = F STORAGE_R(f, t, SV_DPMS_EROSION) + 1.0;
                /* St re  f running t tal impact angle; calculation of running average */
                F UDSI f,t,iart    F_UDSI(f,t,iart) + andeg;
                F UDSI f,t,iarav  = F UDSI(f,t,iart) / F UDSI(f,t,pcnt);
                C UDSI c ,t ,iart  - C UDSI(c0,t ,iart) + andeg;
                C UDSI c ,t ,iarav    C UDSI(c0,t0,iart) / C_UDSI(c0,t0,pcnt);
                /* St re  f runnıng t tal impact velocity; calculation of running average */
                F_UDSI f,t,ivrt    F UDSI(f,t,ivrt) + Vmag;
                F_UDSI f,t,ivrav    F UDSI(f,t,ivrt) / F_UDSI(f,t,pcnt);
                C_UDSI(c ,t0,ivrt  - C_UDSI(c0,t0,ivrt) + Vmag;
                C_UDSI(c0,t0,ivrav)   C_UDSI(c0,t0,ivrt) / C UDSI(c0,t0,pcnt);
        }
}

DEFINE DPM EROSION(M tcA 2d_1, p, t, f, normal, alpha, Vmag, mdot)
{
        double A[ND ND];
        double fa;
        double andeg;
        double mlyear;
        double penrate = 0.0;
        double matdens   14930.0;
        double et   0.0;
        double lowang   2.0, ninety   90.0;
        double lowvel   1.0, hivel = 148.0;
        double oneghty   180.0;
        int newpid   p->part_id;
        int oldpid;
        cell t c0   RP CELL(&(p->cCell));
        Thread *t0   RP THREAD(&(p->cCell));
        andeg   alpha * oneghty / mypi;
        if ((andeg >  lowang) && (andeg <  ninety))
        {
                if ((Vmag >  lowvel) && (Vmag < hivel))
                {
                        et   1000 * mdot * tcA_2d_1(Vmag); /* mdot is in kg/s; convert to g/s */
```

```
                }
                else
                {
                        et   0.0;
                }
                mlyear   et * 60.0 * 60.0 * 24.0 * 365;
                F UDSI(f,t,errat)   F UDSI(f,t,errat) + et;
                F UDSI(f,t,mloss)   F UDSI(f,t,mloss) + (et * 60.0 * 60.0 * hours); /* mass loss in mg */
                C UDSI(c0,t0,errat) - C UDSI(c0,t0,errat) + et;
                C UDSI(c0,t0,mloss)   C UDSI(c0,t0,mloss) + (et * 60.0 * 60.0 * hours);
                F AREA(A, f, t);
                fa   NV MAG(A);
                penrate   1000.0 * (mlyear / (1000.0 * 1000.0 * matdens * fa));
                C UDSI(c0,t0,prate)   C UDSI(c0,t0,prate) + penrate;
                F UDSI(f,t,prate)   F UDSI(f,t,prate) + penrate;
                        /* Following calculates the accretion rate */
                F STORAGE R(f, t, SV DPMS ACCRETION) - F_STORAGE_R(f, t, SV_DPMS_ACCRETION) +
                        (mdot / fa);
                /* Foll wing stores count of particles impacting a face */
                F UDSI(f,t,pcnt)   F UDSI(f,t,pcnt) + 1.0;
                C UDSI(c0,t0,pcnt)   C UDSI(c0,t0,pcnt) + 1.0;
                F STORAGE R(f, t, SV DPMS EROSION)   F STORAGE R(f, t, SV DPMS_EROSION) + 1.0;
                /* Store of running total impact angle; calculation of running average */
                F UDSI(f,t,iart    F UDSI(f,t,iart) + andeg;
                F UDSI(f,t,iarav)   F_UDSI(f,t,iart) / F_UDSI(f,t,pcnt);
                C UDSI(c ,t ,iart)   C UDSI c0,t0,iart) + andeg;
                C UDSI(c ,t0,iarav    C UDSI(c0,t0,iart) / C UDSI(c0,t0,pcnt);
                /* Store  f running t tal impact velocity; calculation of running average */
                F UDSI f,t,ivrt    F UDSI f,t,ivrt) + Vmag;
                F UDSI f,t,ivrav    F UDSI(f,t,ivrt) / F UDSI(f,t,pcnt);
                C UDSI c ,t ,ivrt    C UDSI(c0,t0,ivrt) + Vmag;
                C UDSI c ,t0,ivrav    C UDSI(c ,t0,ivrt) / C_UDSI(c0,t0,pcnt);
        }
}

DEFINE DPM EROSION(M tcA 2d 2, p, t, f, normal, alpha, Vmag, mdot)
{
        d uble A[ND ND ;
        d uble fa;
        double andeg;
        d uble mlyear;
        d uble penrate    . ;
        d uble matdens   1493 . ;
        d uble et    . ;
        double lowang   2. , ninety = 9 .0;
        d uble l wvel   1. , hivel   63. ;
        d uble  neghty   18 . ;
        int newpid   p->part id;
        int  ldpid;
        ce l t c    RP CELL & p->cCell  ;
        Thread *t0   RP THREAD & p->cCell );
        andeg   alpha * oneghty / mypi;
        if  (andeg >  l wang  &&  andeg <= ninety)
        {
                if ( Vmag >  l wvel  && (Vmag < hivel))
                {
                        et   1    * md t * tcA_2d_2 Vmag); /* md t is in kg/s; c nvert to g/s */
                }
                else
                {
                        et - 0.0;
                }
                mlyear   et * 60.0 * 60.0 * 24.0 * 365;
                F UDSI(f,t,errat    F UDSI(f,t,errat) + et;
                F UDSI(f,t,ml ss    F UDSI(f,t,mloss) + (et * 60.0 * 60.0 * hours); /* mass loss in mg */
                C UDSI c0,t ,errat    C UDSI(c0,t0,errat) + et;
                C UDSI(c0,t0,mloss) - C_UDSI(c0,t0,mloss) + (et * 60.0 * 60.0 * hours);
                F AREA(A, f, t);
                fa   NV_MAG A ;
                penrate   1   .0 * (mlyear / (1000.0 * 1000.0 * matdens * fa));
                C_UDSI(c0,t ,prate)   C_UDSI(c0,t0,prate) + penrate;
                F UDSI(f,t,prate) - F UDSI(f,t,prate) + penrate;
                        /* Following calculates the accretion rate */
                F STORAGE R f, t, SV DPMS ACCRETION) = F_STORAGE_R(f, t, SV_DPMS ACCRETION) +
                        (mdot / fa);
                /* Following stores c unt of particles impacting a face */
                F_UDSI(f,t,pcnt) - F_UDSI(f,t,pcnt) + 1.0;
                C UDSI(c0,t0,pcnt)   C UDSI(c0,t0,pcnt) + 1.0;
                F STORAGE R(f, t, SV DPMS EROSION) - F STORAGE_R(f, t, SV_DPMS_EROSION) + 1.0;
                /* Store of running total impact angle; calculation of running average */
                F UDSI(f,t,iart)   F_UDSI(f,t,iart) + andeg;
                F UDSI(f,t,iarav)   F UDSI(f,t,iart) / F UDSI(f,t,pcnt);
                C_UDSI(c0,t0,iart)   C_UDSI(c0,t0,iart) + andeg;
                C UDSI(c0,t0,iarav) - C_UDSI(c0,t0,iart) / C_UDSI(c0,t0,pcnt);
                /* Store of running total impact velocity; calculation of running average */
                F UDSI(f,t,ivrt)   F UDSI(f,t,ivrt) + Vmag;
                F_UDSI(f,t,ivrav) - F_UDSI(f,t,ivrt) / F_UDSI(f,t,pcnt);
                C UDSI(c0,t0,ivrt) - C UDSI(c0,t0,ivrt) + Vmag;
```

```
                C_UDSI(c0,t0,ivrav)    C UDSI(c0,t0,ivrt) / C UDSI(c0,t0,pcnt);
        }
}

DEFINE_DPM_EROSION(M_tcB 2d_1, p, t, f, normal, alpha, Vmag, mdot)
{
        double A[ND_ND];
        double fa;
        double andeg;
        double mlyear;
        double penrate   0.0;
        double matdens   14340.0;
        double et - 0.0;
        double lowang   2.0, ninety   90.0;
        double lowvel   1.0, hivel   268;
        double oneghty   180.0;
        int newpid - p->part_id;
        int oldpid;
        cell_t c0   RP CELL(& p->cCell));
        Thread *t0   RP THREAD(&(p->cCell));
        andeg - alpha * oneghty / mypi;
        if ((andeg >  1 wang) && (andeg <- ninety))
        {
                if ((Vmag >  lowvel) && (Vmag < hivel))
                {
                        et   1  0 * md t * tcB 2d 1(Vmag); /* mdot is in kg/s; convert to g/s */
                }
                else
                {
                        et    . ;
                }
                mlyear   et * 60.  * 60.0 * 24.0 * 365;
                F UDSI f,t,errat    F UDSI(f,t,errat) + et;
                F UDSI f,t,ml ss    F UDSI f,t,mloss) + (et * 60.0 * 60.0 * hours); /* mass loss in mg */
                C UDSI c ,t ,errat    C_UDSI(c0,t ,errat) + et;
                C UDSI c ,t ,ml ss    C UDSI(c0,t ,ml ss) + (et * 60.0 * 60.0 * hours);
                F AREA A, f, t ;
                fa   NV MAG A ;
                penrate   1   .  *  mlyear /  1    .  * 1000.0 * matdens * fa));
                C UDSI c0,t ,prate    C UDSI(c0,t0,prate) + penrate;
                F UDSI f,t,prate    F UDSI f,t,prate) + penrate;
                        /* F 11 wing calculates the accretion rate */
                F ST RAGE R f, t, SV DPMS ACCRETION    F_STORAGE_R(f, t, SV_DPMS_ACCRETION) +
                         md t / fa ;
                /* F 11 wing st res c unt of particles impacting a face */
                F UDSI f,t,pcnt    F UDSI(f,t,pcnt) + 1.0;
                C UDSI c ,t ,pcnt    C UDSI(c0,t0,pcnt) + 1.0;
                F STORAGE R f, t, SV DPMS EROSION  = F_STORAGE_R(f, t, SV_DPMS_EROSION) + 1.0;
                /* St re  f running t tal impact angle; calculation of running average */
                F UDSI f,t,iart    F UDSI f,t,iart) + andeg;
                F UDSI f,t,iarav    F_UDSI(f,t,iart) / F_UDSI(f,t,pcnt);
                C UDSI c0,t ,iart  - C UDSI(c0,t0,iart) + andeg;
                C UDSI c0,t0,iarav  - C UDSI c0,t ,iart) / C_UDSI(c0,t0,pcnt);
                /* St re  f runnıng total impact velocity; calculation of running average */
                F UDSI(f,t,ivrt  - F UDSI f,t,ivrt  + Vmag;
                F UDSI f,t,ivrav    F UDSI(f,t,ivrt  / F_UDSI(f,t,pcnt ;
                C_UDSI c ,t ,ivrt)   C UDSI(c0,t0,ivrt) + Vmag;
                C UDSI(c ,t ,ivrav    C UDSI(c ,t ,ivrt) / C UDSI c0,t0,pcnt);
        }
}

DEFINE DPM EROSION(M tcC_2d 1, p, t, f, normal, alpha, Vmag, mdot)
{
        double A[ND ND];
        double fa;
        double andeg;
        double mlyear;
        double penrate   0.0;
        double matdens   15 10.0;
        double et   0.0;
        double lowang   2.0, ninety - 90.0;
        double lowvel - 1.0, hivel = 148.0;
        double oneghty   180.0;
        int newpid = p->part_id;
        int oldpid;
        cell t c0 = RP_CELL(& p->cCell));
        Thread *t0   RP THREAD(&(p->cCell));
        andeg   alpha * oneghty / mypi;
        if ((andeg >  lowang) && (andeg <- ninety))
        {
                if ((Vmag >  lowvel) && (Vmag < hivel))
                {
                        et   1000 * mdot * tcC 2d 1(Vmag); /* mdot is in kg/s; convert to g/s */
                }
                else
                {
                        et - 0.0;
                }
```

```
                mlyear   et * 60.0 * 60.0 * 24.0 * 365;
                F UDSI(f,t,errat)   F UDSI(f,t,errat) + et;
                F_UDSI(f,t,mloss)   F_UDSI(f,t,mloss) + (et * 60.0 * 60.0 * hours); /* mass loss in mg */
                C UDSI(c0,t0,errat)   C UDSI(c0,t0,errat) + et;
                C_UDSI(c0,t0,mloss) = C_UDSI(c0,t0,mloss) + (et * 60.0 * 60.0 * hours);
                F AREA(A, f, t);
                fa   NV MAG(A);
                penrate - 1000.0 * (mlyear / (1000.0 * 1000.0 * matdens * fa));
                C UDSI(c0,t0,prate) = C UDSI(c0,t0,prate) + penrate;
                F UDSI(f,t,prate)   F UDSI(f,t,prate) + penrate;
                        /* Following calculates the accretion rate */
                F STORAGE R(f, t, SV DPMS ACCRETION)   F_STORAGE_R(f, t, SV_DPMS_ACCRETION) +
                        (mdot / fa);
                /* Following stores count of particles impacting a face */
                F_UDSI(f,t,pcnt)   F_UDSI(f,t,pcnt) + 1.0;
                C UDSI(c0,t0,pcnt)   C UDSI(c0,t0,pcnt) + 1.0;
                F_STORAGE R(f, t, SV DPMS_EROSION) - F STORAGE R(f, t, SV_DPMS EROSION) + 1.0;
                /* St re  f running total impact angle; calculation of running average */
                F UDSI(f,t,iart)   F UDSI(f,t,iart) + andeg;
                F UDSI(f,t,iarav)   F UDSI(f,t,iart) / F_UDSI(f,t,pcnt);
                C UDSI(c0,t0,iart)   C_UDSI(c0,t0,iart) + andeg;
                C UDSI(c0,t0,iarav) - C UDSI(c0,t0,iart) / C UDSI(c0,t0,pcnt);
                /* Store of running t tal impact velocity; calculation of running average */
                F UDSI(f,t,ivrt)   F UDSI(f,t,ivrt) + Vmag;
                F UDSI f,t,ivrav)   F UDSI(f,t,ivrt) / F_UDSI(f,t,pcnt);
                C UDSI c0,t0,ivrt)   C UDSI(c0,t0,ivrt) + Vmag;
                C UDSI c ,t0,ivrav    C UDSI(c0,t0,ivrt) / C_UDSI(c0,t0,pcnt);
        }
}

DEFINE DPM EROSION(M tcC 3d 1, p, t, f, normal, alpha, Vmag, mdot)
{
        d uble A ND ND ;
        d uble fa;
        d uble andeg;
        d uble mlyear;
        d uble penrate    . ;
        d uble matdens   15 1 . ;
        d uble et    . ;
        double l wang   1. , ninety   9 . ;
        d uble l wvel   1. , hivel   148. ;
        d uble  neghty   18 . ;
        int newpid   p  part id;
        int oldpid;
        cell t c    RP CELL(& p->cCell );
        Thread *t    RP THREAD & p->cCell );
        andeg   alpha *  neghty / mypi;
        if ((andeg >  l wang  && (andeg <  ninety))
        {
                if ( Vmag >  l wvel  && (Vmag < hivel))
                {
                        et   1 0  * md t * tcC_3d_1(Vmag, andeg); /* mdot is in kg/s; convert to g/s */
                }
                else
                {
                        et - 0.0;
                }
                mlyear   et * 60.  * 6 .0 * 24.0 * 365;
                F UDSI f,t,errat    F UDSI(f,t,errat) + et;
                F UDSI f,t,ml ss    F UDSI(f,t,ml ss) + (et * 60.0 * 60.0 * hours); /* mass loss in mg */
                C UDSI c0,t0,errat  - C UDSI(c0,t0,errat) + et;
                C UDSI c ,t ,mloss)   C_UDSI(c0,t0,mloss) + (et * 60.0 * 60.0 * hours);
                F AREA A, f, t ;
                fa   NV MAG A ;
                penrate   10  .0 * (mlyear / (1000.0 * 1000.0 * matdens * fa));
                C UDSI(c ,t0,prate)   C UDSI(c0,t0,prate) + penrate;
                F_UDSI f,t,prate  = F UDSI(f,t,prate) + penrate;
                        /* Following calculates the accretion rate */
                F_STORAGE R f, t, SV DPMS ACCRETION) - F_STORAGE_R(f, t, SV_DPMS_ACCRETION) +
                        (md t / fa);
                /* Following stores count of particles impacting a face */
                F UDSI(f,t,pcnt)   F UDSI(f,t,pcnt) + 1.0;
                C UDSI(c0,t0,pcnt) - C UDSI(c0,t0,pcnt) + 1.0;
                F STORAGE R f, t, SV DPMS EROSION) - F_STORAGE R(f, t, SV_DPMS_EROSION) + 1.0;
                /* St re of running t tal impact angle; calculation of running average */
                F UDSI(f,t,iart    F UDSI(f,t,iart) + andeg;
                F_UDSI f,t,iarav)   F_UDSI(f,t,iart) / F_UDSI(f,t,pcnt);
                C UDSI(c0,t ,iart)   C UDSI(c0,t0,iart) + andeg;
                C UDSI(c0,t ,iarav) = C UDSI(c0,t0,iart) / C_UDSI(c0,t0,pcnt);
                /* Store of running t tal impact velocity; calculation of running average */
                F_UDSI f,t,ıvrt)   F_UDSI(f,t,ivrt) + Vmag;
                F UDSI f,t,ivrav)   F UDSI(f,t,ivrt) / F UDSI(f,t,pcnt);
                C UDSI(c0,t0,ivrt)   C_UDSI(c0,t0,ivrt) + Vmag;
                C UDSI(c0,t0,ivrav)   C UDSI(c0,t0,ivrt) / C_UDSI(c0,t0,pcnt);
```

```
DEFINE DPM_EROSION(M_dupf51_2d_1, p, t, f, normal, alpha, Vmag, mdot)
{
        double A[ND ND];
        double fa;
        double andeg;
        double mlyear;
        double penrate - 0.0;
        double matdens   7780.0;
        double et   0. ;
        d uble lowang   2.0, ninety = 90.0;
        d uble lowvel - 1.0, hivel - 268.0;
        double oneghty   180.0;
        int newpid   p->part id;
        int oldpid;
        cell t c0   RP CELL(&(p->cCell));
        Thread *t0   RP THREAD(&(p->cCell));
        andeg   alpha *  neghty / mypi;
        if ((andeg >  l wang) &&  andeg <  ninety))
        {
                if ( Vmag >  lowvel) && (Vmag < hivel))
                {
                        et   10   * mdot * dupf51 2d 1(Vmag); /* mdot is in kg/s; convert to g/s */
                }
                else
                {
                        et    .0;
                }
                mlyear   et * 60.0 * 60.0 * 24.0 * 365;
                F UDSI(f,t,errat)   F UDSI(f,t,errat) + et;
                F UDSI f,t,ml ss)   F_UDSI(f,t,mloss) + (et * 60.0 * 60.0 * hours); /* mass loss in mg */
                C UDSI c ,t ,errat) - C_UDSI(c0,t0,errat) + et;
                C UDSI c ,t0,mloss  - C UDSI c0,t0,mloss) + (et * 60.0 * 60.0 * hours);
                F AREA A, f, t ;
                fa   NV MAG A ;
                penrate   1   .0 *  mlyear /  10  .0 * 1000.0 * matdens * fa));
                C UDSI c ,t ,prate  - C UDSI(c0,t0,prate) + penrate;
                F UDSI f,t,prate    F_UDSI(f,t,prate) + penrate;
                        * Foll wing calculates the accretion rate */
                F STORAGE R f, t, SV_DPMS_ACCRETION)   F_STORAGE_R(f, t, SV_DPMS_ACCRETION) +
                        md t / fa ;
                 * F ll wing st res c unt of particles impacting a face */
                F UDSI f,t,pcnt    F UDSI(f,t,pcnt) + 1.0;
                C U SI c ,t ,pcnt    C_UDSI c0,t0,pcnt) + 1.0;
                F ST RAGE R f, t, SV_DPMS_EROSION    F_STORAGE_R(f, t, SV DPMS_EROSION) + 1.0;
                /* St re  f running total impact angle; calculation of running average */
                F UDSI f,t,iart  - F UDSI f,t,iart) + andeg;
                F_UDSI f,t,iarav    F_UDSI f,t,iart) / F_UDSI(f,t,pcnt);
                C UDSI c ,t0,iart    C_UDSI(c0,t0,iart) + andeg;
                C UDSI c ,t0,iarav  - C_UDSI c0,t0,iart) / C_UDSI(c0,t0,pcnt);
                /* St re  f runnıng t tal impact velocity; calculation of running average */
                F UDSI f,t,ivrt)   F_UDSI f,t,ivrt  + Vmag;
                F UDSI f,t,ivrav    F UDSI f,t,ivrt) / F_UDSI(f,t,pcnt);
                C_UDSI c ,t ,ivrt    C_UDSI c0,t0,ivrt) + Vmag;
                C UDSI c ,t ,ivrav    C_UDSI(c0,t0,ivrt) / C_UDSI(c0,t0,pcnt);
        }
}

DEFINE DPM ER SI N M dupf51_3d_1, p, t, f, normal, alpha, Vmag, mdot)
{
        d uble A ND_ND];
        d uble fa;
        d uble andeg;
        double mlyear;
        double penrate - 0. ;
        double matdens   7780.0;
        double et - 0. ;
        double lowang   1. , ninety = 90.0;
        d uble lowvel   1.0, hivel = 148.0;
        double  neghty   180.0;
        int newpid   p->part_id;
        int oldpid;
        cell_t c0 = RP_CELL &(p->cCell));
        Thread *t0 = RP_THREAD(& p->cCell));
        andeg - alpha *  neghty / mypi;
        if ( andeg >  lowang) && (andeg <- ninety))
        {
                if ((Vmag >  lowvel) && (Vmag < hivel))
                {
                        et - 1000 * mdot * dupf51 3d 1(Vmag, andeg); /* mdot is in kg/s; convert to g/s */
                }
                else
                {
                        et   0.0;
                }
                mlyear   et * 60.0 * 60.0 * 24.0 * 365;
                F_UDSI(f,t,errat) - F_UDSI(f,t,errat) + et;
                F UDSI(f,t,mloss) - F_UDSI(f,t,mloss) + (et * 60.0 * 60.0 * hours); /* mass loss in mg */
```

```
                C UDSI(c0,t0,errat)   C UDSI(c0,t0,errat) + et;
                C UDSI(c0,t0,mloss)   C_UDSI(c0,t0,mloss) + (et * 60.0 * 60.0 * hours);
                F_AREA(A, f, t);
                fa   NV MAG(A);
                penrate   1000.0 * (mlyear / (1000.0 * 1000.0 * matdens * fa));
                C UDSI(c0,t0,prate) - C UDSI(c0,t0,prate) + penrate;
                F UDSI(f,t,prate)   F UDSI(f,t,prate) + penrate;
                        /* Following calculates the accretion rate */
                F_STORAGE_R(f, t, SV DPMS_ACCRETION) - F_STORAGE_R(f, t, SV_DPMS_ACCRETION) +
                        (mdot / fa);
                /* Following stores count of particles impacting a face */
                F UDSI(f,t,pcnt)   F UDSI(f,t,pcnt) + 1.0;
                C UDSI(c0,t0,pcnt) - C_UDSI(c0,t0,pcnt) + 1.0;
                F STORAGE R(f, t, SV DPMS_EROSION) - F_STORAGE R(f, t, SV_DPMS_EROSION) + 1.0;
                /* Store of running total impact angle; calculation of running average */
                F UDSI(f,t,iart)   F UDSI(f,t,iart) + andeg;
                F_UDSI(f,t,iarav)   F_UDSI(f,t,iart) / F_UDSI(f,t,pcnt);
                C UDSI(c0,t0,iart)   C UDSI(c0,t0,iart) + andeg;
                C UDSI(c0,t0,iarav) - C UDSI(c0,t0,iart) / C UDSI(c0,t0,pcnt);
                /* Store of running total impact velocity; calculation of running average */
                F UDSI(f,t,ivrt)   F UDSI(f,t,ivrt) + Vmag;
                F UDSI(f,t,ivrav)   F_UDSI(f,t,ivrt) / F_UDSI(f,t,pcnt);
                C UDSI(c ,t0,ivrt) - C_UDSI(c0,t0,ivrt) + Vmag;
                C UDSI(c0,t0,ivrav) - C UDSI(c0,t0,ivrt) / C UDSI(c0,t0,pcnt);
        }
}

DEFINE DPM EROSION(M aisi 3d 1, p, t, f, normal, alpha, Vmag, mdot)
{
        double A[ND ND];
        double fa;
        double andeg;
        d uble mlyear;
        d uble penrate    . ;
        d uble matdens   7 9 . ;
        d uble et    .0;
        d uble l wang   1.0, ninety   90.0;
        d uble l wvel   1. , hivel   148.0;
        d uble  neghty   18 . ;
        int newpid   p->part id;
        int  ldpid;
        cell t c    RP CELL & p- cCell  ;
        Thread *t    RP THREAD & p->cCell) ;
        andeg   alpha *  neghty / mypi;
        if ((andeg >  l wang  &&  andeg <  ninety
        {
                if ( Vmag >  l wvel  &&  Vmag < hivel))
                {
                        et   1  0 * md t * aisi_3d_l(Vmag, andeg); /* mdot is in kg/s; convert to g/s */
                }
                else
                {
                        et    .0;
                }
                m year   et * 6 .0 * 60.0 * 24.0 * 365;
                F UDSI f,t,errat    F UDSI(f,t,errat  + et;
                F UDSI f,t,ml ss  - F_UDSI(f,t,mloss  + (et * 60.0 * 60.0 * hours); /* mass loss in mg */
                C UDSI c ,t ,errat    C UDSI(c0,t0,errat) + et;
                C_UDSI c ,t0,ml ss    C_UDSI(c0,t0,mloss) + (et * 60.0 * 60.0 * hours);
                F AREA A, f, t ;
                fa   NV_MAG A ;
                penrate - 1 00.0 * (mlyear / (1000.0 * 1000.0 * matdens * fa));
                C UDSI c0,t0,prate    C_UDSI(c0,t0,prate) + penrate;
                F UDSI f,t,prate    F_UDSI(f,t,prate) + penrate;
                         * F ll wing calculates the accretion rate */
                F ST RAGE R(f, t, SV DPMS_ACCRETION) = F STORAGE R(f, t, SV_DPMS_ACCRETION) +
                        mdot / fa ;
                /* Following st res count of particles impacting a face */
                F_UDSI f,t,pcnt  - F_UDSI(f,t,pcnt) + 1.0;
                C UDSI c0,t0,pcnt)   C UDSI(c0,t0,pcnt) + 1.0;
                F STORAGE R f, t, SV DPMS_EROSION) = F_STORAGE R(f, t, SV DPMS_EROSION) + 1.0;
                /* Store of running total impact angle; calculation of running average */
                F_UDSI(f,t,iart  - F UDSI f,t,iart) + andeg;
                F UDSI f,t,iarav)   F UDSI(f,t,iart) / F_UDSI(f,t,pcnt);
                C_UDSI(c0,t0,iart)   C_UDSI(c0,t0,iart) + andeg;
                C UDSI(c0,t0,iarav) - C UDSI(c0,t0,iart) / C UDSI(c0,t0,pcnt);
                /* Store of running total impact velocity; calculation of running average */
                F UDSI f,t,ivrt)   F UDSI(f,t,ivrt) + Vmag;
                F_UDSI(f,t,ivrav)   F_UDSI(f,t,ivrt) / F_UDSI(f,t,pcnt);
                C UDSI(c0,t0,ivrt) - C_UDSI(c0,t0,ivrt) + Vmag;
                C UDSI(c0,t0,ivrav)   C UDSI(c0,t0,ivrt) / C_UDSI(c0,t0,pcnt);
        }
}

DEFINE DPM EROSION(M ph105k, p, t, f, normal, alpha, Vmag, mdot)
{
        double A[ND ND];
```

```
        double fa;
        double andeg;
        double mlyear;
        double penrate   0.0;
        double matdens   7730.0;
        double et   0.0;
        double lowang - 1.0, ninety = 90.0;
        double lowvel   1.0, hivel = 268.0;
        double oneghty   180.0;
        int newpid   p->part id;
        int oldpid;
        cell t c0   RP CELL(&(p->cCell));
        Thread *t0   RP_THREAD(&(p->cCell));
        andeg   alpha *  neghty / mypi;
        if ((andeg >  lowang) && (andeg <- ninety))
        {
                if ((Vmag >  lowvel) && (Vmag < hivel))
                {
                        et   10   * mdot * ph105k 3d_2(Vmag, andeg); /* mdot is in kg/s; convert to g/s */
                }
                else
                {
                        et   0.0;
                }
                mlyear   et * 6 .0 * 60.0 * 24.0 * 365;
                F UDSI f,t,errat)   F UDSI(f,t,errat) + et;
                F UDSI f,t,mi ss)   F UDSI(f,t,mloss) + (et * 60.0 * 60.0 * hours); /* mass loss in mg */
                C UDSI c ,t0,errat)   C UDSI(c0,t0,errat) + et;
                C_UDSI(c ,t0,mloss) - C_UDSI(c0,t0,mloss) + (et * 60.0 * 60.0 * hours);
                F AREA A, f, t ;
                fa   NV MAG A ;
                penrate   1   .0 * (mlyear / (1000.0 * 1000.0 * matdens * fa));
                C UDSI c0,t ,prate    C UDSI c0,t0,prate) + penrate;
                F UDSI f,t,prate    F UDSI(f,t,prate) + penrate;
                        /* F ll wing calculates the accretion rate */
                F STORAGE R(f, t, SV DPMS ACCRETION) - F_STORAGE_R(f, t, SV_DPMS ACCRETION) +
                         md t / fa ;
                /* F ll wing st res c unt of particles impacting a face */
                F_UDSI f,t,pcnt    F UDSI(f,t,pcnt) + 1.0;
                C UDSI c ,t ,pcnt    C UDSI(c0,t0,pcnt) + 1.0;
                F ST RAGE R f, t, SV_DPMS ER SION  - F_STORAGE R(f, t, SV_DPMS_EROSION) + 1.0;
                /* St re  f runnıng t tal impact angle; calculation of running average */
                F UDSI f,t,iart    F UDSI(f,t,iart) + andeg;
                F UDSI f,t,iarav    F UDSI(f,t,iart) / F_UDSI(f,t,pcnt);
                C UDSI c0,t ,iart)   C UDSI(c0,t0,iart) + andeg;
                C UDSI c ,t0,iarav  - C UDSI(c0,t0,iart) / C UDSI(c0,t0,pcnt);
                /* St re  f running t tal impact velocity; calculation of running average */
                F UDSI f,t,ivrt    F UDSI f,t,ivrt  + Vmag;
                F UDSI f,t,ivrav    F_UDSI(f,t,ivrt) / F_UDSI f,t,pcnt);
                C UDSI c ,t ,ıvrt    C UDSI(c0,t0,ivrt) + Vmag;
                C UDSI c0,t0,ivrav)   C_UDSI c ,t ,ivrt) / C_UDSI(c0,t0,pcnt);
        }
}

DEFINE DPM EROSION(M tcA 2d 3, p, t, f, normal, alpha, Vmag, mdot
{
        d uble A ND_ND];
        d uble fa;
        d uble andeg;
        d uble mlyear;
        double penrate - 0. ;
        d uble matdens - 1493 . ;
        double et   0.0;
        double lowang - 2.0, ninety   90.0;
        d uble lowvel = 1.0, midvel - 22.58955, hivel = 148.0;
        d uble oneghty   180.0;
        int newpid   p->part_id;
        int oldpid;
        cell_t c0   RP_CELL(& p->cCell));
        Thread *t0 - RP THREAD & p->cCell));
        andeg   alpha * oneghty / mypi;
        if ((andeg >  l wang  && (andeg <= ninety )
        {
                if ((Vmag >  lowvel) && (Vmag <  midvel))
                {
                        et - 1000.0 * mdot * tcA_2d_3(Vmag); /* mdot is in kg/s; convert to g/s */
                }
                else if ((Vmag > midvel) && (Vmag <= hivel))
                {
                        et = 1000.0 * mdot * tcA_2d_4(Vmag);
                }
                else
                {
                        et   0.0;
                }
                mlyear   et * 60.0 * 60.0 * 24.0 * 365;
                F_UDSI(f,t,errat) - F_UDSI(f,t,errat) + et;
                F UDSI(f,t,mloss) - F_UDSI(f,t,mloss) + (et * 60.0 * 60.0 * hours); /* mass loss in mg */
```

```
                C_UDSI(c0,t0,errat) - C_UDSI(c0,t0,errat) + et;
                C_UDSI(c0,t0,mloss)   C_UDSI(c0,t0,mloss) + (et * 60.0 * 60.0 * hours);
                F_AREA(A, f, t);
                fa   NV_MAG(A);
                penrate - 1000.0 * (mlyear / (1000.0 * 1000.0 * matdens * fa)); /* mm/year */
                C_UDSI(c0,t0,prate) - C_UDSI(c0,t0,prate) + penrate;
                F_UDSI(f,t,prate)   F_UDSI(f,t,prate) + penrate;
                        /* Following calculates the accretion rate */
                F_STORAGE_R(f, t, SV_DPMS_ACCRETION) - F_STORAGE_R(f, t, SV_DPMS_ACCRETION) +
                        (mdot / fa);
                /* Following stores count of particles impacting a face */
                F_UDSI(f,t,pcnt)    F_UDSI(f,t,pcnt) + 1.0;
                C_UDSI(c0,t0,pcnt)   C_UDSI(c0,t0,pcnt) + 1.0;
                F_STORAGE_R(f, t, SV_DPMS_EROSION) - F_STORAGE_R(f, t, SV_DPMS_EROSION) + 1.0;
                /* Store of running total impact angle; calculation of running average */
                F_UDSI(f,t,iart)    F_UDSI(f,t,iart) + andeg;
                F_UDSI(f,t,iarav)    F_UDSI(f,t,iart) / F_UDSI(f,t,pcnt);
                C_UDSI(c0,t0,iart)   C_UDSI(c0,t0,iart) + andeg;
                C_UDSI(c0,t0,iarav) - C_UDSI(c0,t0,iart) / C_UDSI(c0,t0,pcnt);
                /* Store of running total impact velocity; calculation of running average */
                F_UDSI(f,t,ivrt)    F_UDSI(f,t,ivrt) + Vmag;
                F_UDSI(f,t,ivrav)    F_UDSI(f,t,ivrt) / F_UDSI(f,t,pcnt);
                C_UDSI(c0,t0,ivrt)   C_UDSI(c0,t0,ivrt) + Vmag;
                C_UDSI(c0,t0,ivrav) - C_UDSI(c0,t0,ivrt) / C_UDSI(c0,t0,pcnt);
        }
}

/*--------------------------------------------------------------*/
d uble mean2d lowvel(d uble x)
/*--------------------------------------------------------------*
Mean equation for slurry data  nly.
2D equation.
Equati n 4.4 in thesis.

   TableCurve Function: C:  Malc lm  Inconel\\ov mean sldata eq2.c Apr 4, 2000 11:41:57 AM
   C:\\Malc lm\\Inc nel  transferl.xls
   X  V (m/s
   Y  MLEM (mg/g
   Eqn# 33  lny a+bx ( .5
   r  0.999785891286629
   r2ad' 0.999 71 825 3  81
   StdErr 6.1157761 4898 3E- 5
   Fstat 4669.524539875134
   a   13.63455579611177
   b  1.819147229884 34
 *--------------------------------------------------------------*/
{
  d uble y;
  d uble x1;
  x1 sqrt x ;
  y -13.634555796111 7+1.819147229884034*x1;
  return(exp(y));
}

/*--------------------------------------------------------------*/
double mean2d highvel(d uble x
 *-------------------------------------------------------------*
Mean equati n f r high energy slurry data and all air-sand data.
2D equation.
Equati n 4.5 in thesis.

   TableCurve Functi n: C:\\Malc lm\\Inconel\\ov_mean_slair_eq2.c Apr 4, 2000 11:53:02 AM
   C:\\Malcolm\\Inc nel\\transferl.xls
   X  V (m/s)
   Y  MLEM (mg/g)
   Eqn# 1628  y^(-1) a+blnx/x 2+c/x^2
   r2 0.9999997068008751
   r2adj 0.9999991204 26254
   StdErr 0.0009916930944745616
   Fstat 1705325.190355547
   a  0.6238585727611144
   b  -31627.07541769815
   c  163632.6923590128
 *-------------------------------------------------------------- /
{
  double y;
  double x1,x2;
  x1 log(x)/(x*x);
  x2 1.0/(x*x);
  y 0.6238585727611144-31627.07541769815*x1
    +163632.6923590128*x2;
  return(1.0/y);
}

        /*--------------------------------------------------------------*/
        double mean3d_lowvel(double x, double y)
        /*--------------------------------------------------------------*
```

```
      Equation 4.7 in thesis.
      TableCurve 3D
      File Source  c:\malcolm\transfer.xls
      Date  Mar 31, 2000
      Time- 12:00:05 PM
      Data Set  C:\Malcolm\transfer.xls
      X  v (m/s)
      Y  Angle (deg)
      Z  MLEM (mg/g)
      Eqn#  151233887
         Eqn  lnz a+bx+clny+d/y
         r2 0.9811684962111972
         r2adj 0.9727989389717293
         StdErr 0.0004127131137572369
         Fstat 173.6750124003371
         a  -4.992940638903024
         b  0.1970341418018689
         c   0.9291219112122218
         d  -36.20324 8158502
       *-------- ----------------------------------------------------*/
      {
        double z;
        double f1,f2,f3;
        f1 x;
        f2 log(y);
        f3 1.0/y;
        z -4.9929406389 3 24+0.1970341418018689*f1
              -0.9291219112122218*f2-36.20324081585020*f3;
        return exp(z);
      }

      /*--- --- ----------------------------------------------------*/
      d uble mean3d highvel d uble x, double y)
      /* ----        -  ------------------------------------------*
         Equati n 4.9 in thesis.
         TableCurve 3D
         File S urce  c: malc lm transfer.xls
         Date  Apr 14, 2
         Time  11:1 :53 AM
         Data Set  C: Malcolm transfer.xls
         X  V (m/s)
         Y  Angle  deg
         Z  Er si n  mg/g
         Eqn#  296259 63
         Eqn  lnz a+b lnx)^2+clnx+d/x^(0.5)+elnx/x+f/x+gy^(0.5)lny+hy/lny+ilny
         r2  .9998598 9 498 34
         r2adj 0.9998178436748354
         StdErr 0.0 754289 273816813
         Fstat 2765 .94289 33 39
         a  -845.6141 5 1 163
         b  -13.24336 14889272
         c  201. 87 03 384821
         d  2278.4 34  538543
         e  -638.26876722 8533
         f  -1457.711478293632
         g  -1.434 7645752 656
         h  2.48651 757 42481
         i  6.03704911 819493
       *-------------------------------------------------------------*/
      {
        d uble z;
        double f1,f2,f3,f4,f5,f6,f7,f8;
        f1 log(x *log x ;
        f2 log(x);
        f3 1.0/sqrt x);
        f4 log(x)/x;
        f5 1.0/x;
        f6 sqrt(y)*l g(y);
        f7 y/log(y);
        f8 log(y);
        z--845.6141050151630-13.24336014889272*f1
              +201.0870030384821*f2+2278.403400538543*f3
              -638.2687672208533*f4-1457.711478293632*f5
              -1.434076457520656*f6+2.486510757042481*f7
              +6.037049110819493*f8;
        return exp(z);
      }

/*-------------------------------------------------------------*/
double tcA 2d 1(double x)
/*-------------------------------------------------------------*

  Equation C.1 in thesis.
  Tungsten Carbide SMS-25A.

   TableCurve Function: C:\\Malcolm\\duplex\\tcc6f 2dmnad_1.c Apr 11, 2000 3:56:09 PM
   C:\\Malcolm\\duplex\\transfer.xls
   X- Vel (m/s)
```

```
   Y  Av. MLEM (mg/g)
   Eqn# 1304  lny a+bx^(2.5)+c(lnx)^2
   r2-0.9904010114123589
   r2adj 0.9616040456494357
   StdErr 0.001099430739164515
   Fstat 103.1776423494787
   a  -11.5499066166913
   b  -2.682056802679185E-06
   c- 0.3287339620359856
 *-------------------------------------------------------------*/
{
  double y;
  double x1,x2;
  x1 x*x*sqrt(x);
  x2 log(x)*log(x);
  y -11.54990661669130-2.682056802679185E-06*x1
    +0.3287339620359856*x2;
  return(exp(y));
}

/*---- ---------------------- ---------------------------------*/
double tcA 2d 2(double x)
/*-------------------------------------------------------------*

  Equation C.3 in thesis.
  Tungsten Carbide SMS-25A.

   TableCurve Function: C: \Malcolm\\duplex\\tcc6f_2dmnssd_2.c Apr 11, 2000 4:13:59 PM
   C:\\Malcolm\\duplex\\transfer.xls
   X  Vel (m/s)
   Y  Av. MLEM (mg/g
   Eqn# 1630  y (-1  a+b/x^2+ce^(-x
   r2  .999999999998575
   r2adj 0.9999999999957265
   StdErr 9.39008325 13139 E-1
   Fstat 35099933^26 .5141
   a  916.2334955570653
   b  33 469.2563233395
   c  13201780749.61625
 *-------------------------------------------------------------*/
{
  d uble y;
  d uble x1,x2;
  x1 1. /(x*x);
  x2 exp(-x);
  y 916.233495557 653+332469.2563233395*x1
    +1320178 749.61625*x2;
  return(1.0/y);
}

/*-  ----------------------------------------------------------*/
d uble tcB 2d 1(double x)
/*-------------------------------------------------------------*

  Equati n 4.12 in thesis.
  Tungsten Carbide VC-8 8

   TableCurve Functi n: C:\\Malcolm\\duplex\\tcyc8_2dmnsd_1.c Apr 11, 2000 4:29:42 PM
   C:\\Malc lm\\duplex\\transfer.xls
   X  Vel (m/s)
   Y  Av. MLEM (mg/g)
   Eqn# 8074  [Sigmoid_] y-a/(1+exp(-(x-b)/c))
   r2 0.9999999248674422
   r2adj 0.9999997746023267
   StdErr 2.513986088850049E-06
   Fstat 6654904.041508356
   a  0.01028103061295968
   b  128.6473045204041
   c  17.29360230675784
   Constraint: c<>0
 *-------------------------------------------------------------*/
{
  double y;
  y 0.01028103061295968/(1.0+exp(-(x-
    128.6473045204041)/17.29360230675784));
  return(y);
}


/*-------------------------------------------------------------*/
double tcC 2d 1(double x)
/*-------------------------------------------------------------*

  Equation 4.13 in thesis.
  Tungsten Carbide DC(Z)05.

   TableCurve Function: C:\\Malcolm\\duplex\\tcalmet_2dmnad_1.c Apr 11, 2000 4:19:28 PM
   C:\\Malcolm\\duplex\\transfer.xls
```

```
   X  Vel (m/s)
   Y- Av. MLEM (mg/g)
   Eqn# 1259  lny a+bx^(1.5)+clnx
   r2 0.999999993887404
   r2adj 0.9999999816622119
   StdErr 7.883728128541115E-07
   Fstat 81798305.52904612
   a  -19.43724233303847
   b  -0.0006098485445141236
   c  3.164436665687039
 *-------------------------------------------------------------*/
{
  double y;
  double x1,x2;
  x1 x*sqrt(x);
  x2 log(x);
  y -19.437242333 3847- .00 6098485445141236*x1
    +3.164436665687 39*x2;
  return(exp(y );
}

/*- ------------ ---------------- ------------------------------*/
d uble tcC 3d 1 d uble x, d uble y)
/*-------------------------------------------------------------*

  Equati n 4.14 in thesis.
  Tungsten Carbide DC Z  5.

   TableCurve 3D
   File Source  c:\malc lm transfer.xls
   Date  May 1 , 2
   Time  9:56:32 AM
   Data Set  C: Malcolm\transfer.xls
   X  Velocity  m s
   Y  Angle  deg
   Z  MLEM  mg/g
   Eqn#  15123868
   Eqn  lnz a+bx   .5 lnx+cx   .5 +dlny
   r   .9998164836365 3
   r2adj  .99971161714315
   StdErr 5.620312968367776E-05
   Fstat 14  8.28 9642 684
   a  -23.3464542533825
   b  -0.5 2 6238 411239
   c  3.83 383986388 62
   d  0.63 9297539823 95
 *--------    ----------------------------------------------*/
{
  d uble z;
  d uble f1,f2,f3;
  f1 sqrt x *l g x ;
  f  sqrt x ;
  f3 l g y ;
  z -23.34645425338250-0.5025623854112395*f1
    +3.83 383986388 62*f2+0.63 9297539823795*f3;
  return exp(z ;
}

/* ------- - ----------------------------------------------------*/
d uble dupf51 2d 1 d uble x
/*-------------------------------------------------------------*

  Equation C.4 in thesis.
  Duplex F51 across all vel cities.

   TableCurve Function: C:\\Malcolm\\duplexf51_mnad_2.c Apr 5, 2000 11:36:25 AM
   C:\\Malc lm\\transfer8.xls
   X  Vel city (m/s)
   Y  Avg. MLEM (mg/g)
   Eqn# 1276  lny a+bx^2+clnx
   r2 0.999999513979 711
   r2adj 0.999999 279581422
   StdErr 0.0 07451079996225974
   Fstat 4115 47.128722872
   a- -15.39286941108583
   b  -2.332924653237152E-05
   c- 3.198397531042844
 *-------------------------------------------------------------*/
{
  double y;
  double x1,x2;
  x1 x*x;
  x2 l g(x);
  y -15.39286941108583-2.332924653237152E-05*x1
    +3.198397531042844*x2;
  return(exp(y));
}
```

```
/*----------------------------------------------------------------*/
double dupf51 3d 1(double x, double y)
/*----------------------------------------------------------------*

  Equation 4.15 in thesis
  Duplex F51, 3D equation.

   TableCurve 3D
   File Source  c:\malcolm\transfer.xls
   Date  May 17, 2000
   Time  10:25:55 AM
   Data Set- C:\Malcolm\transfer.xls
   X  Velocity
   Y  Angle
   Z  Avg. MLEM
   Eqn#  151334900
   Eqn  lnz a+blnx+cylny+dy^(0.5)lny+ey^(0.5)
   r2 0.9999993110230097
   r2adj 0.9999989665345146
   StdErr 0.000419136446883669
   Fstat 3991422.274028258
   a  -23.78876133835871
   b  2.891249919427044
   c  0.02450592327622955
   d  -1.217081173354619
   e  5.417749421775348
 *----------------------------------------------------------------*/
{
  d uble z;
  d uble f1,f2,f3,f4;
  f1 log(x);
  f2 y*log(y);
  f3 sqrt(y)*l g(y ;
  f4 sqrt(y);
  z  23.78876133835871+2.891249919427044*f1
    +0.024505923 7622955*f2-1.217081173354619*f3
    +5.417749421 75348*f4;
  return exp(z);
}


/*- -  --   ---- ------------------------------------------------*/
d uble aisi 3d 1(d uble x, d uble y
/*--- ----------------------------------------------------------*

  Equation C.5 in thesis.
  AISI 413  3D equati n  sec nd  ne).

   TableCurve 3D
   File S urce- c:\malc lm transfer.xls
   Date  May 17, 2
   Time  10:36:02 AM
   Data Set  C:\Malcolm\transfer.xls
   X  Velocity
   Y  Angle
   Z  Avg. MLEM
   Eqn#  151334318
   Eqn  lnz a+blnx+cy+dylny+ey^ 0.5)
   r2 0.9999498456037136
   r2adj 0.999927 481508562
   StdErr 0.003146145222429 64
   Fstat 59812.2948122422
   a  -21.17241125052738
   b  2.619645442911337
   c  -1.171072970984215
   d  0.1666624171082744
   e  4.8 0561025107296
 *----------------------------------------------------------------*/
{
  double z;
  double f1,f2,f3,f4;
  f1 log(x);
  f2 y;
  f3 y*log(y);
  f4 sqrt(y);
  z -21.17241125052738+2.619645442911337*f1
    -1.171072970984215*f2+0.1666624171082744*f3
    +4.820561025107296*f4;
  return exp(z);
}


double mean3d_lowvel_comp(double v, double angle)
{
        /* Equation 4.8 in thesis */
        double erosion;
        double cfa, n;
        cfa   3.4771E-08;
```

```
        n   3.9059;
        erosion   cfa * (pow(v, n) * mean3d_lvw(angle));

        return erosion;
}


/*----------------------------------------------------------------*/
double mean3d lvw(double x)
/*--  -   ----------   ---------------------------------------*
   TableCurve Function: C:\\Malcolm\\angles\\angle eq1.c Sep 13, 2000 4:48:19 PM
   C:\\Malcolm\\transfer1.xls
   X  Angle
   Y  Erosion
   Eqn# 8036  [Pulse ] y 4an(1-n) n exp(-(x-b)/c)
   r2 0.9976668398857628
   r2adj 0.99300 51965 2883
   StdErr 0.0281137876272147
   Fstat 213.8016233429232
   a  0.9999051635732754
   b  0.01088680367213678
   c  39.65707988611664
   Constraints: x> b,c
 *----------------------------------------------------------------*/
{
  d uble y;
  double n;
  n exp(-(x- . 1 8868 367213678)/39.65707988611664);
  y 4.0*0.9999 516357327 4*n* 1.0-n);
  return(y);
}

/*----  ---  --  ----------------------------------------------*/
d uble ph1 5k 3d 2 d uble x, d uble y)
/*------------ --  ---------------------------------------*
   Equati n C.6 in the ıs.
   TableCurve 3D
   File S urce  c: malc lm transfer.xls
   Date  May 17, 2
   Time  10:58:46 AM
   Data Set  C: Malc lm transfer.xls
   X  Vel city
   Y  Angle
   Z  Avg. MLEM
   Eqn#  151240851
   Eqn  lnz a+blnx+cy^ 0.5 lny+dlny
   r2 0.9999548 8911 66
   r2adj 0.999918656 399197
   StdErr  . 03899 5 2 9 91362
   Fstat 44254.5126  94691
   a  -16.54489554487179
   b  2.657235373524691
   c  -0.08295079168679964
   d  1.457263253776583
 *----------------------------------------------------------------*(
{
  d uble z;
  d uble f1,f2,f3;
  f1 l g x);
  f2 sqrt(y)*l g y ;
  f3 log(y ;
  z--16.54489554487179+2.657235373524691*f1
    -0.08295079168679964*f2+1.457263253776583*f3;
  return exp(z);
}

/*----------------------------------------------------------------*/
d uble tcA 2d 3(double x)
/*----------------------------------------------------------------*
   Equation 4.10 in thesis.
   TableCurve Function: C:\\Malcolm\\FurtherEquations\\tcA_2d_3.c Sep 8, 2000 3:57:14 PM
   C:\\Malcolm\\transfer.xls
   X  Vel (m/s)
   Y  MLEM (mg/g)
   Eqn# 33  lny a+bx^(0.5)
   r2 0.9999991284732841
   r2adj 0.9999982569465682
   StdErr 4.360402252794302E-07
   Fstat=1147410.756550723
   a  -14.64553133803784
   b  1.532546207763015
 *----------------------------------------------------------------*/
{
  double y;
  double x1;
  x1 sqrt(x);
  y=-14.64553133803784+1.532546207763015*x1;
  return(exp(y));
```

```
}

/*----------------------------------------------------------------*/
double tcA_2d_4(double x)
/*----------------------------------------------------------------*
   Equation 4.11 in thesis.
   TableCurve Function: C:\\Malcolm\\FurtherEquations\\tcA_2d_4.c Sep 8, 2000 4:01:36 PM
   C:\\Malcolm\\transfer.xls
   X  Vel (m/s)
   Y  MLEM (mg/g)
   Eqn# 26  lny=a+bx^2lnx
   r2 0.9999999546185705
   r2adj 0.9999999092371409
   StdErr 2.878251628934133E-06
   Fstat 22035444.124102 6
   a  -7.410363370034293
   b  3.06687915759 651E-05
 *----------------------------------------------------------------*/
{
  double y;
  double x1;
  x1 x*x*log(x);
  y -7.410363370034293+3.066879157590651E-05*x1;
  return(exp(y));
}
```